Foundations of Vision (1995)

Brian Wandell

1995-10-26

Contents

How to study vision

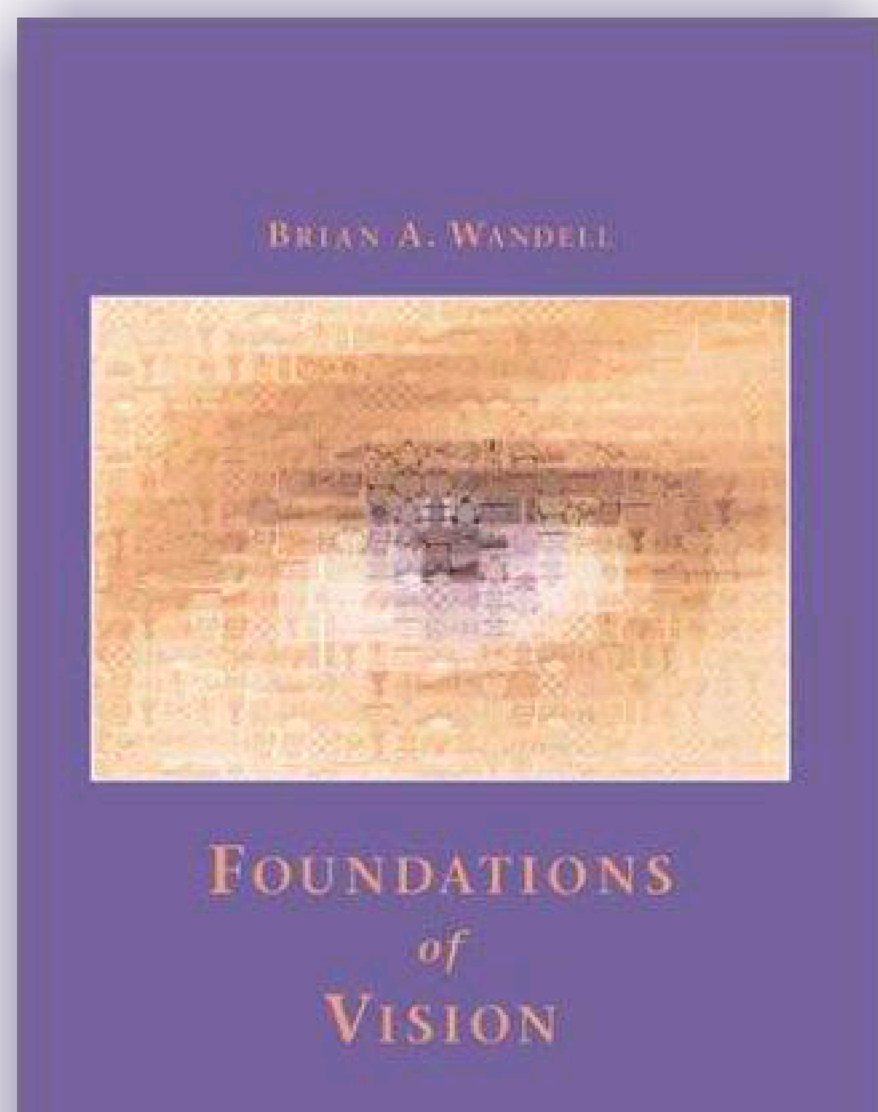

How to study vision

While working to bring this book together, I was inspired and overwhelmed by the breadth and vibrancy of vision science. Vision scientists solve problems across the fields of biology, psychology, and engineering. Our field takes on problems ranging from the nature of consciousness to the hurry-up-and-ship-it applications needed to keep a company afloat. In selecting from the huge amount of material available, I decided to write this book for the student who wishes to know *how* to study vision. The pages are filled with measurements and facts; but, my goal in writing this book is to explain to the student how we learned these facts, not the facts themselves. To organize the material presented, I have divided the book into three sections. My division reflects three of the basic problems of vision: encoding, representation, and interpretation.

Encoding

Part One describes how the retinal image is encoded by the visual pathways. The material in this section is particularly important for three reasons. First, how the visual system encodes light has implications for everything else the visual pathways do. Distortions that are introduced into the signal by poor optics, sparse and uneven spatial sampling of the image, or meager wavelength encoding become part of the signal that must be represented and interpreted by the central visual pathways. We can't understand the central nervous system without understanding the quality of information encoded within the eye.

Second, the properties of the visual encoding have implications for the design of instruments that display visual information. The quality of the representation of pattern and color in display media must be structured to satisfy, but not exceed, the limits of the human visual system. For example, the industry of color imaging, including visual displays, film, and color printing, relies on the fact that human color vision uses three types of cone photopigments to encode light. As a result of this sparse representation of wavelength, color reproductions need not represent the wavelength composition of the original in order to provide a satisfactory appearance match. This is but one example of many in which the initial encoding of the image in the human eye defines practical limits whose properties determine the character of imaging devices.

Third, the methods and standards of proof that are used to understand image encoding set an important example concerning the standards of explanation we aim to achieve at all levels of vision science. The questions of methods and standards of proof are very important an an interdisciplinary field like vision science, which draws on expertise from many different areas. The first section of this book contains several examples that combine physical calculations, biological experiments, and behavioral studies. By examining how these fields come together when we measure the quality of the retinal image formed by the optics of the eye, and again when we establish that human color vision is trichromatic, we see how these diverse fields can forge strong links that define important aspects of visual function. We can learn from these examples as we move on to other problems in vision science.

Representation

Part Two of this volume reviews how the encoded image is represented by the neural response within the peripheral visual pathways. Our understanding of the neural representation is based on work in several different disciplines. This section begins with a review of the anatomical and electrophysiological measurements of the image representation within the retina and primary visual cortex. These measurements characterize the neural hardware of the visual representation and demonstrate that there are several distinct categories of neurons called *visual streams*. The neurons in these visual streams respond to light stimulation in differnt ways, and their signals are communicated to different destinations.

The second half of this section reviews psychological and computational studies of image representation. The behavioral studies of image representation involve the simplest performances, such as detection, discrimination and simple recognition. These experiments have led to various proposals about how pattern and color information is represented within the retina and early cortical areas. The computational studies of image representation cover fundamental issues in efficient image coding and other image operations.

Interpretation

Perception is an interpretation of the retinal image, not a description. The third section of this book contains examples of how we interpret the retinal image to assign perceptual properties such as color, motion, and shape to objects.

Information in the retinal image may be interpreted in many different ways. Because we begin with ambiguous information, we cannot make deducations from the retinal image, only inferences. When we create algorithms to interpret image data -say, to infer the color, motion, and shape of objects- we confront the same challenges as the visual pathways. The success of the visual system in intpreting image data represents a remarkable achievement.

By studying computations designed to infer object properties, we have learned that the visual system succeeds in interpreting images because of statistical regularities present in the visual environment and hence in the retinal image. These regularities permit the visual system to use the fragmentary information present in the retinal image to draw accurate inferences about the physical cause of the image. For example, when we make inferences from the retinal image, the knowledge that we live in a three-dimensional world is essential to the correct interpretation of the image. Often, we are made aware of the existence of these powerful interpretations and their assumptions when they are in error, that is, when we discover a visual illusion.

The range of material in this book

The material I have chosen to include in this book comes from three sources: theory, data, and fruitful applications that are grounded in theoretical and empirical vision science. Portions of this book are written with the expectation that the reader has had some experience with linear algebra and calculus. In most sections of the book, however, I have tried to provide the reader with the basic ideas without using mathematical symbols or formal arguments.

Theory

Certain theoretical and empirical methods appear repeatedly within vision science. The most important theoretical method, which appears across all areas of vision science, is linear systems theory. Whether characterizing optics, neurophysiology, color vision, spatial vision, image compression, or pattern analysis, linear systems play an important role. There is little possibility of understanding the current foundations of vision science without understanding linear systems. I introduce the principles of linear systems in the first chapter and I refer to them throughout the book.

Linear methods are not a theory of vision; linear systems methods consist of a set of experiments that one should use to analyze a system. If the system's performance satisfies certain experimental properties, such as the principle of superposition, then we can use linear methods to characterize the system completely. Even if the system turns out to be nonlinear, it is useful to begin studying the system using summation experiments to obtain some insights as to the nature of the nonlinearities.

A linear characterization of a system is rarely a satisfactory scientific account of the system. There are usually many theoretical questions that require further explanation before the scientist is done. This will be evident in the first section on image encoding. Optical image formation, photoreceptor sampling and color matching are all fundamentally linear and thus we can characterize the performance of these system components. Even when this work is done, we still must explain the measurements in terms of the purpose of these elements and how their properties serve the goals of visual perception.

In part, the emphasis on linear systems methods is my choice; in part, this emphasis is inevitable because of a second choice I made in selecting the material. I have tried to include important problems that vision science has solved, or that I think are close to being solved. At present linear methods are much better understood than nonlinear methods. Consequently, we understand those problems which yield to linear analysis much better than we understand nonlinear problems.

A linear characterization of a system is rarely a complete cientific account of the system. There are usually many theoretical questions that require further explanation before the scientist is done. This will be evident in the first section on image encoding. Optical image formation, photoreceptor sampling, and color matching are all fundamentally linear, and thus we can characterize the performance of these system components. However, even when this work is done, we still must expolain the measurements in terms of the purpose of these elements and how their properties serve the goals of visual perception.

While linear analyses are central, there are some significant examples of successful nonlinear analyses. The first example is the analysis of the relationship between color matching and the cone photocurrent treatment in Chapter 4. This system consists of an initial linear encoding followed by a fixed non-linearity. These types of nonlinear systems can also be treated very thoroughly. The review of pattern sensitivity, in Chapter 7, also includes models that begin with linear encodings followed by a nonlinear stage. In the appendix to Chapter 7 I treat the profoundly nonlinear act of classification. Applications of Bayesian classification to interpret image data is likely to be a very important area in the future.

Data

The field of vision draws on experimental results from many separate disciplines, each with its own standards and methods. The tools of anatomy, electrophysiology, behavior, and computation are so different that no one can be an expert in all of these disciplines. To be a good vision scientist, however, one must appreciate the standards and methods of each discipline. The psychologist must understand whether an anatomical measurement is sufficiently thorough to serve as a good standard for comparison in a behavioral experiment; the computational theorist must understand the generality of a result from electrophysiology.

I have included empirical studies from all of the disciplines of vision. I have tried to describe these results, and their theoretical implications, in enough detail so that the advanced student can learn something about the standards of each of the fields. By placing these results together in a single volume I hope to explain what is special about the interdisciplinary field of vision.

Applications

As I selected problems to review, I did not distinguish strongly between those that are called basic from those that are called applied. I share Edwin Land's frustration with this distinction. After a theoretical lecture on color appearance, Land, who was both a brilliant inventor and entrepreneur, was asked to explain what applied problem his work would solve and he replied quickly that the work had a wonderful application. He then paused while the audience leaned forward to decide whether to invest in Polaroid stock. If the theory is right, Land whispered confidentially, we'll finally understand what we are doing.

Vision science finds applications in at least three important areas that I will draw on throughout the book. The first area is medicine. If we are to help the blind, we must understand how the visual portion of the brain functions, including the anatomy and functional properties of nerve cells. Equally important, we must understand how information is represented within the brain results in behavior. The results of behavioral experiments can answer questions about the organization of information within the visual pathways that are inaccessible to the anatomist or the electrophysiologist. Together, these results can guide the development of medical diagnostic tools and prosthetic devices. Tom Cornsweet's beautiful book, Visual Perception, was a guide to most of my generation as we first learned about the systematic analysis of the visual pathways, ranging from the visual pathways to behavior. In this book I hope to explain to the new student why so many of us found Cornsweet's presentation exhilirating and to build on Cornsweet's review.

A second area of application is the design of computer algorithms capable of analyzing information in an image. Typical applications range from part inspections in a factory to the identification of a tumor in a medical image. David Marr's book, Vision, stimulated the interest of many young scientists in this area. He presented a bold overview that related biological concepts and computer algorithms of visual processing. The contrast between the broad scope of Marr's imagination and the elegant, meticulous discussions by Cornsweet captures something of the creative tension that can arise when different disciplines contribute to a broad scientific endeavor.

The third area of application is the design of visual display devices to communicate information to the human visual system. When two electronic components communicate, the components must be designed to accommodate a set of communication protocols. In the case of communication between an electronic display medium, (e.g. a television display) and the human visual system, the designer can only re-design one of the two components. To communicate information efficiently between the electronic system and the human visual system, we must build displays that are matched to human capabilities. A remarkable harmony between vision science and applications technology has been achieved in some areas, such as color science. I hope that this book will contribute to the further coordination of our basic understanding of vision and the design of useful and efficient visual displays.

A Guide to the Principles of Vision

Much of vision science is predicated on the principle that the components of the visual system that limit or govern performance in various tasks can be quite different. In some experiments performance is limited by the lens, while in other experiments performance is limited by a computation in performed in visual cortex. Different visual tasks may be limited by completely distinct components of the visual pathways. Hence, a static diagram of the visual pathways, in which zero-crossings are inexorably followed by a primal sketch, and so forth, with all the components play the same role across tasks, does not capture the flexibility and adaptability of the visual pathways.

There are, however, several general principles that I found useful as I wrote and organized this volume. Some of these principles are embedded in the organization of the book, repeated in the introductions to the three sections, and repeated within the chapters themselves. This is the time, however, to introduce you to the principles, briefly, in one place.

The Inescapable Components of Image Encoding

The properties of image encoding, such as the blurring by the lens, receptor sampling, and trichromacy, shape the information available to the rest of the nervous system. The first third of the book is devoted to describing these aspects of vision. The properties of image formation set the stage for what the rest of the nervous system must confront.

The limits of image encoding set limits on the image information available to the visual pathways. As we shall see, the image encoding is a very partial description of the light incident at the eye: There is only a narrow region of high visual acuity in the fovea; the dynamic range of the sensors is very small; the representation of wavelength is very coarse. You would never buy a camera with such poor optics and coarse spatial sampling. Yet, the visual algorithms can interpret the properties of objects from this poor encoding.

Whether you wish to study the eye, or study algorithms embedded in the central nervous system, you will not go wrong by studying image encoding and thinking further about its implications for vision.

Adaptation and Flexibility

The visual pathways compensate for the poor quality of the image encoding by their flexibility. Nearly all of the peripheral elements of the visual pathways adapt in response to the viewing conditions. The lens accomodates, the strength of the retinal signal varies as the mean illumination level varies, the eye moves to bring the high visual acuity portion of the retina into a favorable viewing position. The flexible responses of the visual system overcome the mediocre image encoding.

The visual system's adjustments, or adaptations, to the environment are fundamental to its design. We see adaptation throughout the visual representation, not just in the peripheral components. Because adaptation is so widespread, it is impossible to characterize the visual system as a static device. The ability to adapt in response to a changing environment is a fundamental design principle of the visual pathways, beginning at the earliest stages. Such adaptation is also an important property of central brain representations.

Image representation: Visual Streams

As we review the visual representation of the image, we will find that the neural pathways are organized into several distinct pathways. These pathways, sometimes called visual streams, can be identified based on anatomical studies. Some cells have different shapes from others; some cells send their outputs this way and others send their outputs that way.

Many of the most important discoveries about vision concern the the identification of visual streams. Many of the important contemporary challenges in vision concern explanations of the functional significance of these streams. Segregation of visual information into these visual streams begins with the photoreceptors (rods and cones). Clarifications concerning the visual streams within the optic nerve have revolutionized our understanding of the visual representation. Understanding the organization of visual information with respect to these visual streams is one of most hotly debated topics in modern visual neuroscience. Identifying new visual streams and understanding their function is an important challenge to vision scientists.

Image interpretation: Statistical Inferences

To me, vision science is about how we see things. The interpretations of the image, or as Helmholtz called them, the unconscious inferences, are the purpose of vision. I study vision in order to understand the methods of interpreting images to objects and their properties.

Since the retinal image is often ambiguous, the visual system's success in interpreting images must be because it makes good assumptions about the likely properties of objects in the world. Not all configurations of objects are equally likely; we exist in a three-dimensional world. Not all surface reflectance functions are equally likely; there are regularities in the wavelength properties of surfaces and illuminants. Not all types of motion are equally likely; hard objects cannot pass through one another. The unequal probabilities of different interpretations make it possible to make informed guesses about the color, motion, position and shape of objects. The probabilities of different events are sufficiently skewed so that the visual system succeeds at interpreting the image data. Understanding these regularities, and understanding how to use them to interpret the retinal image, is central to vision science.

My devotion to image encoding and representation, the first two parts of this volume, flows from my conviction that we will not understand visual interpretations of the image without understanding encoding and representation. The encoding and representation define the environment in which image interpretation takes place. The encoding and representation must be structured to permit image interpretation to succeed. As you look through each section of this volume, you will find ideas about image interpretation. The material in this book will seem unified to you if you continue to ask how image encoding and the image representation serve the ultimate goal of image interpretation.

Image Encoding

Introduction to Image Encoding

The first section of this book describes the initial encoding of light by the eye. Chapter reviews the image formation process, that is, the process by which light incident at the eye is focused onto the retina. Chapter and Chapter review the basic properties of the conversion of light into a neural signal by the light-sensitive elements of the eye, the *photoreceptors*. This image encoding establishes essential limits on vision; the consequences of the image formation process can be found in many parts of the visual neural representation.

The early chapters introduce and make use of the principles of linear systems. Linear methods are fundamental to vision science, as they are to much of science. The well-designed experiment provides a method of extrapolating beyond the experimental measurements, and linear systems methods provide such a method. A notion of how to extrapolate beyond the experimental measurements is necessary because we can rarely measure the response to every important stimulus. The significance of linear systems methods is that they permit us to evaluate whether we can use the response to a few stimuli to predict the responses to other stimuli.

Since the linear methods apply well to image formation, it seems natural to introduce linear systems as a solution to the problem of measuring the properties of eye. The principles come up again in multiple sections, including analyses of the properties of color, pattern, and motion perception. Thus the reader will have several opportunities to see the application of these ideas.

Since the first edition of this book, new technologies to measure image encoding, and new facts about the image encoding, have been discovered. A particularly impactful technology, adaptive optics, has enabled measurements in the living human eye that were not possible at the time of the 1st edition. In this edition I explain the principles of adaptive optics and describe how it is used both to measure the properties of image formation and to use this knowledge to deliver stimuli with remarkable precision.

In addition, a new class of photosensitive cells was discovered. These cells are not photoreceptors, rather they are ganglion cells that contain a light sensitive pigment distributed across their entire extent. The discovery of these intrinsically photosensitive retinal ganglion cells (ipRGCs) is an important development with implications for vision and other behaviors that depend on light sensitivity.

Finally, this 2nd edition is more firmly connected to computational methods. As we introduce many of the concepts of optics and encoding, we provide the reader with a set of software methods that can be used to calculate the encoding and responses quantitatively.

Image formation

The quality and general properties of the image formed at the retina establish the basic image parameters that the rest of the nervous system must use to make inferences about objects. Because the image formation process is linear, we can characterize its properties fairly thoroughly. Measurements from the eye show that even when optical focus is at its best, the image of a point is spread across eight or more photoreceptors. It follows that the image formation process attenuates the contrast of patterns that vary rapidly across space. This leaves the nervous system with only a small contrast range available in the fine spatial detail of an image, while there is a substantial contrast range present in slowly varying spatial patterns. Finally, the precise meaning of high and low frequency varies with the wavelength of the incident light because the quality of the retinal image varies strongly with wavelength. Under ordinary viewing conditions the short wavelength light (blue portion of the spectrum) is blurred strongly so that very little pattern information is available in this part of the spectrum compared to longer wavelengths of light (green, yellow and red parts of the spectrum).

The Spatial Mosaic of Photoreceptors

Chapter reviews the spatial arrangement of the light-sensitive elements of the photoreceptors. There are two fundamentally different types of receptors, the rods and cones. The spatial organization of the rod and cone photoreceptor mosaics differ; each mosaic reflects the main goal of the visual stream it initiates.

The rod visual stream initiates vision under low illumination conditions when relative few quanta are available. The rods are present in high density to capture more quanta, not to achieve high spatial resolution. Indeed, the spatial resolution of the rod pathway is fairly coarse since the outputs of many rod photoreceptors converge onto single retinal cells.

The visual streams initiated by the cone mosaic ordinarily operate at high light levels where there are plenty of quanta. The organization of the cone mosaic can be understood in terms of the goal of representing fine spatial detail rather than capturing more quanta. This goal is reflected separately in the spatial arrangement of the separate mosaics of the three different types of cones, the L, M, and S cones. The density of the short-wavelength sensitive S cones is lowest, matching the poor resolution of the optics in the short-wavelength region. Only the L and M cones are present in the very central fovea, where they have a very high sampling density and form a locally regular sampling grid. The sampling density of the L and M cones is also a good match to the quality of the image passed by the optics of the eye in the portion of the wavelength spectrum where they have their peak sensitivity. Signals from individual cones in the fovea do not converge onto retinal neurons, but instead these signals are communicated along private neural channels to the cortex.

Wavelength Encoding

Chapter reviews how the visual pathways encode the wavelength of light, a process that greatly influences color appearance. The behavioral predictions that the eye contains three types of cones, as well as behavioral predictions of the way these cones encode wavelength, have been confirmed in a stunning set of experiments that represent an intellectual collaboration between very different disciplines. The nexus of results from physics, psychology, and biology concerning wavelength encoding form one of most beautiful and satisfying stories in science. The successful interactions between these disciplines is a remarkable intellectual achievement. The facts concerning how the visual pathways encode wavelength has been important for all color imaging technologies. The scientific methods that link the color matching experiment to the cone photocurrents are important for all of us who wish to relate behavior and brain.

Image Formation

Image Formation Overview

The cornea and lens are the interface between the physical world of light and the visual encoding. The cornea and lens bring light into focus at the light sensitive receptors in the retina. These cells initiate a series of visual events that result in our visual experience.

The initial encoding of light at the retina is but the first in a series of visual transformations: The stimulus incident at the cornea is transformed into an image at the retina. The retinal image is transformed into a neural response by the light sensitive elements of the eye, the photoreceptors. The photoreceptor responses are transformed to a neural response on the optic nerve. The optic nerve representation is transformed into a cortical representation, and so forth. We can describe most of our understanding of these transformations, and thus most of our understanding of the early encoding of light by the visual pathways by using linear systems theory. Because all of our visual experience is limited by the image formation within our eye, we begin by describing this transformation of the light signal and we will use this analysis as an introduction to linear methods.

Optical Components of the Eye

Figure 1 contains an overview of the imaging components of the eye. Light from a source arrives at the cornea and is focused by the cornea and lens onto the photoreceptors, a collection of light sensitive neurons. The photoreceptors are part of a thin layer of neural tissue, called the retina. The photoreceptor signals are communicated through the several layers of retinal neurons to the neurons whose output fibers makes up the optic nerve. The optic nerve fibers exit through a hole in the retina called the optic disk. The optical imaging of light incident at the cornea into an image at the retinal photoreceptors is the first visual transformation. Since all of our visual experiences are influenced by this transformation, we begin the study of vision by analyzing the properties of image formation.

When we study transformations, we must specify their inputs and outputs. As an example, we will consider how simple one-dimensional intensity patterns displayed on a video display monitor are imaged onto the retina (Figure 2 (a)). In this case the input is the light signal incident at the cornea. One-dimensional patterns have a constant intensity along the, say, horizontal dimension and varies along the perpendicular (vertical) dimension. We will call

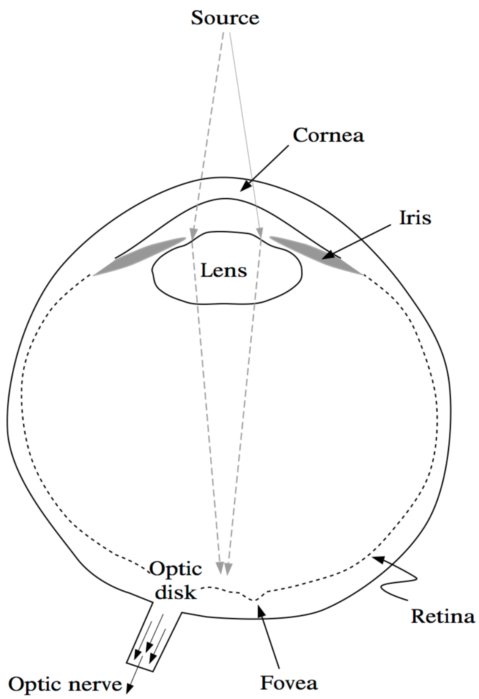

Figure 1: The image formation components of the eye. The cornea and lens focus the image onto the retina. The cornea initiates the bending of the light rays from the source. The rays must pass through the pupil which is bordered by the iris. The flexible lens then further bends the rays. In this image, the rays are focused near the fovea, a region that is specialized for high visual acuity. The retinal output fibers come together to form a bundle that exits through a hole in the retina at the optic disk (or blindspot). The fiber bundle is the optic nerve.

the pattern of light intensity we measure at the monitor screen the monitor image. We can measure the intensity of the one-dimensional image by placing a light-sensitive device called a photodetector at different positions on the screen. The vertical graph in Figure 2 (b) shows a measurement of the intensity of the monitor image at all screen locations.

The output of the optical transformation is the image formed at the retina. When the input image is one-dimensional, the retinal image will be one-dimensional, too. Hence, we can represent it using a curve as in Figure 2 (c). We will discuss the optical components of the visual system in more detail later in this chapter, but from simply looking at a picture of the eye in Figure 1 we can see that the monitor image passes through a lot of biological material before arriving at the retina. Because the optics of the eye are not perfect, the retinal image is not an exact copy of the monitor image: The retinal image is a blurred copy of the input image.

The image in Figure 2 (b) shows one example of an infinite array of possible input images. Since there is no hope of measuring the response to every possible input, to characterize optical blurring completely we must build a model that specifies how any input image is transformed into a retinal image. We will use linear systems methods to develop a method of predicting the retinal image from any input image.

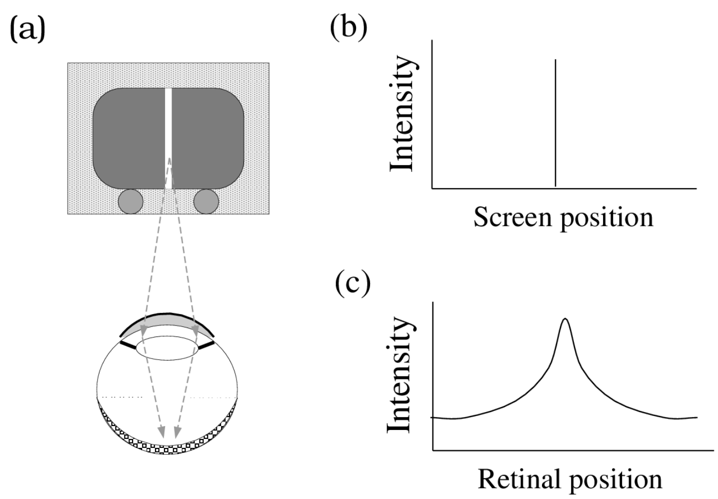

Figure 2: Retinal image formation illustrated with a single-line input image. (a) A one-dimensional monitor image consists of a set of lines at different intensities. The image is brought to focus on the retina by the cornea and lens. (b) We can represent the intensity of a one-dimensional image using a simple graph that shows the light as a function of horizontal screen position. Only a single value is plotted since the one-dimensional image is constant along the vertical dimension. (c) The retinal image is a blurred version of the one-dimensional input image. The retinal image is also one-dimensional and is also represented by a single curve.monitor.to.retina

Reflections From the Eye

To study the optics of a human eye you will need an experimental eye, so you might invite a friend to dinner. In addition, you will need a light source, such as a candle, as a stimulus to present to your friend's eye. If you look directly into your friend's eye, you will see a mysterious darkness that has beguiled poets and befuddled visual scientists. The reason for the darkness can be understood by considering the problem of ophthalmoscope design illustrated in Figure 3(a).

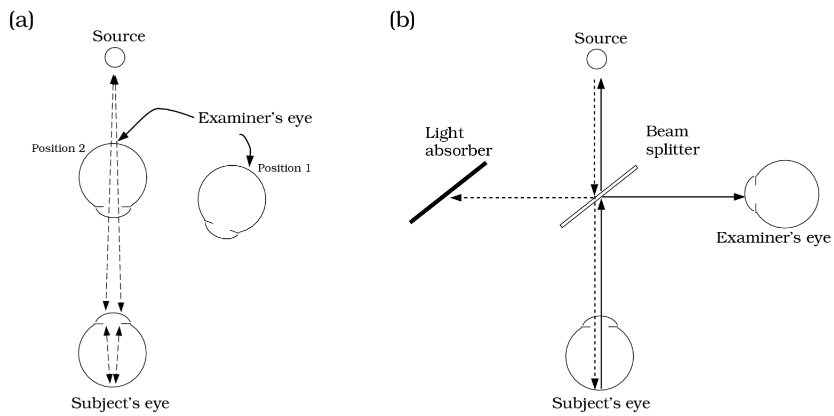

Figure 3: An ophthalmoscope is used to see an image reflected from the interior of the eye. (a) When we look directly into the eye, we cast a shadow making it impossible to see light reflected from the interior of the eye. (b) The ophthalmoscope permits us to see light reflected from the interior of the eye. Helmholtz invented the first ophthalmoscope. (After Cornsweet (1970))

If the light source is behind you, so that your head is between the light source and the eye you are studying, then your head will cast a shadow that interferes with the light from the point source arriving at your friend's eye. As a result, when you look in to measure the retinal image you see nothing beyond what is in your heart. If you move to the side of the light path, the image at the back of your friend's eye will be reflected towards the light source, following a reversible path. Since you are now on the side, out of the path of the light source, no light will be sent towards your eye.

Flamant (1955) first measured the retinal image using a modified ophthalmoscope. She modified the instrument by placing a light sensitive recording, a photodetector, at the position normally reserved for the ophthalmologist's eye. In this way, she measured the intensity pattern of the light reflected from the back of the observer's eye. Campbell and Gubisch (1966) used Flamant's method to build their apparatus, which is sketched in Figure 4. Campbell and Gubisch measured the reflection of a single bright line, that served the input stimulus in their experiment. As shown in the figure, a beam-splitter placed between the input light and the observer's eye divides the input stimulus into two parts. The beam-splitter causes some of the

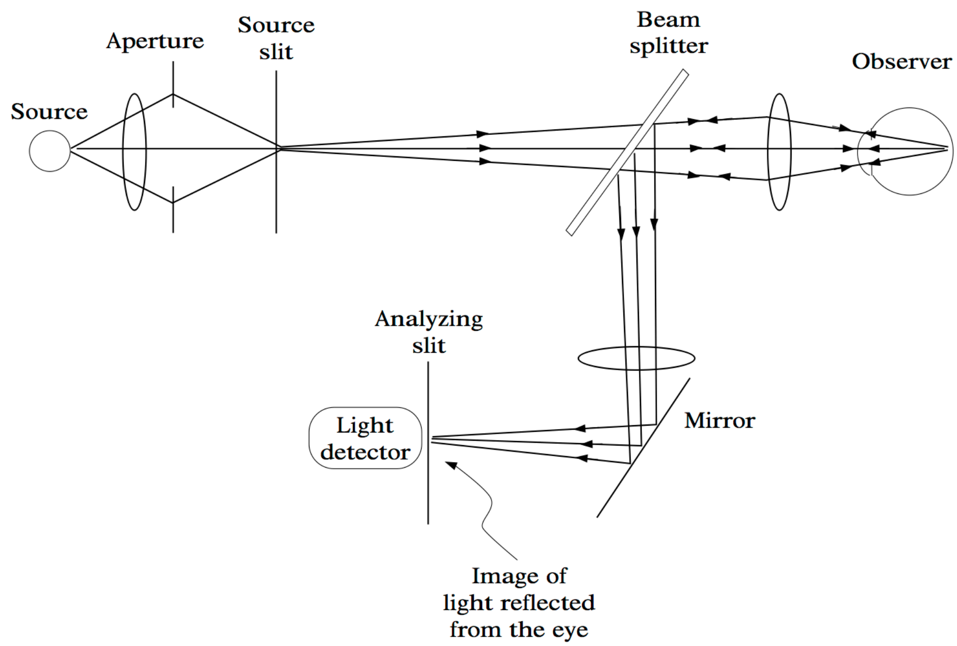

Figure 4: A modified opthalmoscope measures the human retinal image. Light from a bright source passes through a slit and into the eye. A fraction of the light is reflected from the retina and is imaged. The intensity of the reflected light is measured at dif- ferent spatial positions by varying the location of the analyzing slit. (After Campbell and Gubisch (1966), Fig. 2)

light to be turned away from the observer and lost; this stray light is absorbed by a light baffle. The rest of the light continues toward the observer. When the light travels in this direction, the beam-splitter is an annoyance, serving only to lose some of the light; it will accomplish its function on the return trip.

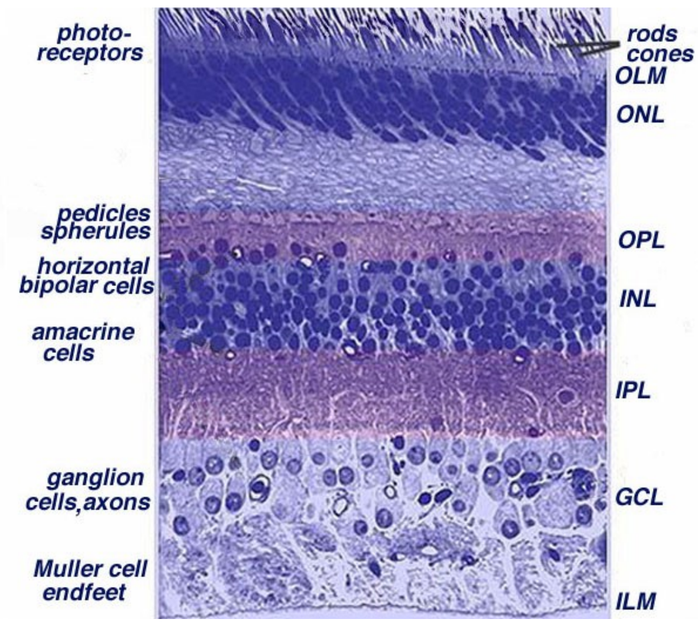

Figure 5: The retina contains the light sensitive photoreceptors where light is focussed. This cross-section of a monkey retina outside the fovea shows there are several layers of neurons in the optical path between the lens and the photoreceptors. As we will see later, in the central fovea these neurons are displaced to leaving a clear optical path from the lens to the photoreceptors (Source: Kolb et al. (2011)).

The light that enters the observer's eye is brought to a good focus on the retina by a lens. A small fraction of the light incident on the retina is reflected and passes – a second time – through the optics of the eye. On the return path of the light, the beam-splitter now plays its functional role. The reflected image would normally return to a focus at the light source. But the beam-splitter divides the returning beam so that a portion of it is brought to focus in a measurement plane to one side of the apparatus. Using a very fine slit in the measurement plane, with a photodetector behind it, Campbell and Gubisch measured the reflected light and used the measurements of the reflected light to infer the shape of the image on the retinal surface.

What part of the eye reflects the image? In Figure 5 we see a cross-section of the peripheral retina. In normal vision, the image is focused on the retina at the level of the photoreceptors. The light measured by Campbell and Gubisch probably contains components from several different planes at the back of the eye. Thus, their measurements probably underestimate the quality of the image at the level of the photoreceptors Figure 6 shows several examples of

Campbell and Gubisch's measurements of the light reflected from the eye when the observer is looking at a very fine line. The different curves show measurements for different pupil sizes. When the pupil was wide open (top, 6.6mm diameter) the reflected light is blurred more strongly than when the pupil is closed (middle, 2.0mm). Notice that the measurements made with a large pupil opening are less noisy; when the pupil is wide open more light passes into the eye and more light is reflected, improving the quality of the measurements. The light measured in Figure 6 passed through the optical elements of the eye twice, while the retinal image passes through the optics only once. It follows that the spread in these curves is wider than the spread we would observe had we measured at the retina. How can we use these doublepass measurements to estimate the blur at the retina? To solve this problem, we must understand the general features of their experiment. It is time for some theory.

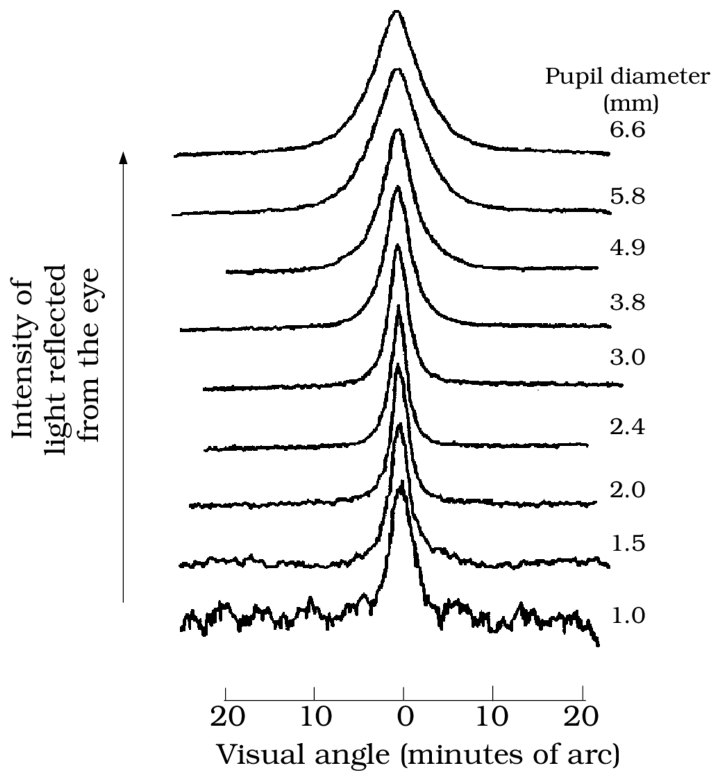

Figure 6: Experimental measurements of light that has been reflected from a human eye looking at a fine line. The reflected light has been blurred by double passage through the optics of the eye. (Source: Campbell and Gubisch (1966)).

Linear Systems Methods

A good theoretical account of a transformation, such as the mapping from monitor image to retinal image, should have two important features. First, the theoretical account should suggest to us which measurements we should make to characterize the transformation fully. Second, the theoretical account should tell us how to use these measurements to predict the retinal image distribution for all other monitor images.

In this section we will develop a set of general tools, referred to as linear systems methods. These tools will permit us to solve the problem of estimating the optical transformation from the monitor to the retinal image. The tools are sufficiently general, however, that we will be able to use them repeatedly throughout this book.

There is no single theory that applies to all measurement situations. But, linear systems theory does apply to many important experiments. Best of all, we have a simple experimental test that permits us to decide whether linear systems theory is appropriate to our measurements. To see whether linear systems theory is appropriate, we must check to see that our data satisfy the two properties of homogeneity and superposition.

Homogeneity

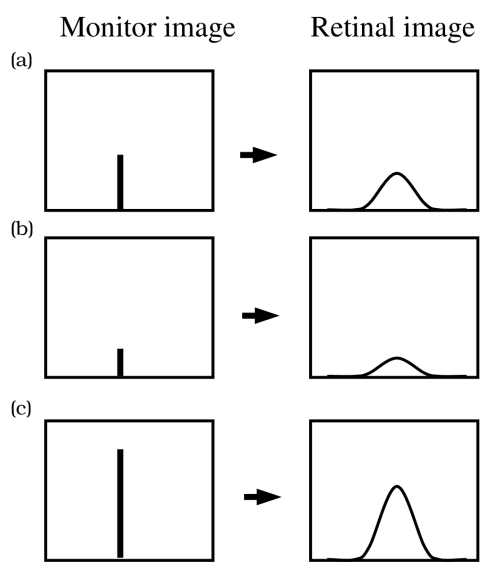

Figure 7: The principle of homogeneity. An input stimulus and corresponding retinal image are shown in each part of the figure. The three input stimuli are the same except for a scale factor. Homogeneity is satisfied when the corresponding retinal images are scaled by the same factor. Part (a) shows an input image at unit intensity, while (b) and (c) show the image scaled by 0.5 and 2.0 respectively

A test of *homogeneity* is illustrated in Figure 7. The left-hand panels show a series of monitor images, and the right-hand panels show the corresponding measurements of reflected light. Suppose we represent the intensities of the lines in the one-dimensional monitor image using the vector p (upper left) and we represent the retinal image measurements by the vector r. Now, suppose we scale the input signal by a factor a, so that the new input is ap. We say that the system satisfies homogeneity if the output signal is also scaled by the same factor of a, and thus the new output is ar. For example, if we halve the input intensity, then the reflected light measured at their photodetector should be one-half the intensity (middle panel). If we double the light intensity, the response should double (bottom panel). Campbell and Gubisch's measurements of light reflected from the human eye satisfy homogeneity.

> **Vector notation**
>
> We will use vectors and matrices in our calculations to eliminate burdensome notation. Matrices will be denoted by boldface, upper case Roman letters, $\mathbf{M}$. Column vectors will be denoted using lower case boldface Roman letters, $\mathbf{v}$. The transpose operation will be denoted by a superscript T, $\mathbf{v}^T$. Scalar values will be in normal typeface, and they will usually be denoted using Roman characters (a) except when tradition demands the use of Greek symbols (α). The i^{th} entry of a vector, $\mathbf{v}$, is a scalar and will be denoted as v_i. The i^{th} column of a matrix, $\mathbf{M}$, is a vector that we denote as $\mathbf{m}_i$. The scalar entry in the i^{th} row and j^{th} column of the matrix $\mathbf{M}$ will be denoted m_{ij}.

Superposition

Superposition, used as both an experimental procedure and a theoretical tool, is probably the single most important idea in this book. You will see it again and again in many forms. We describe it here for the first time.

Suppose we measure the response to two different input stimuli. For example, suppose we find that input pattern p (top left) generates the response r (top right), and input pattern p' (middle left) generates response r' (middle right). Now we measure the response to a new input stimulus equal to the sum of p and p'. If the response to the new stimulus is the sum of the responses measured singly, $r + r'$, then the system is a *linear system*. By measuring the responses to stimuli individually and then the response to the sum of the stimuli, we test superposition. When the response to the sum of the stimuli equals the sum of the individual responses, then we say the system satisfies superposition. Campbell and Gubisch's measurements of light reflected from the eye satisfy this principle.

We can summarize homogeneity and superposition succinctly using two equations. Write the linear optical transformation that maps the input image to the light intensity at each of the receptors as

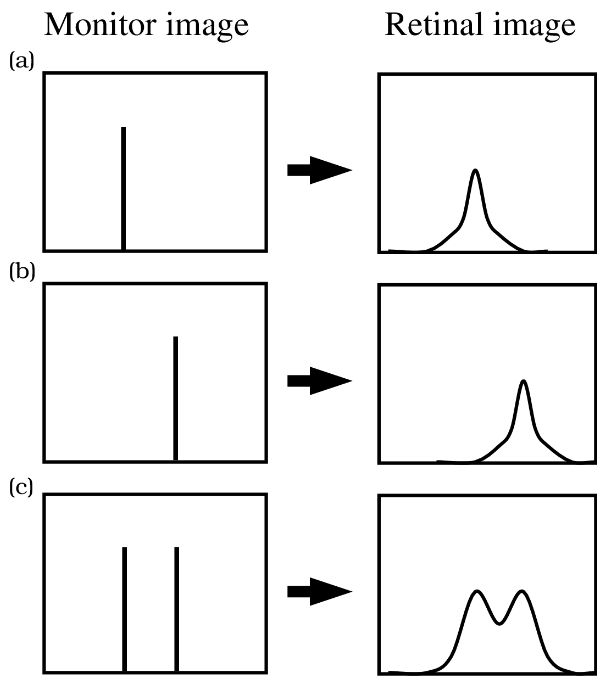

Figure 8: The principle of superposition. Each of the three parts of the picture shows an input stimulus and the corresponding retinal image. The stimulus in part (a) is a single-line image and in part (b) the stimulus is a second line displaced from the first. The stimulus in part (c) is the sum of the first two lines. Superposition holds if the retinal image in part (c) is the sum of the retinal images in parts (a) and (b).

$$\mathbf{r} = L(\mathbf{p}) \tag{0.1}$$

Homogeneity and superposition are defined by the pair of equations:

$$L(a, \mathbf{p}) = a\ L(\mathbf{p}) \quad \text{(Homogeneity)} \tag{0.2}$$

$$L(\mathbf{p} + \mathbf{p}') = L(\mathbf{p}) + L(\mathbf{p}') \quad \text{(Superposition)} \tag{0.3}$$

Implications of Homogeneity and Superposition

Figure 9 illustrates how we will use linear systems methods to characterize the relationship between the input signal from a monitor, light reflected from the eye (we analyze a one-dimensional monitor image to simplify the notation. The principles remain the same, but the notation becomes cumbersome when we consider two-dimensional images.). First, we make an initial set of measurements of the light reflected from the eye for each single-line monitor image, with the line set to unit intensity. If we know the images from single-line images, and we know the system is linear, then we can calculate the light reflected from the eye from any monitor image: Any one-dimensional image is the sum of a collection of lines.

Consider an arbitrary one-dimensional image, as illustrated at the top of Figure 9. We can conceive of this image as the sum of a set of single-line monitor images, each at its own intensity, p_i. We have measured the reflected light from each single-line image alone, call this $\mathbf{r}_i$ for the i^{th} line. By homogeneity it follows that the reflected light from the i^{th} line will be a scaled version of this response, namely $p_i\mathbf{r}_i$. Next, we combine the light reflected from the single-line images. By superposition, we know that the light reflected from the original monitor image, $\mathbf{r}$, is the sum of the light reflected from the single-line images,

$$\mathbf{r} = \sum_{i}^{N} p_i \mathbf{r}_i. \tag{0.4}$$

Equation 0.4 defines a transformation that maps the input stimulus, p, into the measurement, r. Because of the properties of homogeneity and superposition, the transformation is the weighted sum of a fixed collection of vectors: When the monitor image varies, only the weights in the formula, p_i, vary but the vectors r_i, the reflections from single-line stimuli, remain the same. Hence, the reflected light will always be the weighted sum of these reflections.

To represent the weighted sum of a set of vectors, we use the mathematical notation of *matrix multiplication*. Multiplying a matrix times a vector computes the weighted sum of the matrix columns; the entries of the vector define the weights. Matrix multiplication and linear systems methods are closely linked. In fact, the set of all possible matrices define the set of all possible linear transformations of the input vectors.

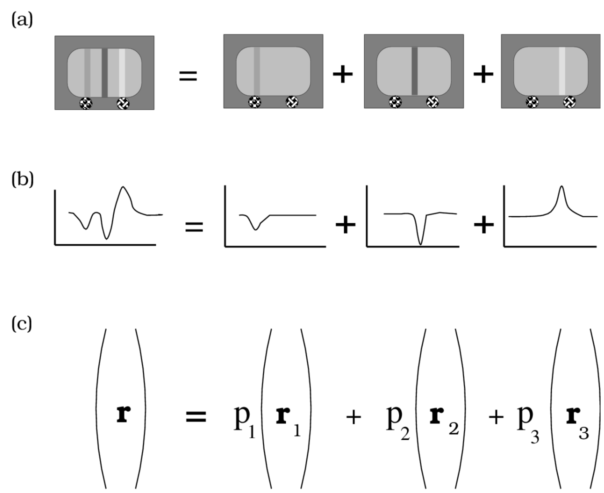

Figure 9: A one-dimensional monitor image is the weighted sum of a set of lines. An example of a one-dimensional image is shown on the left and the individual monitor lines comprising the monitor image are shown separately on the right. (b) Each line in the component monitor image contributes to the retinal image. The retinal images created by the individual lines are shown below the individual monitors. The sum of the retinal images is shown on the left. (c) The retinal image generated by the \$i^{th} monitor line at unit intensity is $\mathbf{r}_i$. The intensity of the ith monitor line is p_i. By homogeneity, the retinal image of the i^{th} monitor line is $p_i\mathbf{r}_i$. By superposition, the retinal image of the collection of mointor lines is the sum of the individual retinal images, $\sum_i p_i\mathbf{r}_i$

Matrix multiplication has a shorthand notation to replace the explicit sum of vectors in Equation 0.4. In the example here, we define a matrix, $\mathbf{R}$, whose columns are the responses to individual monitor lines at unit intensity, $\mathbf{r}_i$. The matrix $\mathbf{R}$ is called the system matrix. Matrix multiplication of the input vector, $\mathbf{p}$, times the system matrix $\mathbf{R}$, transforms the input vector into the output vector. Matrix multiplication is written using the notation

$$\mathbf{r} = \mathbf{R}\mathbf{p} \tag{0.5}$$

Matrix multiplication follows naturally from the properties of homogeneity and superposition. Hence, if a system satisfies homogeneity and superposition, we can describe the system response by creating a *system matrix* that transforms the input to the output.

Why Linear Methods are Useful

Let's use a specific numerical example to illustrate the principle of matrix multiplication. This will also help explain why the method is so useful.

Suppose we measure a monitor that displays only three lines. We can describe the monitor image using a column vector with three entries, $p = (p_1, p_2, p_3)^T$. The three lines of unit intensity are $(1, 0, 0)^T$, $(0, 1, 0)^T$, and $(0, 0, 1)^T$.

We measure the response to these input vectors to build the *system matrix*. Suppose the measurements for these three lines are $(0.1, 0.2, 0.5, 0.3, 0, 0)^T$, $(0, 0.1, 0.2, 0.5, 0.1, 0)^T$, and $(0, 0, 0.2, 0.5, 0.3, 0)^T$ respectively. We place these responses into the columns of the system matrix:

$$\mathbf{R} = \begin{pmatrix} 0.1 & 0 & 0 \\ 0.2 & 0.1 & 0 \\ 0.5 & 0.2 & 0.2 \\ 0.3 & 0.5 & 0.5 \\ 0 & 0.1 & 0.3 \\ 0 & 0 & 0 \end{pmatrix} \tag{0.6}$$

Because the system is linear, we can predict the response to any monitor image using the system matrix. For example, if the monitor image is $\mathbf{p} = (0.5, 1.0, 0.2)^T$ we multiply the input vector and the system matrix to obtain the response, on the left side of Equation 0.7.

$$\begin{pmatrix} 0.05 \\ 0.20 \\ 0.49 \\ 0.75 \\ 0.16 \\ 0 \end{pmatrix} = \begin{pmatrix} 0.1 & 0 & 0 \\ 0.2 & 0.1 & 0 \\ 0.5 & 0.2 & 0.2 \\ 0.3 & 0.5 & 0.5 \\ 0 & 0.1 & 0.3 \\ 0 & 0 & 0 \end{pmatrix} \begin{pmatrix} 0.5 \\ 1.0 \\ 0.2 \end{pmatrix} \tag{0.7}$$

From this example we see why linear systems methods are a good starting point for answering an essential scientific question: How can we generalize from the results of measurements using a few stimuli to predict the results we will obtain when we measure using novel stimuli? Linear systems methods tell us to examine homogeneity and superposition. If these empirical properties hold in our experiment, then we will be able to measure responses to a few stimuli and predict responses to many other stimuli.

This is very important advice. Quantitative scientific theories are attempts to *characterize* and then *explain* systems with many possible input stimuli. Linear systems methods tell us how to organize experiments to characterize our system: measure the responses to a few individual stimuli, and then measure the responses to mixtures of these stimuli. If superposition holds, then we can obtain a good characterization of the system we are studying. If superposition fails, your work will not be wasted since you will need to explain the results of superposition experiments to obtain a complete characterization of the measurements.

To explain a system, we need to understand the general organizational principles concerning the system parts and how the system works in relationship to other systems. Achieving such an explanation is a creative act that goes beyond simple characterization of the input and output relationships. But, any explanation must begin with a good characterization of the processing the system performs.

Shift-Invariant Linear Transformations

Shift-Invariant Systems: Definition

Since homogeneity and superposition are well satisfied by Campbell and Gubisch's experimental data, we can predict the result of any input stimulus by measuring the system matrix that describes the mapping from the input signal to the measurements at the photodetector. But the experimental data are measurements of light that has passed through the optical elements of the eye twice, and we want to know the transformation when we pass through the optics once. To correct for the effects of double passage, we will take advantage of a special property of optics of the eye, *shift-invariance*. Shift-invariant linear systems are an important class of linear systems, and they have several properties that make them simpler than general linear systems. The following section briefly describes these properties and how we take advantage of them. The mathematics underlying these properties is not hard; I sketch proofs of these properties in the Appendix.

Suppose we start to measure the system matrix for the Campbell and Gubisch experiment by measuring responses to different lines near the center of the monitor. Because the quality of the optics of our eye is fairly uniform near the fovea, we will find that our measurements, and by implication the retinal images, are nearly the same for all single-line monitor images. The only way they will differ is that as the position of the input translates, the position of the output will translate by a corresponding amount. The shape of the output, however, will not change. An example of two measurements we might find when we measure using two lines on the monitor is illustrated in the top two rows of Figure 9 . As we shift the input line, the measured output shifts. This shift is a good feature for a lens to have, because as an object's position changes, the recorded image should remain the same (except for a shift). When we shift the input and the form of the output is invariant, we call the system shift-invariant.

Shift-Invariant Systems: Properties

We can define the system matrix of a shift-invariant system from the response to a single stimulus. Ordinarily, we need to build the system matrix by combining the responses to many individual lines. The system matrix of a linear shift-invariant system is simple to estimate since these responses are all the same except for a shift. Hence, if we measure a single column of the matrix, we can fill in the rest of the matrix. For a shift-invariant system, there is only one response to a line. This response is called the linespread of the system. We can use the linespread function to fill in the entire system matrix.

The response to a harmonic function at frequency f is a harmonic function at the same frequency. Sinusoids and cosinusoids are called *harmonics* or *harmonic functions*. When the input to shift-invariant system is a harmonic at frequency f, the output will be a harmonic at the same frequency. The output may be scaled in amplitude and shifted in position, but it still will be a harmonic at the input frequency.

For example, when the input stimulus is defined at N points and at these points its values are sinusoidal, $S_f(i, N)$. Then, the response of a shift-invariant system will be a scaled and shifted sinusoid, $s_f \sin(\frac{2\pi f i}{N} + \phi_f)$. There is some uncertainty concerning the output because there are two unknown values, the scale factor, s_f, and phase shift, ϕ_f. But, for each sinusoidal input we know a lot about the output; the output will be a sinusoid of the same frequency as the input.

We can express this same result another useful way. Expanding the sinusoidal output using the summation rule we have

$$s_f \sin(\frac{2\pi f i}{N} + \phi_f) = a_f \cos(\frac{2\pi f i}{N}) + b_f \sin(\frac{2\pi f i}{N}) \tag{0.8}$$

where

$$\begin{aligned} a_f &= s_f \sin(\phi_f) \\ b_f &= s_f \cos(\phi_f) \end{aligned} \tag{0.9}$$

In other words, when the input is a sinusoid at frequency f the output is the weighted sum of a sinusoid and a cosinusoid, both at the same frequency as the input. In this representation, the two unknown values are the weights of the sinusoid and the cosinusoid:

$$s_f \sin(\frac{2\pi f i}{N} + \phi_f) = a_f \cos(\frac{2\pi f i}{N}) + b_f \sin(\frac{2\pi f i}{N}) \tag{0.10}$$

For many optical systems, such as the human eye, the relationship between harmonic inputs and the output is even simpler. When the input is a harmonic function at frequency f, the output is a scaled copy of the function and there is no shift in spatial phase. For example, when the input is $\sin\left(\frac{2\pi f i}{N}\right)$, the output will be

$$s_f \sin\left(\frac{2\pi f i}{N}\right) \tag{0.11}$$

$$s_f \sin(\frac{2\pi f i}{N}) \tag{0.12}$$

The Optical Quality of the Eye

We are now ready to correct the measurements for the effects of double passage through the optics of the eye. To make the method easy to understand, we will analyze how to do the correction by first making the assumption that the optics introduce no phase shift into the retinal image; this means, for example, that a cosinusoidal stimulus creates a cosinusoidal retinal image, scaled in amplitude. It is not necessary to assume that there is no phase shift but the assumption is reasonable and the main principles of the analysis are easier to see if we assume there is no phase shift.

To understand how to correct for double passage, consider a hypothetical alternative experiment Campbell and Gubisch might have done (Figure 10). Suppose Campbell and Gubisch had used input stimuli equal to cosinusoids at various spatial frequencies, f. Because the optics are shift-invariant and there is no frequency-dependent phase shift, the retinal image of a cosinusoid at frequency f is a cosinusoid scaled by a factor s_f. The retinal image passes back through the optics and is scaled again, so that the measurement would be a cosinusoid scaled by the factor s_f^2. Hence, had Campbell and Gubisch used a cosinusoidal input stimulus, we could deduce the retinal image from the measured image easily: The retinal image would be a cosinusoid with an amplitude equal to the square root of the amplitude of the measurement.

Campbell and Gubisch used a single line, not a set of cosinusoidal stimuli. But, we can still apply the basic idea of the hypothetical experiment to their measurements. Their input stimulus, defined over N locations, is

$$\mathbf{p}_i = \begin{cases} 1 & \text{if } i = 0 \\ 0 & \text{if } 1 \leq i < N \end{cases} \tag{0.13}$$

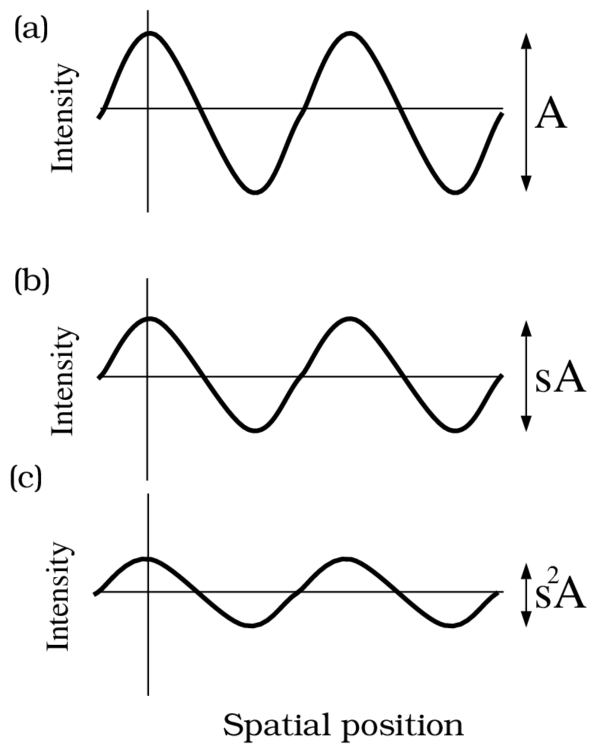

Figure 10: Sinusoids and Double Passage (a) The amplitude, A, of an input cosinusoid stimulus is scaled by a factor, s, after passing through even-symmetric shift-invariant symmetric optics as shown in part (b). (c) Passage through the optics a second time scales the amplitude again, resulting in a signal with amplitude s^2 A.

As I describe in the appendix, we can express the stimulus as the weighted sum of harmonic functions by using the *discrete Fourier series.* The representation of a single line is equal to the sum of cosinusoidal functions

$$\mathbf{p}_i = 0.5 + \sum_{f=1}^{N-1} \cos\left(2\pi f \frac{i}{N}\right) \tag{0.14}$$

Because the system is shift-invariant, the retinal image of each cosinusoid was a scaled cosinusoid, say with scale factor s_f. The retinal image was scaled again during the second pass through the optics, to form the cosinusoidal term they measured.[1]

Using the discrete Fourier series, we also can express the measurement as the sum of cosinusoidal functions,

$$\text{Measurement} = 0.5 + \sum_{f=1}^{N-1} (s_f)^2 \cos\left(2\pi f \frac{i}{N}\right) \tag{0.15}$$

We know the values of s_f^2, since this was Campbell and Gubisch's measurement. The image of the line at the retina, then, must have been

$$\mathbf{l}_i = 0.5 + \sum_{f=1}^{N-1} s_f \cos\left(2\pi f \frac{i}{N}\right) \tag{0.16}$$

The values $\mathbf{l}_i$ define the linespread function of the eye's optics. We can correct for the double passage and estimate the linespread because the system is linear and shift-invariant.

As you read further about experimental and computational methods in vision science, remember that there is nothing inherently important about sinusoids as visual stimuli; we must not confuse the stimulus with the system or with the theory we use to analyze the system. When the system is a shift-invariant linear system, sinusoids can be helpful in simplifying our calculations and reasoning, as we have just seen. The sinusoidal stimuli are important only insofar as they help us to measure or clarify the properties of the system. And if the system is not shift-invariant, the sinusoids may not be important at all.

[1] Be bothered by the fact that the discrete Fourier series approximation is an infinite set of pulses, rather than a single line. To understand why, consult the Appendix.

The Linespread Function

Figure 11 contains Campbell and Gubisch's estimates of the linespread functions of the eye. Notice that as the pupil size increases, the width of the linespread function increases which indicates that the focus is worse for larger pupil sizes. As the pupil size increases, light reaches the retina through larger and larger sections of the lens. As the area of the lens affecting the passage of light increases, the amount of blurring increases.

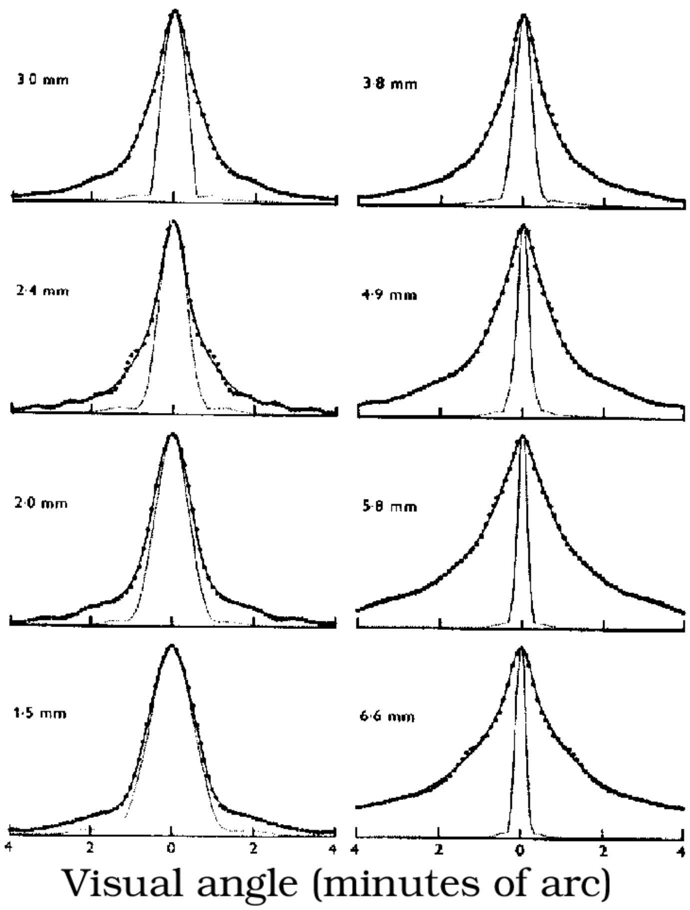

Figure 11: The linespread function of the human eye: The solid line in each panel is a measurement of the linespread. The dotted lines are the diffraction-limited linespread for a pupil of that diameter. (Diffraction is explained later in the text). The different panels show measurements for a variety of pupil diameters (From Campbell and Gubisch (1966)).

The measured linespread functions, $\mathbf{l}_i$, along with our belief that we are studying a shift-invariant linear system, permit us to predict the retinal image for any one-dimensional input image. To calculate these predictions, it is convenient to have a function that describes the linespread of the human eye. G. Westheimer (Westheimer (1986)) suggested the following formula to describe the measured linespread function of the human eye, when in good focus, and when the pupil diameter is near 3mm[2].

$$\mathbf{l}_i = 0.47e^{-3.3i^2} + 0.53e^{-0.93|i|} \tag{0.17}$$

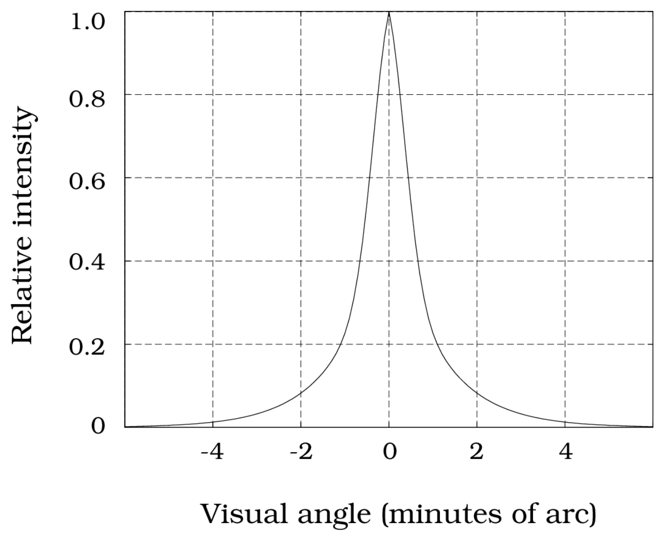

Figure 12: Westheimer's Linespread Function. Analytic approximation of the human linespread function for an eye with a 3.0mm diameter pupil (Westheimer and Tanzman (1956)).

The linespread function is given by:

$$\mathbf{l}_i = 0.47e^{-3.3i^2} + 0.53e^{-0.93|i|} \tag{0.18}$$

where the variable i refers to position on the retina specified in terms of minutes of visual angle. A graph of this linespread function is shown in Equation 0.17.

The Modulation Transfer Function

In correcting for double passage, we thought about the measurements in two separate ways. Since our main objective was to derive the linespread function, a function of spatial position, we spent most of our time thinking of the measurements in terms of light intensity as a

[2]Westheimer's linespread function is for an average observer under one set of viewing conditions. As the pupil changes size and as observer's age, the linespread function can vary. Consult IJspeert et al. (1993) and Williams et al. (1994) for alternatives to Westheimer's formula.

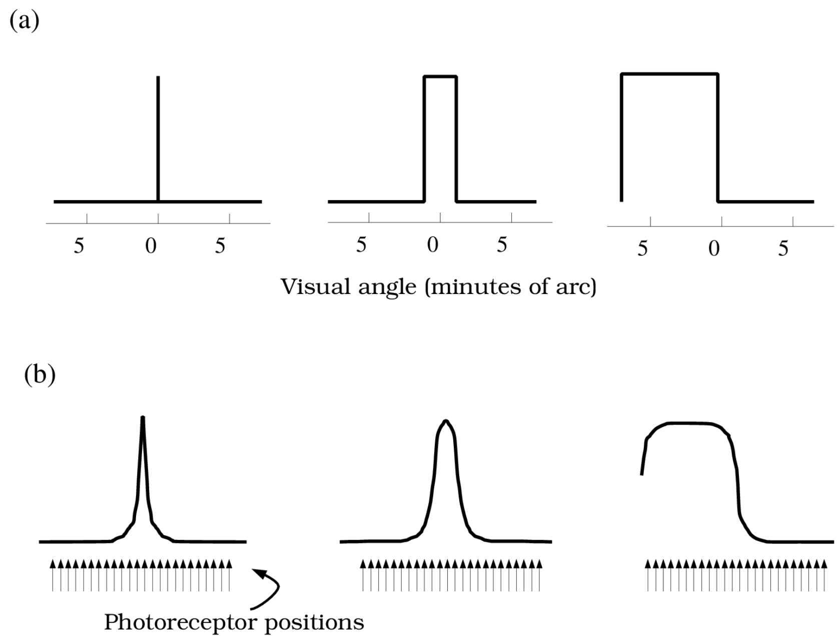

Figure 13: Retinal Images. Examples of the effect of optical blurring. (a) Images of a line, edge and a bar pattern. (b) The estimated retinal image of the images after blurring by Westheimer's linespread function. The spacing of the photoreceptors in the retina is shown by the stylized arrows.

function of spatial position. When we corrected for double passage through the optics, however, we also considered a hypothetical experiment in which the stimuli were harmonic functions (cosinusoids). To perform this calculation, we found that it was easier to correct for double passage by thinking of the stimuli as the sum of harmonic functions, rather than as a function of spatial position.

These two ways of looking at the system, in terms of spatial functions or sums of harmonic functions, are equivalent to one another. To see this, notice that we can use the linespread function to derive the retinal image to any input image. Hence, we can use the linespread to compute the scale factors of the harmonic functions. Conversely, we already saw that by measuring how the system responds to the harmonic functions, we can derive the linespread function. It is convenient to be able to reason about system performance in both ways.

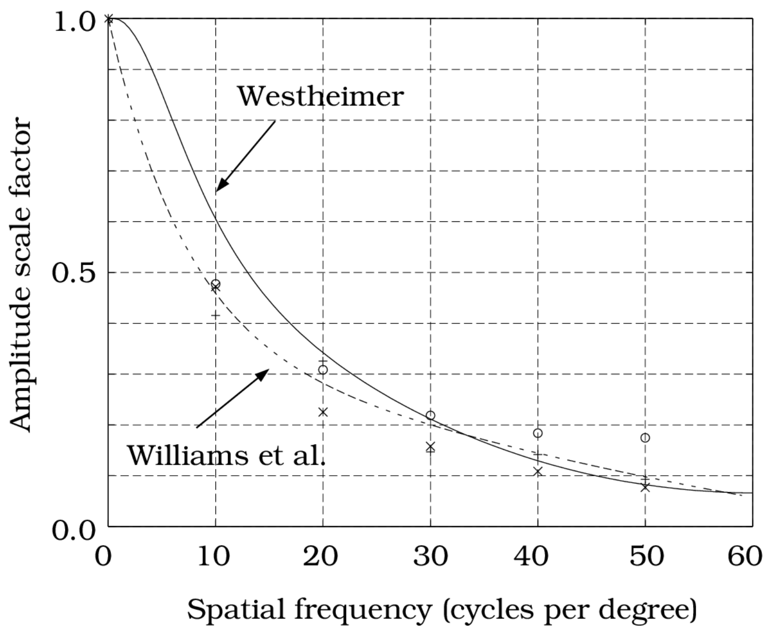

Figure 14: Modulation transfer function measurements of the optical quality of the lens made using visual interferometry (Williams et al. (1994); described in Chapter). The data are compared with the predictions from the linespread suggested by Westheimer (1986) and a curve fit through the data by Williams et al. (1994).

The *optical transfer function* defines the system's complete response to harmonic functions. The optical transfer function is a complex-valued function of spatial frequency. The complex values code both the scale factor and the phase shift the system induces in each harmonic function.

When the linespread function of the eye is an even-symmetric function, there is no phase shift of the harmonic functions. In this case, we can describe the system completely using a real valued function, the *modulation transfer function*. This function defines the scale factors applied to each spatial frequency. The data points in Figure 14 show measurements of the modulation transfer function of the human eye. These data points were measured using a method called *visual interferometry* that is described in Chapter . Along with the data points in Figure 14, I have plotted the predicted modulation transfer function using Westheimer's linespread function and a curve fit to the data by Williams et al. (1994). The curve derived by Westheimer (1986) using completely different data sets differs from the measurements by Williams et al. (1994) by no more than about twenty percent. This should tell you something about the relative precision of these descriptions of the optical quality of the lens.

The linespread function and the modulation transfer function offer us two different ways to think about the optical quality of the lines. The linespread function in Figure 14, describes defocus as the spread of light from a fine slit across the photoreceptors: the light is spread across three to five photoreceptors. The modulation transfer function in Figure 14 describes defocus as an amplitude reduction of harmonic stimuli: beyond 12 cycles per degree the amplitude is reduced by more than a factor of two.

Lenses, Diffraction and Aberrations

Lenses and Accommodation

What prevents the optics of our eye from focusing the image perfectly? To answer this question we should consider why a lens is useful in bringing objects to focus at all.

As a ray of light is reflected from an object, it will travel along along a straight line until it reaches a new material boundary. At that point, the ray may be either absorbed by the new medium, reflected, or refracted. The latter two possibilities are illustrated in part (a) of Figure 15. We call the angle between the incident ray of light and the perpendicular to the surface the *angle of incidence*. The angle between the reflected ray and the perpendicular to the surface is called the *angle of reflection*, and it equals the angle of incidence. Of course, reflected light is not useful for image formation at all.

The useful rays for imaging must pass from the first medium into the second. As they pass from between the two media, the ray's direction is *refracted*. The angle between the refracted ray and the perpendicular to the surface is called the *angle of refraction*.

The relationship between the angle of incidence and the angle of refraction was first discovered by a Dutch astronomer and mathematician, Willebrord Snell in 1621. He observed that when ϕ is the angle of incidence, and ϕ' is the angle of refraction, then

$$\frac{\sin \phi}{\sin \phi'} = \frac{\nu'}{\nu} \tag{0.19}$$

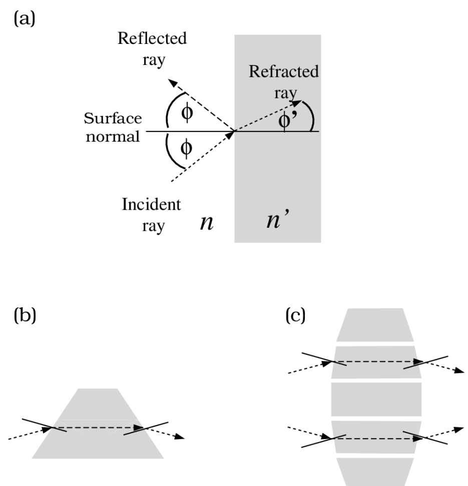

Figure 15: Snell's law. The solid lines indicate surface normals and the dashed lines indicate the light ray. (a) When a light ray passes from one medium to another, the ray can be refracted so that the angle of incidence (phi) does not equal the angle of refraction (phi ‘). Instead, the angle of refraction depends on the refractive indices of the new media (n and n') a relationship called Snell's law that is defined in Equation 0.19 (after Jenkins and White (1937) figures 1H page 15 and 2H page 30.) (b) A prism causes two refractions of the light ray and can reverse the ray's direction from upward to downward. (c) A lens combines the effect of many prisms in order to converge the rays diverging from a point source. (After Jenkins and White (1937) figure 1F, page 12.)

The terms ν' and ν in Equation 0.19 are the *refractive indices* of the two media. The refractive index of an optical medium is the ratio of the speed of light in a vacuum to the speed of light in the optical medium. The refractive index of glass is 1.520, for water the refractive index is 1.333 and for air it is nearly 1.000. The refractive index of the human cornea is 1.376, which is quite similar to water, the main content of our eyes.

Now, consider the consequence of applying Snell's law twice in a row as light passes into and then out of a prism, as illustrated in part (b) of Figure 15. We can draw the path of the ray as it enters the prism using Snell's law. The symmetry of the prism and the reversibility of the light path makes it easy to draw the exit path. Passage through the prism bends the ray's path downward. The prism causes the light to deviate significantly from a straight path; the amount of the deviation depends upon the angle of incidence and the angle between the two sides of the prism.

We can build a lens by smoothly combining many infintesimally small prisms to form a convex lens, as illustrated in part (c) of Figure 15. In constructing such a lens, any deviations from the smooth shape, or imperfections in the material used to build the lens, will cause the individual rays to be brought to focus at slightly different points in the image plane. These small deviations of shape or materials are a source of the imperfections in the image.

Objects at different depths are focused at different distances behind the lens. The *thin lens equation* relates the distance between the source and the lens with the distance between the image and the lens. The thin lens equation relating these two distances depends on the *focal length* of the lens. Call the distance from the center of the lens to the source d_s, the distance to the image d_i, and the focal length of the lens, f. Then the thin lens equation is

$$\frac{1}{d_s} + \frac{1}{d_i} = \frac{1}{f} \tag{0.20}$$

From this equation, notice that we can measure the focal length of a convex thin lens by using it to image a very distant object. In that case, the term $\frac{1}{d_s}$ is zero so that the image distance is equal to the focal length. When I first moved to California, I spent a lot of time measuring the focal length of the lenses in my laboratory by going outside and imaging the sun on a piece of paper behind the lens; the sun was a convenient source at optical infinity. It had been a less reliable source for me in my previous home.

The optical *power* of a lens is a measure of how strongly the lens bends the incoming rays. Since a short focal length lens bends the incident ray more than a long focal length lens, the optical power is inversely related to focal length. The optical power is defined as the reciprocal of the focal length measured in meters and is specified in units of *diopters*. When we view far away objects, the distance from the middle of the cornea and the flexible lens to the retina is 0.017 m. Hence, the optical power of the human eye is $\frac{1}{0.017} = 58.8$, or roughly 60 diopters.

From the optical power of the eye $(1/f)$ and the thin lens equation, we can calculate the image distance of a source at distance. For example, the top curve in Figure 16 shows the relationship

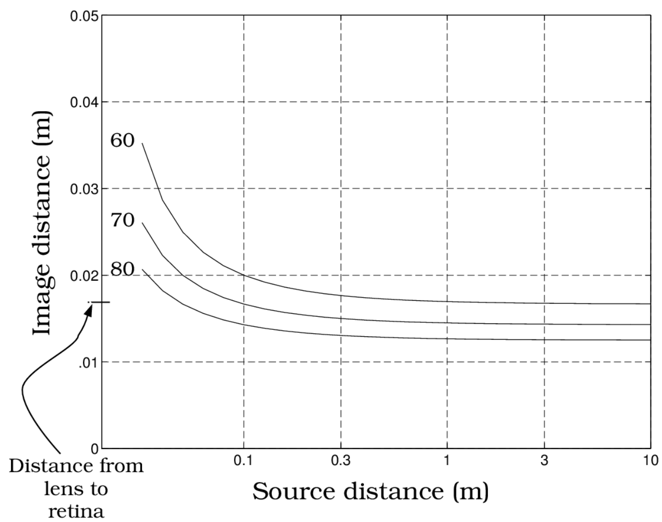

Figure 16: Depth of Field in the Human Eye. Image distance is shown as a function of source distance. The bar on the vertical axis shows the distance of the retina from the lens center. A lens power of 60 diopters brings distant objects into focus, but not nearby objects; to bring nearby objects into focus the power of the lens must increase. The depth of field, namely the distance over which objects will continue to be in reasonable focus, can be estimated from the slope of the curve.

between image distance d_i and source distance d_s for a 60 diopter lens. Sources beyond 1.0m are imaged at essentially the same distance behind the optics. Sources closer than 1.0m are imaged at a longer distance, so that the retinal image is blurred.

To bring nearby sources into focus on the retina, muscles attached to the lens change its shape and thus change the power of the lens. The bottom two curves in Figure 16 illustrate that sources closer than 1.0m can be focused onto the retina by increasing the power of the lens. The process of adjusting the focal length of the lens is called *accommodation*. You can see the effect of accommodation by first focusing on your finger placed near your noise and noticing that objects in the distance appear blurred. Then, while leaving your finger in place, focus on the distant objects. You will notice that your finger now appears blurred.

Pinhole Optics and Diffraction

The only way to remove lens imperfections completely is to remove the lens. It is possible to focus images without any lens at all by using *pinhole* optics, as illustrated in Figure 17.

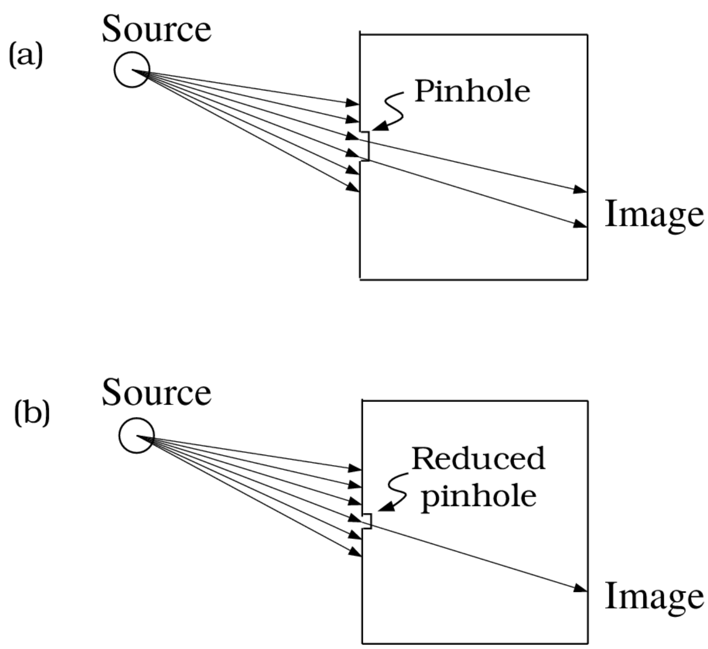

Figure 17: Pinhole Optics. Using ray-tracing, we see that only a small pencil of rays passes through a pinhole. (a) If we widen the pinhole, light from the source spread across the image, making it blurry. (b) If we narrow the pinhole, only a small amount of light is let in. The image is sharp; the sharpness is limited by diffraction.

A pinhole serves as a useful focusing element because only the rays passing within a narrow angle are used to form the image. As the pinhole is made smaller, the angular deviation is reduced. Reducing the size of the pinhole serves to reduce the amount of blur due to the deviation amongst the rays. Another advantage of using pinhole optics is that no matter how distant the source point is from the pinhole, the source is rendered in sharp focus. Since the focusing is due to selecting out a thin pencil of rays, the distance of the point from the pinhole is irrelevant and accommodation is unnecessary.

But the pinhole design has two disadvantages. First, as the pinhole aperture is reduced, less and less of the light emitted from the source is used to form the image. The reduction of signal has many disadvantages for sensitivity and acuity.

A second fundamental limit to the pinhole design is a physical phenomenon. When light passes through a small aperture, or near the edge of an aperture, the rays do not travel in a single straight line. Instead, the light from a single ray is scattered into many directions and produces a blurry image. The dispersion of light rays that pass by an edge or narrow aperture is called *diffraction*. Diffraction scatters the rays coming from a small source across the retinal image and therefore serves to defocus the image. The effect of diffraction when we take an image using pinhole optics is shown in Figure 18.

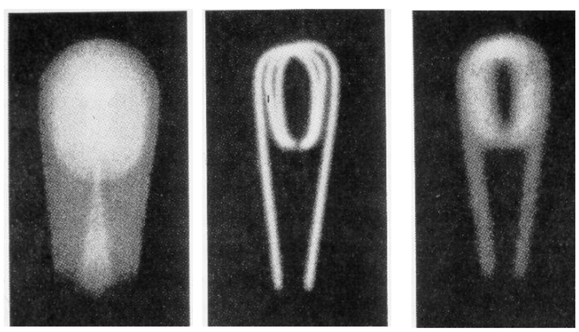

Figure 18: Diffraction limits the quality of pinhole optics. The three images of a bulb filament were imaged using pinholes with decreasing size. (a) When the pinhole is relatively large, the image rays are not properly converged and the image is blurred. (b) Reducing the pinhole improves the focus. (c) Reducing the pinhole further worsens the focus due to diffraction.

Diffraction can be explained in two different ways. First, diffraction can be explained by thinking of light as a wave phenomenon. A wave exiting from a small aperture expands in all directions; a pair of coherent waves from adjacent apertures create an interference pattern. Second diffraction can be understood in terms of quantum mechanics; indeed, the explanation of diffraction is one of the important achievements of quantum mechanics. Quantum mechanics supposes that there are limits to how well we may know both the position and direction of travel of a photon of light. The more we know about a photon's position, the less we can know about its direction. If we know that a photon has passed through a small aperture, then we know something about the photon's position and we must pay a price in terms of our uncertainty concerning its direction of travel. As the aperture becomes smaller, our certainty concerning the position of the photon becomes greater; this uncertainty takes the form of the scattering of the direction of travel of the photons as they pass through the aperture. For very small apertures, for which our position certainty is high, the photon's direction of travel is very broad producing a very blurry image.

There is a close relationship between the uncertainty in the direction of travel and the shape of the aperture (Figure 19). In all cases, however, when the aperture is relatively large, our knowledge of the spatial position of the photons is insignificant and diffraction does not contribute to defocus. As the pupil size decreases, and we know more about the position of the photons, the diffraction pattern becomes broader and spoils the focus.

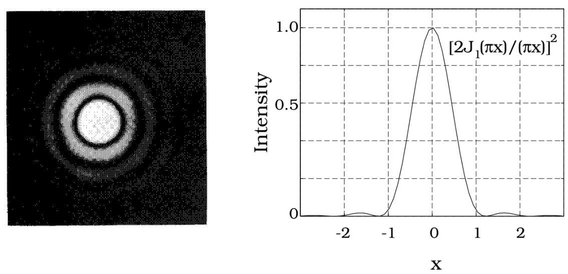

Figure 19: Diffraction: Diffraction pattern caused by a circular aperture. (a) The image of a diffraction pattern measured through a circular aperture. (b) A graph of the cross-sectional intensity of the diffraction pattern. (After Goodman (1968)).

In the human eye diffraction occurs because light must pass through the circular aperture defined by the pupil. When the ambient light intensity is high, the pupil may become as small as 2 mm in diameter. For a pupil opening this small, the optical blurring in the human eye is due only to the small region of the cornea and lens near the center of our visual field. With this small an opening of the pupil, the quality of the cornea and lens is rather good and the main source of image blur is diffraction. At low light intensities, the pupil diameter is as large as 8 mm. When the pupil is open quite wide, the distortion due to cornea and lens imperfections is large compared to the defocus due to diffraction.

One way to evaluate the quality of the optics is to compare the blurring of the eye to the blurring from diffraction alone. The dashed lines in Figure 6 plot the blurring expected from diffraction for different pupil widths. Notice that when the pupil is 2.4~mm, the observed linespread is about equal to the amount expected by diffraction alone; the lens causes no further distortion. As the pupil opens, the observed linespread is worse than the blurring expected by diffraction alone. For these pupil sizes the defocus is due mainly to imperfections in the optics[3].

[3]Helmholtz calculated that this was so long before any precise measurements of the optical quality of the eye were possible. He wrote, "The limit of the visual capacity of the eye as imposed by diffraction, as far as it can be calculated, is attained by the visual acuity of the normal eye with a pupil of the size corresponding to a good illumination." From Helmholtz, Phys. Optics I, page 442 (Helmholtz (1866/1911), p. 442).

The Pointspread Function and Astigmatism

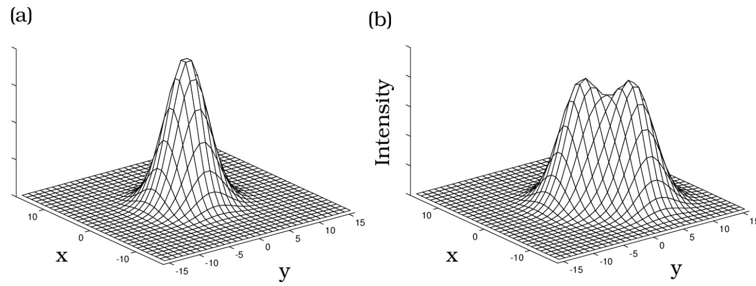

Figure 20: Pointspread Function: A pointspread function. (a) and the sum of two pointspreads (b). The pointspread function is the image created by a source consisting of a small point of light. When the optics shift-invariant, the image to any stimulus can be predicted from the pointspread function.

Most images, of course, are not composed of weighted sums of lines. The set of images that can be formed from sums of lines oriented in the same direction are all one-dimensional patterns. To create more complex images, we must either use lines with different orientations or use a different fundamental stimulus: the point.

Any two-dimensional image can be described as the sum of a set of points. If the system we are studying is linear and shift-invariant, we can use the response to a point and the principle of superposition to predict the response of a system to any two-dimensional image. The measured response to a point input is called the *pointspread*}* function. A pointspread function and the superposition of two nearby pointspreads are illustrated in Figure 20.

Since lines can be formed by adding together many different points, we can compute the system's linespread function from the pointspread. In general, we cannot deduce the pointspread function from the linespread because there is no way to add a set of lines, all oriented in the same direction, to form a point. If it is know that a pointspread function is circularly symmetric, however, a unique pointspread function can be deduced from the linespread function. The calculation is described in the beginning of Goodman (1968) and in Yellott et al. (1984).

When the pointspread functions is not circularly symmetric, measurements of the linespread function will vary with the orientation of the test line (Figure 21). It may be possible to adjust the accommodation of this type of system so that any single orientation is in good focus, but it will be impossible to bring all orientations into good focus at the same time. For the human eye, astigmatism can usually be modeled by describing the defocus as being derived from the contributions of two one-dimensional systems at right angles to one another. The defocus in intermediate angles can be predicted from the defocus of these two systems.

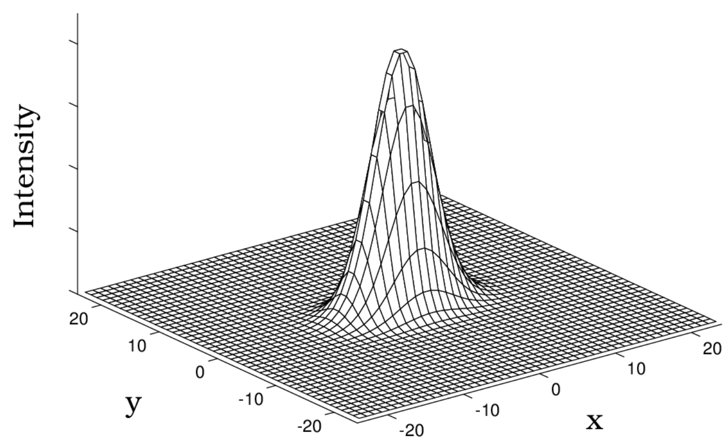

Figure 21: Astigmatism: Astigmatism implies an asymmetric pointspread function. The pointspread shown here is narrow in one direction and wide in another. The spatial resolution of an astigmatic system is better in the narrow direction than the wide direction.

Chromatic Aberration

The light incident at the eye is usually a mixture of different wavelengths. When we measure the system response, there is no guarantee that the linespread or pointspread function we measure with different wavelengths will be the same. Indeed, for most biological eyes the pointspread function is very different as we measure using different wavelengths of light. When the pointspread function of different wavelengths of light is quite different, then the lens is said to exhibit *chromatic aberration*.

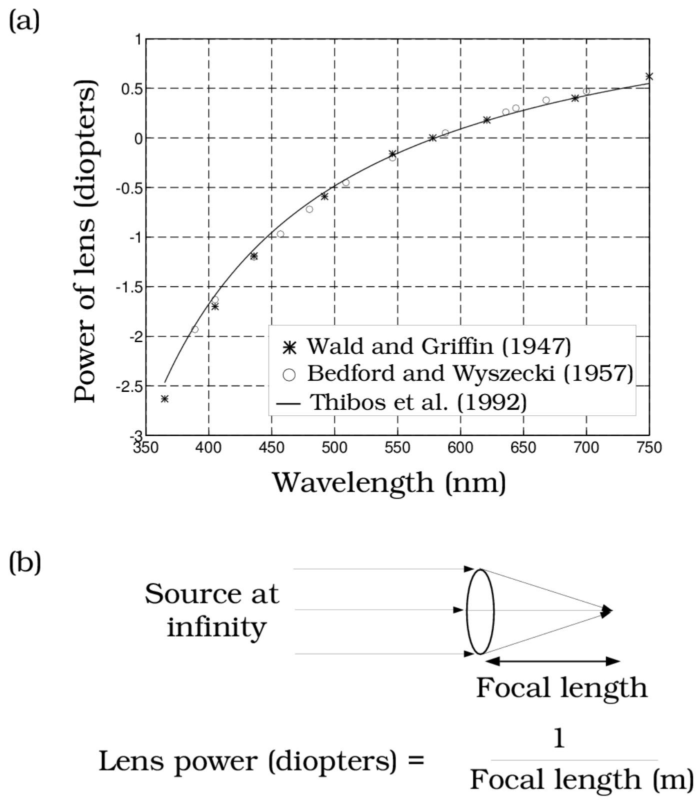

Figure 22: Chromatic Aberration: Chromatic aberration of the human eye. (a) The data points are from Wald and Griffin (1947), and Bedford and Wyszecki (1957). The smooth curve plots the formula used by Thibos et al. (1992), D( ) = p − q / (− c) where is wavelength in micrometers, D( ) is the defocus in diopters, p =1.7312, q = 0.63346, and c = 0.21410. This formula implies an in-focus wavelength of 578 nm. (b) The power of a thin lens is the reciprocal of its focal length, which is the image distance from a source at infinity. (After Marimont and Wandell (1992)).

When the incident light is the mixture of many different wavelengths, say white light, then we can see a chromatic fringe at edges. The fringe occurs because the different wavelength components of the white light are focused more or less sharply. Figure 22 a plots one measure of the chromatic aberration. The smooth curve plots the lens power, measured in units of *em diopters* needed to bring each wavelength into focus along with a 578nm light.

Figure 22 shows the optical power of a lens necessary to correct for the chromatic aberration of the eye. When the various wavelengths pass through the correcting lens, the optics will have the same power as the eye's optics at 578nm. The two sets of measurements agree well with one another and are similar to what would be expected if the eye were simply a bowl of water. The smooth curve through the data is a curve used by Thibos et al. (1992) to predict the data.

An alternative method of representing the axial chromatic aberration of the eye is to plot the modulation transfer function at different wavelengths. The two surface plots in Figure 23 shows the modulation transfer function at a series of wavelengths. The plots show the same data, but seen from different points of view so that you can see around the hill. The calculation in the figure is based on an eye with a pupil diameter of 3.0mm, the same chromatic aberration as the human eye, and in perfect focus except for diffraction at 580nm.

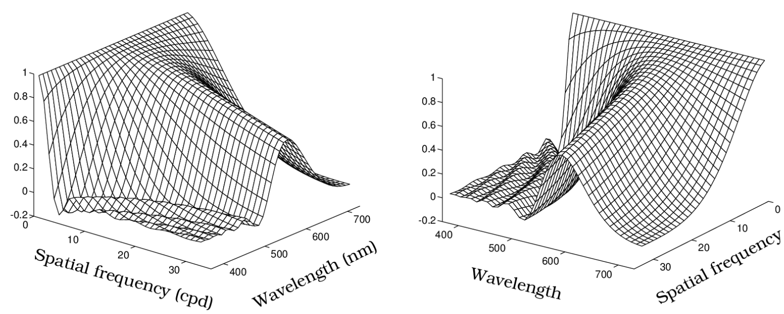

Figure 23: OTF of Chromatic Aberration: Two views of the modulation transfer function of a model eye at various wavelengths. The model eye has the same chromatic aberration as the human eye (Figure 22) and a 3.0mm pupil diameter. The eye is in focus at 580nm; the curve at 580nm is diffraction limited. The retinal image has no contrast beyond four cycles per degree at short wavelengths.(From Marimont and Wandell (1993)).

The retinal image contains very poor spatial information at wavelengths that are far from the best plane of focus. By accommodation, the human eye can place any wavelength into good focus, but it is impossible to focus all wavelengths simultaneously[4].

[4] A possible method of improving the spatial resolution of the eye to different wavelengths of light is to place the different classes of photoreceptors in slightly different image planes. Ahnelt et al. (1987) and Curcio et al. (1991) have observed that the short-wavelength photoreceptors have a slightly different shape and length from the middle- and long-wavelength photoreceptors. In principle, this difference could play a role to compensate for the chromatic aberration of the eye. But, the difference is very small, and it is unlikely that it plays any significant role in correcting for axial chromatic aberration.

The Photoreceptor Mosaic

In Chapter we reviewed Campbell and Gubisch (1966) measurements of the optical linespread function. Their data are presented in Figure 6, as smooth curves, but the actual measurements must have taken place at a series of finely spaced intervals called sample points. In designing their experiment, Campbell and Gubisch must have considered carefully how to space their sample points because they wanted to space their measurement samples only finely enough to capture the intensity variations in the measurement plane. Had they positioned their samples too widely, then they would have missed significant variations in the data. On the other hand, spacing the sample positions too closely would have made the measurement process wasteful of time and resources.

Just as Campbell and Gubisch sampled their linespread measurements, so too the retinal image is sampled by the nervous system. Since only those portions of the retinal image that stimulate the visual photoreceptors can influence vision, the sample positions are determined by the positions of the photoreceptors. If the photoreceptors are spaced too widely, the image encoding will miss significant variation present in the retinal image. On the other hand, if the photoreceptors are spaced very close to one another compared to the spatial variation that is possible given the inevitable optical blurring, then the image encoding will be redundant, using more neurons than necessary to do the job. In this chapter we will consider how the spatial arrangement of the photoreceptors, called the photoreceptor mosaic, limits our ability to infer the spatial pattern of light intensity present in the retinal image.

We will consider separately the photoreceptor mosaics of each of the different types of photoreceptors. There are two fundamentally different types of photoreceptors in our eye, the rods and the cones. There are approximately 5 million cones and 100 million rods in each eye. The positions of these two types of photoreceptors differ in many ways across the retina. Figure 1 shows how the relative densities of cone photoreceptors and rod photoreceptors vary across the retina.

The rods initiate vision under low illumination levels, called scotopic light levels, while the cones initiate vision under higher, photopic light levels. The range of intensities in which both rods and cones can initiate vision is called mesopic intensity levels. At most wavelengths of light, the cones are less sensitive to light than the rods. This sensitivity difference, coupled with the fact that there are no rods in the fovea, explains why we can not see very dim sources, such as weak starlight, when we fixate our fovea directly on them. These sources are too dim to be visible through the all cone fovea. The dim source only becomes visible when it is placed in the periphery and be detected by the rods. Rods are very sensitive light detectors: they

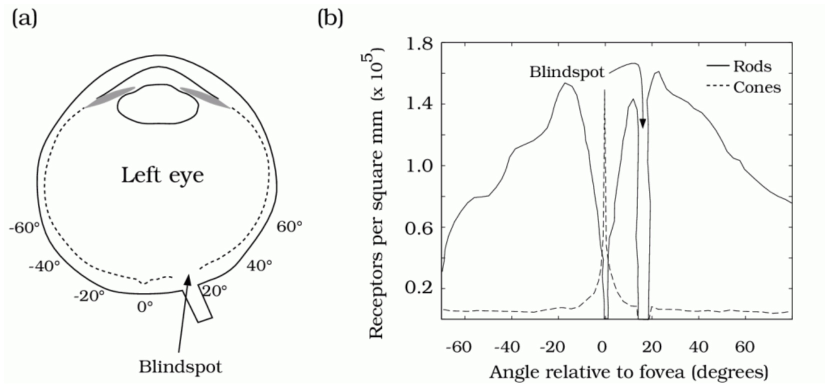

Figure 1: The distribution of rod and cone photorceptors across the human retina. (a) The density of the receptors is shown in degrees of visual angle relative to the position of the fovea for the left eye. (b) The cone receptors are concentrated in the fovea. The rod photoreceptors are absent from the fovea and reach their highest density 10 to 20 degrees peripheral to the fovea. No photoreceptors are present in the blindspot.

generate a detectable photocurrent response when they absorb a single photon of light (Hecht et al. (1942); Schwartz (1977); Baylor (1987)).

The region of highest visual acuity in the human retina is the *fovea*. As Figure 1 shows, the fovea contains no rods, but it does contain the highest concentration of cones. There are approximately 50,000 cones in the human fovea. Since there are no photoreceptors at the optic disk, where the ganglion cell axons exit the retina, there is a blindspot in that region of the retina Chapter .

Figure 2 shows schematics of a mammalian rod and a cone photoreceptor. Light imaged by the cornea and lens is shown entering the receptors through the *inner segments*. The light passes into the *outer segment* which contain light absorbing *photopigments*. As light passes from the inner to the outer segment of the photoreceptor, it will either be absorbed by one of the photopigment molecules in the outer segment or it will simply continue through the photoreceptor and exit out the other side. Some light imaged by the optics will pass between the photoreceptors. Overall, less than ten percent of the light entering the eye is absorbed by the photoreceptor photopigments (Baylor (1987)).

The rod photoreceptors contain a photopigment called rhodopsin. The rods are small, there are many of them, and they sample the retinal image very finely. Yet, visual acuity under scotopic viewing conditions is very poor compared to visual acuity under photopic conditions. The reason for this is that the signals from many rods converge onto a single neuron within the retina, so that there is a many-to-one relationship between rod receptors and neurons in the optic nerve fibers. The density of rods and the convergence of their signals onto single neurons improves the sensitivity of rod-initiated vision. Hence, rod-initiated vision does not resolve fine spatial detail.

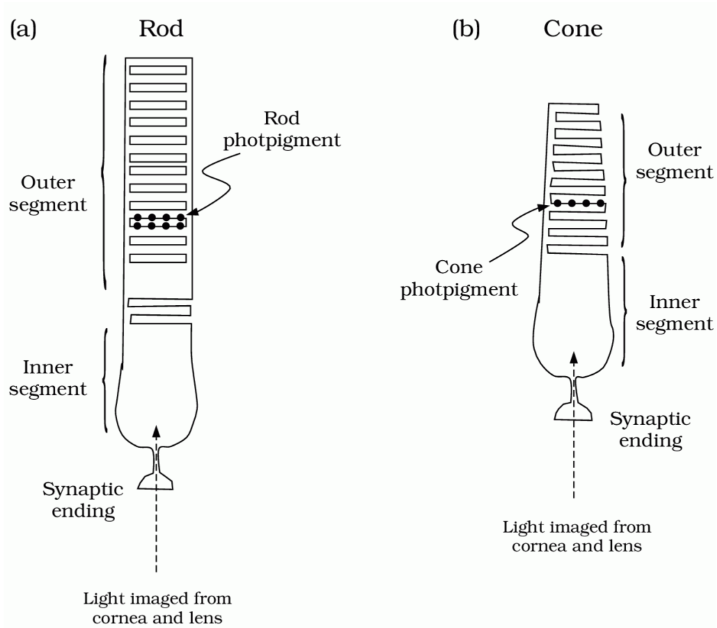

Figure 2: Mammalian rod and cone photoreceptors contain the light absorbing pigment that initiates vision. Light enters the photoreceptors through the inner segment and is funneled to the outer segment that contains the photopigment. (After Baylor (1987))

The foveal cone signals do not converge onto single neurons. Instead, several neurons encode the signal from each cone, so that there is a one-to-many relationship between the foveal cones and optic tract neurons. The dense representation of the foveal cones suggests that the spatial sampling of the cones must be an important aspect of the visual encoding.

There are three types of cone photoreceptors within the human retina. Each cone can be classified based on the wavelength sensitivity of the photopigment in its outer segment. Estimates of the spectral sensitivity of the three types of cone photoreceptors are shown in Figure 3. These curves are measured from the cornea, so they include light loss due to the cornea, lens and inert materials of the eye. In the next chapter we will study how color vision depends upon the differences in wavelength selectivity of the three types of cones. Throughout this book I will refer to the three types of photoreceptors as the L, M and S cones.

(The letters refer to **L**ong-wavelength, **M**iddle-wavelength and **S**hort-wavelength peak sensitivity.)

Because light is absorbed after passing through the inner segment, the position of the inner segment determines the spatial sampling position of the photoreceptor. Figure 4 shows cross-sections of the human cone photoreceptors at the level of the inner segment in the human fovea (part a) and just outside the fovea (part b). In the fovea, cross-section shows that the inner segments are very tightly packed and form a regular sampling array. A cross-section

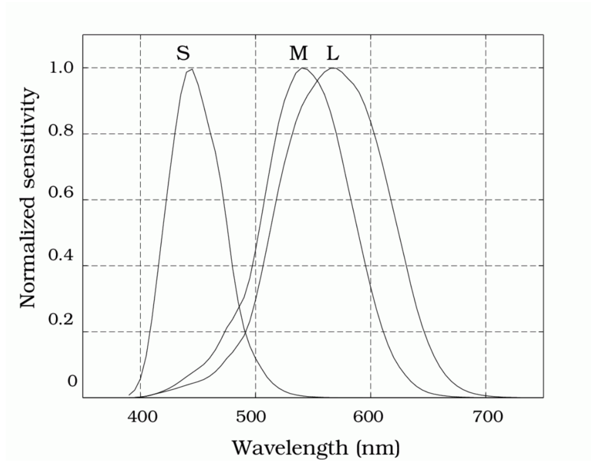

Figure 3: Spectral sensitivities of the L, M and S cones in the human eye. The measurements are based on a light source at the cornea, so that the wavelength loss due to the cornea, lens and other inert pigments of the eye play a role in determining the sensitivity. (Source: Stockman et al. (1993)).

just outside the fovea shows that the rod photoreceptors fill the spaces between the cones and disrupt the regular packing arrangement. The scale bar represents 10 μm; the cone photoreceptor inner segments in the fovea are approximately 2.3 μm wide with a minimum center to center spacing of about 2.5 μm. Figure 4 (c) shows plots of the cone densities from several different human retinae as a function of the distance from the foveal center. The cone density varies across individuals.

Units of Visual Angle

We can convert these cone sizes and separations into degrees of visual angle as follows. The distance from the effective center of of the eye's optics to the retina is 1.7×10^{-2} m (17 mm). We compute the visual angle spanned by one cone, ϕ, from the trigonometric relationship in Figure 5: the tangent of an angle in a right triangle is equal to the ratio of the lengths of the sides opposite and adjacent to the angle. This leads to the following equation:

$$\tan(\phi) = \frac{2.5 \times 10^{-6}\ \text{m}}{1.7 \times 10^{-2}\ \text{m}} = 1.47 \times 10^{-4} \tag{0.1}$$

The width of a cone in degrees of visual angle, ϕ, is approximately 0.0084 degrees, or roughly one-half minute of visual angle. In the center of the eye, then, where the photoreceptors are packed densely, the cone photoreceptors are tightly packed and their centers are separated by one-half minute of visual angle.

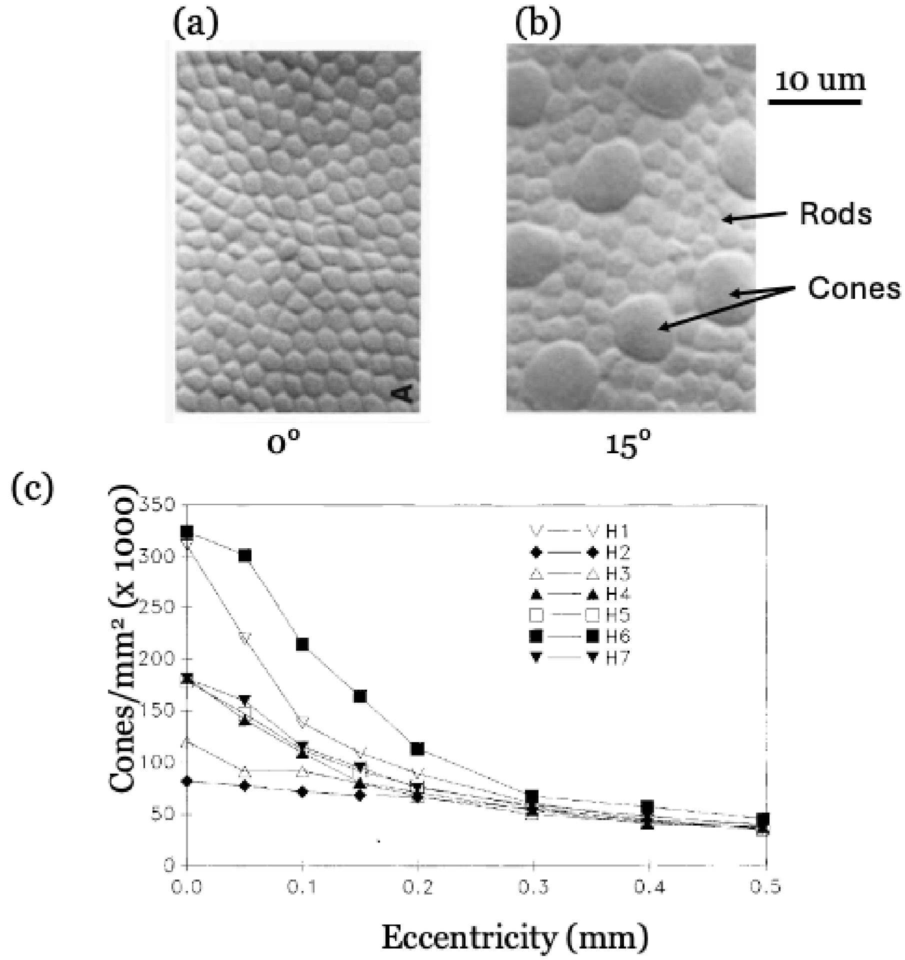

Figure 4: Photoreceptor Sampling: The spatial mosaic of the human cones. A cross-section of the human retina at the level of the inner segments. Cones in the fovea (a) are smaller than cones in the periphery (b). As the separation between cones grows, the rod receptors fill in the spaces. (c) The cone density varies with distance from the fovea. Cone density is plotted as a function of eccentricity for seven human retinae (After Curcio and Allen (1990)).

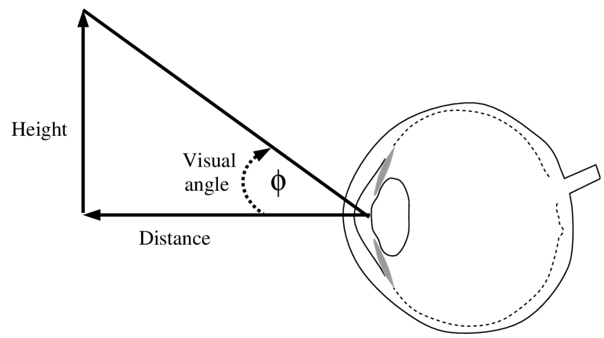

Figure 5: Calculating Viewing Angle: By trigonometry, the tangent of the viewing angle, ϕ, is equal to the ratio of height to distance in the right triangle shown. Therefore, ϕ is the inverse tangent of that ratio (Equation 0.1).

The S Cone Mosaic

Behavioral Measurements

Just as the rods and cones have different spatial sampling distributions, so too the three types of cone photoreceptors have different spatial sampling distributions. The sampling distribution of the short-wavelength cones was the first to be measured empirically, and it has been measured both with behavioral and physiological methods. The behavioral experiments were carried out as part of D. Williams dissertation at the University of California in San Diego. Williams et al. (1981) took advantage of several features of the short-wavelength photoreceptors. As background to their work, we first describe several features of the photoreceptors.

The photopigment in the short-wavelength photoreceptors is significantly different from the photopigment in the other two types of photoreceptors. Notice that the wavelength sensitivity of the L and M photopigments are very nearly the same (Figure 3). The sensitivity of the S photopigment is significantly higher in the short-wavelength part of the spectrum than the sensitivity of the other two photopigments. As a result, if we present the visual system with a very weak light, containing energy only in the short-wavelength portion of the spectrum, the S cones will absorb relatively more quanta than the other two classes. Indeed, the discrepancy in the absorptions is so large that it is reasonable to suppose that when short-wavelength light is barely visible, at detection threshold, perception is initiated uniquely from a signal that originates in the short-wavelength receptors.

We can give the short-wavelength receptors an even greater sensitivity advantage by presenting a blue test target on a steady yellow background. As we will discuss in later chapters, steady backgrounds suppress visual sensitivity. By using a yellow background, we can suppress the sensitivity of the L and M cones and the rods and yet spare the sensitivity of the S cones. This improves the relative sensitivity advantage of the short-wavelength receptors in detecting the short-wavelength test light. It is reasonable to suppose that when short-wavelength light is barely visible, at detection threshold, perception is initiated uniquely from a signal that originates in the short-wavelength receptors.

During the experiment, the subjects visually fixated on a small mark. They were then presented with short-wavelength test lights that were likely to be seen with a signal initiated by the S cones. After the eye was perfectly fixated, the subject pressed a button and initiated a stimulus presentation. The test stimulus was a tiny point of light, presented very briefly (10 ms). The test light was presented at different points in the visual field. If light from the short-wavelength test fell upon a region that contained S cones, sensitivity should be relatively high. On the other hand, if that region of the retina contained no S cones, sensitivity should be rather low. Hence, from the spatial pattern of visual sensitivity, Williams, Hayhoe and Macleod inferred the spacing of the S cones.

The sensitivity measurements are shown in Figure 6. First, notice that in the very center of the visual field, in the central fovea, there is a large valley of low sensitivity. In this region, there appear to be no short-wavelength cones at all. Second, beginning about half a degree from the center of the visual field there are small, punctate spatial regions of high sensitivity. We interpret these results by assuming that these peaks correspond to the positions of this observer's S cones. The gaps in between, where the observer has rather low sensitivity are likely to be patches of L and M cones. Around the central fovea, the typical separation between the inferred S cones is about 8 to 12 minutes of visual angle. Thus, there are five to seven S cones per degree of visual angle.

Biological Measurements

There have been several biological measurements of the short-wavelength cone mosaic, and we can compare these with the behavioral measurements. Marc and Sperling (1977) used a stain that is taken up by cones when they are active. They applied this stain to a baboon retina and then stimulated the retina with short-wavelength light in the hopes of staining only the short-wavelength receptors. They found that only a few cones were stained when the stimulus was a short-wavelength light. The typical separation between the stained cones was about 6 minutes of arc. This value is smaller than the separation that Williams et al. (1981) observed and may be a species-related difference.

Monasterio et al. (1981) discovered that when the dye procion yellow is applied to the retina, the dye is absorbed in the outer segments of all the photoreceptors, but it stains only a small subset of the photoreceptors completely. Figure 7 shows a group of stained photoreceptors in cross-section.

The indirect arguments identifying these special cones as S cones are rather compelling. But, a more certain procedure was developed by C. Curcio and her colleagues. They used a biological marker, developed based on knowledge of the genetic code for the S cone photopigment, to label selectively the S cones in the human retina (Curcio et al. (1991)). Their measurements agree

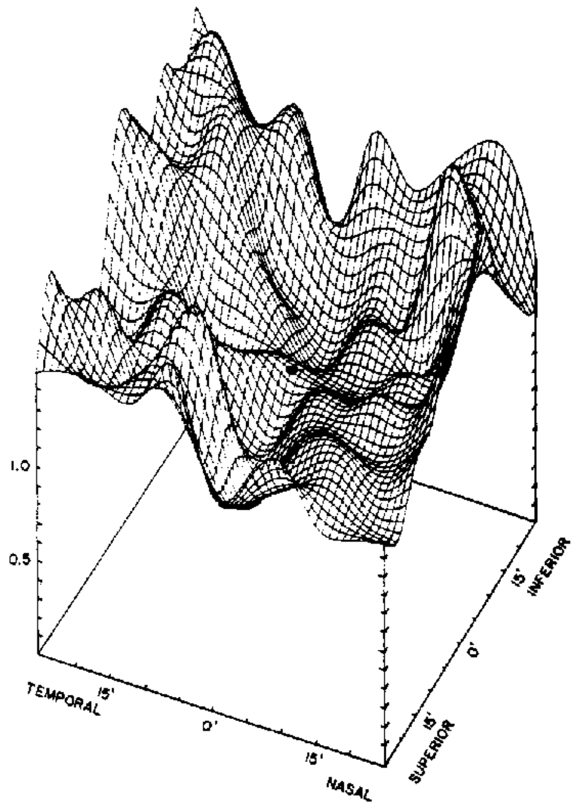

Figure 6: Short-wavelength Cone Mosaic: Psychophysical estimate of the spatial mosaic of the S cones. The height of the surface represents the observer's threshold sensitivity to a short wavelength test light presented on a yellow background. The test was presented at a series of locations spanning a grid around the fovea (black dot). The peaks in sensitivity probably correspond to the positions of the S cones. (From Williams et al. (1981)).

well quantitatively with Williams' psychophysical measurements, namely that the average spacing between the S cones is 10 minutes of visual angle. Curcio and her colleagues could also confirm some early anatomical observations that the size and shape of the S cones differ slightly from the L and M cones. The S cones have a wider inner segment, and they appear to be inserted within an orderly sampling arrangement of their own between the sampling mosaics of the other two cone types (Ahnelt et al. (1987)).

Why are the S cones widely spaced?

The spacing between the S cones is much larger than the spacing between the L and M cones. Why should this be? The large spacing between the S cones is consistent with the strong blurring of the short-wavelength component of the image due to the axial chromatic aberration of the lens. Recall that axial chromatic aberration of the lens blurs the short-wavelength portion of the retinal image, the part S cones are particularly sensitive to, more than the middle- and long-wavelength portion of the image (Figure 22). In fact, under normal viewing conditions the retinal image of a fine line at 450 nm falls to one half its peak intensity nearly 10 minutes of visual angle away from the location of its peak intensity. At that wavelength, the retinal image only contains significant contrast at spatial frequency components below 3 cycles per degree of visual angle. The optical defocus force the wavelength components of the retinal image the S cones encode to vary smoothly across space. Consequently, the S cones can sample the image only six times per degree and still recover the spatial variation passed by the cornea and lens.

Interestingly, the *spatial* defocus of the short-wavelength component of the image also implies that signals initiated by the S cones will vary slowly over *time*. In natural scenes, temporal variation occurs mainly because of movement of the observer or an object. When a sharp boundary moves across a cone position, the light intensity changes rapidly at that point. But, if the boundary is blurred, changing gradually over space, then the light intensity changes more slowly. Since the short-wavelength signal is blurred by the optics, and temporal variation is mainly due to motion of objects, the S cones will generally be coding slower temporal variations than the L and M cones.

At the very earliest stages of vision, we see that the properties of different components of the visual pathway fit smoothly together. The optics set an important limit on visual acuity, and the S cone sampling mosaic can be understood as a consequence of the optical limitations. As we shall see, the L and M cone mosaic densities also make sense in terms of the optical quality of the eye.

This explanation of the S cone mosaic flows from our assumption that visual acuity is the main factor governing the photoreceptor mosaic. For the visual streams initiated by the cones, this is a reasonable assumption. There are other important factors, however, that can play a role in the design of a visual pathway. For example, acuity is not the dominant factor in the visual stream initiated by rod vision. In principle the resolution available in the rod encoding is

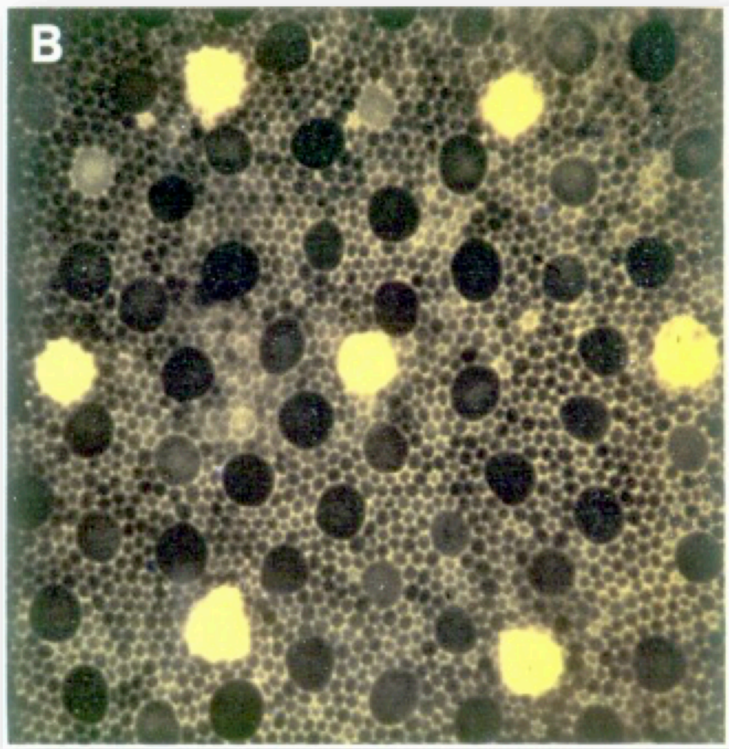

Figure 7: Short-Wavelength Cone Mosaic: Procion Yellow Stains. Biological estimate of the spatial mosaic of the S cones in the macaque retina. A small fraction of the cones absorb the procion yellow stain; these are shown as the dark spots in this image. These cones, thought to be the$S$ cones, are shown in a cross-section through the inner segment layer of the retina. (From Monasterio et al. (1981))

comparable to the acuity available in the cone responses; but, visual acuity using rod-initiated signals is very poor compared to acuity using cone-initiated signals. Hence, we shouldn't think of the rod sampling mosaic in terms of visual acuity. Instead, the high density of the rods and their convergence onto individual neurons suggests that we think of the imperative of rod-initiated vision in terms of improving the signal-to-noise under low light levels. In the rod-initiated signals, the visual system trades visual acuity for an increase in the signal-to-noise ratio. In the earliest stages of the visual pathways, then, we can see structure, function and design criteria coming together.

When we ask why the visual system has a particular property, we need to relate observations from the different disciplines that make up vision science. Questions about anatomy require us to think about the behavior the anatomical structure serves. Similarly, behavior must be explained in terms of algorithms and the anatomical and physiological responses of the visual pathway. By considering the visual pathways from multiple points of view, we piece together a complete picture of how system functions.

Visual Interferometry

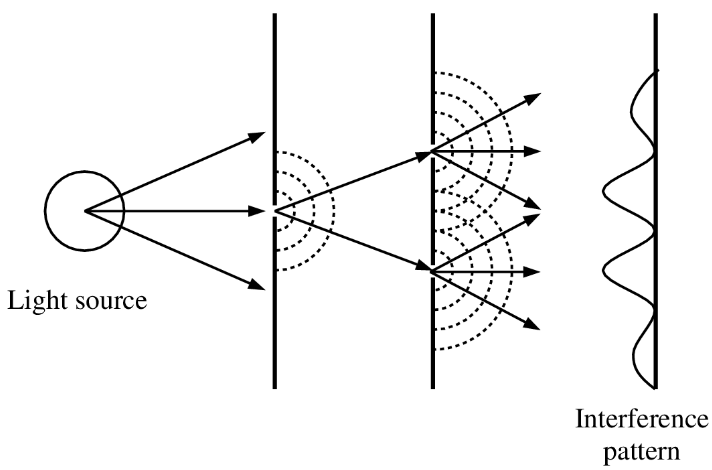

Figure 8: Young's double-slit experiment uses a pair of coherent light sources to create an interference pattern of light. The intensity of the resulting image is nearly sinusoidal, and its spatial frequency depends upon the spacing between the two slits.

Thomas Young, the brilliant scientist, physician, and classicist demonstrated to the Royal Society that when two beams of coherent light generate an image on a surface such as the retinal surface, the resulting image is an interference pattern Young (1804). His experiment is often called the *double-slit* or *double-pinhole* experiment. Using an ordinary light source, Young passed the light through a small pinhole first and then through a pair of slits, as illustrated in Figure 9. In the experiment, the first pinhole serves as the source of light; the double pinholes then pass the light from the common original source. Because they share this common source, light emitted from the double pinholes are in a coherent phase relationship and their wavefronts interfere with one another. This interference results in an image that varies nearly sinusoidally in intensity.

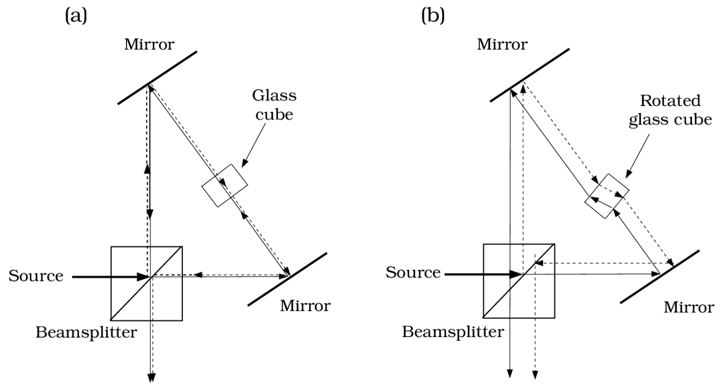

Figure 9: A visual interferometer creates an interference pattern as in Young's double-slit experiment. In the device shown here the original beam is split into two paths shown as the solid and dashed lines. (a) When the glass cube is at right angles to the light path, the two beams traverse an equal path and are imaged at the same point after exiting the interferometer. (b) When the glass is rotated, the two beams traverse slightly different paths causing the images of the two coherent beams to be displaced and thus create an interference pattern. (After Macleod et al. (1992)).

We can also achieve this narrow pinhole effect by using a laser as the original source. The key elements of a visual interferometer used by Macleod et al. (1992) are shown in Figure 9. Light from a laser enters the beamsplitter and is divided into one part that continues along a straight path (solid line) and a second path that is reflected along a path to the right (dashed line). These two beams, originating from a common source, will be the pair of sources to create the interference pattern on the retina.

Light from each beam is reflected from a mirror towards a glass cube. By varying the orientation of the glass cube, the experimenter can vary the path of the two beams. When the glass cube is at right angles to the light path, as is shown in part (a), the beams continue in a straight path along opposite directions and emerge from the beamsplitter at the same position. When the glass cube is rotated, as is shown in part (b), the refraction due to the glass cube symmetrically changes the beam paths; they emerge from the beamsplitter at slightly different locations and act as a pair of point sources. This configuration creates two coherent beams that act like the two slits in Thomas Young's experiment, creating an interference pattern. The amount of rotation of the glass cube controls the separation between the two beams.

Each beam passes through only a very small section of the cornea and lens. The usual optical blurring mechanisms do not interfere with the image formation, since the lens does not serve to converge the light (see the section on lenses in Chapter . Instead, the pattern that is formed depends upon the diffraction due to the restricted spatial region of the light source.

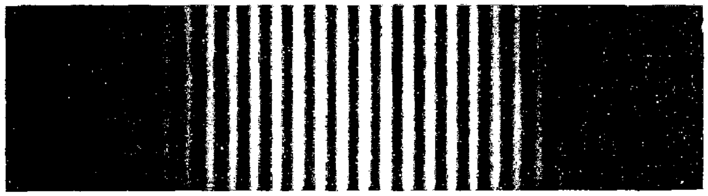

Figure 10: Sinusoidal Interference Pattern. An interference pattern. The image was created using a double-slit apparatus. The intensity of the pattern is nearly sinusoidal. (From Jenkins and White (1937))

We can use diffraction to create retinal images with much higher spatial frequencies than are possible through ordinary optical imaging by the cornea and lens. Figure 10 is an image of a diffraction pattern created by a pair of two slits. The intensity of the pattern is nearly a sinusoidal function of retinal position. The spatial frequency of the retinal image can be controlled by varying the separation between the focal points; the smaller the separation between the slit, the lower the spatial frequency in the interference pattern. Thus, by rotating the glass cube in the interferometer and changing the separation of the two beams we can control the spatial frequency of the retinal image.

Visual interferometry permits us to image fine spatial patterns at much higher contrast than when we image these patterns using ordinary optical methods. For example, Figure 14 shows that a 60 cycles per degree sinusoid cannot exceed 10% contrast when imaged through the optics. Using a visual interferometer, we can present patterns at frequencies considerably higher than 60 cycles per degree at 100% contrast.

However, a challenge remains: the interferometric patterns are not fine lines or points, but rather extended patterns (cosinusoids). Therefore, we cannot use the same logic as Williams et al. and map the receptors by carefully positioning the stimulus. We need to think a little bit more about how to use the cosinusoidal interferometric patterns to infer the structure of the cone mosaic.

Sampling and Aliasing

The most basic observation concerning sampling and aliasing is this: we can measure only that portion of the input signal that falls over the sample positions. Figure 11 shows one-dimensional examples of aliasing and sampling. Parts (a) and (b) contain two different cosinusoidal signals (left) and the locations of the sample points. The values of these two cosinusoids at the sample points are shown by the height of the arrows on the right. Although the two continuous cosinusoids are quite different, they have the same values at the sample positions.

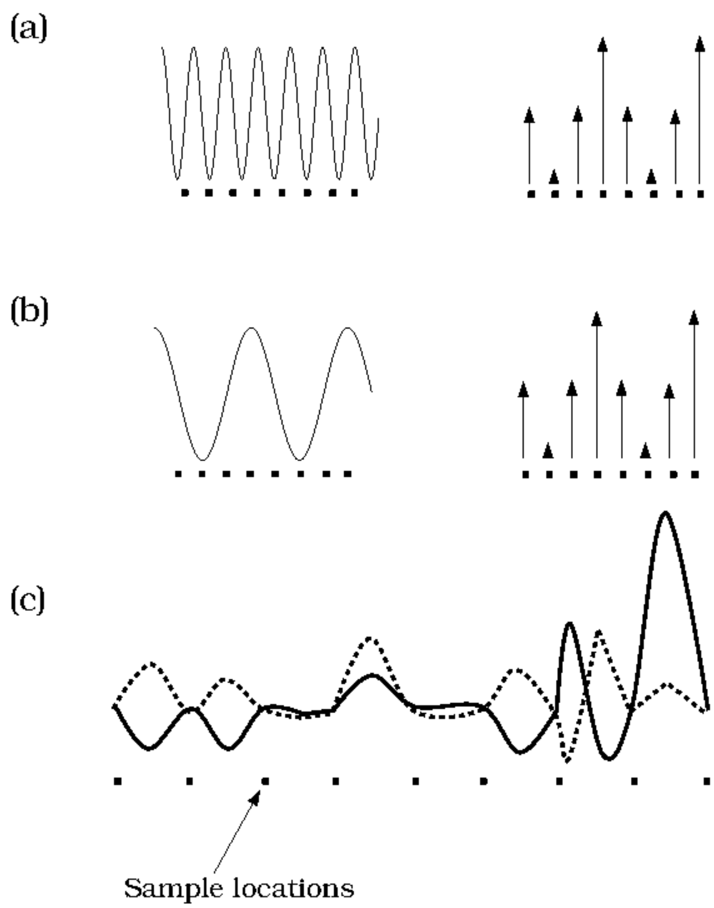

Figure 11: Aliasing of signals results when sampled values are the same but in-between values are not. (a,b) The continuous sinusoids on the left have the same values at the sample positions indicated by the black squares. The values of the two functions at the sample positions are shown by the height of the stylized arrows on the right. (c) Undersampling may cause us to confuse various functions, not just sinusoids. The two curves at the bottom have the same values at the sampled points, differing only in between the sample positions.

Hence, if cones are only present at the sample positions, the cone responses will not distinguish between these two inputs. We say that these two continuous signals are an *aliased* pair. Aliased pairs of signals are indistinguishable after sampling. Hence, sampling degrades our ability to discriminate between sinusoidal signals.

Figure 12 shows that sampling degrades our ability to discriminate between signals in general, not just between sinusoids. Whenever two signals agree at the sample points, their sampled representations agree. The basic phenomenon of aliasing is this: Signals that only differ between the sample points are indistinguishable after sampling.

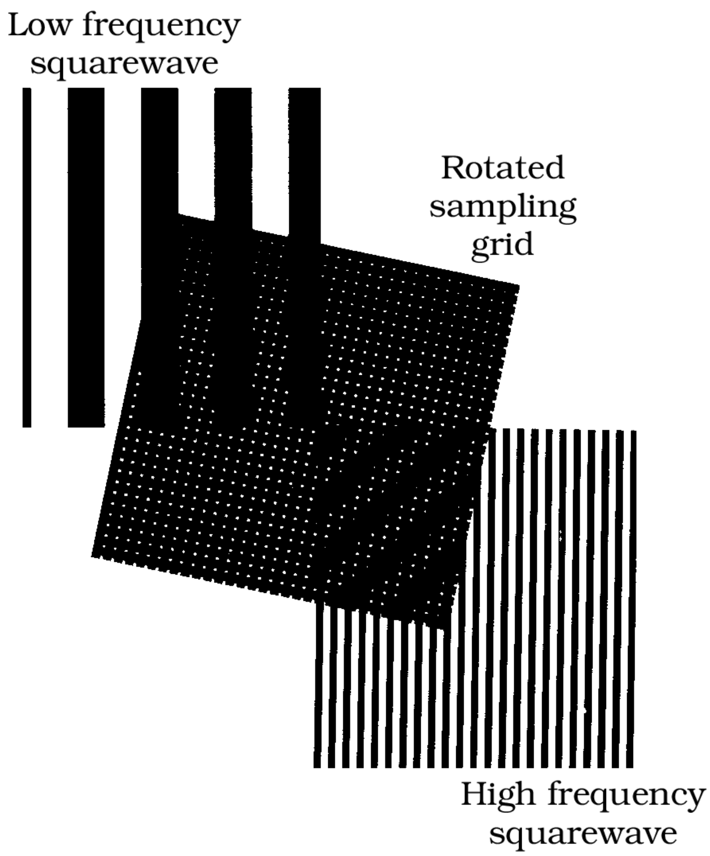

Figure 12: Square-wave aliasing. The squarewave on top is seen accurately through the grid. The squarewave on the bottom is at a higher spatial frequency than the grid sampling. When seen through the grid, the pattern appears at a lower spatial frequency and rotated.

The exercises at the end of this chapter include some computer programs that can help you make sampling demonstrations like the one in Figure 12. If you print out squarewave patterns and various sampling arrays, using the programs provided, you can print various patterns onto overhead transparencies and explore the effects of sampling. Figure 12 shows an example of two squarewave patterns seen through a sampling grid. After sampling, the high frequency pattern appears to be a rotated, low frequency signal.

Sampling is a Linear Operation

The sampling transformation takes the retinal image as input and generates a portion of the retinal image as output. Sampling is a linear operation as the following thought experiment reveals. Suppose we measure the sample values at the cone positions when we present image A; call the intensities at the sample positions $S(A)$. Now, measure the intensities at the sample positions for a second image, B; call the sample intensities $S(B)$. If we add together the two images, the new image, $A + B$, contains the sum of the intensities in the original images. The values picked out by sampling will be the sum of the two sample vectors, $S(A) + S(B)$.

Since sampling is a linear transformation, we can express it as a matrix multiplication. In our simple description, each position in the retinal image either falls within a cone inner segment or not. The sampling matrix consists of N rows representing the N sampled values. Each row is all zero except at the entry corresponding to that row's sampling position, where the value is 1.

Aliasing of harmonic functions

For uniform sampling arrays we have already observed that some pairs of sinusoidal stimuli are aliases of one another (part (a) of Figure 11). We can analyze precisely which pairs of sinusoids form alias pairs using a little bit of algebra. Suppose that the continuous input signal is $\cos(2\pi f x)$. When we sample the stimulus at regular intervals, the output values will be the value of the cosinusoid at those regularly spaced sample points. Suppose that within a single unit of distance there are N sample points, so that our measurements of the stimulus takes place every $1/N$ units. Then the sampled values will be $S_f(k) = \cos\left(2\pi f \frac{k}{N}\right)$. A second cosinusoid, at frequency f' will be an alias if its sample values are equal, that is, if $S_{f'}(k) = S_f(k)$.

With a little trigonometry, we can prove that the sample values for any pair of cosinusoids with frequencies $\frac{N}{2} - f$ and $\frac{N}{2} + f$ will be equal. That is,

$$\cos\left(2\pi\left(\frac{N}{2} + f\right)\frac{k}{N}\right) = \cos\left(2\pi\left(\frac{N}{2} - f\right)\frac{k}{N}\right) \tag{0.2}$$

(To prove this we must use the cosine addition law. The steps in the verification are in Exercise 5 at the end of the chapter.)

The frequency $f = N/2$ is called the *Nyquist frequency* of the uniform sampling array; sometimes it is referred to as the *folding frequency*. Cosinusoidal stimuli whose frequencies differ by equal amounts above and below the Nyquist frequency of a uniform sampling array will have identical sample responses.

Experimental Implications

The aliasing calculations suggest an experimental method to measure the spacing of the cones in the eye. If the cone spacing is uniform, then pairs of stimuli separated by equal amounts above and below the Nyquist frequency should appear indistinguishable. Specifically, a signal $\cos\left(2\pi\left(\frac{N}{2}+f\right)\right)$ that is above the Nyquist frequency will appear the same as the signal $\cos\left(2\pi\left(\frac{N}{2}-f\right)\right)$ that is an equal amount below the Nyquist frequency. Thus, as subjects view interferometric patterns of increasing frequency, as we cross the Nyquist frequency the perceived spatial frequency should begin to decrease even though the physical spatial frequency of the diffraction pattern increases.

Yellott (1982) examined the aliasing prediction in a nice graphical way. He made a sampling grid from Polyak's (Polyak (1957)) anatomical estimate of the cone positions. He simply poked small holes in the paper at the cone positions in one of Polyak's anatomical drawings. We can place any image we like, for example patterns of light and dark bars, behind the grid. The bits of the image that we see are only those that would be seen by the visual system. Any pair of images that differ only in the regions between the holes will be an aliased pair. Yellott introduced the method and proper analysis, but he used the Polyak (1957) data on the outer segment positions rather than on the positions of the inner segments (Miller and Bernard (1983)).

This experiment is relatively straightforward for the **S** cones. Since these cones are separated by about 10 minutes of visual angle, there are about six **S** cones per degree of visual angle. Hence, their Nyquist frequency is 3 cycles per degree of visual angle (cpd). It is possible to correct for chromatic aberration and to present spatial patterns at these low frequencies through the lens. Such experiments confirm the basic predictions that we will see aliased patterns (Williams and Collier (1983)).

The L and M Cone Mosaic

Experiments using a visual interferometer to image a high frequency pattern at high contrast on the retina are a powerful way to analyze the sampling mosaic of L and M cones. But, even before this was technical feat was possible, Helmholtz' (Helmholtz (1866/1911)) noticed that extremely fine patterns, looked at without any special apparatus, can appear wavy. He attributed this observation to sampling by the cone mosaic. His perception of a fine pattern and his graphical explanation of the waviness in terms of cone sampling are shown in part (a) of Figure 13 (boxed drawings).

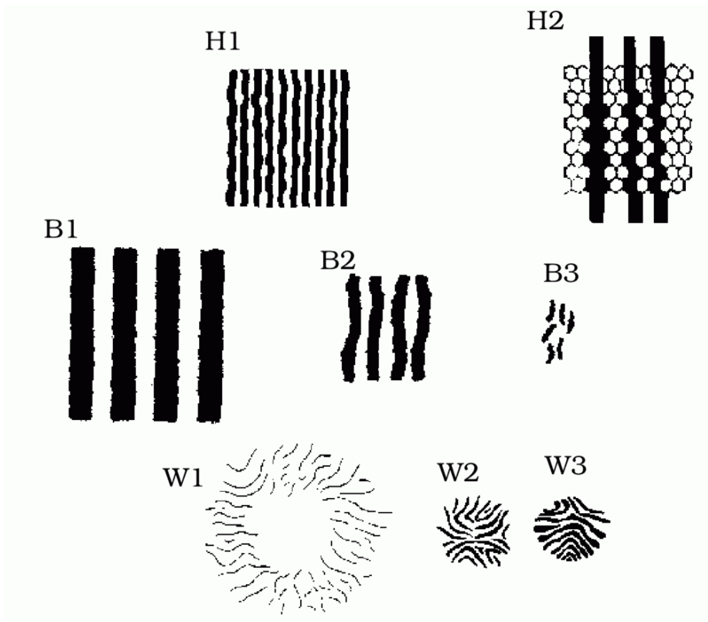

Figure 13: Drawings of perceived aliasing patterns by several different observers. Helmholtz' observed aliasing of fine patterns which he drew in part H1. He offered an explanation of his observations, in terms of cone sampling, in H2 (Helmholtz (1866/1911)). The Byram (1944) drawings of three interference patterns at 40, 85 and 150 cpd are labeled B1, B2, and B3. Drawings W1,W2 and W3 are by subjects in Williams' laboratory who drew their impression of aliasing of an 80 cpd and two patterns at 110 cpd (williams1985b-aliasing)

G. Byram was the first to describe the appearance of high frequency interference gratings (Byram (1944)). His drawings of the appearance of these patterns are shown in part (b) of the figure. The image on the left shows the appearance of a low frequency pattern diffraction pattern. The apparent spatial frequency of this stimulus is faithful to the stimulus. Byram noted that as the spatial frequency increases towards 60 cpd, the pattern still appears to be a set of fine lines, but they are difficult to see (middle drawing). When the pattern significantly exceeds the Nyquist frequency, it becomes visible again but looks like the low-frequency pattern drawn on the right. Further, he reports that the pattern shimmers and is unstable, probably due to the motion of the pattern with respect to the cone mosaic (Byram (1944), Williams (1985a)).

Over the last 10 years D. Williams' group has replicated and extended these measurements using an improved visual interferometer. Their fundamental observations are consistent with both Helmholtz and Byram's reports, but greatly extend and quantify the earlier measurements. The two illustrations on the left of part (c) of Figure 13 show Williams' drawing of 80 cpd and 110 cpd sinusoidal gratings created on the retina using a visual interferometer. The third figure shows an artist's drawing of a 110 cpd grating. The drawing on the left covers a large portion of the visual field, and the appearance of the patterns varies across the visual field. For example, at 80 cpd the observer sees high contrast stripes at some positions, while the field appears uniform in other parts of the field. The appearance varies, but the stimulus itself is quite uniform. The variation in appearance is due to changes in the sampling density of the cone mosaic. Cone sampling density is lower in the periphery than in the central visual field, so aliasing begins at lower spatial frequencies in the periphery than in the central visual field. If we present a stimulus at a high enough spatial frequency we observe aliasing in the central and peripheral visual field, as the drawings of the 110 cpd patterns in Figure 13 show.

There are two extensions of these ideas on aliasing you should consider. First, the cone packing in the fovea occurs in two dimensions, of course, so that we must ask what the appearance of the aliasing will be at different orientations of the sinusoidal stimuli. As the images in Figure 12 show, the orientation of the low frequency alias does not correspond with the orientation of the input. By trying the demonstration yourself and rotating the sampling grid, you will see that the direction of motion of the alias does not correspond with the motion of the input stimulus[1]. These kinds of aliasing confusions have also been reported using visual interferometry (Coletta and Williams (1987)).

Second, our analysis of foveal sampling has been based on some rather strict assumptions concerning the cone mosaic. We have assumed that the cones are all of the same type, that

[1]To describe a general linear receptive field, we must measure the neuron's response using both sinusoidal and cosinusoidal contrast patterns. The receptive fields of retinal ganglion cells can be measured using only cosinusoids centered on the peak because the receptive fields are *even-symmetric*. A function is said to have even symmetry if $f(x) = f(-x)$. A function has *odd symmetry* if $f(x) = -f(-x)$. When a receptive field is even-symmetric, it will have zero response to any odd-symmetric inputs, so we need to measure only the response to even-symmetric inputs. For retinal ganglion cells, then, the contrast sensitivity function is a complete description of the receptive field in this case.

their spacing is perfectly uniform, and that they have very narrow sampling apertures. The general model presented in this chapter can be adapted if any one of these assumptions fails to hold true. As an exercise for yourself, a new analysis with altered assumptions might change the properties of the sampling matrix.

Visual Interferometry: Measurements of Human Optics

There is one last idea you should take away from this chapter: Using interferometry, we can estimate the quality of the optics of the eye.

Suppose we ask an observer to set the contrast of a sinusoidal grating, imaged using normal incoherent light. The observer's sensitivity to the target will depend on the contrast reduction at the optics and the observer's neural sensitivity to the target. Now, suppose that we create the same sinusoidal pattern using an interferometer. The interferometric stimulus bypasses the contrast reduction due to the optics. In this second experiment, then, the observer's sensitivity is limited only by the observer's neural sensitivity. Hence, the sensitivity difference between these two experiments is an estimate of the loss due to the optics.

The visual interferometric method of measuring the quality of the optics has been used on several occasions. While the interferometric estimates are similar to estimates using reflections from the eye, they do differ somewhat. The difference is shown in Abdelhamed et al. (2021), which includes the Westheimer's estimate of the modulation transfer function, created by fitting data from reflections, along with data and a modulation transfer function obtained from interferometric measurements. The current consensus is that the optical modulation transfer function is somewhat closer to the visual interferometric measurements than the reflection measurements. The reasons for the differences are discussed in several papers (e.g. Campbell and Green (1965); Williams (1985b), Williams (1985a); Williams et al. (1994)).

Summary and Discussion

The **S** cones are present at a much lower sampling density, and they are absent in the very center of the fovea. Because they are sparse, we can measure the **S** cone positions behaviorally using small points of light. The behavioral estimates of the **S** cones are also consistent with anatomical estimates of the **S** cone spacing.

The wide spacing of the **S** cones can be understood in terms of the chromatic aberration of the eye. The eye is ordinarily in focus for the middle-wavelength part of the visual spectrum, and there is very little contrast beyond 2-3 cycles per degree in the short-wavelength part of the spectrum. The sparse **S** cone spacing is matched to the poor quality of the retinal image in the short-wavelength portion of the spectrum.

The **L** and **M** cones are tightly packed in the central fovea, forming a triangular grid that efficiently samples the retinal image. Ordinarily, optical defocus protects us from aliasing in the fovea. Once aliasing between two signals occurs, the confusion cannot be undone. The two signals have created precisely the same spatial pattern of photopigment absorptions; hence, no subsequent processing, through cone to cone interactions or later neural interpolation, can undo the confusion. The optical defocus prevents high spatial frequencies that might alias from being imaged on the retina.

By creating stimuli with a visual interferometer, we bypass the optical defocus and image patterns at very high spatial frequencies on the cone mosaic. From the aliasing properties of these patterns, we can deduce some of the properties of the **L** and **M** cone mosaics. The aliasing demonstrations show that the foveal sampling grid is regular and contains approximately 120 cones per degree of visual angle. These measurements, in the living human eye, are consistent with the anatomical images obtained of the human eye reported by Curcio and her colleagues (Curcio et al. (1991)).

The precise arrangement of **L** and **M** cones within the human retina is unknown, though data on this point should arrive shortly (e.g., Mollon and Bowmaker (1992)). Current behavioral estimates of the relative number of **L** and **M** cones suggest that there are about twice as many **L** cones as **M** cones (Cicerone and Nerger (1989)).

The cone sampling grid becomes more coarse and irregular outside the fovea where rods and other cells enter the spaces between the cones. In these portions of the retina, high frequency patterns presented through interferometry no longer appear as regular low frequency frequency patterns. Rather, because of the disarray in the cone spacing, the high frequency patterns appear to be mottled noise. In the periphery, the cone spacing falls off rapidly enough so that it should be possible to observe aliasing without the use of an interferometer (Yellott (1982)).

In analyzing photoreceptor sampling, we have ignored eye movements. In principle, the variation in receptor intensities during these small eye movements can provide information to permit us to discriminate between the alias pairs. (You can check this effect by studying the images you observe when you experiment with the sampling grids.) The effects of eye movements are often minimized in experiments by flashing the targets briefly. But, even when one examines the interferometric pattern for substantial amounts of time, the aliasing persists. The information available from small eye movements could be very useful; but, the analysis assuming a static eye offers a good account of current empirical measurements, This suggests that the nervous system does not integrate information across minute eye movements to improve visual resolution (Packer and Williams (2003)).

Wavelength Encoding

Wavelength encoding overview

Sir Isaac Newton's sketch in Figure 1 summarizes his investigations into the properties of light. In these experiments, Newton separated daylight into its fundamental components by passing it through a prism and creating a rainbow. Newton's demonstration that light can be decomposed into rays of different wavelength is at the foundation of our understanding of light and color.

To perform these experiments, Newton placed a shutter containing a small hole in the window in his room at Cambridge. The light emerging from the hole in the window shutter served as a point source to illuminate his apparatus. The key elements of the apparatus are featured prominently in the center of the figure: the lens and prism. Newton's drawing shows that when the daylight passed through the prism, it formed an image of a rainbow on his wall. With two experimental manipulations, he showed that the components of the rainbow were fundamental constituents of light. In the upper left of the sketch, we see a series of holes that Newton drilled in the wall permitting part of the rainbow to continue through to a second prism. This ray of light was cast upon a second surface, but the new image did not produce a second rainbow; rather, as Newton wrote:

> *"the color of the light was never changed in the least. If any part of the red light was refracted, it remained totally of the same red color as before. No orange, no yellow, no green or blue, nor other new color was produced by that refraction." (Newton (1984))*

From this experiment, Newton concluded that the pass through the first prism had separated the daylight into its fundamental components. No further change was observed when the ray passed through a second prism.

At the bottom of the sketch Newton illustrated that the decomposition is reversible: passing light through the prism does not destroy the character of the light. To show this Newton converged the rays following their passage through the prism to form a new image; he found that the color of the image same is the same as that of the source. Newton concluded that:

> *"Light being transmitted through the parallel surfaces of two prisms … if it suffered any change by the refraction by one surface, it lost that impression by the contrary refraction of the other surface."(Newton (1984))*

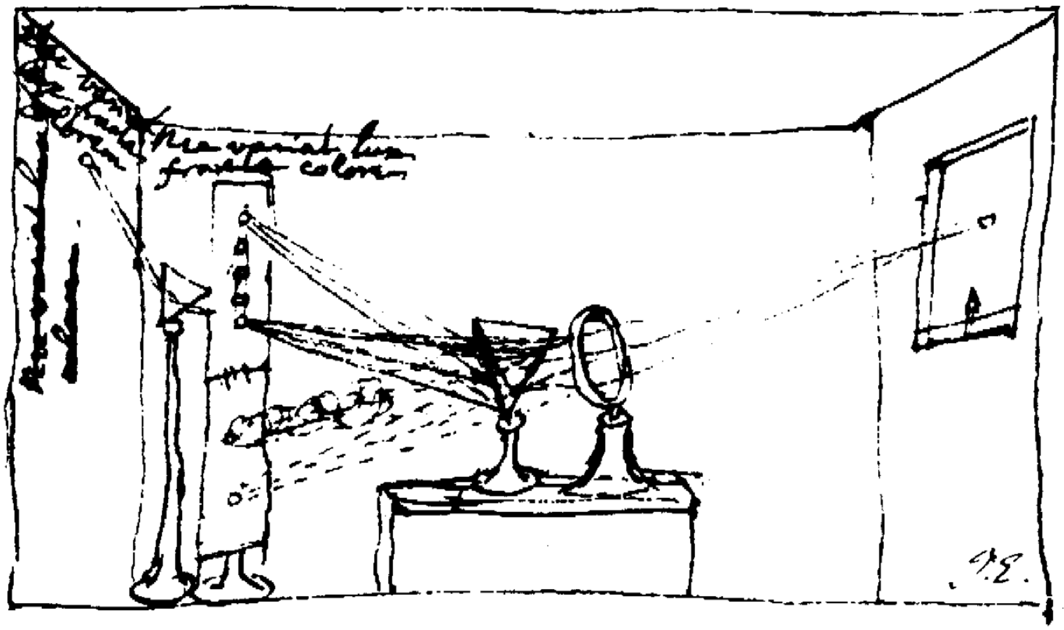

Figure 1: Newton's summary drawing of his experiments with light. Using a point source of light and a prism, Newton separated sunlight into its fundamental components. By reconverging the rays, he also showed that the decomposition is reversible.

From the second experiment, he concluded that passage through the prism had not destroyed, but merely revealed, the character of the light.

We now know that Newton succeeded in decomposing the sunlight into its *spectral* components, each with its own characteristic wavelength. The prism separates the rays because the prism bends each wavelength of light by a different amount. (See the section on Snell's law in Chapter). When we see the spectral components separately, they each have a different color appearance. Light with relatively long wavelengths appears red when viewed against a dark background. Light with relatively short wavelengths appears blue when viewed against a dark background. Shorter wavelengths of light are refracted more strongly than longer wavelengths. A spectral light, with energy only at a single wavelength, is also called a *monochromatic light*.

Newton's apparatus suggests a simple device we might build to measure the amount of power a light has in each of the different wavelength bands. As illustrated on the top of Figure 2, by proper use of lenses and prisms, we can form a focused image of the spectral components in an image plane with a movable slit placed in front of a photodetecting sensor. To measure the energy at different wavelengths, we move the slit passing only some of the spectral components at each position, and thus we measure the energy of the source at different wavelengths of light. In the visible region, the wavelength of light is on the order of a few hundred billionths of a meter, or *nanometers* (nm).

(a)

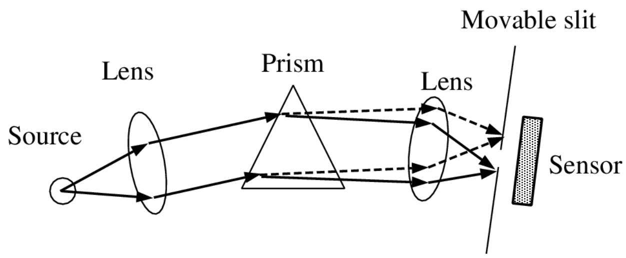

(b)

Wavelength (nm)	Color [a]
700	red
610	orange
580	yellow
540	green
480	blue
400	violet

[a] Viewed in isolation

Figure 2: A spectroradiometer is used to measure the spectral power distribution of light. (a) A schematic design of a spectroradiometer includes a means for separating the input light into its different wavelengths and a detector for measuring the energy at each of the separate wavelengths. (b) The color names associated with the appearance of lights at a variety of wavelengths are shown (After Wyszecki and Stiles (1982)).

The *spectral power distribution* of a light is the function that defines the power (Watts = Joules/sec) in the light in each wavelength band. In the modern theory of physics, the wavelength of light can be thought of in two different ways. We describe the light as if it were a continuous wave as it passes through a medium. When the light exchanges energy with some material, say by giving up its energy to be absorbed, we describe the light as if it were a discrete object called a *photon* or *quantum* of light. The amount of energy given up by the photon is predicted by the wavelength of the light.

The experimental aspect of light measurement that makes it useful and predictable is that the measurement satisfies the principle of superposition. We can demonstrate the superposition of light measurement as follows. First, measure the spectral power distributions of two lights separately. Then, mix the two lights together and measure again. The spectral power distribution of the mixture will be the sum of the first two spectral power distributions. This property of light mixture is illustrated in Figure 3. Superposition is a crucial property of light measurement because it implies that we can measure the energy of a light at each wavelength separately, and then combine the individual measurements to predict spectral power distribution when the spectral components are mixed together.

Suppose we wish to measure the spectral power distribution of a light source. How many wavelengths should we measure? Or, equivalently, how finely do we have to sample along the wavelength dimension? The answer to this question is important for both practical and theoretical reasons because the number of samples can be quite large. For example, to sample the visible spectrum from 400 nm to 700 nm in 1 nm steps, we need about 300 measurements. To sample in 10 nm steps, we need about 30 measurements.

The answer to this sampling question depends on the same set of issues as the sampling questions we addressed in Chapter on the spatial sampling of the retinal image by the photoreceptor mosaics. If the energy in the light varies rapidly as a function of wavelength, then

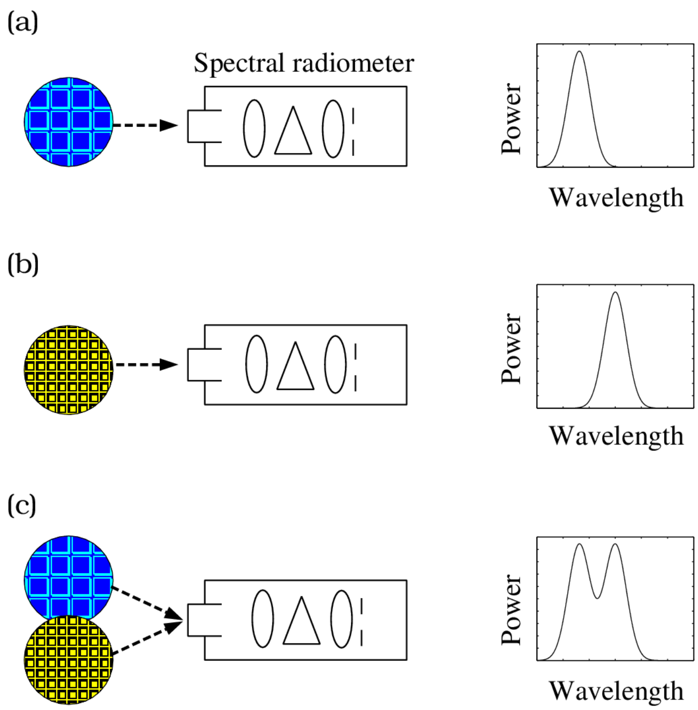

Figure 3: Principle of Superposition. The measurement of light spectral power distributions satisfies the principle of superposition. The spectral power distributions of two lights measured separately are shown in (a) and (b) and together in (c). The spectral power distribution of the mixture is the sum of the individual measurements, thus demonstrating that superposition holds true.

we may have to sample quite finely to measure accurately; if the functions vary slowly, then only a few measurements are necessary. Also, the precision of the representation requires that we know how sensitive the photopigments in the are to rapid changes in the energy as a function of wavelength.

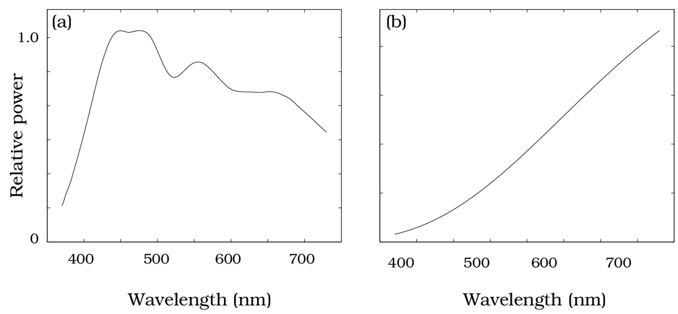

Figure 4: The spectral power distribution of two important light sources are shown: blue skylight (a) and the yellow disk of the sun (b).

It is difficult to make accurate generalizations about how spectral power distributions vary as a function of wavelength, but it is believed widely that for practical purposes we can approximate spectral power distributions using smooth, regular functions as shown in Figure 4. Also, it is known that the photopigments integrate broadly across the wavelength spectrum. Consequently, international standards organizations suggest making measurements every 5 nm to achieve an excellent representation of the signal. Practical measurements often rely on measurements spaced every 10 or 20 nm. We will consider this issue much more completely when we review color appearance, in Chapter .

Scotopic Wavelength Encoding

What information do we encode about the spectral power distribution when rods initiate vision, under *scotopic* conditions? We can answer this question by an experiment designed to measure how well people can discriminate different spectral power distributions. In the *scotopic matching* experiment, we present an observer with two lights, side by side in a *bipartite* field. One side of the field contains the *test* light; it may have any spectral power distribution whatsoever. The second side of the field contains the *primary* light; it has a fixed relative spectral power distribution and can vary only by an overall intensity factor. The observer's task in the *scotopic matching experiment* is to adjust the primary light intensity so that the primary light appears indistinguishable from the test light. The observer can adjust only the intensity of the primary light, so when the match is achieved the spectral power distributions of the test and primary lights that match are still different.

Under scotopic conditions, observers can adjust the primary intensity so that the primary matches any test light. Since subjects can always make this match, we have a simple answer to our question: The rods encode nothing about the relative spectral density of a light. An observer can adjust the intensity of a primary light to match the appearance of a test light with any spectral power distribution. The relative spectral power distribution is immaterial, all that matters is the relative intensities of the two lights.

Matching: Homogeneity and superposition

We can learn more about scotopic wavelength encoding by studying the quantitative properties of the matching experiment. To characterize the matching experiment completely, we must be able to predict how a subject will adjust the primary intensity to match any test light. We treat the experiment as a transformation by identifying the spectral power distribution of the test light as the input and the intensity of the primary light as the output. A quantitative description of the experiment tells us how to map the input to the output.

Naturally, we first ask whether we can characterize the matching experiment transformation using linear systems methods. Denote the spectral power distribution of the test and primary lights using the vectors $\mathbf{t}$ and $\mathbf{p}$ respectively. The n_λ entries of these vectors describe the power at each of the n_λ sample wavelengths. To test linearity, we evaluate whether the scotopic matching experiment satisfies the linear systems properties of homogeneity and superposition. We can evaluate these properties from the following experimental tests:

- (Homogeneity) If $\mathbf{t}$ matches $e\mathbf{p}$, will $a\mathbf{t}$ match $a(e\mathbf{p})$?
- (Superposition) If $\mathbf{t}$ matches $e\mathbf{p}'$, and $\mathbf{t}'$ matches $e'\mathbf{p}'$, will $\mathbf{t} + \mathbf{t}'$ match $(e\mathbf{p}) + (e'\mathbf{p})$?

An hypothetical test of homogeneity is shown in Figure 5. The separate panels show the intensity of the test light on the horizontal axis and the intensity of the matching primary light on the vertical axis. Each panel plots the results using spectral test lights at a series of wavelengths and a 510 nm primary light. In the scotopic matching experiment the data will fall on a straight line, consistent with the prediction from homogeneity. The slope of the line defines the relative scotopic sensitivity to the test and the primary lights. For example, in panel (c) the hypothetical results from an experiment with a 580 nm test light are shown. The slope of the line shows that we need 8.3 units of energy at 580 nm to have the same effect as one unit of energy at 510 nm. Hence, the light at 510 nm is 8.3 times more effective, per unit energy, than the light at 580 nm.

Because the scotopic matching experiment is linear, there must be a system matrix, $\mathbf{R}$ that maps the input ($\mathbf{t}$, the test spectral power distribution), to the output (e, the primary light intensity). The system matrix, call it $\mathbf{R}$, must have one row and n_λ columns. The test light, system matrix, and primary intensity are related by the product, $e = \mathbf{Rt}$.

We can relate the measurements in the scotopic matching experiment to the entries of the system matrix as follows. Write the matrix product $\mathbf{Rt}$ as a summation over the sample wavelengths,

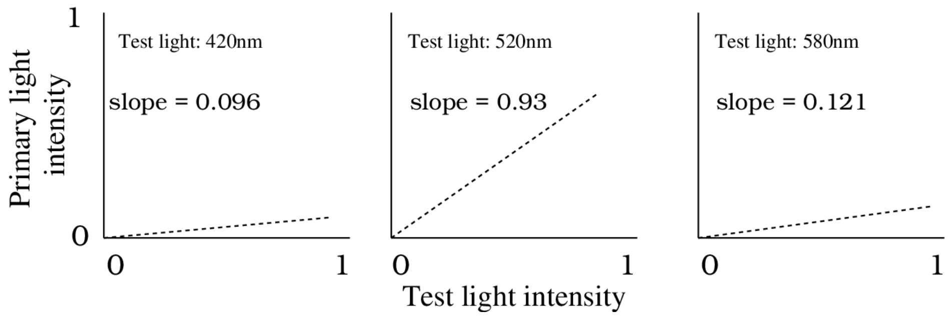

Figure 5: Hypothetical scotopic matching experiment. The horizontal scale measures the intensity of a monochromatic test light and the vertical scale measures the intensity a matching 510 nm primary light. Since the scotopic matching experiment satisfies homogeneity, the data will fall along a straight line. The slope of the line defines the relative scotopic sensitivity to each test wavelength.

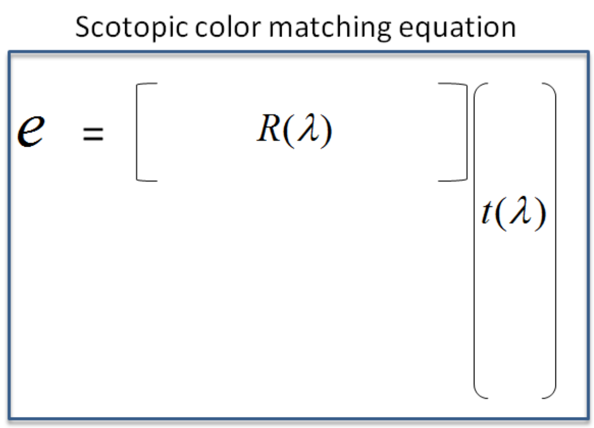

Figure 6: Matrix tableau of the scotopic matching experiment. The primary light intensity, e, equals the product of the $1 \times n_\lambda$ scotopic matching system matrix and the $n_\lambda \times 1$ vector representing the test light spectral power distribution.

$$e = \sum_{i=1}^{i=n_\lambda} R_i \mathbf{t}_i \tag{0.1}$$

Suppose we use a monochromatic test light of unit intensity, that is, an input $\mathbf{t}$ that has only a single non-zero wavelength, $(0, 0, ..., 0, 1, 0, ...0)^T$. Then Equation 0.1 becomes simply $e = R_i \mathbf{t}_i$. This shows that the slope of the line relating the monochromatic test intensity, $\mathbf{t}_i$, to the primary intensity, e, is the system matrix entry, R_i. Hence, we can estimate the system matrix from the slopes of the experimental lines we measure in the test of homogeneity shown in Figure 5.

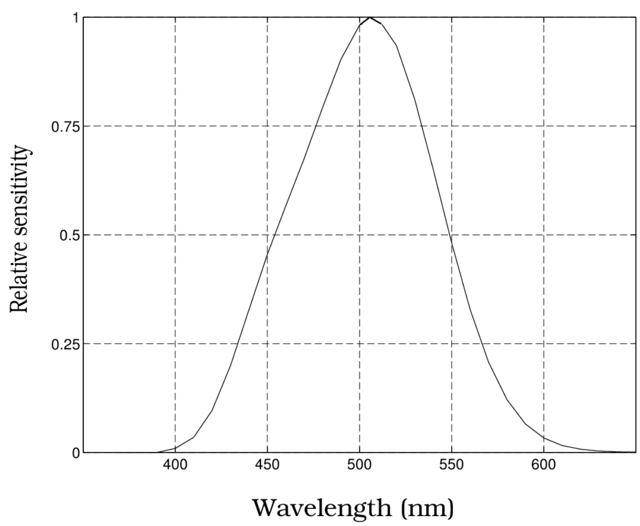

Figure 7: The scotopic spectral sensitivity function defines the human wavelength sensitivity under scotopic viewing conditions. The curve is a plot of the entries of the scotopic system matrix.

Figure 7 is a graphical method of representing the system matrix of the scotopic matching experiment. The curve shows the entries of $\mathbf{R}$ as a function of wavelength, interpolated from experimental measurements at many sample wavelengths. The curve is called the *scotopic sensitivity function*.

Once we measure the system matrix, $\mathbf{R}$, we can predict whether any pair of lights will match under scotopic conditions. The matrix tableau shows how we use the system matrix to predict the intensity of a primary light needed to match a test light. Suppose we have two test lights, $\mathbf{t}$ and $\mathbf{t}'$. Two lights will match when they are matched by the same intensity of the primary light. So, these two lights will match when $\mathbf{Rt} = \mathbf{Rt}'$.

Uniqueness

The hypothetical experiment illustrated in Figure 6 assumed a 510 nm primary light. Suppose that we perform the scotopic matching experiment using a different primary light. How will this effect the system matrix, $\mathbf{R}$?

We can answer this question by a thought experiment. Call the second primary light $\mathbf{p}'$. We can set a match between the new primary light, $\mathbf{p}'$, and the first primary light $\mathbf{p}$. We will find that there is some scalar, k, such that $k\mathbf{p}'$ matches $\mathbf{p}$, and we expect that whenever $a\mathbf{p}$ matches a test light, $\mathbf{t}$, then $a(k\mathbf{p}')$ will match $\mathbf{t}$. In particular, since $R_i\mathbf{p}$ matches the i^{th} monochromatic test light, we expect that $R_i k\mathbf{p}'$ will match the i^{th} monochromatic test light as well. It follows that the entries of the new system matrix will be kR_i, equal to the original except for a constant scale factor, k. Hence, the new system matrix will be $k\mathbf{R}$, and we say that the estimate of $\mathbf{R}$ is unique up to an unknown scale factor.

The Biological Basis of Scotopic Matching

Color Plate 1 is a photograph of the photopigment contained in the rod outer segments. In part (a) of the figure the photopigment is photographed in the eye of an alligator. Because the back of the alligator's eye contains a white reflective surface, called the *tapetum*, it is possible to see the color of the rod photopigment. Cats too have a white tapetum, which is why cats eyes appear to glow so brightly when they catch the beam of a car's headlights. The alligator shown in the picture had been kept in a dark closet for 24 hours so that the photopigment would be fully regenerated and easy to photograph. The closet was opened briefly, a flash picture taken, and then I suppose the door was shut again. Whew.

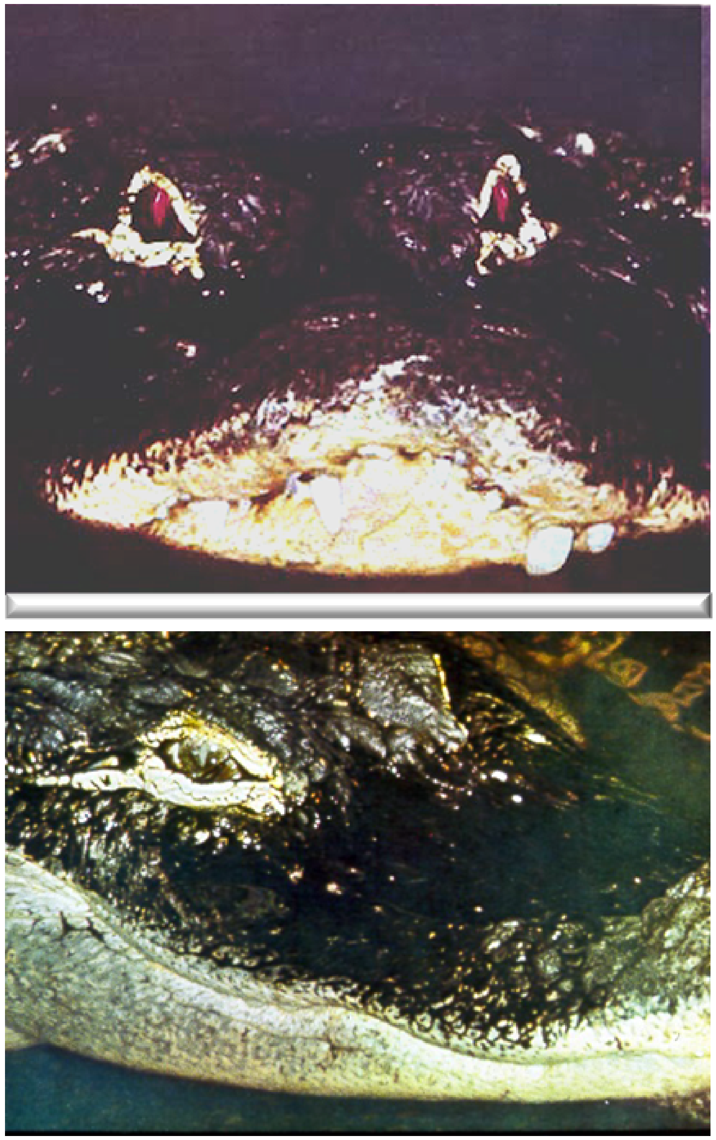

Figure 8: **Color Plate 1.** The scotopic matching experiment is remarkable in its simplicity. We can understand the biological basis of the experimental matches by studying the properties of the rod photopigment, rhodopsin.

Rod photopigment is present in much higher density than any of the cone photopigments. Thus, researchers have been able to isolate and extract the rod photopigment for fifty years, whereas the cone photopigments have only become available recently through the methods of genetic engineering (Merbs and Nathans (1992)). Characteristically, when the rod photopigment is exposed to light, it undergoes a series of rapid changes in chemical state (Hubbard and Wald (1951); Wald and Brown (1958); Wald (1968)). Whenever a quantum of light is absorbed by the rhodopsin photopigment, it undergoes a specific sequence of events resulting in the decomposition of the rhodopsin molecule into opsin and vitamin A. Color Plate 1 (b) shows the same alligator after its eye has been exposed to light. The rhodopsin is been broken into two parts and the resulting products are clear, rather than purple. In this state, the white tapetum of the eye is evident. It is the wavelength selectivity of the rhodopsin photopigment that provides the biological basis of scotopic matching. The relationship between the behavioral experiment and the properties of the rod photopigment is based on an important property called *univariance*.

W. Rushton emphasized that when a photopigment molecule absorbs light, the effect upon the photopigment is the same no matter what the wavelength of the absorbed light might be. Thus, even though quanta at 400 nm possess more energy than quanta at 700 nm, the sequence of rhodopsin reactions to absorption of a 400 nm quantum is the same as the sequence of reactions to a 700 nm quantum. Rushton used the word *univariance* for this principle to remind us that a single photopigment makes only a single-variable response to the incoming light. The photopigment maps all spectral lights into a single-variable output, the *rate of absorptions*. The response of a single photopigment does not encode any information about the relative spectral composition of the light. This explains why we cannot discriminate between lights with different spectral power distributions under scotopic viewing conditions (Rushton (1965); Naka and Rushton (1966)).

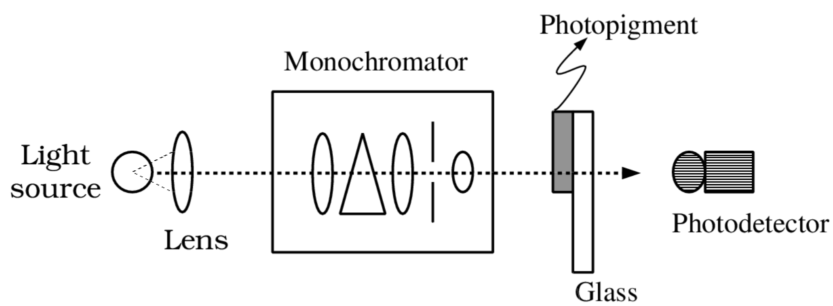

Figure 9: An apparatus to measure the spectral absorption of a photopigment. Using the monochromator, one can select light at one wavelength from the light source. To estimate the fraction of photons absorbed by the photopigment at that wavelength, we divide the number of photons detected through the glass and photopigment by the number detected after passing through the glass alone.

Univariance does not mean, however, that the photopigment responds equally well to all spectral lights. The photopigment is much more likely to absorb some wavelengths of light than others. Univariance asserts that once absorbed, however, all quanta have same visual effect.

We can measure the probability of absorption using the experimental apparatus shown in

Figure 9. We place a thin layer of photopigment on a clear plate of glass. We create a monochromatic light by passing the light from an ordinary source through a *monochromator*. The monochromator can be constructed using prisms or diffraction gratings to separate the incident light into its separate wavelengths, much as in Newton's original experiments. We measure the amount of monochromatic light passed through the photopigment and the glass plate by means of a photodetector at the rear of the apparatus. We then move the glass plate upwards, to remove the photopigment from the light path, and measure again. The difference in the photodetector signal measured in these two conditions is proportional to the amount of light absorbed by the photopigment.

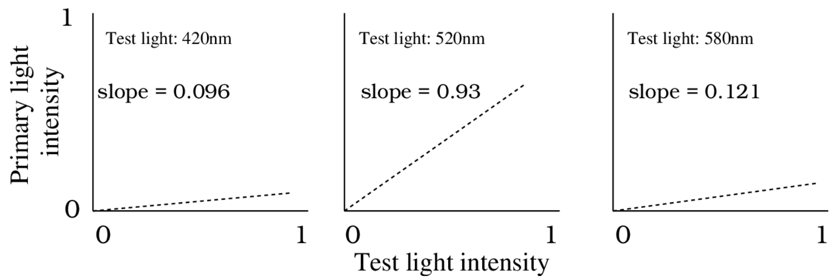

Figure 10: Rhodopsin absorptions at different wavelengths. The number of absorptions in a thin layer of photopigment are proportional to the intensity of the input light and thus satisfy the principle of homogeneity. The slope of the linear relationship between the light intensity and the number of absorptions describes the fraction of photon absorptions. The slope varies with the wavelength of the test light, thus defining the photopigment wavelength sensitivity.

If only a thin layer of photopigment is present, the experimental measurements of the absorptions will satisfy homogeneity and superposition. To test homogeneity, we increase the intensity of the test light. We will find that the number of absorptions will increase proportionately over a significant range. To test superposition, we measure the photopigment absorptions to a test light $\mathbf{t}$ to be a, and the number of absorptions to a second light $\mathbf{t}'$ to be a'. When we superimpose the two input lights, we will measure $a + a'$ absorptions. Since the measurement process is linear, we can estimate the system matrix of this absorption process, $\mathbf{A}$, just as we measured the system matrix of the scotopic matching experiment, $\mathbf{R}$.

We can predict the matches in the scotopic matching experiment from the absorptions of the rhodopsin photopigment. A test and primary light match in the scotopic matching experiment when the two lights create the same number of absorptions in the rhodopsin photopigment. We can demonstrate this by comparing the system matrices of the scotopic matching experiment and the rhodopsin absorption experiment. After we correct for the effects of the wavelength sensitive elements of the eye, mainly the lens, we can plot the system matrices of the scotopic matching experiment $\mathbf{R}$, and the rhodopsin absorption experiment, $\mathbf{A}$, on the same graph. Wald and Brown (1958) made this comparison in the graph shown in Figure 11. The filled circles in the graph plot the measurements of the system matrix from the rhodopsin absorption

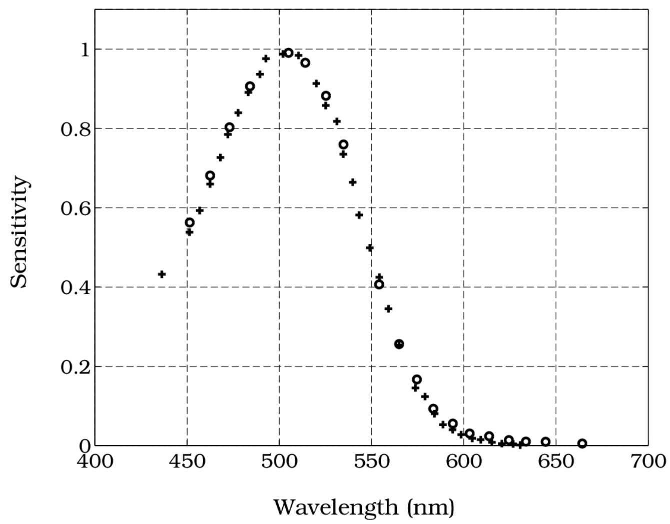

Figure 11: Comparisons of scotopic matching and rhodopsin wavelength sensitivity. The filled circles show human rhodopsin absorption measured as in Figure 10. The open circles show human scotopic sensitivity, corrected for light loss at the lens and optical media. (Source: Wald and Brown (1958))

experiment, **A**. The completely open circles plot estimates of the entries of **R** after correcting for the fact that the lens absorbs a significant amount of light in the short-wavelength part of the spectrum.

The agreement between the measurements of the rhodopsin photopigment and the scotopic matching experiment confirm a simple model of the observer's behavior. Under scotopic viewing conditions the observer's perception of the two halves of the bipartite field depends on a signal initiated by the rod photopigment absorptions. The two sides of the field appear identical when the rhodopsin absorption rates on the two sides of the bipartite field are equal. During the experiment, then, the observer adjusts the intensity of the matching light to equalize the rod absorption rates on the two sides of the bipartite field. Since the absorption of the light is a linear process, the observer's behavior is linear, too.

The precise quantitative match between the scotopic matches and the rod photopigment make a very strong connection between performance and biological encoding of the light. This type of precise quantitative relationship between behavior and the biological encoding of light serves as a good standard to use when we consider the relationship between behavior and biology in other conditions.

Photopic Wavelength Encoding

When the cones initiate vision, under photopic conditions, we do encode some information about the relative spectral power distribution of the incident light. Changes in the relative spectral power distributions result in changes of the color appearance of the light. Several of the important properties of color appearance can be traced to the way cone photoreceptors encode the relative spectral power distribution of light[1].

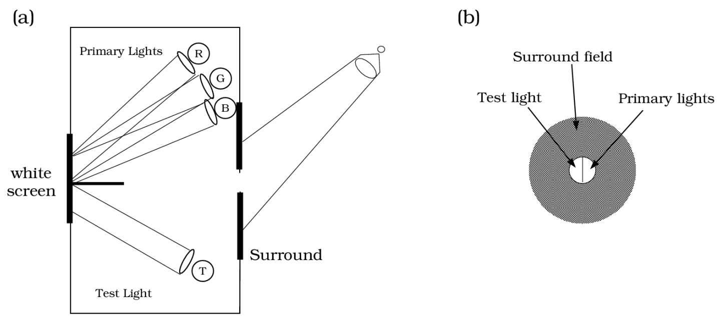

Figure 12: The color-matching experiment. The observer views a bipartite field and adjusts the intensities of the three primary lights to match the appearance of the test light. (a) A side-view of the experimental apparatus. (b) The appearance of the stimuli to the observer. (After Judd and Wyszecki (1975))

We will relate the human ability to discriminate lights to the properties of the cones just as we did with the rods. First, we will review the matching experiments that characterize how well people can discriminate between lights with spectral power distributions. When we measure under photopic conditions, the experiment is called the *color-matching* experiment. The color-matching experiment is the foundation of color science and of direct significance to many color applications (see the Appendix). Second, we will relate the properties of the color-matching experiment to the properties of the cone photopigments. The analysis of photopic wavelength encoding parallels the analysis of scotopic wavelength encoding. The main differences are that (a) we must keep track of the photopigment absorptions in three cone photopigments rather than the single rod photopigment, and (b) until quite recently the cone photopigments were not present in sufficient quantity to define their properties with any certainty (Merbs and Nathans (1992)). Hence, the problem of relating color-matching and the cone photopigments was solved using other indirect biological measurements. We can learn a great deal from studying the logic of these methods.

Figure 12 shows a simple apparatus that can be used to perform the color-matching experiment. The observer views a bipartite visual field with the test light on one side. The test light may have any spectral power distribution. The second half of the bipartite field contains a mixture of *three* primary lights. Throughout the experiment, the relative spectral power distribution

[1] Color appearance is not a simple consequence of the spectral power distribution of the incident light. We will discuss color appearance broadly in Chapter .

of each primary light is constant; only the absolute level of the primary lights can be adjusted. The observer's task is to adjust the intensities of the three primary lights so that the two sides of the bipartite field appear identical.

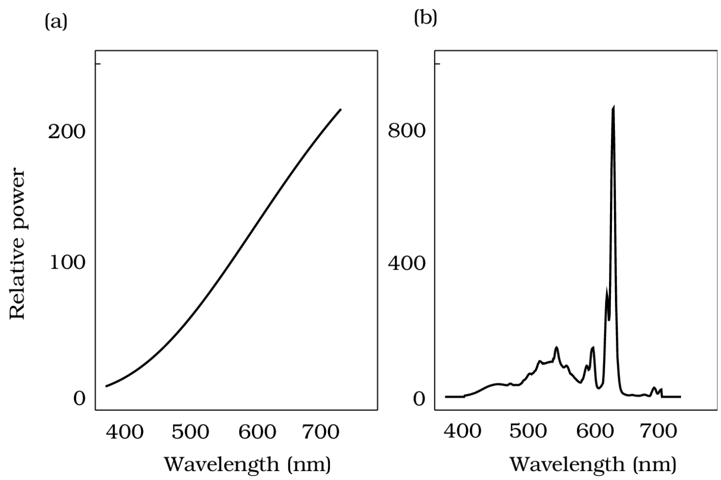

Figure 13: Metameric lights. Two lights with these spectral power distributions appear identical to most observers and are called metamers. The curve in part (a) is an approximation to the spectral power distribution of the sun. The curve in part (b) is the spectral power distribution of a light emitted from a conventional television monitor whose three phosphor intensities were set to match the light in (a) in appearance.

When the observer has completed setting an appearance match, the lights on the two sides of the bipartite field are not physically the same. The test light can have any spectral power distribution, while the mixture of primaries can only have a limited number of spectral power distributions determined by the possible weighted sums of the three primary light spectral power distributions. Lights that are photopic appearance matches, but that are physically different, are called *metamers*. Figure 13 contains a pair of spectral power distributions that match visually but differ physically, i.e. a pair of metamers.

The metamers in Figure 13 illustrate that even under photopic viewing conditions we fail to discriminate between very different spectral power distributions. To understand the behavioral aspects of photopic wavelength encoding, we must try to predict which spectral power distributions we can discriminate. The first question we ask is whether we can predict performance in the photopic color-matching experiment using linear systems methods.

We can define the experimental measurements in the color-matching experiment in direct analogy with the definitions we used in the scotopic matching experiment. The input variable in the color-matching experiment is the light $\mathbf{t}$, just as in scotopic matching. In the color-matching experiment, however, the subject's responses consist of three numbers, not just one. So, we record the responses using a three-dimensional vector, $\mathbf{e}$. The entries of $\mathbf{e}$ are the

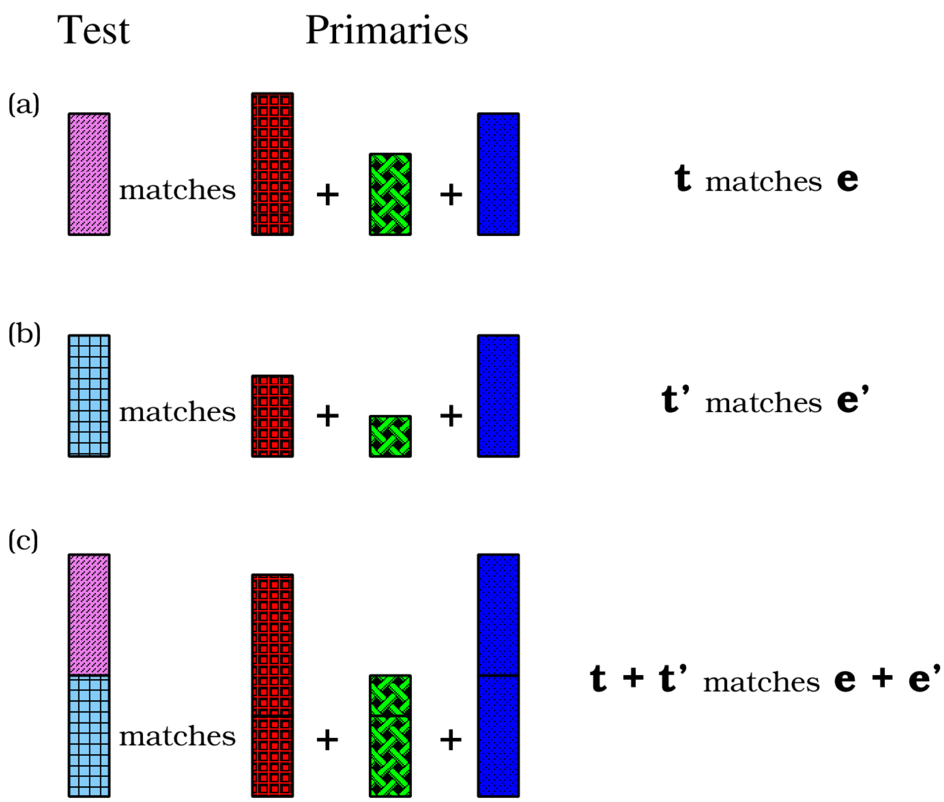

Figure 14: The color-matching experiment satisfies the principle of superposition. In parts (a) and (b) test lights are matched by a mixture of three primary lights. In part (c) the sum of the test lights is matched by the additive mixture of the primaries, demonstrating superposition.

intensities of the three primary lights ($e1, e2, e3$). To test superposition in the color-matching experiment we follow the logic illustrated in Figure 14. We obtain a match to a $\mathbf{t}$ by adjusting the primary intensities to the levels in $\mathbf{e}$. We then obtain a match to $\mathbf{t}'$ by adjusting the three primary intensities to $\mathbf{e}'$. We test additivity by verifying that the match to $\mathbf{t} + \mathbf{t}'$; is $\mathbf{e} + \mathbf{e}'$. Photopic color-matching satisfies homogeneity and superposition. We honor the person who first understood the importance of superposition in color-matching by calling this empirical property *Grassmann's additivity law.*

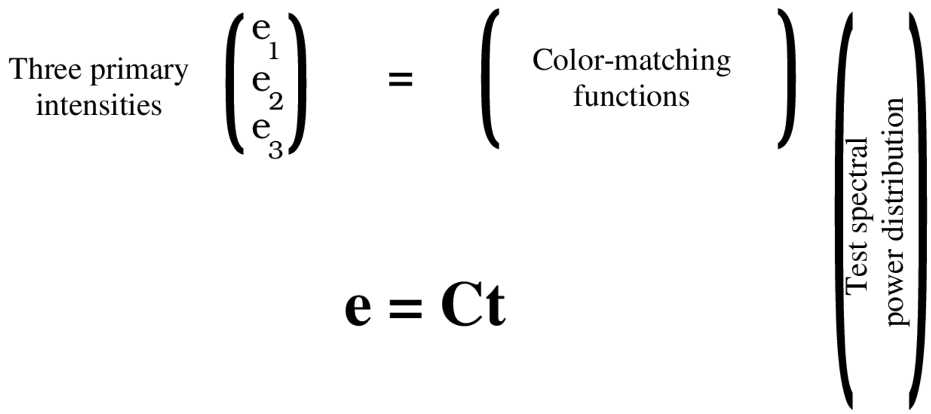

Figure 15: Matrix tableau of color-matching. The photopic color-matching experiment defines a linear mapping from the test light spectral power distribution to the intensity of the three primary lights. The rows of the system matrix are called the color-matching functions. These functions can be estimated by setting matches to many different test lights and solving a set of linear equations.

Because the color-matching experiment linearly maps the physical stimulus $\mathbf{t}$ to the primary intensities, $\mathbf{e}$, there must be a system matrix that maps the input vector $\mathbf{t}$ to the output vector $\mathbf{e}$. The matrix tableau shows the input-output relationship for the photopic color-matching experiment in matrix tableau. We will call the $3 \times n_\lambda$ system matrix $\mathbf{C}$.

We can estimate the system matrix $\mathbf{C}$ from the color-matches in the same way as we estimated the scotopic system matrix: by setting matches to a collection of monochromatic test lights with unit intensity. Since the vector representing a monochromatic test light is zero at each entry but one, the product of the system matrix and the monochromatic test light vector equals a single column of the system matrix. Thus, by matching a series of unit intensity monochromatic lights, we can define each of the columns of the system matrix, $\mathbf{C}$.

It is also useful to think of the system matrix in terms of its rows, which are called the *color-*

matching functions. Each row of the matrix defines the intensity of a single primary light that was set to match the monochromatic test lights. We will relate the rows of the photopic system matrix to the properties of the cone photopigments just as we related the single row of the scotopic system matrix to the rhodopsin photopigment. However, to make the connection between the cone photopigments and the color-matching functions will require a little more work.

Measurements of the Color-Matching Functions

Two important caveats arise when we measure the color-matching functions. These are only a minor theoretical nuisance, but they have important implications for the laboratory experiment and for practical applications.

The first issue concerns the selection primary lights. We should chose lights that are visually *independent*: that is, no additive mixture of two of the primary lights should be a visual match to the third primary. This is an obvious but important constraint: it would be unreasonable to choose the second primary light that looked the same as the first except for an intensity scale factor. This choice would be foolish since we could always replace the second light by an intensity-scaled version of the first primary light, adding nothing to the range of visual matches we can obtain. Similarly, a primary that can be matched by a mixture of the first two adds nothing. We must choose our primary lights so that they are independent of one another.

Even among collections of primary lights that are independent, some are more convenient than others. Empirically, it turns out that no matter which primary lights we choose, there will always be some test lights that cannot be matched by an additive mixture of the three primaries. To match these test lights, we must move one or even two of the primary lights from the matching side of the bipartite field to the test side of the bipartite field. Thus, ordinarily we obtain a visual matches of the form

$$\mathbf{t} = e_1\mathbf{p}_1 + e_2\mathbf{p}_2 + e_3\mathbf{p}_3. \tag{0.2}$$

Shifting one of the primaries to the other side of the bipartite field means that our match has the form

$$\mathbf{t} + e_1\mathbf{p}_1 = e_2\mathbf{p}_2 + e_3\mathbf{p}_3. \tag{0.3}$$

To a mathematician, Equation 0.3 is the same as

$$\mathbf{t} = -e_1\mathbf{p}_1 + e_2\mathbf{p}_2 + e_3\mathbf{p}_3. \tag{0.4}$$

Hence, when we encode the intensity of the primary light that has been shifted to the other side of the test field we denote the match using a negative intensity value[2].

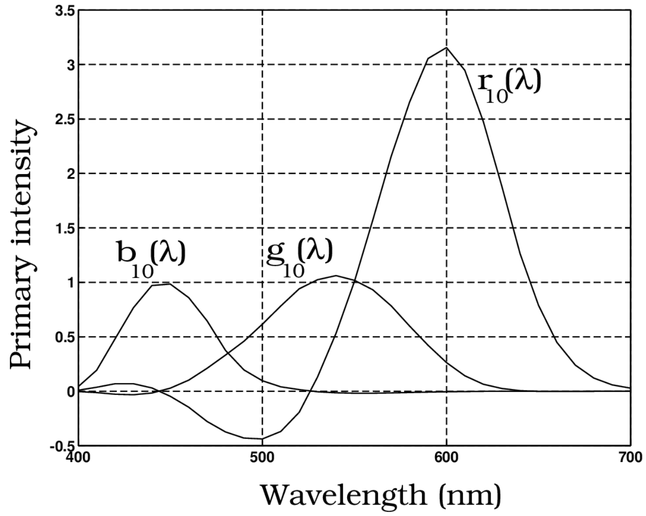

Figure 16: The color-matching functions are the rows of the color-matching system matrix. The functions measured by Stiles and Burch (1959) using a 10 deg bipartite field and primary lights at the wavelengths 645.2 nm, 526.3 nm, and 444.4 nm with unit radiant power are shown.

Figure 16 plots color-matching functions measured by Stiles and Burch (1959) using three monochromatic primary lights at 645.2 nm, 525.3 nm and 444.4 nm. Each function describes the intensity of one of the primary lights used to match various monochromatic test lights. Notice that the intensity of the red primary, at 645.2 nm nm, is negative over a region of test light wavelengths, indicating that over this range of test lights the 645.2 nm primary light was added to the test field.

The color-matching functions are extremely important in color technology, such as creating images on color monitors and color printers. I review the application of these methods to color monitors in the Appendix.

Uniqueness of the Color-Matching Functions

Suppose two research groups measure the color-matching functions using different sets of primary lights. One group measures the color-matching functions using three primary lights

[2]Changing the sign of the primary intensity is a trivial matter for the theorist. It is a nuisance in the laboratory, however, and usually impossible in technological applications such as color displays. Thus, the issue of selecting primaries to minimize the number of times we must make this adjustment is of great practical interest.

$\mathbf{p}_i$, while the second group uses a different set of primary lights, $\mathbf{p}'_i$. How will the two sets of color matching functions be related?

We can answer this question by the following thought experiment. First, create a matrix whose columns contain the spectral power distributions of the first group's primary lights, and call this matrix $\mathbf{P}$. The spectral power distribution of a mixture of the primaries, with primary intensities $\mathbf{e}$, is the weighted sum of the columns. We can express this mixture using the matrix product $\mathbf{Pe}$. Now, we can use the color-matching functions to predict when a test light will match the mixture of three primaries. The test and primaries will match when

$$\mathbf{Ct} = \mathbf{CPe} \tag{0.5}$$

Suppose the second group of researchers can also established matches to this test light using their primaries. To describe their measurements, we create a second matrix whose columns contain the spectral power distributions of the second group's primary lights, $\mathbf{P}'$. Call the primary intensities used to match the test with the second primaries $\mathbf{e}'$. Since the light $\mathbf{P}'\mathbf{e}'$ is a visual matched to the test light, we know that

$$\mathbf{Ct} = \mathbf{CP}'\mathbf{e}' \tag{0.6}$$

By combining Equation 0.5 and Equation 0.6, we find that the two vectors of primary intensities, $\mathbf{e}$ and $\mathbf{e}'$, are related by a linear transformation,

$$\mathbf{e} = (\mathbf{CP})^{-1}\mathbf{CP}'\mathbf{e}' \tag{0.7}$$

With a little more algebra, one can show that the color-matching functions are related by the following linear transformation:

$$\mathbf{C} = (\mathbf{CP}')\mathbf{C}' \tag{0.8}$$

The 3×3 matrix relating the two sets of color-matching functions, $\mathbf{CP}'$, has a simple empirical interpretation; its columns contain the intensities of the new primaries needed to match the original primaries. To see this, remember that each column of $\mathbf{P}'$ is the spectral power distribution of one of the primary lights, $\mathbf{p}'_i$. Thus, the first column of $\mathbf{CP}'$ is the vector of intensities of the first group of primaries needed to match $\mathbf{p}'_1$. Similarly, the second and third columns of $\mathbf{CP}'$ contain the intensities of the first group of primaries needed to match the corresponding primaries in $\mathbf{P}'$. The matrix $\mathbf{CP}'$ contains three columns equal to the primary intensities of $\mathbf{p}_i$ needed to match the new primary lights, $\mathbf{p}'_i$.

The photopic color-matching functions are not unique; when we measure using different sets of primaries we will obtain different color-matching functions. But, the color-matching functions are not completely free to vary either, since different pairs of color-matching functions will always be related by a linear transformation. We say that the color-matching functions are unique up to a free linear transformation

A Standard Set of Color-Matching Functions

When the members of the Committe Internationale d'Eclairage (CIE; an international standards organization) met in 1931, they were fully aware that the color-matching functions were not unique. To facilitate communication about color, the CIE defined a standard system of color representation based on one particular set of color-matching functions, that everyone should use. This set of color-matching functions defines the *XYZ tristimulus coordinate system*. The color-matching functions in this system are called $\bar{x}(\lambda)$, $\bar{y}(\lambda)$, and $\bar{z}(\lambda)$ respectively. They define one of the many possible system matrices of the color-matching experiment. Figure 17 shows the three standard color-matching functions, $\bar{x}(\lambda)$, $\bar{y}(\lambda)$, and $\bar{z}(\lambda)$.

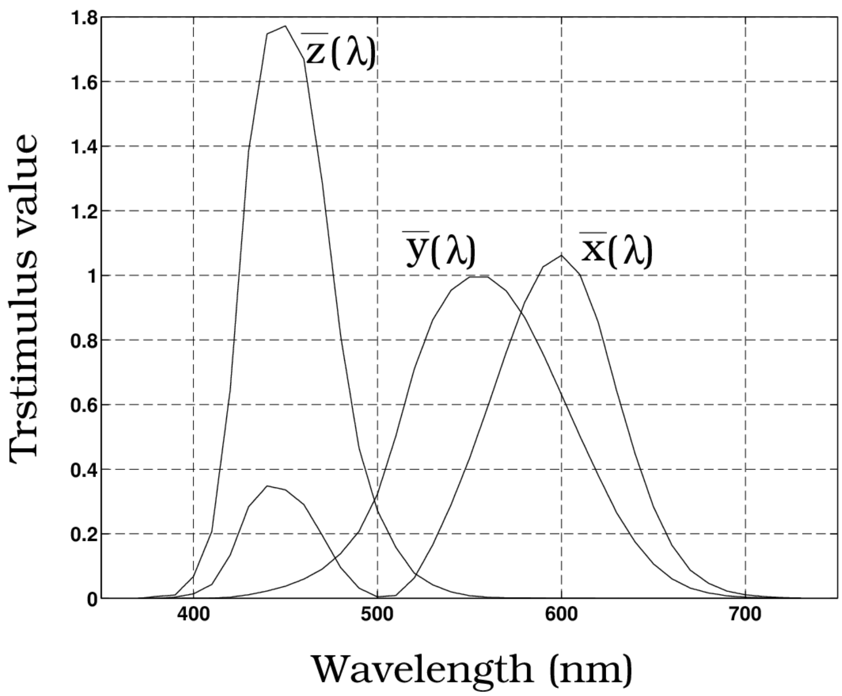

Figure 17: The XYZ standard color-matching functions. In 1931 the CIE standardized a set of color-matching functions for image interchange. These color-matching functions are called $\bar{x}(\lambda)$, $\bar{y}(\lambda)$, and $\bar{z}(\lambda)$. Industrial applications commonly describe the color properties of a light source using the three primary intensities needed to match the light source that can be computed from the XYZ color-matching functions.

The standard color-matching functions were chosen for several reasons. First, $\bar{y}(\lambda)$ is a rough approximation to the brightness of monochromatic lights of equal size and duration. A second important reason is that the functions are non-negative, which simplified some aspects of the design of instruments to measure the tristimulus coordinates. But, as with any standards decision, there are some irritating aspects of the XYZ color-matching functions as well. One serious drawback is that there is no set of physically realizable primary lights that by direct measurement will yield the color-matching functions. Primary lights that would yield these functions would have to have negative energy at some wavelengths and cannot be instrumented. Another problem is that these early estimates have been improved upon. Specifically, Judd (1951) noted that the functions are inaccurate in the short-wavelength region and he proposed a modified set of functions that are often used by scientists, although they have not displaced the industrial standard. Also, and perhaps most significantly, there is very little that is intuitive about the XYZ color-matching functions. Although they have served us quite well as a technical standard, and are understood by the mandarins of our discipline, they have served us quite poorly in explaining the discipline to new students and colleagues.

The Biological Basis of Photopic Color-matching

Just as we can explain the scotopic color-matching experiment in terms of the light absorption properties of the rhodopsin photopigment, we also would like to explain the photopic color-matching experiment in terms of the light absorption properties of the cone photopigments. We related the photopigments and the behavior by studying the system matrices of the two experiments. We found that two lights were scotopic matches when $\mathbf{Rt} = \mathbf{Rt}'$, and we then showed that the entries in the $1 \times n_\lambda$ scotopic matching matrix, $\mathbf{R}$, was the same as the rhodopsin absorption function $\mathbf{A}$. For photopic vision, we use the same general approach. But, there are two complications: there are three cone photopigments, not just one; the photopic matching matrix is not unique.

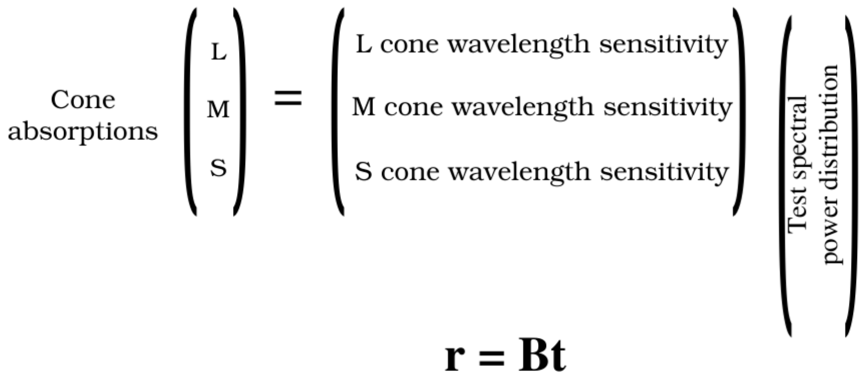

Figure 18: Cone photopigments and the color-matching functions. If we measure the wavelength sensitivity of each of the cone photopigments, we can create a $3 \times N$ system matrix to describe the cone absorptions. Then, we can evaluate whether the cone absorption system matrix can serve to explain the results of the color-matching experiment.

Extending our analysis to account for three cone photopigments instead of one rod photopigment is straightforward. We measure the absorption properties of each of the three cone photopigments, and we create a system matrix, **B**, with three rows to define the three cone photopigment absorption functions. This matrix generalizes the rhodopsin system matrix **A**. Then, we compare the cone absorption system matrix, **B**, with the color-matching experiment system matrix, **C**. We must evaluate whether the cone photopigment matrix can explain the color-matching data.

From our analysis of color-matching, we know that the color-matching system matrix is not unique; there is a collection of equivalent system matrices, all related by a linear transformation. Hence, to evaluate whether the cone absorption matrix can explain the color-matching experiment, we must evaluate whether the color-matching system matrix, **C**, is related to **B** by a linear transformation. Our next task, then, is to measure the cone absorption system matrix, **B**.

Measuring Cone Photocurrents

Currently, the best estimate of the cone photopigment absorptions is derived from measurements of the cone photocurrent, that is the change in the current flow through the membrane of individual cones as they are stimulated by light. Relating the photocurrent to the photopigment absorptions requires some careful analysis because the photocurrent depends nonlinearly on the photopigment absorptions in the cone. In this section we will develop new theoretical methods to interpret the nonlinear cone photocurrent measurements and infer the linear properties of the cone photopigments.

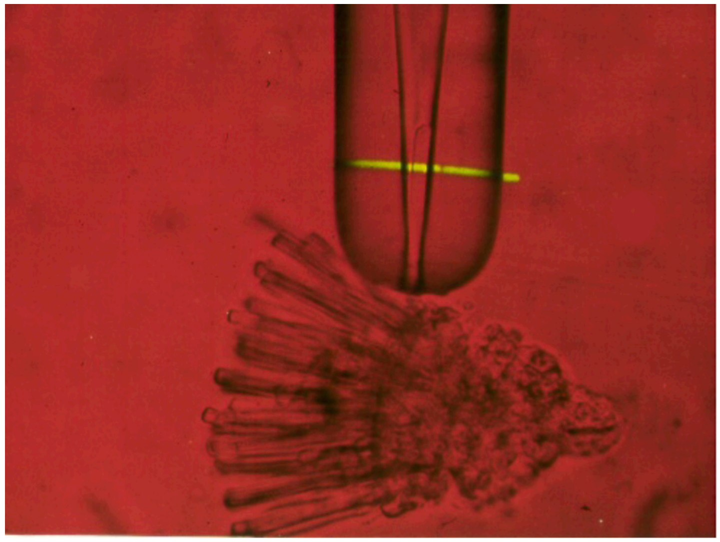

Figure 19: Measurement instruments for detecting the photocurrent generated by a macaque photoreceptor. The image shows a portion of the retina suspended in solution. A single photoreceptor from this retinal section has been drawn into the microelectrode and is being stimulated by a beam of light passing transversely through the photoreceptor and microelectrode (Image courtesy of D. Baylor).

Baylor et al. (1987) and Baylor (1987) were the first to measure the cone photocurrents in the macaque retina. The macaque has three types of cones and its behavior on most color tasks is quite similar to human behavior Thus, the comparison between the properties of the macaque photoreceptors and human behavior is a good place to begin (De Valois and Jacobs (1971)).

To measure the cone photocurrent, Baylor, Nunn and Schnapf removed the retina from the eye and chopped it into fine pieces about 100 μm across. The pieces are placed in a chamber containing special solutions that support the metabolism of the cells. Even though the retina has been dissected from the eye and chopped into pieces, the electrical response of the photoreceptors remains vigorous for several hours. Baylor and his colleagues recorded the photocurrent of individual cells using the experimental technique pictured in Figure 19. The figure shows a glass micropipette approaching a single photoreceptor. The inner diameter of the micropipette is between 2 and 6 μm, only ten times as wide as the wavelength of visible light. A single photoreceptor outer segment is held inside the micropipette, and there is a thin ray of light passing transversely through the photoreceptor and stimulating it.

Figure 20 shows the result of stimulating the photoreceptor with a brief impulse of light. The curves illustrate the membrane photocurrent following a brief light flash. The curves in part

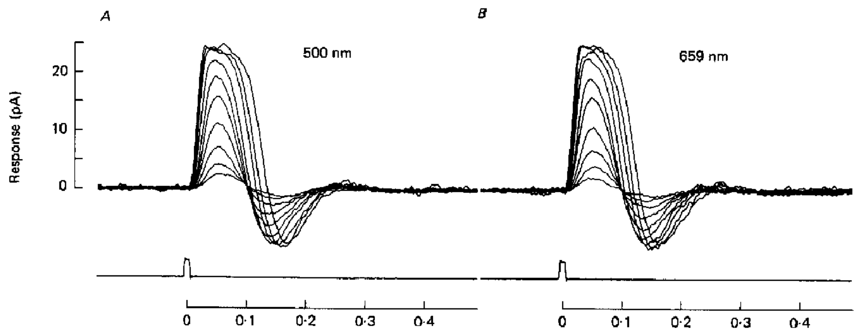

Figure 20: The timecourse of cone photocurrent in response to a brief test flash is biphasic. The amplitude of the photocurrent response increases with the stimulus intensity. The response functions are the same for different wavelengths of light, such as at 500 nm and 659 nm in parts (a) and (b), respectively. The stimulus timecourse is shown below the photocurrent plots. (Source: Baylor et al. (1987))

(a) of the figure plot the response to 500 nm light at a range of intensities. The curves in part (b) plot the response to 659 nm light at a range of intensities. Before the stimulus is presented, there is a steady inward flow of current consisting of a stream of positively charged sodium ions entering the photoreceptor through ion channels in the cell membrane. This steady level in the absence of light is called the dark current. It represents a baseline level and is denoted as zero in the graph. The plotted values are biphasic, varying both above and below the baseline.

When the photopigment absorbs light from the flash, the inward flow of sodium ions is slowed. The sodium current in darkness reduces the negative electrical polarization of the cell interior. When light blocks the inward flow, the negative voltage difference between the inside and outside of the cell increases. Thus, the initial photoreceptor response to light is a hyperpolarization. After the initial blockage of inward flowing sodium current, the current flow is actively restored. The mechanism that restores balance overcompensates; during the second phase of the response the total photocurrent flow reverses direction. Thus the photocurrent response first flows in one direction and then the opposite direction, leading to the biphasic impulse response.

In this experiment the test light is the input, $\mathbf{t}$, and the cone photocurrent response is the output. We can evaluate whether the input-output relationship satisfies one of the requirements of a linear system, homogeneity, from the graphs in Figure 20. Suppose the input signal is $\mathbf{t}$ and the photocurrent response is $\mathbf{c}$, a vector representing the photocurrent as a function of time following the stimulus. To test homogeneity we should measure the response to the scaled input, $k\mathbf{t}$. If the system is linear, then we expect that the photocurrent response will be $k\mathbf{c}$. From a visual inspection of the curves in Figure 20 we can see that homogeneity fails. There are two features of the curves that should make this evident to you. First, notice that as the test intensity increases, the peak deviation reaches a maximum of about 25 pA and then saturates. Saturation is inconsistent with a strictly linear relationship between input intensity and output photocurrent. A second way to see that linearity fails is to consider the point of the biphasic response at which the output crosses the zero level at baseline. If the output photocurrent is proportional to the input intensity, points with a zero response level should always have a zero response level: multiplying zero by any intensity still yields zero. Hence, we expect that the zero-crossing should not change its position as we increase the test intensity. This prediction is true for lower test intensities, but as the input intensity increases to fairly high levels, the zero-crossing shifts its position in time.

How surprising: Human performance in the color-matching experiment satisfies the principles of a linear system, homogeneity and superposition, yet the cone photocurrent responses a part of the chain of biological events that mediate the behavior, fail the simplest tests of linearity. How can the behavior be linear when the components mediating the behavior are nonlinear? We will answer this question in the following section. The answer is given specifically for color-matching, but the principles we will review are quite general. They will be helpful again when we consider the relationship between behavior and other neural responses throughout this book.

Static Nonlinearities: Photocurrents and Photopigments

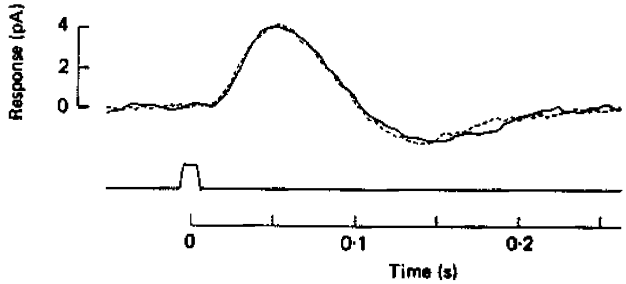

Figure 21: The principle of univariance states that a photon absorption leads to the same neural response, no matter what the wavelength of the photon. The principle predicts that two stimuli at different wavelengths can be adjusted to equate the photocurrent response throughout its timecourse. This is shown here as the match between photocurrents in response to 550 nm (dashed) and 659 nm (solid) test lights set to a nine to one intensity ratio (Source: Baylor et al. (1987)).

By comparing the sets of photocurrent responses on the top and bottom of Figure 20, it appears that as we vary the level of the test signal we sweep out the same set of curves. The similarity of the measured photocurrent responses to the two test lights suggests that we can perform a color-matching experiment at the level of the photocurrent response. We can perform such an experiment by choosing a test light and a primary light and adjusting the intensity of the primary light light until the photocurrent responses of the test and primary are the same. The curves in Figure 21 show one example of such a match using a primary light at 500 nm and a test light at 659 nm.

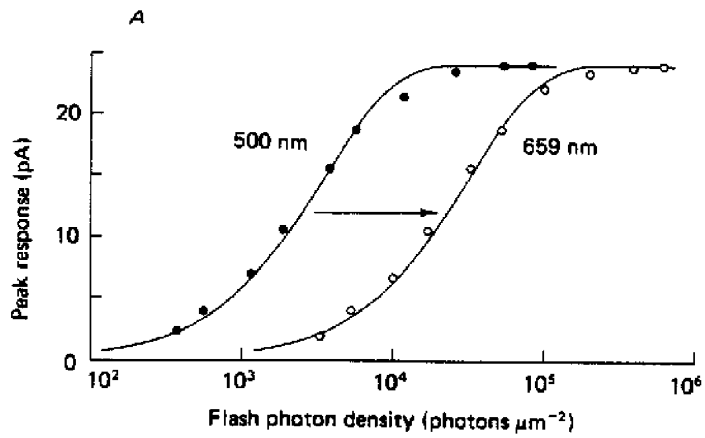

Figure 22: A matching experiment using the cone photocurrent as response. Lights at different wavelengths have equivalent effects on the cone photocurrent when the light intensity ratio is set properly. For this cone, the 659 nm light must be nine times more intense than the 500 nm light to have an equivalent effect (Source: Baylor et al. (1987)).

The physiological preparation is very delicate and it is difficult to keep the photoreceptors alive and functioning. This makes it impossible to set full photocurrent matches for arbitrary test and primary combinations. But, it is possible to carry out an efficient approximation of the full experiment. The two curves in Figure 22 summarize the photocurrent responses to a 659 nm test light and the 500nm primary light at a series of different intensity levels. The data points shows the peak value of the photocurrent response as a function of intensity; the peak value summarizes the full photocurrent timecourse. The smooth curves drawn through the points interpolate the peak response at any intensity level. From these interpolated measurements, we can estimate the intensity levels needed to obtain complete matches between the test and primary lights.

If the matching experiment performed at the level of the photocurrent satisfies homogeneity, the intensity of the test and primary lights that match should be proportional to one another. We can estimate the intensity of the test and primary lights that match at different response levels by drawing a horizontal line across the graph and noting the intensity levels that produce the same peak photocurrent. The curves through the two sets of data points in Figure 22 are parallel on a logarithmic intensity axis, so that the intensities of pairs of points that match are separated by a constant amount. Since the axis is logarithmic, equal separation implies that when the photocurrents match the test and primary light intensities are in a particular ratio, precisely as required by homogeneity. Hence, the photocurrent matching experiment satisfies homogeneity even though the photocurrent response itself is nonlinear.

From the separation between the two curves, we see that more 659 nm photons are needed than 500 nm photons to evoke the same response. For this pair of wavelengths the curves are separated by 0.97 log units that corresponds to a ratio of 9.3. It takes 9.3 times as many 659 nm quanta to equal the photocurrent produced by a number of 500 nm quanta. By repeating this experiment using test lights at many different wavelengths, we can estimate the complete spectral responsivity curves for the cone photoreceptors. From a collection of such measurements we can estimate the wavelength sensitivity of the cone receptor. The wavelength sensitivity is due to the properties of the cone photopigment, so in this way we can derive the cone photopigment absorption function from the photocurrent measurements.

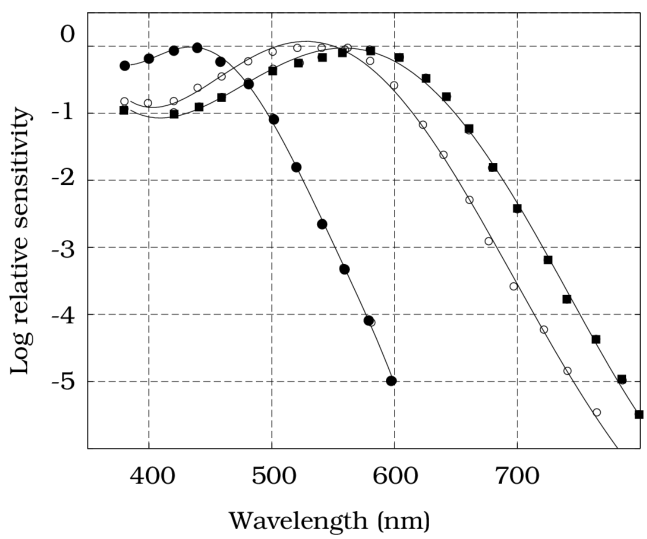

Figure 23: Cone photocurrent spectral responsivities. The measurement range spans a factor of one million. The S cone sensitivity at short wavelengths is high compared to behavioral measurements because in behavioral conditions the lens absorbs short wavelength light strongly. (After Baylor (1987)).

The reader will not be surprised to learn that Baylor, Nunn and Schnapf found cones with three distinct spectral response functions: these measurements are plotted in Figure 23. Notice that the vertical axis spans six logarithmic units, so that they measured sensitivities varying over a factor of one million, an extraordinary technical measurement achievement.

Static Nonlinearities: The principle

We can analyze the photopigment sensitivity from the photocurrent response because the nonlinear relationship between the test light and the photocurrent signal is very simple: The photons are absorbed by a linear process; the linear encoding is followed by a nonlinear process that converts the photopigment absorption rate into membrane photocurrent. The properties of the nonlinear process are independent of the linear encoding step, and thus we call this process a static nonlinearity. When a system is a linear process followed by a static nonlinearity, we can characterize the system performance completely.

It is worth spending a little time thinking about why we can characterize this type of nonlinear system. First, consider the linear process of photopigment absorption. There is a photopigment system matrix, say, $\mathbf{A}$, that maps the test light into a photon absorption rate, $\mathbf{At}$. Second, the static nonlinearity converts the photopigment absorption rate into a peak photocurrent response. Together, these two processes define the nonlinear system response, $F(\mathbf{At})$.

When we set a match between the peak photocurrent from the test light and the primary light, we establish an equation of the form

$$F(\mathbf{At}) = F(a\mathbf{Ap}) \tag{0.9}$$

where a is the intensity of the primary light needed to match the test light. Since the nonlinear function F is monotonic, we can remove it from both sides of Equation 0.9 and write

$$\mathbf{At} = a\mathbf{Ap} \tag{0.10}$$

From this equation we see that there is a linear relationship between the primary and test light intensities, since if $\mathbf{t}$ matches $a\mathbf{p}$, then $k\mathbf{t}$ will match $ka\mathbf{p}$. Thus, even if a system has a static nonlinearity, the system's performance in a matching experiment will satisfy the test of homogeneity. We can also show that in a matching experiment a system with a static nonlinearity will satisfy superposition.

Cone Photopigments and Color-matching

How well do the spectral sensitivity of the cone photopigments predict performance in the photopic color-matching experiment? We predict that two lights are metamers when they have the same effect on the three types of cone photopigments. To answer how well the cone photopigments predict the color-matching results, we can perform the following calculation.

Create a matrix, $\mathbf{B}$, whose three rows are the cone photopigment spectral sensitivities. We use this matrix to calculate the cone absorptions to a test light, so that $\mathbf{Bt}$ is a 3×1 vector containing the cone sensitivities to the test light. We predict that two lights $\mathbf{t}$ and $\mathbf{t}'$ will be a visual match when they have equivalent effects on the cone photopigments. Thus, two lights will be metamers when

$$\mathbf{B}\,\mathbf{t} = \mathbf{B}\,\mathbf{t}'$$

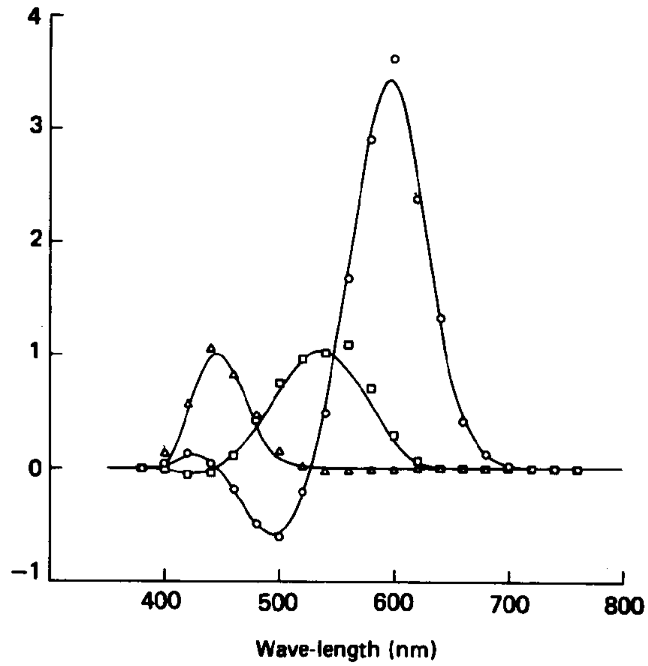

Figure 24: Comparison of cone photocurrent responses and the color-matching functions. The cone photocurrent spectral responsivities are within a linear transformation of the color-matching functions, after a correction has been made for the optics and inert pigments in the eye. The smooth curves show the Stiles and Burch (1959) 10 deg color-matching functions. The symbols show the matches predicted from the photocurrents of the three monkey cones. The predictions included a correction for absorption by the lens and other inert pigments in the eye (Source: Baylor (1987)).

It follows that the cone absorption matrix $\mathbf{B}$ is a system matrix for the color-matching experiment. This is precisely what we mean when we say that the cone photopigments can explain the color-matching experiment. Earlier in this chapter, we showed that the color-matching functions are all related by a 3×3 linear transformation. Thus, there should be a linear transformation, say $\mathbf{Q}$, that maps the cone absorption curves to the system matrix of the color-matching experiment, namely $\mathbf{C} = \mathbf{Q}\,\mathbf{B}$.

Baylor, Nunn and Schnapf made this comparison[3]. They found a linear transformation to convert their cone photopigment measurements into the color-matching functions. Figure 24 shows the color-matching functions along with the linearly transformed cone photopigment sensitivity curves. From the agreement between the two data sets, we can conclude that the photopigment spectral responsivities are a satisfactory biological basis to explain the photopic color-matching experiment.

Why this is a big deal

The methods we have used to connect cone photopigments and color-matching are a wonderful example of how to relate physiological and behavioral data precisely. To make the connection between the behavioral and physiological data we have had to reason through some challenging issues. Still, we have obtained a close quantitative agreement between the behavioral and physiological measurements.

Notice that as we began our analysis, the properties of the neural measurements and the behavioral measurements appeared different. The linearity of the color-matching experiment contrasts with the nonlinearity of the photocurrent response. But by comparing stimuli that cause equal-performance responses, rather than comparing behavioral matches with raw photocurrent levels, we can see past the dissimilarities and understand their profound relationship. In this case, we know how to connect these two different measurements and the simplicity and clarity of the relationship is easy to see. It makes sense, then, to ask what we can learn from this successful analysis that might help us when we move on to try to relate other behavioral and biological measurements.

We should remember that the relationship between behavior and biology may not always be found at the level of the measurements that are natural within each discipline. Direct comparisons between the intensity of the primary lights and the photocurrent signals do not help us to explain the relationship, even though each measure is natural within its own experiment. To make a deep connection we needed to look at the structural properties of the experiment. When we perform the color-matching experiment, we learn about the equivalence of different stimuli. This equivalence is preserved under many transformations. Thus, we succeed at comparing the behavior and the biology when we compare the results at this level, although they seem different when we use other quantitative measures.

[3]After correcting for the absorptions by the lens and inert pigments in the eye.

How do we know when we have the right set of biological and behavioral measures? There are many related physiological measures we might use to characterize the photoreceptors, and there are many variants of the behavioral color-matching experiment. For example, we could have asked the subject whether the brightness of the test light doubles when we double the intensity (the answer is no). Or we could have asked the subject to assess the change in redness or greenness. Just as the input-output relationship of the photocurrent may violate linearity for intense stimuli, so too many behavioral measures violate linearity. Finding the right measures to reveal the common properties of the two data sets is in part science and in part art. We learn about connections between these disciplines by trying to recast our experiments using different methods until the relationships become evident.

As we study the neural response in more central parts of the nervous system, you may be tempted to interpret a physiological measurement as a direct predictor of some percept. The rate at which a neuron responds or the stimulus that drives a neuron powerfully are natural biological measures. Remember, however, that there is no simple relationship between the photocurrent response and the intensity level of a primary light. We achieved a good link between the physiological and behavioral measures by structuring a theory of the information that is preserved in each set of experimental measurements. Understanding our measurements in terms of this level of abstraction — what information is present in the signal — is a harder but better way to forge links between different disciplines. Color science has been fortunate to have workers in both disciplines who seek to forge these links. We should take advantage of their experience when we relate behavior and biology in other domains.

Color Deficiencies

I have emphasized the fact that for most observers color-matching under the standard viewing conditions requires three primary lights to form a match and we call color vision *trichromatic*. There are some viewing conditions in which only two different primary lights are necessary. Under these viewing conditions, color vision is *dichromatic*. Finally, when only a single primary is required, as under rod viewing conditions, performance is *monochromatic*.

Small field dichromacy

Perhaps the most important of case of dichromacy occurs when we reduce the size of the bipartite field used in the color-matching experiment. If the field is greatly reduced in size, from 2 degrees to only 20 minutes of visual angle, then observers no longer need three independent primary lights: two primary lights suffice. Under these circumstances, observers act as if they have only two classes of photoreceptors rather than three.

Why should observers behave as if they had only two classes of receptors when the field is very small? If this observation surprises you, go back to Chapter and re-read the section on the S cone mosaic. You will find that there are very few short-wavelength cones, and there are none in the central fovea. Oddly, we encode less about the spectral properties of the incident light in the central fovea than we record just slightly peripheral to the fovea. In the central fovea, people are dichromatic.

Dichromatic observers

Some observers find that they can perform the color-matching experiment using only two primary lights throughout their entire visual field. Such observers are called *dichromats*. The vast majority of dichromats are male. By studying the family relationships of dichromats, it has been found dichromacy is a sex-linked genetic trait (Pokorny et al. (1979)). Dichromatic observers can be missing the long-wavelength photopigment (*protanopes*), the middle-wavelength photopigment (*deuteranopes*), or short-wavelength photopigment (*tritanopes*). Tritanopes are much more rare than either protanopes or deuteranopes. The difference in the probabilities arises because the gene responsible for the creation of the short-wavelength photopigment is on a different chromosome (Nathans et al. (1992)).

It is possible to use the color-matching functions measured from dichromatic observers to estimate the photoreceptor spectral responsivities. Suppose we have two dichromatic observers: the first observer has only the R and G photoreceptors, and the second observer has only the R and B photoreceptors. Since the photoreceptor sensitivities are linearly related to the color matching functions, a weighted sum of the first observer's color-matching functions will equal the R cone absorption function, and a different weighted sum of the second observer's color-matching functions will equal the R cone absorption function, too. This establishes a linear equation we can use to estimate the R cone absorption function. Similarly, from a pair of dichromats who share only the G cones, we can estimate the G cone sensitivity, and so forth.

Pseudoisochromatic Plates.

For some purposes, we do not need the complete results of a color matching experiment to learn about the observer's color vision. A much simpler test for dichromacy is to have a subject examine a set of colored images called the *Ishihara Plates*. These plates were designed based on the results of the color matching experiment and can be used to identify different types of dichromats based on a few simple judgments.

Each plate consists of a colored test pattern drawn against a colored background. The test and background are both made up of circles of random sizes; the test and background are distinguished only by their colors. Observers with red-green color deficiencies havedifficulty perceiving the test pattern based. Because this test iseasy to administer, it is commonly used as a quick screening tool todiscriminate normals from protanopes and deuteranopes.

Farnsworth-Munsell 100 Hue test

The *Farnsworth-Munsell 100 Hue test* is also commonly used to test for dichromacy. In this test, which is much more challenging than the Ishihara plates, the observer is presented with a collection of cylindrical objects, roughly the size of bottle caps and often called *caps*. The colors of the caps can be organized into a hue circle, from red, to orange, yellow, green, blue-green, blue, purple and back to red. Despite the name of the test, there are a total of 85 caps, each numbered according to its position around the hue circle. The color of the caps differ by roughly equal perceptual steps.

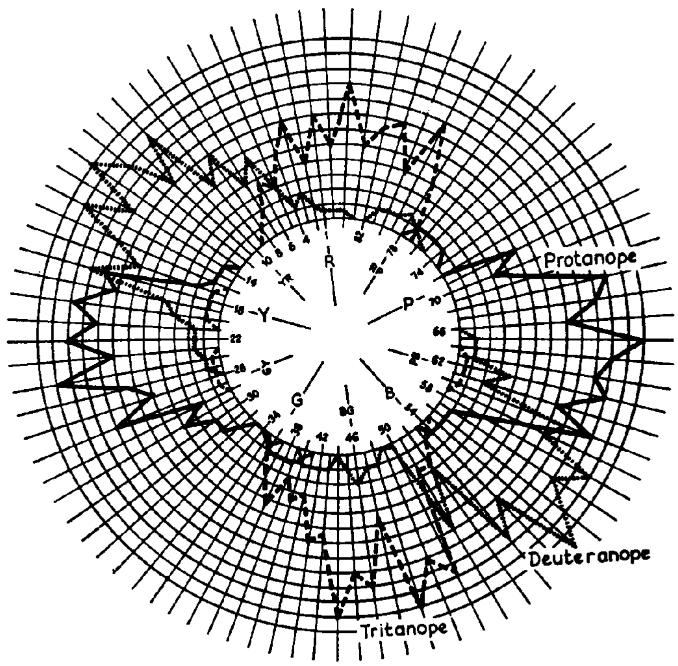

Figure 25: Representing errors in the Farnsworth-Munsell 100 Hue test. Each of the test objects, called caps, is assigned a position around the circle. The error score is indicated by the radial distance of the line from the center of the circle. Observers with normal color vision rarely have an error score greater than two. Errors characteristic of an observer missing the L cone photopigment (protanope), the M cone photopigment (deuteranope) and the S cone photopigment (tritanope) are shown. (Source: Kalmus (1965)).

The observer's task is to take a random arrangement of the caps and to place them into order around the color circle. At the beginning of the task, four of the caps (1,23,43, and 64) are used to establish anchor points for the color circle. The subject is asked to arrange the remaining color caps "to form a continuous series of colors."

The hue steps separating the colors of the caps are fairly small; subjects with normal color vision often make mistakes. After the subject finishes sorting the caps, the experimenter computes an error for each of the 85 positions along the hue circle. The error score is equal to the sum of the absolute differences between the number on the cap and its neighbors. For example, in the correct series 1-2-3-4-5-6 the error score for caps 2 through 5 is 2, the smallest error score. With a single misodering, say 1-3-2-4-5-6, the error scores for caps 2 to 4 are 3, and the error score for 5 remains 2. Normal observers do not produce an error greater than 2 or 3 at any location.

The subject's error scores are plotted at 85 positions on a circular chart as in Figure 25. An error score of zero plots at the innermost circle and increasing error scores plot further away from the center. Subjects missing the L cones (protanopes), M cones (deuteranopes), and S cones (tritanopes) show characteristically different error patterns that cluster along different portions of the hue circle.

Anomalous Observers

Dichromatic observers have only two types of cones. The slightly larger population of observers, who are called *anomalous*, have three types of cones and require three primaries in the color-matching experiment. The matches that they set are stable, but they are well outside of the range set by most of the population. These observers have cone photopigments that are slightly different in structure from most of the population, which is why they are called anomalous. The color-matching functions for anomalous observers are not within a linear transformation of the normal color-matching functions. This is equivalent to the experimental observation that lights that visually match for these observers do not match for normal observers, and vice versa.

Neitz et al. (1993) have argued on genetic grounds that many people contain small amounts of the anomalous photopigments so that there are more than three cone photopigment types in the normal eye. Because the anomalous photopigments are not very different from the normal, it is hard to discern their presence in all but the most sensitive experimental tasks. They attribute the trichromatic behavior in the color-matching experiment to a neural bottleneck rather than a limit on the number of photopigment types. Since the differences between the normal and anomalous photopigments are very small, however, this hypothesis will be difficult to prove or disprove and it will have very little impact on color technologies.

The relationship between anomalous observers and normal observers parallels the relationship between color cameras and normal observers. The spectral responsivities of the color sensors in most color cameras differ from the spectral responsivity of the human cone photoreceptors. Worse yet, the camera sensors are not within a linear transformation of the cone photopigments. As a result, lights that cause the same effect on the camera, that is lights that are visual matches when measured at the camera sensors, may be discriminable to the human observer. Conversely, there will be pairs of lights that are visual matches but that cause different responses in the camera sensors. I will return to discuss this topic when we return to discuss color appearance in Chapter .

Color Appearance

Color-matching provides a standard of precision to strive for when we analyze the relationship between behavior and physiology. The work in color-matching is also important because it has had an impact well beyond basic science, into engineering and technology that touch our lives.

The success of color-matching and its explanation is so impressive, that there is a tendency to believe that color-matching explains more than it does. The theory and data of photopic color-matching provide a remarkably complete explanation of when two lights will match. But, the theory is silent about what the lights look like.

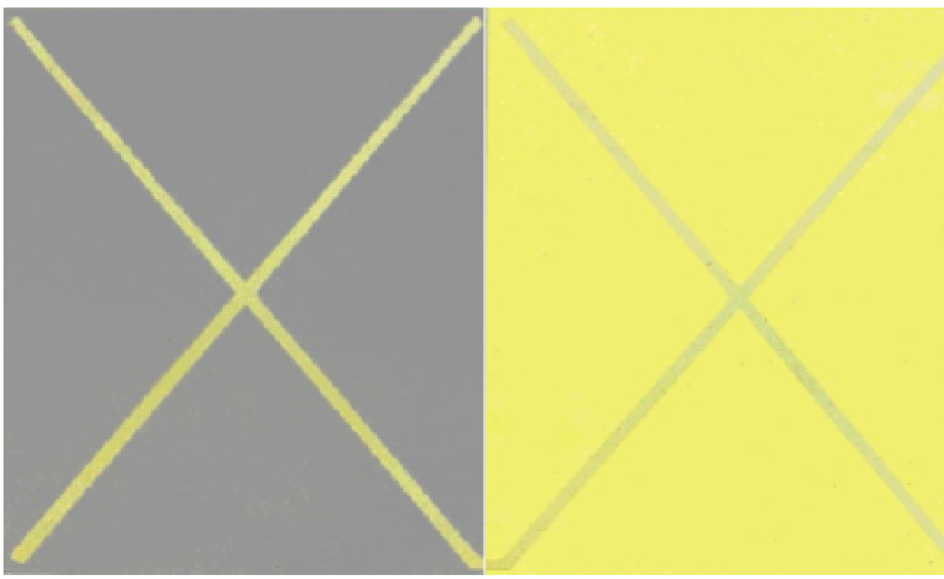

Figure 26: **Color Plate 2**. Color-matching does not predict color appearance. The X's are physically the same (notice where they join) and thus have the same effect on the photopigments; but, their appearance differs. The photopigment responses at a point do not determine the color appearance at that point. Appearance instead depends on the spatial structure in the image. (Source: Albers (1975)).

Often, students who are introduced to color-matching for the first time are surprised that the words brightness, saturation and hue never enter the discussion. The logic of the color-matching experiment, and what the color-matching experiment tells us about human vision, does not speak to color appearance. What we learn from color-matching is fundamental, but it is not everything we want to know. For many purposes we want to know An understanding of color-matching is necessary for an understanding color appearance; but, it is not a solution to the problem.

To emphasize the separation between color-matching and color appearance, consider the following experiment. Suppose that we form a color-match between two lights that are presented as a pair of crossing lines against one background. Such a pair is illustrated on the left hand side of Color Plate 2. On the left, the lines both appear gray. Now, move this pair of lines to a new background. Color-matching assures us that the two lights will continue to match one another as we move them about.

But we should not be assured that their appearance remains the same. For example, on the right of the figure we find that the pair of lights now have quite a different color appearance. By examining the point where the lines come together at the top of Color Plate 2, which is a painting by the artist Joseph Albers, you can see that the lines are physically identical on both sides of the painting.

Color-matching is different from color appearance. To build theories of color appearance we will need to incorporate experimental factors — such as the viewing context — that are not included in either the theory or experimental manipulations of the color-matching experiment. It is precisely because the important discoveries recounted in this chapter do not solve the problem of color appearance that the chapter is so oddly titled. We will review the topic of color in Chapter .

Image Representation

Introduction to Image Representation

Our understanding of how the visual pathways represent images is based upon a diverse collection of methods, drawn from several different fields. Four broad principles emerge from the studies in these different disciplines.

- Anatomical studies show that the neurons in the visual pathway are segregated into different *visual streams*. The functional role of the visual streams must be inferred from the anatomical properties along with the way the neurons in these separate streams respond to light stimulation.
- The most important information represented by the visual pathways is the image *contrast*, not the absolute light level. The image contrast is the ratio of the local intensity and the average image intensity. To represent the image contrast, neurons in the visual pathway change their sensitivity to compensate for changes in the mean illumination level. This process, called *visual adpatation*, permits the visual system to represent information in terms of the relative intensity of different portions of the visual field, i.e., the contrast, rather than the absolute intensity.
- Behavioral and electrophysiolgical measurements suggest that contrast information is represented at different spatial scales and orientations.
- As we try to integrate information from these diverse areas, we will consider the question of what standards we can apply to merge measurements from these different fields of study.

Visual Streams

The visual system consists of a collection of pathways, each responsible for analyzing different aspects of the retinal image. The specialization of the visual pathways begins at the peripheral stages of the visual encoding with the segregation into rods and cones. The segregation is elaborated in the retina and continues into the cortical areas.

The distinction between rod and cone vision is clear: the division of labor between rods and cones permit us to extend the range of illumination conditions where we can see. It seems likely that the visual streams throughout the visual pathways exist to meet various functional requirements. How can we establish their roles?

One visual stream in the retina contains the signals communicated to control eye movements. The spatio-temporal image information needed to control eye movements differs from the information needed to analyze fine detail and color in spatial patterns. This visual stream can be identified based in part on its anatomical connections and in part from the fact that the neurons in this stream respond to light differently from the neurons that signal pattern and shape information.

In the primate retina, one pair of visual streams, based on two specialized types ganglion cells whose inputs are kept separate into primary visual cortex, has been studied extensively. One stream represents contrast information that varies slowly over space but rapidly over time, while the other represents information that varies rapidly over space but slowly over time. The specialization of these visual streams, too, must serve a purpose in extending visual performance.

Separate visual areas exist within the visual cortex as well. These areas can be identified from their unique patterns of interconnection. The functional significance of these areas is an important question in modern vision science, and we will review some of the hypotheses about these areas in the later chapters.

Adaptation and Contrast

It would be impractical to create a new visual stream to meet every visual challenge. Neurons within individual pathways must be able to adjust to their sensitivity to light stimulation in response to changes in the imaging conditions.

The most salient adjustment of the image representation is the compensation in response to variation in the illumination level, *visual adaptation.* As the mean illumination level increases, the light sensitivity of individual neurons in the visual pathway, and of the whole observer, decreases.

Under many conditions the change in sensitivity achieves a constant representation of image *contrast*, rather than image light level. Image contrast is the ratio of the light at a point compared to the light at nearby points. Since this ratio is preserved as the level of ambient illumination decreases, preserving image contrast enhances our ability to distinguish and recognize objects in the image.

Multiresolution representations

Behavioral studies of contrast sensitivity suggest that image contrast is represented within separate visual streams that specialize in coding the information within a certain range of spatial frequencies and orientations. This *multiresolution* representation is qualitatively consistent with measurements of receptive field properties in primary visual cortex.

Multiresolution image representations have become a standard tool in computational applications, including image compression, segmentation, and analysis. To understand the implications of multiresolution for the visual pathways, we will spend some time thinking about how these computational applications can be designed to work with multiresolution representations.

Linking Hypotheses

Within vision science, biological and behavioral measurements data are frequently compared. G.S. Brindley called hypotheses that relate measurements in these fields *linking hypotheses*. He advised that we adopt a very conservative position in drawing connections between biological from behavioral measurements.

This conservatism is far from universally accepted. For example, Zeki argues that a fearless attitude in speculating about linking hypothesis is to be admired and emulated. Begin by formulating guesses about brain and perception, he argues. The number of views on this matter exceeds the number of vision scientists.

The next few chapters contain many examples in which behavior and physiology are compared. What standard should we adopt before we accept a neural phenomena as corresponding to a behavioral phenomenon?

A necessary condition for accepting a neural measurement as an explanation of a behavioral measurement is this: the logic of the separate experiments must stand on their own. An analogy between a few behavioral measurements and the receptive field properties of a neuron may be suggestive, but it should only serve as an inspiration for more perspiration.

Use the relationship between color-matching behavior and photopigment sensitivities as your model of a complete story. The linking hypothesis for color-matching is built by connecting a quantitative set of behavioral measurements and a quantitative set of physiological measurements. For each type of measurement, we can derive a clear set of rules that define how the system will respond to a wide range of stimuli. When each analysis stands on its own, the link between behavior and physiology is strongest.

Retina

Retinal overview

In this chapter we will review the structure of the retina and its role in organizing visual information. The retina is a thin layer of neural tissue that lines the eye. After the retinal image is encoded by the photoreceptors, neurons within the retina transform the photoreceptor signals into a new representation that is carried by the optic nerve to a variety of locations in the brain. The retina is important for several reasons. First, the retina is important to neuroscientists because it is a very accessible part of the central nervous system making it an important site for scientific study Second, the retina is important to clinicians since it is the only part of the central nervous system that can be examined directly, by using an opthalmoscope. Third, the retina is important to vision scientists because it has several important visual functions, including encoding the image and transforming it into a collection of separate pathways that send information about the entire retinal image to the brain. Since retinal neurons develop from the same progenitor cells that give rise to the brain, the organization of information within these retinal pathways is also an important clue about the organization within the brain as well.

Retinal structure

Over most of its extent, the primate retina is approximately 0.5 mm thick and consists of three layers of cell bodies and two layers containing the synaptic interconnections between the neurons. Near the optical axis of the eye, however, the primate retina contains a specialized region, the fovea, consisting of only a single layer of neurons, the cone photoreceptors. Both of these structural properties of the retina can be seen in the anatomical cross-section section of a human retina shown in Figure 1.

Figure 2 shows two types of retinal neurons and identifies some of their parts, including the dendritic fields, cell bodies, and axon. The dendritic fields receive input from other neurons; the axon, which may branch, carries the neuron's output to its destination[1].

[1] Some neurons have no axon, exerting their influence only at local interconnections at synapses within the dendritic field. The shape of a neuron's dendritic field and its axonal branches are generally important features for distinguishing broad classes of neurons. We will use many features, including the locations of cell bodies, dendrites and axons; the size and shape of their cell bodies and dendritic fields; and, their interconnections with other neurons, to classify and understand retinal neurons.

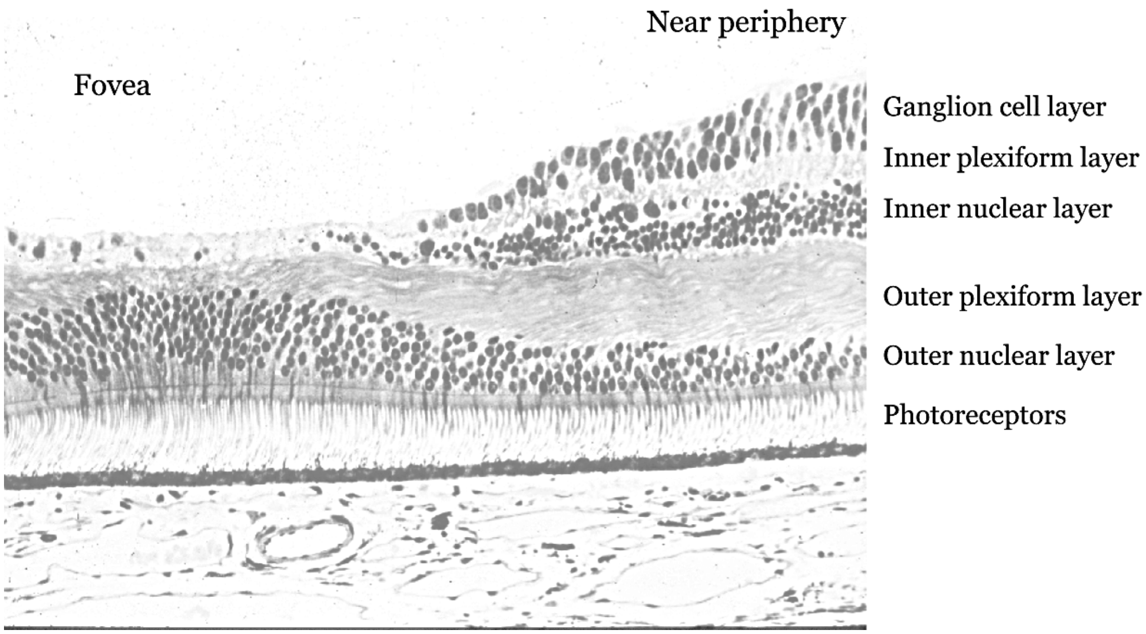

Figure 1: The human retina is a thin layer of neural tissue that lines the back of the eye. In the near periphery and periphery the retina is a layered structure. The cornea and lens would be at the top of this picture, so that in the periphery light must pass through the retinal layers before being absorbed by the photoreceptors. In the fovea the retina consists of only a single layer of photoreceptors as the neurons responsible for carrying the responses of the foveal cones are displaced to the side, out of the light path. (Source: A. Hendrickson, personal communication).

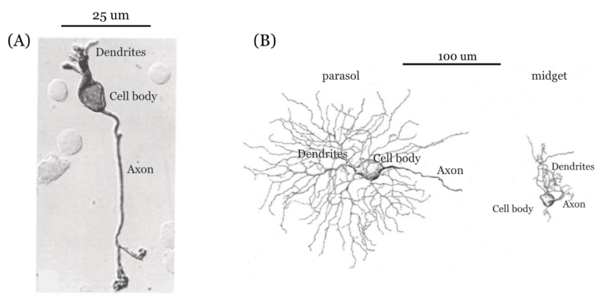

Figure 2: Retinal neurons have many different shapes and sizes. A midget bipolar and a parasol-type ganglion cell are shown. (a) The cell body of a bipolar cell resides in the inner nuclear layer. Its dendrites make contact with the photoreceptors and horizontal cells and its axon carries the output of the bipolar cell to the inner plexiform layer where it contacts the dendritic field of a ganglion cell. There are several different types of bipolar cells; the cell shown is a midget bipolar whose dendritic tree makes contact with a single photoreceptor and whose axon makes contact with a single ganglion cell. (Source: Yamashita and Wässle (1991)). (b) The retinal ganglion cell bodies reside in the ganglion cell layer of the retina. The axons of the retinal ganglion cells comprise the optic nerve. Several types of retinal ganglion cells can be distinguished based on the properties of their dendritic fields, their interconnections, and their cell bodies. The cells drawn here are midget and parasol cell (Source: Dacey and Petersen (1992)).

There are five basic categories of retinal neurons, although each category has several subclassifications. The major categories of retinal neurons are distinguished by the location of their cell bodies, dendritic fields, and axon terminals. The photoreceptors' cell bodies are located in the *outer nuclear layer* of the retina. The synaptic terminals of the photoreceptors make contact with the dendritic fields of the *bipolar* and *horizontal* cells in the *outer plexiform layer*. The cell bodies of the bipolar and horizontal cells are located in the *inner nuclear layer*. Both the dendrites and the branching axon terminals of the horizontal cells make connections with cells in the outer nuclear layer. The bipolar cells, however, make connections onto the the dendrites of the *ganglion cells* within the *inner plexiform layer*. Since only the bipolar cells link the signals in the outer and inner plexiform layers, all visual signals must pass through the bipolar cells.

The *amacrine* cell bodies are also located in the inner nuclear layer. Santiago Ramon y Cajal gave these cells their name to indicate that they have no identifiable axons, but only dendrites. The dendritic fields of the amacrine cells make connections with the dendritic fields of the ganglion cells in the inner plexiform layer. The retinal *ganglion* cell bodies are located in the *ganglion cell layer*, and their dendritic fields connect with the axon terminals of the bipolars and the dendritic fields of the amacrine cells.

The axons of the retinal ganglion cells provide the only retinal output signal. The ganglion cell axons comprise the *optic nerve* and they exit from the retina at a single location in the retina called the *optic disk*. There are no photoreceptors at the optic disk, so we do not encode or perceive the light that falls there. Consequently, the optic disk is also called the *blindspot*. We are not aware of the blindspot in our eyes ordinarily since the portion of the visual field falling in the blindspot of one eye falls on functional a retina in the other eye. You can perceive your blindspot by closing one eye and then carefully fixating with the other eye on the "x" in Figure 3. Move the screen to a viewing distance where the white square disappears, roughly 25 cm from your nose. Notice that the white square and dot within the texture pattern fill in, while the dots at a comparable visual eccentricity are still visible. Thus, the dot disappears because of the blindspot and not because of a loss of visual acuity in the periphery.

Retinal function: specialization

The retina segregates visual information into parallel neural pathways specialized for different visual tasks. In earlier chapters, we reviewed one example of neural specialization in the retina: there are two different types of photoreceptors, the rods and the cones, that both sample the image. These two photoreceptors types are responsible for encoding the visual image in different intensity ranges.

The segregation of rod and cone signals continues through several synaptic connections within the retina. Kolb and her collaborators have shown that the signals initiated within the rods follow a separate rod pathway within the retina until the signals arrive at the retinal ganglion cells (see Figure 4). The rods make connections with a class of bipolars, the rod bipolars, that

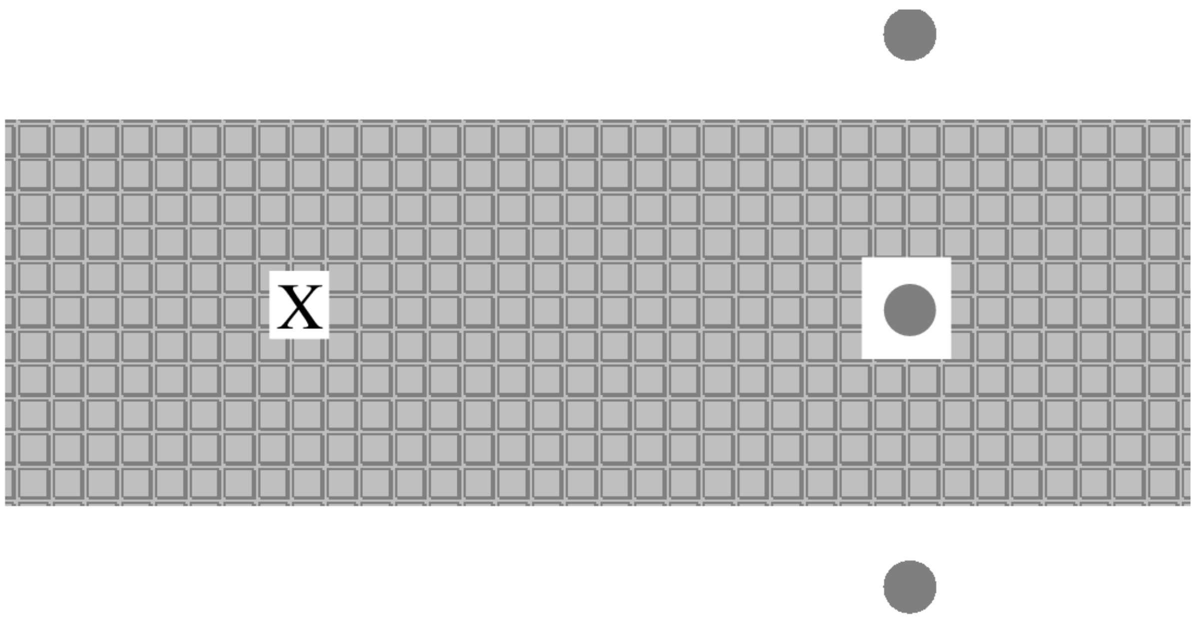

Figure 3: A demonstration of the blindspot. Place the page about 25 cm from your eye. Then close your left eye and fixate the X: the white spot in the texture will disappear. If it does not, then slowly move the book back and forth, carefully maintaining fixation, until the spot does disappear. The two squares above and below become hard to see in the periphery, but they do not disappear. This demonstrates that the disappearance of the central square is not merely due to a general loss of visibility at this eccentricity.

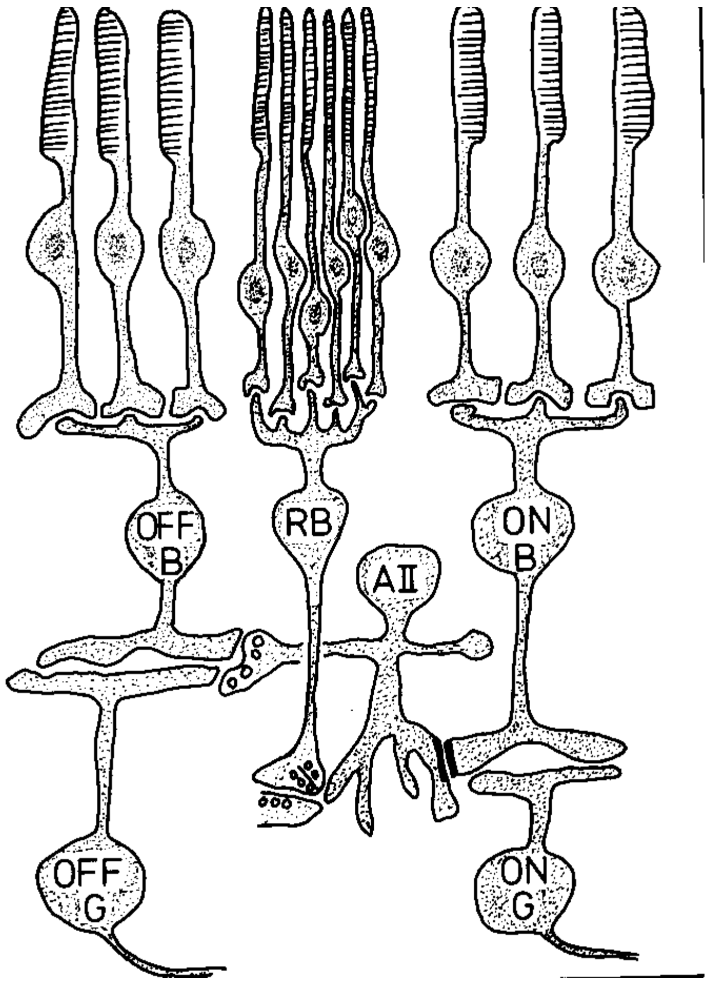

Figure 4: A rod-initiated pathway in the vertebrate retina. Axons from more than 1000 rods converge upon a single rod bipolar cell. The rod bipolar send their outputs to a specialized amacrine cell, the AII, located in the inner plexiform layer. The AII amacrine cell communicates the rod-initiated signal to two types of ganglion cells, one whose dendritic field is in the upper layers of the inner plexiform layer and another whose dendritic field is in the lower layers. The responses of ganglion cells whose dendritic fields are in the upper layer are decreased by light, while responses of ganglion cells whose dendritic fields are in the lower layer are increased by light (Source: Wässle and Boycott (1991)).

integrate the responses of many different rod photoreceptors. Presumably, pooling the signals from many rods enhances the sensitivity of this rod pathway. The rod bipolars synapse directly onto type AII amacrine cells, but unlike other bipolars the rod bipolars do not synapse directly onto ganglion cells. The rod bipolars synapse on the AII amacrine cells within a narrow level of the inner plexiform layer. Finally, the AII amacrines synapse onto retinal ganglion cells both within the same level of the inner plexiform layer and also at a a second level of the inner plexiform layer. The ganglion cells that connect with the AII amacrine cells also receive signals via a cone-initiated pathway. Hence, the rod pathway merges with a cone-initiated pathway and disappears as a unique entity at this point.

By examining the properties of the rod pathway, we can see certain general features that might also be true of the organization of other visual pathways. First, the rod pathway only exists over a few synapses, serving its function and then merging with the main visual signal. By converging onto the main processing stream, central processing elements that define shape, form, and so forth can analyze both the rod and cone signals and need not be duplicated. Thus, a visual pathway may serve its purpose within a few synapses and then disappear.

Second, we see that visual streams may be created to serve fairly rudimentary functions, such as enhancing some aspect of the information in the image. The strong convergence of signals within the rod pathway — a single rod bipolar may integrate the signal from 1500 rods — makes the rod pathway well-suited to capturing information at low light levels while paying a penalty in terms of visual acuity. Hence, visual pathways may be created to achieve a special computational goal.

There are probably many types of information, in addition to the illumination level, that are formed for special computational purposes. For example, some types of behaviors may require precise visual information of one sort; say, to track a moving object. To improve this type of performance, one may require a pathway with excellent temporal resolution. Other behaviors may require precise visual information of another sort; say, to identify a texture pattern may require high spatial acuity. This might require a pathway with very high spatial sampling resolution. Rodieck et al. (1993) estimate that there may be as many as twenty pathways originating within the retina, and that each of these pathways communicates its signal to a different location in the central nervous system. Like the rods and cones, each subcategory of retinal ganglion cell obtains a fairly complete copy of the retinal image. We may presume that each subcategory of ganglion cell type specializes in communicating about certain types of visual information.

We will refer to the connected series of neurons carrying information in parallel as *visual streams* or *visual pathways*. The precise site where information is segregated into different visual streams within the retina is not certain, but it seems likely that the segregation begins immediately at the output of the rods and cones. In fact, there appear to be about 15 to 20 different bipolars that make contact with each cone. The information encoded by each of the bipolars may serve as the starting point for the visual streams that have been identified at points further along the visual pathway (Rodieck et al. (1993); Wässle and Boycott (1991)).

Evidently, one of the important functions of the retina is to organize the information encoded by the photoreceptors into a collection of visual streams. Presumably, the purpose of these separate visual streams is to communicate relevant image information efficiently to brain areas engaged in specialized types of visual processing. This observation reinforces the view that the existence of these visual streams can be an important clue about the functional organization of the visual pathways. We presume that each visual stream carries an efficient representation of the spatio-temporal component of the image that is most relevant for task carried out in visual area where the ganglion cell output is sent. Hence, by studying the response sensitivity to different kinds of stimuli of the neurons within a visual stream, we learn something about the functional role of that stream.

Retinal function: image contrast and adaptation

There are some visual challenges that are common to the information carried on all of the specialized visual streams. It makes sense to try to solve these types of problems when the signals are close together, as in the retina, rather than after the visual signals have reached widely separated destinations within the brain.

A fundamental challenge that is common to the signals carried by all retinal neurons is this: they must remain sensitive as the ambient light intensity varies over many orders of magnitude. This is a challenge for the nervous system because neurons have a very limited response range.

Neurons in the peripheral visual system solve this problem, in part, by signaling the local contrast in the image rather than the absolute stimulus level. The local contrast is the percent change in the image intensity relative to the local average. The range of contrasts in a typical image is constant as ambient illumination level changes and typically spans no more than two orders of magnitude. By coding contrast, rather than absolute level, neurons with small dynamic range can convey essential information about the retinal image despite enormous variations in the absolute level. In later chapters we will review computational issues and we will find that in contrast is an important signal in its own right. The contrast signal is closely coupled to the properties of surfaces, and surfaces are often the visual entity we want to identify or recognize[2].

[2] In some books the dynamic range problem is treated by explaining that the photoreceptors respond to light intensity using a compressive function of intensity, such as a logarithmic or power function. A compressive function maps a light stimulus ranging over six orders of magnitude into neural responses of one to two orders of magnitude above their intrinsic variability. In the modern literature, this view has been substantially replaced by a formulation based on stimulus and response contrast.

Visual Streams

We will begin by reviewing the kinds of methods we can use to classify retinal neurons. Then, we will review the principal features of the information carried within two specific visual streams, the *parvocellular pathway* and the *magnocellular pathway*. We focus on these two streams because we know most about them and because their output represents a very large fraction of the total output of the retina.

Methods of classifying neurons

The form and structure of a neuron, including its dendritic field, cell body, and axonal projections, are called the neuron's *morphology*, The most fundamental method of distinguishing categories of neurons is simply to study their morphology. A second type of data we can use is the neuron's electrical responsiveness to different signals, that is its *electrophysiology*. A third type of data we can use is to study the chemical substances used to build the neuron, that is the neuron's *biochemistry*. A fourth type of data is the *anatomical* pattern of interconnections a neuron makes with other neurons. The most satisfying classification of neurons occurs when the evidence from these different sources converge.

We used all of these methods to distinguish the photoreceptors into rods and cones. The rods and cones can be classified based on their morphology of the cell (rod-like shape versus cone-like shape), the type of photopigment they contain, their electrical response to light, and their interconnections (rods make no connections in the fovea). Taken together, the classification of rods and cones also suggests a difference in function, namely that cones carry visual information used for high acuity tasks and rods are specialized for low illumination conditions.

It is natural to use our successes at peripheral levels to guide our next analysis of cellular function. So, we begin the analysis of the retinal ganglion cells by considering how we can use the measurements to categorize the retinal ganglion cells into groups serving various visual functions.

Morphology of Parasol and Midget Ganglion Cells

When examining the retinal ganglion cell layer using a light microscope, one sees ganglion cells of many different sizes, shapes and patterns of dendritic fields. In an extraordinary set of studies, Santiago Ramon y Cajal examined the retinal cell types in many mammalian eyes, but no primates, and identified the basic anatomical structure of the retina. To classify neurons, Cajal used several morphological properties, relying mainly on the location of the dendritic arbor terminations. Figure 5 shows Cajal at work, along with one of his sketches of the mammalian retina.

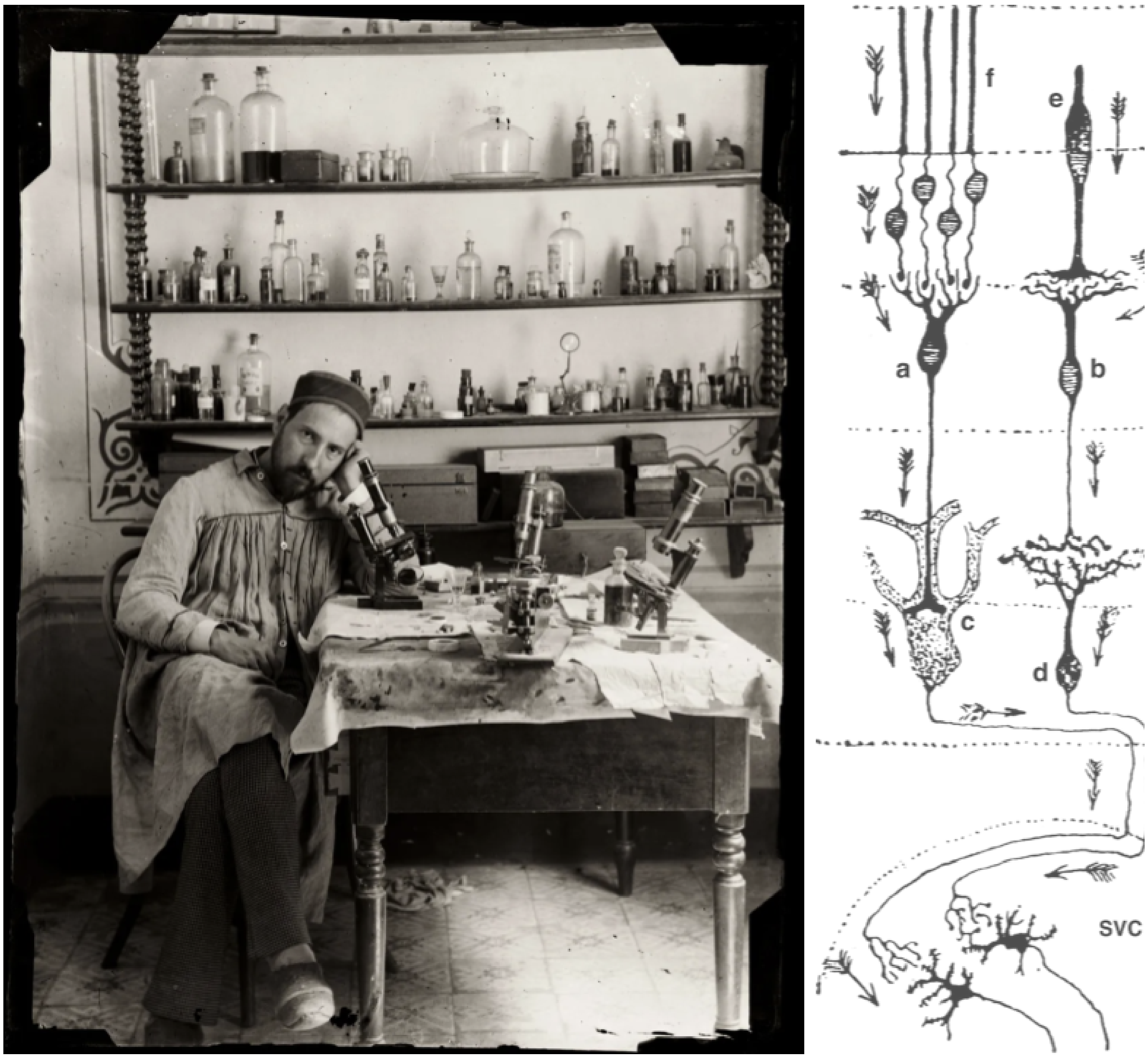

Figure 5: Ramon y Cajal and one of his drawings. Cajal is shown at his lab bench along with a drawing he made of the direction of visual signals in a mammalian retina. The labeled cells in part A of Cajal's drawings are (a) rod bipolar, (b) cone bipolar, (c) and (d) ganglion cells. The connections with a subcortical visual center are shown in part B (Source: Popova (2017) and Reichenbach and Bringmann (2022)).

The modern era of anatomical studies in the primate retina began with the work of Stephen Polyak (Polyak (1941); Polyak (1957)) who wrote a remarkable pair of books describing his investigations into the primate visual system. Polyak described many aspects of the anatomical structure of the retina specifically and the primate vertebrate visual system generally. In his work on the retinal ganglion cells, Polyak identified five different categories of cells using the size of their cell bodies and the properties of their dendritic fields. One of the principal classifications he made, and the one that will concern us here, was based on the size and spread of the retinal ganglion cell dendritic arborizations. At most locations within the retina one can identify some neurons whose dendritic fields are relatively dense and compact compared to other retinal ganglion cells. Near the fovea these neurons are particularly conspicuous since they make contact with only a single bipolar which in turn makes contact with only a single cone. Polyak was the first to identify these retinal ganglion cells which are abundant in the primate but absent in other mammals. Polyak named these cells *midget* ganglion cells. Several midget ganglion cells at different positions within the retina are illustrated in Figure 6 (a).

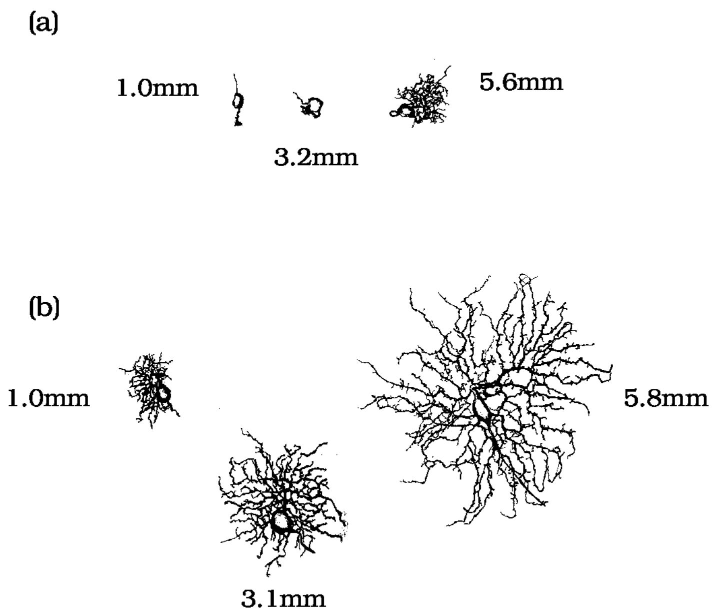

Figure 6: A comparison of midget and parasol retinal ganglion cell morphology at various retinal eccentricities. (a) Midget ganglion cells and (b) parasol ganglion cells from a series of positions within the retina are shown as camera lucida drawings. At comparable positions within the retina, the dendritic tree of the midget ganglion cell is smaller and denser than that of the parasol cell. For both types of cells, however, the absolute size of the dendritic field increases with eccentricity. (Source: Watanabe and Rodieck (1989)).

The morphology of the midget ganglion cells contrasts with a second class of ganglion cells shown in Figure 6 (b) and called *parasol* cells by Polyak. The parasol cells have a sparse dendritic tree and medium to large cell bodies. The drawings in Figure 6 compare a sampling of the midget and parasol cells at several distances from the fovea.

Variation with retinal eccentricity

As Polyak noted, the size of many types of retinal neurons increases with distance from the fovea. For example, a cell body or dendritic field that is relatively large in the fovea will be relatively small in the periphery. While Polyak says that the midget ganglion cells are present throughout the retina, due to retinal inhomogeneity the midget ganglion cells in the periphery are larger than the parasol cells near the fovea. If absolute size is not a reliable indicator, what measurement can we use to decide whether neurons at different eccentricities are of the same type? In a seminal paper, Boycott and Wässle (1974) showed how to make such a measurement in the retina of the domestic cat. The idea is simple and elegant: make measurements that span a wide range of retinal eccentricities and compare the trends within the population. Boycott and Wässle's methods and observations have been extended from cat to the primate and human (Perry and Cowey (1981), Perry and Cowey (1984); Levinthal et al. (1981); Rodieck et al. (1985); Watanabe and Rodieck (1989); Dacey and Petersen (1992)).

Figure 7 shows that the size of dendritic fields of the midget and parasol ganglion cells increase with eccentricity in the human retina. Although both cell types increase in size, within each cell type the dendritic field size varies smoothly and at each retinal eccentricity the sizes of the two populations remain distinct. The graph in Figure 7 suggests that the signals from the midget cells form one unified visual stream and the parasol cells form a second visual stream (Dacey and Petersen (1992)).

Further evidence that these two classes of neurons form independent visual streams comes from their coverage of the retinal image. Both midget and parasol cells are present at every location within the retina. Thus, each class of neuron encodes a complete copy of the retinal image.

Although the two populations both receive a complete copy of the image, they do not encode the image at the same spatial resolution. In the fovea, midget ganglion cells receive input from a single cone (N.B. This does not mean that a cone sends its output to a single bipolar or ganglion!). From the spread of their dendritic fields, we see that the parasol cells receive convergent input from a much wider area of the retina. The fine resolution achieved by the midget ganglion cells means that more of them than parasol cells are needed to encode the entire retinal image. There appear to be 7 or 9 times as many midget cells as parasol cells (Sterling et al. (1994); Perry et al. (1984)). The midget ganglion cells encode the spatial image up to the full sampling resolution of the photoreceptors, roughly 60 cycles per degree. The smaller number of parasol cells are capable of encoding the signal up to a spatial resolution of 20 cycles per degree.

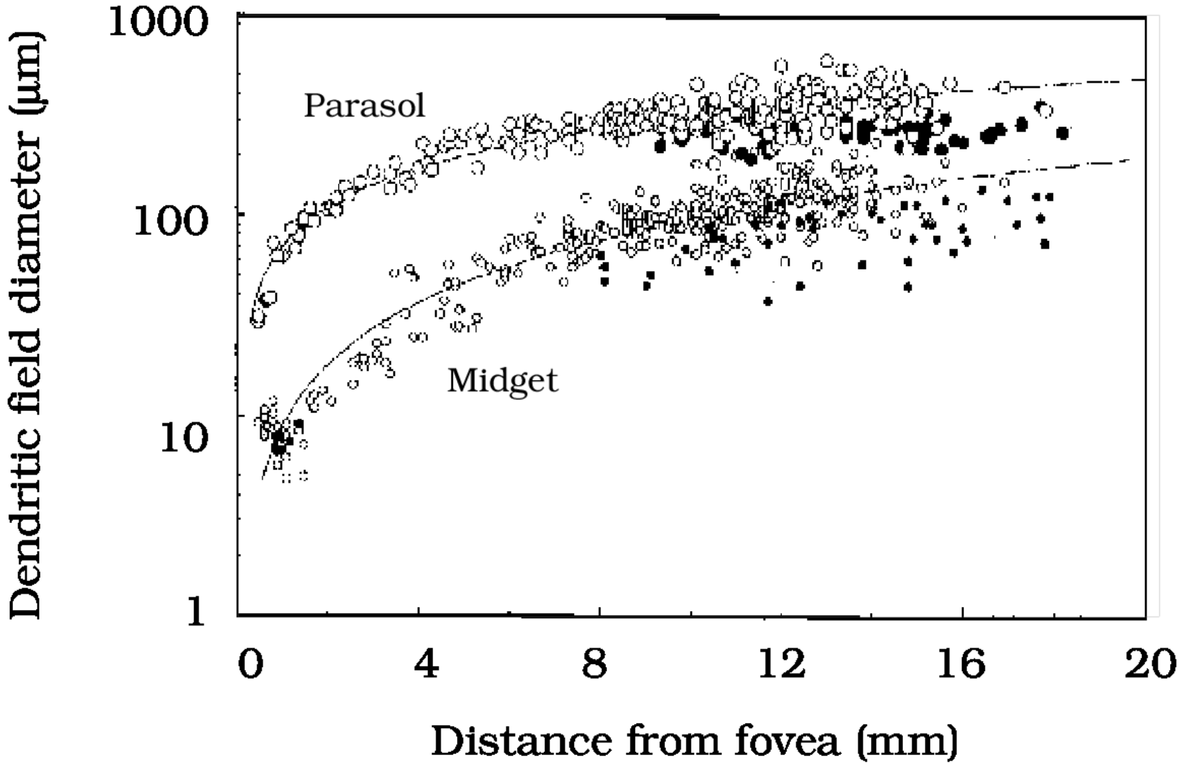

Figure 7: Dendritic field size as a function of eccentricity in the human retina. The graph shows the dendritic field size of midget and parasol neurons. The dendritic field size increases with eccentricity for both types of neurons, but at each eccentricity the sizes are easily classified. (Source: Dacey and Petersen (1992)).

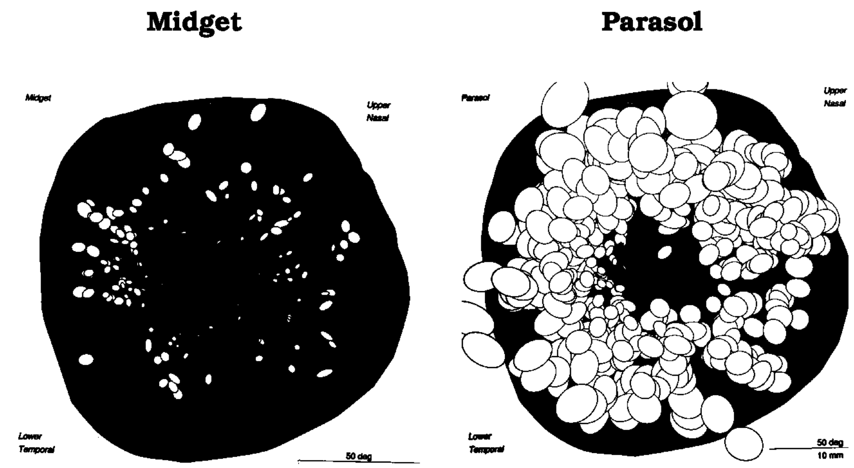

Figure 8: Midget and parasol dendritic fields both sample the entire retinal image. The dendritic fields of the midget ganglion cells (a) are small compared to the dendritic fields of the parasol cells (b). Parasol cells have much larger dendritic fields at each retinal location, so that fewer are needed to cover the entire retina (From Watanabe and Rodieck (1989)).

Central Projections

A second method of identifying visual streams originating in the ganglion cell layers is to consider how the retinal ganglion By injecting tracer substances that are carried from the brain back to the retina, we can identify where each type of retinal ganglion cell sends its outputs.

Perry et al. (1984) studied how different cell types send their axons to brain structures. They injected a tracer substance called *horseradish peroxidase* into the optic nerve. When horseradish peroxidase is absorbed by a neuron, it is transported throughout the neuron. Thus, if the horseradish peroxidase is absorbed in an axon, it is transported back to the cell body. Conversely if the horseradish peroxidase is absorbed in the cell body, it will be transported down to the axon terminals. The presence of horseradish peroxidase within a neuron can be established by appropriate histochemistry. By injecting the tracer into the optic nerve, they could identify the appearance of all cell types when stained by horseradish peroxidase.

Perry et al. (1984) also introduced horseradish peroxidase into the lateral geniculate, a nucleus located in the *thalamus*, that is a major recipient of axons from the retina. The majority of the retinal ganglion cells make a connection with this nucleus, so that the horseradish peroxidase was transported to many retinal ganglion cells. They estimate that 90 percent of monkey retinal ganglion cells send their axons to the lateral geniculate layers. While the preponderance of retinal ganglion cells containing horseradish peroxidase could be classified as either parasol or midget, there is some evidence that at least two other types of retinal ganglion cells also send their outputs to the lateral geniculate nucleus (Rodieck et al. (1993)).

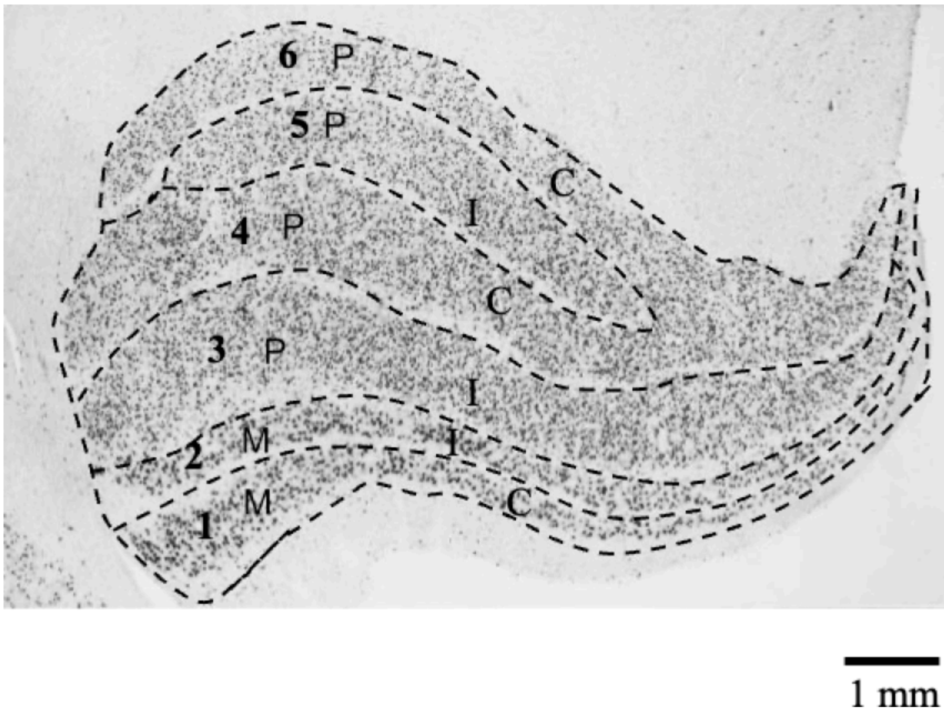

Figure 9: The lateral geniculate nucleus (LGN) is located in the thalamus. In primates, most retinal ganglion cell axons terminate in the LGN. Using a Golgi stain, the LGN shows six distinct layers: the four upper layers are the **parvocellular layers (P)**, which contain small cell bodies and receive input mainly from midget ganglion cells; the two lower layers are the **magnocellular layers (M)**, which contain large cell bodies and receive input mainly from parasol ganglion cells. Each layer receives input from only one eye—either the same side (I, ipsilateral) or the opposite side (C, contralateral). Neurons are also found between these layers in regions called intercalated zones, which require specialized markers to visualize. (Adapted from Andrews et al. (1997))

There is considerable regularity in the distribution of axons from the parasol and midget neurons within the primate lateral geniculate nucleus. The primate lateral geniculate nucleus contains six different layers (see Figure 9). The four superficial layers contain neurons with small cell bodies and are called the *parvocellular layers*. The two deeper layers contain neurons with large cell bodies and are called the *magnocellular layers*. The axons of parasol and midget retinal ganglion cells make connections in different layers of the lateral geniculate nucleus. The axons of the midget retinal ganglion cells terminate in the parvocellular layers, while the axons of the parasol cells terminate in the magnocellular layers. In addition to the cell bodies within parvocellular and magnocellular layers, there are also cell bodies that fall in between in regions called the *intercalated zones*. These zones may receive signals from yet another class of retinal ganglion cells.

The consistency in the shape of the cells and their central projections suggests that the midget and parasol cells form separate visual streams. The pathway that begins with the midget ganglion cells and terminate within the parvocellular layers of the lateral geniculate nucleus is called the *parvocellular pathway*, while the pathway that begins within the parasol cells and terminate within the magnocellular layers of the lateral geniculate is called the *magnocellular pathway*. The significance of these pathways for visual perception is the source of much current experiment and speculation. How far within the visual pathways are these signals segregated? Do the signals on these pathways carry information with different and specialized perceptual significance? In the next sections I will review some of the differences in how these neurons respond to light. I will discuss experiments that address the broader topic of the perceptual significance of these pathways at several points throughout the book.

Although the majority of retinal ganglion cells send their outputs to the lateral geniculate, there are many other destinations for the optic tract fibers. For example, Perry and Cowey (1980) introduced horseradish peroxidase into the monkey superior colliculus a nucleus in the *mid-brain* that is known to receive input from retinal ganglion cells. They found that about ten percent of the retinal ganglion cells send axons that terminate in the superior colliculus. None of the labeled cells were midget or parasol ganglion cells. Rodieck et al. (1993) review a broad range of measurements concerning visual streams of retinal origin. They conclude that each subcategory of ganglion cell sends its output to a single destination in the brain, making the morphology of retinal ganglion cells a very important clue in determining the organization of the visual streams that originate in the retina.

The majority of the retinal output is sent to the lateral geniculate nucleus. But, the retinal connections in the lateral geniculate nucleus account for only about 10 percent of the synapses. Nearly 60 percent of the synapses in the lateral geniculate are signals from the cortex and the remaining synapses are connections with other parts of the brain (Sherman and Koch (1990)).

Conduction Time and Contrast Gain

There are several differences in the way neurons in the parvo- and magnocellular pathways code information. These differences are clues about the kind of visual information represented by these visual streams and the function these streams serve in vision.

First, the conduction time for electrical signals traveling from the optic chiasm to the parvocellular layers of the lateral geniculate nucleus is longer than the conduction time to the magnocellular neurons. Schiller and Malpeli (1978) measured the conduction time for an electrical stimulus originating in the optic chiasm to travel to different layers in the lateral geniculate nucleus. The signal arrives later in the parvocellular layers than it does in the magnocellular layers, as illustrated by the histograms in Figure 10.

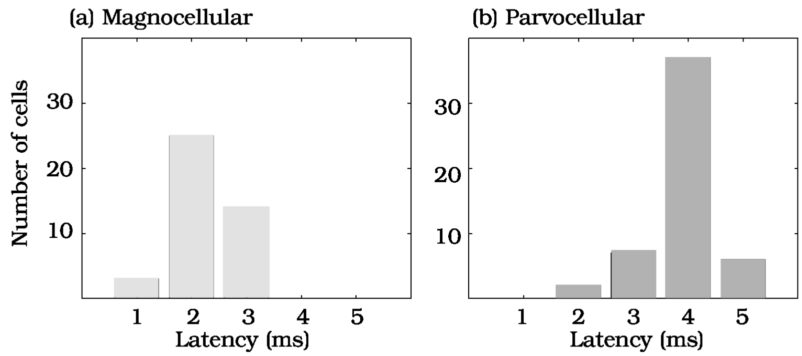

Figure 10: The conduction time for an electrical stimulus to travel from the optic chiasm to the magnocellular and parvocellular layers of the lateral geniculate. The responses of neurons in the parvocellular layers (a) are delayed compared to the responses of neurons in the magnocellular layers (Source: Schiller and Malpeli (1978)).

Second, the response of neurons in these two pathways to contrast patterns differs reliably. Kaplan and Shapley (1982) and Kaplan and Shapley (1986) observed that as the stimulus contrast of a sinusoidal grating pattern increases, the response of neurons in the magnocellular pathway changes more rapidly than neurons in the parvocellular pathway. Figure 11 compares the *contrast-response curves* of a neuron in the parvocellular pathway and a neuron in the magnocellular pathway. The horizontal axis measures the stimulus contrast and the vertical axis measures the neuron's response as a percent change from the spontaneous response level. The contrast-response curve of the neuron in the magnocellular pathway increases more rapidly with stimulus contrast and also saturates at a lower contrast. The slope of the contrast-response curve is called the neuron's *contrast-gain*. We can summarize the results in Figure 11 by saying that magnocellular neurons have higher contrast-gain than parvocellular neurons; the contrast-gain ratio is approximately eight.

While they original observed the difference in contrast-gain in the lateral geniculate nucleus, Kaplan and Shapley went on to show that this difference can be traced to differences in the response gains of the midget and parasol neurons within the primate retina. Quite possibly, the differences in these signals may begin at the bipolar connection to the cones themselves.

Visual Information Encoded by the Parvocellular and Magnocellular Pathways

Anatomical and physiological measurements suggest that the parvocellular and magnocellular pathways carry different types of information to the brain. We can try to evaluate this hypothesis by removing one of the pathways by introducing a lesion in to the pathway and studying the changes in an animal's performance due to the lesion.

When we perform a lesion, we must be careful not to damage fibers that are merely passing by, or else we will have lesioned remote sites that are the source or destination of the fibers. The

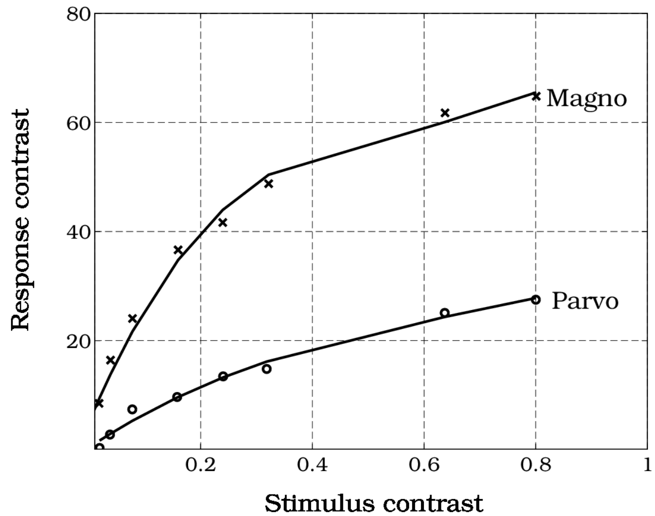

Figure 11: Contrast-response functions of neurons in the lateral geniculate nucleus. The contrast-responses of magnocellular neurons (filled squares) increase more rapidly than the contrast-responses of parvocellular neurons. (Source: Shapley (1990))

substance *ibotenic acid* is particularly useful for lesion studies because it destroys cell bodies of neurons but spares axons. Ibotenic acid has been applied to lesion neurons in the magnocellular or parvocellular layers. By studying changes in performance after ibotenic lesions of the parvocellular and magnocellular pathways, we learn something about the information present on these two visual streams (Schiller and Logothetis (1990); Merigan et al. (1991a), Merigan et al. (1991b); Lynch et al. (1992)).

When cells in the parvocellular layers of a monkey's lateral geniculate nucleus are destroyed, performance deteriorates on a variety of tasks, such as color discrimination and pattern detection. Since the parvocellular pathway includes more than seventy percent of the retinal ganglion cells, perhaps this result is not terribly surprising. When cell bodies in the magnocellular layers are destroyed many visual performances are unaffected. The results of several behavioral measurements before and after these lesions are summarized in Figure 12 (Merigan et al. (1991a)).

The most informative result is this: when neurons in the magnocellular layers are destroyed, the animal is less sensitive to rapidly flickering low spatial frequency targets. This loss of sensitivity shows that the magnocellular pathway contains the best information about this aspect of the image. This suggests that the magnocellular pathway is a specialization that improves our ability to perform tasks requiring high temporal frequency information.

What type behaviors depend on the low spatial frequency and high temporal frequency information represented by the magnocellular pathway? Two examples of visual tasks that require precise and rapid information about rapidly varying image signals are motion detection and motion-tracking. The central projections of the magnocellular pathway we will review later, coupled with the significance of the perceptual signals, suggest that the magnocellular pathway plays an important role in providing high quality information used in motion perception.

What conclusion can we draw from these lesion studies? The information carried by the neurons in the magnocellular pathway provide the *best* information in the low temporal and high spatial frequency components of the image. Performance on motion tasks and other tasks that require this information is better when the magnocellular pathway signal is available. The signals are not absolutely necessary to perform the task. This was shown by Merigan et al. (1991a), who studied motion perception in monkeys with magnocellular pathway lesions. They found that performance deficits on motion tasks could be compensated for simply by increasing the stimulus contrast; that is, one can compensate for the loss of information on the magnocellular pathway by improving the quality of the information on the parvocellular pathway. Hence, the magnocellular pathway contains information that is particularly useful for certain kinds visual tasks, such as motion perception. Discovering where these signals are sent in the central brain should provide us with some useful ideas about where we compute and perceive motion, as well as other visual tasks requiring this type of information.

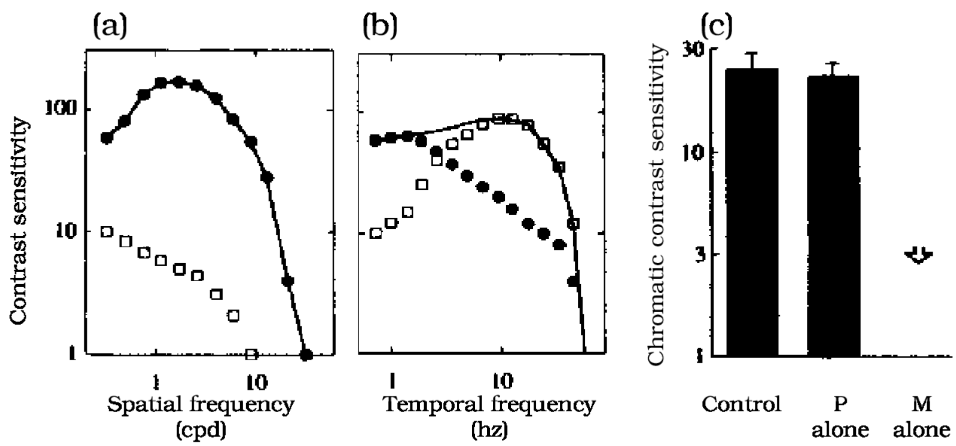

Figure 12: The effect of lesions in the parvocellular and magnocellular layers of the monkey lateral geniculate nucleus. (a)~The smooth curve defines the control monkey's performance when detecting a stationary grating. Filled circles show performance following lesion of the magnocellular pathway. Open squares show performance following lesion of the parvocellular pathway. (b)~The smooth curve defines the control monkey's performance when detecting a low spatial frequency target at various flicker rates. Filled circles show performance following lesion of the magnocellular pathway and open squares show performance following lesion of the parvocellular pathway. (c)~Comparison of sensitivity in detecting color contrast in the control and lesion conditions. (Source: Merigan and Maunsell (1993))

Retinal Ganglion Cell Response To Light

The output of the retinal ganglion cells consists of a series of discrete electrical impulses called *action potentials* or *spikes*. We measure ganglion cell responses by recording the temporal pattern of action potentials caused by light stimulation. Retinal ganglion cells form part of a pathway that transforms the light into a temporal series of electrical pulses. The properties of the neural transformation from a light signal to a pattern of action potentials is one of the main types of evidence we have about a neuron's functional significance, and hence the pathway's role in vision.

Within the field of *electrophysiology*, the field that studies the electrical response of neurons, the transformation associated with a neuron is called the neuron's *receptive field*. The receptive field concept, first used in vision by Hartline (1938), is a cornerstone of the electrophysiolgist's description of the action of visual neurons. The receptive field concept, like the notion of a transformation is quite general. Hence, the receptive field notion is used also to describe neural properties in other sensory and motor areas as well (Mountcastle (1957)).

Classically, the visual receptive field of a neuron was defined as the retinal area in which light influences the neuron's response. This region can be defined by positioning small flashes of light and simple moving bars and evaluating when the neuron responds and fails to respond. The responses of many neurons in the visual pathway are influenced only by light falling within narrow regions of the retina, and hence small regions of the visual field. The region of the visual field in which these flashes of light and bars influence the neuron's response is called the neuron's classically-defined receptive field. This description is relatively easy to obtain and provides a useful preliminary description of the neuron's transformation.

Although we refer to a *neuron's* receptive field, in fact the receptive field depends on the properties of the entire visual pathway, beginning with the optics and including the transformation by the neuron itself. In some cases, when there is feedback descending upon the neuron from central brain regions, the receptive field we measure at a neuron includes contributions from many places within the visual pathways (though there is no feedback to the retinal ganglion cells).

Center-Surround Organization

Several important properties of ganglion cell receptive fields were discovered by measuring the classically defined receptive field. In this section we will consider how one important property, *center-surround* organization, was measured.

There are two locations in the visual pathways where one can conveniently record the spiking activity of retinal ganglion cells (see Figure 13). One can measure the electrical activity from the cell bodies of the retinal ganglion cells, which are on the surface of the retina closest to the cornea, or one can insert the microelectrode in the optic nerve which contains the axonal fibers that emerge from the cell bodies and carry the signal to the cortex. When the electrode

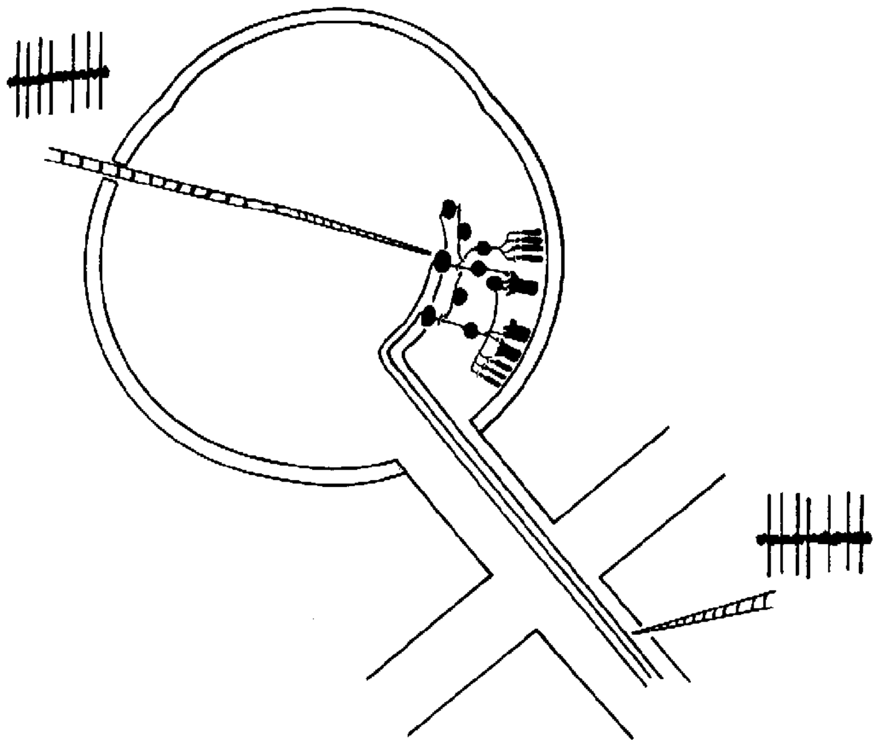

Figure 13: Retinal ganglion cell action potentials can be recorded with a microelectrode at the two locations shown. One location is near the cell bodies in the ganglion cell layer of the retina. A second position is near the optic nerve (Source: Enroth-Cugell and Robson (1984)).

is positioned properly with respect to the cell body of a neuron, or an axon in the optic nerve, we can record action potentials.

When the stimulus is a large uniform field, most retinal ganglion cells respond with a random stream of action potentials. A typical retinal ganglion cell response to uniform illumination might consist of 50 spikes per second. For most retinal ganglion cells, the temporal sequence of the spiking activity has no systematic temporal structure, so that the chance of a spike occurring in the next brief interval of time is approximately constant. We call the average number of action potentials per unit time, in the presence of a constant field, the *spontaneous firing rate* of the retinal ganglion cell.

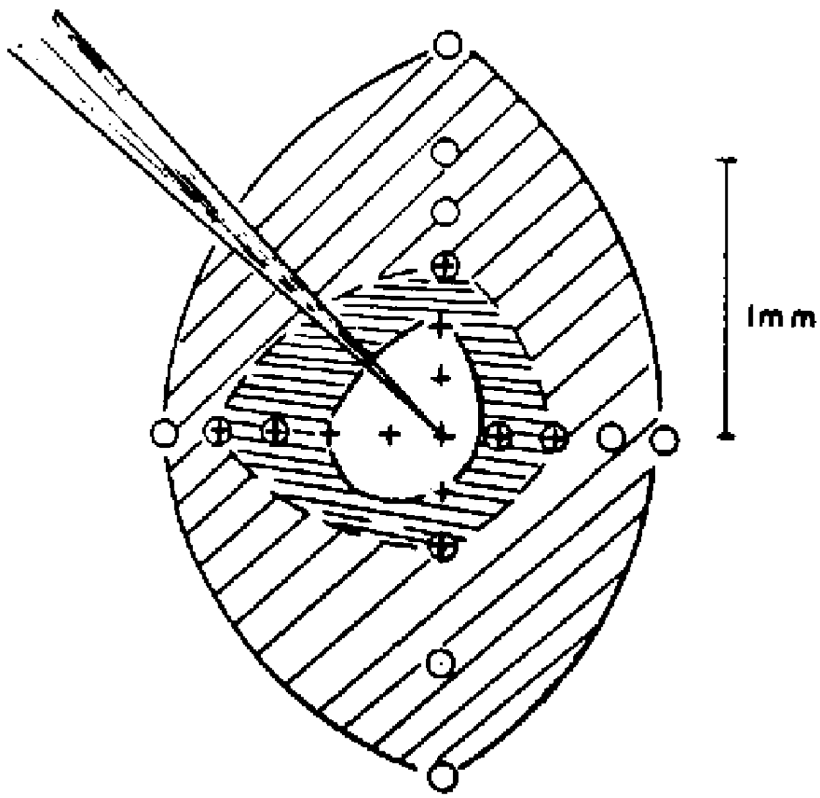

Figure 14: The receptive field of mammalian retinal ganglion cells have a center-surround organization. In a small central region of the retina, light stimulation may excite or inhibit a neuron. In a surrounding annular region light stimulation will have an opposing effect to that of the center. The receptive field shown here has an on-center and an off-surround cell. (Source: Kuffler (1953)).

S. Kuffler was the first to define the receptive field of of mammalian retinal ganglion cells. They used small points of light flashed at different retinal positions, and they recorded the difference between the spontaneous firing rate and the response when the point of light was presented at different points on the retinal surface. An example from Kuffler's measurements is shown in Figure 14. A small spot of light flashed within a central region of the receptive field causes an increase in firing relative to the spontaneous activity. When the spot is placed on a surrounding area, there is a measurable decrease in the cell's activity. The intermediate region showed some excitation at the beginning of the stimulus and some inhibition at stimulus extinction (Kuffler (1953); Barlow et al. (1957)).

The responses illustrated in Figure 14 define an *on-center, off-surround* receptive field. About half of the retinal ganglion cells respond this way. The remaining ganglion cells are inhibited by light falling on the center and excited by light falling on the surround. These are called *off-center, on-surround* cells. Most mammalian retinal ganglion cells exhibit the basic *center-surround* organization.

The dendritic fields of retinal ganglion cells with on-center are segregated in the inner plexiform layer of the retina from retinal ganglion cells with off-center receptive fields. Ganglion cells that make connections in the upper portion of the inner plexiform layer have an off-center, while neurons that synapse in the lower half of the inner plexiform layer have on-center receptive fields. Hence, the anatomy and electrophysiology suggest that there are at least two types of visual pathways, an on-center and an off-center pathway, emerging from the retina.

Measurements of Receptive Fields

The classical receptive field is only a partial description of the neuron's response properties. To understand a neuron's transformation of the light signal completely, we would like to predict the pattern of action potentials in response to any visual stimulus. To describe the transformation from light to neural activation completely, we need to develop a more systematic method of measuring the neuron's response. Since there are many possible visual stimuli, we need to develop a method so that we can make a small set of measurements and then use these measurements to predict the responses to all other stimuli.

Linear systems theory provides some guidance on the question of how to measure the receptive field completely. If a neuron's responses to light satisfies the principle of superposition, then we can use a few measurements to predict how the neuron will respond to many other visual stimuli. As we shall see, in the primate retina and lateral geniculate nucleus, linearity provides a satisfactory account of a large part of the neural response.

How do we test whether the input-output relationship of a retinal ganglion cell satisfies the principle of superposition? A simple and direct test, for one pair of stimuli, is shown in Figure 15. In this study Enroth-Cugell and Pinto (1970) examined the center-surround antagonism of cat retinal ganglion cells. They studied the superposition of two stimuli: a spot placed in the center of the ganglion cell receptive field and an annulus placed in the antagonistic surround. The response to the spot is illustrated in part (a) of the figure and the response to the annulus is illustrated in part (b).

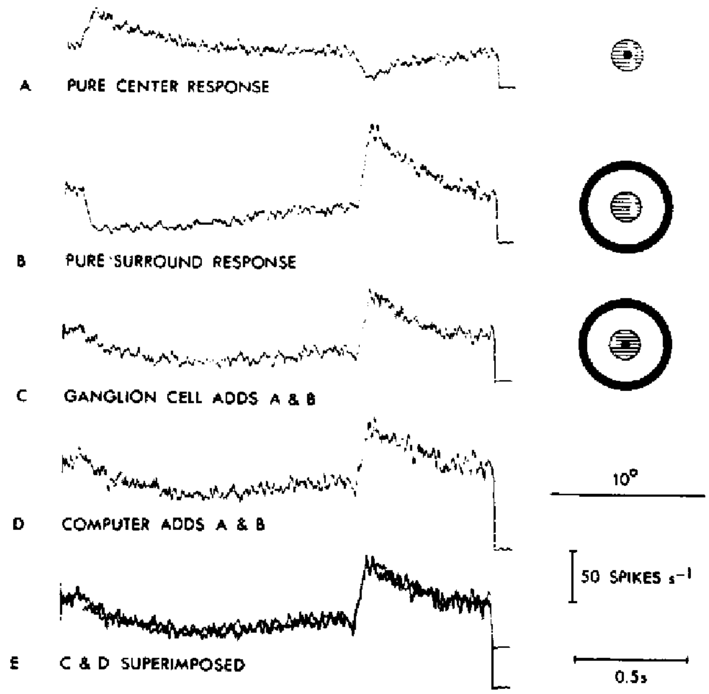

Figure 15: A test of superposition of the response of a retinal ganglion cell. (a)~The PSTH to a disk of light flashed in the center of the receptive field. (b)~The PSTH to an annulus flashed in the surround of the receptive field. (c)~The PSTH to simultaneous presentation of the disk and the annulus. (d)~The sum of the responses in (a) and (b). (e)~A comparison of the predicted and observed response to the sum of the stimuli. (Source: Enroth-Cugell and Pinto (1970)).

If the ganglion cell response obeys the principle of superposition, we should be able to predict the temporal response when we present the spot and the annulus together. The observed response and the predicted response are shown in panels (c) and (d) of the figure. They are compared in panel (e) of the figure. For this pair of stimuli, and this retinal ganglion cell, the principle of superposition predicts the neuron's complete response very well.

Steady-state Measurements

To build a complete description of the neural response properties, we must include time in our characterization of the neuron's receptive field. We will consider the full space-time receptive field later in this chapter. But, it is simpler to begin with an example in which we eliminate time as a variable; we will consider only the response after the stimulus has been presented for several seconds and the neuron's response has stabilized. This asymptotic response is called the *steady-state* response of the neuron. By measuring the steady-state response of the neuron, we remove time as a factor in our analysis.

As in all cases of linear systems studies, we must specify both the input and output signals carefully. One of the important advances in recent years has been discovering insightful definitions for the input and output stimuli we use to measure the neurons receptive fields. Both of these definitions are based on the notion of *contrast*.

The stimulus.

We use a spatial image as the input stimulus. We will represent the spatial image as the sum of two components. One part is the average light level of the stimulus, and the second part is the variation of the intensity about the mean. The mean level of the stimulus is always a positive number. The variation around the average light level is the *stimulus contrast* pattern. The stimulus contrast contains both positive and negative values.

Consider the simple case of a one-dimensional stimulus that varies along one spatial dimension and is constant in the second dimension. We can specify the stimulus contrast with respect to a single spatial variable, say x. The formula that relates the stimulus intensity to the mean background intensity and the stimulus contrast is

$$I = [1 + c]\ \mu, \tag{0.1}$$

where I is the stimulus intensity, μ is the mean background intensity, and c is the stimulus contrast.

The response.

Suppose that a neuron's spontaneous firing rate is r_0. Now, suppose we introduce a contrast pattern, c, and the neuron's steady-state response becomes r spikes per second. We define the change in the retinal ganglion cell rate of response, $\Delta r = r - r_0$, as the neuron's response. Thus, just as we consider the input to be the stimulus change from the mean background level, so too we consider the neuron's output to be the change from the average spontaneous response of the neuron.

Testing contrast linearity.

To test superposition, we must measure the response to two different contrast patterns and their sum. Suppose we use two contrast patterns, c_1 and c_2 and corresponding changes in the steady-state response of Δr_1 and Δr_2. To test superposition we combine the two contrast patterns to form a new stimulus,

$$[1 + c_1 + c_2]\ \mu. \tag{0.2}$$

We expect that the steady-state response to the new test pattern will be $\Delta r_1 + \Delta r_2$. Be sure to compare Equation 0.1 and Equation 0.2; the new stimulus pattern is formed by adding together the **contrast terms**, c_1 and c_2, not the two intensity patterns.

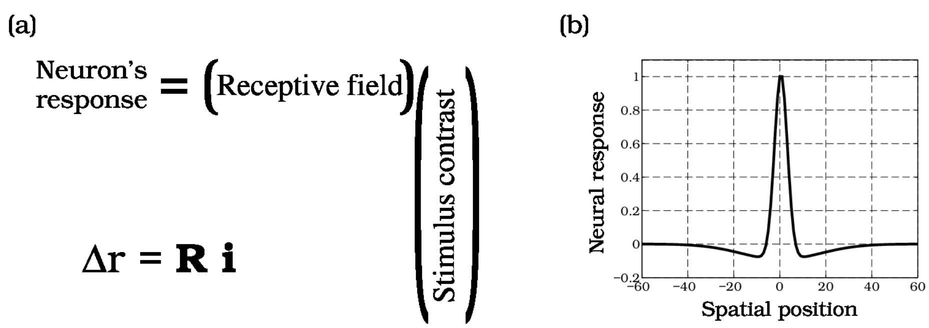

Figure 16: The steady-state contrast response of primate retinal ganglion cells are often linear. We can predict the response to contrast patterns by measuring the system-matrix that maps the stimulus contrast into the increased firing rate of the neuron. Since the change in firing rate is a single number, the system matrix is a row-vector. The entries of the system matrix define the one-dimensional, steady-state, receptive field of the neuron.

If the change in the neuron's response satisfies the principle of superposition, we can model the response to any contrast pattern by defining a system matrix that describes the neuron's transformation, i.e., receptive field. The relationship between the contrast stimulus, the system matrix, and the response is shown in Figure 16. We represent the one-dimensional stimulus contrast pattern as a column vector. The output is the retinal ganglion cell response. If the neuron is linear, there is a matrix that maps the input contrast vector to the neural response. The system matrix is a $1 \times N$ matrix $\mathbf{R}$ whose entries define the one-dimensional receptive field of the neuron. We can use the system matrix to predict how the neuron will respond to any one-dimensional contrast pattern. We say that the entries of the matrix $\mathbf{R}$ define the *linear, steady-state, receptive field* of the neuron.

By examining the matrix tableau, you can see that to estimate the entries of the system matrix we need to measure the response to a series of lines at different positions on the retina. The response to each line defines the corresponding entry in the system matrix. The curve in Figure 16 (b) is a graphical representation of the entries of the system matrix, that is, of the neuron's one-dimensional receptive field.

The Two-Dimensional Receptive Field

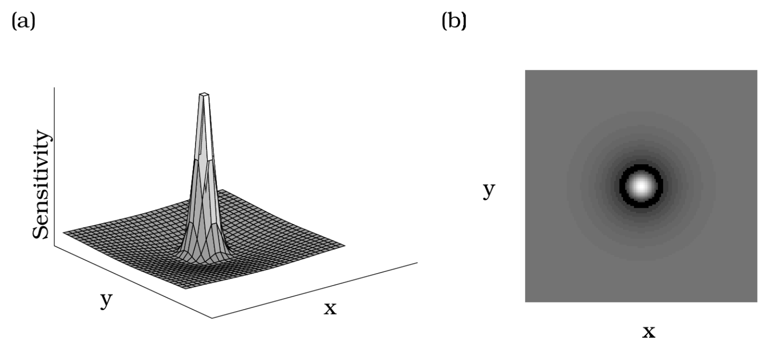

Figure 17: The two-dimensional steady-state receptive field of an on-center off-surround retinal ganglion cell is represented in two different ways. (a) A surface plot shows the spatial sensitivity by the height of the surface. The inhibitory surround covers a large area compared to the center, but its general effect on the neuron's response is small compared to the center. (b) An image shows the spatial sensitivity of the receptive field by the image intensity. A light color denotes a retinal location where light excites the neuron, a dark color is a location where light inhibits the neuron, and gray locations are places where light has no influence on the neuron's response.

By measuring with points of light rather than lines, we can measure a two-dimensional steady-state receptive field. Figure 17 shows two ways to represent the two-dimensional receptive field of a retinal ganglion cell. The height of the curve in Figure 17 (a) shows change neuron's light response as we stimulate with a point of light at different locations in the visual field. The large positive values in the center of the diagram indicate that this neuron is excited by stimuli in a central region. The negative values in the surrounding region show the inhibition by point stimuli surrounding the central region. Notice that the effect at each point in the inhibitory surround is very small, but the inhibitory surround covers large area compared to the excitatory center. The picture captures quantitatively the center-surround antagonism that Kuffler discovered in cat retinal ganglion cells. Figure 17 (b) represents the same measurements as an image. Light regions show where the neuron is excited by a spot and a dark regions show where the neuron is inhibited.

Contrast Sensitivity Functions

Often, it is useful to characterize the response of a linear system in terms of the system's response to harmonic functions. It is helpful to understand the information encoded by neurons by plotting their response to harmonic functions as well.

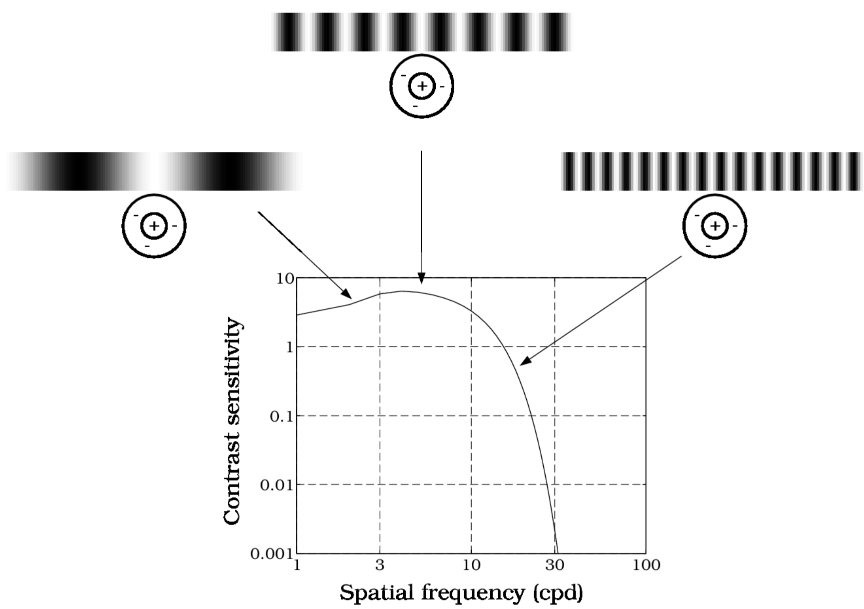

Figure 18: The contrast sensitivity function describes a neuron's sensitivity to harmonic stimuli. In the example illustrated, a linear on-center neuron responds best to an intermediate spatial frequency whose bright bars fall over the on-center and whose dark bars fall over the opposing surround. When the spatial frequency is low, the signals from the center and surround oppose one another thus diminishing sensitivity. When the spatial frequency is high, the stimulus is averaged by the center again diminishing the response. From the response to harmonic stimuli, one can derive the spatial structure of the receptive field.

To measure a neuron's contrast sensitivity function, we determine the amount of contrast necessary in the stimulus that is required to elicit a criterion level of response from the neuron. When a contrast pattern is ineffective at influencing the neuron, we need to present the pattern at high contrast to elicit the response. When a pattern is well-suited to the neuron's receptive field, a small amount of contrast will elicit the criterion response level. We call the amount of necessary to elicit the criterion response the *contrast threshold*. The inverse of contrast threshold is called *contrast sensitivity*.

From Figure 18, you can see how a center-surround ganglion cell will respond to cosinusoidal patterns whose peak is centered over the receptive field of the neuron. When the spatial frequency is very low, a bright bar in the stimulus covers both the excitatory center and the inhibitory surround and the steady-state response is small. The most effective spatial frequency has bright bars imaged on the excitatory part of the linear receptive field, and dark bars on the opposing surround. This spatial frequency is well-matched to the receptive field and we will observe a strong neural response. If the frequency is higher still, parts of the cosinusoid greater and less than the mean both fall within the excitatory and inhibitory regions. The net effect of the stimulus averages out to a small response, so that high spatial frequencies are ineffective stimuli.

We summarize the neuron's response to harmonic functions at a range of spatial frequencies using the *contrast sensitivity function*. Different aspects of the function provide us with information about the neuron's spatial receptive field. The most effective spatial frequency provides information about the overall size of the receptive field. The extent of the fall off in sensitivity at low spatial frequencies provides information about the strength of the opposing surround. Finally, the fall-off in sensitivity at high spatial frequencies describes the size of the receptive field center since the highest spatial frequency the cell responds to is limited by the size of the receptive field center. Neurons with small receptive field centers respond well to high spatial frequency targets, while neurons with large centers do not.

Figure 19 shows a contrast sensitivity function from a linear cells in the parvocellular layers of a monkey lateral geniculate nucleus. The receptive fields of these neurons are indistinguishable from the receptive fields of midget ganglion cells[3].

The contrast sensitivity function of a retinal ganglion cell is an alternative way to represent the cell's receptive field. There are several characteristic features of retinal ganglion cell contrast sensitivity functions. First, retinal ganglion cell contrast sensitivity functions are single-peaked. Single-peaked contrast sensitivity functions are called *bandpass* and the peak-frequency is called

[3]To describe a general linear receptive field, we must measure the neuron's response using both sinusoidal and cosinusoidal contrast patterns. The receptive fields of retinal ganglion cells can be measured using only cosinusoids centered on the peak because the receptive fields are *even-symmetric*. A function is said to have even symmetry if $f(x) = f(-x)$. A function has *odd symmetry* if $f(x) = -f(-x)$. When a receptive field is even-symmetric, it will have zero response to any odd-symmetric inputs, so we need to measure only the response to even-symmetric inputs. For retinal ganglion cells, then, the contrast sensitivity function is a complete description of the receptive field in this case.

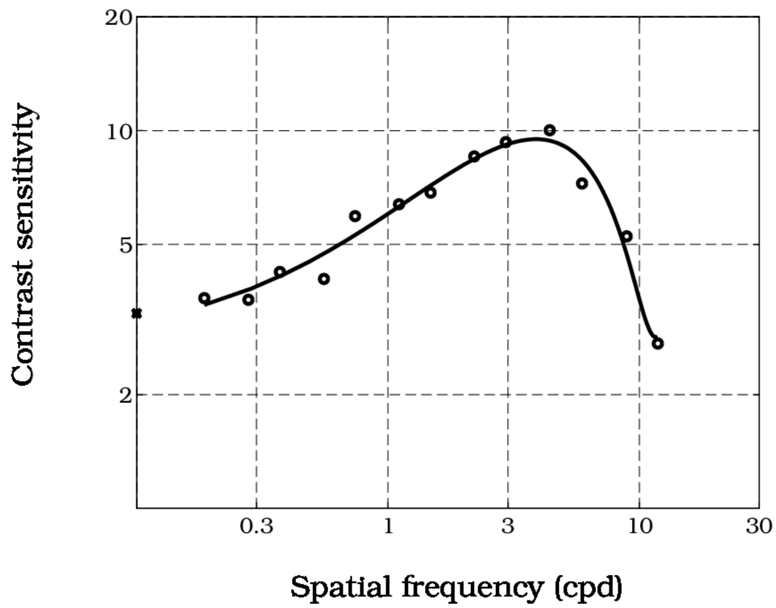

Figure 19: Contrast sensitivity function of a neuron in the parvocellular layers of the monkey lateral geniculate nucleus. This neuron responds best to a spatial frequency near 5 cycles per degree. Notice that the opposing surround reduces the sensitivity to low spatial frequency patterns. Each grating pattern drifted across the retina at a velocity so that each point on the retina saw one 5.2 cycles of the pattern each second. The symbol on the vertical axis is the contrast sensitivity to a uniform spatial pattern flickering at 5.2 Hz. (Source: Derrington and Lennie (1984)).

the *center* frequency. With experience, the contrast sensitivity function becomes an intuitive way to understand some aspects of the neuron's receptive field.

Why contrast patterns are important

In early studies of the neural response to light, the stimulus intensity, I, was treated as the input variable. In this case, the linear systems methods fail severely. If we wish to apply linear methods to characterizing the responses of retinal ganglion cells, it is important to fix the mean level, and to treat the stimulus contrast, c, as the input.

Formulating our experiments in terms of contrast does not make a nonlinear system linear. The nonlinear behavior of neurons becomes quite clear when we compare measurements at different mean levels. But, by organizing our measurements around the contrast responses at a fixed mean level, we can use linear methods to characterize the receptive field for perturbations around the mean level. To describe the neuron fully, we must combine the neuron's response across many mean intensity levels. This forces us to acknowledge the nonlinear aspects of the neuron's response.

The change in the system performance as we vary the mean stimulus level is called *visual adaptation*. We can measure the effects of visual adaptation in individual neurons, beginning in the retina, as well as in the behavior of animals and people. The way in which performance of neurons and people change as the mean illumination varies, that is visual adaptation, is one of the most important topics in vision. By formulating our stimulus in terms of a mean intensity level and a contrast pattern, we segregate out the effects of visual adaptation from the local contrast effects. Thus, formulating our experimental input this way is an important decision that has ramifications for how we study many important aspects of vision.

Most of modern vision science relies uses contrast as the key experimental parameter. The linearities that I will describe in this chapter and the following chapters are usually measured in the contrast domain, at a fixed mean level. As we change the mean level, the properties of the linear system we estimate change as well. This is a fundamental non-linearity in the system's behavior. A complete theory must weave together how the locally linear responses, on a single mean background, vary with the mean. We will review this topic, called *adaptation*, at the end of this chapter and then again in later chapters.

Connections to Different Cone Types

In the primate fovea, the center response of the midget ganglion cells depends on the light captured by a single cone. Hence, the centers will inherit the wavelength sensitivity of the photopigment in that cone's outer segment. Parvocellular Pathway neurons with receptive fields near the primate fovea often have a center response that is either an R or G cone. roughly equal to the optical blur imposed by diffraction (2.4 – 4.2 minutes of arc), which is consistent with the center response being due to a single cone.

There are two views concerning the connections of cones to the opponent-surround responses in ganglion cell receptive fields. Lennie (1980) suggested that the surround is driven by a random collection of cones, including both the R and G types. Reid and Shapley (1992) attempted to measure the surround and concluded that only a single class of cones contributes to the surround response. When the center response of a cell in the parvocellular pathway is from a R cone, the surround response is due to G cones. Conversely, when the center is from the G the surround is from the R. At the moment, the question of the segregation of cone signals in the surround of parvocellular pathway neurons is unresolved (see also, Gouras and Evers (1989)).

There is some agreement that the centers and surround of neurons in the magnocellular pathway receive a signal from both cone types. An on-center parasol cell receives an excitatory signal from the R and G cones, while the the surround signal is inhibitory and originates in both of these cone classes. The relative strength of the signals from these cone classes to the surround may vary (Derrington et al. (1984)).

Mariani (1984) and Dacey and Lee (1994) have shown that the signals from the B cones are coded within a specialized visual stream. Neurons that receive a signal from the B cones have large receptive fields (18 min). As I noted in Chapter , the chromatic aberration of the optics is very strong in the short-wavelength region. Since the image from a short-wavelength light source will be blurred, the large size of these receptive fields is not necessarily a disadvantage. Mariani's anatomical studies described the existence of bipolar neurons that make contact with a few widely spaced cones that appeared to be consistent with the B cone mosaic. His observations suggest that the spatial connectivity of the B cone signals also plays a role in creating large center receptive fields (see also, Kouyama and Marschak (1992)).

D. Dacey and B. Lee have confirmed the existence of a visual stream specialized for carrying information about the B cone signal and made several important and novel observations. First, Dacey showed that there is a morphologically distinct type of retinal ganglion responsible for carrying the B cone signal. These *bistratified* ganglion cells have dendritic trees that are stratified into two tiers near the inner and outer borders of the inner plexiform layer where the on- and off-center receptive field neurons stratify. Based on the anatomical connectivity of these neurons, Dacey suggested that these neurons carry a B cone excitatory signal. Using electrophysiological measurements, Dacey and Lee made two additional and surprising observations. First, their sample of midget and parasol ganglion cells contained no input from the B cones. Second, they showed that all of the bistratified ganglion cells had a B excitatory input (Dacey (1993); Dacey and Lee (1994)).

The bistratified neurons send their outputs to the parvocellular layers of the lateral geniculate nucleus (Rodieck et al. (1993)). Using electrophysiological methods, one can measure receptive fields in that nucleus whose excitatory centers are driven by signals from the B cones. It is also possible that these neurons project to the intercalated zones of the lateral geniculate. Because the sampling resolution of the B cone mosaic is poor, we do not expect these neurons to make up a large fraction of the total population. Nonetheless, they are important since at present they are the only cell class known to carry the B cone signal (Wiesel and Hubel (1966); Gouras (1968); Derrington et al. (1984)).

Spatio-Temporal Analysis: Lines and Spots

Up to now, we have considered only the steady-state response, thus excluding time in order to simplify our analysis. Now we consider how to include the temporal response of the neuron in our measurement of the receptive field.

Figure 15 illustrates an average temporal response of a cat retinal ganglion cell to a flashed target. To obtain the curves shown in the figure, the experimenters presented the test light and recorded the resulting neural activity. If we present the test flash repeatedly, we will find that the resulting pattern of spikes differs slightly each time. The differences will be small, however, so that we can sum together all of the responses obtained from, say, 50 repetitions of the test flash. We can compute the average number of action potentials at each moment in time following the flash, and plot this as a curve. This curve is called the *peri-stimulus time histogram, (PSTH).*

The data in Figure 15 and other experimental measurements have shown that for certain cells in the cat retina, linearity holds rather well (Enroth-Cugell and Robson (1984)). Linearity has not been extensively tested in primate retina. To a fair approximation, linearity has been confirmed in measurements in the parvocellular pathway within the primate lateral geniculate nucleus (Derrington and Lennie (1984)). Hence, based on linear methods we can measure the responses to a collection of basic stimuli and use these responses to predict the responses to many other stimuli.

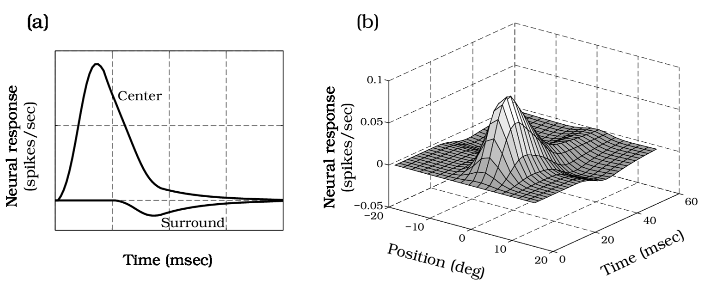

Figure 20: The space-time receptive field of a linear neuron can be estimated by measuring the temporal responses to briefly flashed lines. (a) A simulation of the temporal response to briefly flashed lines positioned either in the center or the surround portion of the receptive field. (b) A surface plot showing simulated temporal responses to individual lines at different positions within the receptive field. Such a collection of measurements can be used to predict a linear neuron's response to any one-dimensional time-varying stimulus. Hence, these measurements are one way to define the space-time receptive field of the neuron.

Panel (a) of Figure 20 shows two simulated PSTHs for an on-center cell response to a briefly flashed line. One PSTH shows the simulated response to a line flashed over the center of the receptive field, and the second PSTH is for a line flashed over the opposing surround. By measuring the responses to briefly flashed lines at many receptive field positions, we can specify the *space-time receptive field* of the neuron (Stevens and Gerstein (1976)). I have collected a series of these simulated responses in a surface plot shown in panel (b) of Figure 20. One axis of the figure measures time and the second axis describes spatial position of the test line. Each curve along the time axis shows a simulated PSTH for a single spatial position of the line. When the position of the line is in the receptive field center, the simulated response is large and begins soon after the stimulus. When the line is positioned over the receptive field surround, the simulated response is weaker, delayed, and of opposite sign.

Since any one-dimensional time-varying stimulus is the sum of a set of briefly flashed lines, a collection of measurements like the simulations in panel (b) Figure 20 permit us to predict the response to any such stimulus. Such measurements define the space-time receptive field of this simulated neuron for one spatial dimension. This method of defining space-time receptive fields has been applied mainly to study the cat visual pathway (Stevens and Gerstein (1976); Palmer and Davis (1981); Emerson et al. (1992)).

Spatio-Temporal Measurements: Harmonic Functions

It is also possible to measure receptive field properties using harmonic functions, though in this case, we need to use harmonic functions in space and time. We can create space-time harmonic functions by multiplying cosinusoidal contrast patterns in space and time, creating a stimulus called a *contrast-reversing grating*. Such a pattern is the product of a spatial harmonic with frequency f_x cycles per degree and a temporal harmonic with frequency f_t Hz. The formula for a contrast-reversing grating made from cosinusoids is

$$I(x) = [1.0 + \cos(2\pi f_t t)\cos(2\pi f_x x)]\,\mu.$$

where μ is the mean background intensity.

Figure 21 shows the contrast-reversing in two different forms. At each moment in time the grating is a one-dimensional spatial frequency grating, with spatial frequency f_x. At each point in space the time-varying contrast is a cosinusoidal function of time, with temporal frequency f_t. In part (a) of the figure the function is shown as a surface plot. One axis of the plot represents time and the other space. Individual lines in both of these dimensions are sinusoidal. In part (b) of the figure the function is shown as an intensity image. Again, one dimension of the image represents time and the other space. The image intensity is bright at those points where the function has positive contrast and dark where the function has negative contrast.

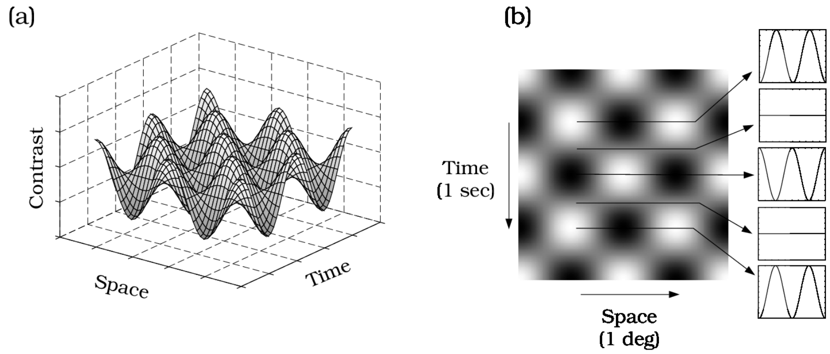

Figure 21: Space-time representations of a contrast-reversing grating. At each moment in time this image is a cosinusoidal spatial pattern; the amplitude of the spatial pattern varies cosinusoidally over time. The contrast-reversing space-time pattern is represented as a two-dimensional surface plot in (a) and as an intensity image in (b).

Neurons in the lateral geniculate nucleus respond linearly for stimuli as high as 30 percent contrast. Hence, it is appropriate to use linear methods to measure the spatial-receptive fields of these neurons. Moreover, since the receptive field of neurons in the retinal and lateral geniculate nucleus in the parvocellular pathway are even-symmetric, we can measure the space-time contrast sensitivity function using only cosinusoidal functions centered on the receptive field. Because the neurons are linear and temporally shift-invariant, the PSTH is a harmonic function at the same temporal frequency of the input stimulus, f_t. The amplitude and phase of the PSTH modulation depends on the temporal and spatial frequency of the contrast-reversing pattern used as an input.

The response to contrast-reversing patterns of a parvocellular neuron in the monkey lateral geniculate nucleus is shown in Figure 22. This surface plot was derived by interpolating measurements reported by Derrington and Lennie (1984). This cell responded to temporal and spatial modulations up to 15 Hz and 15 cycles per degree. From the shape of the neuron we can make several observations about the neuron's responsivity. First, the reduced sensitivity at low spatial frequencies shows that the neuron had a significant opponent surround. Second, the neuron responds well to all tested temporal frequencies when we measured with a low spatial frequency stimulus, but the neuron responds poorly at high temporal frequencies when measured using a high spatial frequency stimulus. Since the response to the high spatial frequency stimulus is mediated through the on-center, the data show that the temporal sensitivity from the on-center and opposing surround may be different. It is time to consider the general question of the interdependence of spatial and temporal sensitivity.

Space-time separability

We have defined the neuron's receptive using two complementary representations. In one case, the we have defined the receptive field using briefly flashed lines, and in the second case we

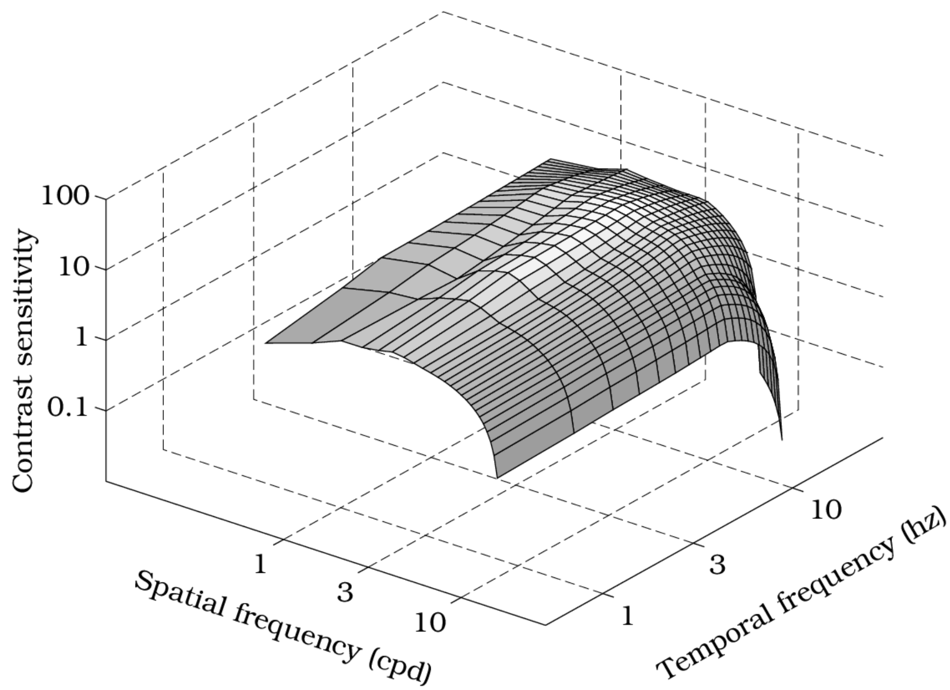

Figure 22: The response to contrast-reversing harmonic patterns of a neuron in the parvocellular layers of the lateral geniculate nucleus. The two horizontal axes measure the spatial and temporal frequency of the contrast-reversing pattern. The height of the surface measures the response amplitude of the neuron's PSTH. Notice that the loss of temporal frequency sensitivity depends on the spatial frequency: the temporal sensitivity falls off more rapidly at higher spatial frequencies. The surface plot was created by interpolating measurements reported by Derrington and Lennie (1984).

have defined the receptive field using harmonic functions of space-time. We can use either method to measure and describe a linear neuron's receptive field.

No matter which description we use, the neuron's sensitivity depends jointly on space and time. When our description of the receptive field includes both space and time, how can we define a neuron's spatial receptive field? Or, how can we define its temporal receptive field?

Suppose that we refer to the neuron's space-time receptive field, illustrated in Figure 20 (b), using the function $\mathbf{R}(x,t)$. This function defines the response of the neuron to a line briefly flashed at position x at time t following the flash. We can ask whether a neuron has a unique *spatial* receptive field by examining this function at several different moments in time. That is, we might fix time at a value of t_1 and consider the function of position, $\mathbf{R}(x,t_1)$, that defines the spatial receptive field at time t_1. We can compare this spatial receptive field with the measurements at a second time, say, $\mathbf{R}(x,t_2)$. We would say that the neuron has a unique spatial receptive field when the two functions are essentially the same, say,

$$\mathbf{R}(x,t_1) = a\mathbf{R}(x,t_2)$$

where a is a scalar constant. If the spatial receptive field at each moment in time is the same except for a constant scale factor, then we say the neuron has a well-defined spatial receptive field.

A neuron will only have a well-defined spatial receptive field when the space-time receptive field is a *separable* function of space and time. Separability means that the receptive field function can be written as the product of two functions, one that depends only on space and the other that depends only on time, namely

$$\mathbf{R}(x,t) = S(x)T(t) \tag{0.3}$$

If the space-time receptive field is separable, then, it follows from the definition that the spatial receptive fields at two times will always be related by the scale factor $T(t_1)/T(t_2)$. In this case the function $S(x)$ is a meaningful definition of the neuron's spatial receptive field. The function $T(t)$ is a meaningful definition of the neuron's temporal impulse response function. If the space-time receptive field is separable, then it is possible to show that the space-time contrast sensitivity function will also be separable.

As the plots in panel (b) of Figure 20 and Figure 22 show, the space-time receptive fields of neurons in the parvocellular pathway are not space-time separable. Hence, these neurons do not have unique spatial or temporal response properties[4]. In part because of this complexity, it is important to go beyond the descriptions of the neuron's response we obtain from linear measurements, and to build a model to predict the neuron's response to space-time patterns.

[4]Although I will not go into the details here, by considering the connections to specific cone types you can convince yourself that the receptive fields will not be separable with respect to space and wavelength.

The Difference of Gaussian Model

In the mid 1960s, R. W. Rodieck and Enroth-Cugell and Robson introduced a linear receptive field model that has served as the basis for most subsequent models of linear retinal ganglion cells. The basic model is important in vision science broadly since the ideas in the model have been used in many different areas including work in the visual psychophysics of spatial perception and in computer vision vision work addressed to edge-detection and image segmentation. The receptive field model is now called the *Difference of Gaussian* model (Rodieck (1965); Enroth-Cugell and Robson (1966), Enroth-Cugell et al. (1983)).

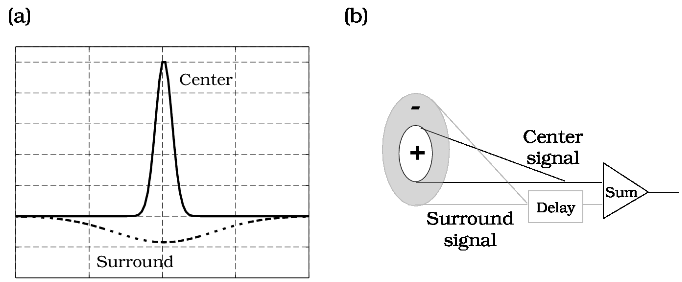

Figure 23: A linear model of the space-time receptive field. The neural response depends on the linear sum of two independent mechanisms, a center and an opposing surround. (a) The spatial sensitivity of the center and surround mechanism both follow a Gaussian curve. The linespreads of the two mechanism are shown here. (b) The signals are summed separately within the center mechanism and the surround mechanism. The signal from the surround mechanism is temporally delayed and added to the signal from the center mechanism.

The difference of Gaussian model supposes that the neural response results from the combined signal of two separate mechanisms called the *center* and the *surround*. The center mechanism receives all of its input from a small central region and the surround mechanism receives its input from a region that includes the center and the surrounding region.

Both the center and surround are assumed to respond to contrast stimuli as space-time separable linear systems. Because each mechanism is separable, we can describe them as having meaningful spatial and temporal sensitivities. The curves describing the spatial sensitivity of the center and surround mechanisms are shown in Figure 23 (a). Both curves follow the shape of a *Gaussian distribution*, also known as the *normal* curve.

According to the difference of Gaussian model, the output of the neuron can be predicted by summing together the temporal response from the center mechanism with a temporal signal from the surround mechanism. The model further assumes that the temporal response from the surround is different from the temporal response of the center, generally being slower to develop over time. Because of this delay between the center and surround responses, the behavior of the cell as a whole is not space-time separable even though the responses of the component mechanisms are space-time separable. Hence, the model neuron does not have a unique spatial receptive field, nor does it have a unique temporal response function.

The difference of Gaussian model has been useful to vision scientists in several different ways. First, the model simplifies our calculations and thinking about receptive fields. The difference of Gaussian model predicts the response of neurons from a calculation that requires us to specify only a few unknown parameters, such as the width of the center and surround mechanisms receptive fields. The model provides a very efficient method of describing neural space-time receptive fields, and thus a convenient way of comparing the receptive fields of neurons.

Just as important, the model provides a framework for posing new and interesting questions. You should notice that the idea of a center and surround mechanism are entirely theoretical. I have not offered any direct proof of their existence. By building a model to efficiently describe the results, we have generated a new hypothesis about how the responses of neurons are created. In probing to identify whether these are merely useful theoretical tools, or whether there are true anatomical center and surround pathways, we will be led to explore new and interesting aspects of the visual encoding of light in the retina.

Finally, the model is specified in enough detail that it can be used in a variety of branches of vision science. As we shall see in later chapters, the difference of Gaussian model has been used as a key element to describe some of the limitations in human visual sensitivity to patterns. The model has also been used to describe certain aspects of how computational models of how images are represented in the visual pathways.

Retinal Light Adaptation

We have divided the study of receptive fields into two parts. We began by studying the neuron's response to contrast patterns presented on a fixed mean background. Contrast patterns are perturbations about the mean background field; by studying the responses to these stimuli we have been able to apply linear methods successfully to specify the transformation from light signal to neural impulses.

When we measure with respect to contrast instead of absolute intensity tests of linearity have a better chance of succeeding. To a significant degree, this is because contrast stimuli limit the range of intensities in the the image. For example, the peak intensity in a 100 percent contrast sinusoidal pattern is only a factor of 2 greater than the mean background intensity. The range of contrasts that we encode in a typical image, from the least contrast we can detect to 100 percent contrast, is no more than 2 orders of magnitude.

Through the course of a day, however, the range of image absolute intensities we experience typically exceeds 6 orders of magnitude. The visual pathways do not remain linear over this enormous range. When we study the response to contrast stimuli, we are attending to the local response of a globally nonlinear system. To fully understand the properties of neurons, we must also analyze how their responses change as we vary the mean background level. The changing neural and behavioral responses as a function of mean background intensity varies is called *visual adaptation*. In this section we will consider how to the locally linear measures we have developed using contrast must be extended when we consider the visual pathways over a wider range of mean signal levels.

Contrast Sensitivity: Dependence on Mean Intensity

Figure 24 (a) shows several contrast sensitivity functions from a cat retinal ganglion cell. These functions were measured on a wide range of mean intensities. When the mean intensity is relatively low, the neuron responds poorly to relatively high spatial frequencies[5]. At low background intensities the contrast sensitivity function shows little bandpass behavior, suggesting that there is little effect of the inhibitory surround. As the background intensity increases, the contrast sensitivity function changes shape. The reduced sensitivity to low frequency sensitivity stimuli becomes apparent, indicating that the opponent surround is more significant.

The change in the contrast sensitivity function with mean background intensity is a clue about how visual adaptation compensates for the change in mean background intensity. At low mean levels the neuron simply sums all of the quanta incident within the receptive field. At these low levels there is little surround inhibition, and thus there is little fall-off in the low frequency portion of the contrast sensitivity function. At higher mean levels, when quanta are more abundant, and the spatial receptive field of the neuron becomes relatively more sensitive to stimuli whose intensity varies within the receptive field. The opposing surround means that the neuron no longer sums the response to every quantum. Instead, the neuron responds better when there is variation in the intensity level within the spatial receptive field.

At the high mean background intensities, the contrast sensitivity functions are rather similar. For example, the three highest mean intensities used in the measurements in Figure 24 differ by a factor of 100. Yet, in the low spatial frequency range the contrast sensitivity curves measured at these levels differ only by about a factor of three. Panel (b) in the figure shows the relatively small change in contrast sensitivity with mean background by comparing the cell's contrast sensitivity to a 0.2 cpd pattern measured on different background intensities. As mean intensity changes over five orders of magnitude, the contrast sensitivity to this pattern varies one order of magnitude.

The relative constancy in contrast sensitivity reinforces the view that the response of the neuron is more closely coupled to the stimulus contrast than the absolute intensity level. This suggests that the contrast variable may be the key stimulus variable represented by the neuron's activity.

[5] In general, cats have very poor spatial resolution compared to primates. The spatial frequency range of this neuron, and cats' performance as measured behaviorally, is far below the normal range for primate visual acuity.

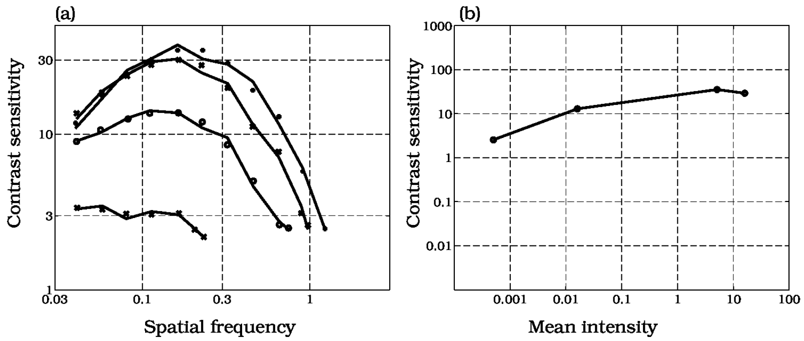

Figure 24: Contrast sensitivity function of a cat retinal ganglion cell measured at different mean intensity levels. (a) The curves correspond to contrast sensitivity measurements made on backgrounds at 16, 5.1, 0.016, and 0.0005 candelas per meter squared. The shape of the contrast sensitivity function becomes increasingly lowpass, and less bandpass, as the background illumination decreases. (b) The contrast sensitivity to a 0.2 cpd spatial pattern varies by less than a factor of ten as the mean level varies over near five orders of magnitude. (Source: Enroth-Cugell and Robson (1966)).

Image contrast and image intensity are inter-related quantities. The relatively constant sensitivity to contrast implies that the neuron's sensitivity to absolute light level varies with changes in mean intensity level; Figure 25 shows this variation in sensitivity to light. The vertical axis of the graph measures the logarithm of the light intensity of an incremental flash needed to cause a fixed increase in firing rate from the spontaneous rate. This is a measurement of the threshold sensitivity to the incremental test flash. The horizontal axis of the graph measures logarithm of the mean background intensity. Since the slope of the increasing portion of the graph is close to one, we can conclude that the threshold increases roughly in proportion to mean background intensity. This relationship between threshold and background level was first discovered from measurements of human behavior. The relationship is called *Weber's law*, to honor the scientist who first discovered the principle.

As the mean intensity of the background varies, we can find other aspects to the change in the neural response as well. Plotted as insets to the figure are the PSTHs of the measurements to these incremental threshold flashes. The timecourse of the response to the incremental flash varies with mean intensity level, becoming somewhat brisker with sharper signals at the onset and offset of the test flash. Thus, we see that the temporal response of the neuron, like the spatial contrast sensitivity, varies with mean intensity level. These adaptations probably occur to take advantage of the improved quality of the signal available at higher light levels.

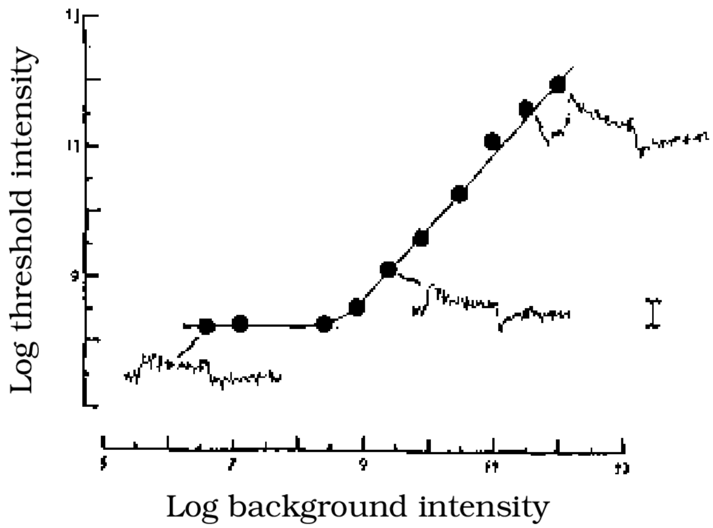

Figure 25: Threshold sensitivity as a function of background intensity measured on a cat retinal ganglion cell. The threshold intensity of an incremental test flash required to elicit a criterion peak firing rate in a retinal ganglion cell was measured. The test flash was presented on a large steady background, The logarithm of the threshold intensity of the test flash grows linearly with the logarithm of the mean background intensity, and the slope is close to one. Hence, the threshold is intensity is proportional to the background intensity. The insets within the figure show the PSTH and demonstrate that the timecourse of the ganglion cell changes with intensity level. On higher backgrounds, transient overshoots and undershoots are evident. (Source: Enroth-Cugell et al. (1977)).

Comparison with Behavioral Contrast Sensitivity

Sensitivity to contrast and sensitivity to absolute light level are complementary measures. When the threshold to the absolute light level is proportional to the background, as Weber's law predicts, sensitivity to contrast will be precisely constant. In most cases, however, Weber's Law is only a rough approximation. For example, consider the contrast sensitivity functions plotted in Figure 24. Were Weber's law exact, all of the contrast sensitivity functions would overlap. Plainly, this is not so. Moreover, the quality of the Weber's law approximation depends on the spatial pattern of the stimulus. The approximation is better for low spatial frequency patterns than for high spatial frequency patterns.

Reasoning based on these types of approximations is part of the challenge confronting the student of biological systems. The laws we discover don't have the same precision as physical laws. It is often a question of judgment as to whether the approximation to a law we see in a biological measurement is adequate to support a principled view about the function of a neuron or a visual pathway. In this case, there is some consensus that contrast is a key variable reported out by the retinal ganglion cells. In part, the consensus has developed from the neural response data we have reviewed in this chapter. And, in part, the consensus depends on the analysis that we will undertake later in this volume, in which we consider the important signals for visual function.

There is a third type of evidence that we should consider as well: this is the question of whether the properties of the contrast sensitivity function we measure at the level of individual neurons can be detected in the properties of the animal's behavior. In Chapter and Chapter , and Chapter we have seen several succesful comparisons between human behavior and physiological measurements.

The retinal ganglion cell contrast sensitivity functions have a counterpart in the behavioral contrast sensitivity functions. Pasternak and Merigan (1981) measured behavioral contrast sensitivity functions in the cat on a variety of mean background intensities (see Figure 26). The behavioral contrast sensitivity functions parallel the neural contrast sensitivity functions. For example, as the mean background intensity increases the behaviorally measured contrast sensitivity functions become more bandpass. Also, as the mean background intensity varies over six orders of magnitude, the contrast sensitivity changes by only one order of magnitude. Hence, there is good qualitative agreement between the response sensitivities of individual retinal ganglion cells and the animal as a whole.

The agreement between neural measurements and behavioral measurements demonstrates that the information present in the responses of individual neurons is similar to the information available to the cat making its behavioral judgments concerning the presence of the contrast pattern. This does not mean, however, that the responses of individual retinal ganglion cells govern the animal's behavior. We have already seen, for example, that the information encoded about wavelength by the cone photoreceptors is equivalent to the information available to the human when making a color-match. Yet, it is certain that when we formulate our conscious

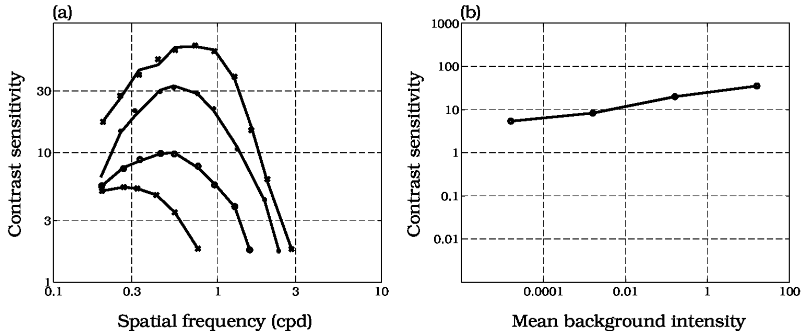

Figure 26: Behavioral contrast sensitivity functions of the cat measured on a variety of mean background intensities. Individual behavioral contrast sensitivity functions show the same qualitative properties as the contrast sensitivity functions of individual retinal ganglion cells. As the mean background intensity increases the contrast sensitivity function becomes increasingly bandpass (panel a). As the mean background intensity varies over six orders of magnitude, the contrast sensitivity of a 0.3 cpd target changes by only one order of magnitude (panel b). (Source: Pasternak and Merigan (1981)).

decisions about a color-match we do not have access to the information at the cones themselves. The agreement between neural and behavioral responses is an abstract one, an agreement at a theoretical level. We shall see this type of comparison again as we move on to study visual cortex and human behavior. As we do, remember that a good method of comparing neural and behavioral responses is to analyze the information available at a point in the visual pathway with the information available to the human making a behavioral decision.

Cortical Representation

Cortical representation overview

In this chapter we will review the representation of information in visual cortex. There have been many advances in our understanding of visual cortex over the last twenty-five years. Even today, our view of visual cortex is changing rapidly; new results that change our overall view sometimes seem to arrive weekly. In the beginning of this chapter, I will review what is commonly accepted concerning visual cortex. Towards the end, I will introduce some of the broader claims that have been made about the relationship between visual cortex and perception. We will take up the issue of connecting cortex, computation, and seeing again in the later chapters.

Visual cortex

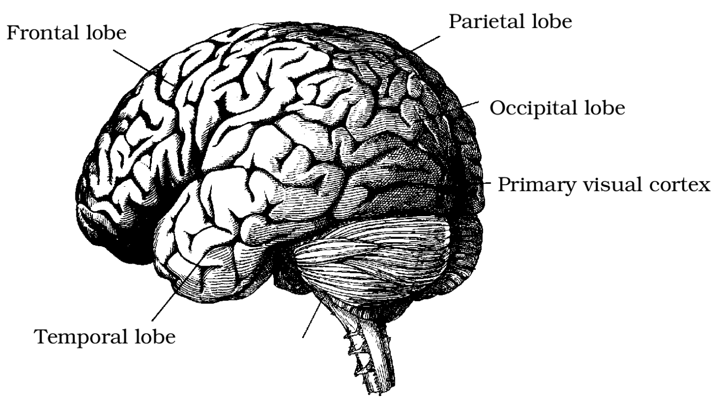

Figure 1: The cortex is shown in lateral view. Based on its overall shape, anatomists divide the human brain into four regions called the occipital, temporal, parietal and frontal lobes. Based on its internal connections, the cortex can be further divided into many anatomically distinct areas. Visual input to the brain arrives in primary visual cortex, area V1, which is located in the occipital lobe.

A lateral view of the brain is sketched in Figure 1. The human cortex is a 2.5mm (range: 1-4.5mm) thick sheet of neurons with a surface area of 1400 square centimeters. Rather than lining the skull, as the retina lines the eye, the visual cortex is like a crumpled sheet stuffed into the skull. Each location where the folded cortex forms a ridge visible from the exterior is called a *gyrus*, while each shallow furrow that separates a pair of gyri is called a *sulcus*. The pattern of sulci and gyri differ considerably across species: the human brain contains more sulci than other primate brains. There are also significant differences between human brains, although the broad outlines of the sulcal and gyral patterns are usually present and recognizable across different people. The gyri and sulci are convenient landmarks, but it is not established that they have a functional significance.

The most visible sulci serve as markers to partition the human brain into four *lobes*. The lobes are called *frontal, parietal, temporal* and *occipital* to describe their relative positions (see Figure 1). Each lobe contains many distinct brain *areas*, that is contiguous groups of cortical neurons that appear to function in an interrelated manner. A cortical area is identified in several ways, though perhaps the most significant is by its anatomical connections with other parts of the brain. Each brain area makes a distinctive pattern of anatomical connections with other brain areas. The inputs arriving to one area come from only a few other places in the brain, and the outputs emerging from that area are sent to a specific set of destination areas.

In the primate, the great part of the visual signal from the retina and the lateral geniculate nucleus arrives at a single area within the occipital lobe of the cortex called, or *primary visual cortex*. This is a large cortical area, comprising roughly 1.5 x 108 neurons, many more than the 106 neurons in the lateral geniculate nucleus. Area V1 can be identified by a prominent striation made up of a dense collection of myelinated axons within one of the layers of visual cortex. The striation is coextensive with area V1 and appears as a white band to the naked eye. Because area V1 was defined by the presence of this striation, it is sometimes called *striate cortex*. The stripe is also called the *Stria of Gennari*. Because of its prominence, important anatomical location and large size (18 square centimeters), area V1 has been the subject of intense study. We will begin this chapter with a review of the anatomical and electrophysiological features of area V1.

In addition to area V1, more than twenty cortical areas have been discovered that receive a strong visual input. The anatomy, electrophysiology and computational purpose of these areas are now under active study and will be an important topic for study for many years to come. We will review some of the preliminary experiments that have been performed in these visual areas at the end of this chapter. In later chapters concerning motion and color, we will return to consider the functional role of these visual areas as well (Zeki (1978), Zeki (1990); Felleman and Van Essen (1991)).

Most of what we know about cortical visual areas comes from experimental studies of cat and monkey. There are significant differences in the anatomy and functional properties of the cortices of different species. These differences can be demonstrated in simple experimental manipulations. For example, Sprague et al. (1977) have shown that removal of the cat primary visual cortex does not blind the cat: the animal jumps, runs, and appears normal to the casual observer. Humphrey (1974) has studied the behavior of a monkey whose area V1 was removed.

Initially the lesion appeared to blind the monkey completely. Over time, however, the monkey recovered some visual function and was able to walk around objects, climb a tree, and even find and pick up small candy pellets in her play area. In human, the loss of area V1 is devastating to all visual function. Because of these differences, I describe measurements of the human brain whenever possible, and mainly I have restricted this review to primate.

The Architecture of Primary Visual Cortex

There is a great deal of precision in the interconnections of cortical visual areas. The specific pattern of connections received by area V1 from the two retinae via the lateral geniculate nucleus results in certain regularities of the architecture of primary visual cortex. We review the anatomical structure of area V1 first. Then, we review how the pattern of connections from the two retinae imposes an overall organization on the visual information represented in cortical area V1.

The layers of area V1

Like cortex in general, area V1 is a layered structure. Figure 2 (a) shows a cross section of the visual cortex. Several major layers can be identified easily. Area V1 is segregated into six layers based on differences in the relative density of neurons, axons and synapses and interconnections to the rest of the brain. The superficial layer 1 has very few neurons but many axons, dendrites and synapses, which collectively are called *neuropil*. Layers 2 and 3 consists of a dense array of cell bodies and many local dendritic interconnections. These layers appear to receive a direct input from the intercalated layers of the lateral geniculate as well (Fitzpatrick et al. (1983); Hendry and Yoshioka (1994)), and the outputs from layers 2 and 3 are sent to other cortical areas. Layers 2 and 3 are hard to distinguish based on simple histological stains of the cortex. Functionally, layers 1-3 are often grouped together and simply called the *superficial layers* of the cortex.

Layer 4 has been subdivided into several parts as the interconnections with other brain areas and layers have become clarified. Layer 4C receives the primary input from the parvocellular and magnocellular layers of the lateral geniculate. The magnocellular neurons send their output to the upper half of this layer, which is called 4C[α] while the parvocellular neurons make connections in the lower half, called 4C[β]. Layer 4B receives a large input from 4C[α] and sends its output to other cortical areas. Layer 4B can be defined anatomically by the presence of the large Stria of Gennari, which is composed mainly of cortical axons.

Layer 5 contains relatively few cell bodies compared to the surrounding layers. It sends a major output to the superior colliculus, a structure in the midbrain. Layer 6 is dense with cells and sends a large output back to the lateral geniculate nucleus (Toyama et al. (1969)). As a general though not absolute rule, forward outputs to new cortical areas tend to come from the superficial layers and terminate in layer 4. The feedback projections tend to come

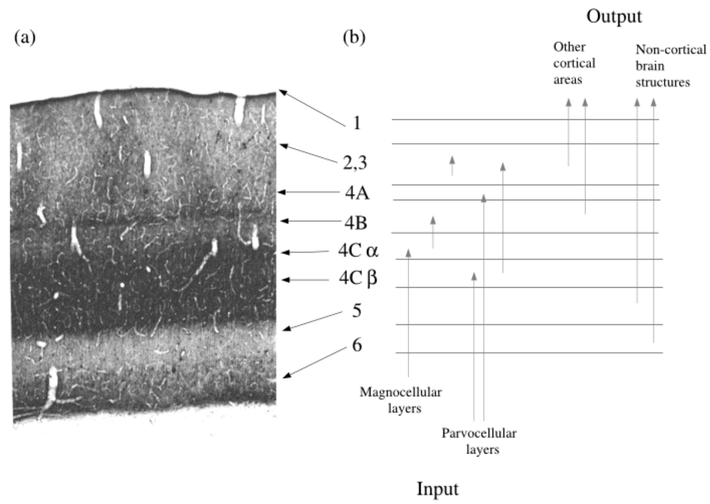

Figure 2: Area V1 is a layered structure. (a) A stained cross-section of the visual cortex in macaque shows the individual layers. Each layer has different proportions of cell bodies, dendrites and axons and may be distinguished by the density of the staining and other properties. The light areas are blood vessels. (Source: J. Lund, personal communication). (b) The organization of the neural inputs and outputs to area V1 are shown. The parvocellular and magnocellular inputs make connections in layer 4C. The intercalated neurons make connections in the superficial layers. The outputs are sent to other cortical areas, back to the lateral geniculate nucleus and other subcortical nuclei.

from the deep layers and terminate in layers 1 and 6 (Rockland and Pandya (1979); Felleman and Van Essen (1991)).

The wiring diagram in Figure 2 (b) shows that the signals to and from area V1 are complex and highly specific. One must suppose that the interconnections within area V1 are specific, too. Roughly twenty-five percent of the neurons in all layers are inhibitory interneurons, and their interconnections must be governed by the presence of biochemical markers that identify which neurons should connect and how. Anatomical classification of the cell types within the visual cortex, and identification of the local circuitry, will provide us with many more clues about the functional significance of this area.

The pathway to area V1

The structure of the anatomical pathways leading from the two retinae to the cortex defines many of the fundamental properties of area V1. Among the most significant properties is that area V1 in each hemisphere has only a restricted field of view. Area V1 in the left (right) hemisphere only receives visual input concerning the right (left) half of the visual field.

We can see how this arises by considering how retinal signals make their way to area V1. The optic tract fibers from the two retinae come together at the *optic chiasm*, as shown in Figure 3. There the fibers are sorted into two new groups that each connect to only one side of the brain. Axons from ganglion cells whose receptive fields are located in the *left visual field* send their outputs towards the lateral geniculate nucleus on the right side of the brain, while axons of ganglion cells with receptive fields in the right visual field communicate their output to the left side of the brain. Consequently, each lateral geniculate nucleus receives a retinal signal derived from both eyes, but only one half of the visual field.

The signals reaching the cortex from the retina respect three other basic organizational principles. The pattern of interconnections are organized with respect to (a) the eye of origin, (b) the class of ganglion cell, and (c) the spatial position of the ganglion cell within the retina. Figure 3 illustrates the pattern of connections schematically, starting at the retinae and continuing to area V1.

Eye of origin

Within the lateral geniculate nucleus information about the eye of origin is preserved since fibers from each eye make connections in different layers of the lateral geniculate nucleus. The parvocellular and magnocellular layers, which are numbered as 1-6, receive input from the retina on the [same,opposite,opposite,same,opposite,same] side of head, respectively. The connections of these layers for the left lateral geniculate nucleus are illustrated in Figure 3. Why this particular pattern of ocular connections exists is a mystery. The eye-of-origin for the intercalated layers, which fall between the parvocellular and magnocellular layers, has not yet been demonstrated.

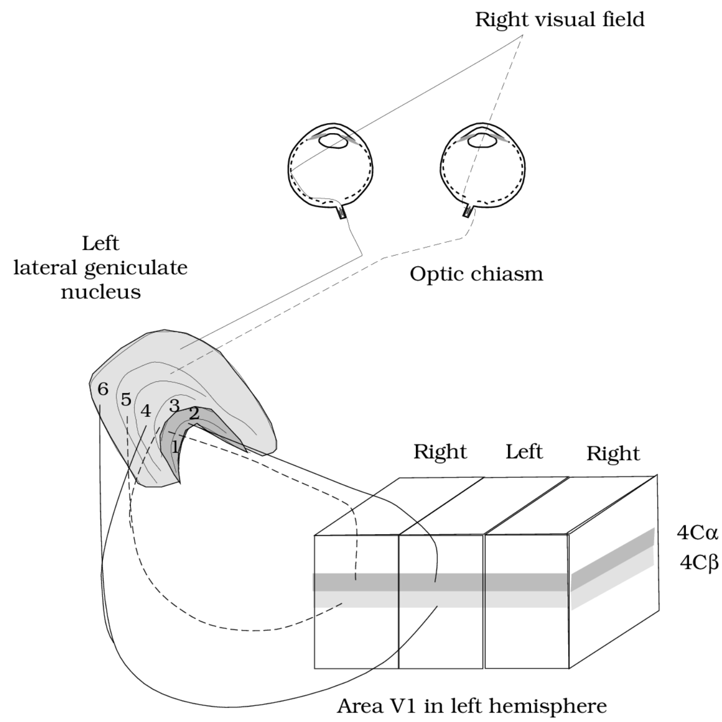

Figure 3: The signals from the two retinae are communicated to area V1 via the lateral geniculate nucleus (LGN). Points in the right visual field are imaged on the temporal side of the left eye and the nasal side of the right eye. Axons from ganglion cells in these retinal regions make connections with separate layers in the left lateral geniculate nucleus, which are also segregated by eye of origin. Neurons in the magnocellular and parvocellular layers of the lateral geniculate send their outputs to cortical layers 4Cα and 4Cβ, respectively. The signals from each eye are segregated into different bands within area V1. Signals from these bands converge on individual neurons in the superficial layers of the cortex.

The signals from the two eyes remain segregated as they arrive at the input layers of area V1. One can observe this segregation by measuring the electrophysiological responses of the units in layer 4C. As the recording electrode travels within layer 4C, there is an abrupt shift as to which eye drives the unit. In layer 4C The shift from one eye to the other takes place over a distance of less than 50
mum. Above and below layer 4C the signals from the two eyes converge onto single neurons, although there is still a tendency for individual neurons to receive inputs predominantly from one eye or another and this pattern is aligned with the input pattern. The transition between eye of origin is less abrupt in the superficial layers, perhaps extending over 100
mum. The relative segregation of information across the columns with respect to the eye of origin is called *ocular dominance columns* (Hubel and Wiesel (1977); Bishop (1984)). %Review article by bishop

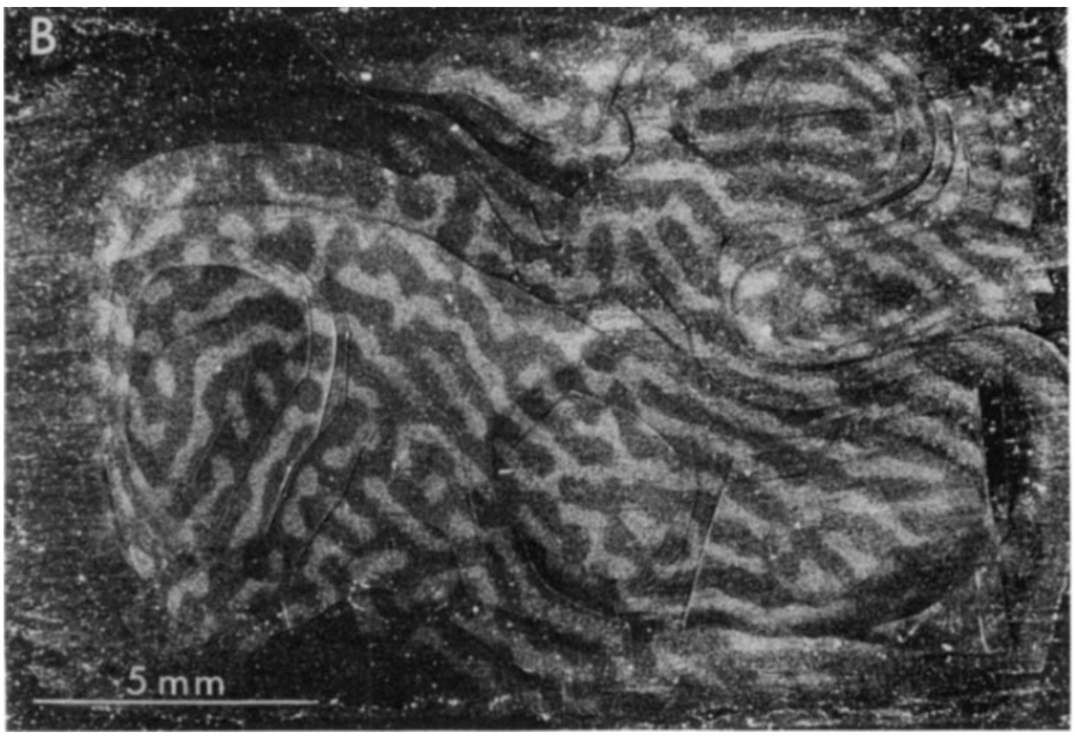

Figure 4: The ocular dominance columns in area V1 can be visualized using a radioactive marker, tritiated proline. When the marker is injected into one eye it is transported via the lateral geniculate nucleus to the cortex. The radioactive uptake is revealed in this dark field photograph. The light bands in this tangential section show the places where the radioactive marker was located and thus reveal the ocular dominance columns. (Source: Hubel et al. (1978))

In addition to evidence from electrophysiological measurements, one also can use anatomical methods to visualize the ocular dominance columns and demonstrate their existence. After injection into one eye, the the tritiated amino acid proline will be transported from the retina to the cortex across the synaptic connections. By sectioning the visual cortex tangentially through at layer 4C, and exposing the section to a photographic emulsion, we can develop a pattern of light and dark stripes that correspond to the presence and absence of the tritiated proline. Figure 4 shows a pattern of light bands that mark regions receiving input from the injected eye; the intervening dark areas receive input from the opposite eye. In the monkey these bands each span approximately 400 μm, though in the human they span approximately one millimeter (Hubel et al. (1978); Horton and Hoyt (1991a)).

In the superficial layers of area V1 many neurons respond to stimuli from both eyes; in the normal monkey eighty percent of the neurons in the superificial layers of area V1 are binocularly driven. The development of the interconnections necessary to drive the binocular neurons depends upon experience during maturation. Hubel and Wiesel (1965) showed that artifically closing one eye or cutting an ocular muscle strongly affects the development of neurons in area V1. Specifically, the binocular neurons fail to develop. Behaviorally, if one eye is kept closed for a critical period during development, the animal will remain blind in this eye for the rest of its life. This is quite different from the result of closing an adult eye for a few months; this has no significant effect (Hubel et al. (1977); Shatz and Stryker (1978); Mitchell (1988); Movshon and Van Sluyters (1981)). In the cat, normal development of ocular dominance columns, and presumably the binocular interconnections as well, depends upon neural activity originating in the two retina (Stryker and Harris (1986)).

Ganglion cell classification

Information from different classes of retinal ganglion cells remains segregated along the path to the cortex. Neurons in the magnocellular layers receive fibers from the parasol cells; neurons in the parvocellular layers receive fibers from the midget ganglion cells. It is uncertain precisely which retinal ganglion cells project to the intercalated layers. The segregation of signals continues to the input of area V1. Within layer 4C, the upper half (4Cα) receives the axons from the magnocellular layers while the lower half (4Cβ) receives the parvocellular input. The neurons in the intercalated layers send their output to the superficial layers 2 and 3.

Retinotopic organization

The spatial position of the ganglion cell within the retina is preserved by the spatial organization of the neurons within the lateral geniculate nucleus layers. The back of the nucleus contains neurons whose receptive fields are near the fovea. As we measure towards the front of the nucleus, the receptive field locations become increasingly peripheral. This spatial layout is called *retinotopic* organization because the topological organization of the receptive fields in the lateral geniculate parallels the organization in the retina.

The signals in area V1 are also retinotopically arranged. From electrophysiology in monkeys, one can measure the location of receptive fields with an electrode that penetrates tangentially through layer 4C, traversing through the ocular dominance columns. The receptive field centers of neurons along this path are located systematically from the fovea to the periphery. This trend is interrupted locally by small, abrupt jumps at the ocular dominance borders. Within the first ocular dominance column the receptive field center positions change smoothly; as one passes into the next ocular dominance region there is an abrupt shift of the receptive field positions equal to about half of the space spanned by receptive fields in the first column. Hubel and Wiesel (1977) describe this organization and refer to it as "two steps forward and one step back."

In the last fifteen years, it has become possible to estimate spatially localized activity in the human brain. Beginning with *positron emission tomography* (*PET*) studies, and more recently by using *functional magnetic resonance imaging* (*fMRI*), we can measure activity in volumes of the cortex as small as 10 cubic millimeters, containing a few hundred thousand neurons.[1]

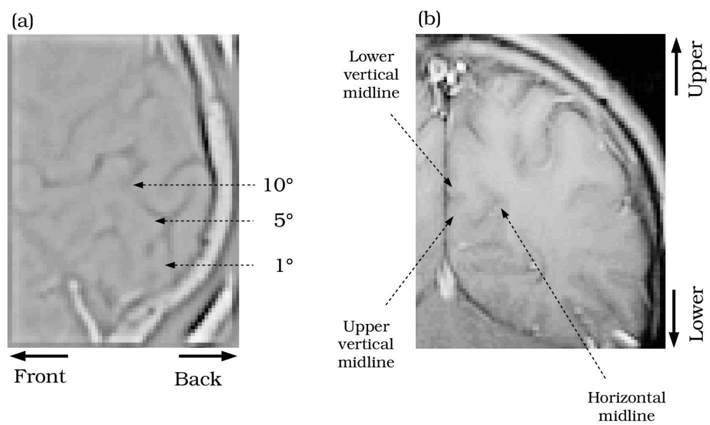

Figure 5: Human area V1 is located mainly in the calcarine sulcus, and in some individuals it may extend onto the occipital pole. (a) Seen in sagittal view, the calcarine is a long sulcus that extends roughly 4 cm. The visual eccentricities of the receptive fields of neurons at different locations in the calcarine are shown. (b) In the coronal plane the calcarine sulcus appears as an indentation of the medial wall of the brain. At a given distance along the calcarine, the receptive fields of neurons fall along a semi-circle within the visual field. Each hemisphere represents one half of the visual field. Neurons with receptive fields on the upper, middle, and lower sections of a semi-circle of constant eccentricity are found on the lower, middle and upper portions of the calcarine, respectively.

[1]Both of these methods are based on indirect measures of neural activation. With the PET method, an observer receives a low dose of radiation in his blood stream and neural activity is indicated by brain regions showing increased radioactivity. The fMRI signal detects differences in the local concentration of blood oxygen. Both the increased radioactivity and the change in local blood oxygenation are due to vascular responses to the neural activity (Posner and Raichle (1994); Ogawa et al. (1992); Kwong et al. (1992)).

Human area V1 is located within the *calcarine* sulcus in the occipital lobe. The calcarine sulcus in my brain, and its retinotopic organization, is shown in Figure 5. Neurons with receptive fields in the central visual field are located in the posterior calcarine sulcus, while neurons with receptive fields in the periphery are located in the anterior portions of the sulcus. At a given distance along the sulcus, the receptive fields are located along a semi-circle in the visual field. Neurons with receptive fields on the upper, middle, and lower sections of the semi-circle, are found on the lower, middle and upper portions of the calcarine, respectively. (Holmes (1918), Holmes (1945); Horton and Hoyt (1991b); Inouye (1909))

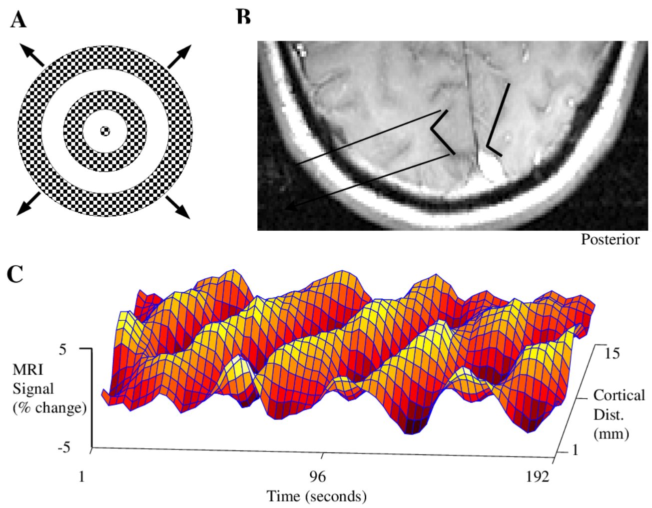

Figure 6: Receptive field locations of neurons in human calcarine sulcus can be measured by functional magnetic resonance imaging. (a) The observer viewed a series of concentric expanding annuli presented on a gray background. Each annulus contained a high contrast flickering radial checkerboard pattern. As an annulus expanded beyond the edge of the display, a new annulus emerged in the center creating a periodic image sequence. The sequence was repeated four times in a single experiment. (b) An image within the plane of the calcarine sulcus. The dark lines indicate points identified as following the left calcarine sulcus. (c) The fMRI temporal signal at different points within the calcarine sulcus. The fMRI signal follows the timecourse of the stimulus; the phase of the signal is delayed as we measure from the posterior to the anterior calcarine sulcus.

Engel et al. (1994) measured the human retinotopic organization from fovea to periphery by using the stimulus shown in Figure 6 (a). The stimulus consisted of a series of slowly expanding rings; each ring was a collection of flickering squares. The ring began as a small spot located at the fixation mark, and then it grew until it traveled beyond the edge of the visual field. As a ring faded from view, it was replaced by a new ring starting at the center. Because of the retinotopic organization of the calcarine, each ring causes a traveling wave of neural activity beginning in the posterior calcarine and traveling in the anterior direction.

We can detect the traveling wave of activation by measuring the fMRI signal at different points along the calcarine sulcus. Figure 6 (b) is an image of the brain within the plane of the calcarine sulcus. Positions within the calcarine sulcus are highlighted in black. The fMRI signal at each point within the sulcus, plotted as a function of time, is shown in the mesh plot in Figure 6 (c). Notice that the amplitude of the fMRI signal covaries with the stimulus; the fMRI signal waxes and wanes four times through the four periods of the expanding annulus. The temporal phase of the fMRI signal varies systematically from the posterior to anterior portions of the sulcus: Activity in the posterior portion of the sulcus is advanced in time compared to activity in the anterior portion. This traveling wave occurs because the stimulus creates activity in the posterior part of the sulcus first, and then later in the anterior part of the sulcus.

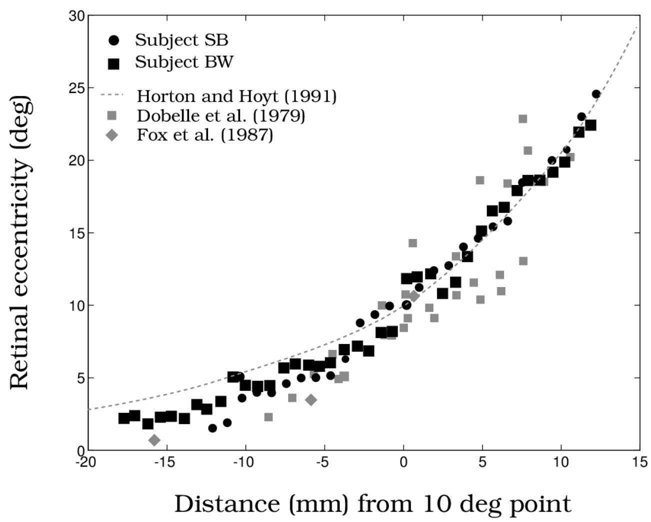

Figure 7: Several methods have been used to estimate the receptive field location of neurons in the calcarine sulcus. The filled symbols show measurements from two observers using the fMRI method (Engel et al. (1994)). The squares are from a microstimulation study on a blind volunteer (Dobelle et al. (1979)). The diamonds are measurements averaged from 5 observers using PET (Fox and Raichle (1984)). The dashed curve is an estimate based on studying the locations of scotoma in stroke patients and single-cell data from non-human primates (Horton and Hoyt (1991b)). (Source: Engel et al. (1994))

In addition to fMRI, there are several other estimates of the mapping from visual field eccentricity to location in the calcarine sulcus. These estimates are compared in Figure 7. The fMRI measurements from two observers are shown as the filled circles. Estimates from direct electrical stimulation of the cortex are shown as gray squares (Dobelle et al. (1979)). In these experiments the volunteer observer's brain was stimulated and he indicated the location of the perceived visual stimulation within the visual field (see also Brindley and Lewin (1968)). The three gray diamonds are show measurements using PET. These data represent the average of five different observers, normalized for differences in brain size. The dashed line shows an estimate by Horton and Hoyt (1991b) by studying the positions of scotoma in observers with localized brain lesions and extrapolating from monkey. These estimates are in good agreement, and they all show that considerably more cortical area is allocated to the foveal representation than to the peripheral representation.

The allocation of more cortical area to the foveal than the peripheral representation seems a natural consequence of the fact that more photoreceptors and retinal ganglion cells represent the fovea than the periphery. Wässle et al. (1990) (see also Schein (1988)) suggested that the expanded foveal representation can be explained by assuming that every ganglion cell is allocated an equal amount of cortical area. More recently, Azzopardi and Cowey (1993) suggest that there is a further expansion of the foveal representation, and that foveal ganglion cells are allocated three to six times more cortical area than peripheral ganglion cells.

Electrical stimulation of Human Area V1

Direct electrical stimulation of the visual cortex causes the sensation of vision. When a visual impression is generated by non-photic stimulation, say by pressing on the eyeball or by electrical stimulation, the resulting perception is called a *visual phosphene*. In order to develop visual prostheses for individuals with incurable retinal diseases, several research groups have studied the visual properties of phosphenes created by electrical stimulation of the visual cortex (Brindley and Lewin (1968); Dobelle et al. (1979); Bak et al. (1990)).

Brindley and Lewin (1968) describe experiments with a human volunteer who was diabetic and suffered from bi-lateral glaucoma, a right retinal detachment, and was effectively blind. When she suffered a stroke, she required an operation that would expose her visual cortex. With the patient's consent, Brindley and Lewin built and implanted a stimulator that could deliver current to the surface of her brain, near the patient's primary visual cortex. They asked her to describe the appearance of the electrical stimulation following stimulation by the different electrodes, at various positions within her primary visual cortex. She reported that electrical stimulation caused her to perceive a phosphene that appeared to be a point of light or a blob in space. Her description of the visual impression caused by most of the electrodes was "like a grain of rice at arm's length." Occasionally one electrode might cause a slightly longer impression, "like half a matchstick at arm's length."

As might be expected from the retinotopic organization of the visual cortex, the position of the phosphenes varied with the position of the stimulating electrodes. The observer told the experimenters where she perceived the phosphenes to be using a simple procedure. She grasped a knob with her right hand and imagined she was fixating on that hand. She then pointed to the location of the phosphenes relative to the fixation point using her left hand.

Figure 8 shows the positions of the electrodes and the corresponding phosphenes. The pattern of results follows the expectations from the retinotopic organization of the calcarine sulcus.

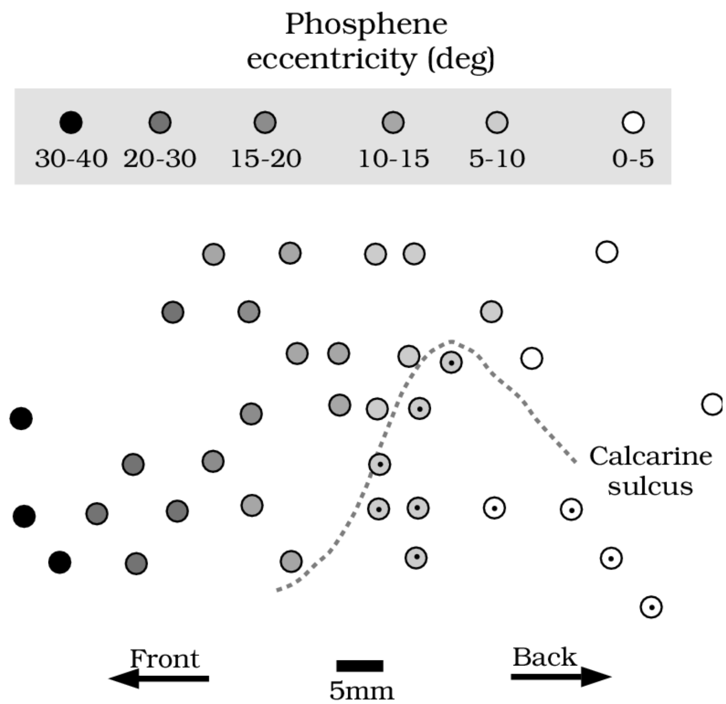

Figure 8: Electrical stimulation of human area V1 using chronically implanted microelectrodes reveals the retinotopic organization of human cortex. The symbols are plotted at the electrode positions on the medial wall of the brain. The shading of the symbol indicates the visual eccentricity of the phosphene created by electrode stimulation. A dot within the symbol means that the phosphene was perceived in the upper visual field. The dashed curve shows the inferred position of the calcarine sulcus (Source: Brindley and Lewin (1968)).

Stimulation by electrodes near the back of the brain created phosphenes in the central five degrees; stimulation by forward electrodes created phosphenes in more eccentric portions. More cortical area is devoted to the central than peripheral regions of vision.

Brindley and Lewin tested the effects of superposition by stimulating with separate electrodes and then stimulating with both electrodes at once. When electrodes were far apart, the visual phosphene generated by stimulating both electrodes at once could be predicted from the phosphenes generated by stimulating individually. Superposition also held for some closely spaced electrodes, but not all. The test of superposition is particularly important for practical development of a prosthetic device. To build up complex visual patterns from stimulation of V1, it is necessary to use multiple electrodes. If linearity holds, then we can measure the appearance from single electrode stimulations and predict the appearance to multiple stimulations. That superposition held approximately suggests that it may be possible to predict the appearance of the multiple electrode stimulation from measurements using individual electrodes. Without superposition, we have no logical basis for creating a an image from the intensity at a set of single points.

There have been a few recent reports of stimulation of the human visual cortex. For example, Bak et al. (1990) stimulated using very fine microelectrodes (37.5 μm) inserted within the cortex during to stimulate visual percepts. They experimented on patients who were having epileptic foci removed. These patients were under local anaesthesia and could report on their visual sensations. Bak et al. observed that when the stimulation was embedded within the visual cortex, visual sensations could be obtained with quite low current levels. Brindley and Lewin used about 2 mA of current, but Bak et al. found thresholds about 100 times lower, near 20 μA. The appearance of the visual phosphene was steady in these patients, and some of them appeared colored. Time was quite limited in these studies and only a few experimental manipulations were possible. But, they report that when the microelectrodes were separated by more than 0.7 mm, the two phosphenes could be seen as distinct, while separations of 0.3 mm were seen as a single spot. For one subject, nearly all of the phosphenes were reported to be strongly colored, unlike the phosphenes reported by Brindley and Lewin's patient. While the subjects were stimulated, they could also perceive light stimuli. The phosphenes were visible against the backdrop of the normal visual field.

Receptive Fields in Primary Visual Cortex

The receptive fields of neurons in area V1 are qualitatively different from those in the lateral geniculate nucleus. For example, lateral geniculate neurons have circularly symmetric receptive fields, but most V1 receptive fields do not. Unlike lateral geniculate neurons, some neurons in area V1 respond well to stimuli moving in one direction but fail to respond to stimuli moving in the opposite direction. Some area V1 neurons are binocular, responding to stimuli from both eyes. These new receptive field properties must be related to the visual computations performed within the cortex such as the analysis of form and texture, the perception of motion, and the estimation of stereo depth. We might expect that these new receptive field properties have a functional role in these visual computations.

Much of what we know about cortical receptive fields comes from Hubel and Wiesel's measurements during their 25 year collaboration. Others had accomplished the difficult feat of recording from cortical neurons first; but the initial experiments used diffuse illumination, say turning on the room lights, as a source of stimulation. As we have seen, pattern contrast is an important variable in the retinal neural representation; consequently, cortical cells respond poorly to diffuse illumination (von Baumgarten and Jung (1952)). Hubel and Wiesel made rapid progress in elucidating the responses of cortical neurons by using stimuli of great relevance to vision and by being extremely insightful. Hubel and Wiesel's papers chart a remarkable series of advances in our understanding of the visual cortex. Their studies have defined the major ways in which area V1 receptive fields differ from lateral geniculate nucleus receptive fields. Their qualitative methods for studying the cortex continue to dominate experimental physiology (Hubel and Wiesel (1959), Hubel and Wiesel (1962), Hubel and Wiesel (1968), Hubel and Wiesel (1977); Hubel (1982)).

Hubel and Wiesel recorded the activity of cortical neurons while displaying patterned stimuli, mainly line segments and spots, on a screen that was imaged through the animal's cornea and lens onto the retina. As the microelectrode penetrated the visual cortex, they presented line segments whose width and length could be adjusted. First, they varied the position of the stimulus on the screen, searching for the neuron's receptive field. Once the receptive field position was established, they measured the response of the neuron to a lines, bars and spots presented individually.

One important goal of their work was to classify the cortical neurons based on their responses to the small collection of stimuli. They sought classifications that represented the neurons' receptive field properties and that also helped to clarify the neurons' function in seeing. Classification of the receptive field types was an important theme when we considered the responses of retinal ganglion cells as well. It is of great current interest to try to understand whether the classifications of cortical neurons and retinal neurons can be brought together to form a clear picture of this entire section of the visual pathways.

A second important aspect of characterizing cortical neurons is to measure the transformation from pattern contrast stimulus to firing activity. We used linear systems methods to design experiments and create quantitative models of this transformation for retinal ganglion cells. Linearity is an important idea when applied to cortical receptive fields, too. The most important application of linearity is Hubel and Wiesel's classification of cortical neurons into two categories, called *simple* and *complex*. This classification is based, in large part, on an informal test of linearity (Skottun et al. (1991)). As Hubel writes, "For the most part, we can predict the responses of simple cells to complicated shapes from their responses to small-spot stimuli (Hubel (1988), p. 72)." Complex cells, on the other hand, do not satisfy superposition. The response obtained by sweeping a line across the cell's receptive field can not be predicted accurately from the responses to individual flashes of a line.

Orientation selectivity

Since simple cells are approximately linear, we can measure their receptive fields using the methods described in Chapter . Simple cell receptive fields consist of adjacent excitatory and inhibitory areas, as illustrated in Figure 9. Simple cells have *oriented* receptive fields and hence they respond to stimuli in some orientations better than others. This receptive field property is called *orientation selectivity.* The orientation of the stimulus the evokes the most powerful response is called the cell's *preferred orientation.*

Orientation selectivity of cortical neurons is a new receptive field property. Lateral geniculate neurons and retinal neurons have circularly symmetric receptive fields and they respond almost equally well to all stimulus orientations. Orientation selective neurons are found throughout layers 2 and 3, though they are relatively rare in the primary inputs within layer 4C.

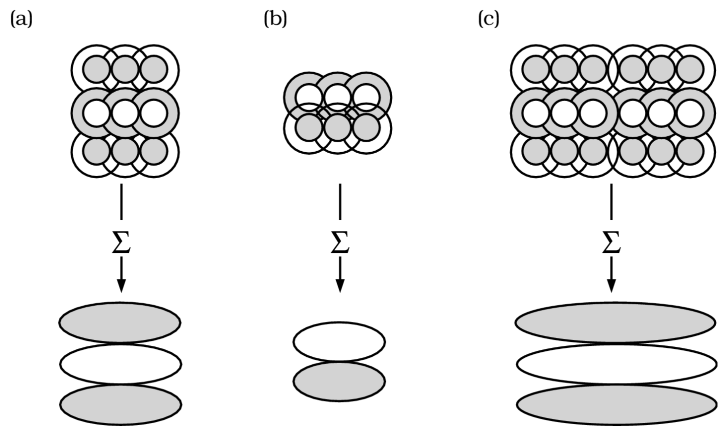

Figure 9: Orientation selective receptive fields can be created by summing the responses of neurons with non-oriented, circularly symmetric receptive fields. The receptive fields of three hypothetical neurons are shown. Each hypothetical receptive field has an adjacent excitatory and inhibitory region. (a) and (c) illustrate that the degree of orientation selectivity can vary depending on the number of neurons combined along the main axis.

Figure 9 shows several orientation selective linear receptive fields and how these might be constructed from the outputs of lateral geniculate neurons. The simple cell receptive fields consist of adjacent excitatory and inhibitory regions that are longer in one direction than the other. The main axis of the receptive fields defines the preferred orientation; stimuli oriented along the main axis of these receptive fields are more effective at exciting or inhibiting the cell than stimuli in other orientations. The figure shows the excitatory regions as resulting from the combined output of neurons with excitatory centers and the inhibitory regions resulting from the combined output of neurons with inhibitory centers[2].

[2]In principle, one might construct an oriented receptive field from the outputs of a single line of lateral geniculate neurons. But, recall that the receptive fields of lateral geniculate neurons have a weak opposing

By comparing the three panels in Figure 9 you will see that receptive fields sharing a common preferred orientation can differ in a number of other ways. Panels (a) and (b) show two receptive fields with the same preferred orientation but different spatial arrangements of the excitatory and inhibitory regions. Panels (a) and (c) show two receptive fields with the same preferred orientation and arrangement of excitatory and inhibitory regions, but differing in the overall length of the receptive field. The neuron with the longer receptive field will respond well to a narrower range of stimulus orientations than the neuron with the shorter receptive field.

Complex cells also show orientation selectivity. Complex cells are nonlinear, so to explain the behavior of complex cells, including orientation selectivity, will require more complex models than the simple sums of neural outputs used in Figure 9.

The preferred orientation of neurons varies in an orderly way that depends on the neuron's position within the cortical sheet. Figure 10 shows the preferred orientation of a collection of neurons measured during a single, long, tangential penetration through the cortex. In any small region of layers 2 and 3, the preferred orientation is similar. As the electrode passes tangentially through the cortical sheet, the preferred orientation changes systematically, varying through all angles. Figure 10 (a) shows an extensive set of measurements of preferred orientation made during a single tangential penetration (Hubel and Wiesel (1977)). The change in preferred orientation is very systematic as the electrode passes tangentially through the cortex. Upon later review, Hubel and Livingstone (1987) noted that during these measurements there were certain intervals during which the receptive field orientation was ambiguous. Figure 10 (b) shows a second penetration in which regions with no preferred receptive field orientation are identified. As we shall see, Hubel and Livingstone also report that the regions lacking orientation selecitivity coincide with locations in layers 2 and 3 cortex where an enzyme called *cytochrome oxidase* is present in high density. However, there is some debate whether these measurements represent true differences in the receptive fields of individual neurons, or whether they represent differents in the distribution of activity in local collections of neurons (O'Keefe et al. (1993); Leventhal et al. (1993)).

The alternative interpretation is based on measurements of the spatial organization of cortical regions with common orientation preference. Obermayer and Blasdel (1993) measured regions with a common orientation preference using a high resolution optical imaging method. In this method, a voltage sensitive dye is applied to cortex. Local neural activity causes reflectance changes in the dye, and these can be visualized by reflecting light from the exposed cortex. By stimulating with visual signals in different orientations and measuring the changes in reflectance, Obermayer and Blasdel (1993) visualized regions with common orientation preference; by stimulating with images in originating in different eyes, they could identify ocular dominance columns (see also Hubel and Wiesel (1977)).

surround. The inhibitory and excitatory regions of the cortical neurons often are more nearly balanced in their effect. Hence, I have constructed these regions by combining the outputs from separate groups of neurons.

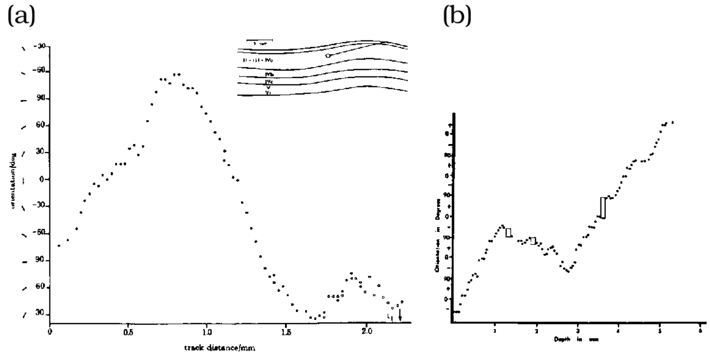

Figure 10: The preferred orientation of neurons in area V1 measured during a single tangential penetration. The horizontal axis shows the distance along the tangential penetration and the vertical axis shows the orientation of the receptive field.

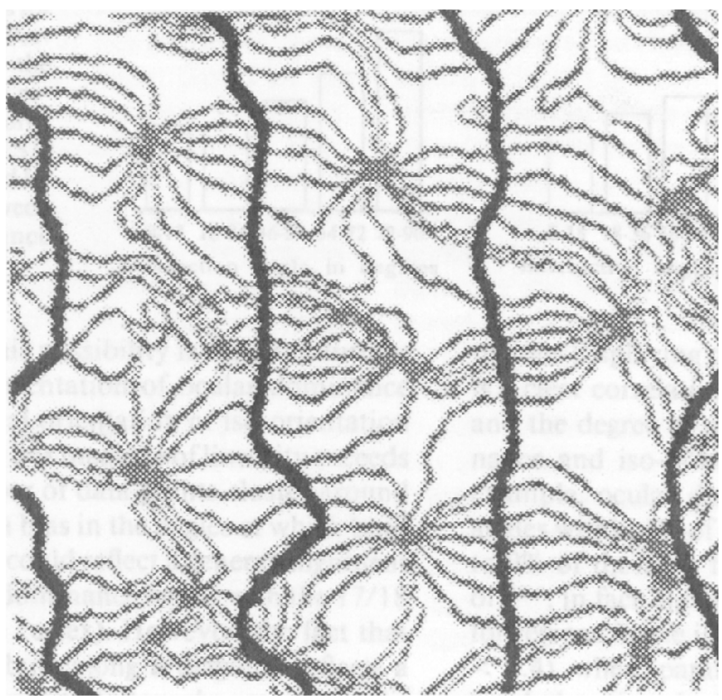

Figure 11: Regions with common orientation preference are shown as the gray lines in this contour plot. The dark lines show the boundaries of ocular dominance columns. At the edges of the ocular dominance columns, regions with common orientation are arranged in parallel lines that are nearly perpendicular to the ocular dominance columns. These lines converge to singular points located near the center of the ocular dominance columns. (Source: Obermayer and Blasdel (1993)).

Figure 11 represents the Obermayer and Blasdel (1993) measurements as a contour plot. Regions with common orientation preference are shown as gray iso-orientation lines, and the boundaries of the ocular dominance columns are shown as dark lines. The figure shows that the variation in preferred orientation is synchronized with the variation in ocular dominance. A full range of preferred orientations takes place within about 1 mm of the cortex, about equal to one ocular dominance column. Near the edges of the ocular dominance columns, the iso-orientation lines are arranged in linear, parallel strips extending roughly 0.5 – 1 mm. These linear strips are oriented nearly perpendicular to the edge of the ocular dominance edge. In the middle of the ocular dominance columns, the iso-orientation lines converge toward single points called *singularities*. In these regions, neurons with receptive fields with different preferred orientations are brought close to one another, and they may also be the position of the high density of cytochrome oxidase (Blasdel (1992)). These regions will have high metabolic activity since, for any stimulus orientation some of the neurons in the region will be active. This is an alternative explanation of the colocation of regions of high density cytochrome oxidase and regions of reduced orientation selectivity of the neural response.

There are a number of broad questions that remain unanswered about the orientation selectivity in the visual cortex. First, we might ask how are the receptive field properties of cortical neurons constructed from the cortical inputs? Figure 9 shows that we can explain orientation selectivity theoretically since combining signals from center-surround neurons with adjacent receptive field locations results in an oriented receptive field. But, there is no empirical counterpart to this theoretcal explanation. Second, the regularity of the iso-orientation contours shows that the orientation preferences of neurons is created in an highly regular and organized pattern. What are the rules for making the interconnections that lead to this spatial organization of orientation selectivity? What functional role to they have in perceptual processing? Is this spatial organization essential for neural computations, or is it merely a convenient wiring diagram for an area whose output is communicated to other processing modules?

Direction selectivity

Hubel and Wiesel (1968) also found a second specialization that emerges in the receptive fields of V1 neurons. Certain cortical neurons in the monkey respond well when a stimulus moves in one direction and poorly or not at all when the same stimulus is moved in the opposite direction. This feature is called *direction selectivity*. Figure 12 shows the response of a neuron in monkey area V1 to a line first moving in one direction and then in the opposite direction. Notice that the cell shows orientation selectivity, it only responds well to the line in one orientation. In addition, the cell shows direction selectivity. When the line moves up and to the right the cell responds well but when the same line moves down and to the left the cell responds poorly. Because of the low spontaneous response rate of this neuron, which is characteristic of many cortical neurons, we cannot tell from these measurements whether the neuron simply fails to respond or if it is actively inhibited by the stimulus moving in the wrong direction.

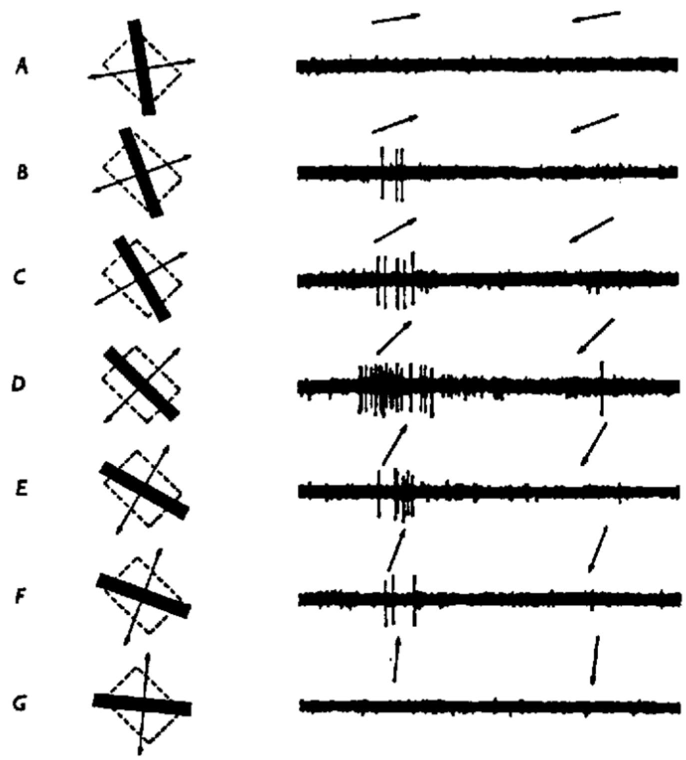

Figure 12: Direction selectivity of a cortical neuron's response. The firing pattern in response to movement in opposite directions, indicated by the arrows, are shown. The left hand portion of each panel shows the receptive field location, the orientation of the line stimulus, and the two motion directions. The action potentials shown on the right are the neuron's response to motion in each of the two opposite directions. The neuron's response depends upon the direction of motion and the orientation of the line (From Hubel and Wiesel (1968)).

The direction selective neurons are found mainly in certain layers of the cortex and are quite rare or absent from others. The main layers containing direction selective neurons are 4A, 4B, 4Cα and layer 6 (Hawken et al. (1988)). These layers receive the main input from the magnocellular pathway and send their outputs to selected brain areas. Hence, these neurons may be part of a visual stream that is specialized to carry information about motion.

Direction selectivity of the receptive field response may arise from neural connections that are analogous to the connections used underlying orientation selectivity. A cell with a direction selective receptive field can be built by sending the outputs of neurons with spatially displaced receptive fields onto a single cortical neuron and introducing temporal delays into the path of some of the input neurons. The temporal delays of the signal are a displacement of the signal in time. As we will review in more detail in Chapter , the result of a combined spatial and temporal displacement is to create a cortical neuron that responds better to stimuli moving in one direction, when the delay reinforces the signal, than to stimuli moving in the opposite direction, when the delay works against the two signals. This scheme for connecting neurons is plausible; but like the mechanisms of orientation selectivity, the precise neural wiring used to achieve direction selectivity have not been demonstrated in primate cortical neurons.

Contrast Sensitivity of Cortical Cells

Perhaps the most straightforward way to classify simple and complex cells is based on their responses to contrast-reversing sinusoidal patterns. Examples of the response of a simple and a complex cell to a contrast-reversing pattern are shown in Figure 13.

Recall from Chapter that contrast-reversing patterns are periodic in both space and time. The stimulus used to create the neural responses shown in Figure 13 had a temporal period of 0.5 seconds. Figure 13 (a) shows the firing rate of a simple cell averaged over many repetitions of the contrast reversing stimulus. Were the simple cell perfectly linear, the variation in firing rate would be sinusoidal and one period of the response would equal one period of the stimulus. This sinusoidal variation is impossible, however, because the spontaneous discharge rate of the neuron is close to zero; hence, the firing rate cannot fall below the spontaneous rate. The response shown in the figure is typical of cortical simple cells because many have a low spontaneous discharge rate. When a signal follows only the positive part of the sinusoid, and has a zero response to the negative part, it is called *half-wave rectified*. The response of many simple cells shows this half-wave rectification.

Figure 13 (b) shows the average response of a complex cell during one period of the stimulus. Unlike the simple cell, the complex cell response does not vary at the same frequency as the input stimulus; the cell's response is elevated during both phases of the flickering contrast. This response pattern is called *full-wave* rectification, and the temporal response varies at twice the temporal frequency of the stimulus. This nonlinear *frequency doubling* is typical of complex cells. These cells make up a large proportion of the neurons in area V1.

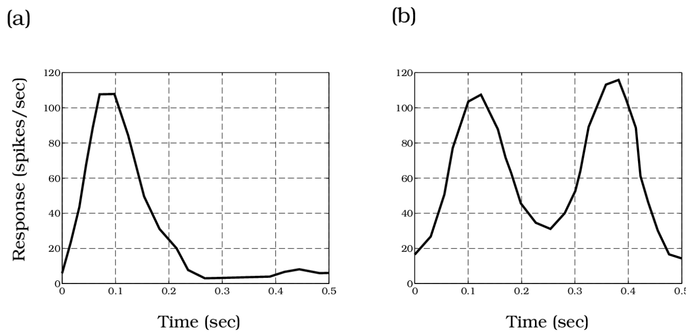

Figure 13: The timecourse of response of cortical cells to a contrast-reversing spatial frequency pattern at a period of 0.5 seconds. (a) The response of a simple cell is a half-wave rectified sinusoid. (b) The response of the complex cell is full-wave rectified. Consequently, the temporal response is at twice the frequency of the stimulus. (Source: De Valois et al. (1982)).

De Valois et al. (1982) measured the spatial contrast sensitivity functions of cortical neurons. Figure 14 shows a sample of these measurements, for both simple and complex cortical neurons. The contrast sensitivity functions of these neurons are narrower than those of retinal ganglion cells. Moreover, even though these measurements were made from neurons close to one another in the cortex, there is considerable heterogeneity in the most effective spatial frequency of the stimulus. This variation in spatial tuning is not true of retinal neurons from a single class. This may be due to a new specialization in the cortex, or it may be that we have not yet identified the classes of cortical neurons properly. In either case, the different peak spatial frequencies of the contrast sensitivity functions raises the question of how the signals from retinal neurons within a small patch are recombined to form cortical neurons with such varied spatial receptive field properties.

Movshon et al. (1978a), Movshon et al. (1978b), and Tolhurst and Dean (1987) tested the linearity of cat simple cells. Taking into account the low spontaneous rate and the resulting half-wave rectification, they found that they could predict quantitatively a range of simple simple cell responses from measurements of the contrast sensitivity function. The predictions work well for stimuli with moderate to weak contrast, that is stimuli that evoke a response that is less than half of the maximum response rate of the neuron. There have not been extensive tests of linear receptive fields in the monkey cortex, but contrast sensitivity curves are probably adequate to predict monkey simple cell responses, too.

Figure 14 also includes contrast sensitivity functions of nonlinear complex neurons. Recall from our discussion in earlier chapters that when a system is nonlinear, its response to sinusoidal patterns is not a fundamental measurement of the neuron's performance: we cannot use it to predict the response to other stimuli. For these nonlinear neurons, the contrast sensitivity function defines the response of the cell to an interesting collection of stimuli. And, these measurements may help us understand the nature of the nonlinearity. But, the contrast

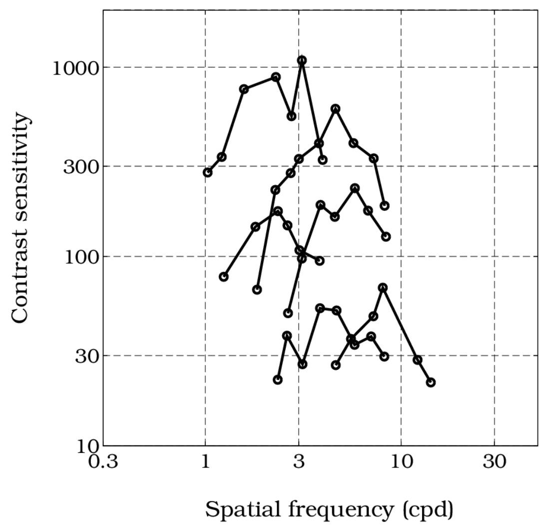

Figure 14: Spatial frequency selectivity of six neurons cells in area V1 of the monkey. These responses were recorded at nearby locations within the cortex, yet the neurons have different spatial frequency selectivity. (Source: De Valois et al. (1982)).

response function of a nonlinear system is not a complete quantitative measurement of the cell's receptive field.

Contrast Normalization

Taking into account the low spontaneous firing rate, simple cells are approximately linear for moderate contrast stimuli. As one expands the stimulus range, however, several important response properties of cortical simple cells are nonlinear. One deviation from linearity, called *contrast normalization*, can be demonstrated by measuring the contrast-response function (cf. Figure 22).

Figure 15 shows the contrast response function of a neuron in area V1 to four different sinusoidal grating patterns. The stimulus contrast and neuronal responses are plotted on logarithmic axes. The rightward displacements of the curves indicate that the neuron is differentially sensitive to the spatial patterns used as test stimuli. This shift is what we expect from a simple linear system followed by a static nonlinearity (see the discussion in Chapter near Figure 22).

The entire set of data is not consistent with such a model, however, because the response saturation level depends on the spatial frequency of the stimulus. Were the nonlinearity static, then the response saturation level would be the same no matter which stimulus we used. Since the saturation level is stimulus-dependent, it cannot be based on the neuron's intrinsic properties. Rather, it must be mediated through an active process (Albrecht and Geisler (1991); Heeger (1992)). This process is called *contrast normalization*.

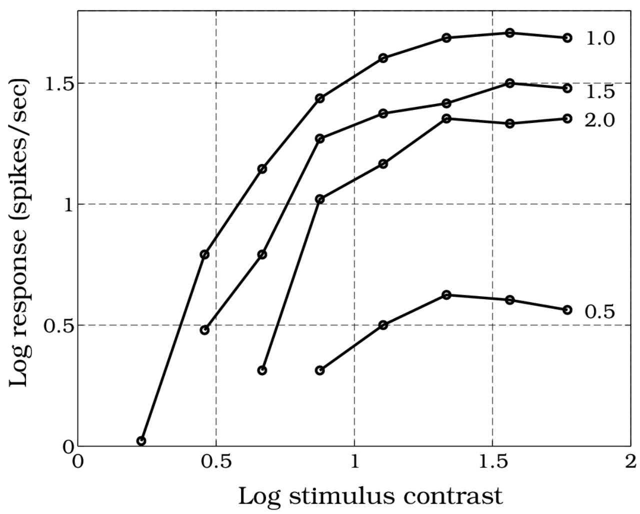

Figure 15: Contrast response functions of a neuron in area V1. Each curve shows the responses measured using a different spatial frequency gratings. The spatial frequencies of the stimuli are shown at the right. The neuron's sensitivity and maximum response depend on the stimulus spatial frequency (Source: Albrecht and Hamilton (1982)).

Heeger (1992) has described a model of this process (see Figure 16). The model assumes that the neuron's response is initiated by a linear process. This linear signal is divided by a second signal whose value depends on the pooled activity of the population of cortical neurons. This is a nonlinear term. It is not a static nonlinearity because the divisive term depends on the contrast of the stimulus.

This model explains the data in Figure 15 as follows. First, the sensitivity of the neuron varies with the spatial frequency of the stimulus because the initial linear receptive field will respond better to some stimuli than others. This causes the response to be displaced along the horizontal axis in the log-log plot. Second, the response saturation level depends on the ratio of the neuron's intrinsic sensitivity to the stimulus and the neural population's sensitivity to the stimulus. This saturation level is set by the normalization process. If the neuron is relatively insensitive to the stimulus compared to the population as a whole, then the peak response of the neuron will be suppressed by the divisive signal. Finally, the overall shape of the response function is determined by the nature of the static nonlinearity that follows.

What purpose does the contrast-response nonlinearity serve? From the data in Figure 15, notice that the response ratio remains approximately constant at all stimulus contrast levels. Without the contrast normalization process, the neuron's response would saturate at the same level, independent of the stimulus. In this case, the response ratios at different contrast levels

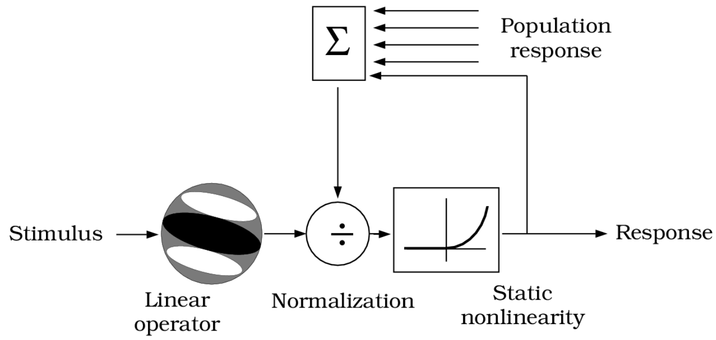

Figure 16: A model of contrast normalization is shown. According to this model, each neuron's response is derived from an initial linear encoding of the stimulus. The linear response is divided by a factor that depends on the activity of the neural population. Finally, the entire signal is modified by a static nonlinearity (Source: Heeger (1992), Heeger (1994)).

would vary. For example, at high contrast levels all of the neurons would be saturated and their signals would be nondiscriminative with respect to the input signal. The normalization process adjusts saturation level so that it depends on the neuron's sensitivity; in this way the ratio of the neuronal responses remain constant across a wide range of contrast levels.

Binocular Receptive Fields

At the input layers of the visual cortex, signals from the two eyes are spatially segregated. Within the superficial layers, however, many neurons respond to light presented to either eye. These neurons have *binocular* receptive fields. Cortical area V1 is the first point in the visual pathways where individual neurons receive binocular input. One might guess that these binocular neurons may play a role in our perception of stereo depth. What binocular information is present that neurons might use to deduce depth?

First, consider the two retinae as illustrated in Figure 17 (a). We can label points on the two retina with respect to their distance from the fovea. We say that a pair of points on the two retinae fall at corresponding locations if they are displaced from the fovea by the same amount. Otherwise, the two points fall at non-corresponding positions.

Now, suppose that the two eyes are positioned so that a point F casts an image on the two foveae. By definition, then, the images of the point F fall on corresponding retinal locations. By tracing a ray from the corresponding retinal positions back into space, we can find the points in space whose images are cast on corresponding retinal positions (Figure 17 (b)). These points sweeps out an arc about the viewer that is called the *horopter*.

The image of a point closer or further than the horopter will fall on non-corresponding retinal positions. The difference between the image locations and the corresponding locations is

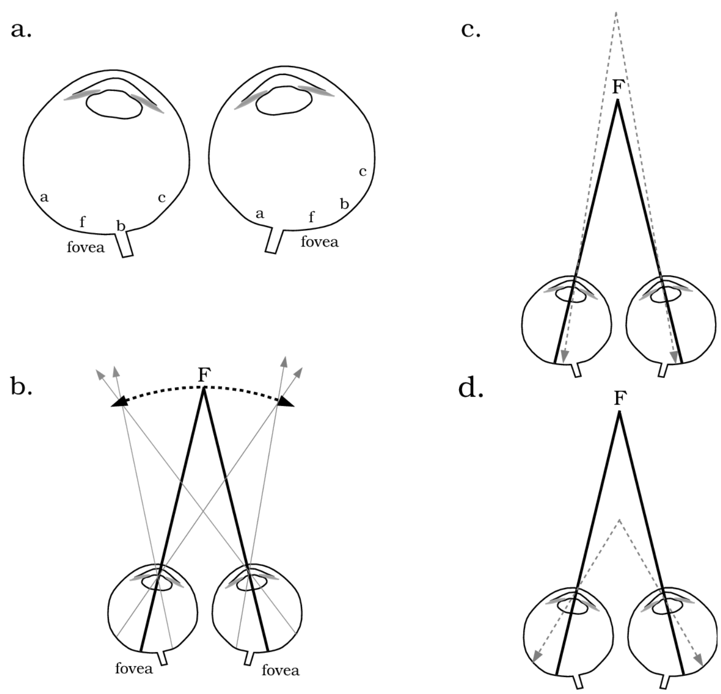

Figure 17: Retinal disparity and the horopter are explained. (a) The fovea and three pairs of points at corresponding retinal locations are shown. (b) When the eyes are fixated at a point F, rays originating at corresponding points on the two retinae and passing through the lens center intersect on the horopter (dashed curve). The images of points located farther (c) or closer (d) than the horopter do not fall at corresponding retinal locations.

called the *retinal disparity*. Because the main separation between the two eyes is horizontal, the retinal disparities are mainly in the horizontal direction as well. The horopter is the set of points whose images have zero retinal disparity.

Figure 17 (c,d) show two examples in which image points fall on noncorresponding retinal points. Figure 17 (c) shows an example when both images fall on the nasal side of the foveae, and Figure 17 (d) shows an example when both images fall on the temporal side of the fovea. These panels show that the size and nature of the horizontal retinal disparity varies with the distance from the visual horopter. Hence, the horizontal retinal disparity is a binocular clue for estimating the distance to an image point[3]

Do binocular neurons represent stereo depth information by measuring horizontal disparity? There are two types of experimental measurements we can make to answer this question. First, we can measure the receptive fields of individual binocular neurons. If retinal disparity is used to estimate depth, then the receptive fields of the binocular neurons should show some selectivity for horizontal disparity. Second, we can look at the properties of the population of binocular neurons. While no single neuron alone can code depth information, the population of binocular neurons should include enough information to permit the population to estimate image depth.

A complete characterization of binocular receptive fields requires many measurements. First, one would like to measure the spatial receptive fields of the neuron when stimulated by each eye alone. These are called the *monocular* receptive fields of the binocular neuron. Then, we should characterize how the binocular neuron responds to simultaneous stimulation of the two eyes. In practice there have been very few complete measurements of binocular neurons' receptive fields. The vast majority of investigations have been limited to localization of the monocular receptive field centers that are then used to derive the retinal disparities between the monocular field centers.

Given the variability inherent in biological systems, the two monocular receptive fields will not be in perfect register. We would like to decide whether the observed horizontal disparities are purposeful, or whether they are due to unavoidable random variation. To answer this question several groups have measured both the horizontal and the vertical disparities of binocular neurons in the cat cortex (Barlow et al. (1967); Joshua and Bishop (1970); von der Heydt et al. (1978)). The histograms in Figure 18 (a) show the initial measurements from Barlow et al. (1967). They observed more variability in the horizontal disparity than vertical disparity, and they concluded that the horizontal variation was purposeful and used for processing depth.

Joshua and Bishop (1970) and von der Heydt et al. (1978) saw no difference in the range of disparities in the horizontal and vertical directions. A scatter plot of the retinal disparities observed by Joshua and Bishop (1970) is shown in Figure 18 (b). While these data do not show

[3]You can demonstrate the relative shift in retinal positions to yourself as follows. Focus on a nearby object, say your finger placed in front of your nose. Then, alternately look through one eye and then the other. Although your finger remains in the fovea, the relative positions of points nearer or further than your finger will change as you look through each eye in turn.

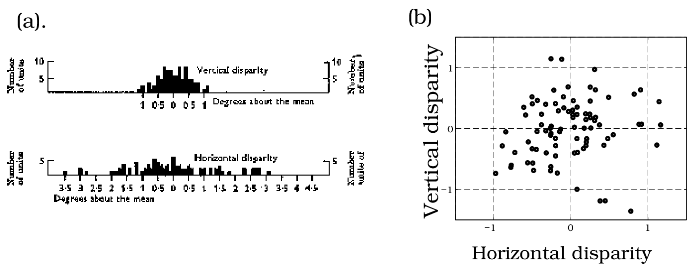

Figure 18: The horizontal and vertical disparities of binocular neurons in the cat visual cortex are shown. (a) Histograms of the horizontal and vertical disparities of binocular neurons in cat cortex (Source: Barlow et al. (1967)). (b) A scatter diagram of the vertical and horizontal disparities of cells in cat cortex with receptive fields located within 4 degrees of the cat's best region of visual acuity. (Source: Bishop (1973))

any systematic difference between the horizontal and vertical disparity distributions, these authors do not dispute Barlow et al.'s hypothesis that variations in the horizontal disparity are used for stereo depth detection[4]

For the moment, let's accept the premise that the variation in horizontal disparity of these binocular neurons is a neural basis for stereo depth. How might we design the binocular response properties of these neurons to estimate depth?

One possibility is to create a collection of neurons that each responds to only a single disparity. One might estimate the local disparity by identifying the neuron with the largest response. An alternative possibility, suggested by Richards (1971), is that one might measure disparity by creating a few *pools* of neurons with coarse disparity tuning. One pool might consist of neurons that respond when an object feature is beyond the horopter, and a second pool consists of neurons that respond when the feature is in front of it. The third pool might respond only when the feature is close to the horopter. To estimate depth, one would compare the relative responses in the three neural pools.

Some support for Richards' hypothesis comes from measurements of individual neurons in areas V1 and the adjacent area V2 of a monkey brain. Poggio and Fischer (1977) (see also Ferster (1981)) measured how well individual neurons respond to stimuli with different amounts of disparity. They used experimental stimuli consisting of bar patterns whose width and velocity were set to generate a strong response from the individual neuron. The experimenters varied the retinal disparity between the two bars presented to the two eyes. They plotted the binocular neuron's response to the moving bars as a function of their retinal disparity. The curves in Figure 19, plotting response as a function of retinal disparity, are called *disparity tuning* curves.

[4]A frequently suggested alternative is that these disparity cues serve to converge the two eyes. Since the same cues are used to converge the eyes and estimate depth, this alternative hypothesis is virtually impossible to rule out.

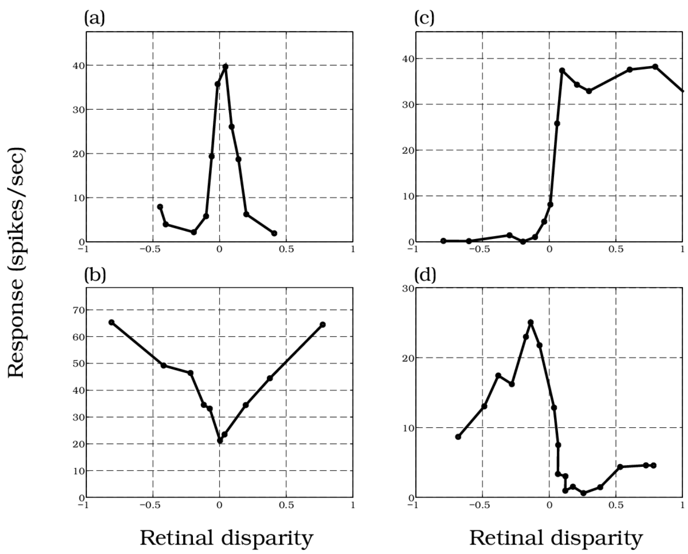

Figure 19: Disparity tuning curves of binocular neurons in areas V1 and V2 in monkey. Each panel plots the response of a different neuron to moving bar patterns. The independent variable is the retinal disparity of the stimulus. (a) and (b) show the responses of neurons that respond best to stimuli with near zero disparity, that is near the horopter. Responses of a neuron that responds best to stimuli with positive disparity (c) and a neuron with negative disparity (d) are also shown. The curves represent data measured using binocular stimulation. (Source: Poggio and Talbot (1981)).

Poggio and Talbot (1981) found that the disparity tuning curves could be grouped into a small number of categories. Typical tuning curves from each of these categories are are illustrated in the separate panels of Figure 19. The two neurons illustrated in the left panels respond to disparities near the fixation plane; for these neurons stimuli near the horopter stimulate or inhibit the cell. The two panels on the right illustrate neurons with opponent tuning. One neuron is excited by a bar whose disparity places the object beyond the horopter and the neuron is inhibited by bars in front of the horopter. The second neuron shows approximately the complementary excitation pattern. The neuron is excited by objects nearer than the horopter and inhibited by objects further. Poggio and his colleagues view their measurements in monkey as support for Richards' hypothesis that binocular depth is coded based on the response of neurons organized in disparity pools (see also Ferster (1981)).

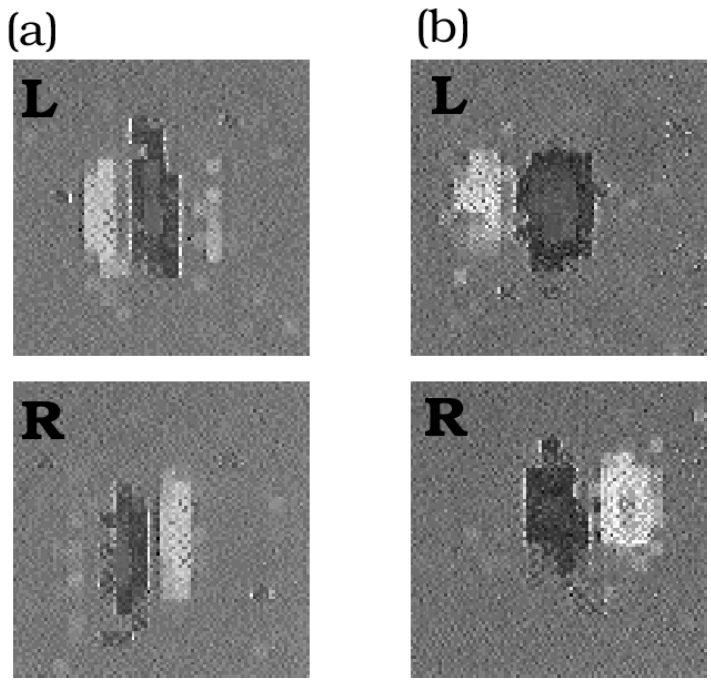

Figure 20: Monocular spatial receptive fields of two binocular neurons in cat cortex. (a) and (b) show examples of left (L) and right (R) monocular receptive fields whose centers are displaced horizontally and thus have non-zero retinal disparity. In addition to the disparity, the left and right monocular spatial receptive fields differ. (Source: Freeman and Ohzawa (1990)).

We have been paying attention mainly to the retinal disparity of the binocular neurons. But, disparity tuning is only one measure of the receptive field properties of these neurons. In addition, the receptive fields must have spatial, temporal and chromatic selectivities. To fully understand the responses of these neurons we must make some progress in measuring all of these properties.

To obtain a more complete description of binocular neurons, Freeman and Ohzawa (1990) and DeAngelis et al. (1991) studied the monocular spatial receptive fields of cat binocular neurons. They found that the spatial receptive fields measured in the two eyes can be quite different. Figure 20 shows an example of the differences they observed between the spatial monocular receptive fields. The left eye spatial receptive field and the right eye monocular field are displaced relative to one another. If we only concern ourselves with disparity, we will report that this cell's receptive field has significant horizontal disparity. But, notice that the spatial receptive fields are different from one another. The spatial receptive field in the left eye is a mirror-reversal of the field in the right eye.

Freeman and Ohzawa suggest that these different receptive spatial monocular receptive fields are important to the way in which stereo depth is estimated by the nervous system. They hypothesize that stereo depth depends on having neurons with different monocular spatial receptive fields. Perhaps most important, however, their measurements reminds us that to understand the biological computation of stereopsis, we must study more than just the center position of the monocular receptive fields.

Visual Streams in the Cortex

We have reviewed two major principles that characterize the flow of information from retina to cortex. First, visual information is organized into separate visual streams. These streams begin in the retina and continue along separate neural pathways into the brain. Second, the receptive field properties of neurons become progressively more sophisticated. Receptive fields of cortical neurons show selective responses to stimulus properties that are more complex than retinal neurons. The new receptive field properties are clues about the specialization of the computations performed within the visual cortex.

As we study visual processing within the cortex we should expect to see both of these principles extended. First, we should expect to find new visual streams that play a role in the cortical computations. Some new visual streams will arise in visual cortex, and some, like the rod pathway in the retina, will have served their purpose and merge with other streams. Second, as we explore the cortex we should expect to find neurons with new receptive field properties. We will need to characterize these receptive fields adequately in order to understand their computational role in vision.

Our understanding of cortical visual areas is in an early and exciting phase of scientific study. In this section, we will review some of the basic organizational principles of the cortical areas. In particular, we will review how information from area V1 is distributed to other cortical areas and we will review the experimental and logical methods that relate activity within these cortical areas to what we see. We will review some of the more recent data and speculative theories in Chapter and Chapter .

The fate of the parvocellular and magnocellular pathways

The segregation of visual information into separate streams is an important organizing principle of neural representation. Two of the best understood streams are the magnocellular and parvocellular pathways whose axons terminate in layers 4Cα and 4Cβ within area V1. What happens to the signals from these pathways within the visual cortex?

Along one branch, signals from the magnocellular pathway continue from area V1 directly to a distinct cortical area. The magnocellular pathway in layer 4Cα makes a connection to neurons in layer 4B where there are many direction selective neurons. These neurons then send a strong projection to cortical area MT (medial temporal). It seems reasonable to suppose, then, that the information contained within the magnocellular stream is of particular relevance for the visual processing in area MT. As we saw in Chapter , the magnocellular pathway has particularly good information about the high temporal frequency components of the image. Earlier in this chapter we saw that neurons in layer 4B show strong direction selectivity, as do the neurons in area MT (Zeki (1974)). Taken together, these observations have led to the hypothesis that area MT plays a role in motion perception. We will discuss this point more fully in Chapter .

While one branch of the magnocellular stream continues on an independent path, another branch of this stream converges with the parvocellular pathway in the superficial layers of area V1. Malpeli et al. (1981) and Nealey and Maunsell (1994) made physiological measurements demonstrating that signals from the parvocellular and magnocellular streams converge on individual neurons. In these experiments parvocellular or magnocellular signals were blocked either by application of a local anaesthetic (Malpeli et al. (1981); lidocaine hydrochloride) or GABA (Nealey and Maunsell (1994)) to small regions of the lateral geniculate nucleus. Both studies report instances of neurons whose responses are influenced by both parvocellular and magnocellular blocking. Anatomical paths for this signal have also been identified. Lachica et al. (1992) injected retrograde anatomical tracers into the superficial layers of visual cortex, that is tracers that are carried from the injection site towards the inputs to the injection site. They concluded that the magnocellular and parvocellular neurons contribute inputs into overlapping regions within the superficial layers of the visual cortex. Hence, these anatomical pathways could be the route for the physiological signals.

Just as the rod pathways are segregated for a time, and then they merge with the cone pathways, so too signals from the magnocellular stream merge with parvocellular signals. The purpose of the peripheral segregation of the parvocellular and magnocellular signals, then, may be to communicate rapidly certain type of image information to area MT. After the signal has been efficiently communicated, the same information may be used by other cortical areas, in combination with information from the parvocellular pathways.

The function of the visual areas

Even when the computation performed in a visual area is not part of our conscious experience, we would still like to know what the area does. Over the last fifteen years, there have been a broad variety of hypotheses concerning the perceptual significance of the cortical areas. Mainly, we have seen a flurry of proposals suggesting that individual visual areas are responsible for the computation of specific perceptual features, such as color, stereo, and form and so forth.

What is the logical and experimental basis for reasoning about the perceptual significance of visual areas? Barlow (1972) has set forth one specific doctrine to relate neurons to perception, the *neuron doctrine.* This doctrine asserts that *a neuron's receptive field describes the percept caused by excitation of the neuron.* You will see the idea expressed many times as you read through the primary literature and study how investigators interpret the perceptual significance of neural responses.

Our understanding of the peripheral representation lends little support to the neuron doctrine. For example, the principle does not serve us well when analyzing color appearance. In that case, we know with some certainty that a large response from an R photoreceptor does not imply that the observer will perceive red at the corresponding location in the visual field. Rather, the color appearance depends upon stimulation at many adjacent points of the retina. The conditions for a red percept include a pattern of peripheral neural responses, including more R and less G. Data from the periphery is generally more consistent with the notion of a distributed representation in which an experience depends on the response of a collection of neurons.

Oddly, the failure of the neuron doctrine in the periphery, is often used to support the neuron doctrine. After all, the argument goes, the periphery is not the site of our conscious awareness. so failures of the doctrine in the periphery are to be expected. The neuron doctrine's significance depends on the idea that there will be a special place, probably located in the cortex, where the receptive fields of a neuron predicts conscious experience when that neuron is active. This location in the brain should only exist at a point after the perceptual computations needed to see features we perceive — color, form, depth — have taken place.

In the past, secondary texts sometimes used Hubel and Wiesel's work in area V1 as a location where the neuron doctrine might hold. The receptive fields in area V1 seem like basic perceptual features; orientation, motion selectivity, binocularity, complex cells, all emerge for the first time in area V1 [5]. Consequently, secondary texts often described the receptive fields in area V1 as a theory of vision, with the receptive fields defining salient perceptual features. The logical basis for this connection between V1 receptive fields and visual features is the neuron doctrine.

By 1979 the significance of the other cortical areas had become undeniable (Zeki (1974), Zeki (1978); Felleman and Van Essen (1991); Van Essen et al. (1992)). In reviewing the visual pathways, Hubel and Wiesel wrote

[5] See Hubel's Nobel lecture for a marvelous description of the paradigm prior to their work.

> The lateral geniculate cells in turn send their axons directly to the primary visual cortex. From there, after several synapses, the messages are sent to a number of further destinations: neighboring cortical areas and also several targets deep in the brain. One contingent even projects back to the lateral geniculate bodies; the function of this feedback path is not known. The main point for the moment is that the primary visual cortex is in no sense the end of the visual path. It is just one stage, probably an early one in terms of the degree of abstraction of the information it handles. (Hubel and Wiesel (1979)).

Acknowledging this point leads one to ask what is the function of these cortical areas. The answer to this question has relied, mainly, on the neuron doctrine. For example, when Zeki (Zeki (1980); Zeki (1983); Zeki (1993)) found that color contrast was a particularly effective stimulus in area V4, he argued that this area is responsible for color perception. Since movement was particularly effective in stimulating neurons in area MT, that become the motion area (Dubner and Zeki (1971)). The logic of the neuron doctrine permits one to interpret receptive field properties in terms of perceptual function.

Among the most vigorous application of the neuron doctrine is contained in articles by Livingstone and Hubel (Livingstone and Hubel (1984a), Hubel and Livingstone (1987), Livingstone and Hubel (1988)). They supported Zeki's basic view and added new hypotheses of their own. Their hypothesis, which continues to evolve, is summarized in the elaborate anatomical/perceptual diagram shown in Figure 21. In this diagram anatomical connections in visual cortex are labeled with perceptual tags, including color, motion, and form. The logical basis for associating perceptual tags with these anatomical streams is the neuron doctrine. Receptive fields of neurons in one stream were orientation selective, hence the stream was tagged with form perception. Neurons in a different stream were motion selective and hence the stream was tagged with motion perception.

The perceptual-anatomical hypotheses proposed by Zeki and Livingstone and Hubel define a new view of cortex. On this view, the relationship between cortical neurons and perception should be made at the level of perceptual features. These investigators did not study the computation within the neural streams, but rather, like tailors labeling a suit, they summarized what they felt were the main features of the pathway (see Hubel and Wiesel (1977) for a description of this approach).

The use of the neuron doctrine to interpret brain function is very widespread, but there is very little evidence in direct support of the doctrine (Martin (1992)). The main virtue of the hypothesis is the absence of an articulated alternative. The most frequently cited alternative is the proposal that perceptual experience is represented by the activity of many neurons, so that no individual neuron's response corresponds to a conscious perceptual event. These types of models are often called *distributed* processing models; they are not widely used by neurophysiologists since they do not provide the specific guidance for interpreting experimental measurements from single neurons, the neurophysiologist's stock-in-trade. The neuron doctrine, on the other hand, provides an immediate answer.

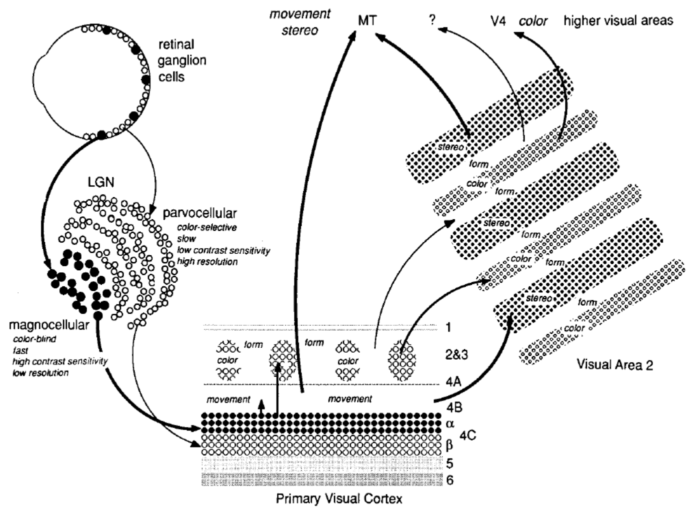

Figure 21: Functional Specialization. An anatomical-perceptual model of the visual cortex. In this speculative model, visual streams within the cortex are identified with specific perceptual features. The anatomical streams are identified using anatomical markers; the perceptual properties are associated with the streams by applying the neuron doctrine (Source: Livingstone and Hubel (1988)).

In my own thinking about brain function, I am more inclined to wonder about the brain's computational methods than the mapping between perceptual features and tentatively identified visual streams. I find it satisfying to learn that the magnocellular pathway contains the best representation of high temporal frequencies, but less satisfying to summarize the pathway as the motion pathway since this information may also be used in many other types of performance tasks. The questions I find fundamental concerning computation are how, not where. How are essential signal processing tasks, such as multiplication, addition and signal synchronization, carried out by the cortical circuitry? What means are used to store temporary results, and what means are used to represent the final results of computations? What decision mechanisms are used to route information from one place to another?

My advice, then, as you read and think about brain function is this: Don't be distracted by the neuron doctrine or its application. The doctrine is widely used because it is an easy tool to relate perception and brain function. But, the doctrine distracts us from the most important question about visual function: how do we *compute* perceptual features like color, stereo and form? Even if it turns out that a neuron's receptive field is predictive of experience, the question we should be asking is how the neuron's receptive field properties arise. Answering these computational questions will help us most in designing practical applications that range from sensory prostheses to robotics applications. We should view the specific structures within the visual pathways as a means of implementing these principles, rather than as having an intrinsic importance.

Hubel and Wiesel once expressed something like this view. While reviewing their accomplishments in the study of area V1, they wrote:

> What happens beyond the primary visual area, and how is the information on orientation exploited at later stages? Is one to imagine ultimately finding a cell that responds specifically to some very particular item? (Usually one's grandmother is selected as the particular item, for reasons that escape us.) Our answer is that we doubt there is such a cell, but we have no good alternative to offer. To speculate broadly on how the brain may work is fortunately not the only course open to investigators. To explore the brain is more fun and seems to be more profitable.
>
> There was a time, not so long ago, when one looked at the millions of neurons in the various layers of the cortex and wondered if anyone would ever have any idea of their function. Did they all work in parallel, like the cells of the liver or the kidney, achieving their objectives by pure bulk, or where they each doing something special? For the visual cortex the answer seems now to be known in broad outline: Particular stimuli turn neurons on or off; groups of neurons do indeed perform particular transformations. It seems reasonable to think that if the secrets of a few regions such as this one can be unlocked, other regions will also in time give up their secrets. [ibid., p. 23].

In the remaining chapters, we will see how other areas of vision science, based on behavioral and computational studies, might help us to unlock the secrets of vision.

Pattern Vision

Pattern vision overview

In this chapter we will consider measurements and models of human visual sensitivity to spatial and temporal patterns. We have covered topics relevant to pattern sensitivity in earlier chapters as we reviewed image formation and the receptor mosaic. Here, we will extend our analysis by reviewing a collection of behavioral studies designed to reveal how the visual system as a whole detects and discriminates spatio-temporal patterns.

The spatial pattern vision literature is dominated by detection and discrimination experiments, not by experiments on what things look like. There are probably two reasons why these measurements make up such a large part of the literature. First, many visual technologies (e.g. televisions, printers, etc.) are capable of reproducing images that appear similar to the original, but not exactly the same. The question of which approximation to the original is *visually best* is important and often guides the engineering development of the device. As a result, there is considerable interest in developing a complete theory to predict when two different images will appear very similar. When we cannot reproduce the image exactly a theory of discrimination helps the device designer; the discriminability theory selects the image the device can reproduce that appears most similar to the original. Threshold and discrimination experiments are indispensable to the design of discrimination theories.

Second, many authors believe that threshold and discrimination tasks can play a special role in analyzing the neurophysiological mechanisms of vision. The rationale for using threshold and discrimination to analyze the physiological mechanisms of vision is rarely stated and thus rarely debated, but the argument can be put something like this. Suppose the nervous system is built from a set of components, or *mechanisms*, that analyze the spatial pattern of light on the retina. Then we should identify and analyze these putative mechanisms to understand how they contribute to perception of spatial patterns. Threshold performance offers us the best chance of isolating the mechanisms because, at threshold, only the most sensitive mechanisms contribute to visibility. If threshold performance depends upon the stimulation of a single mechanism or small number of mechanisms, then threshold studies can serve as a psychologist's dissecting instrument: At threshold we can isolate different parts of the visual pathways. After understanding the component mechanisms, we can seek a unified theory of the visual system's operation.

I am not sure whether this rationale in terms of visual mechanisms adequately justifies the startling emphasis on threshold measurements. But, I think it is plain that by now we have learned a lot from detection and discrimination experiments (De Valois and De Valois (1990); Graham (1989)). Many of the basic ideas used in image representation and computer vision were derived from the work on detection and discrimination of spatial patterns. This chapter is devoted to an exposition of some of those experiments and ideas. In In Chapter and Chapter we will take up the question of what things look like.

Single Resolution Theory

The problem of predicting human sensitivity to spatial contrast patterns has much in common with other problems we have studied: image formation, color-matching, or single unit neurophysiological responses. We want to make a small number of measurements, say sensitivity to a small number of spatial contrast patterns, and then use these measurements to predict sensitivity to all other spatial contrast patterns.

In 1956, Otto Schade had some ideas about how to make these predictions and he set out to build a photoelectric analog of the visual system in order to predict visual sensitivity. His idea was to use the device to predict whether small changes in the design parameters of a display would be noticeable to a human observer. For example, in designing a new display monitor an engineer might want to alter the spatial resolution of the device. To answer whether this difference is noticeable to a human observer, Schade needed a way to predict the sensitivity of human observers to the effect of the engineering change.

Figure 1 shows a schematic diagram of Schade's computational eye. I include the diagram to show that Schade created a very extensive model that incorporated many visual functions, such as optical image formation, transduction, how to combine signals from the different cone types, adaptation, spatial integration, negative feedback, and even some thoughts about correction, interpretation and correlation of the signals with stored information (i.e. memory). In this sense, his work was a precursor to the computational vision models set forth by Marr (2010) and his colleagues.

The neural image

A fundamental part of Schade's computation — and one that has been retained by the field of spatial pattern vision — is his suggestion that we can summarize the effects of the many visual components using a single representation now called the *neural image*[1]. A real image and several neural images are drawn suggestively in Figure 2. The idea is that there is a collection of neurons whose responses, taken as a population, capture the image information available to the observer. The responses of a collection of neurons with similar receptive fields, differing only in that the receptive fields are centered at various positions, make up a neural image.

[1]To the best of my knowledge, John Robson suggested the phrase neural image.

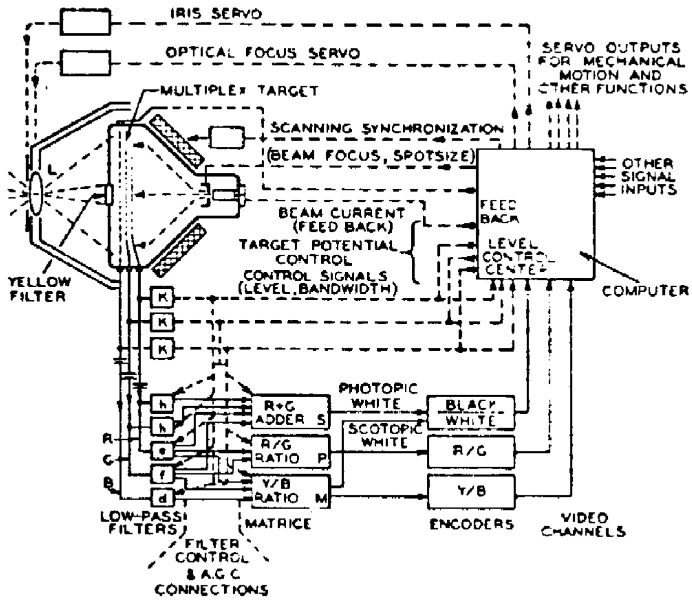

Figure 1: A computational model of the human visual system. Otto Schade designed a visual simulator to predict human visual sensitivity to patterns. His model incorporated many features of the visual pathway, and it may be the earliest computational model of human vision (From H. (1956)).

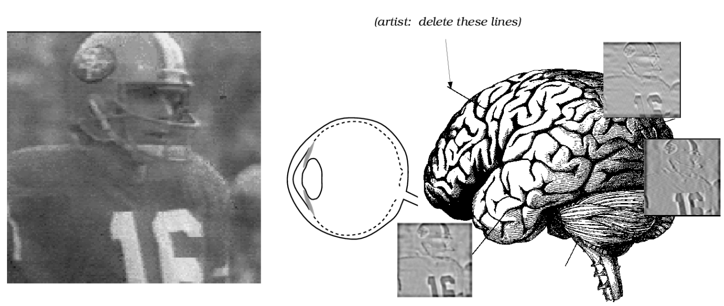

Figure 2: The neural image is a psychophysical construct. The activity of a hypothetical array of neurons, whose properties are selected to mimic some collection of neurons in the visual pathway, are represented as an image. The intensity at each location in the neural image is proportional to the response of a neuron whose receptive field is centered at that image point.

Figure 2 shows how the neural image concept permits us to visualize the neural response to an input image. At several places within the figure, I have represented the neural responses as an image. The intensity at each point in these neural images represents the response of a neuron single whose receptive field is centered at the corresponding image point. A bright value represents a neuron whose response is increased by the stimulus and a dark value a neuron whose response is decreased.

The assumptions we make concerning the receptive field properties of neurons comprising the neural image permit us to calculate the neural image using linear methods. For example, suppose the receptive fields of a collection of neurons are identical except for the position of the receptive field centers; further, suppose these are uniformly spaced. In that case, we can calculate the mapping from the real image to the responses of these neurons using a shift-invariant linear mapping, i.e. convolution.

The neural images shown in Figure 2 illustrate the idea that different populations of neurons may represent different types of information. One neural image is shown near the optic nerve; this neural image is drawn to represent the responses of the midget ganglion cells in a small region of the retina near the fovea. Near the fovea, the receptive fields of the midget cells are all about the same, except for displacements of the center of the receptive field; this neural image is a shift-invariant linear transformation of the input image. The neural images located near the cortical areas are transformed using oriented receptive fields. Of course, the information represented in the neural image at coritcal locations depends on transformations of the signal that take place all along the visual pathway, including lens defocus, sampling by the photoreceptor mosaic, and noisy signaling by visual neurons.

Schade's single resolution theory

Schade's theory of pattern sensitivity is formulated mainly for foveal vision. Schade assumed that foveal pattern sensitivity could be predicted by the information available in a single neural image. He assumed that for this portion of the visual field, the relevant neural image could be represented by a shift-invariant transformation of the retinal image, much like the neural image shown near the optic nerve in Figure 2. In this section we review the significance of this hypothesis and also some empirical tests of it.

We know that a neural image spanning the entire visual field cannot really be shift-invariant. In earlier chapters, we reviewed measurements showing that the fovea contains many more photoreceptors and retinal ganglion cells than the perihpery, and also that there is much more cortical area devoted to the fovea than the periphery. Consequently, a neural image can have a shift-invariant representation only over a relatively small portion of the visual field, say within the fovea or a small patch of the peripheral visual field.

Still, a model of pattern discrimination in the fovea is a good place to begin. First, the theory will be much simpler because we can avoid the complexities of visual field inhomogeneities. Second, because of our continual use of eye movements in normal viewing the fovea is our main source of pattern information. So, we begin by reviewing theory and measurements of foveal pattern sensitivity in the fovea. Later, we will consider how acuity varies across the visual field later in this chapter.

There are several ways the shift-invariant neural image hypothesis help us predict contrast sensitivity. Perhaps the most important is an idea we have seen several times before: If the mapping from image to neural image is shift-invariant, then the mapping from image to neural image is defined by knowing the shape of a single receptive field. In a shift-invariant neural image there is only one basic receptive field shape. Neurons that make up the neural image differ only with respect to their receptive field positions.

The analogy between shift-invariant calculations and neural receptive fields is useful. But, we should remember that we are reasoning about behavioral measurements, not real neural receptive fields. Hence, it is useful to phrase our measurements using the slightly more abstract language of linear computation. In these calculations, the linear receptive field is equivalent to the *convolution kernel* of the shift-invariant mapping. The shift-invariance hypothesis tells us that to understand the neural image, we must estimate the convolution kernel. Its properties determine which information is represented by the neural image and which information is not.

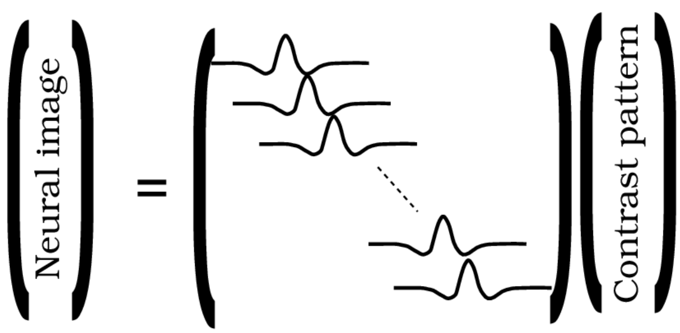

Figure 3: A shift-invariant linear neural image is formed by the responses of neurons whose receptive fields are the same except for their spatial position. The matrix tableau illustrates the computation of a shift-invariant linear transformation of a one-dimensional image. The rows of the system matrix are the one-dimensional spatial receptive fields of the neurons.

As we have done several times earlier in this book, we will begin our analysis using one-dimensional stimuli: vertical sinusoids varying only in the x-direction. If we use only one-dimensional stimuli as inputs, then we can estimate only the one-dimensional receptive field of the transformation. We can write the shift-invariant transformation that maps the one-dimensional contrast stimulus, a_x, to the one-dimensional neural image, n_x, using the summation formula,

$$n_x = \sum_y l_y a_{x-y} \tag{0.1}$$

where l_x is the one-dimensional receptive field. We also can express the transformation in matrix tableau (see Figure 3). In matrix tableau it becomes clear that the system matrix is very simple; the rows and columns are essentially all equal to the receptive field (i.e., convolution kernel) except for a shift or a reversal. Hence, by estimating the convolution kernel, we will be able to predict the transformation from contrast image to neural image.

The overall plan for predicting an observer's pattern sensitivity is this: First, we will measure sensitivity to a collection of sinusoidal contrast patterns. These measurements will define the observer's contrast sensitivity function (see Chapter and Chapter and the Appendix), we can use the contrast sensitivity function to estimate the convolution kernel of the shift-invariant linear transformation from image to neural image, l_x. Finally, we will use the estimated kernel to calculate the neural image and predict the observer's sensitivity to other one-dimensional contrast patterns. This final step will provide a test of the theory.

Shortly, it will become clear that we must make a few additional assumptions before we can use the observer's contrast sensitivity measurements to estimate the convolution kernel. But, first, let's review some measurements of the human spatial contrast sensitivity function.

Spatial contrast sensitivity functions

Schade measured the contrast threshold sensitivity function by asking observers to judge the visibility of sinusoidal patterns of varying contrast. The observer's task was to decide what contrast was necessary to render the pattern just barely visible. Because of optical and neural factors, observers are not equally sensitive to all spatial frequency patterns; the threshold contrast depends upon the pattern's spatial frequency.

To get a sense of the informal nature of Schade's experiments, it is interesting to read his description of the methods.

> The test pattern is faded in by increasing the electrical modulation at a fixed rate and observed on the modulation meter; the observer under test gives a signal at the instant he recognizes the line test pattern, and the person conducting the test reads and remembers the corresponding modulation reading. The modulation is returned to zero, and within seconds it is increased again at the same fixed rate to make a new observation. By averaging 10 to 15 readings mentally and recording the average reading directly on graph paper, the [contrast sensitivity] function …
>
> can be observed in a short time and inconsistencies are discovered immediately and checked by additional observations.

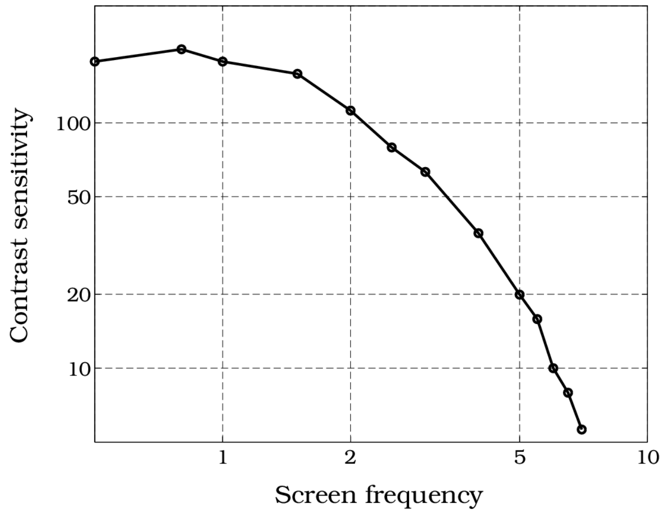

Figure 4: Contrast threshold and contrast sensitivity measurements of a human observer. The contrast thresholds are plotted with respect to spatial frequency on the display rather than cycles per degree of visual angle (Source: H. (1956)).

The contrast sensitivity function he measured is shown Figure 4. The horizontal axis is spatial frequency as measured in terms of the display device. The vertical axis is contrast sensitivity, namely $\log(1/c) = -\log c$ where c is the contrast of the pattern at detection threshold. The contrast sensitivity function has two striking features. First, there is a fall-off in sensitivity as the spatial frequency of the test pattern increases. This effect is large, but it should not surprise you since we already know many different components in the visual pathways are insensitive to high spatial frequency targets: the optical blurring of the lens reduces the contrast of high spatial frequency targets; retinal ganglion cells with center-surround receptive fields are less sensitive to high spatial frequency targets.

Second, and somewhat more surprisingly, is that there is no improvement of sensitivity at low spatial frequencies; there is even a small loss of contrast sensitivity at the lowest spatial frequency. The eye's optical image formation does not reduce sensitivity at low frequencies, so the fall in contrast sensitivity at low spatial frequencies is due to neural factors. Center-surround receptive fields are one possible reason for this low frequency fall-off.

Schade's measurements were made using a steadily presented test pattern or a drifting pattern. Robson (1966) (see also Kelly (1961a)) made additional measurements using flickering *contrast-reversing* gratings. Contrast-reversing patterns are harmonic spatial patterns with harmonic amplitude variation (see Chapter). For example, suppose the mean illumination is μ. Then the **intensity** of the contrast-reversing stimulus at spatial frequency f_x, temporal frequency f_t, and contrast a is

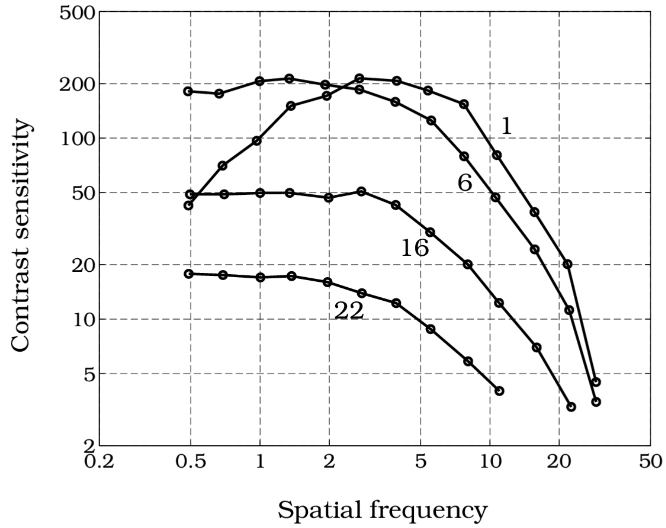

Figure 5: Temporal variations change the shape of the human spatial contrast sensitivity function. The contrast sensitivity functions shown here were measured with contrast-reversing targets at several different temporal frequencies. At low temporal frequencies the contrast sensitivity function is bandpass. At high temporal frequencies the function is lowpass (Source: Robson (1966)).

$$[1.0 + a\cos(2\pi f_t t)\cos(2\pi f_x x)]\,\mu \tag{0.2}$$

The intensity is always positive. The spatiotemporal **contrast** of the pattern is

$$a\cos(2\pi f_t t)\cos(2\pi f_x x) \tag{0.3}$$

The contrast can be both positive and negative.

As the data in Figure 5 show, the spatial sensitivity falls at low frequencies when we measure at a low temporal frequency (1 Hz). At high temporal frequencies, say as one might encounter during a series of rapid eye movements, there is no low frequency sensitivity loss. As we shall see later, the contrast sensitivity function also varies with other stimulus parameters such as the mean illumination level and the wavelength composition of the stimulus.

The psychophysical linespread function

Now, let's return to the problem of using the contrast sensitivity data to calculate the convolution kernel, l_x. Because this kernel defines both the rows and the columns of the shift-invariant linear transformation, it is also called the *psychophysical linespread function*, in analogy with the optical linespread function (see Chapter). By now you have noticed that each time we apply linear systems theory, some special feature of the measurement situation requires us to devise some slightly different approach to calculating the system properties. The calculations involved in using contrast sensitivity measurements to predict sensitivity to all contrast patterns are no exception.

Let's work out what we need to do to estimate the psychophysical linespread function. The general linear problem is illustrated in the matrix tableau in Figure 3. The input stimulus is shown as a column vector, specifying the one-dimensional spatial contrast pattern. The matrix describes how the stimulus is transformed into the neural image. We want to make a small number of measurements in order to estimate the entries of the system matrix.

We have solved this problem before, but in this case we have a special challenge. In our previous attempts to estimate linear transformations we have been able to specify both the stimulus and the response. When we obtain the contrast sensitivity measurements, however, we never measure the output neural image. We only measure the input threshold stimulus and the observer's detection threshold. Hence, we have fairly limited information available.

Because we assumed that the neural image is a shift-invariant mapping, we do know something about the neural image: when the input stimulus is a harmonic function, the output must be a harmonic function at the same frequency. But, we do not know the amplitude or phase of the harmonic function in the hypothetical neural image. To estimate the psychophysical linespread function, we must make additional assumptions about the properties of a neural image that render it at detection threshold. From these assumptions, we will then specify the phase and amplitude of the neural image at detection threshold.

Two additional assumptions are commonly made. First, we assume that the spatial phase of the neural image is the same as the spatial phase of the input spatial contrast pattern.[2] Specifically, when the input pattern is a one-dimensional cosinusoid, $\cos(2\pi f i/N)$, we assume the neural image output pattern is a scaled copy of the input pattern, $n_i = a_f \cos(2\pi f i/N)$. The scale factor, a_f, depends on the frequency of the input signal.

Second, we must specify the amplitude of the neural image at detection threshold. The amplitude of the neural image should be related to the visibility of the pattern, and we can list a few properties that should be associated with pattern visibility. For example, whether the change introduced by the signal increases or decreases the firing rate should be irrelevant; any change from the spontaneous rate ought to be detectable. Also, detectability should depend on responses pooled across the neural image rather than the response of a single neuron. The squared *vector-length* of the responses of the neural image is a measure that has both of these properties. The squared vector-length of the neural image, d^2, is defined by the formula

[2]We used the same assumption to infer the properties of the lens in Chapter . Specifically, when the input pattern is a one-dimensional cosinusoid, $\cos(2\pi f i/N)$, we assume the neural image output pattern is a scaled copy of the input pattern, $n_i = a_f \cos(2\pi f i/N)$. The scale factor, a_f, depends on the frequency of the input signal.

$$d^2 = \sum_{i=1}^{N} n_i^2. \tag{0.4}$$

This formula satisfies both of our requirements since (a) the signs of the individual neural responses, n_i, are not important because the neural image entry is squared, and (b) the formula incorporates the responses from different neurons. Other measures are possible. For example, one might assume that at detection threshold the sum of the absolute values of the neural image is equal to a constant, or one might make up a completely different rule. But, one must make some assumption and the vector-length rule is a useful place to begin.

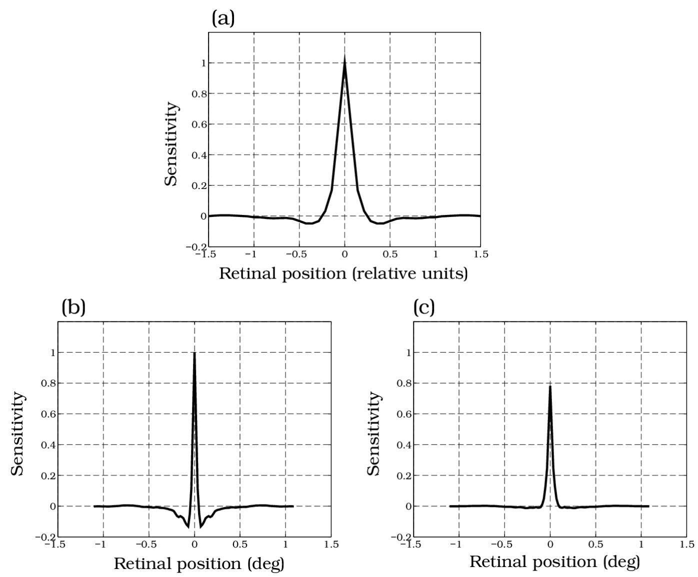

Figure 6: The psychophysical linespread function can be estimated from the contrast sensitivity function. (a) A linespread estimated from Schade's measurements. The horizontal axis is in arbitrary units because the spatial frequency of the contrast sensitivity function was reported in arbitrary units. (b,c) Linespread functions for contrast-reversing targets at 1 and 6 Hz derived from Robson's measurements. The horizontal axis is in degrees of visual angle.

If we assume that at contrast detection threshold all neural images have the same vector-length, then we can specify the amplitude of the harmonic functions in the neural image. Hence, at this point we have made enough assumptions so that we can specify the complete neural image and solve for the psychophysical linespread function. Figure 6 shows three linespread functions estimated using these assumptions. Figure 6 (a) shows a psychophysical linespread computed from Schade's measurements (note that the spatial dimension is uncalibrated). Figure 6 (b,c) show psychophysical linespreads, plotted in terms of degrees of visual angle, derived from Robson's measurements using 1 Hz and 6 Hz contrast-reversing functions. No single linespread function applies to all stimulus conditions. We will consider how the linespread function changes with the stimulus conditions later in this chapter.

H. (1956) suggested that the general shape of the psychophysical linespread function can be described using the difference of two Gaussian functions. This description is the same one used by Rodieck (1965) and Enroth-Cugell and Robson (1966) to model retinal ganglion cell receptive fields. The correspondence between the psychophysical linespread function, derived from the behavioral measurement of contrast sensitivity, and the receptive field functions of retinal ganglion cells, derived from retinal physiology, is encouraging.

Discussion of the theory: Static nonlinearities

To estimate the convolution kernel of Schade's hypothetical neural image, without being able to measure the neural image directly, we have been forced make several assumptions. It is wise to remember the three strong assumptions we have made:

(a) the neural image is a shift-invariant linear encoding,
(b) zero phase shift of the linear encoding, and
(c) vector-length rule determines visibility.

Taken as a whole, this is a nonlinear theory of pattern sensitivity. Although the neural image is a linear representation of the input, indeed it is even a shift-invariant representation, the vector-length rule linking the neural image to performance is nonlinear. You can verify this by noting that when a stimulus vector $\mathbf{s}_1$ has length d_1 and vector $\mathbf{s}_2$ has length d_2, the vector $\mathbf{s}_1 + \mathbf{s}_2$ need not have length $d_1 + d_2$. Thus, even when $\mathbf{s}_1$ and $\mathbf{s}_2$ are at one half threshold, $\mathbf{s}_1 + \mathbf{s}_2$ may not be at threshold[3].

The vector-length calculation is a static nonlinearity applied after a linear calculation (see Chapter). This is a relatively simple nonlinearity, so that it is straightforward to make certain general predictions about performance even though the theory is nonlinear. In the next section, we consider some of these predictions as well as experimental tests of them.

Experimental Tests

The contrast sensitivity function by itself offers no test of Schade's theory other than reasonableness: do the inferred linespread functions seem plausible? We have seen that the linespread functions are plausible since they are quite similar to the receptive fields of visual neurons. But, because we have made so many assumptions, it is important to find general properties of the theory that we can test experimentally and in that way gain confidence in the theory's usefulness.

[3]The only case in which the lengths will add is when the vectors representing the neural images point in the same direction.

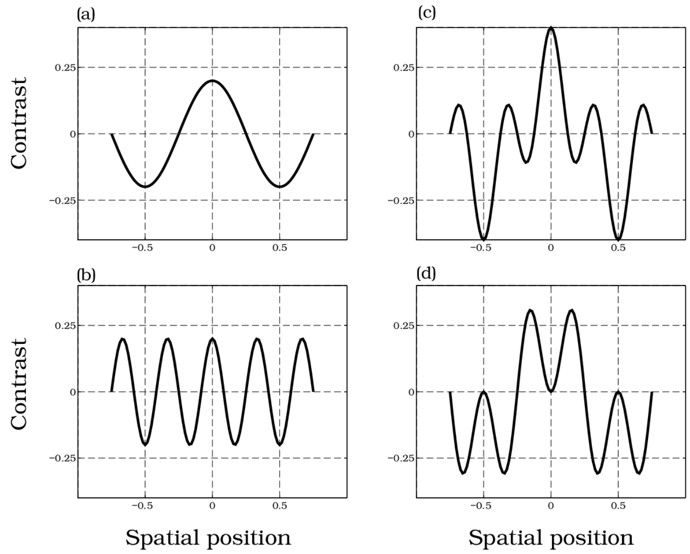

Figure 7: Mixtures of spatial contrast patterns can be used to test theories about pattern sensitivity. Panels (a) and (b) show the contrast of cosinusoidal stimuli at 1 and 3 cpd. The spatial contrasts of these two stimuli are shown added together in peaks add spatial phase (c) and peaks subtract spatial phase (d).

Harmonic functions will play a special role in testing the theory. There are two separate reasons why harmonics are important for our new test. (1) Given the assumed shift-invariance, the neural image of a harmonic is also a harmonic. We have seen this property many times before and it will be important again. (2) Harmonic functions at different frequencies are orthogonal to one another. Geometrically, orthogonality means that the vectors are oriented perpendicular to one another. Algebraically, we say two vectors, a_x and b_x are orthogonal when $0 = \sum a_x b_x$. Sinusoids and cosinusoids are orthogonal to one another, and any pair of harmonic functions at different frequencies are orthogonal to one another. We will use these two properties, combined with the vector-length rule, to test Schade's basic theory.

Suppose we create a stimulus equal to the sum of two sinusoids at frequencies, f_i, and contrasts, c_i, for $i = 1, 2$. According to the shift-invariant theory, the neural image of these two sinusoids is the weighted sum of two sinusoids. Each sinusoid is scaled by a factor, s_i, that defines how well the stimulus is passed by the shift-invariant system. The squared vector-length of the neural image created by the sum of the two sinusoids is

$$d^2 = \sum_{i=1}^{N} \left(c_1 s_1 \sin\left(2\pi f_1 \frac{i}{N}\right) + c_2 s_2 \sin\left(2\pi f_2 \frac{i}{N}\right) \right)^2 \tag{0.5}$$

The squared term in the summation can be expanded into three terms

$$
\begin{aligned}
d^2 = & (c_1 s_1 \sum_{i=1}^{N} \sin(2\pi f_1 i/N))^2 \\
& + (c_2 s_2 \sum_{i=1}^{N} \sin(2\pi f_2 i/N))^2 \\
& + 2 c_1 c_2 s_1 s_2 \left(\sum_{i=1}^{N} \sin(2\pi f_1 i/N) \sin(2\pi f_2 i/N) \right)
\end{aligned} \tag{0.6}
$$

Because sinusoids at different frequencies are orthogonal functions, the third term is zero, leaving only

$$
d^2 = \left(c_1 s_1 \sum_{i=1}^{N} \sin\left(2\pi f_1 \frac{i}{N}\right) \right)^2 + \left(c_2 s_2 \sum_{i=1}^{N} \sin\left(2\pi f_2 \frac{i}{N}\right) \right)^2 \tag{0.7}
$$

We can group some terms to define a new equation,

$$
d^2 = (c_1 a_1)^2 + (c_2 a_2)^2 \tag{0.8}
$$

where a_i is a constant, namely $s_i \sum_{j=1}^{N} \sin^2\left(2\pi f_i \frac{j}{N}\right)$.

Equation 0.8 tells us when a pair of contrasts of the two sinusoids, (c_1, c_2), should be at detection threshold. Figure 8 is a graphical representation of these predictions. The axes of the graph represent the contrast levels of the two sinusoidal components used in the mixture. The solutions to Equation 0.8 sweep out a curve called a *detection contour*. As shown in Figure 8, Equation 0.8 defines an ellipse whose principal axes are aligned with the axes of the graph. The two unknown quantities, the scale factors a_i, are related to the lengths of the principal axes. Hence, if we scale the contrast of the sinusoidal components so that threshold contrast for each sinusoidal component is arbitrarily set to one, the predicted detection contour will fall on a circle (Graham and Nachmias (1971), Nielsen and Wandell (1988)).

Many alternative theories are possible. Had we supposed that threshold is determined by the peak contrast of the pattern, then the detection contour would fall along the diamond shape shown in Figure 8. The important point is that the shape of the detection contour depends on the basic theory. The prediction using Schade's theory is clear, so that we can use the prediction to test the theory.

Graham et al. (1978) and Graham and Nachmias (1971) measured sensitivity to mixtures of sinusoidal gratings at 1 cpd and 3 cpd. They measured thresholds using a careful psychophysical threshold estimation procedure called a *two-interval, forced-choice* design. In this procedure each trial is divided into two temporal periods, usually indicated by a tone that defines the onset of the first temporal period, a second tone that defines the onset of the second temporal

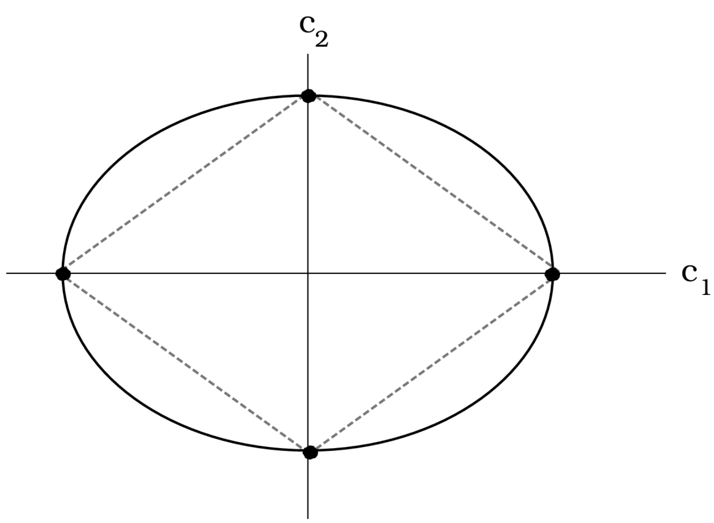

Figure 8: The spatial test-mixture experiment provides a test of contrast sensitivity models. We measure the visibility of a test-mixture whose sinusoidal components have contrasts c_1 and c_2. The set of contrast pairs such that the mixture stimulus is at detection threshold define the detection contour. Schade's hypothesis predicts that the detection contour is an ellipse aligned with the axes of the graph, as shown by the solid curve. If the peak stimulus contrast determines contrast sensitivity to the pair, then detection contour should fall along the contour indicated by the dotted lines.

period, and a final tone that indicates the end of the trial. A test stimulus is presented during one of the two temporal intervals, and the observer must watch the display and decide which interval contained the test stimulus. When the contrast of the test pattern is very low, the observer is forced to guess and so performance is at chance. When the contrast is very high, the observer will nearly always identify the correct temporal interval. Hence, as the test pattern contrast increases, performance varies from 0.5 to 1.0. The threshold performance level is arbitrary, but for technical reasons described in their paper, Graham et al. defined threshold to be the contrast level at which the observer was correct with probability 0.81.

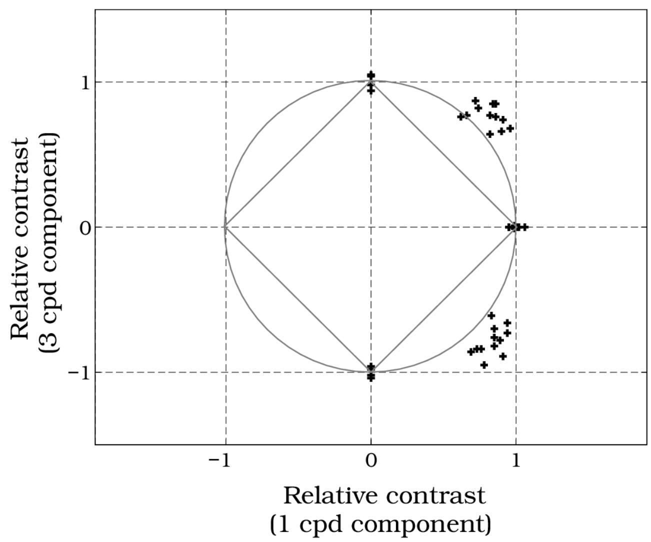

Figure 9: Spatial test-mixture thresholds measured using a 1 cpd and 3 cpd grating. The thresholds fall outside of the detection contour predicted by the shift-invariant hypothesis and vector length rule (Source: Graham et al. (1978)).

The test-mixture data in Figure 9 do not fall precisely along the predicted circular detection contour predicted by Schade's single-resolution theory. Specifically, thresholds measured in the 45 degree direction tend to fall just outside the predicted detection contour; thresholds are a little too high compared to the prediction. The theory predicts that the threshold contrasts of the individual components should be reduced by a factor of 1.414, but thresholds are reduced by only a factor of 1.2. These data are typical for these types of experimental measurements.

Is this an important difference? The point of this theory is to measure sensitivity to a small number of spatial patterns and to use these measurements to predict sensitivity to all other spatial patterns. If we see failures when we measure sensitivity to a mixture of only two test patterns, we should be concerned. The theory must be precise enough to tolerate decomposition of an arbitrary pattern into a sum of many sinusoidal patterns, and then predict sensitivity to the mixtures of the multiple components. If we already see failures with two components, we should worry about how well the theory will do when we measure with three components.

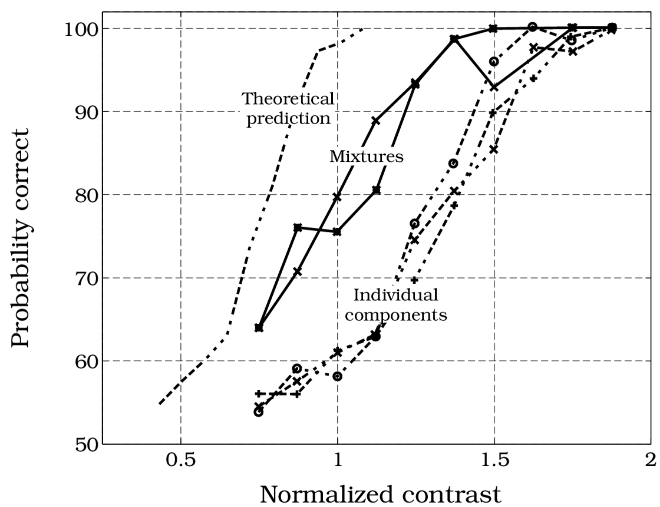

Figure 10: A three component spatial test-mixture experiment. The probability of correct detection in a two-interval forced choice is shown as a function of normalized contrast. The dashed lines on the right show detection for three simple sinusoidal gratings at frequencies of 1.33, 4, and 12 cpd. The two solid lines show the probability of detecting mixtures of these three components in cosine phase and sine phase. The dot-dash curve on the left shows the predicted sensitivity using the shift-invariant model and the vector-length rule (Source: Graham (1989)).

The data in Figure 10 illustrate sensitivity measurements to the combination of three sinusoidal gratings. In this case, the data are plotted as three *psychometric* functions. Shown in this format, the dependence of performance on contrast is explicit. The data points connected by the dashed curves show the observer's probability of correctly detecting the individual sinusoidal grating patterns at 1.33, 4.0, or 12 cpd. The horizontal axis measures the scaled contrast of the sinusoids in which the scale factor has been chosen to make the three curves align.

The visibility of two patterns formed by the mixtures of all three sinusoidal patterns, whose contrast ratios have been adjusted to make the three sinusoidal patterns equally visible, are shown as solid lines. One sum was formed with the peak contrasts all aligned (cosine phase) and the other with their zero-crossings aligned (sine phase).

Again, because the input signals are sinusoids or sums of sinusoids, we can predict performance based on the shift-invariant neural image and the vector-length rule. The neural image of the sum of three sinusoidal gratings will be the weighted sum of three sinusoidal neural images. The predicted threshold to the mixture of the three patterns is shown by the dot-dashed curve at the left of Figure 10. The vector-length rule also predicts that the probability correct will be the same in both sine and cosine phase.

The model prediction is not completely wrong; the phase relationship of the gratings does not have a significant influence on detection threshold for the mixture of three targets. But the mixture patterns are less visible than predicted by the theory: The contrasts of the three component mixtures are reduced by a factor of about 1.4 compared to their individual thresholds, while the theory predicts a contrast reduction of 1.73. The basic theory has some good features, but the quantitative predictions fail more and more as we apply the theory to increasingly complex patterns.

Intermediate Summary

We have begun formulating psychophysical theory using the simple computational ideas of shift-invariance followed by a static nonlinearity. These ideas are reminiscent of the properties of certain neurons in the visual pathway. While this theoretical formulation is a vast simplification of what we know about the nervous system, it is a reasonable place to begin. The nervous system is complex and contains many different types of computational elements. While Schade's effort to capture all of the nuances of the neural representation is inspiring, it was perhaps a bit premature. Much of the neural representation must be irrelevant to the tasks we are studying. By beginning with simpler formulations, we can use psychophysical model to discover those aspects of the neural representation that are essential for predicting the behavior. By comparing and contrasting the behavioral data and the neural data, we can discern the important functional elements of the neural representation for different types of visual tasks.

While the shift-invariant theory did not succeed, it has served the useful purpose of organizing some of our thinking and suggesting some experiments we should try. And, for those of us who need to make some approximate predictions quickly rather than precise predictions slowly, there are some good aspects of the calculation. For example, the inferred psychophysical line-spread is similar to the receptive fields of some peripheral neurons. Also, for simple mixtures the theoretical predictions are only off by by a modest factor. Still, the shift-invariant theory plainly does not fit the data very well, and its performance will only deteriorate when we apply it to complex stimuli, such as natural images. We need to find new insights and experiments that might suggest how to elaborate the theory.

Multiresolution Theory

Schade's single resolution theory of pattern sensitivity does not predict the pattern sensitivity data accurately. But, the theory is not so far wrong that we should abandon it entirely. The question we consider now is how to generalize the single resolution theory, keeping the good parts.

The most widely adopted generalization of expanding the initial linear encoding. Modern theories generally use an initial linear encoding consisting of a collection of shift-invariant linear transformations, not just a single one. Each shift-invariant linear transformations has its own convolution kernel and hence forms its own neural image. We will refer to the data represented by the individual shift-invariant representations as a *component-image* of the full theory.

To fully specify the properties of the more general theory, we need to select convolution kernels associated with each of the shift-invariant linear transformations and the static nonlinearities that follow. Also, we need to specify how the outputs of the different component-images are combined to form a single detection decision. For reasons I will explain next, the properties of the convolution kernels of the component-images are usually selected so that the expanded theory is a *multiresolution* representation of the image, a term I will explain shortly.

Pattern Adaptation

The motivation for building a multiresolution theory comes from a collection of empirical observations, such as the one illustrated in Figure 11. That figure demonstrates a phenomenon called *pattern adaptation*. To see the illusion, first notice that the bars in the patterns on top and bottom of panel (b) are the same width. Next, stare at the fixation target between the patterns in panel (a) for a minute or so. These patterns are called the *adapting patterns*. When you stare, allow your eye to wander across the dot between patterns, but do not let your gaze wander too far. After you have spent a minute or so examining the adapting patterns, look at the patterns in panel (b) again. Particularly at first, you will notice that the bars at the top and bottom of the middle pattern will appear to have different sizes. You can try the

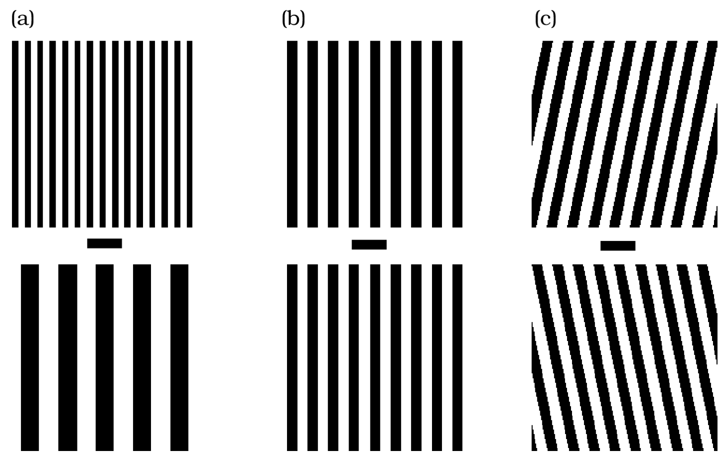

Figure 11: A size illusion and an orientation illusion based on visual pattern adaptation. The bar widths and orientations of the two squarewave patterns in the middle are the same. Stare at the fixation point between the two patterns in (a) for a minute, adapting to the two patterns in your upper and lower visual fields. When you shift your gaze to the patterns in (b) the patterns will appear to have different bar widths. Then, stare at the fixation point between the two patterns in (c) and then examine the middle pattern. When you shift your gaze to (b) the patterns will appear to have different orientations (After Blakemore and Sutton (1969); see also De Valois (1977)).

same experiment by fixating between the adapting patterns in panel (c) for a minute or so. When you examine the bars in the middle, the top and bottom will appear to have different orientation (Blakemore and Campbell (1969); Blakemore and Sutton (1969); Blakemore et al. (1970); Gilinsky (1968); Pantle and Sekuler (1968))

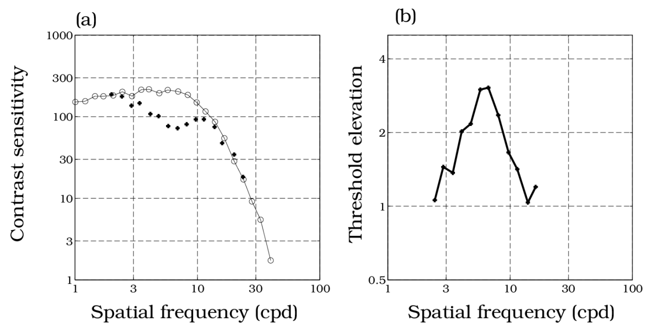

Figure 12: The effect of pattern adaptation on the contrast sensitivity function. (a) The curve through the open circles shows the observer's contrast sensitivity function before pattern adaptation. The plus symbols show contrast sensitivity following adaptation to a sinusoidal pattern 7.1 cpd. (b) Threshold elevation, that is the ratio of contrast sensitivity before and after adaptation, is plotted as a function of spatial frequency. Threshold is to test frequencies near the frequency of the adapting stimulus (Source: Blakemore and Campbell (1969)).

The effect of pattern adaptation can be measured by comparing the contrast sensitivity function before and after adaptation. The curve through the open symbols in Figure 12 (a) shows the contrast sensitivity function prior to pattern adaptation. After adapting for several minutes to a sinusoidal contrast pattern, much as you adapted to the patterns in Figure 11 (a), the observer's contrast sensitivity to stimuli near the frequency of the adapting pattern is reduced while contrast sensitivity to other spatial frequency patterns remains unchanged (the '+' symbol). The ratio of contrast sensitivity before and after adaptation is shown in Figure 11 (b). When this experiment is repeated, using adapting patterns at other spatial frequencies, contrast sensitivity falls for test patterns whose spatial frequency is similar to that of the adapting pattern (Blakemore and Campbell (1969)).

The results of the pattern adaptation measurements suggest one way to generalize the neural image from a single resolution theory to a multiresolution theory: Use a neural representation that consists of a collection of component-images, each sensitive to a narrow band of spatial frequencies and orientations. This separation of the visual image information can be achieved by using a variety of convolution kernels, each of which emphasizes a different spatial frequency range in the image. This calculation might be implemented in the nervous system by creating neurons with a variety of receptive field properties, much as we have found in the variety of receptive fields of linear simple cells in the visual cortex; these cells have both orientation and spatial frequency preferences (Chapter). Because the individual component-images are assumed to represent different spatial frequency resolutions, we say that the neural image is a *multiresolution* representation.

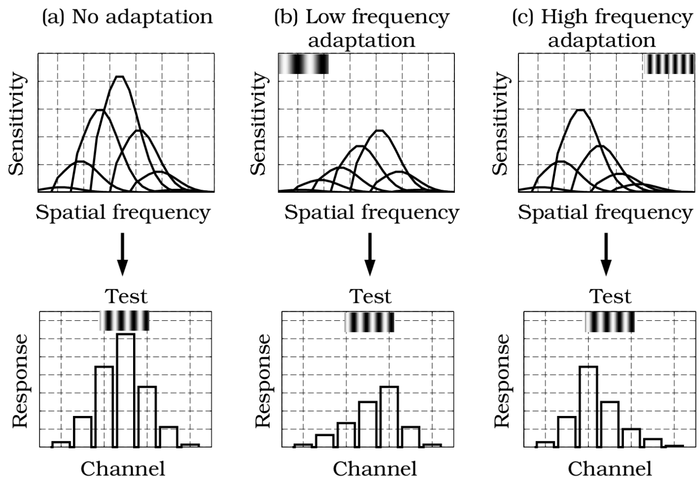

Figure 13: A multiresolution model can explain certain aspects of pattern adaptation. (a) In normal viewing, the bar width is inferred from the relative responses of a collection of component-images, each responding best to a selected spatial frequency band. The spatial frequency selectivity of each component-image is shown above and the amplitude of the component-image encoding of the test stimulus is shown in the bar graph below. (b) Following adaptation to a low frequency stimulus (shown in inset), the sensitivity of the neurons comprising certain component-images is reduced. Considering the responses of all the component-images, the response to the test is similar to the unadapted response to a high frequency target. (c) Following adaptation to a high frequency pattern (shown in inset), the neural representation is consistent with the unadapted response to a low frequency target.

Multiresolution representations provide a simple framework to explain pattern adaptation (see Figure 13). The visual system ordinarily encodes the image using a collection of shift-invariant whose contrast sensitivity curves are shown on the top of Figure 13 (a). Before adaptation, each of the component images represents the squarewave at an amplitude that depends on the squarewave frequency and the channel sensitivity. The amplitude of the component-image representations to the test pattern before adaptation is plotted at the bottom of part (a) as the bar plot.

Adaptation to a low frequency squarewave suppresses sensitivity of some of the component-images, as shown in the top of part (b) Consequently, the responses to the test frequency following adaptation changes, as shown in the bottom of part (b). The new pattern of responses is consistent with the responses that would be caused by the unadapted response to a finer squarewave pattern. This is the explanation of the observation that following adaptation to a low frequency squarewave the test pattern appears to shift to a higher spatial frequency. Figure 13 (c) illustrates the component-image sensitivities following adaptation to a high frequency squarewave (top) and how the amplitude of the component image responses are altered (bottom). In this case, the pattern of responses is consistent with the unadapted encoding of a lower frequency target.

According to the multiresolution model, pattern adaptation is much like a lesion experiment. Adaptation reduces or eliminates the contribution of one set of neurons, altering the balance of activity and producing a change in the perceptual response. Following adaptation to a low frequency target, the excitation in component-images at higher spatial frequencies is relatively greater, giving the test bars a narrower appearance. Conversely, following adaptation to a high frequency target, the pattern the excitation in component-images representing low spatial frequencies is relatively greater, giving the test bars a wider appearance.

In summary, the empirical observations using pattern adaptation suggest that squarewave or sinusoidal adapting patterns only influence the contrast sensitivity of patterns of roughly the same spatial frequency. This observation suggests that the component-images might be organized at multiple spatial resolutions.

Pattern Discrimination and Masking

There are several other experimental observations, in addition to pattern adaptation, that can be used to support multiresolution representations for human perception. Historically, one of the most important papers on this point was Campbell and Robson (1968) detection and discrimination measurements using squarewave gratings and other periodic spatial patterns. Squarewaves, like all periodic stimuli, can be expressed as the weighted sum of sinusoidal components using the Discrete Fourier Series. A squarewave, $sq(x)$, that oscillates between plus and minus one, with a frequency of f, can be expressed in terms of sinusoidal components as

$$sq(x) = \frac{4}{\pi} \sum_{n=0}^{\infty} \frac{1}{2n+1} \sin(2\pi(2n+1)fx) \tag{0.9}$$

A squarewave at frequency f is equal to the sum of a series of sinusoids at the odd numbered frequencies, f, $3f$, $5f$, and so forth. The amplitude of the sinusoids declines with increasing frequency; the amplitude of the $3f$ sinusoid is one-third the amplitude of the component at f, the amplitude of the $5f$ sinusoid is one-fifth, and so forth. When the overall contrast of the squarewave is very low, the amplitude of the higher order terms is extremely small and they can be ignored. At low contrast values, then, the squarewave pattern can be well-approximated by the pattern

$$sq(x) \approx \frac{4}{\pi} \left[\sin(2\pi fx) + \frac{1}{3} \sin(2\pi(3f)x) + \frac{1}{5} \sin(2\pi(5f)x) \right] \tag{0.10}$$

Campbell and Robson used squarewaves (and other periodic patterns) to test the multiresolution hypothesis in several ways. First, they measured the smallest contrast level at which

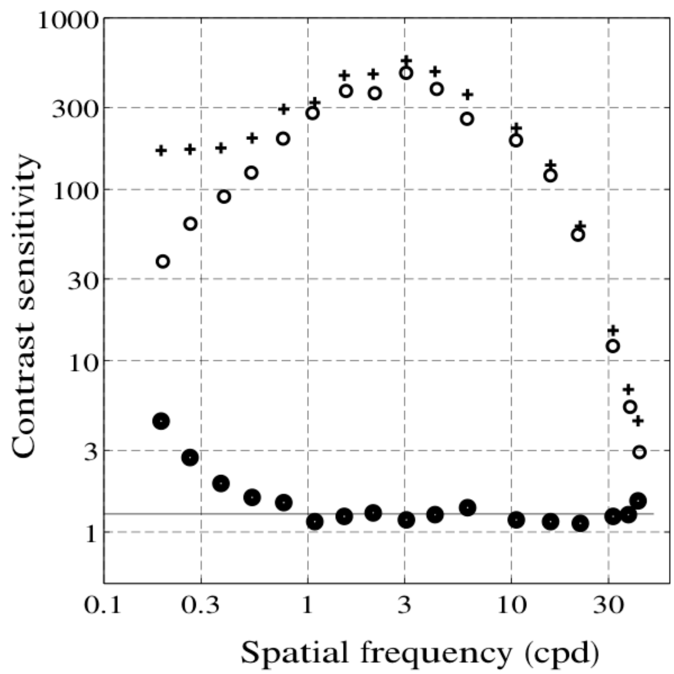

Figure 14: Contrast sensitivity measured using squarewave gratings greater than 1 cpd can be predicted from the contrast of squarewave fundamental frequency. The plus signs and open circles show contrast sensitivity to squarewaves and sinewaves, respectively. The filled circles show the ratio of contrast sensitivities at each spatial frequency. The solid line is drawn at a value of 4/\pi \approx 1.273, the amplitude of a squarewave fundamental in a unit contrast squarewave (Source: Campbell and Robson (1968)).

observers could detect the squarewave grating. Notice that the amplitude of the lowest frequency component, which is called the *fundamental*, is $4/\pi$. Since the fundamental has the largest contrast, and for patterns above 1 cpd sensitivity begins to decrease, Campbell and Robson argued that the neurons whose receptive field size are well-matched to the fundamental component will signal the presence of the squarewave first. If this is the most important term in defining the visibility of the squarewave, then the threshold contrast of the squarewave should be $4/\pi$ times the threshold contrast of a sinusoidal grating at the same frequency. The data in Figure 14 show contrast sensitivity functions to both sinusoidal and squarewave targets, and the ratios of the contrast sensitivities. As predicted[4], for patterns above 1 cpd the ratio of contrasts at detection threshold is $1.28 \approx 4/\pi$.

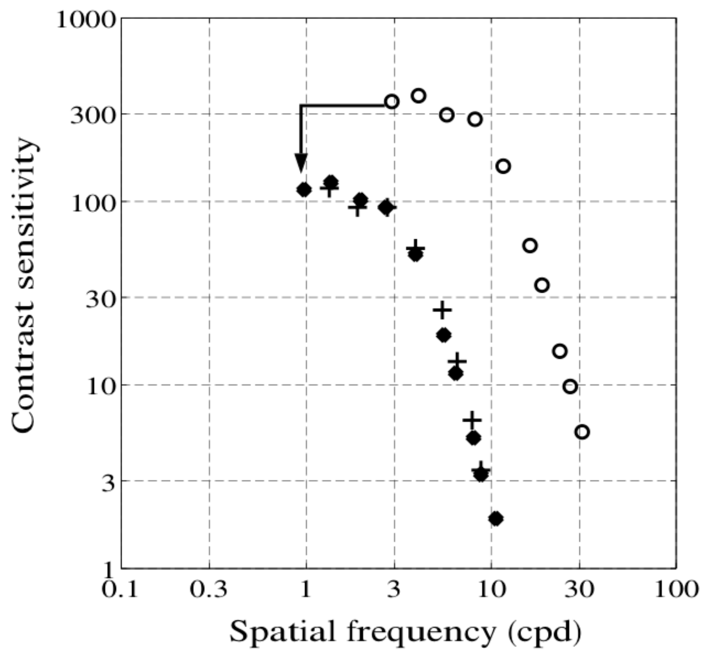

Figure 15: Discrimination of sinusoidal and squarewave gratings becomes possible when the third harmonic in the squarewave reaches its own independent threshold. The open circles plot contrast sensitivity function. The plus signs show the contrast level at which a squarewave can be discriminated from its fundamental frequency. The filled circles show the squarewave discrimination data shifted by a factor of 3 in both frequency and contrast. The alignment of the shifted curve with the contrast sensitivity function suggests that squarewaves are discriminated when the third harmonic reaches its own threshold level (Source: Campbell and Robson (1968)).

[4]Campbell and Robson's squarewave detection experiment is a special case of the test-mixture experiment we reviewed earlier. The results show that the $3f$ and higher frequency components do not help the observer detect the squarewave grating. The more general question of how different frequency components combine is answered by test-mixture experiments, such as those performed by Graham and Nachmias (1971), in which the relative contrast of all the components are varied freely.

In addition to detection thresholds, Campbell and Robson also measured how well observers can discriminate between squarewaves and sinusoids. In these experiments, observers were presented with a squarewave and a sinewave at frequency f. The two patterns were set in a contrast ratio of $4/\pi$, insuring that the fundamental component of the square and the sinusoid had equal contrast. The observers adjusted the contrast of the two patterns, maintaining this fixed contrast ratio, until the squarewave and sinusoid were barely discriminable. Since the contrast of the squarewave fundamental was held equal to the contrast of the sinusoid, the stimuli could only be discriminated based on the frequency components at $3f$ and higher.

Campbell and Robson found that observers discriminated between the sinusoid and the squarewave when the contrast in the third harmonic reached its own threshold level. Their conclusions are based on the measurements shown in Figure 15. The filled circles show the contrast sensitivity function. The open circles show the contrast of the squarewave when it is just discriminable from the sinusoid. Evidently, the squarewave contrast needed to discriminate the two patterns exceeds the contrast needed to detect the squarewave. But, we can explain the increased contrast by considering the contrast in the $3f$ component of the squarewave. Recall that this component has $1/3$ the contrast of the squarewave. By shifting the squarewave discrimination data (open circles) to the left by a factor of three for spatial frequency, and downwards by a factor of three for contrast, we compensate for these two factors. The plus signs show the open circles shifted in this way. The plus signs align with the original contrast sensitivity measurements. From the alignment of the shifted discrimination data with the contrast sensitivity measurements, we can conclude that the squarewave can be discriminated from the sinusoid when the $3f$ component is at detection threshold visible.

Masking and facilitation

Campbell and Robson's discrimination results are consistent with a multiresolution representation of the pattern. It is as if the fundamental and third harmonics are encoded by different component-images. Because the amplitude of the fundamental component is the same in the squarewave and sinusoid, the observer cannot use that information to discriminate between them. When the contrast of the third harmonic exceeds its own independent threshold, the observer can use the information and discriminate the two patterns.

Although multiresolution representations are consistent with this result, we should ask whether the evidence is powerful. Specifically, we should ask whether the data might be explained by simpler theories. One more general hypothesis we should consider is this: observers discriminate two spatial patterns, S and $S + \Delta S$, whenever ΔS is at its own threshold. This is the phenomenon that Campbell and Robson report for their when S and ΔS are low contrast stimuli, widely separated in spatial frequency. Can subjects always discriminate S from $S + \Delta S$ when ΔS is at its own threshold hold generally?

No. In fact, the case described by Campbell and Robson is very rare. In many cases the two patterns S and $S + \Delta S$ cannot be discriminated even though ΔS, seen alone, is plainly visible.

In this case, we say the stimulus S *masks* the stimulus ΔS. There are also cases when S and $S+\Delta S$ can be discriminated even though ΔS, seen alone, cannot be detected. In this case, we say the stimulus S *facilitates* the detection of ΔS. Masking and facilitation are quite common; the absence of masking and facilitation, as in the data reported by Campbell and Robson, are fairly unusual.

The images in Figure 16 (a) demonstrate the phenomenon of visual masking. The pattern shown on the left is the target contrast pattern, ΔS. This contrast pattern is added into one of the masking patterns shown in the middle column. The masking pattern on the top is similar to the target in orientation, but different by a factor of three in spatial frequency. If you look carefully, you will see a difference between the mask alone and the mask plus the target: Specifically, near the center of the pattern several of the bars on the left appear darkened and several bars on the right appear lightened. The second mask is similar to the target in both orientation and spatial frequency. In this case, it is harder to see the added contrast, ΔS. The third mask is similar in spatial frequency but different in orientation. In this case, it is easy to detect the added target.

Figure 16 (b) shows measurements of masking and facilitation between patterns with similar spatial frequency and the same orientation (Legge and Foley (1981)). Observers discriminated a mask, S, from a mask plus a two cycle per degree sinusoidal target, $S + \Delta S$. The vertical axis measures the threshold contrast of the target needed to make the discrimination and the horizontal axis measures the contrast of the masking stimulus S. The different curves show results for maskers of various spatial frequencies. In general, the presence of S facilitates detection at low contrasts and masks detection at high contrasts. When the spatial frequencies of ΔS and S differ by a factor of two, the amount of facilitation is small, though there is still considerable masking. Other experimental measurements show that when the spatial frequencies of the test and mask differ by a factor of three, the effect of masking is reduced (Wilson et al. (1983); De Valois (1977)). We will discuss the effect of orientation on masking later in this chapter.

The implications of these experiments for multiresolution models can be summarized in two parts. First, Campbell and Robson's data show no facilitation or masking when S and ΔS are low contrast and widely separated in spatial frequency. Second, the Legge and Foley data show that for many stimulus pairs more similar in spatial frequency, S influences the visibility of an increment ΔS. Taken together, these results are consistent with the idea that stimuli with widely different spatial frequencies are encoded by different component-images.

The Conceptual Advantage of Multiresolution Theories

Today, many different disciplines represent images using the multiresolution format; that is, by separating the original data into a collection of component-images that differ mainly in their peak spatial frequency selectivity. The multiresolution representation has opened up a large set of research issues, and I will discuss several of these in Chapter . While the behavioral

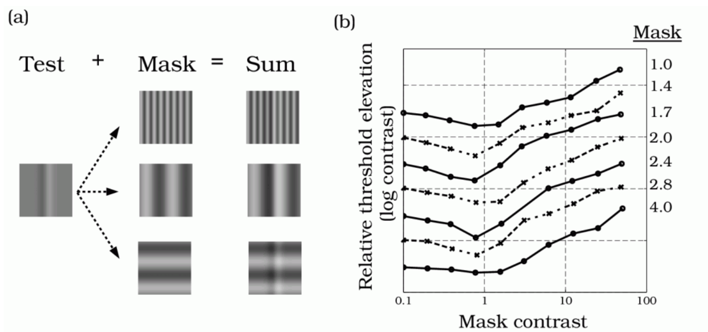

Figure 16: Masking and facilitation. (a) These images illustrate visual masking. The test contrast pattern is shown on the left, and three different masking contrast patterns are shown in the middle column. The sum of the test and mask contrasts are shown in the right column. When the spatial frequency of the test and mask differ by a factor of three (top), it is possible to see the effect of the test pattern. When the spatial frequency of the test and mask are similar (middle) it is difficult to perceive the added test. When the orientations of the test and mask are very different (bottom) it is very easy to see the added test. (b) The contrast needed to detect a 2 cpd target (Delta S, vertical axis) depends on the contrast of the masking pattern (S, horizontal axis). Each curve measures the effect of a different spatial frequency pattern, S. When S is of low contrast and similar spatial frequency and orientation, it facilitates detection of the target; when it is of high contrast pattern it masks detection of the target. The curves have been displaced along the vertical axis so that each can be seen clearly (Source: Legge and Foley (1980)).

evidence for multiresolution is interesting, it is hardly enough to explain why multiresolution hypothesis have led to something of a revolution in vision science. Rather, I think that it is the conceptual advantages of multiresolution representations, described below, that have made them an important part of vision science.

When theorists abandon the simple shift-invariance hypothesis for the initial linear encoding, two problems arise. First, the set of possible encoding functions, even just linear encoding functions, becomes enormous. How can one choose among all of the possible linear transformations? Second, without shift-invariance, the theorist loses considerable predictive power, some many important derivations we have made depend on shift-invariance. For example, without shift-invariance we can not derive the same quantitative prediction to the test-mixture threshold of a pair of sinusoids (Equation 0.8).

Simply abandoning shift-invariance opens up the set of possible encodings too far; theorists need some method of organizing their choices amongst the set of possible linear encodings. The multiresolution structure helps to organize the theorist's choices. To specify a multiresolution model we must specify the properties of the collection of shift-invariant calculations that make up the multiresolution theory. This organization helps the theorist reason and describe the properties of the linear encoding.

The multiresolution hypothesis also permits theorists to introduce organizational properties into the component-images that make these images seem more like the cortical response of nerve cells. A model with only a single shift-invariant model can not have an orientation selective convolution kernel or a single frequency selective kernel. If the convolution kernel (i.e., neural receptive field) encodes one orientation more effectively than others, or one spatial resolution more strongly, then the observer also must be more sensitive to stimuli with this orientation. Since observers show no strong orientation or resolution bias, a shift-invariant model must use a circularly symmetric pointspread function with fairly broad spatial resolution.

Multiresolution theories, however, can incorporate receptive fields with a variety of orientations and resolutions. As long as all orientations are represented, the model as a whole will retain equal sensitivity to all orientations. The use of oriented convolution kernels with restricted spatial resolution makes the analogy between the convolution kernels and cortical receptive fields much closer (see Chapter).

The complexity of the calculations is an important challenge in developing multiresolution models of human pattern sensitivity. Figure 17 is an overview of a fairly simple multiresolution model described by Wilson and Regan (1984) (Wilson and Gelb (1984); Watson (1983); Foley and Legge (1981); Watt and Morgan (1985)). The initial image is transformed linearly into a neural image comprising a set of component-images. In a recent implementation of this model, Wilson and Regan (1984) suggest that the neural image consists of forty-eight component-images, organized by six spatial scales and eight orientations (i.e. all scales at all orientations). Each component-image is followed by a static nonlinearity that are modifications of the vector-length measure. To see the development of an even more extensive model, the reader should consult the work by Watson and his colleagues (e.g. Watson (1983); Watson and

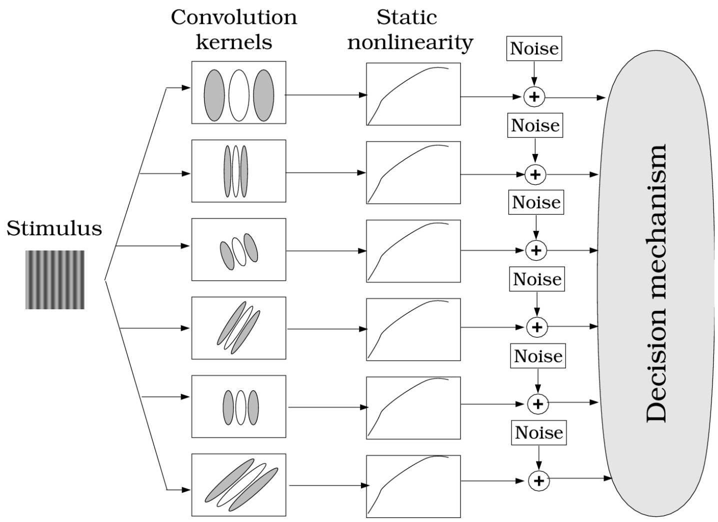

Figure 17: A multiresolution model of spatial pattern sensitivity. The stimulus is convolved with a collection of spatial filters with different peak spatial frequency sensitivity. The filter outputs are modified by a nonlinear compression, noise is added, and the result is combined into a neural image (Source: Spillmann and). (2012)).

Ahumada (1989)). They have developed a substantially larger multiresolution model, using very sophisticated assumptions concerning the observer's internal noise and decision-making capabilities.

It is difficult to reason about the performance of these multiresolution models from first principles (though see Nielsen and Wandell (1988); Bowne (1990)). Consequently, most of the predictions from these models are derived using computer simulation. Analyzing the model properties closely could easily fill up a book; and, in fact, Graham (1989) has completed an authoritative account of the present status of work in this area. I am pleased to refer the reader to her account.

Challenges to Multiresolution Theory

Multiresolution theories are the main tool that theorists use to reason about pattern sensitivity. As we reviewed in the preceding section, multiresolution representations have many useful features and they can be used to explain several important experimental results. There are, however, a number of empirical challenges to the multiresolution theories. In this section, I will describe a few of the measurements that represent a challenge to multiresolution theories of human pattern sensitivity. As you will see, many of these challenges derive from the same source as challenges to a shift-invariant theory: mixture experiments.

Pattern Adaptation to Mixtures

If we are to use pattern adaptation to justify multiresolution theories, then we should spend a little more time studying the general properties of pattern adaptation measurements. Perhaps the first step we should take is to extend the pattern adaptation measurements from simple sinusoids to more general patterns consisting of the mixture of two patterns.

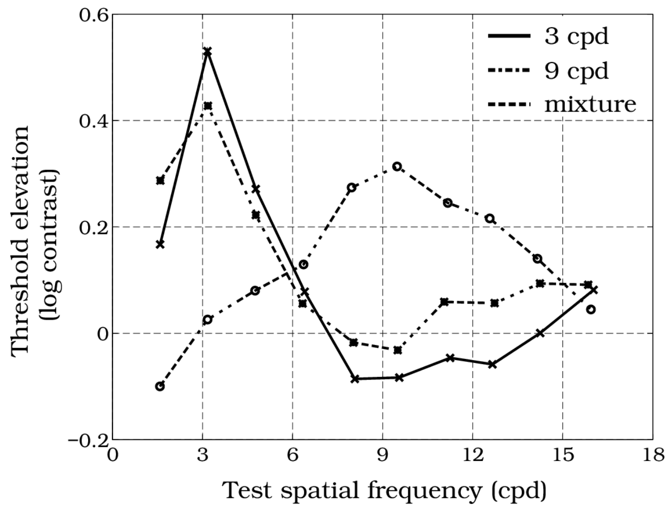

Figure 18: Pattern adaptation mixture experiments. These curves measure log threshold contrast elevation at various test frequencies following adaptation. The curves show the results following adaptation to a 3 cpd sinusoid (solid), a 9 cpd sinusoid (dash), and their sum (dot-dash). Threshold elevation following adaptation to the sum is smaller than threshold elevation following adaptation to the individual components (Source: Nachmias et al. (1973)).

Nachmias et al. (1973) performed a pattern adaptation experiment using individual sinusoidal stimuli and their mixtures as adapting stimuli. The question they pose, as in all mixture experiments, is whether we can use the individual measurements to predict the behavioral performance to the sum.

The results of their measurements are shown in Figure 18. Each curve in Figure 18 represents threshold elevation of sinusoidal test gratings at different spatial frequencies. The solid curve measures threshold elevation when the adapting stimulus was a three cycles per degree sinusoidal grating. Confirming Blakemore and Campbell (1969), there is considerable threshold elevation at 3 cycles per degree and less adaptation at both higher and lower spatial frequencies. The dashed curve measures threshold elevation when the adapting field was a 9 cycle per degree grating. For historical reasons, the contrast of this grating was one third the contrast of the grating at the fundamental. Even at this reduced contrast, the nine cycle per degree grating also causes a significant threshold elevation for nine cycles per degree test stimuli.

The dot-dash curve shows the threshold elevation following adaptation to the mixture of the two adapting stimuli. For this observer, adaptation to the mixture shows no threshold elevation to test gratings at 9 cpd. For all of the observers in this study, the threshold elevation at 9 cpd following adaptation to the mixture is smaller than the threshold elevation following adaptation to the 3 cpd adapting stimulus. The mixture of 3 and 9 is *less* potent than adapting to 9 alone.

This result is difficult to reconcile with the simple interpretation of adaptation and spatial frequency channels in Figure 17. If the adaptation to 3 cpd stimulates a different set of neurons from adaptation to 9 cpd, then why should adapting to 3 cpd and 9 cpd improve sensitivity at 3 cpd? I am unaware of any explanations of this phenomenon that also preserve the basic logical structure of the multiresolution representations.

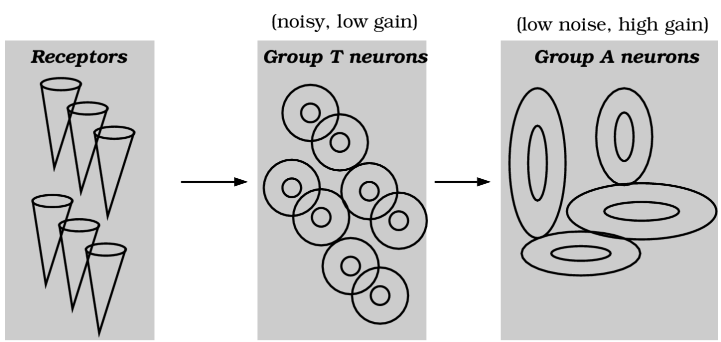

Figure 19: The neurons that limit detection and those that cause pattern adaptation may not be the same. For example, one group of neurons (Group T) may be noisy and have low contrast gain. Because of their noise properties, this group would limit detection threshold. Neurons in a second population (Group A) may integrate the responses of the first group of neurons and have high contrast gain. Because of their high gain, this group of neurons may fatigue easily and be the neural basis of pattern adaptation. If the neural units that limit these two types of behavioral responses are different, then the spatial receptive fields of neurons that are inferred from detection and pattern adaptation experiments may well be different.

The results of these mixture experiments should motivate us to rethink the basic mechanisms of pattern adaptation. If we plan on using this experimental method to provide support for a notion as significant as multiresolution representation of pattern, then we should understand the adaptation phenomenon. Figure 19 illustrates one of the difficulties we face when we try to integrate results from detection and adaptation experiments. When we group results from detection and adaptation experiments, we assume implicitly that the visual mechanisms that limit detection are the same as those that alter visual sensitivity following pattern adaptation. But behavioral measurements provide no direct evidence that the neurons that limit sensitivity are the same as those that underly adaptation.

The diagram in Figure 19 illustrates one way in which this assumption may fail. Suppose that neurons indicated as *Group T* are located early in the visual pathways, and that these neurons are noisy and have low contrast gain. If these are the least reliable neurons in the pathway, then the sensitivity may be limited by their properties. In that case, we can improve the observer's detection performance by testing with stimuli that are well-matched to response properties of the Group T neurons.

We have assumed that the effects of pattern adaptation are due to neural fatigue caused by strong stimulus excitation. Because the Group T neurons have relatively low gain, they will not respond very strongly to most stimuli and consequently they may not be susceptible to pattern adaptation. Instead, it may be that another group of neurons, *Group A* neurons, are the ones most influenced by the adapting pattern. I have shown these neurons in Figure 19 at a later stage in the visual pathways. The spatial spatial properties of the pattern adaptation experiment, for example the way test sensitivity varies with the spatial properties of the adapting pattern, may be due to the spatial receptive field properties of the Group A neurons. Group T and Group A neurons may have quite different spatial receptive fields[5].

From this analysis, it should be clear that the spatial properties of the neural encoding derived from pattern adaptation may differ from the spatial properties of the neural encoding derived from detection tasks, To argue that the mechanisms limiting detection and mediating pattern adaptation are the same, we must find behavioral experimental measurements that prove this point. In that case, we can piece together the results from detection and pattern adaptation to infer the organization within multiresolution models.

Masking with Mixtures

In the Campbell and Robson (1968) discrimination experiment, the observer was asked to distinguish between two stimuli S and $S + \Delta S$, where S and ΔS, effectively, were sinusoidal patterns. Campbell and Robson found that when S and ΔS were sinusoidal stimuli at well-separated spatial frequencies the two patterns were discriminable when ΔS was at its own threshold. In reviewing their experiments we considered how masking depends on the relative spatial frequency of the test and masking patterns (@Figure 16).

The data in Figure 20 show how masking depends on the relative orientation of the target and masker (Phillips and Wilson (1984)). In this study, the masker S and test ΔS were at the same spatial frequency. Phillips and Wilson measured the contrast needed in the test to discriminate $S + \Delta S$ from S for various orientations of the masker. The horizontal axis in Figure 20 measures the orientation of the masking stimulus, S. The vertical axis measures the threshold elevation of the test. As the difference in orientation between the test stimulus ΔS and masking stimulus S increases, the masking effect decreases. In this data set, when the

[5] You should also consider the possibility that the basic mechanism of neural fatigue is not the main source of pattern adaptation. Recently, Barlow and Földiák (1989) have put forward an entirely different explanation of pattern adaptation that is based on learning principles, not on neural fatigue. While the work on this topic is too preliminary for me to include in this volume, I think this line of research has great potential for clarifying many visual phenomena.

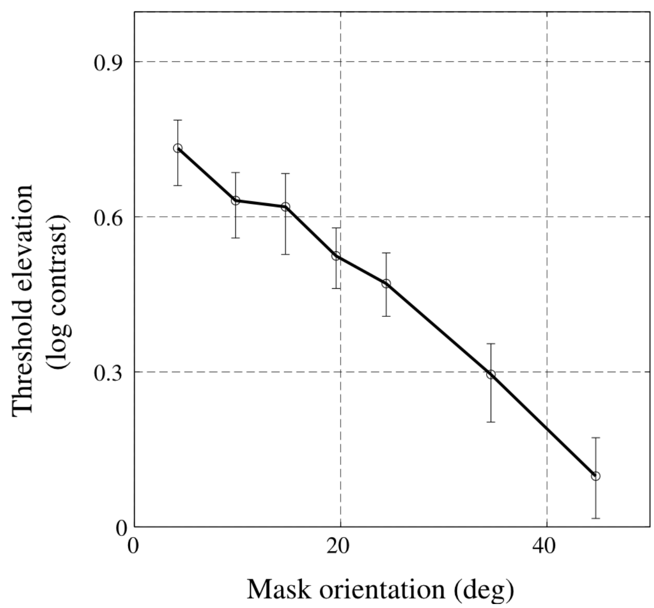

Figure 20: Orientation tuning in the masking experiment. Threshold elevation to a 2 cpd test as a function of the orientation of a 2 cpd masking stimulus. The data include only maskers with positive orientations since masking is symmetric with respect to the orientation of the masking stimulus. The two curves show data from two observers and the error bars are one standard error of the mean (Source: Phillips and Wilson (1984)).

orientation difference exceeds 40 degrees $S + \Delta S$ can be discriminated from S when ΔS is at its own threshold level.

Based on these measurements, one might suspect that one-dimensional contrast patterns separated in orientation by 40 degrees are encoded by separate neurons. Experimental results like these might be used to determine the orientation selectivity properties of convolution kernels used in multiresolution models.

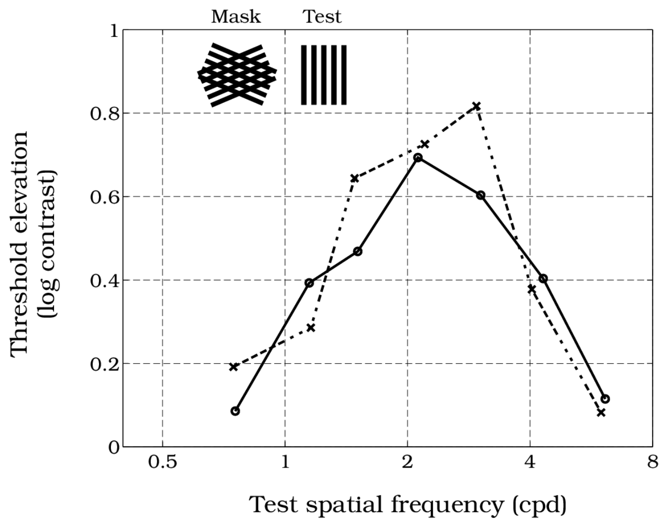

Figure 21: Masking mixture experiments. When a test and masking grating are separated in orientation by 67.5 deg, the masker has no influence on the visibility of the test. But, the combination of two masking gratings at 67.5 deg, neither of which alone has any effect, acts as a powerful masker. (Source: Derrington and Henning (1989)).

Results from test-mixture experiments based on visual masking challenge the validity of this conclusion. Derrington and Henning (1989) report mixture experiments in which they measured threshold elevation using two separate masking patterns and their mixture. The individual masking patterns were 3 cpd sinusoidal gratings; one grating was oriented at plus 67.5 degrees and the other minus 67.5 degrees relative to vertical. They measured the effect of these masking patterns on a variety of vertically oriented sinusoidal gratings.

If the two masking stimuli are represented by neurons that are different from those that represent the vertical test patterns, then the superposition of these two masking stimuli should not influence the target visibility. The data in Figure 21 show that this is not the case. The mixture of the two masking patterns is a potent mask even though each alone fails to have any effect[6].

[6] Similar difficulties in interpreting the effects of masking, but with respect to mixtures of sinusoidal gratings, have been studied by Nachmias and Rogowitz (1983) and Perkins and Landy (1991).

Multiresolution Theory: Current status

The multiresolution representations are very important theoretical tool. They help us think about the general problem of pattern sensitivity and they provide a framework for organizing computational models of pattern sensitivity and other pattern-related tasks. There is some evidence that these representations are an important part of the human visual pathways. But, there is a bewildering array of experimental methods — ranging from detection to pattern adaptation to masking — whose results are inconsistent with the central notions of multiresolution representations. As we have seen, mixture experiments using pattern adaptation and masking are difficult to understand if we believe that components of the image in spatial frequency and orientation bands are encoded by independent sets of neurons.

The conflicting pattern of experimental results show us that we haven't yet achieved a complete understanding of the basic neural processes that cause adaptation and masking. Nor do we understand how these neural processes are related to the neural processes that limit pattern sensitivity. Achieving this understanding is important because these experiments provide the key results that support multiresolution representations. Perhaps, once we understand the properties these separate experimental methods more fully, we will understand the role of multiresolution representations and find a way to make sense of complete set of experimental findings. Up to this point, I think you should see that we are well underway in understanding these issues, but many questions remain unanswered.

Pattern Sensitivity Depends on Other Viewing Parameters

Next, we will review how pattern sensitivity depends on other aspects of the viewing conditions, such as the mean illumination level, the temporal parameters of the stimulus, and the wavelength properties of the pattern. In each of these cases, we will use some form of the contrast sensitivity function as a summary of the observer's behavior.

In the remainder of this chapter, the contrast sensitivity function plays a different role from the way we have used it up to now. To this point, I have emphasized the special role of the contrast sensitivity function in linear systems theories. If we understand the structure of the data well enough, then the contrast sensitivity function can be used to predict sensitivity to many other different patterns. A clear example of this is Schade's use of the contrast sensitivity function: if visual sensitivity is limited by a shift-invariant neural image, then we can use the contrast sensitivity function to predict sensitivity to any other pattern.

We do not have yet a complete theory that permits us to use the contrast sensitivity function to characterize behavior generally. My purpose in continuing to describe pattern sensitivity in terms of the contrast sensitivity function now is that it serves as a summary measure of visual pattern sensitivity. Hence, in the remainder of this chapter, we will not look at the contrast sensitivity function as a complete description of the observer's pattern sensitivity. Rather, we will use it as a descriptive tool to help us learn something about the general pattern sensitivity of the visual system.

Part of the reason for standardizing on the contrast sensitivity function is this: The measure is used widely in both physiology and psychophysics. Hence, behavioral measurements of the contrast sensitivity function can provide us with a measure that we can compare with the neural response at different points in the visual pathway. If a particular class of neurons, say retinal ganglion cells, limit visual sensitivity, we should expect behavioral contrast sensitivity curves and neural contrast sensitivity curves to covary as we change the experimental conditions.

Light Adaptation

Figure 22 shows that the contrast sensitivity function changes when it is measured at different mean background intensities. The curve in the lower left shows a contrast sensitivity function measured at a low mean luminance level (9×10^{-4} trolands) when rods dominate vision. Under these conditions the contrast sensitivity function peaks at 1–3 cpd and the curve is lowpass rather than bandpass. The curve on the upper right shows a contrast sensitivity function measured on a bright photopic background, one million times more intense. Under these conditions the peak of the contrast sensitivity function is near 6–8 cpd and the shape of the curve is bandpass. At mean background intensities higher than 1000 trolands, the contrast sensitivity function remains unchanged (Westheimer (1960); Nes and Bouman (1967)).

The change in the shape of the contrast sensitivity function is consistent with a few simple imaging principles. The first principle concerns the importance of achieving adequate signal under the ambient viewing conditions. At very low light levels, the observer needs to integrate light across the retina in order to achieve a reliable signal. If the observer must spatially average the light signal to obtain a reliable signal, then the observer cannot also resolve high spatial frequencies. Consequently, under dim, scotopic conditions the observer should have poor sensitivity to high spatial frequencies, as they do. On more intense backgrounds, when quanta are plentiful, the observer can integrate information over smaller spatial regions and spatial frequency resolution improves.

The second principle concerns the importance of contrast, rather than absolute intensity, for visual processing. Figure 22 shows that contrast sensitivity of low spatial frequency patterns (below 1 cpd) rises with mean luminance and then becomes constant. The range in which contrast sensitivity becomes constant is called the *Weber's law* regime. For low spatial frequency patterns, Weber's law is a good description of the results. At higher spatial frequencies, contrast sensitivity continues to rise with the mean luminance. For these patterns Weber's law is not a precise description of behavior of sensitivity.

Even though Weber's law is imprecise it does contain a kernel of truth. Consider the overall dynamic ranges we are measuring. The background intensities used in these experiments vary by a factor of one million, i.e., six orders of magnitude. Yet, the contrast sensitivity generally varies by only a factor of 20 or so, only one order of magnitude while sensitivity

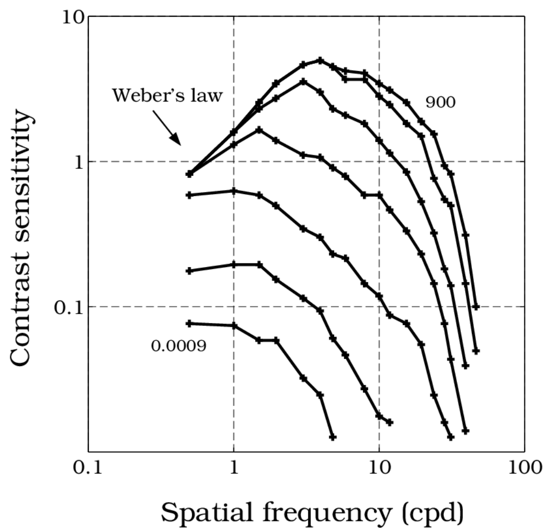

Figure 22: Contrast Sensitivity at Various Mean Field Levels: Human contrast sensitivity varies with mean field luminance. Each curve shows a contrast sensitivity function at a different mean field luminance level ranging from 9×10^{-4} trolands to 9×10^{2} trolands, increasing by a factor of ten from curve to curve. The stimulus consisted of monochromatic light at 525 nm. At the lowest level, under scotopic conditions, the contrast sensitivity function is lowpass and peaks near 1 cpd. On intense photopic backgrounds the curve is bandpass and peaks near 8 cpd. Above these mean background levels, the contrast sensitivity function remains constant (Source: Nes and Bouman (1967)).

to absolute light level varies by 4 or 5 orders of magnitude. The pattern of results suggests that the visual system preserves contrast sensitivity, as suggested by Weber's law, rather than absolute intensity. The visual system succeeds quite well at Weber's law behavior at low spatial frequencies, and it comes close at high spatial frequencies. The significance of contrast rather than absolute intensity for vision confirms the general view we have adopted, beginning with measurements of contrast sensitivity in retinal ganglion cells and cat behavior described in Chapter .

Spatio-temporal contrast sensitivity

Figure 5 showed several contrast sensitivity functions measured using contrast-reversing sinusoids. Those data illustrate how the contrast sensitivity function varies when we measure at a few different temporal frequencies. Figure 23 contains a surface plot that represents how spatial contrast sensitivity function when we measure at many different temporal frequencies. One axis of the graph shows the spatial frequency of the test pattern, a second axis shows the test pattern's temporal frequency. The height of the surface represents the observer's contrast sensitivity. The surface represents the observer's *spatiotemporal contrast sensitivity function*. This single surface represents a large range of spatial and temporal contrast sensitivity functions. Paths through the surface running parallel to the spatial frequency axis represent the spatial contrast sensitivity function; paths through the surface running parallel to the temporal frequency axis represent temporal contrast sensitivity functions. Kelly (1979a) and Kelly (1979b) derived the analytic curve that yields the surface shape from an extensive set of psychophysical measurements.

If the spatial contrast sensitivity functions had the same shape up to a scale factor, and similarly for the temporal contrast sensitivity functions, we would say that human spatio-temporal contrast sensitivity is space-time *separable*[7]. From the shape of the contrast sensitivity surface, it is apparent that the spatial contrast sensitivity curves have different shapes when measured at different temporal frequencies (cf. Figure 5). Hence, human contrast sensitivity is not space-time separable (Kelly and Burbeck (1984)).

There are several considerations that make space-time separability an important property. First, in Chapter I explained that only space-time separable systems have unique spatial and temporal sensitivity functions. When a system is not separable it does not have a unique contrast sensitivity function; rather it has a different function for each temporal measurement condition.

Second, space-time separability is significant because it simplifies computations and representations. For example, suppose we want to represent the spatiotemporal contrast sensitivity function at $N = 60$ spatial and $N = 60$ temporal frequencies. If the contrast sensitivity function is not separable, we may need to store as many as $N^2 = 3600$ values of the sensitivity function. But, if the function is space-time separable, we need to represent only the the spatial

[7]See Section , (Equation 0.3) for a discussion of space-time separability of receptive fields.

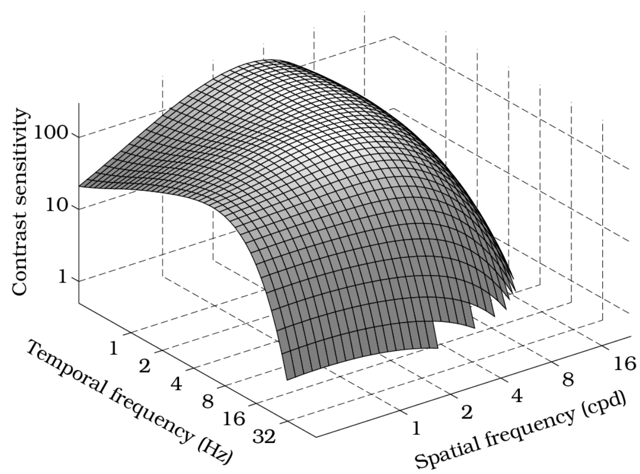

Figure 23: Human spatiotemporal contrast sensitivity function. The two lower axes represent the spatial and temporal frequencies of a contrast-reversing pattern. The vertical axis represents the observer's contrast sensitivity to each of the contrast reversing patterns. The data used to estimate this surface were made on a mean background luminance of 1000 trolands. Curves running parallel to the spatial frequency axis define a set of spatial contrast sensitivity functions measured at different temporal frequencies (cf. Figure 5). Curves running parallel to the temporal frequency axis represent the temporal contrast sensitivity measured at different spatial frequencies. Human spatiotemporal contrast sensitivity is not space-time separable (Source: Kelly (1966); Kelly (1979a), Kelly (1979b)).

contrast sensitivity function and the temporal contrast sensitivity function ($2N = 120$). Sensitivity to any space-time pattern can be calculated from the products of these two functions.

While the observer's behavior as a whole is not space-time separable, it is not necessary that we forego all of the advantages of space-time separability. Thus, even though the observer's performance as a whole is not space-time separable, we may be able to describe the observer's performance as if it depends on the combination of a few space-time separable mechanisms[8]. We first saw this approach in Chapter when we studied the receptive field of retinal ganglion cells. Although their receptive fields are not space-time separable, we could model them as comprised of two space-time separable components, namely the center and surround.

Kelly (Kelly (1971a), Kelly (1971b), Kelly (1979a), Kelly (1979b); Kelly and Burbeck (1984)) has modeled the human spatiotemporal contrast sensitivity function as if visual sensitivity is limited by contributions from two space-time separable component. This description of contrast sensitivity is a single-resolution description, much like Schade's. The convolution kernel of the system is composed of a central and a surround region, much like a difference of Gaussian, in which the two components are each space-time separable. When the two components are summed, as for retinal ganglion cells, the resulting convolution is not separable. Using suitable parameters for the Gaussians and temporal parameters, it is possible to approximate the the contrast sensitivity surface by computing the output of the convolution kernel. This single-resolution convolution kernel provides a convenient method for computing the surface, but as we have seen in other parts of this chapter the single-resolution system does not generalize well to predict sensitivity to other space-time patterns.

Temporal Sensitivity and Mean luminance

The *temporal contrast sensitivity function* measures sensitivity to temporal sinusoidal variations in the stimulus contrast. Figure 24 (a) shows the temporal contrast sensitivity function measured at a variety of mean background intensities.

First, consider how contrast sensitivity to the lowest temporal frequencies varies with background intensity. At the very lowest background levels, contrast sensitivity increases with mean luminance. Once the mean background luminance reaches 5 trolands, contrast sensitivity to low frequencies changes by less than a factor of two while the background intensity changes over a factor of 100. For low temporal frequencies, contrast sensitivity remains relatively constant across changes in the mean background intensity. This is the form of light adaptation called Weber's Law.

Second, consider the contrast sensitivity at high temporal frequencies. For these tests, contrast sensitivity increases systematically at all background levels, a deviation from Weber's Law. The nature of the deviation can be clarified by replotting the data as shown in Figure 24 (b) where sensitivity is plotted as a function of the *amplitude* of the high frequency flicker, not

[8] Indeed, it is possible to show this is always a theoretical possibility. The result follows from an important representation in linear algebra called the *singular value decomposition*.

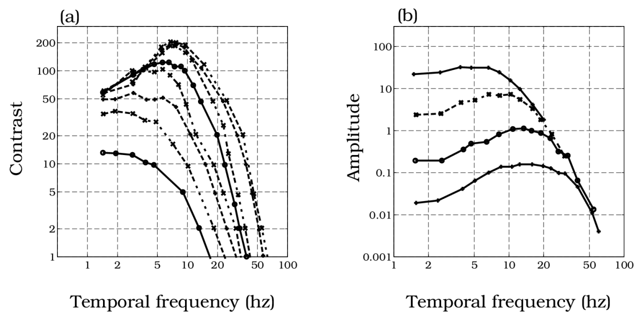

Figure 24: Human temporal sensitivity measured at various mean background illuminance levels. (a) Temporal contrast sensitivity. The spatial pattern was a two degree disk presented on a large background. Each curve measures contrast sensitivity (vertical axis) as a function of temporal frequency (horizontal axis). The curves show measurements on a variety of backgrounds In sequence from lowest curve to highest the mean luminance was 0.375, 1, 3.75, 10, 37.5, 100, 1000, 10,000 tds. Once the background illumination reaches roughly 5 trolands, contrast sensitivity to low temporal frequencies remains constant, consistent with Weber's law (Source: de Lange (1958)). (b) Temporal amplitude sensitivity. The spatial pattern was a 60 degree disk. Each curve measures the threshold amplitude, not contrast, as a function of temporal frequency. The mean background levels are 0.85, 7.1, 8.5 and 850 trolands. Notice that at high temporal frequencies the threshold amplitude appear to fall along a single curve, independent of the mean background level. This convergence is consistent with a purely linear response, involving and no light adaptation, for high temporal frequency stimuli (Source: Kelly (1961b)).

contrast (which is the amplitude divided by the mean level). When plotted as a function of amplitude, the temporal flicker sensitivity curves converge at high temporal frequencies. The convergence of the functions measured at many different mean luminance levels implies that sensitivity to high temporal frequency signals is predicted by the amplitude of the signal, not its contrast. This is the behavior one expects from a pure linear system, without light adaptation. In this temporal frequency range, then, Weber's Law does not describe the data well at all. These data show that light adaptation does not play a significant role in determining the visibility of high temporal frequency flicker.

Pattern-Color Sensitivity

There is a very powerful relationship between the wavelength composition of a target and our sensitivity to pattern. In Chapter we reviewed one of the most important factors that relates wavelength and pattern sensitivity: the chromatic aberration of the optics. The consequences of chromatic aberration are quite significant for the organization of the entire visual pathways. For example, based on the measurements we reviewed in earlier chapters, the chromatic aberration of the lens, coupled with the wide spacing of the B cones, imply that a signal beginning in the B cones can only represent signals less than 3–4 cycles per degree (cf. Figure 23). This compares to the basic optical and sampling limit of nearly 50 cpd for signals initiated by a mixture of R and G cones. The consequences of these neural limitations and others can be measured easily in people's ability to detect, discriminate and perceive colored patterns: People's ability to resolve short-wavelength patterns is very poor (Williams (1986)).

While it is easy to understand some of the relationship between pattern and color in terms of the optics and the cone mosaic, the limitations that relate color and pattern are best understood by thinking about the neural pathways that encode color, rather than the cones. A great deal of physiological and behavioral evidence (see Chapter and Chapter) demonstrate that we perceive color via neural pathways that combine the signals from the three cone classes. One pathway carries the sum of the cone signals, while other pathways, called *color opponent-pathways*, carry signals representing the difference between cone signals. Signals are represented on these pathways at very different spatial resolution (Mullen (1985); Noorlander and Koenderink (1983); Poirson and Wandell (1993); Sekiguchi et al. (1993b)).

High spatial frequency signals (20–60 cpd) appear to excite only the pathway formed by summing the cone signals. We experience these patterns as light-dark modulations around the mean luminance. Spatial frequency patterns below 12 cpd can excite a pathway that encodes the difference between L and M signals. Only the lowest spatial frequencies excite the third pathway, a pathway that includes the S cones.

These effects have been roughly understood for many years. For example, the color television broadcast system that is transmitted into many homes is organized into three color signals that correspond to a light-dark signal and two color difference signals. Only the light-dark signal includes high spatial frequency information about the image; the two color channels represent only low spatial frequency information. This representation is very efficient for transmission since leaving out high spatial frequencies in two of the signals permits a large compression in the bandwidth of the signal. Despite the missing spatial frequency information, the broadcast images do not appear spatially blurred. The reason is that the high spatial frequency color information that is omitted in the transmission is not ordinarily perceived.

The color pathways also differ in their temporal sensitivity. Perhaps the most important observation is based on the *flicker photometry* experiment. In this experimental procedure a pair of test lights alternate with one another. When the lights are alternated slowly the pattern appears to change between the colors of the two lights. When the lights alternate rapidly, observers fail to see the color modulation, and all differences appear as a light-dark modulation upon a steady colored background. Our temporal resolution for distinguishing blue-yellow flicker is poorest, red-green in the middle, and light-dark is best.

The relationship between spatial resolution and temporal resolution suggest a hypothesis that we considered in Chapter : namely, that spatial and temporal resolution covary because they are both related through the rigid motion of objects. If the most important source of temporal variation in the image is due to motions of the eye or motions of an object, temporal frequency and spatial frequency resolution should covary. At a single velocity, the motion of a low spatial frequency image produces a slower temporal variation than motion of a high spatial frequency image. Hence, in those wavelength bands where only low spatial frequencies are imaged the visual system may not require high temporal frequency resolution.

I have summarized the covariation of color, space and time in the color image shown in Figure 25. The image represents how color appearance varies across different spatiotemporal frequency ranges. We are trichromatic only in a relatively small range of low spatial and temporal frequencies represented near the origin of the figure. As the spatial or temporal frequency increases we fail to see blue-yellow variation and vision becomes dichromatic. At the higher spatial and temporal frequencies we are monochromatic, and we see only light-dark variation.

Retinal Eccentricity

The contrast senstivity measurements we have reviewed were all made using small patches of sinusoidal grating presented within the central few degrees of the visual field. As one measures contrast sensitivity at increasingly peripheral locations in the visual field, sensitivity decreases. There are a number of neural factors[9] that conspire to reduce both absolute sensitivity and spatial resolution. The density of the cone mosaic falls off rapidly as a function of visual eccentricity, so that there are fewer sensors available to encode the signal. The retinal ganglion cell density falls as well, as does the amount of cortical area devoted to representing the periphery. Approximately one half of primary visual cortex represents only the central ten

[9]The quality of the optics does not appear to decline significantly over the first 20 degrees of visual angle (Jennings and Charman (1981)).

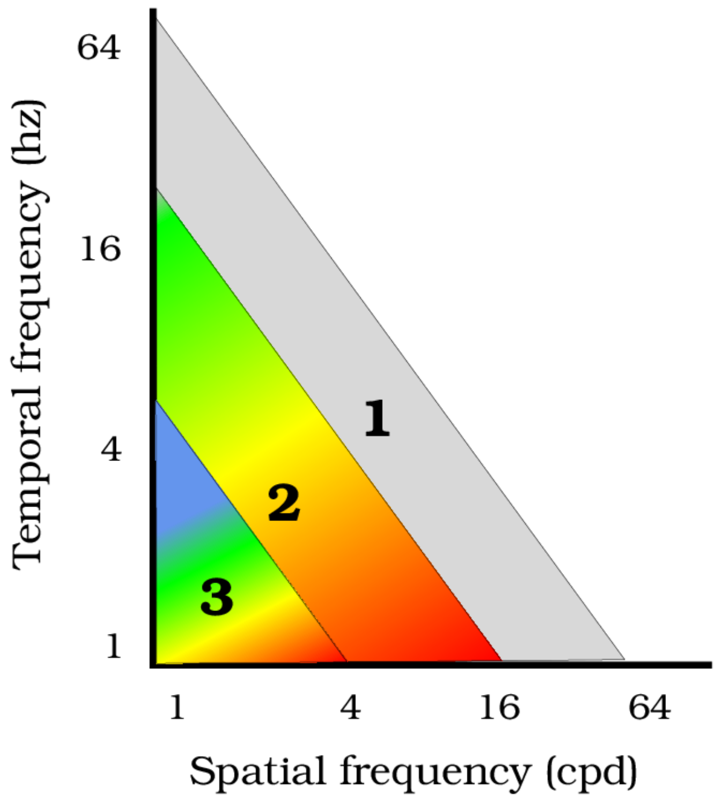

Figure 25: Color sensitivity and appearance depends on the spatiotemporal pattern. We perceive blue-yellow, red-green and light-dark variations at the lowest spatiotemporal frequencies. When the spatial frequency of the pattern exceeds 3 or 4 cpd, we fail to see blue-yellow variation. For spatial (temporal) frequencies greater than 16 cpd (Hz), we see the world only as light-dark modulations about the mean color. In this spatiotemporal region our perception is monochromatic.

degrees of the visual field (314 square degrees), while the remaing half of visual cortex must represents the rest of the visual field, which extends to a radius of 80 degrees (20,000 square degrees; see Chapter and Chapter .

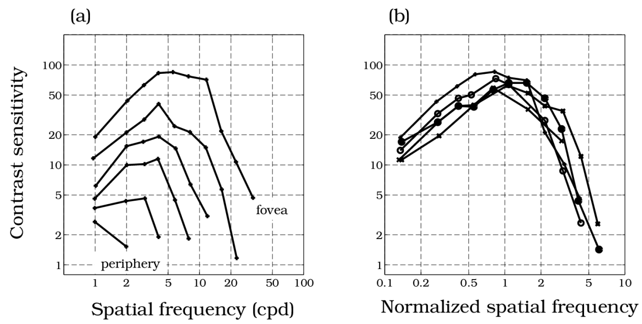

Figure 26: The contrast sensitivity function varies with retinal eccentricity. (a) Contrast sensitivity functions measured using a 1 deg x 2 deg grating patch at retinal eccentricities of 0, 1.5, 4, 7.5, 14, and 30 degrees retinal eccentricity are shown. Contrast sensitivity measured using this stimulus is highest in the fovea and falls dramatically with retinal eccentricity. (b) Contrast sensitivity functions measured with test stimulus scaled in size and spatial frequency in order to compensate roughly for the reduced cortical area devoted to different retinal eccentricities (Source: Rovamo et al. (1978)).

Figure 26 (a) shows a set of contrast sensitivity functions measured using a small grating patch at several different visual eccentricities. The top curve shows the observer's contrast sensitivity in the fovea. The observer's peak contrast sensitivity is 100 for gratings near 5-8 cpd, meaning that the observer can detect these at one percent contrast. In the fovea, the observer can resolve gratings as fine as 40-60 cpd. When the same stimulus is used to make measurements in the visual periphery, observers become less sensitive in all regards so that stimuli 30 degrees in the periphery have a peak sensitivity of 3 and an upper limit of 2 cpd.

We don't notice ordinarily this decrease in contrast sensitivity. When asked, most people believe that their spatial resolution is fairly uniform over a much wider extent of the image than just 2 degrees (their thumb nail at arms length). Yet, from the curves in Figure 26 (a), it is plain that our visual resolution is very poor by 7-10 degrees (a fist at arms length). Hence, our impression of seeing sharply over a large spatial extent must be due in part to our ability to integrate spatial information using eye movements.

Rovamo et al. (1978), Rovamo and Virsu (1979) and Virsu and Rovamo (1979) suggested that the decrease in contrast sensitivity with eccentric viewing can be explained quantitatively by the reduced representation of the visual field in the cortex. Qualitatively, the decrease in contrast sensitivity and the coarse neural representation of the periphery do parallel one another. The rough agreement between these factors is demonstrated by the results in Figure 26 (b). These contrast sensitivity functions, like those in Figure 26 (a), were made at different retinal eccentricities. For these measurements, however, the size and spatial frequency of the grating patch were scaled to compensate for the reduced cortical representation at that retinal eccentricity. When the size and spatial frequency of the stimulus are adjusted to compensate for the reduced cortical representation, the contrast sensitivity functions become fairly similar.

Visual performance deteriorates with eccentricity for all known spatial-acuity tasks and spatial localization tasks that we will review later in this chapter; but, the performance decrease as a function of retinal eccentricity varies considerably across observers and across tasks. The reduced representation of the periphery is present in all of the neural representations beginning with the photoreceptors and continuing into the central nervous system. The variance in observers' performance coupled with the wide number of neural representations with similar decrease in the peripheral representation, make it difficult to attribute the decline in performance with any single anatomical structure. The decline of acuity with eccentric viewing is an important and widespread feature of the visual system; it may not be possible to localize its cause to a single site in the visual pathways (e.g., Farrell and Desmarais (1990); Ludvigh (1941); Legge and Kersten (1987); Levi et al. (1985); Westheimer (1979), Yap et al. (1989)).

Linking Hypotheses

We have now reviewed several instances in which the variation of behavioral contrast sensitivity functions with stimulus conditions is similar to the variation of retinal ganglion cell responses. These correlations suggests that there is a causal relationship between the retinal ganglion cells receptive fields and the behavioral measurements. But, such a relationship is quite difficult to prove with the certainty that we would like to have. At this point, I think it is worth reviewing what we have learned about making such inferences.

Behavioral and neural theorizing supplement one another. Psychophysicists measure behavioral responses and then build theories about neural mechanisms. The properties of the theoretical neural mechanisms summarize the data and lead to new behavioral predictions. Neurophysiological measurements tell us about the neural activity directly. But, we must theorize about how the neural activity influences behavior. Each field contributes part of the information about visual function.

In an influential chapter in his book, Brindley (1960) called hypotheses that connect measurements in the two fields *linking hypotheses*. He took a very conservative view concerning the type of experiments that could be used to reason about physiology from performance. His comments initiated a discussion that continues to this day (Westheimer (1990); Teller (1990)). Brindley felt that the only truly secure argument connecting physiology and perception is this:

> ... whenever two stimuli cause physically indistinguishable signals to be sent from the sense organs to the brain, the sensations produced by these stimuli, as reported by the subject in words, symbols, or actions, must also be indistinguishable (Brindley (1970), p. 133.)

By stating his hypothesis clearly and forcefully, Brindley has drawn a great deal of attention to the problem of linking results between the separate disciplines. My purpose in writing this section is to question whether he may have succeeded too well; the emphasis on linking results from behavioral and physiological studies sometimes distracts us from assuring that the experimental logic within each discipline is complete.

We establish the most secure links between behavior and physiology when we first understand the separate measurements very well. For example, the relationship between the color-matching functions and photopigment sensitivities are strong because we have extensive quantitative studies, ranging over many measurement conditions, that tell us about each set of measurement conditions on their own. The color-matching experiment stands no matter what the photochemist observers, and the cone photopigment measurements stand no matter what the psychophysicist observes. Because each set of results stands powerfully on its own, we can feel confident that their relationship is a strong case for a connection between the two fields. If we require that the analysis within each discipline stands on its own, then when it comes time to join the two sets of observations we can have greater confidence in the link.

I mean to contrast the view stated here with an alternative approach in which the behaviorist uses the discovery of a particular neural response as the logical basis for a purely behavioral experiment. Or, conversely the case in which a physiologist explains a set of recordings in terms of some potentially related behavioral measure. Such ideas may be useful in the background to help formulate specific experimental measurements. But, the logic of theories and experiments based on a web of interconnections from behavior to physiology often serve to entangle our thinking.

Given this standard, what should we think about the connection between behavioral contrast sensitivity and neural receptive fields? In this chapter we have found that there is a powerful theory underlying behavioral contrast sensitivity functions. This theory is a good match to the logic of receptive field organization we reviewed in earlier chapters. The psychophysical results based on the contrast sensitivity function, however, do not fully support the basic theory. We cannot yet generalize from contrast sensitivity functions to sensitivity to other stimuli. Hence, the association between receptive field properties and contrast sensitivity functions are far more tentative than the connection between the color-matching functions and the photopigment spectral sensitivities.

Having stated this limitation in our current understanding, I don't think we should be discouraged. The similarities between the properties of the contrast sensitivity functions and neural receptive fields are too striking to ignore. By continuing to improve on the models for behavior and receptive fields separately, the links we forge and quantitative comparisons we make could well turn out to form a complete model, linking behavioral pattern sensitivity and neural receptive fields.

Spatial Localization

In this section we will review how well human observers can localize the position of a target. Wülfing (1892) showed that human observers can make surprisingly fine discriminations between the positions of two objects. Observers can reliably distinguish spatial offsets between a pair of lines as small as one fifth the width of a single cone photoreceptor. Moreover, people can distinguish this spatial offset even when the objects are moving (Westheimer (1979)).

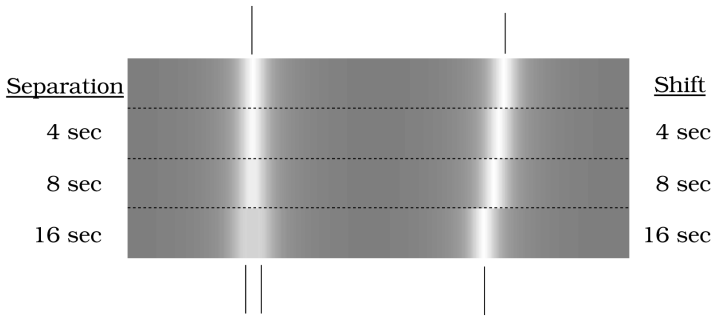

Figure 27: A comparison of localization and spatial resolution experiments. In a two-line spatial acuity experiment, the observer distinguishes between a stimulus consisting of a single line from a stimulus consisting of a pair of lines separated by a small amount. The images on the left side show the estimated retinal light distribution of a reference line and of three pairs of lines separated by increasing amounts. In a localization experiment, the observer distinguishes the position of a single line from the position of a displaced line. The images on the right side of the figure show a reference line and the estimated retinal light distribution of three offset lines.

The ability to discriminate between targets at different spatial positions is an aspect of human spatial resolution. It is important to recognize that that the ability to *localize* a target is different kind of resolution from the spatial resolution we measure when we ask observers to discriminate a pattern from a uniform background[10]. The differences between the tasks are illustrated in Figure 27 .The left side of the image in Figure 27 shows the estimated retinal light distributions of several stimuli a subject might be shown in a spatial resolution task. In this experiment, the subject must discriminate between the light distribution of a single dine line (top left) from the light distribution of a line-pair in which the two lines are separated by a small amount (bottom left). In this task, the stimuli are all centered at the same point, so there is no difference in where they are located. The right side of the image in Figure 27 (b) shows the retinal light distributions of stimuli a subject might be shown in a spatial localization task. In this experiment, the subject must discriminate the position of the retinal light distribution

[10]The terminology associated with these two types of spatial tasks can be confusing. The word *hyperacuity* refers to the fact that people localize spatial position with very high precision. Unfortunately, acuity is also used to refer to the spatial frequency sensitivity of the observer, which is a different matter. Here, I will use the term *localization* to refer to spatial resolution for position.

created by reference line (top right) from the positions of the light distributions of a line that is offset (bottom right).

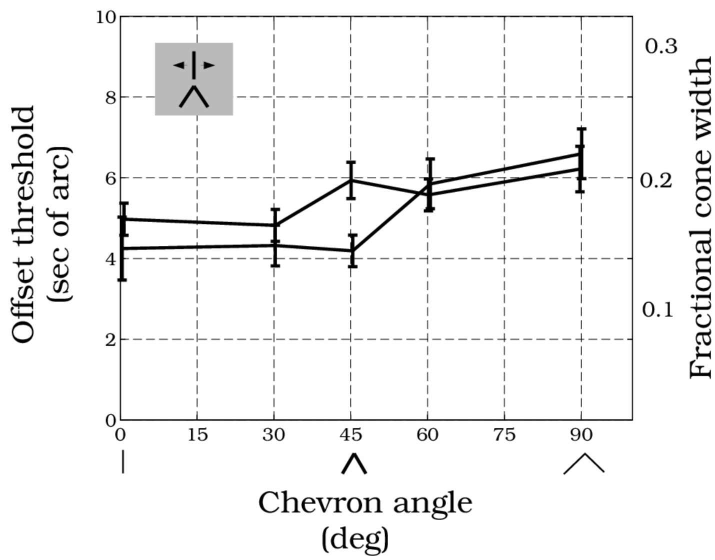

Figure 28: Localization sensitivity. Subjects detected whether a line was offset to the right or left of the tip of a chevron for a variety of angles of the opening of the chevron. Data from two observers are shown. Both observers could reliably report offsets as small as six seconds of arc (left vertical scale) which is one-fifth the width of a single photoreceptor (right vertical scale) (Source: Westheimer and McKee (1977)).

Westheimer and McKee (1977) measured observers ability to localize a line (see Figure 28). Subjects judged whether a line was located to the right or left of the tip of a chevron (see inset in the figure). The vertical axis of the graph measures the displacement needed to discriminate reliably when the line is offset from the middle of the chevron. This task was repeated for chevrons with various angles; for all angles, the offsets thresholds are on the order of 5 seconds of arc, roughly one-fifth the width of a single cone. Performance does not vary much as we change the stimulus. This suggests that localization performance is robust with respect to spatial manipulations of the target. This very fine localization applies to many different kinds of stimuli, including the relative positions of a pair of vertical lines, moving lines, and many other targets (Westheimer (1979)).

At first, it seems surprising to learn that we can localize targets at a finer resolution than the spacing of the cone mosaic. We know that the sampling grid determined by the cone mosaic imposes a fundamental limit on spatial pattern resolution through the phenomenon of aliasing (see Chapter). Shouldn't the cone mosaic also impose a limitation on our ability to localize position?

In fact, a coarse sampling grid does not eliminate the possibility of localizing a target precisely.

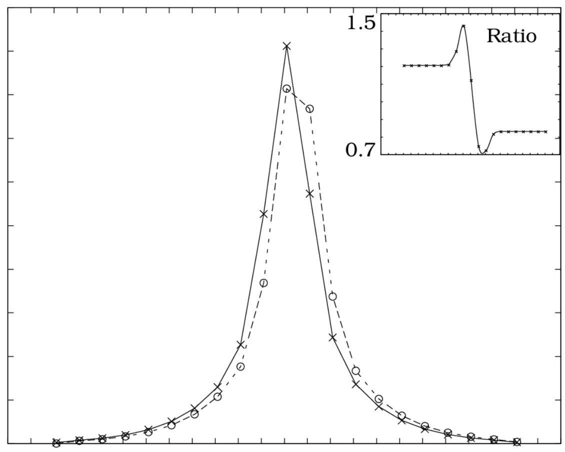

Figure 29: A physical basis for localization in localization tasks. The points in the main graph show the estimated rate of light absorption by foveal cones to a fine line. The x's show absorptions to a reference line and the open circles show the absorptions to a line offset by 12 seconds of arc. The tick marks on the horizontal axis are separated by the width of a single cone. The solid and dashed lines linearly connect the estimated absorption rates. The inset shows the ratio of cone absorptions from the reference line and the displaced line at each cone position. The graphs shows that a 12 sec shift, roughly 1/3 the width of a photoreceptor, changes the cone absorption rate by as much as 50 percent. This information can be used to localize the position of the line at a resolution that is substantially finer than the separation between cones.

The physical principles we can use to achieve fine spatial localization on a coarse sampling grid are illustrated in Figure 29. The main portion of the figure shows the pattern of cone absorptions we expect in response to a reference line centered over a cone and a line that is displaced to the right by 12 sec of arc. The separation between the tick-marks on the horizontal axis are set at 30 sec, the size of an individual cone. The values were calculated using Westheimer's optical linespread function (Chapter).

Because the offset is very small compared to the sampling, the same cones respond to the reference line and the offset line. It follows that the identity of the cones cannot be used to estimate the locations of the two lines. Although the same cones respond to the two lines, the spatial pattern of cone absorptions when the lines are in these two positions is quite different. The inset to Figure 29 shows the ratio of the cone absorptions to the two different lines. A small spatial shift of 12 sec of arc causes a fifty percent change in the absorption rate at an individual cone. Hence, the *spatial pattern of absorption rates* is a reliable signal that can be interpreted to infer that the line position at a resolution finer than the spacing of the cone mosaic.

Notice that the optical blurring of the light distribution is essential if we wish to localize the line at positions finer than the sampling grid. Were there no optical blurring, the image of a line would fall within the width of a photoreceptor and spatial displacements less than a photoreceptor width would not be detectable. Optical blur, which seems like a nuisance when we consider spatial resolution of contrast patterns, is a help when we consider spatial resolution to localize targets.

Our ability to localize the position of edges and lines is very robust with respect to various stimulus manipulations. If we vary the target contrast, set the display into motion, or flash the display briefly, performance remains excellent. Since performance is robust with respect to these experimental manipulations, it is clear that the simple calculation shown in Figure 29 is only a demonstration of how localization is possible. The visual system must use a much more sophisticated and robust method to calculate position than the simple calculation described in the figure. Eye movements during examination of a static display, or tracking errors during examination of a visual display, will make it impossible to compare the outputs of a single small set of cones. Rather, people must be capable of estimating the position at fine precision even though the precise identity of the cones mediating the signal varies. Although we have some basic principles to work from, how we estimate the relative position of moving targets using active eyes remains an important challenge to study.

Summary

Theories of human pattern sensitivity are organized around a few basic principles. In the earliest and simplest theories, the visibility of different types of test patterns was explained by the properties of a single shift-invariant linear system. This type of theory is simple for computation and also parallels nicely our understanding of the initial encoding of light by retinal nerve cells in certain visual streams. The convolution kernel of the shift-invariant linear system and the neural receptive field play analogous roles and provide a natural basis for comparison of behavioral and physiological data. By using common experimental measures, such as contrast sensitivity functions, the properties of neural mechanisms and behavioral theories can be compared directly.

While certain aspects of single-resolution theories provide a reasonable description of human pattern sensitivity, they fail a number of direct empirical tests. Consequently, theorists have tried to assemble new theories in which the pattern representation is based on a collection of shift-invariant representations, not just a single one. This idea parallels the physiological notion that the visual system contains a set of visual streams. The more complex modern theories must specify a larger number of convolution kernels (receptive fields). To keep these organized, and to parallel some of the properties of cortical receptive fields, theorists generally choose convolution kernels that respond best to restricted bands of spatial frequency and to restricted stimulus orientations. These theories can predict more experimental results, but there remain many computational and experimental challenges before we will have a complete satisfactory theory of pattern sensitivity.

Because human vision constantly adapts to new viewing conditions, human pattern sensitivity cannot be described by a single pattern sensitivity function. Pattern sensitivity covaries with the temporal properties of the test stimulus, the mean background level, and with the wavelength composition of the stimulus. Thus, a general specification of human pattern sensitivity must take all of these factors into account.

Behavioral experiments show that people are also exquisitely sensitive the spatial location of targets. Observers can localize test stimuli to a resolution that is considerably finer than the spacing of the cone mosaic. The ability to localize is quite robust, surviving many different stimulus manipulations. The principles of how one might local to a very fine resolution are clear, but the methods that the visual pathways use to acquire the necessary information remain to be determined.

Multiresolution Representations

Multiresolution overview

Our review of the organization of neural and behavioral data have led us to several specific hypotheses about how the visual system represents pattern information. Neural evidence suggests that visual information is segregated into a number of different visual streams that are specialized for different tasks. Behavioral evidence suggests that within the streams that are specialized for pattern sensitivity, information is further organized by local orientation and spatial scale and color. All of the evidence we have reviewed to this point suggest that image contrast, rather than image intensity, is the key variable represented by the visual pathways.

We will spend this chapter mainly just thinking about how these and other organizational principles might be relevant to solving various visual tasks. In addition to the intrinsic and practical interest of solving visual problems, finding principled solutions for visual tasks can also be helpful in understanding and interpreting the organization of the human visual pathways.

But, which tasks should we consider? There are many types of visual problems; only some of these have to do with tasks that are essential for human vision. One approach to thinking about visual algorithms, then, is to adopt a general approach to vision, sometimes called *computational vision*, in which we do not restrict our thinking to those problems that are important for human vision. Instead, we open our minds to visual algorithms that may have no biological counterpart.

In this book, however, we will restrict our analysis to the subset of algorithms that is related to human vision. While this is not the broadest possible class, it is a very important one because there are many potential applications for visual algorithms that emulate human performance. For example, suppose a person who wants to search through a database of images to find images with "red vehicles." To assist the person, the computer program must have some algorithmic representation related to human vision; after all, the words "red" and "vehicle" are defined by human perception. This is but one example from the set of computer vision algorithms that can serve to augment the human ability to manipulate, analyze, search and create images. These algorithms will be of tremendous importance over the next few decades.

There is a second reason for paying special attention to visual problems related to human vision. Many investigators have argued that studying the visual pathways and visual behavior is an efficient method for discovering novel algorithms for computational vision. The idea is that by studying the specific properties of a successful visual system, we will be led to an understanding of the general design principles of computational vision. This process is analogous to the idea of *reverse-engineering* that is often used to improve instrument design in manufacturing. This view has been suggested by many authors, but Marr (2010) has argued particularly forcefully that biology is a good source of ideas for engineering design. I have never been persuaded by this argument; it seems to me that reverse-engineering methods are most successful when one understands the fundamental principles and only wishes to improve the implementation. It is very difficult to analyze how a system works from the implementation unless one already has a set of general principles as a guide. I think engineering algorithms have done more for understanding the neuroscience than neuroscience has done for engineering algorithms.

Whichever way the benefits flow, from neuroscience to engineering or the other way around, just the presence of a flow is a good reason for the vision scientist and imaging engineer to be familiar with biological, behavioral, and computational issues. In the remainder of this book, we will spend more time engaged in thinking about computational issues related to human vision. In this chapter I will describe ideas and algorithms related to multiresolution image representations. In the following chapters I will describe work on color appearance, motion and objects. Algorithms for all of these topics continue be an important part of vision science and engineering.

Efficient Image Representations

In this chapter we will consider several different multiresolution representations. Multiresolution representations have been used as part of a variety of visual algorithms ranging from image segmentation to stereo depth and motion (e.g., Burt (1988); Vetterli and Metin UZ (1992)). To unify the introduction of these various representations, however, I will introduce them all by considering how they solve a single engineering problem: efficient storage of image image information.

Efficient image representations are important for systems with finite resources, which is to say all systems. No matter how much computer memory or how many visual neurons we have, we can always perform better computations, transmit more information, or store higher quality images if we use efficient storage algorithms. If we fail to consider efficiency, then we waste resource that could improve performance.

Image compression algorithms transform image data from one representation to a new one that requires less storage space. To evaluate the efficiency of a compression algorithm, we need some way to describe the amount of space required to store an image. The most common way to measure the amount of storage space necessary to encode an image is to count the total number of bytes used to represent the image[1]. Color images acquired from cameras or

[1] A bit is a single **b**inary dig**it**, that is, 0 or 1. A byte is 8 bits and represents 256 levels (2^8). A megabyte is 10^6 bytes, while a gigabyte is 10^9 bytes.

scanners, or color images that are about to be displayed on a monitor, are represented in terms of the intensities at a set of picture locations, called *pixels*. The color data are represented in three color bands, usually called the red, green and blue bands. We can compute the number of bytes data represented in a single image fairly easily. Suppose we have a modest size image of 512 rows and 512 columns, and that each color band represents intensity using one byte. The image representation within a single color band requires $512 \times 512 \times 3$ bytes of data, or approximately 0.75 Megabytes of data. If we have an image comprising 1024 rows and columns, we will require 3.0 Megabytes to represent the image. In a movie clip, in which we update the image sixty times a second, the numbers grow at an alarming rate; one minute requires 10 Gigabytes of information, and one hour requires 600 Gigabytes.

Notice that color image encoding already uses a significant amount of image compression that is made possible by the special characteristics of human vision. The physical signal consists of light with energy at many wavelengths, i.e., a complete spectral power distribution. The image data, however, does not encode the complete spectral power distribution of the displayed or acquired color signal. The data represent only three color bands, a very compressed representation of the image. The results of the color-matching experiment justifies the compression of information (see Chapter 4). This part of compression is so well understood, it is rarely mentioned explicitly in discussions of image compression.

In addition to color trichromacy, two main factors permit us to compress images with little loss of quality. First, adjacent pixels in natural images tend to have similar intensity levels. We say that there is considerable *spatial redundancy* in these images. This redundancy is part of the signal, and it may be removed without any loss of information in order to obtain more efficient representations. Second, we know that human spatial resolution to certain spatial patterns is very poor (see Chapter and Chapter). People have very poor spatial resolution to short-wavelength light, and only limited spatial resolution for colored patterns in general. Representing this information in the stored image is unnecessary because the receiver, that is the visual system, cannot detect it. By eliminating this information, we improve the efficiency of the image representation.

In this chapter we will consider efficient encoding algorithms of monochrome images, spending most of our time on issues of intensity and spatial redundancy. In the next Chapter , which is devoted to color broadly, we will again touch on some of the issues of color image representation.

Intensity Redundancy in Image Data

Suppose that we have an image we wish to encode efficiently, such as the image in Figure 1 (a). The camera I used to acquire this image codes up to 256 different intensity levels (8 bits). You might imagine, therefore, that this is an 8 bit image. To see why that is not the case, let's look at the distribution of pixel levels in the image.

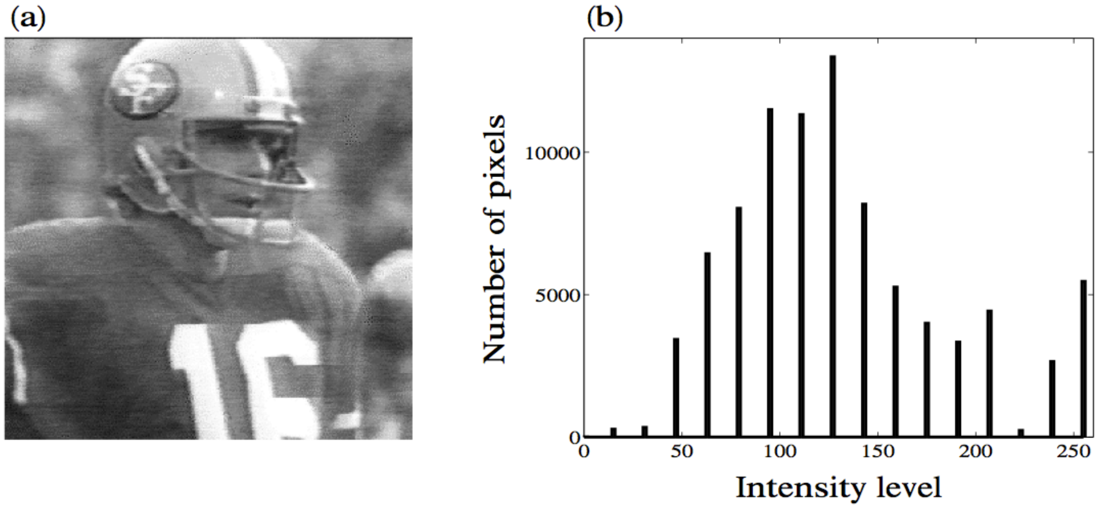

Figure 1: The distribution of image intensities is an important factor in obtaining an efficient image representation. (a) This image was acquired by a device capable of reproducing 256 gray-levels. But, the image data consists of only 16 different gray levels. (b) A histogram of the gray levels used to code the image shown in (a). Device properties limit the gray-level resolution; they do not enforce a resolution.

In Figure 1 (b) I have plotted the number of points in the image at each of the 256 intensity levels the device can represent. This graph is called the image's *intensity histogram*. The histogram shows that intensity level 128 occurs quite frequently and only a few other levels occur at all.

Although the device used to acquire this image could potentially represent 256 different intensity levels, the image itself does not contain this many levels. We do not need to represent the data at the device resolution, but only at the intrinsic resolution of the image, which is considerably smaller. Since the image in Figure 1 (a) contains 16 levels, not 256, we can represent it using 4 bits per image point rather than the 8 bit resolution the device can manage. This saves us a factor of two in storage space.

The first savings in efficiency is easy to understand; we must not allocate storage space to intensity levels that do not occur in the image. We can refine this idea by taking advantage of the fact that the different intensity levels do not occur with equal frequency. Consider one method to take advantage of the fact that some intensity levels are more likely than others. Assign the one-bit sequence, 1, to code level 128. Encode the other levels using a five bit sequence that starts with a zero, say $0xxxx$, where $xxxx$ is the original four bit code. For example, the level 5 is coded by the five bit sequence 00101. We can unambiguously decode an input stream as follows. When the first bit is a one, then the current value is 128. When the first bit is a zero, read four more bits to define the intensity level at that pixel.

In this image, the intensity level 128 occupies sixty percent of the pixels. Our encoding scheme reduces the space devoted to coding these pixels from 4 bits to 1 bit, saving 3 bits at 60 percent of the locations. The encoding method costs us 1 bit of storage for 40 percent of the pixels. The average savings across the entire image is $0.6 \times 3 - 0.4 \times 1 = 1.2$ bits per pixel. Using these very simple rules, we have reduced our storage requirements to 2.8 bits per pixel.

The example I have provided here is very simple; many more elaborate and efficient algorithms exist for taking advantage of the redundancies in a data set. In general, the more we know about the input distribution the better we can do at designing efficient codes. A great deal of thought has been to the question of designing efficient coding strategies for single images and also for various classes of images such as business documents and natural images. I will not review them here, but you will find references to books on this topic in the bibliography.

Spatial Redundancy in Image Data

Normally, intensity histograms of natural images are not as coarsely discretized as the example in Figure 1. In natural images, intensity distributions range across many intensity levels and strategies that rely only on intensity redundancy do not save much storage space.

But there are *spatial redundancies* in natural images, and we can use the same general encoding principles we have been discussing to take advantage of these redundancies as well. Specifically, certain spatial patterns of pixel intensities are much more likely than others. There are various formal and informal ways to convince oneself of the existence of these spatial redundancies. First, consider the image in Figure 2. This figure contains a picture of Professor Horace Barlow, an eminent visual scientist. A few of the pixel intensities have been set randomly to a new intensity value. Kersten (1987) has shown that naive observers are quite good at adjusting the intensity of these pixels back to their original intensity. With one percent of the pixels deleted, observers correct the pixel intensity to its original value nearly 80 percent of the time. Even with forty percent of the pixels deleted observers set the proper intensity level more than half the time.

Second, we can measure the spatial redundancy in natural images by comparing intensities at neighboring pixels. Figure 3 (a) shows the pixel intensities from the image shown in the center of the figure. Measured one at a time, the pixel intensities are distributed across many values and do not contain a great deal of redundancy. Figure 3 (b) shows an image *cross-correlogram* that measures the intensity of a pixel, $p(x, y)$, on the horizontal axis and the intensity of its neighboring pixel, $p(x, y + 1)$, on the vertical axis. Because adjacent pixels tend to have the same intensity level, the points in the cross-correlogram cluster near the identity line. Because the intensity of one pixel tells us a great deal about the probable intensity level of an adjacent pixel, we know that the pixel intensity levels are redundant.

We can improve the efficiency of the image representation by removing this spatial redundancy. One way of removing the redundancy is to transform the image representation. For example, instead of coding the intensities at the two pixels at adjacent locations independently, we can

Figure 2: Experimental measurement of spatial redundancy in an image. The image shows Professor Horace Barlow; random noise is added to the picture. Subjects were asked to adjust the intensity of the noisy pixels to the level they thought must have been present in the original image. Subjects are very accurate at this task, using the information present in nearby pixels. This is an experimental demonstration that people can take advantage of the spatial redundancy in image data (Source: Kersten (1987)).

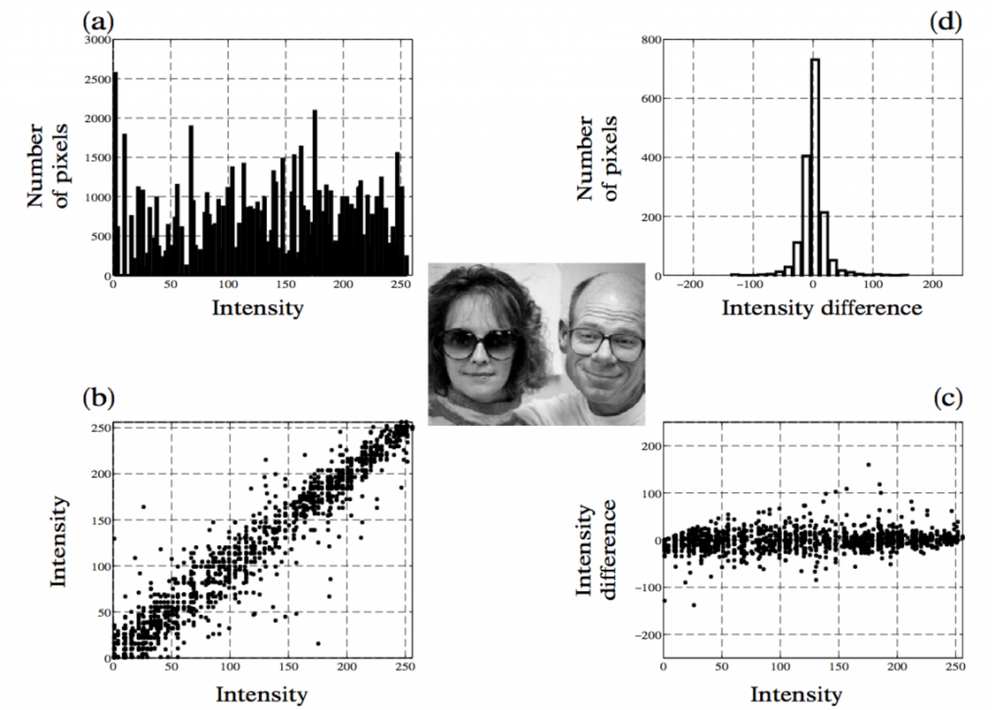

Figure 3: Computational measurement of spatial redundancies in a natural image. The natural image used for these computations is shown in the middle. (a) The image intensity histogram shows the distribution of image intensities. (b) A correlogram of the intensity at a pixel located at position (x,y) and the intensity of a pixel located at position (x,y+1). (c) A correlogram of the intensity at a pixel located at position (x,y) and the intensity difference between it and the adjacent pixel at (x,y+1). (d) A histogram of the intensity differences showing that they are concentrated near the zero level.

code one pixel level, $p(x, y)$ and the difference between the adjacent pixel values, $p(x, y+1) - p(x, y)$. This pair of values preserves the image information since we can recover the original from $p(x, y)$ and $p(x, y+1) - p(x, y)$ by a simple subtraction.

After transforming the data, the number of bits needed to code $p(x, y)$ is unchanged. But the difference, $p(x, y+1) - p(x, y)$, can fall in a larger range, anywhere between 255 and -255 so that we may need as many as 9 bits to store this value. In principle, requiring an additional bit is worse, but in practice the difference between most adjacent pixels is quite small. This point is illustrated by the cross-correlogram of the transformed values shown in Figure 3 (c). The horizontal axis measures the pixel intensity $p(x, y)$, and the vertical axis measures the difference value, $p(x, y+1) - p(x, y)$. First, notice that most of the values of the intensity difference cluster near zero. Second, notice that there is virtually no correlation between the transformed values; knowing the value of $p(x, y)$ does not help us know the value of the difference.

To build an efficient representation, we can use the same strategy I outlined in the previous section. We use a short code (say, 5 bits) to encode the small difference values that occur frequently. We use a longer code (say, 10 bits) to encode the rarely occurring large values. Because most of the pixel differences are small, the representation will more efficient.[2]

Decorrelating Transformations

We can divide the image compression strategies I have discussed into two parts. First, we linearly transformed the image intensities to a new representation by a linear transformation. The linear transformation computes $p(x, y)$ and $p(x, y) - p(x, y+1)$ from $p(x, y)$ and $p(x, y+1)$. The matrix form of this transformation is simply

$$\begin{pmatrix} p(x, y) \\ p(x, y+1) - p(x, y) \end{pmatrix} = \begin{pmatrix} 1 & 0 \\ -1 & 1 \end{pmatrix} \begin{pmatrix} p(x, y) \\ p(x, y+1) \end{pmatrix} \tag{0.1}$$

We apply the linear transformation because the correlation of the transformed values is much smaller than the correlation in the original representation.

Second, we find a more efficient representation of the transformed representation. Because we have removed the correlation, in natural images the variation of the transformed values will be smaller than the variation of the original pixel intensities. Hence we will be able to encode the transformed data more efficiently than the original data.

[2]We could improve even this coding strategy in many different ways. For example, after the first pair of pixels we never need to encode an absolute pixel level, we can always encode only differences between adjacent pixels. This is called Differential Pulse Code Modulation, or *DPCM*. Or, we could consider the pair of pixels as a vector, calculate the frequency distribution of all possible vectors, and build an efficient code for sending communicating the values of these vectors. This is called Vector Quantization, or *VQ*. All of these methods trade on the fact that natural images are more likely to contain some spatial patterns than others.

From our example, we can identify a key property of the linear transformation that is essential for achieving efficient coding. The new transformation should convert the data to *decorrelated* values. Values are decorrelated when we gain no advantage in predicting one value from knowing the other. It should seem intuitive that decorrelation is important part of efficiency: if we can predict one value from the another, there is no reason to encode both. Generalizing this idea, if we can predict approximately predict one value from another, we can achieve some efficiencies in our representation. In our example we found that the value $p(x, y)$ is a good predictor of the value $p(x, y + 1)$. Hence, it is efficient to predict that $p(x, y + 1)$ is equal to $p(x, y)$ and to encode only the error in our prediction. If we have a good predictor (i.e., high correlation) the prediction error will span a smaller range than the data value. Hence, the error can be encoded using fewer bits and we can save storage space.

The transformation in Equation 0.1 does yield a pair of approximately decorrelated values. To make the example simple, I chose a simple linear transformation. We might ask how we might find a decorrelating linear transformation in general. When the set of images we will have to encode is known precisely, then the best linear transformation for lossless image compression can be found using a matrix decomposition called the *singular value decomposition*. The singular value decomposition defines a linear transformation from the data to a new representation with statistically independent values that are concentrated over smaller and smaller ranges. This representation is just what we seek for efficient image encoding. The singular value decomposition is at the heart of principal components analysis and goes by many other names including the Karhunen-Loeve transform and the Hoteling transform. The singular value decomposition may be the most important technique in linear algebra.

In practice, however, the image population is not known precisely. Nor are the image statistics for the set of natural images are known precisely. As a result, the singular value decomposition has no ready application to image compression. As a practical matter, then, selecting a good initial linear transformation remains an engineering skill acquired by experience with algorithm design.

Lossy Compression

To this point, we have reviewed compression methods that transform the original data with no loss of information. Since we can recover the original image data perfectly from the compressed data, the methods are called *lossless* image compression. Ordinarily, we can achieve savings of a factor of two or three based on lossless compression methods, though this number is strongly image dependent.

If we are willing to tolerate some difference between the original image and the stored copy, then we can develop schemes that save considerably more space. Transformations that lose information are called *lossy* image compression methods. Using only three sensor responses to represent color information is the most successful example of a perceptually lossless encoding. We can not recover the original wavelength representation from the encoded signal. Still, we use this lossy representation because we know from the color-matching experiment that when done perfectly there should be no difference between the perceived image and the original image Chapter .

Lossy compression is inappropriate for many types of applications, such as storing bank records. But, some amount of image distortion is acceptable for many applications. It is possible to build lossy image compression algorithms for which the difference between the original and stored image is barely perceptible, and yet the savings in storage space can be as large as a factor of five or ten. Users often judge the efficiency to be worth the image distortion. In cases when the image distortion is not visible, some authors refer to the compression as *perceptually lossless*.

As we reviewed in Chapter and Chapter , the human visual system is very sensitive to some patterns and wavelengths but far less sensitive to others. Perceptually lossless encoding methods are designed to account for these differences in human visual sensitivity. These schemes allocate more storage space to represent highly visible patterns and less storage space to represent poorly visible patterns (Watson and Ahumada (1989); Watson (1990)).

Perceptually lossless image encoding algorithms follow a logic that has much in common with the lossless encoding algorithms. First, the image data are transformed to a new set of values, using a linear transformation. The transformed values are intended to represent *perceptually decorrelated features*. Second, the algorithm allocates different amounts of precision to these transformed values. In this case, the precision allocated to each transformed value depends on the visual salience of the feature the value represents; hence, salient features are allocated more storage space than barely visible features. It is at this point in the process where lossy algorithms differ from lossless algorithms. Lossless algorithms allocate enough storage so that the transformed values are represented perfectly, yet due to the decorrelation they still achieve some savings. Lossy algorithms do not allocate enough storage to perfectly represent the initial information; the image cannot be reconstructed perfectly from the compressed representation. The lossy algorithm is designed, however, so that the lost information would not have been visible anyway. Thus, the new picture will require less storage and still look like the original image.[3]

Perceptually Decorrelated Features

In my overview of perceptually lossless compression algorithms, I used — but did not define — the phrase "perceptually decorrelated features." The notion of a "perceptual feature" is widely used in a very loose way to describe the image properties that are essential for object perception. There is no widely agreed on the specific image features that comprise the perceptual features. In the context of image compression, however, we can use a very useful operational definition

[3]In practice, lossy and lossless compression are concatenated to compress image data. First a lossy compression algorithm is applied, followed by a lossless algorithm.

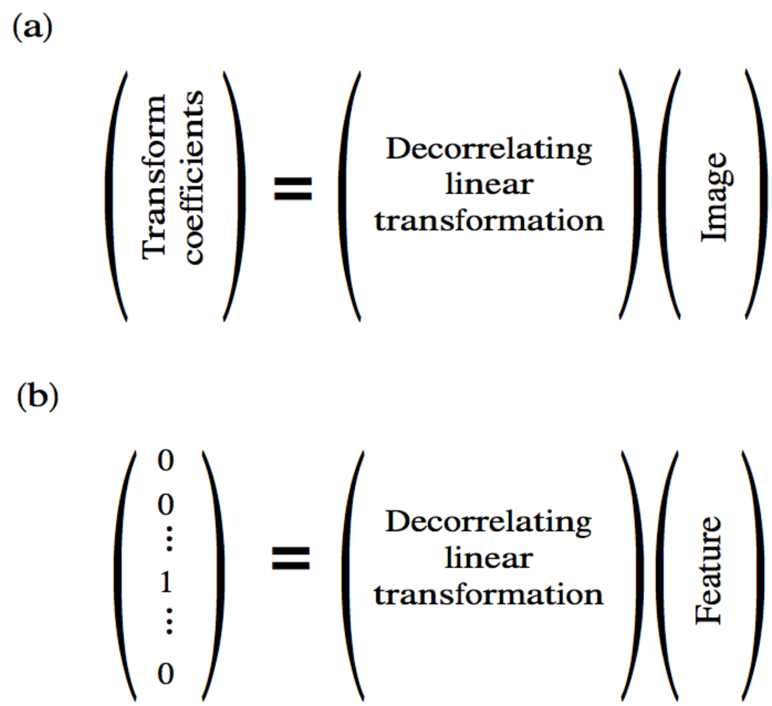

Figure 4: An operational definition of perceptual features. (a) Image compression usually begins with a linear transformation that maps image intensities into a set of transformed coefficients. (b) An operational definition of an image feature, associated with that linear transformation, is to find the image whose transformation results in a representation that is zero at all values except for one transformation coefficient.

for perceptual feature, defined in terms of the linear transformation used to decorrelate the image data. The idea is illustrated in the matrix tableau drawn in Figure 4.

Suppose we represent the original image as a list of intensities, one intensity for each pixel in the image. We then apply a linear transformation to the image data, as shown in Figure 4 (a), to yield a new vector of *transform coefficients*. This is the same procedure we applied in our simple example defined by Equation 0.1.

In the transformed representation, each value represents something about the contents of the input image. One way to represent the visual significance of each transformed value is to identify an input image that is represented by that transform coefficient alone. This idea is illustrated in Figure 4 (b), in which a feature is defined as the input image that is represented by a set of transform coefficients that are zero everywhere except at one location. We call this image the *feature* represented by this transform coefficient. Using this operational definition, features are defined with respect to a particular linear transformation.

Next, we must define what we mean by "perceptually decorrelated" image features. We can use the Kersten (1987) experiment to provide an operational definition. In that experiment subjects adjusted the intensity of certain pixels to estimate the intensity level in the original image. Kersten found that observers inferred the intensity levels of individual pixels quite successfully and that observers perceived a great deal of correlation when comparing individual pixels. We can conclude that pixels are a poor choice to serve as decorrelated features.

Now, suppose we perform a variant of Kersten's experiment. Instead of randomly perturbing pixel values in the image, suppose that we perturb the values of the transform coefficients. And, suppose we ask subjects to adjust the transform coefficient levels to reproduce the original image. This experiment is the same as Kersten's task except except we use the transform coefficients, rather than individual pixels, to control image features.

We concluded that individual pixels do *not* represent perceptually decorrelated features because subjects performed very well. We will conclude that a set of transform coefficients represent decorrelated features only if subjects perform badly. When knowing all the transform coefficients but one does not help the subject set the level of an unknown coefficient, we will say the features represented by the transformation are perceptually independent. I am unaware of perceptual studies analogous to Kersten's that test for the perceptual independence of image features; but, in principle, these experiments offer a means of evaluating the independence of features implicit in different compression algorithms.

The important compression step in perceptually lossless algorithms occurs when we use different numbers of bits to represent the transform coefficients. To decide on the number of bits allocated to a transform coefficient, we consider the visual sensitivity of the image feature represented by that coefficient. Because visual sensitivity to some image features is very poor, we can use very few bits to represent these features with very little degradation in the image appearance. This permits us to achieve very compact representations of image data. By saving information at the level of image features, the perceptual distortion of the image can be quite small while the efficiencies are quite large.

This compression strategy depends on the perceptual independence of the image features. If the features are not independent, then the distortions we introduce into one feature may have unwanted side effects on a second feature. If the observer is sensitive to the second feature, we will introduce unwanted distortions. Hence, discovering a set of image features that are perceptually independent is an important part of the design of a perceptually lossless image representation. If distortions of some features have unwanted effects on the appearance of other features, that is if the representation of a pair of features is perceptually correlated, then the linear transformation is not doing its job.

A Block Transformation: The JPEG-DCT

The Joint Photographic Experts Group (JPEG) committee of the International Standards Organization has defined an image compression algorithm based on a linear transformation called the *Discrete Cosine Transformation* (DCT). Because of the widespread acceptance of this standard, and the existence of hardware to implement the JPEG-DCT compression algorithm is likely to appear on your desk and in your home within the next few years. The JPEG-DCT compression algorithm has a multiresolution character and bears an imprint from work in visual perception[4].

The JPEG-DCT algorithm uses the DCT to transform the data into a set of perceptually independent features. The image features associated with the DCT are shown in Figure 5. The image features are all products of cosinusoids at different spatial frequencies and two orientations. Hence, the independent features implicit in the DCT are loosely analogous to a collection of oriented spatial frequency channels. The features are not the same as the features used to model human vision since the DCT image features are comprised of high and low frequencies, while others contain signals with perpendicular orientations. Still, there is a rough similarity between these features and the oriented spatial frequency organization of models of human multiresolution representations; this is particularly so for the features pictured along the edges and along the diagonal in Figure 5, where the image features are organized along lines of increasing spatial frequency and within a single orientation.

The main steps of the JPEG-DCT algorithm are illustrated in Figure 6. First, the data in the original image are separated into blocks. The computational steps of the algorithm are applied separately to each block of image data, making the algorithm well-suited to parallel implementation. The image block size is usually 8×8 pixels, though it can be larger. Because the algorithm begins by subdividing the image into blocks, it is one of a group of algorithms called *block coding* algorithms.

Next, the data in each image block are transformed using the linear DCT. The transform coefficients for the image block are shown as an image in Figure 6 labeled "Transform coefficients." In this image white means a large absolute value and black means a low absolute

[4] The DCT is similar to the Fourier Series computation reviewed in Chapters Chapter and the **Appendix**.

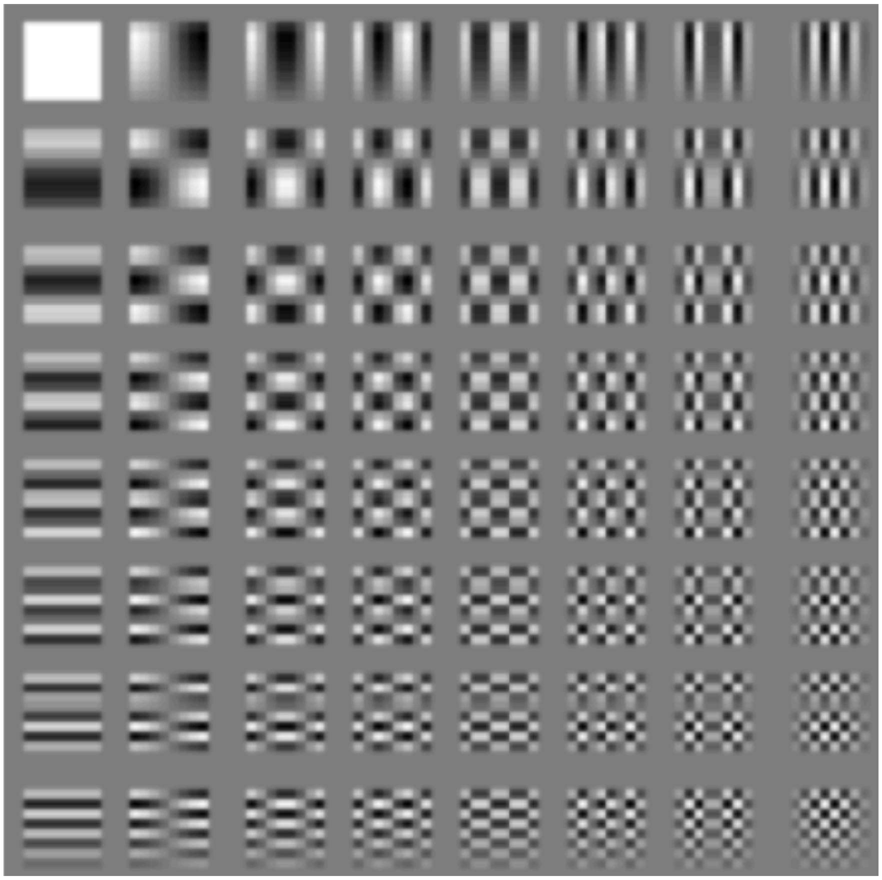

Figure 5: The perceptual features of the DCT. The DCT features are products of harmonic functions, cos(2 f_1 j)cos(2 f_2 k), where j and k refer to position along the horizontal and vertical directions. These functions have both positive and negative values, and they are shown as contrast patterns varying about a constant gray background.

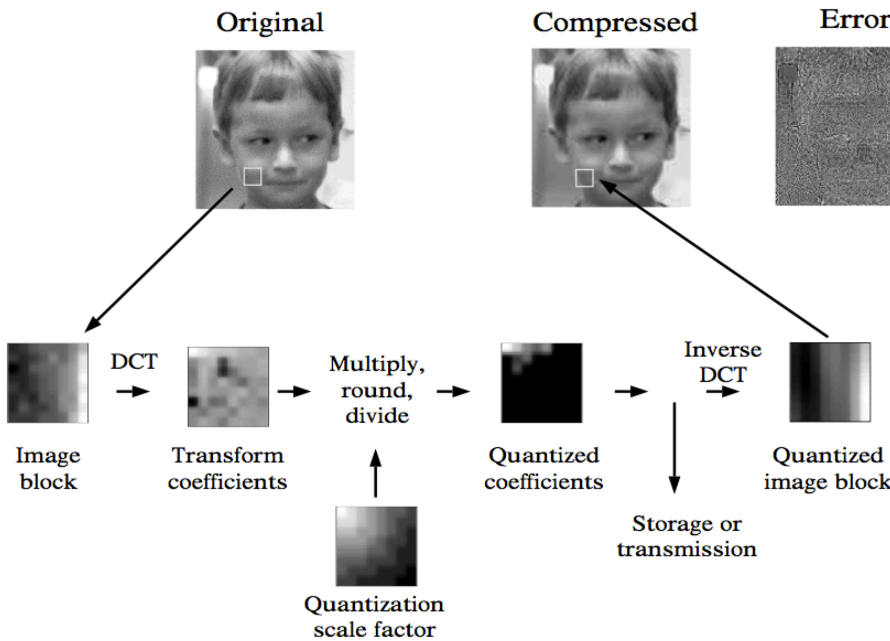

Figure 6: An outline of the JPEG compression algorithm based on the DCT. The original image is divided into a set of nonoverlapping square blocks, usually 8x8 pixels. The image data are transformed using the DCT to a new set of coefficients. The transform coefficients are quantized using a simple multiply-round-divide operation. The quantized coefficients are zeroed by this operation, making the image well-suited for efficient lossless compression applied prior to storage or transmission. To reconstruct the image, the quantized coefficients are converted by the inverse DCT, yielding a new image that approximates the original. The error in the reconstruction, i.e., the difference between the original and the reconstruction, consists of mainly high frequency texture. The error is shown as an image on the right.

value. The coefficients are represented in the same order as the image features in Figure 5; the low spatial frequencies coefficients are in the upper left of the image and the high spatial frequency coefficients are in the lower right.

In the next step, the transform coefficients are quantized. This is one stage of the algorithm where compression is achieved. The quantization is implemented by multiplying each transform coefficient by a scale factor, rounding the result to the nearest integer, and then dividing the result by the scale factor. If the scale factor is small, then the rounding operation has a strong effect and the number of coefficient quantization levels is small. The scalar values for each coefficient are shown in the image marked "Quantization scale factor." For this example, I chose large scalar values corresponding to the low spatial frequency terms (upper left) and small values for the high spatial frequency terms (lower right).

The quantized coefficients are shown in the next image. Notice that many of the quantized values are zero (black). Because there are so many zero coefficients, the quantized coefficients are very suitable for lossless compression. JPEG-DCT algorithm includes a lossless compression algorithm applied to the quantized coefficients. This representation is used to store or transmit the image.

To reconstruct an approximation of the original image, we only need to apply the inverse of the DCT to the quantized coefficients. This yields an approximation to the original image. Because of the quantization, the reconstruction will differ from the original somewhat. Since we have removed information mainly about the high spatial frequency components of the image, the difference between the original and the reconstruction is an image comprised of mainly fine texture. The difference image for this example is labeled "Error" in Figure 6.

One of the most important limiting factors in compressing images arises from the separation of the original image into distinct blocks for independent processing. Pixels located at the edge of these blocks are reconstructed without any information concerning the intensity level of the pixels that are adjacent, in the next block. One of the most important visual artifacts of the reconstruction, then, is the appearance of distortions at the edges of these blocks, which are commonly called *block artifacts*. These artifacts are visible in the reconstructed image shown in Figure 6.

There are two aspects of the JPEG-DCT algorithm that connect it with human vision. First the algorithm uses a roughly multiresolution representation of the image data. One way to see the multiresolution character of the algorithm is to imagine grouping together the coefficients obtained from the separate image blocks. Within each block, there are 64 DCT coefficients corresponding to the 64 image features. By collecting the corresponding transform coefficients from each block, we obtain a measure of the amount of each image feature within the image blocks. Implicitly, then, the DCT coefficients define sixty four images, each describing the contribution of the sixty four image features of the DCT. These implicit images are analogous to the collection of neural images that make up a multiresolution model of spatial vision (Chapter Chapter)[5].

[5]There is something that may strike you as odd when you think about the JPEG representation in this way.

Second, the JPEG-DCT algorithm relies on the assumption that quantization in the high spatial frequency coefficients does not alter the quality of the image features coded by low spatial frequency coefficients. If reduced resolution of the high spatial frequencies influences very visible features in the image, then the algorithm will fail. Hence, the assumption that the transform yields perceptually *independent* features is very important to the success of the algorithm.

The independent features in the JPEG-DCT algorithm do not conform perfectly to the multiresolution organization in models of human spatial vision. High and low frequency components are mixed in some of the features, components at very different orientations are also combined in a single feature. These features are desirable for efficient computation and implementation. In the next section, we will consider multiresolution computations that reflect the character of human vision a bit more closely.

Image Pyramids

Image pyramids are multiresolution image representations. Their format differs from the JPEG-DCT in several ways, perhaps the two most important being that (a) pyramid algorithms do not segment the image into blocks for processing, and (b) the pyramid multiresolution representation is more similar to the human visual representation than that of the JPEG-DCT. In fact, much of the interest in pyramid methods in image coding is born of the belief that the image pyramid structure is well-matched to the human visual encoding. This sentiment is described nicely in Pavlidis and Tanimoto's paper, one of the first on the topic (Tanimoto and Pavlidis (1975)).

> It is our contention that the key to efficient picture analysis lies in a system's ability, first, to find the relevant parts of the picture quickly, and second, to ignore (not waste time with) irrelevant detail. The retina of the human eye is … structured so as to see a wide angle in a low-resolution ("high-level") way using peripheral vision, while simultaneously allowing high-resolution, detailed perception by the fovea. (Tanimoto and Pavlidis 1975, p. 104).

The linear transformations used by pyramid algorithms have image features comprising periodic patterns at a variety of spatial orientations, much like human multiresolution models. Because the coefficients in the image pyramid represent data that fall mainly in separate spatial frequency bands, it is possible to use different numbers of transform coefficients to represent the different spatial frequency bands. Image pyramids use a small number of transform coefficients to represent the low spatial frequency features and many coefficients to represent the

Notice that each block contributes the same number of coefficients to represent low frequency information as high frequency information. Yet, from the Nyquist sampling theorem (see Chapter Chapter), we know that we can represent the low frequency information using many fewer samples than are needed to represent the high frequency information. Why isn't this differential sampling rate is not part of the JPEG representation? The reason is in part due to the block coding, and in part due to the properties of the image features.

high spatial frequency features. It is this feature, namely that decreasing number of coefficients are used to represent high to low spatial frequency features, that invokes the name pyramid.

The Pyramid Operations: General Theory

Image pyramid construction relies on two fundamental operations that are approximately inverses of one another. The first operation blurs and samples the input. The second operation interpolates the blurred and sampled image to estimate the original. Both operations are linear. I will describe the pyramid operations on one-dimensional signals to simplify notation; none of the principles change when we apply these methods to two-dimensional images. At the end of this section, I will illustrate how to extend the one-dimensional analysis to two-dimensional images.

Suppose we begin with a one-dimensional input vector, g_0, containing n entries. The first basic pyramid operation consists of convolving the input with a smoothing kernel and then sampling the result. The blurring and sampling go together, intuitively, because the result of blurring is to create a smoother version of the original, containing fewer high frequency components. Since blurring removes high frequency information, according to the sampling theorem we can represent the blurred data using fewer samples than the are needed for the original. We do this by sampling the blurred image at every other value.

As we have seen in Chapter and Chapter (see also the **Appendix**), both convolution and sampling are linear operations. Therefore, we can represent each by a matrix multiplication. We represent convolution by the matrix multiplication $B_0 g_0$, where the rows of B_0 contain the convolution kernel. We represent sampling by a rectangular matrix, S_0, whose entries are all zeroes and ones. The combined operation of blurring and sampling is summarized by the basic pyramid matrix $P_0 = S_0 B_0$. Multiplication of the input by P_0 yields a reduced version of the original, $g_1 = P_0 g_0$, containing only half as many entries; a matrix tableau representing the blurring and sampling operator, P_0, is shown in Figure 7 (a).

To create the image pyramid, we repeat the convolution and sampling on each resulting image. The first operation creates a reduced image from the original, g_1. To create the next level of the pyramid, we blur and sample g_1 to create g_2; then, we blur and sample g_2 to create g_3, and so forth. When the input is a one-dimensional signal, each successive level contains half as many sample values as the previous level. When the image is two-dimensional, sampling is applied to both the rows and the columns so that the next level of resolution contains only one-quarter as many sample values as the original. This repeated blurring and sampling is shown in matrix tableau in Figure 7 (b).

The second basic pyramid operation, interpolation, serves as an inverse to the blurring and sampling operation. Blurring and sampling transforms a vector with n entries to a vector with only $n/2$ entries. While this operation does not have an exact inverse, still, we can use g_1 to make an informed guess about g_0. If there is a lot of spatial redundancy in the input signals, our guess about the original image may not be too far off the mark. Interpolation is

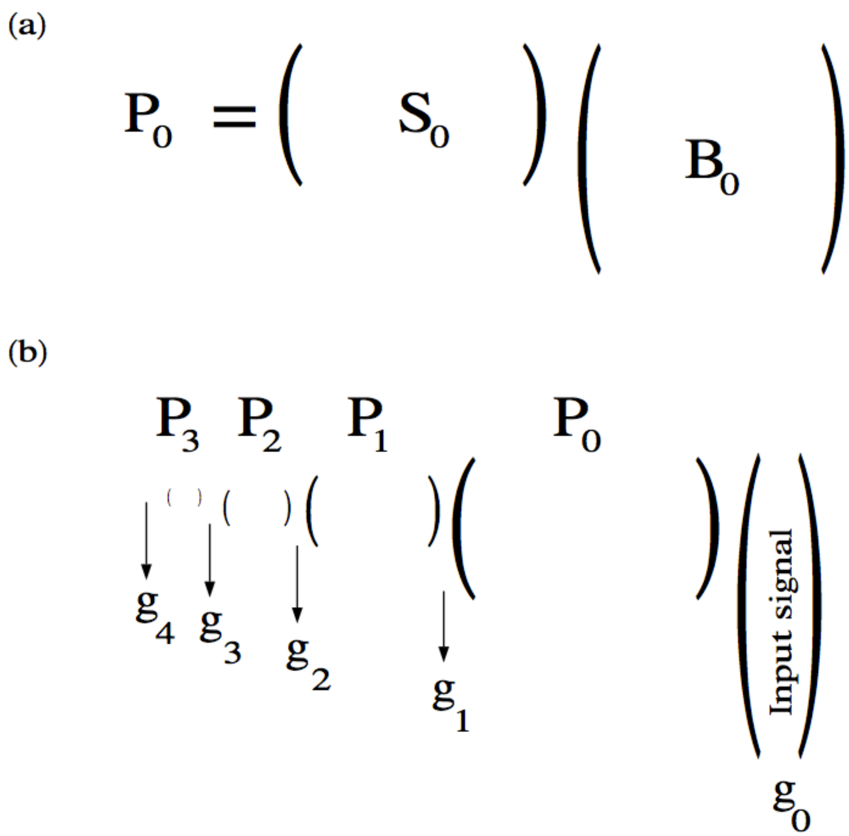

Figure 7: A matrix tableau representation of the one-dimensional pyramid operations. (a) The basic pyramid operation consists of blurring and then sampling the signal. The blurring operation is a convolution that can be represented by a square matrix whose rows are a convolution kernel. The sampling operation can be represented by a rectangular matrix, consisting of zeros and ones, that pulls out the sample values from the blurred result. (b) To create a series of images at decreasing resolution, we apply the blurring and sampling operation recursively.

the process of making an informed guess about the original image from the reduced image. We interpolate by selecting a matrix, call it E_0, to estimate the input. We choose the *interpolating* matrix E_0 so that in general $E_0 g_1 \approx g_0$.

We can now put together the two basic pyramid operations into a constructive sequence will use several times in this chapter. First, we transform the input by convolution and sampling, $g_1 = P_0 g_0$. We then form our best guess about the original using the interpolation matrix, $\hat{g}_0 = E_0 g_1 = E_0 P_0 g_0$. The estimate $\hat{g}_0$ has the same size as the original image. Finally, to preserve all of the information, we create one final image to save the error. The *error* is the difference between the true signal and the interpolated signal, $e_0 = g_0 - \hat{g}_0$. This completes construction of the first level of the pyramid.

To complete the construction of all levels of the pyramid, we apply the same sequence of operations, but now beginning with first level of the pyramid, g_1. We build a new convolution matrix, B_1; we sample using the matrix, S_1; we build $g_2 = S_1 B_1 g_1$; we interpolate g_2 using a matrix E_1; finally, we form the new error image $g_1 - \hat{g}_1$, where $\hat{g}_1 = E_1 g_2$. To construct the entire pyramid we repeat the process, reducing the number of elements at each step. We stop when we decide that the reduced image, g_n, is small enough so that no further blurring and sampling would be useful.

The pyramid construction procedure defines three sequences of signals; the series of blurred and sampled signals whose size is continually being reduced, the interpolated signals, and the error signals. We can summarize their relationship to one another in a few simple equations. First, the reduced image at the i^{th} level is created by applying the basic pyramid operation to the previous level.

$$g_i = P_{i-1} g_{i-1} \tag{0.2}$$

The estimate of the image $\hat{g}_i$ is created from the lower resolution representation by the calculation

$$\hat{g}_i = E_{i+1} g_{i+1} \tag{0.3}$$

Finally, the difference between the original and the estimate is the error image,

$$e_i = g_i - \hat{g}_i = g_i - E_i P_i g_i \tag{0.4}$$

Two different sets of these signals preserve the information in the original. One sequence consists of the original input and the sequence of *reduced signals*, g_0, g_1, g_2, ..., g_n. This sequence provides a description of the original signal at lower and lower resolution. It contains all of the data in the original image trivially since the original image is part of the sequence. This image sequence is of interest when we display low resolution versions of the image.

The second sequence consists of the *error signals*, $e_0, e_1, \ldots, e_{n-1}, g_n$ (note that g_n is part of this sequence, too). Perhaps surprisingly, this sequence also contains all of the information in the original image. To prove this to yourself, notice that we can build the sequence of images, g_i, from the error signals. The terms g_n and e_{n-1} are sufficient to permit us to construct g_{n-1}; g_{n-1} and e_{n-2} can recover g_{n-2}, and so forth. Ultimately, we use e_0 and g_1 to reconstruct the original, g_0. This image sequence is of interest for image compression (Mallat (1989)).

Pyramids: An Example

Figure 8 illustrates the process of constructing a pyramid. The specific calculations used to create this example were suggested by Burt and Adelson (1983a), who were perhaps the first to introduce the general notion of an image pyramid to image coding.

The example in Figure 8 begins with a one-dimensional squarewave input, g_0. This signal is blurred using a Gaussian convolution kernel and then sampled at every other location; the reduced signal, g_1, is shown below. This process is then repeated to form a sequence of reduced signals. When the convolution kernel is a Gaussian function, the sequence of reduced signals is called the *Gaussian pyramid*.

To interpolate the reduced signal to a higher resolution, Burt and Adelson proposed the following ad hoc procedure. Place the data in g_1 into every other entry of a vector with the same number of entries as g_0. The procedure is called *up-sampling*; it is equivalent to multiplying the vector g_i by the transpose of the sampling matrix, S_0^t. Then, convolve the up-sampled vector with (nearly) the same Gaussian that was used to reduce the image. The Gaussian used for interpolation differs from the Gaussian used to blur the signals only in that it is multiplied by a factor of 2 to compensate for the fact that the up-sampled vector only has non-zero values at one out of every two locations. In this important example, then, the interpolation matrix is equal to two times the transpose of the convolution-sampling matrix,

$$E_0 = 2{B_0}^t {S_0}^t = 2{P_0}^t.$$

The interpolated signal, that is, the estimate of the higher resolution signal, is shown in the middle column of Figure 8.

Next, we calculate the error signal, the difference between the estimate and the original. The error signals are shown on the right of Figure 8. The sequence of error signals forms the error pyramid. As I described above, we can reconstruct the original g_0 without error from the signals e_0 and g_1. Burt and Adelson called the error signals created by the combination of Gaussian blurring and interpolation functions the *Laplacian pyramid*.

Figure 9 (a) shows the result of applying the pyramid process to a two-dimensional signal, in this case an image. The sequence of reduced images forming the Gaussian pyramid is shown on the top, with the original image on the left. These images were created by blurring the original and then representing the new data at one half the sampling rate for both the rows and the

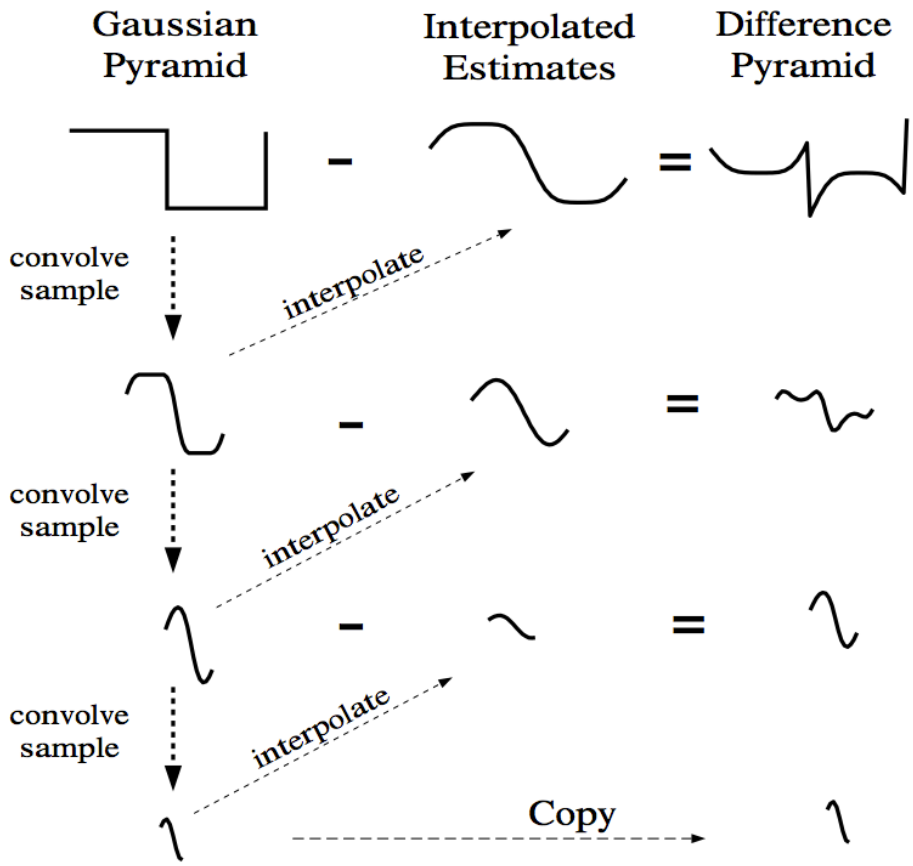

Figure 8: One-dimensional pyramid construction. The input signal (upper left) is convolved with a Gaussian kernel and the result is sampled. This creates a blurred copy of the signal at lower resolution. An estimate of the original is created by interpolating the low resolution signal, and the difference between the original and the estimate is saved in the error pyramid. The process is repeated, beginning with the blurred copy, thus creating series of copies of the original at decreasing resolution (on the left) and a series error images (on the right). The signal at the lowest resolution level is stored as the final element in the error pyramid.

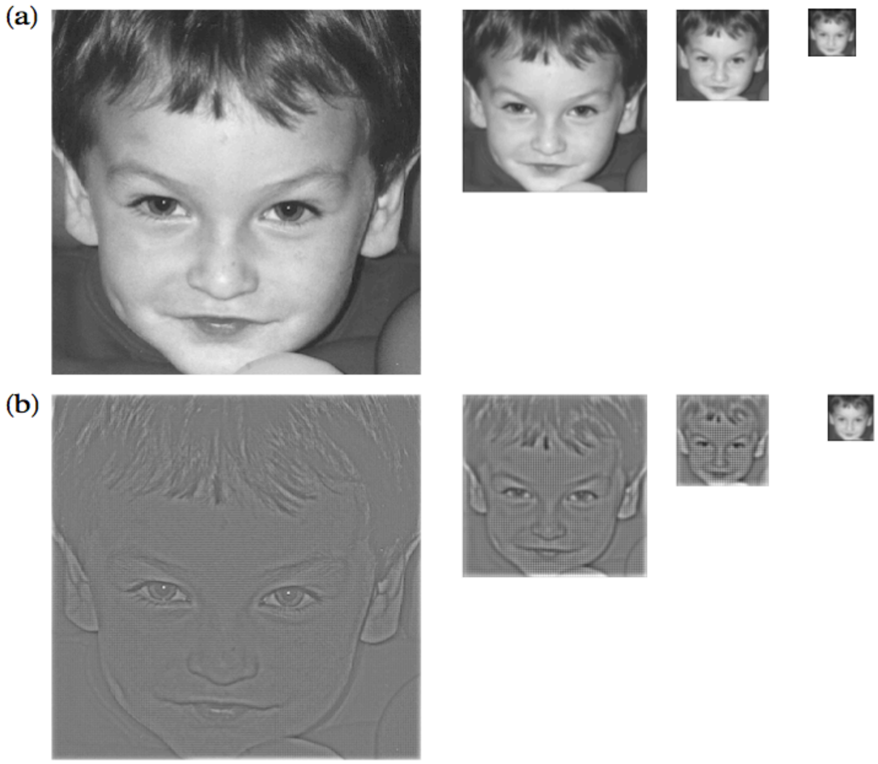

Figure 9: The Gaussian and Laplacian image pyramids. (a) The series of reduced images that form the Gaussian image pyramid begins with the original image, on the left. This image is blurred by a Gaussian convolution kernel and then sampled to form the image at a lower spatial resolution and size. (b) Each reduced image in the Gaussian pyramid can be used to estimate the image at a higher spatial resolution and size. The difference between the estimate the higher resolution image forms an error image, which in the case of Gaussian filtering is called the Laplacian pyramid. These error images can have positive or negative values, so I have shown them as contrast images in which gray represents zero error, while white and black represent positive and negative error respectively. (After Burt and Adelson (1983a)).

columns. Thus, in the two-dimensional case each reduced image contains only one-quarter the number of coefficients as its predecessor[6].

The sequence of error images forming the Laplacian pyramid is shown in Figure 9 (b). Because the interpolation routine uses a smooth Gaussian function to interpolate the lower resolution images, the large errors tend to occur near the edges in the image. And, because the images are mainly smooth (adjacent pixel intensities are correlated) most of the errors are small[7].

Image Compression Using the Error Pyramid

From the point of view of image compression, the sequence of images in the Gaussian pyramid is not very interesting because that sequence contains the original. Rather than the use the entire sequence, we might as well just code the original. The sequence of images in the Laplacian pyramid, however, is interesting for two reasons.

First, the information represented in the Laplacian pyramid varies systematically as we descend in resolution. At the highest levels, containing the most transform coefficients, the Laplacian pyramid represents the fine spatial detail in the image. At the lowest levels, containing the fewest transform coefficients, the Laplacian pyramid represents low spatial resolution information. Intuitively, this is so because the error image is the difference between the original, which contains all of the fine detail, and an estimate of the original based on a slightly blurred copy. The difference between the original and an estimate from a blurred copy represents image information in the resolution band between the two levels. Thus, the Laplacian pyramid is a multiresolution representation of the original image.

Second, the values of the transform coefficients in the error images are distributed over a much smaller range than the pixel intensities in the original image. Figure 10 (a) shows intensity histograms of pixels in the first three elements of the Gaussian pyramid. These intensity histograms are broad and not well-suited to the compression methods we reviewed earlier in this chapter. Figure 10 (b) shows histograms of the pixel intensities in the Laplacian pyramid. The transform coefficients tend to cluster near zero and thus they can be represented very efficiently. The reduced range of transform coefficient values in the Laplacian pyramid arises because of the spatial correlation in natural images. The spatial correlation permits us to do fairly well in approximating images using smooth interpolation. When the approximations are close, the errors are small, and they can be coded efficiently.

There is one obvious problem with using the images in the Laplacian pyramid as an efficient image representation: there are more coefficients in the error pyramid than pixels in the original image. When building an error pyramid from two-dimensional images, for example, we sample every other row and every other column. This forms a sequence of error images equal to 1, 1/4, 1/16 the size of the original; hence, the error pyramid contain 1.33 times

[6] Therefore, in the estimation phase we multiply the interpolation matrix by a factor of 4, not 2, i.e., $E_0 = 4{P_0}^t$.

[7] In order to display the error images, which have negative coefficients, the image intensities are scaled so that black is a negative value, medium gray is zero, and white is positive.

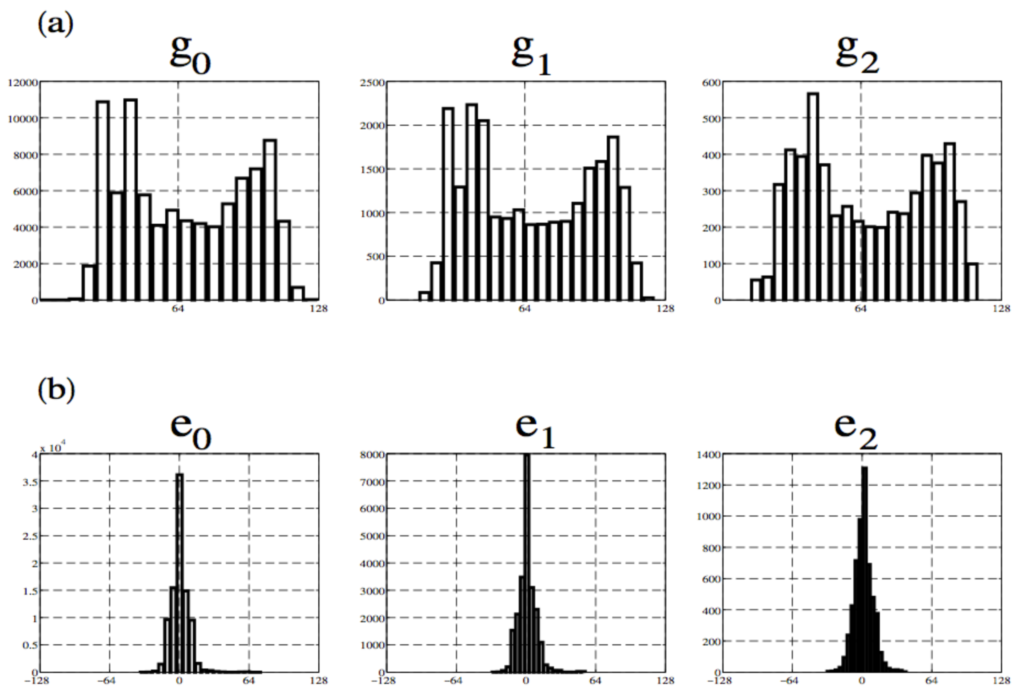

Figure 10: Histograms of the Gaussian and Laplacian pyramids. (a) The separate panels show the intensity histograms at each level of the Gaussian pyramid. The intensities are distributed across a wide range of values, making the intensities difficult to code efficiently. (b) The Laplacian pyramid coefficients are distributed over a modest range near zero and can be coded efficiently.

as many coefficients as the original (see Figure 9). Because of the excess of coefficients, the error image representation is called *overcomplete*. If one is interested in image compression, overcomplete representations seem to be a step in the wrong direction.

Burt and Adelson (1983a) point out, however, that there is an important fact pertaining to human vision that reduces the significance of the overcompleteness: The vast majority of the the transform coefficients represent information in the highest spatial frequency bands where people have poor visual resolution. Therefore, we can quantize these elements very severely without much loss in image quality. Quantization is the key step in image compression, so that having most of the transform coefficients represent information that can be heavily quantized is an advantage.

The ability to quantize severely many of the transform coefficients with little perceptual loss, coupled with the reduced variance of the transform coefficients, make the Laplacian pyramid representation practical for image compression. Computing the pyramid can be more complex than the DCT, depending on the block size, but special purpose hardware has been created for doing the computation efficiently. The pyramid representation performs about as well or slightly better the JPEG computation based on the DCT. It is also applicable to other visual applications, as we will discuss later (Burt (1988)).

QMFs and Orthogonal Wavelets

Pyramid representations using a Gaussian convolution kernel have many useful features; but, they also have several imperfections. By examining the problematic features of Gaussian and Laplacian pyramids, we will see the rationale for using a different convolution kernel, {\em quadrature mirror filters} (QMFs), in creating image pyramids. The first inelegant feature of the Gaussian and Laplacian pyramids is an inconsistency in the blurring and sampling operation. Suppose we had begun our analysis with the estimated image, $\hat{g}_0$, rather than g_0. From the pyramid construction point of view, the estimate should be equivalent to the original image. It seems reasonable to expect, therefore, that the reduced image derived from $\hat{g}_0$ should be the same as the reduced image derived from g_0. We can express this condition as an equation,

$$g_1 = P_0(2{P_0}^t)g_1 = P_0\hat{g}_0 \tag{0.5}$$

Equation 0.5 implies that the square matrix $P_0(2{P_0}^t)$ must be the identity matrix. This implies that the columns of the matrix, P_0, should be *orthogonal* to one another[8]. This is not a property of the Gaussian and Laplacian pyramid.

A second inelegant feature of the Gaussian and Laplacian pyramid is that the representation is overcomplete, i.e., there are more transform coefficients than there are pixels in the original

[8] Orthogonality is defined in Chapter and the Appendix. Two vectors are orthogonal when $a^t b = 0$.

image. The increase in the transform coefficients can be traced to the fact that we represent an image g_i with N_i pixels by a reduced signal and an error signal that contain more than N_i coefficients. For example, we represent the information in the i^{th} level of the pyramid using the reduced image g_{i+1} and the error image e_i.

$$g_i = (2{P_i}^t)g_{i+1} + e_i \tag{0.6}$$

In the one-dimensional case, the error image, e_i, contains N_i transform coefficients. The reduced signal, g_{i+1}, contains $N_i/2$ coefficients. To create an efficient representation, we must represent g_i using N_i transform coefficients, not $1.5N_i$ coefficients as in the Gaussian pyramid.

The error signal and the interpolated signal are intended to code different components of the original input; the interpolated vector $\hat{g}_i = (2{P_i}^t)g_{i+1}$ codes a low resolution version of the original, and e_i codes the higher frequency terms left out by the low resolution version. To improve the efficiency of the representation, we might require that the two terms code completely different types of information about the input. One way to interpret the phrase "completely different" is to require that the two vectors be orthogonal, that is,

$$0 = {e_i}^t \hat{g}_i \tag{0.7}$$

If we require that $\hat{g}_i$ and e_i to be orthogonal, we can obtain significant efficiencies in our representation. By definition, we know that the interpolated image $\hat{g}_i$ is the weighted sum of the columns of ${P_i}^t$. If we the error e_i image is orthogonal to the interpolated image, then the error image must be the weighted sum of a set of column vectors that are all orthogonal to the columns of ${P_i}^t$. In the (one-dimensional) Gaussian pyramid construction, ${P_i}^t$ has $N_i/2$ columns. From basic linear algebra, we know that there are $(1/2)N_i$ vectors perpendicular to the columns of ${P_i}^t$. Hence, if $\hat{g}_i$ is orthogonal to e_i, we can describe both of these images using only N_i transform coefficients, and the representation will no longer overcomplete.

But, what conditions must be met to insure that e_i and $\hat{g}_i$ are orthogonal? By substituting Equation 0.2, Equation 0.3, Equation 0.4 into Equation 0.7 we have

$$\begin{aligned} 0 &= {e_i}^t \hat{g}_i \\ &= (g_i^t(2{P_i}^t)P_i)((2{P_i}^t)P_i g_i - g_i) \\ &= [g_i^t(2{P_i}^t)(P_i(2{P_i}^t))P_i g_i] - [g_i^t(2{P_i}^t)P_i g_i]. \end{aligned} \tag{0.8}$$

If the rows of P_i are an orthogonal set, then by appropriate scaling we can arrange it so that $P_i(2{P_i}^t)$ is equal to the identity matrix. In that case, the final term in Equation 0.8 simplifies and we have

$$\hat{g}_i = [{g_i}^t(2{P_i}^t)P_i g_i] - [{g_i}^t(2{P_i}^t)P_i g_i] = 0 \tag{0.9}$$

thus guaranteeing that the error signal and the interpolated estimate will be orthogonal to one another. For the second time, then, we find that the orthogonality of the rows of the pyramid matrix is a useful property.

We can summarize where we stand as follows. The basic pyramid operation has several desirable features. The rows within each level of the pyramid matrices are shifted copies of one another, simplifying the calculation to nearly a convolution; the pyramid operation represents information at different resolutions, paralleling human multiresolution representations; the rows of the pyramid matrices are localized in space, as are receptive fields, yet they are not sharply localized as the blocks used in the JPEG-DCT algorithm. Finally, from our criticisms of the error pyramid, we have added a new property we would like to have: The rows of each pyramid matrix should be an orthogonal set.

We have accumulated an extensive set of properties we would like the pyramid matrices, P_i, to satisfy. Now, one can have a wish list, but there is no guarantee that there exist any functions that satisfy all our requirements. The most difficult pair of constraints to satisfy is the combination of orthogonality and localization. For example, if we look at convolution operators alone, there are no convolutions that are simultaneously orthogonal and localized in space.

Interestingly there exists a class of discrete-valued functions, called *quadrature mirror filters*, that satisfy all of the properties on our wish list (Esteban and Galand (1977); Simoncelli and Adelson (1990); Vetterli (1986)). The quadrature mirror filter pair splits the input signal into two orthogonal components. One of the filters defines a convolution kernel that we use to blur the original image and obtain the reduced image. The second filter is orthogonal to the first and can be used to calculate an efficient representation of the error signal. Hence, the quadrature mirror filter pair splits the original signal into coefficients that define of the two orthogonal terms, $\hat{g}_i$ and e_i; Each set of coefficients has only $n/2$ terms, so the new representation is an efficient pyramid representation. Figure 11 shows an example of a pair of quadrature mirror filters. The function shown in Figure 11 (a) is the convolution kernel that is used to create the reduced images, g_i. The function in Figure 11 (b) is the convolution kernel needed to calculate the transform coefficients in the error pyramid directly. When the theory of these filters is developed for continuous, rather than discrete, functions the convolution kernels are called *orthogonal wavelets* (Daubechies (1990)).

The discovery of quadrature mirror filters and wavelets was a bit of a surprise. It is known that there are no nontrivial convolution kernels that are orthogonal; i.e., no convolution matrix, B_i, satisfies the property that $B_i B_i^t = I$. Hence it was surprising to discover that convolution kernels do exist for the pyramid operation, which relies so heavily on convolution, can satisfy $P_i {P_i}^t = I$.

The quadrature mirror filter and orthogonal wavelet representations have many fascinating properties and are an interesting area of mathematical study. They may have significant implications for compression because they remove the problem of having an overcomplete representation. But, it is not obvious that once quantization and correlation are accounted

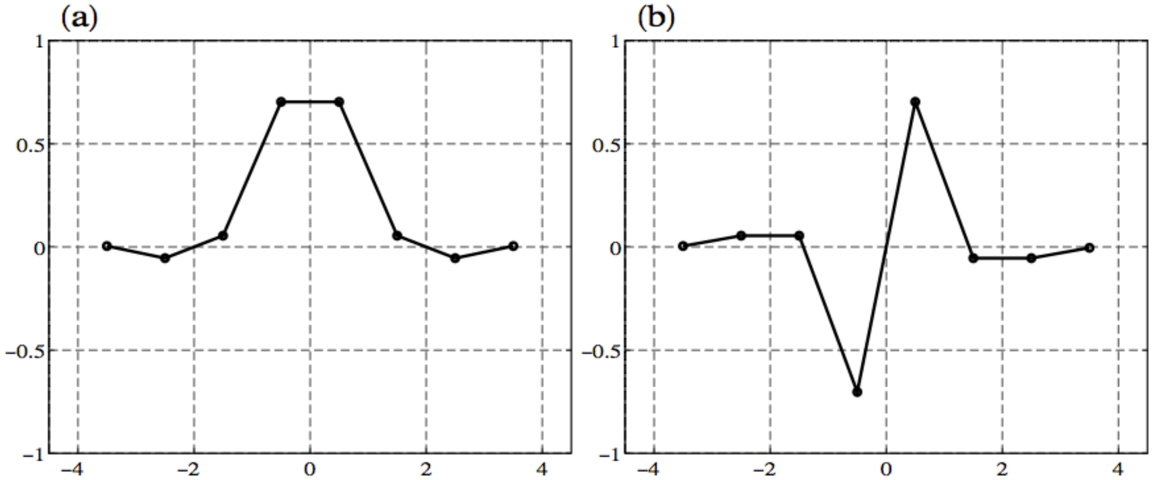

Figure 11: A quadrature mirror filter pair. One can use these two functions as convolution kernels to construct a pyramid. Convolution with the kernel in (a) followed by sampling produces the transform coefficients in the set of reduced signals. Transformation by the kernel in (b) followed by sampling yields the transform coefficients of the error pyramid (Source: Simoncelli (1988)).

for that the savings in the number of coefficients will prove to be significant. For now, the design and evaluation of quadrature mirror filters remains an active area of research in pyramid coding of image data.

Applications of multiresolution representations

The statistical properties of natural images make multiresolution representations efficient. Were efficiency a primary concern, the visual pathways might well have evolved to use the multiresolution format. But, there is no compelling reason to think that the human visual system, with hundreds of millions of cortical neurons available to code the outputs of tens of thousands of cone photoreceptors, was subject to very strong evolutionary pressure to achieve efficient image representations. Understanding the neural multiresolution representation may be helpful when we design image compression algorithms; but, it is unlikely that neural multiresolution representations arose to serve the goal of image compression alone.

If multiresolution representations are present in the visual pathways, what other purpose might they serve? In this section, I will speculate about how multiresolution representations may be a helpful component of several visual algorithms. \comment{It is possible to create a multiresolution version of almost any algorithm, but there are few examples in which the multiresolution representation is essential.}

Image Blending

Imagine blending refers to methods for smoothly connecting several adjacent or overlapping images of a scene into a larger photomosaic (Milgram (1975); Carlbom et al. (1994)). There are several different reasons why we might study the problem of joining together several pieces of an image. For example, in practical imaging applications we may find that a camera's field of view may be too small to capture the entire region of interest. In this case we would like to blend several overlapping pictures to form a complete image.

The human visual system also needs to blend images. As we saw in the early chapters of this volume, spatial acuity is very uneven across the retina. Our best visual acuity is in the fovea, and primate visual systems rely heavily on eye-movements to obtain multiple images of the scene. To form a good high acuity representation of more than the central few degrees, we must gather images from a sequence of overlapping eye fixations. How can the overlapping images acquired through a series of eye movements be joined together into the single, high resolution representation that we perceive?

Burt and Adelson (1983b) showed that multiresolution image representations offer a useful framework for blending images together. They describe some fun examples based on the pyramid representation.

We can see some of the advantages of a multiresolution image blending by comparing the method with a single resolution blend. So, let's begin by defining a simple method of joining the two pictures, based on a single resolution representation. Suppose we decide to join a picture on the left $L(x, y)$ and a picture on the right $R(x, y)$. We will blend the images by mixing their intensity values near the border where the join. A formal rule for to blend the image data must specify how to combine the data from the two images. We do this using a blending function, call it $b(x, y)$, whose values vary between 0 and 1.0. To construct our single-resolution blending algorithm we form a mixture image from the weighted average

$$M(x, y) = b(x, y)L(x, y) + (1 - b(x, y))R(x, y). \tag{0.10}$$

Consider the performance of this type of single resolution blend on an a pair of simulated astronomical images in Figure 12. Each of these images contain 512 rows and columns. The two images were built to simulate the appearance of a starry sky. The images contain three distortions to illustrate some of the advantages of multiresolution methods for blending images.

First, the images contain two kinds of objects (stars and clouds) whose spatial structure places them in rather different spatial frequency bands. Second, the images have different mean levels (the image on the top right being dimmer than the one on the top left). Third, the images are slightly shifted in the vertical direction as if there was some small jitter in the camera position at the time of acquiring the pictures.

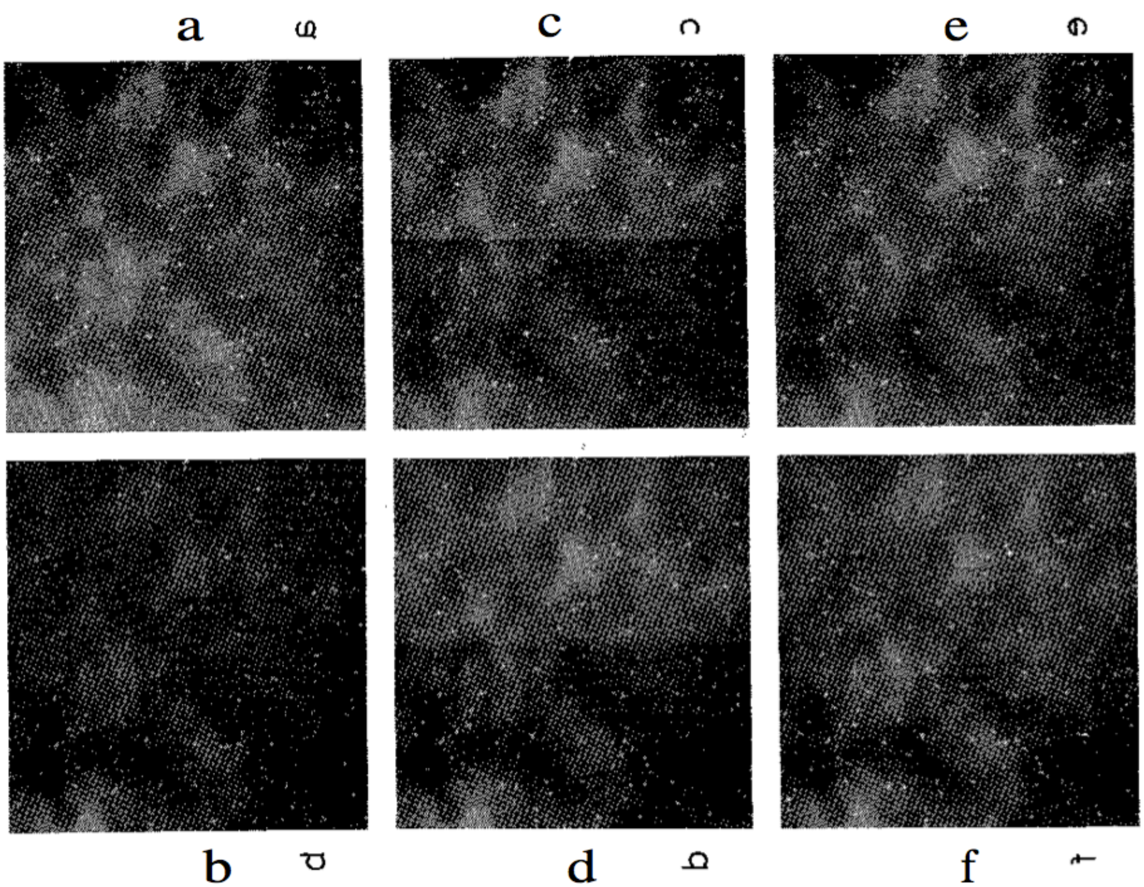

Figure 12: A comparison of single-resolution and multiresolution image blending methods. The images in (a) and (b) have a slightly different mean and are translated vertically. Abutting the right and left halves of the images is shown in (c). Spatial averaging over a small distance across the image boundary is shown in (d). Spatial averaging over a large distance across the image boundary is shown in (e). The multiresolution blend from Burt and Adelson is shown in (f). (Source: Burt and Adelson (1983b)).

Because the images are divided along a vertical line, we need to concern ourselves only with the variation with x and join the images the same way across each row.

The most trivial, and rather ineffective, way of joining the two images is shown in panel (c). In this case the two images are simply divided in half and joined at the dividing line. Simply abutting the two images is equivalent to choosing a function $s(x,y)$ equal to

$$b(x,y) = \begin{cases} 1 & \text{if } x < m \\ 0 & \text{otherwise} \end{cases} \tag{0.11}$$

where m is the midpoint of the image, 256 in this case. This smoothing function leads to a strong artifact at the midpoint because of the difference in mean gray level.

We might use a less drastic blending function for $b(x,y)$. For example, we might choose as function that varied as a linear ramp over some central width of the image.

(13)

$$b(x,y) = \left\{ \begin{array}{ll} 1 & \text{if } x < m - w \\ 1 - \frac{x-m-w}{2w} & \text{if } m - w \leq x \leq m + w \\ 0 & \text{otherwise} \end{array} \right\}. \tag{0.12}$$

Using a ramp to join the images blurs the image at the edge, as illustrated in panels (d) and (e) of Figure 12. In panel (d) the width parameter of the linear ramp, w, is fairly small. When the width is small the edge artifact remains visible. As the width is broadened, the edge artifact is removed (panel (e)) and elements from both images contribute to the image in the central region. At this point the vertical shift between the two images becomes apparent. If you look carefully in the central region, you will see double stars shifted vertically one above the other. Image details that are much smaller than the width of the ramp appear in the blended image and they appear at their shifted locations. The stars are small compared to the width of the linear ramp, so the blended image contains the an artifact due to the shift in the image details.

Multiresolution representations provide a natural, way for combining the two images that avoid some of these artifacts. We can state the multiresolution blending method as an algorithm.

1. Form the pyramid of error images for L and R.
2. Within each level of the pyramid, average the error images with a blend function $b(x,y)$. A simple ramp function, as in Equation 0.12 with $w = 1$, will do as the blend function.
3. Compute the new image by reconstructing the image from the blended pyramid of error images.

The image in panel (f) of Figure 12 contains the results of applying the multiresolution blend to the images. The multiresolution algorithm avoids the previous artifacts because by averaging the two error pyramids, two images combine over different spatial regions in each of the resolution bands. Data from the low resolution level is combined over a wide spatial region of the image, while data from the high resolution levels are combined over a narrow spatial region of the image.

By combining low frequency information over large spatial regions, we remove the edge artifact. By combining high frequency information over narrow spatial regions, we reduce the artifactual doubling of the star images to a much narrower spatial region.

Burt and Adelson (1983b) also describe a method of blending images with different shapes. Figure 13 illustrates one of their amusing images. They combined the woman's eye taken from panel (a) and the hand, taken from panel (b) into a single image shown in panel (d). The method for combining images with different shapes is quite similar to the algorithm I described above. Again, we begin by forming the error images e_i for each of the two images. For the complex region, however, we must a method to define a blend function $s_i(x, y)$, appropriate for combining the data at each resolution of the pyramid over these different shapes. Burt and Adelson have a nifty solution to this problem. Build an overlay image that defines the location where second image is to be placed over the first, as in panel (c) of Figure 13. Build the sequence of pyramid of reduced images, g_i, corresponding to the overlay image. Use the elements of the image sequence g_i to define the blend functions for combining the images at resolution e_i.

Progressive Image Transmission

For many devices, transmitting an image from its stored representation to the viewer can take a noticeable amount of time. And, in some of these cases, transmission delays may hamper our ability to perform the task. Suppose we are scanning through a database for suitable pictures to use in a drawing, or we are checking a directory to find the name of the person who recently waved hello. We may have to look through many pictures before finding a suitable one. If there is a considerable delay before we see each picture, the tasks become onerous; people just won't do them.

Multiresolution image representations are natural candidates to improve the rate of image transmission and display. The reconstruction of an image from its multi-resolution image proceeds through several stages. The representation stores the error images e_i and the lowest reduced image g_n. We reconstruct the original by computing a set of reduced images, g_i. These reduced images are rough approximations of the original, at reduced resolution. They are represented by fewer bits than the original image, so they can be transmitted and displayed much more quickly. We can make these low resolution images available for the observer to see during the reconstruction process. If the observer is convinced that this image is not worth any more time, then he or she can abort the reconstruction and go on to the next image. This offers the observer a way to save considerable time.

We can expand on this use of multiresolution representations by allowing the observer to request a low resolution reconstruction, say at level g_i, rather than a full representation at level g_0. The observer can choose a few of the low resolutions for viewing at high resolution.

Figure 13: Image blending of regions with arbitrary shape. To create a multiresolution blend of the images of the eye and hand, we must define a blending function for each level of the pyramid. The blending function can be created by building the Gaussian pyramid representation of the region where the image of the eye will be inserted. The different levels of the Gaussian pyramid can be used as the blending functions to combine the error pyramids of the two images (Source: Burt and Adelson (1983b)).

Multiresolution representations are efficient because there is little wasted computation. The pyramid reconstruction method permits us to use the work invested in reconstructing the low resolution image as we to reconstruct the original at full resolution.

Th engineering issues that arise in progressive image transmission may be relevant to the internal workings of the human visual system. When we call up an image from memory, or sort through a list of recalled images, we may wish to image low resolution images rather than reconstruct each image in great detail. If the images are stored using a multi-resolution format, our ability to search efficiently through our memory for images may be enhanced.

Threshold and Recognition

Image compression methods link *visual sensitivity* measurements to an engineering application. This makes sense because threshold sensitivity plays a role in image compression; perceptually lossless compression methods, by definition, tolerate threshold level differences between the reconstructed image and the original.

For the applications apart from compression, however, sensitivity is not the key psychological measure. Since low resolution images do not look the same as the high resolution images, sensitivity to differences is not the key behavioral measure. To understand when progressive image transmissions methods work well, or which low resolution version is the best approximation to a high resolution version of an image, we need to be informed about which multiresolution representations permit people to {\em recognize} quickly or {\em search} for an item in a large collection of low resolution images quickly. Just as the design of multiresolution image compression methods requires knowing visual sensitivity to different spatial frequency bands, so too multiresolution methods for progressive image transmission requires knowing how important different resolution bands will be for expressing the information in an image.

As we study these applications, we will learn about new properties of human vision. To emphasize some of the interesting properties that can arise, I will end this section by reviewing a perceptual study by Bruner and Potter (1964). This study illustrates some of the counter-intuitive properties we may discover as we move from threshold to recognition studies.

Bruner and Potter (1964) studied subjects ability to recognize common objects from low resolution images. Their subjects were shown objects using slides projected onto a screen. In 1964 low resolution images were created much more quickly and easily than today; rather than requiring expensive computers and digital framebuffers low resolution images were created by blurring the focus knob on the projector.

Bruner and Potter compared subjects' ability to recognize images in a few ways. I want to abstract from their results two key observations[9].

[9]There are a number of important methodological features of the study I will not repeat here, and I encourage the reader to return to the primary sources to understand more about the design of these experiments.

Figure 14 illustrates three different measurement conditions. Observers in one group saw the image develop from very blurry to only fairly blurry over a two minute period. At the end of this period the subjects were asked to identify the object in the image. They were correct on about a quarter of the images. Observers in a second group only began viewing the image after after 87 seconds. They first saw the image at a somewhat higher resolution, but then they could watch the image develop for only about a half minute. The difference between the second group and the first group, therefore, was whether they saw the image in a very blurry state, during the first 90 seconds. The second group of observers performed substantially better, recognizing the object `r 44` percent of the time rather than `r 25` percent. Surprisingly, the initial 90 seconds of viewing the image come into focus made the recognition task more difficult. A third group was also run. This group only saw the image come into focus during the last 13 seconds. The third group did not see the first 107 seconds as the image came into focus. This group also recognized the images correctly about `r 43` percent of the time.

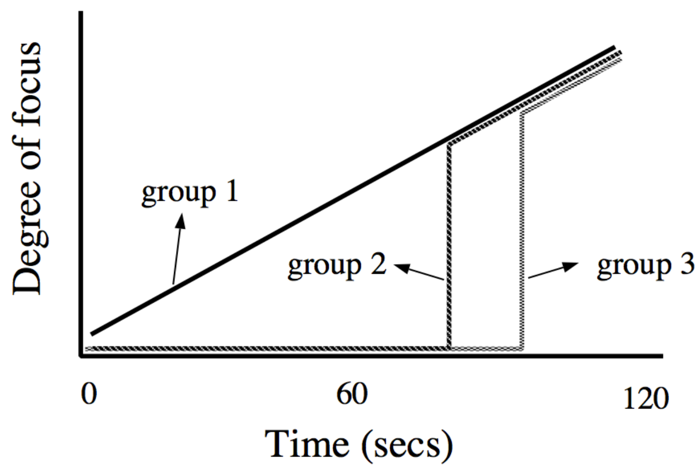

Figure 14: The experimental viewing conditions used by Bruner and Potter in their recognition experiment. One group saw the picture come into slowly and continuously over a period of 122 seconds. A second group saw nothing for 87 seconds and then watched the remainder of the image come into focus. The final group only saw the image 109 seconds. Surprisingly, the group that watched the image come into focus for the full 122 seconds had the lowest recognition rate (Source: Bruner and Potter (1964)).

Seeing these images come into focus slowly made it harder for the observers to recognize the image contents. Observers who saw the images come into focus over a long period of time formulated hypotheses as to the image contents. These hypotheses were often wrong and ultimately interfered with their recognition judgments.

Bruner and Potter illustrated the same phenomenon a different way. They showed one group of observers the image sequence coming into focus and a second group the same image sequence going out of focus. These are the same set of images, shown for the same amount of time. The difference between the stimuli is the time-reversal. Subjects who saw the images come into focus recognized the object correctly 44% of the time. Subjects who saw the image going out of focus recognized the object correctly 76% of the time. Seeing a low resolution version of an image can interfere with our subsequent ability to recognize the contents of an image.

Now, don't draw too strong a conclusion from this study about the problems progressive image enhancement will create. There are a number of features of this particular experiment which make the data quite unlike applications we might plan for progressive image transmission. Most importantly, in this study subjects never saw very clear images. At the best focus, only half of the subjects recognized the pictures at all. Also, the durations over which the images developed were quite slow, lasting minutes. These conditions are sufficiently unlike most planned applications of progressive image transmission that we cannot be certain the results will apply. I mention the result here to emphasize that even after the algorithms are in place, human testing will remain an important element of the system design.

Image Interpretation

Introduction to Image Interepretation

Helmholtz wrote:

> The general rule determining the ideas of vision that are formed whenever an impression is made on the eye, is that *such objects are always imagined as being present in the field of vision as would have to be there in order to produce the same impression on the nervous mechanism* [Italics in the original; Southall, Physiological Optics, Vol. III, p. 2, 1865]

Helmholtz' advice is at the center of much modern vision science. Helmholtz recommends that we think of our perceptions as mental representations of the object most likely to explain the sensory input. To understand the logic of perception, therefore, we should study how to use the retinal image to estimate the object properties. The interest in understanding perceptions as estimates of the physical properties of objects joins computational vision together with physiology and psychology. as we review color appearance, motion and depth perception, and objects in the we will find several ways in which Helmholtz' general advice has succeeded in specific cases.

Like many good ideas, Helmholtz' idea has often been rediscovered. We should be generous in crediting the re-discovery of good ideas, since that is greatly preferable to the rediscovery of bad ideas. Marr's (1980) influential book amplifies Helmholtz' point, and by using the word computational, rather than inferential, Marr also linked vision to the computer metaphor. My colleague Roger Shepard has championed this approach as well in his writings under the banner of *psychophysical complementarity*.

When we pose vision science questions as an estimation problem — what objects could give rise to the sensory input? — we place biology, psychology and computation on common ground. Each discipline can formulate its experiments and theories in terms of a fundamental computational objective. The neural response, the behavior, and the computation all are seen as part of the goal of defining an object and estimating object properties. Even if the computational method turns out to be a poor model of human vision, discovering a new method may still be useful for robotics or other industrial applications.

In the next few chapters, then, we will engage in some free-wheeling abstract thinking about visual inferences. We will ask what sensory information is available in the retinal image that could be used to estimate object properties, first for color, and then for motion and depth. We will consider abstract algorithms to extract this information, and then we will consider how the neural substrate represents and analyzes this information.

Color Appearance

In the next chapter we will analyze the visual inferences that lead to color appearance. The color appearance of an object is predicted better by the object's surface reflectance function than by the light scattered from the object. We will study how the visual system can, in principle, use the light scattered from a surface to infer an object's surface reflectance function, and then, we will compare people's color appearance judgments with this standard.

As is common in biology and behavior, the performance does not match the absolute best limits. But, there are some important similarities, so that we obtain an excellent framework for understanding behavior and the neural representation by beginning with the computational questions. For example, we will consider how computational analyses of color can help us understand some of the basic properties of the neural response to wavelength, such as opponent-colors signals.

We are at the beginning stages of discovering the neural mechanisms of color appearance. The clinical literature documents many cases of individuals who have lost their ability to organize color appearance as a consequence of strokes located in the visual area. We will consider the logic of these clinical cases studies. Then, we will review some of the experimental evidence that seeks to connect color appearance and neural responses. The most important aspect of this review is that it will get us thinking about the general methods we have available to us to relate perception and brain activity.

Motion and Depth

Many of the same issues arise in Chapter 10 as I discuss motion and depth perception. I have grouped motion and depth because estimating motion and depth are closely related computational tasks. Image changes arising from an observer's motion yield a rich source of information about depth.

It will also become clear that just as color is not a direct representation of wavelength, perceived motion is not a direct representation of physical motion. Rather, motion perception is a mental inference that relies on computations implemented in the visual pathways.

For motion perception, more than any other percept, there is strong evidence to identify a particular visual stream as an important component of motion judgments. This visual stream can be traced from the retina to visual area MT. We will review the evidence that this stream plays a role in motion perception, and we will review new experiments that expand our repertoire of techniques for connecting brain activity and behavior.

Objects and Illusions

Color and motion are descriptions of objects. We identify the perceptual color and motion so that we can recognize and interact with objects. Objects have color; objects move. Perhaps the most important question concerning vision, then, is how we decide that something is an object in the first place. We will end by considering an array of visual illusions that offer us hints about object perception, and that make us think about how we see objects.

Color

Color overview

Edwin Land was one of the great inventors and entrepreneurs in US history; he created instant developing film and founded the Polaroid Corporation. The first instant developing film made black and white reproductions, and after a few years Land decided to create a color version of the film. In order to learn about color appearance, Land returned to his laboratory to experiment with color. He was so surprised by his observations that he decided to write a paper summarizing his observations. In a paper published in the Proceedings of the National Academy of Sciences (USA), Land startled many people by arguing that there are only two, not three, types of cones. He further went on to dismiss the significance of the color-matching experiments. He wrote: "We have come to the conclusion that the classical laws of color mixing conceal great basic laws of color vision (Land (1959))." Land's sharp words, an arrow aimed at the heart of color science, provoked heated rejoinders from two leading scientists, Judd (1960) and Walls (1960).

What was it that Land, a brilliant man, found so objectionable about color-matching? It seems to me that Land's reading of the literature led him to believe that the curves we measure in the color-matching experiment can be used to predict color appearance. When he set the textbooks down and began to experiment with color, he was sorely disappointed. He found that the color-matching measurements do not answer many important questions about color appearance.

Land's observation is consistent with our review of color-matching in Chapter . The results from the color-matching experiment can be used to predict when two lights will look the same, but they cannot be used to tell us what the two lights look like. As Color Plate 2 (Albers) illustrates, the experimental results in the color-matching experiment can be explained by the matches between the cone photopigment absorptions at a point, while color appearance forces us to think about the pattern of photopigment absorptions spread across the cone mosaics. Figure 1 illustrates this point again. The two squares in the image reflect the same amount of light to your eye. Yet, because the squares are embedded in different surroundings, we interpret the squares very differently, seeing one as light and the other as dark.

Land's paper contained a set of interesting qualitative demonstrations that illustrate these same points. While the limitations of the color-matching experiment were new to Land and the reviewers of his paper, they were not new to most color scientists. For example, Judd (1940) had worked for years trying to understand these effects. Later in this chapter I will

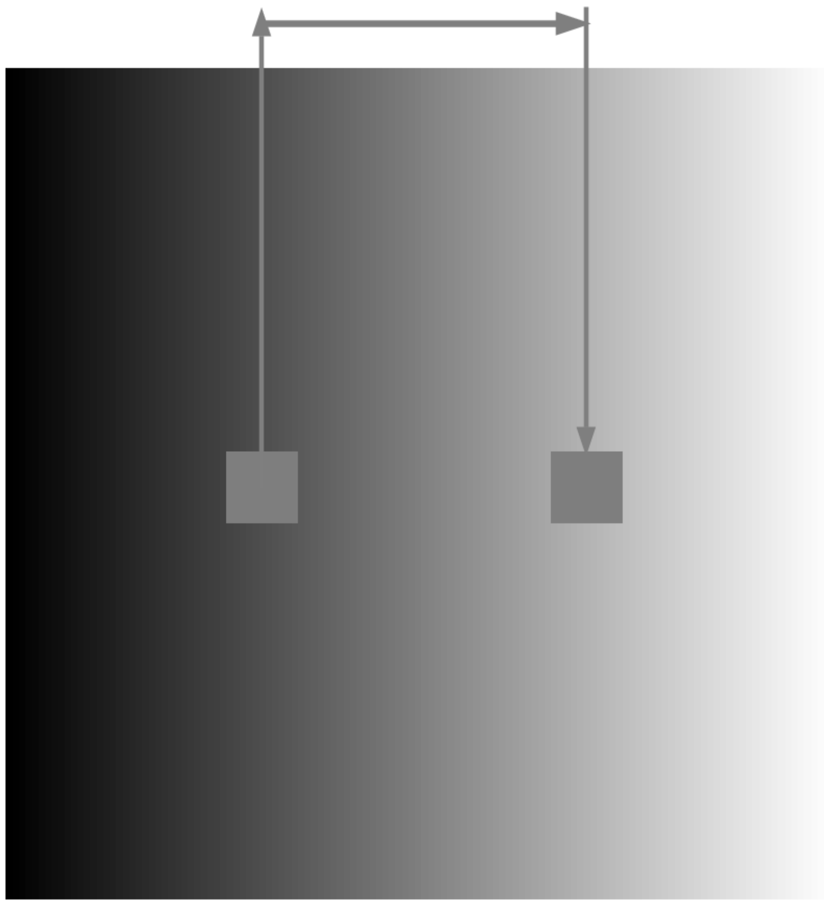

Figure 1: Color appearance in a region depends on the spatial pattern of cone absorptions, not just the absorptions within the region. The two square regions are physically identical and thus create the same local rate of photopigment absorption. Yet, they appear to have different lightness because of the difference in their relative absorptions compared to nearby areas.

review work at Kodak and in academic laboratories, contemporaneous with that of Land, that was designed to elucidate the mechanisms of color appearance. This episode in the history of color science remains important, however, because it reminds us that the phenomena of color appearance are very significant and very compelling, enough so to motivate Edwin Land to challenge whether the color establishment had answered the right questions. As to Land's additional and extraordinary claim in those papers, that there are two not three types of photoreceptors, well, we all have off days[1].

Color Constancy: Theory

If the absolute rates of photopigment absorptions don't explain color appearance, what does? The illusions in Color Plate 2 (Albers) and Figure 1 both suggest that color appearance is related to the *relative* cone absorption rates. Within an image, bright objects generate more cone absorptions than dark objects; red objects create more L cone absorptions and blue objects more S cone absorptions. Hence, one square in Figure 1 appears light because it is associated with more cone absorptions than its neighboring region, while the other appears dark because it is associated with fewer cone absorptions. The relative absorption rate is very closely connected to the idea of the stimulus contrast that has been so important in this book. Color appearance depends more on the local contrast of the cone absorptions than on the absolute level of cone absorptions.

The dependence on relative, rather than absolute, absorption rates is a general phenomenon, not something that is restricted to a few textbook illusions. Consider a simple thought experiment that illustrates the generality of the phenomenon. Suppose you read this book indoors. The white part of the page reflects about 90 percent of the light towards your eye, while the black ink reflects only about 2 percent. Hence, if the ambient illumination inside a reading room is 100 units, the white paper reflects 90 units and the black ink 2 units. When you take the book outside, the illumination level can be 100 times greater, or 10,000 units. Outside the black ink reflects 200 units towards your eye, which far exceeds the level of the white paper when you were indoors. Yet, the ink continues to look black. As we walk about the environment, then, we must constantly be inferring the lightness and color of objects by comparing the spatial pattern of cone absorptions[2].

This thought experiment also illustrates us that the color we perceive informs us mainly about objects. The neural computation of color is structured so that objects retain their color appearance whether we encounter them in shade or sun. When the color appearance of an object changes, we think that the object itself has changed. The defining property of an object is not the absolute amount of light it reflects, but rather how much light it reflects relative to other objects. From our thought experiment, it follows that the color of an object imaged at a point on the retina should be inferred from the relative level of cone absorptions caused by

[1]Of course, even on his off days, Land was worth a billion dollars.
[2]This example was used by Hering (1964).

an object. To compute the relative level of cone absorptions, we must take into account the spatial pattern of cone absorptions, not just the cone absorptions at a single point.

On this view, color appearance is a mental explanation of why an object causes relatively more absorptions in one cone type than another object. The physical attribute of an object that describes how well the object reflects light at different wavelengths is called the object's *surface reflectance*. Generally, objects that reflect light mainly in the long-wavelength part of the spectrum usually appear red; objects that reflect mainly short-wavelength light usually appear blue. Yet, as we shall explore in the next few pages, interpreting the cone absorption rates in terms of the surface reflectance functions is not trivial. How the nervous system makes this interpretation is an essential question in color appearance. A natural place to begin our analysis of color appearance, then, is with the question: how can the central nervous system can infer an object's surface reflectance function from the mosaic of cone absorptions?

Spectral Image Formation

To understand the process of inferring surface reflectance from the light incident at our eyes, we must understand a little about how images are formed. The light incident at our corneas and absorbed by our cones depends in part on the properties of the objects that reflect the light and in part on the wavelength composition of the ambient illumination. We must understand each of these components, and how they fit together, to see what information we might extract from the retinal image about the surface reflectance function. A very simple description of the imaging process is shown in Figure 2 (a).

Ordinarily, image formation begins with a light source. We can describe the spectral properties of the light source in terms of the relative amount of energy emitted at each wavelength, namely the *spectral power distribution* of the light source (see Chapter). The light from the source is either absorbed by the surface or reflected. The fraction of the light reflected by the surface defines the *surface reflectance* function. As a first approximation, we can calculate the light reflected towards the eye by multiplying the spectral power distribution and the surface reflectance function together (Figure 2 (b)). We will call this light the *color signal* because it serves as the signal that ultimately leads to the experience of color. The color signal leads to different amounts of absorptions in the three cone classes, and the interpretation of these cone absorptions by the nervous system is the basis of our color perception.

In Chapter I reviewed some properties of illuminants and sensors. But, this is the first time we have considered the surface reflectance function; it is worth spending time thinking about some of the properties of how surfaces reflect light. Figure 3 shows the reflectance function of four matte papers, that is papers with a smooth even surface free from shine or highlights. Because these curves describe the fraction of light reflected, they range between zero and one. While it is common to refer to an object as having a surface reflectance function, as I have just done, in a certain sense, the notion of a surface reflectance function is a ruse. If you look about the room you are in, you will probably see some surfaces that are shiny or glossy.

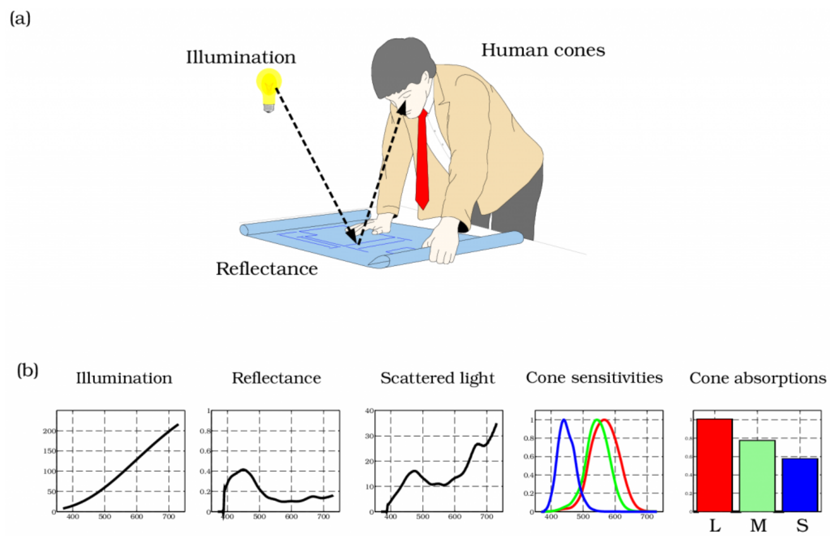

Figure 2: A description of spectral image formation. (a) Light from a source arrives at a surface and is reflected towards an observer. The light at the observer is absorbed by the cones and ultimately leads to a perception of color. (b) The functions associated with the imaging process include the spectral power distribution of the light source, the surface reflectance function of the object, the result of multiplying these two functions to create the color signal incident at the eye, and the cone absorptions caused by the incident signal.

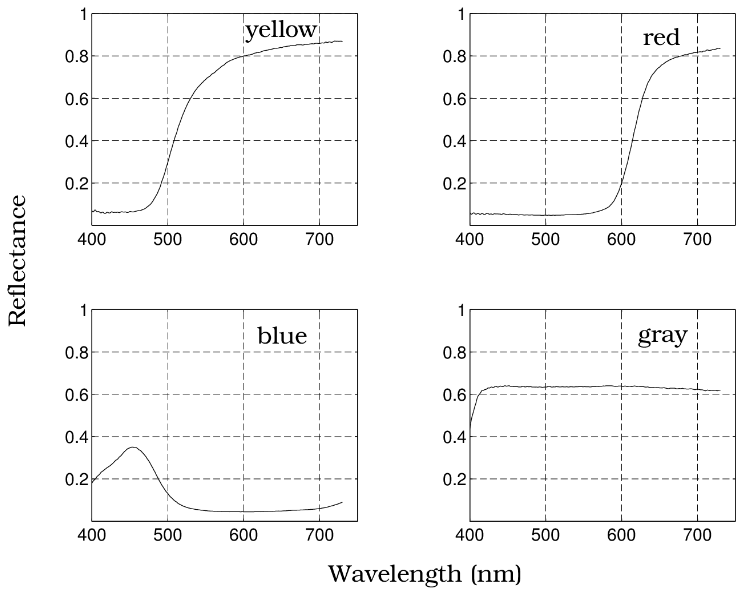

Figure 3: The surface reflectance function measures the proportion of light scattered from a surface at each wavelength. The panels show the surface reflectance functions of various colored papers along with the color name associated with the paper. Surface reflectance correlates with the color appearance; as Newton wrote “colors in the object are nothing but a disposition to reflect this or that sort of ray more copiously than the rest.”

As you move around these surfaces, changing the geometrical relationship between yourself, the lighting, and the surface, the light reflected to your eye changes considerably. Hence, the tendency of the surface to reflect light towards your eye does not depend only on the surface; the light scattered to your eye also depends on the viewing geometry, too[3].

The surface reflectance dependence on viewing geometry because the reflected light arises from several different physical processes that occur when light is incident at the surface. Each of these processes contributes simultaneously to the light scattered from a surface, and each has its own unique properties. The full model describing reflectance appears to be be complex; but, Shafer (1985) has created a simple approximation of the reflection process, called the *dichromatic reflection model*, that captures several important features of surface reflectance. Figure 4 (a) sketches the model, which applies to a broad collection of materials called *dielectric* surfaces[4] (Klinker et al. (1988); Shafer (1985); Nayar and Bolle (1993), Wolff (1994)).

According to the dichromatic reflection model, dielectric material consists of a clear substrate with embedded colorant particles. One way light is scattered from the surface is by a mirror-like reflection at the interface of the surface. This process is called *interface* reflections. A second scattering process takes place when the rays enter the material. These rays are reflected randomly between the colorant particles. A fraction of the incident light is absorbed by the material, heating it up, and part of the light emerges. This process is called *body* reflection.

The spatial distributions of light scattered by these two mechanisms are quite different (Figure 4 (b)). Light scattered by interface reflection is quite restricted in angle, much as a mirror reflects incident rays. Conversely, the light scattered by body reflection emerges equally in all directions. When a surface has no interface reflections, but only body reflections, it is called a *matte* or *Lambertian* surface. Interface reflection is commonly called *specular* reflection and is the reason why some objects appear *glossy*.

The different geometrical distribution in how body and interface reflections are reflected is the reason why specular highlights on a surface appear much brighter than diffuse reflection. Nearly all of the specular scattering is confined to a small angle; the body reflection is divided among many directions. The interface reflections provide a strong signal, but because they can only be seen from certain angles they are not a reliable source of information. As the object and observer change their geometric relationship the specular highlight moves along the surface of the object, or it may disappear altogether.

For many types of materials, interface reflection is not selective for wavelength. The spectral power distribution of the light scattered at the interface is the same as the spectral power distribution of the incident light. This is the reason specular highlights take on the color of the illumination source. Body reflection, on the other hand, does not return all wavelengths uniformly. The particles in the medium absorb light selectively, and it is this property of the material that distinguishes objects in terms of their color appearance. Ordinarily, when people

[3] Also, some types of materials fluoresce, which is to say they absorb light at one wavelength and emit light at another (longer) wavelength. This is also a linear process, but too complex to consider in this discussion.

[4] Dielectrics are non-conducting materials.

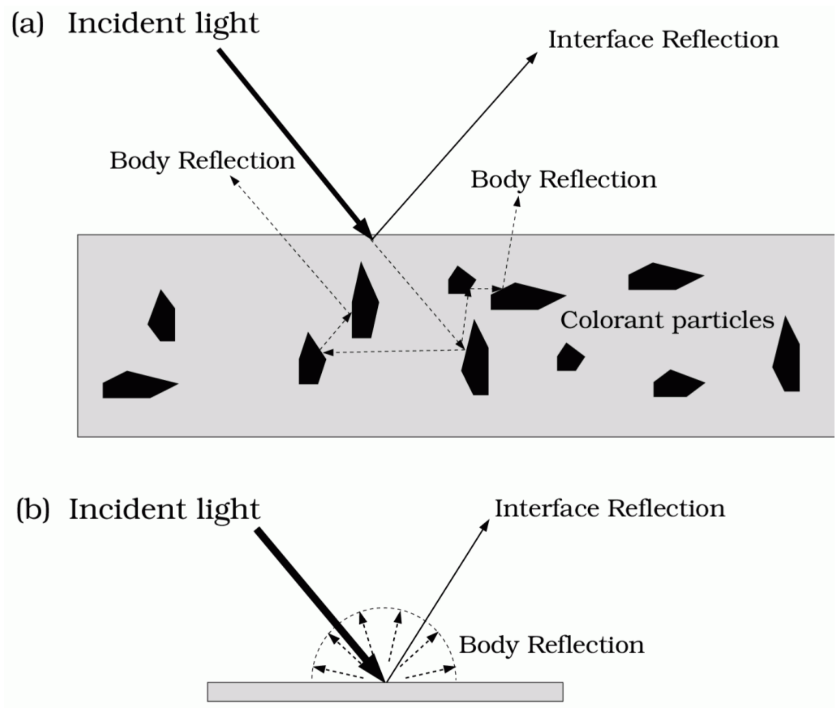

Figure 4: The dichromatic reflection model of surface reflectance in inhomogeneous materials. (a) Light is scattered from a surface by two different mechanisms. Some incident light is reflected at the interface (interface reflection). Other light enters the material, interacts with the embedded particles, and then emerges as reflected light (body reflection). (b) Rays of light reflected by interface reflections is likely to be concentrated in one direction. Rays of light reflected by body reflection are reflected with nearly equal likelihood in many different directions. Because interface reflections are concentrated in certain directions, light reflected by this process can be much more intense than light reflected by body reflection.

refer to the surface reflectance of an object, they mean to refer to the body reflection of the object.

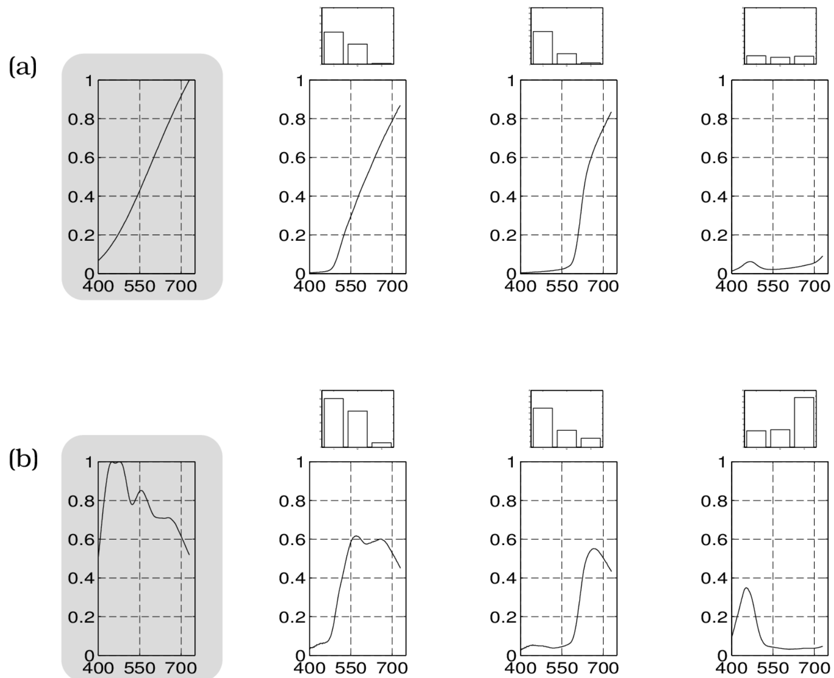

Figure 5: The light reflected from objects changes as the illuminant changes. (a) The shaded panel on the left shows the spectral power distributions of a light source similar to a tungsten bulb. The three graphs on the right show the light reflected from the red, green and yellow papers in Figure 3 when illuminated by this source. The bar plots above the graphs show the three cone absorption rates caused by the color signal. (b) When the light source is similar to the blue sky, as in the shaded panel on the left, the light reflected from the same papers is quite different. These change considerably, too, and are thus an unreliable cue to the surface reflectance of the object.

We can describe the reflection of light by a matte surface with a simple mathematical formula. Suppose that the illuminant spectral power distribution is $ e( ) $. We suppose that the body reflectance is $s( ) $. Then the color signal, that is the light arriving at the eye, is

$$c(\lambda) = s(\lambda)e(\lambda). \tag{0.1}$$

Figure 5 shows several examples of the light reflected from matte surfaces. The shaded graph in Figure 5 (a) is the spectral power distribution of an illuminant similar to a tungsten bulb. The other panels show the spectral power distribution of light that would be reflected from the red, green and yellow papers in Figure 3. The shaded graph in Figure 5 (b) shows the spectral power distribution similar to blue sky illumination and the light reflected from the same three papers. Plainly, the spectral composition of the reflected light changes when the illuminant changes.

We can calculate the cone absorption rates caused by each of these color signals (see Chapter). These rates are shown in the bar plots inset within the individual graphs of reflected light. By comparing the insets in the top and bottom, you can see that the cone absorption rates from each surface changes dramatically when the illumination changes. This observation defines a central problem in understanding color appearance. Color is a property of objects; but, the reflected light, and thus the cone absorptions, varies with the illumination. If color must describe a property of an object, the nervous system must *interpret* the mosaic of photopigment absorptions and estimate something about the surface reflectance function. This is an estimation problem. How can the nervous system use the information in the cone absorptions to infer the surface reflectance function?

Surface reflectance estimation

There are some very strong limitations on what we can achieve when we set out to estimate surface reflectance from cone absorptions. First, notice that the color signal depends on two spectral functions that are continuous functions of wavelength: the spectral power distribution of the ambient illumination and the surface reflectance function. The light incident at the eye is the product of these two functions. So, any illuminant and surface combination that produces this same light will be indistinguishable to the eye.

One easy mathematical way to see why this is so is to consider the color signal. Recall that the color signal is equal to the product of the illuminant spectral power distribution $ e( ) $ and the surface reflectance function $ s( ) $,

$$c(\lambda) = s(\lambda)e(\lambda). \tag{0.2}$$

Suppose we replace the illuminant with a new illuminant, $ f( ) e( ) $ and all of the surfaces with new functions $ s( ) / f( ) $. This change has no effect on the color signal,

$$c(\lambda) = \frac{s(\lambda)}{f(\lambda)} f(\lambda)e(\lambda) = s(\lambda)e(\lambda) \tag{0.3}$$

and thus no effect on the photopigment absorption rates. Hence, there is no way the visual system can discriminate between these two illuminant and surface pairs.

Now, consider a second limitation to the estimation problem. The visual system does not measure the spectral power distribution directly. Rather, the visual system only encodes the absorption rates of the three different cones. Hence, the nervous system cannot be certain which of the many metameric spectral power distributions is responsible for causing the observed cone absorption rates (see Chapter) for a definition of metameric). This creates even more uncertainty for the estimation problem.

In the introduction to this part of the book, I quoted Helmholtz' suggestion: the visual system imagines those objects being present that could give rise to the retinal image. We now find that the difficulty we have in following this advice is not that are no solutions, but rather that there are too many. We encode so little about the color signal that many different objects could all have given rise to the retinal image.

Which of the many possible solutions should we select? The general strategy we should adopt is straightforward: Pick the most likely one. Will this be a helpful estimate, or are there so many likely signals that encoding the most likely one is hardly better than guessing with no information?

Perhaps the most important point that we have learned from color constancy calculations over the last ten years is this: the set of surface and illuminant functions we encounter is not so diverse as to make estimation from the cone catches useless. Some surface reflectance functions and some illuminants are much more likely than others, even with only three types of cones, it is possible to make educated guesses that do more good than harm.

The surface reflectance estimation algorithms we will review are all based on this principle. They differ only in the set of assumptions they make concerning what the observer knows and what we mean by most likely. I review them now because some of the tools are useful and interesting, and some of the summaries of the data are very helpful in practical calculations and experiments.

Linear Models

To estimate which lights and surfaces are more probable, we need to do two things. First, we need to measure the spectral data from lights and surfaces. Second, we need a way to represent the likelihood of observing different surface and illuminant functions.

Since the early part of the 1980s, *linear models* of surface and illuminant functions have been used widely to represent our best guess about the most likely surface and illuminant functions. A linear model of a set of spectral functions, such as surface reflectances, is a method of efficiently approximating the measurements. There are several ways to build linear models, including *principal components analysis*, *centroid analysis*, or *one mode analysis*. These methods have much in common, but they differ slightly in their linear model formulation and error measures (Cohen (1964); Judd et al. (1964); Maloney (1986); Marimont and Wandell (1992)).

As an example of how to build a linear model, we will review a classic paper by Judd et al. (1964). These authors built a linear model of an important source of illumination, daylight spectral power distributions. They collected more than six hundred measurements of the spectral power distribution of daylights at different times of day and under different weather conditions and on different continents. To measure the spectral power distribution of daylight we place an object with a known reflectance outside. It is common to use blocks of pressed magnesium oxide as a standard object because such blocks reflect light of all wavelengths nearly equally. Moreover, the material is essentially a pure diffuser: a quantum of light incident on the surface from any angle is reflected back with equal probability in all other directions above the surface.

Since they were interested in the relative spectral composition, not the absolute level, Judd et al. normalized their measurements so that they were all equal to the value 100 at 560nm. Their main interest was in the wavelength regime visible to the human eye, so they made measurements roughly from 400nm to 700nm. Their measurements were spaced every 10 nm. Hence, they could represent each daylight measurement by a set of thirty-one numbers. Three example daylight spectral power distributions, normalized to coincide at 560nm, are shown in Figure 6.

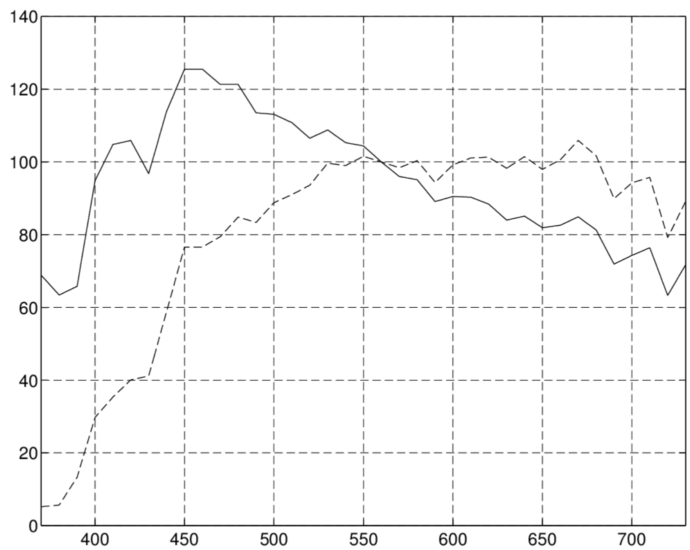

Figure 6: The relative spectral power distribution of three typical daylights. The curves drawn here are typical daylight measured by Judd et al. (1964). The curves are normalized to coincide at 560nm (Source: Judd et al. (1964)).

The data plotted in Figure 6 show that measured daylight relative spectral power distributions can differ depending on the time of day and the weather conditions. But, after examining many daylight functions, Judd et al. found that the curves do not vary wildly and unpredictably; the data are fairly regular. Judd et al. captured the regularities in the data by building a linear model of the observed spectral power distributions. They designed their linear model, a *principal components model*, using the following logic.

First, they decided that they wanted to approximate their observations in the *squared-error sense*. That is, suppose $e(\lambda)$ is a measurement, and $\hat{e}(\lambda)$ is the linear model estimate of the measurement. Then, they decided to select the approximation in order to minimize the *squared error*

$$\sum_{\lambda}(e(\lambda) - \hat{e}(\lambda))^2.$$

When we consider the collection of observations as a whole, the function that approximates the entire data set with the smallest squared error is the mean. The mean observation from Judd et al.'s data set, $ e_{0}( ) $, is the bold curve in Figure 7.

Once we know the mean, we need only to approximate the difference between the mean and each individual measurement. We build the linear model to explain these differences as follows. First, we select a fixed set of *basis functions*. Basis functions, like the mean, are descriptions of the measurements. We approximate a measurement's difference from the mean as the weighted sum of the basis functions. For example, suppose $\Delta e_j(\lambda)$ is the difference between the j^{th} daylight measurement and the mean daylight. Further, suppose we select a set of N basis functions, $E_i(\lambda)$. Then, we approximate the differences from the mean as the weighted sum of these basis functions, namely

$$\Delta e_j(\lambda) \approx \sum_{i=1}^{i=N} w_i E_i(\lambda). \tag{0.4}$$

The basis functions are chosen to make the sum of the squared errors between the *collection* of measurements and their approximations as small as possible. The number of basis functions, N, is called the *dimension* of the linear model. The values w_i are called the linear model *weights*, or *coefficients*. They are chosen to make the squared error between an *individual* measurement and its approximation as small as possible. They serve to describe the properties of the specific measurement.

As the dimension of the linear model increases, the precision of the linear model approximation improves. The dimension one chooses for an application depends on the required precision[5].

Judd et al. found an excellent approximation of the daylight measurements using the mean and two basis functions. The linear model representation expresses the measurements efficiently. The mean and two basis functions are fixed, side conditions of the model. Their linear model approximation of each measurement uses only two weights. The empirical results have been confirmed by other investigators and the results have been adopted by the international color standards organization to create a model of daylights (Dixon (1978); Sastri and Das (1966)). The mean and two basis terms from the international standard are plotted in Figure 7.

[5] The basis functions that minimize the squared error can be found in several ways, most of which are explained in widely available statistical packages. If the data are in the columns of a matrix, one can apply the singular value decomposition to the data matrix and use the left singular vectors. Equivalently, one can find the eigenvectors of the covariance matrix of the data.

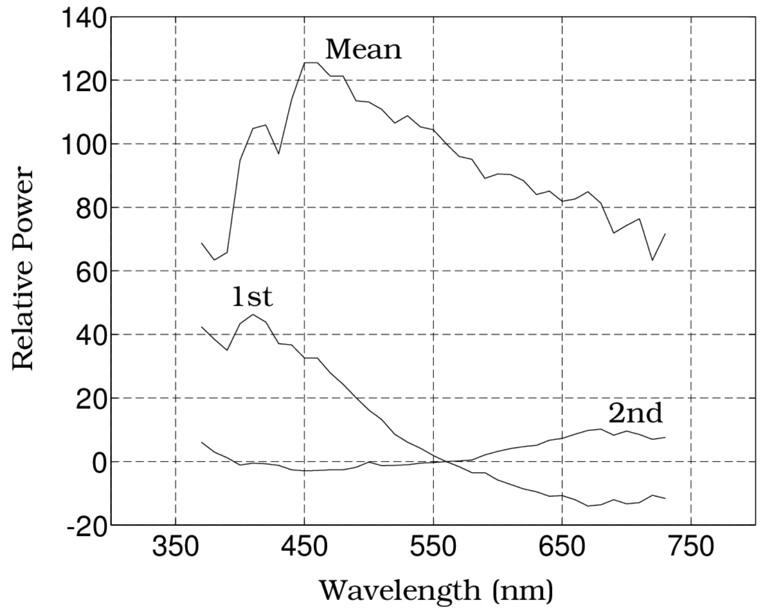

Figure 7: A linear model for daylight spectral power distributions. The curve labeled mean is the mean spectral power distribution of a set of daylights whose spectral power distributions were normalized to a value of 100 at 560nm. The curves labeled 1st and 2nd show the two basis curves used to define a linear model of daylights. By adding together the mean and weighted sums of the two basis functions, one can generate examples of typical relative spectral power distributions of daylight. (Source: Judd et al. (1964)).

Because daylights vary in their absolute spectral power distributions, not just their relative distributions, we should extend Judd et al.'s linear model to a three-dimensional linear model that includes absolute intensity. A three dimensional linear model we might use consists of the mean and the two derived curves. In this case the three-dimensional linear model approximation becomes[6]

$$e(\lambda) = \sum_{i=1}^{3} w_i E_i(\lambda). \tag{0.5}$$

We can express the linear model in Equation 0.5 as a matrix equation, $\mathbf{e} = \mathbf{B_e w}$ in which $\mathbf{e}$ is a vector representing the illuminant spectral power distribution, the three columns of $\mathbf{B_e}$ contain the basis functions $E_i(\lambda)$, and $\mathbf{w}$ is a three dimensional vector containing the linear model coefficients w_i.

We can see why linear models are efficient by writing Equation 0.5 as a matrix tableau.

$$\begin{pmatrix} . \\ . \\ . \\ e(\lambda) \\ . \\ . \\ . \end{pmatrix} = \begin{pmatrix} . & . & . \\ . & . & . \\ . & . & . \\ E_1(\lambda) & E_2(\lambda) & E_3(\lambda) \\ . & . & . \\ . & . & . \\ . & . & . \end{pmatrix} \begin{pmatrix} w_1 \\ w_2 \\ w_3 \end{pmatrix}$$

The single spectral power distribution, the vector on the left, consists of measurements at many different wavelengths. The linear model summarizes each measurement as the weighted sum of the basis functions, which are the same for all measurements, and a few weights, $\mathbf{w}$, which are unique to each measurement. The linear model is efficient because we represent each additional measurement using only three weights, $\mathbf{w}$, rather than the full spectral power distribution.

Simple Illuminant Estimation

Efficiency is useful; but, if efficiency were our only objective we could find more efficient algorithms. The linear models are also important because they lead to very simple estimation algorithms. As an example, consider how we might use a device with three color sensors, like the eye, to estimate the spectral power distribution of daylight. Such a device is vastly simpler than the spectroradiometer Judd et al. needed to make many measurements of the light.

[6]It is possible to improve on this model slightly, but as a practical matter these three curves do quite well as basis functions.

Suppose we have a device with three color sensors, whose spectral responsivities are, say, $r_i(\lambda),\ i = 1 \dots 3$. The three sensor responses will be

$$\begin{aligned} r_1 &= \sum_\lambda R_1(\lambda)\, e(\lambda) \\ r_2 &= \sum_\lambda R_2(\lambda)\, e(\lambda) \\ r_3 &= \sum_\lambda R_3(\lambda)\, e(\lambda) \end{aligned} \tag{0.6}$$

We can group these three linear equations into a single matrix equation

$$r = \mathbf{S}\, e \tag{0.7}$$

where the column vector r contains the sensor responses, the rows of the matrix R are the sensor spectral responsivities, and e is the illuminant spectral power distribution.

Before the Judd et al. study, one might have thought that three sensor responses are insufficient to estimate the illumination. But, from their data we have learned that we can approximate e with a three-dimensional linear model, $e \approx E\,\mathbf{w}$. This reduces the equation to

$$r \approx (\mathbf{SB_e})\,\mathbf{w} \tag{0.8}$$

The matrix $(\mathbf{SB_e})$ is 3×3, and its entries are all known. The sensor responses, r, are also known. The only unknown is w. Hence, we can estimate w, and use these weights to calculate the spectral power distribution, $\mathbf{B_e}\,\mathbf{w}$.

This calculation illustrates two aspects of the role of linear models. First, linear models represent a priori knowledge about the likely set of inputs. Using this information permits us to convert underdetermined linear equations (Equation 0.7) into equations we can solve (Equation 0.8). Linear models are a blunt but useful tool for representing probabilities. Using linear models, it becomes possible to use measurements from only three color sensors to estimate the full relative spectral power distribution of daylight illumination.

Second, linear models work smoothly with the imaging equations. Since the imaging equations are linear, the estimation methods remain linear and simple.

Surface Reflectance Models

The daylights are an important class of signals for vision. For most of the history of the earth, daylight was the only important light source. There is no similar set of surface reflectance functions. I was reminded by this once by the brilliant color scientist, G. Wyszecki. When I was just beginning my study of these issues, I asked him why he had not undertaken a study of surfaces similar to daylight study. He shrugged at me and answered, "How do you sample the universe?"

Wyszecki was right, of course. The daylight measurement study could begin and end in a single paper. There is no specific set of surfaces that of equal importance to the daylights, so we have no way to perform a similar analysis on surfaces. But, there are two related questions we can make some progress on. First, we can ask what the properties are of certain collections of surfaces that are of specific interest to us, say for practical applications. Second, we can ask what the visual system, with only three types of cones, can infer about surfaces.

Over the years linear models for special sets of materials can be used in many applications. Printer and scanner manufacturers may be interested in the reflectance functions of inks. Computer graphics programmers may be interested in the reflectance factors of geological materials, or tea pots. Color scientists have repeatedly measured the reflectance functions of standard color samples used in industry, such as the Munsell chips. These cases can be of practical value and interest in printing and scanning applications (e.g. Marimont and Wandell (1992); Farrell et al. (1992); Vrhel and Trussell (1994); Drew and Funt (1992)). To discover the regularities in surface functions, then, we should measure the body reflection terms. From the studies that have taken place over the last several years, it has become increasingly clear that in the visible wavelength region the surface reflectance functions tend to be quite smooth, and thus exhibit a great deal of regularity. Hence, linear models serve to describe the reflectance functions quite well.

For example, Cohen (1964), Maloney (1986) and Parkkinen et al. (1989) studied the reflectance properties of a variety of surfaces including special samples and some natural objects. For each of the sets studied by these authors the data can be modeled nearly perfectly using a linear model with less than six dimensions. Excellent approximations, though not quite perfect, can be obtained by three-dimensional approximations.

As an example, I have built a linear model to approximate a small collection surface reflectance functions for a color target, the *Macbeth ColorChecker*, that is used widely in industrial applications. The target consists of 24 square patches laid out in a 4 by 6 array. The surfaces in this target were selected to have reflectance functions similar to a range of naturally occurring surfaces. They include reflectances similar to human skin, flora, and other materials (McCamy et al. (1976)).

To create the linear model, I measured the surface reflectance functions of these patches with a spectral radiometer in my laboratory. The original data set, then, consisted of measurements from 370nm to 730nm in 1 nm steps for each of the 24 patches. Then, using conventional

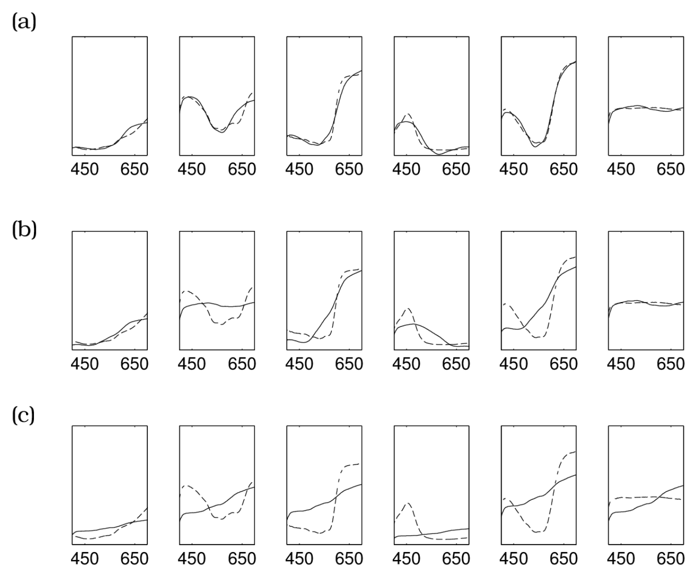

Figure 8: A linear model to approximate the surface reflectances in the Macbeth ColorChecker. The panels in each row of this figure show the surface reflectance functions of six colored surfaces (dashed line) and the approximation to these functions using a linear model (solid lines). The approximations using linear models with three (a), two (b) and one (c) dimension respectively are shown.

statistical packages, I calculated a three-dimensional linear model to fit all of these surface reflectance functions. The linear model basis functions, $S_i(\lambda)$, were selected to minimize the squared error[7].

$$\left(s(\lambda) - \sum_{i=1}^{N} \sigma_i S_i(\lambda) \right)^2 . \tag{0.9}$$

The values σ_i are called the *surface coefficients*, and we will represent them as a vector, $= (\sigma_1, \ldots, \sigma_N)$. There are fewer surface coefficients than data measurements. If we create a matrix whose columns are are the basis functions, $\mathbf{B_s}$, then we can express the linear model approximation as $\mathbf{B_s}$.

The dashed lines in Figure 8 show the reflectance functions of six of the twenty-four surfaces. The smooth curves within each row of the figure contain the approximations using linear models with different dimensionality. The bottom row shows a one-dimensional linear model; in this case the approximations are scaled copies of one another. As we increase the dimensionality of the linear model the approximations become very similar to the originals. The 3-dimensional model the approximations are quite close to the true functions.

The low-dimensional linear model approximates these surface reflectance functions because the functions vary smoothly as a function of wavelength. The linear model consists of a few, slowly varying basis functions shown in Figure 9. The first basis function captures the light-dark variation of the surfaces. The second basis function captures a red-green variation, and the third a blue-yellow variation.

[7] I calculated the singular value decomposition of the matrix whose columns consist of the surface reflectance vectors. I used the left singular vectors as the basis functions.

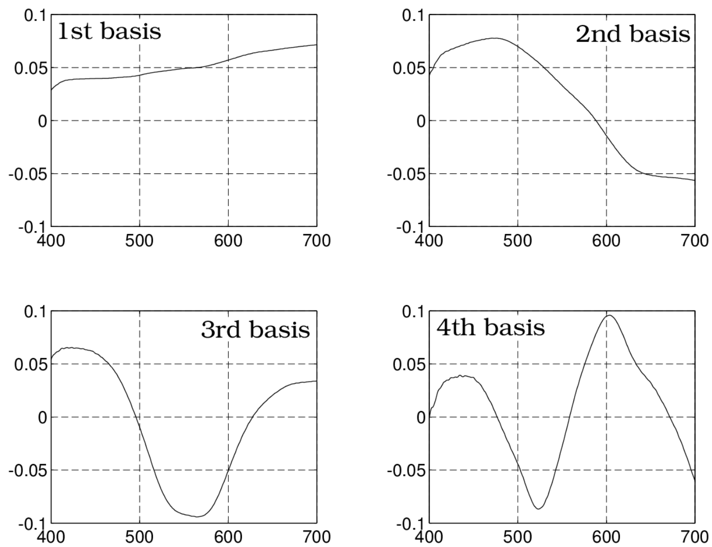

Figure 9: Basis functions of the linear model for the Macbeth ColorChecker. The surface reflectance functions in the collection vary smoothly with wavelength, as do the basis functions. The first basis function is all positive and explains the most variance in the surface reflectance functions. The basis functions are ordered in terms of their relative significance for reducing the error in the linear model approximation to the surfaces.

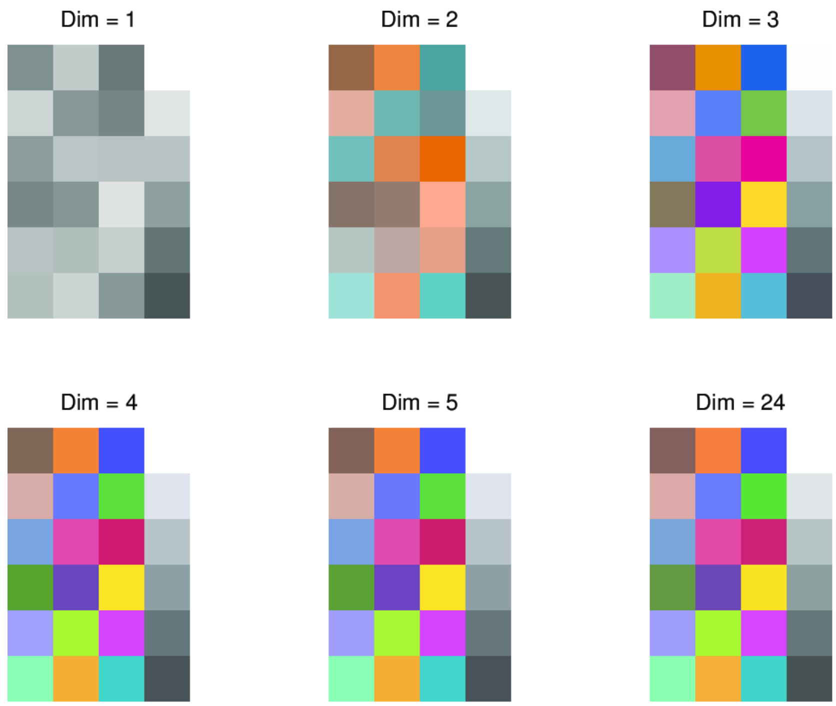

Figure 10: **Color Plate 4.** Color renderings of the linear model approximations to the Macbeth ColorChecker. The linear model approximations are shown rendered under a blue sky illumination. The dimension of the linear model approximation is shown above each image. The one-dimensional approximation the surfaces appear achromatic, varying only in lightness. For this illuminant, and using three or more dimensions in the linear model, the rendering is visually indistinguishable from a complete rendering of the surfaces.

Although the approximations are quite good, there are still differences between the surface reflectance functions and the three dimensional linear model. We might ask whether these differences are visually salient. This question is answered by the renderings of these surface approximations in Color Plate 4. The one-dimensional model looks like a collection of surfaces in various shades of gray. For the blue sky illumination used in the rendering, linear models with three or more dimensions are visually indistinguishable from a rendering using the complete set of data.

Sensor-based error measures

I have described linear models that minimize the squared error between the approximation and the original spectral function. As the last analysis showed, however, when we choose linear models to minimize the spectral error we are not always certain whether we have done a good job in minimizing the visual error. In some applications, the spectral error may not be the objective function that we care most about minimizing. When the final consumer of the image is a human, we may only need to capture that part of the reflectance function that is seen by the sensors.

If we are modeling reflectance functions for a computer graphics application, for example, there is no point in modeling the reflectance function at 300nm since the human visual system cannot sense light in that part of the spectrum anyway. For these applications, we should be careful to model accurately those parts of the function that are most significant for vision. In these cases, one should select a linear model of the surface reflectance by minimizing a different error measure, one that takes into account the selectivity of the eye.

Marimont and Wandell (1992) describe how to create linear models that are appropriate for the eye. They consider how to define linear models that minimize the root mean squared error in the photopigment absorption rates, rather than the root mean squared error of the spectral curves. Their method is called *one-mode analysis*. For many applications, the error measure minimized by one-mode analysis is superior to root mean squared error of the spectral curves.

Surface and Illuminant Estimation Algorithms

There is much regularity in daylight and surface functions; so, it makes sense to evaluate how well we estimate spectral functions from sensor responses. Estimation algorithms rely on two essential components.

First, we need a method of representing our knowledge about the likely surface and illuminant functions. For example, linear models can be used encode our a priori knowledge[8]. Second, all modern estimation methods assume that the illumination varies either slowly or not at all across the image. This assumption is important because it means that the illumination adds very few new parameters to estimate.

Consider an example of an image with p points. We expect to obtain 3 cone absorption rates at each image point, so there are $3p$ measurements. If we can use a surface 3 dimensional model for the surfaces, then there are $3p$ unknown surface coefficients. And, there is a linear relationship between the measurements and the unknown quantities. If the illuminant is known, then the problem is straightforward to solve.

The additional unknown illuminant parameters make the problem a challenge. If the illuminant can vary from point to point, there will be $6p$ unknown parameters and the mismatch between known and unknown parameters will be very great. But, if the illuminant is constant across the image, we only have 3 additional parameters. In this case, by making some modest assumptions

[8]More sophisticated methods are based on using Bayesian estimation as part of the calculation. For example, see Brainard and Freeman (1994) and D'Zmura and Iverson (1993a); D'Zmura and Iverson (1993b); D'Zmura and Iverson (1994).

about the image, we can find ways to infer these three parameters and then proceed to estimate the surface parameters.

Modern estimation algorithms work by find a method to overcome the mismatch between the measurements and the unknowns. We can divide existing estimation algorithms into two groups. The majority of estimation algorithms infer the illumination parameters by making one additional assumption about the image contents. For example, suppose we know the reflectance function of one surface. Then, we can use the sensor responses from that surface to measure the illuminant parameters. Knowing the reflectance function of one surface in the image compensates for the three unknown illuminant parameters. There are several implementations of this principle. The most important is the assumption that the average of all the surfaces in the image is gray, which is called the *gray-world* assumption (Buchsbaum (1980); Land (1977)). Other algorithms are based on the assumption that the brightest surface in the image is a uniform, perfect reflector (McCann et al. (1976)). An interesting variant on both of these assumptions is the idea that we can identify specular or glossy surfaces in the image. Since specularities reflect the illumination directly, often without altering the illuminant's spectral power distribution, the sensor responses to glossy surfaces provide information about the illuminant (Lee (1986); D'Zmura and Lennie (1986); Tominaga and Wandell (1989), Tominaga and Wandell (1990)).

A second group of estimation algorithms compensates for the mismatch in measurements and parameters by suggesting ways to acquire more data. For example, Maloney and I showed that if one adds a fourth sensor (at three spatial locations), one can also estimate the surface and illuminants. D'Zmura and Iverson (1993a) and D'Zmura and Iverson (1993b) explored an interesting variant of this idea. They asked what information is available if we observe the same surface under several illuminants. Changing the illumination on a surface is conceptually equivalent to seeing the surfaces with additional sensors. Pooling information about the same object seen under different illuminants, is much like acquiring additional information from extra sensors (e.g., see Wandell (1987)).

Illuminant correction: An example calculation

Before returning to experimental measurements of color appearance, let's perform an example calculation that is of some practical interest as well as of some interest in understanding how the visual system might compensate for illumination changes. By working this example, we will start to consider what neural operations might permit the visual pathways to compensate for changes in the ambient illumination.

First, let's write down the general expression that shows how the surface and illuminant functions combine to yield the cone absorption rates. The three equations for the three cone types, L, M, and S, are

$$
\begin{aligned}
r_1 &= \sum_{\lambda} R_1(\lambda)E(\lambda)S(\lambda) \\
r_2 &= \sum_{\lambda} R_2(\lambda)E(\lambda)S(\lambda) \\
r_3 &= \sum_{\lambda} R_3(\lambda)E(\lambda)S(\lambda).
\end{aligned}
\tag{0.10}
$$

Next, we replace the illuminant and surface functions in Equation 0.10 with their linear model approximations. This yields a new relationship between the coefficients of the surface reflectance linear model, , and the three-dimensional vector of cone absorptions, **r**,

$$
\mathbf{r} \approx \ _e \ . \tag{0.11}
$$

We call the matrix $_e$ that relates these two vectors the *lighting* matrix. The entries of this matrix depend upon the illumination, **e**. The ij^{th} entry of the lighting matrix is

$$
\sum_{\lambda} \left(\sum_{k} w_k E_k(\lambda) \right) R_i(\lambda) S_j(\lambda). \tag{0.12}
$$

We can compute two lighting matrices (Equation 0.11) from the spectral curves we have been using as examples. For one lighting matrix I used the mean daylight spectral power distribution, and for the other I used the spectral power distribution of a tungsten bulb. I used the linear model of the Macbeth ColorChecker for the surface basis functions and the Stockman and MacLeod cone absorption functions (see the appendix to Chapter). The lighting matrix for the blue sky illumination is

$$
\begin{pmatrix}
591.48 & 223.05 & -643.05 \\
477.62 & 376.93 & -564.48 \\
267.61 & 487.46 & 350.39
\end{pmatrix}
$$

and the lighting matrix for the tungsten bulb is

$$
\begin{pmatrix}
593.45 & 168.37 & -646.71 \\
445.79 & 312.79 & -564.33 \\
152.46 & 278.51 & 185.47
\end{pmatrix}.
$$

Notice that the largest differences between the matrices are in the third row. This is the row that describes the effect of each surface coefficient on the S cone absorptions. The blue sky lighting matrix contains much larger values than matrix for the tungsten bulb. This makes sense because that is the region of the spectrum where these two illuminant spectral power distributions differ the most (see Figure 5).

Imagine, now the following way in which the visual system might compensate for illumination changes. Suppose that the cortical analysis of color is based upon the assumption that the illumination is always that of a blue sky. When the illumination is different from the blue sky, the retina must try to provide a neural signal that is similar to the one that would have been observed under a blue sky. What computation does the retina need to perform in order to transform the cone absorptions obtained under the tungsten bulb illuminant into the cone absorption that would have occurred under the blue sky?

The cone absorptions from a single surface under the two illuminants can be written as

$$
\begin{aligned}
\mathbf{r} &\approx {}_{e}\,, \text{and} \\
\mathbf{r}' &\approx {}_{e'}\,.
\end{aligned}
$$

By inverting the lighting matrices and recombining terms, we find that the cone absorptions under the two illuminants should be related linearly as,

$$
\mathbf{r} \approx {}_{e}\;{}_{e'}^{-1}\,\mathbf{r}'. \tag{0.13}
$$

Hence, we can transform the cone absorptions from a surface illuminated by the tungsten bulb into the cone absorptions of the same surface illuminated by the blue sky by the following:

$$
\mathbf{r} = \begin{pmatrix} 0.8119 & 0.2271 & 0.0550 \\ -0.0803 & 1.1344 & 0.1282 \\ 0.0429 & -0.0755 & 1.8091 \end{pmatrix} \mathbf{r}'. \tag{0.14}
$$

The retina can compensate for the illumination change by linearly transforming the observed cone absorptions, $\mathbf{r}'$, into a new signal, $\mathbf{r}$.

Now, what does it mean for the retina to compute a linear transformation? The linear transformation consists of a simple series of multiplications and additions. For example, consider the third row of the matrix in Equation 0.14. This row defines how the new S cone absorptions should be computed from the observed absorptions. When we write this transformation as a single linear equation we see that the observed and transformed signals are related as

$$
S = .0429\ L' + -0.0755\ M' + 1.8091\ S'. \tag{0.15}
$$

The transformed S cone absorption is mainly a scaled version of the observed absorptions. Because the tungsten bulb emits much less energy in the short-wavelength part of the spectrum, the scale factor is larger than one. In addition, to be absolutely precise, we should add in a small amount of the observed L cone signal and subtract out a small amount of the observed M cone signal. But, these contributions are relatively small compared to the contribution from the S cones. In general, for each of the cone types, the largest contributions to the transformed signal are scaled copies of the same signal type.

In this matrix, and in many practical examples, the only additive term that is not negligible is the contribution of the M cone response to the transformed L signal. As a rough rule, because the diagonal terms are much larger than the off-diagonal terms, we can obtain good first order approximation to the proper transformation by simply scaling the the observed cone absorptions (e.g., Foster and Nascimento (1994)).

Compensating for the illumination change by a purely diagonal scaling of the cone absorptions is called *von Kries Coefficient Law.* The correction is not as precise as the best linear correction, but it frequently provides a good approximation. And, as we shall see in the next section, the von Kries Coefficient Law describes certain aspects of human color appearance measurements as well.

Color Constancy: Experiments

> In woven and embroidered stuffs the appearance of colors is profoundly affected by their juxtaposition with one another (purple, for instance, appears different on white than on black wool), and also by differences of illumination. Thus embroiderers say that they often make mistakes in their colors when they work by lamplight, and use the wrong ones. [Aristotle, c. 350 B.C.E. Meteorologica].

Asymmetric Color-matching Experiments

To formulate some ideas about how the visual pathways compute color appearance, we adopted the view that color appearance is a psychological estimate of the surface reflectance function (body reflectance). By thinking about computational methods of estimating body reflectance, we have discovered how the cone absorptions from an object vary with illuminant changes. Finally, we have seen that it is possible compensate approximately for these changes by a applying linear transformation to the cone absorptions.

From the computational analysis, we have discovered a good principle to examine in experimental studies of color appearance: What is the relationship between the cone absorptions of objects that appear the same under different illuminants? The computational analysis suggests that the cone absorptions of lights with the same color appearance, but seen under different illuminants, are related by a linear transformation.

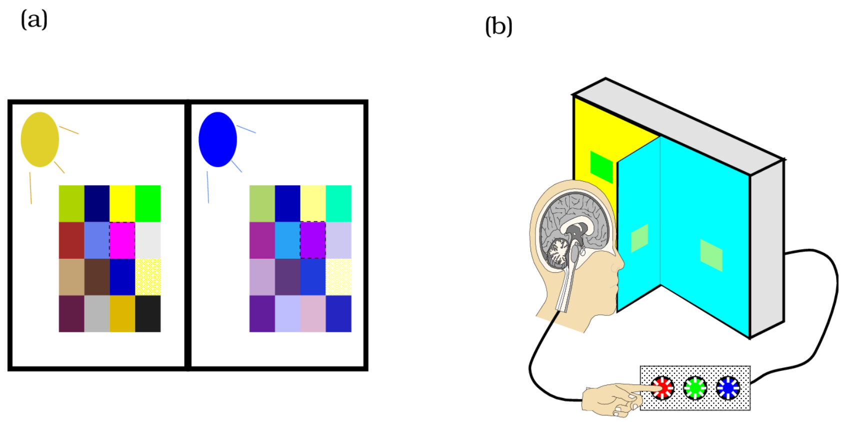

Figure 11: **Color Plate 5.** Two experimental methods for measuring asymmetric color-matches. (a) In a memory matching method, the observer sees a target under one illumination, remembers it, and then identifies a matching target after adapting to a second illumination. (b) In a haploscopic experiment the observer adapts the two eyes separately and makes a simultaneous appearance match. The basic findings from these two types of experiments are the same.

It is up to the experimentalist, then, to find an experimental method to use for measuring the cone absorptions that correspond to the same color appearance when seen in different viewing contexts. Color Plate 5 illustrates two methods of making such measurements. Panel (a) shows a *memory matching* method. In this method, the subject studies the color of a target that is presented under one illumination source and then must select a target that looks the same under a second illumination source. These measurements identify the stimuli, and thus the cone absorptions, of targets that appear the same under the two illuminants. The drawback of the method is that making such matches is very time-consuming because the subject must adapt to the two illumination sources completely, a process which can take two minutes or more.

Color Plate 5 (b) shows a second method called *dichoptic matching*. In this experiment the observer views the two scenes simultaneously in different eyes. One eye is exposed to a large neutral surface illuminated by, say, a daylight lamp. The other eye is exposed to an equivalent large neutral surface illuminated by, say, a tungsten lamp. These surfaces define a background stimulus that is different to each eye. The two backgrounds fuse in appearance, and appear as a single large background. To establish the asymmetric color-matches, the experimenter places a test object on top of the standard background seen by one eye. The observer selects a matching object from an array of choices seen by the second eye. The color appearance mapping is defined by measuring the cone absorptions of the *test* and *matching* objects, usually small colored papers, seen under their respective illuminants.

The dichoptic method has the advantage that the matches may be set quickly, avoiding the tedious delays required for visual adaptation in memory matches. The method has the disadvantage of making the assumption that adaptation occurs independently, prior to binocular combination[9].

The experimental methods illustrated in Color Plate 5 generalize conventional usual color-matching experiment. These methods are called *asymmetric* color-matching because, unlike conventional color-matching, in these experiments the matches are set between stimuli presented in different contexts. As we have already seen, because color appearance discounts estimated changes of the illumination, matches set in the asymmetric color-matching experiment are **not** cone absorption matches. Rather, the observer is establishing a match at a more central site following the correction for the properties of the scene.

The asymmetric color-matching experiment is directly relevant to the questions raised by our computational analysis of color appearance. Moreover, the experiment has a central place in the study of color appearance simply for practical experimental reasons. There are many general questions we might ask about color appearance. For example, we would like to be able to measure which colors are similar to one another; which colors have a common hue, saturation or brightness, and so forth. If we had to study these questions separately under each illuminant, the task would be overwhelming. By beginning with the asymmetric color-matching experiment, we can divide color appearance measurements into two parts and reduce our experimental burden. The asymmetric matches define a mapping between the cone absorptions of objects with the same color appearance seen under different illuminants. From these experiments, we learn how to convert a target seen under one illuminant into an equivalent target under a standard illuminant. This transformations saves a great deal of experimental effort since we can focus most of our questions about color appearance on studies using just one standard illuminant.

The linearity of asymmetric color-matches

We have seen measurements of superposition to test linearity throughout this volume. Tests of linearity in asymmetric color matching appear very early in the color appearance literature. When von Kries (1905) introduced the coefficient law, he listed several testable empirical results. Among the predictions of the basic law he listed the basic test of linearity, namely

> ... there exist several very simple laws, which also appear to be specially adapted for experimental test. Namely, it must be that if L_1 on one retinal region causes the same result as L_2 on another, and similarly M_1, working on the first, causes the same effect as M_2 on the other, in every case also $L_1 + M_1$ must have here the

[9] This binocular method makes sense if one accepts the view that the adjustment for the illumination is mediated primarily before the signals from the two eyes are combined, in the superficial layers of area V1. The coherence of the experimental method can be tested psychophysically by examining transitivity. The observer matches a test on backgrounds L and R_1, and then on backgrounds L and R_2. The experimenter then places R_1 in the left eye and R_2 in the right eye and verifies that the matching lights match one another. There is no guarantee, of course, that these measurements are governed by precisely the same visual mechanisms that govern adaptation under normal viewing conditions.

> same effect as $L_2 + M_2$ there.
> ... The extended studies of Wirth (1900-1903) show that the law can be considered as nearly valid for reacting lights that are not too weak.

Evidently, von Kries not only raised the question of linearity of asymmetric color-matching, but by 1905 he considered it answered affirmatively.

While von Kries considered the question settled, not everyone was persuaded. Over the years, there have been many separate experimental tests of linearity in the asymmetric color-matching experiment. I am particularly impressed by a series of papers by Elaine Wassef, working first in London and then at the University College for Girls in Cairo. Wassef wrote at roughly the same time E. H. Land was working at Polaroid. In her papers, she reports on new studies and a review of the experimental test of asymmetric color-matching linearity[10]. Like von Kries, Wassef asked whether one could predict asymmetric color-matches using the principle of superposition. And, like von Kries, she concluded that the weight of the experimental evidence supported the linearity hypothesis: When the illumination changes, the cone absorptions of the test and matching lights are related by a linear transformation.

I have replotted some of Wassef's data to illustrate the nature of the measurements and the size of the effect (Figure 12). The illuminant spectral power distributions she used in her dichoptic matching experiment are plotted in Figure 12 (a). To plot her results, I have converted Wassef's reported measurements into one absorptions. I have plotted the cone absorptions of the surfaces that matched in color appearance when seen under the two illuminants. Figure 12 (b) shows the L and M cone absorptions of the surfaces under the two illuminants, and @Figure 12 (c) shows the L and S cone absorptions. The cone absorptions for objects seen under a tungsten illuminant are plotted as open circles; the cone absorptions for objects seen under a blue sky illumination are plotted as filled squares. The size of the effect is quite substantial. Two sets of points show the cone absorptions of targets that look identical in their respective contexts. Yet, the cone absorption values from the surfaces under these illuminants don't even overlap in their values.

Taken together, the color matching and asymmetric color-matching show the following. When the objects are in the same context, equating the cone absorptions equate appearance. But, when the two objects are seen under different illuminants, equating cone absorptions does not equate for appearance. Within each context the observer uses the pattern of cone absorptions to infer color appearance, probably by comparing the relative cone absorption rates. Color appearance is an interpretation of the physical properties of the objects in the image.

Von Kries Coefficient Law: Experiments

Through his Coefficient Law, J. Von Kries sought to explain these asymmetric color matches by a simple physiological mechanism. He suggested that the visual pathways adjust to the

[10] Interestingly, one of the largest sets of data she reviewed was a series of experiments performed at the Kodak research laboratories, Polaroid's competitor. (Wassef (1952), Wassef (1958), Wassef (1959))

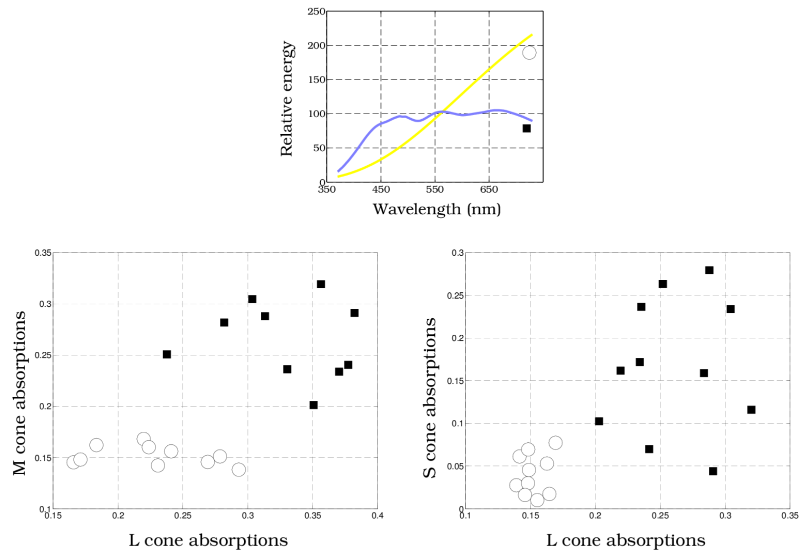

Figure 12: Data from an asymmetric color-matching experiment using the dichoptic method. The test and matching lights are viewed in different contexts and appear identical. But, the two lights have very different cone absorption rates. Hence, appearance matches made across an illuminant change are not cone absorption matches. The spectral power distributions of two illuminants, one approximating mean daylight and the other a tungsten illuminant are shown in panel a. Cone absorptions for targets that appear identical to one another in these two contexts are shown as scatterplots in (b) for the (L, M) cones, and (c) for the (L, S) cones. The points plotted as open circles are cone absorptions for tests seen under the first illuminant; matches seen under the second illuminant are plotted as filled squares. The stimuli represented by the absorptions have the same color appearance, but they correspond to very different cone absorptions (Source: Wassef (1959)).

illumination by scaling the signals from the individual cone classes. This hypothesis has a simple experimental prediction: If we plot, say, the S cone absorptions of the test and match surfaces on a single graph, the data should fall along a straight line through the origin. The slope of the predicted line is the scale factor for the illuminant change.

Neither von Kries or Wassef knew the photopigment spectral curves; hence, they could not create the graph they needed to test the von Kries Coefficient Law directly. But, using an indirect measurement based on estimation of the eigenvectors of the measured linear transformations, Burnham et al. (1957) and Wassef (1959) rejected von Kries scaling. Despite this rejection, von Kries' hypothesis continued to be used widely to explain how color appearance varies with illumination. Among theorists, for example, E. H. Land relied entirely on von Kries scaling as the foundation of his retinex theory (Brewer and Lyle Brewer (1954); Brainard and Wandell (1986); Land (1986a), Land (1986b)).

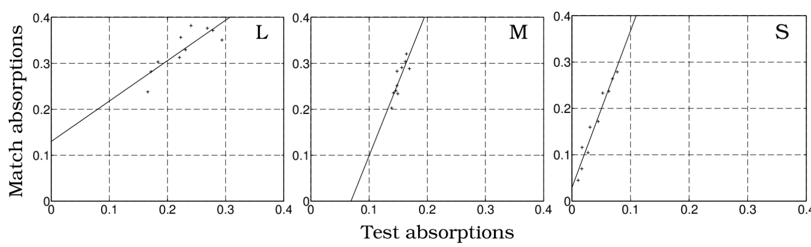

Figure 13: The cone absorptions of the test and match surfaces fall close to a straight line. These appearance matches were made by presenting the test and match objects to different eyes. The illuminant for one eye was similar to a tungsten bulb and the other eye was blue skylight. The Von Kries coefficient law predicts that the line should pass through the origin of the graph; while not precisely correct, the rule is a helpful starting point (Source: Wassef (1959)

Today, we have good estimates of the spectral sensitivities of the cone photopigments and it is possible convert Wassef's data into cone absorptions and analyze von Kries coefficient law directly. Figure 13 shows a graphical evaluation of von Kries hypothesis for the data in Figure 12. Each panel plots the cone absorptions of corresponding test and match targets for one of the three cone types. As predicted by Von Kries, the cone absorptions of the test and match targets fall along a line. Moreover, the slope of the lines relating the cone absorptions also make sense. The slope is largest for the S cones where illuminant change has its largest effect. The data are not perfectly consistent with von Kries scaling, however, because the lines through the data do not pass through the origin, as required by the theory[11].

There is an emerging consensus in many branches of color science that the von Kries coefficient law explains much about how color appearance depends on the illumination. J. von Kries simple hypothesis is important partly because of its practical utility, and partly because of

[11]Indeed, this is equally a failure of the simple linearity that Wassef uses to summarize the data, and more in line with some of the conclusions that Burnham et al. (1957) drew about their data.

its implications for the representation of color appearance within the brain. The hypothesis explains the major adjustments for color constancy to in terms of the photoreceptor signal, and the photoreceptor signals combine within the retina (Chapter). Hence, von Kries hypothesis implies that either (a) the main adjustment takes place very early, or (b) the photoreceptor signals can be separated in the central representation. This topic will come up again later, when we review some of the phenomena concerning color appearance in the central nervous system.

How Color Constant Are We?

Finally, let's consider how well the visual pathways correct for illumination change. On this point there is some consensus: The asymmetric color-matches do not compensate completely for the illumination change. The visual pathways compensate for only part of the illuminant change (Helson (1938); Judd (1940)).

Brainard and Wandell (Brainard and Wandell (1991), Brainard and Wandell (1992)) described this phenomenon using results from a recent experiment. We used an experimental apparatus consisting of simulated surfaces and illuminants and an asymmetric color-matching experiment based on memory-matches. We presented subjects with images of simulated colored papers, rendered under a diffuse daylight illuminant, on a CRT display. The subjects memorized the color appearance of one of the surfaces. Next, we changed the the simulated illuminant, slowly over a period of two minutes, giving subjects a chance to adapt to the new illuminant. Then, the subject adjusted the appearance of a simulated surface to match the color appearance of the surface they had memorized.

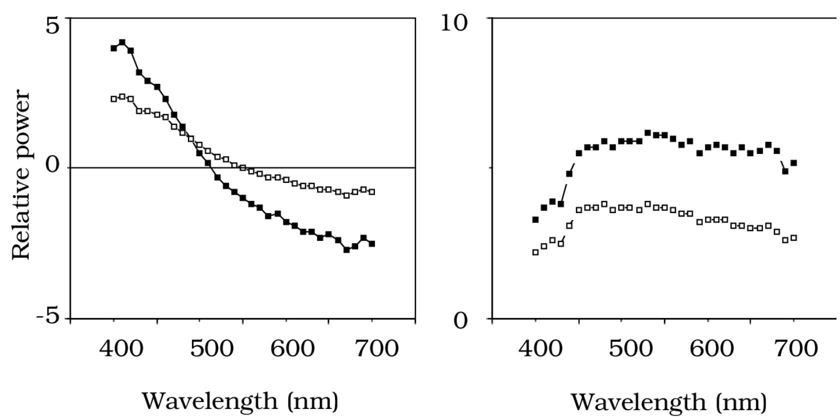

Figure 14: A comparison of the illuminant change and the subjective illuminant change, as inferred from an asymmetric matching experiment. The simulated illuminant change and subjective illuminant changes are shown by the filled squares and open squares respectively. Subjects behave as if the illuminant change is about half of the true illuminant change (Source: Brainard and Wandell (1991)).

We can represent the difference between the two simulated illuminants by plotting the illuminant change. The filled symbols in Figure 14 show the illuminant changes in two experimental conditions. The top panel shows an illuminant change that increased the short-wavelength light and decreased the long-wavelength light. The bottom panel shows an illuminant change that increased the energy at all wavelengths.

Suppose that subjects equated the perceived surface reflectance, but that the illuminant change they estimated was different from the true illuminant change. In that case, we can use the observed matches to infer the the subjects' illuminant estimates, which are plotted as the open symbols in two panels of Figure 14. Subjects are acting as if the illuminant change they are correcting for is similar to the simulated illuminant change but, smaller. Subjects' performance is conservative, correcting for about half the true illuminant change.

Brainard and Wandell's experiments were conducted on display monitors, and the images were far less interesting than full natural scenes (Brainard and Wandell (1991) Brainard and Wandell (1992)). It is possible that given additional clues, subjects may come closer to true illuminant estimation. But, in most laboratory experiments to date, subjects do not compensate fully for changes in the illumination. When the illumination changes color appearance changes less than it might if color was defined by the cone absorptions; but, it changes more than it would if the nervous system used the best possible computational algorithms. The performance of biological systems often seems to fall in this regime. Very poor behavior is forced to change towards a better solution. But, the evolutionary pressure does not force our nervous system to solve estimation problems perfectly. When the marginal return for additional improvements is not great, pretty well seems to do.

The Perceptual Organization of Color

In this section, I will review some of the methods for describing the perceptual organization of color appearance. Specifically, we will review the relationship between different colors and some of the systems for describing color appearance. In addition to the implications this organization has for understanding the neural representation of color appearance, there are also many practical needs for descriptive systems of color appearance. Artists and designers need ways to identify and specify the color appearance of a design. Further, they need ways of organizing colors and finding interesting color harmonies. Engineers need to assess the appearance and discriminability of colors used to highway signs and to label parts, packaging, and software icons.

Language provides us with a useful start at organizing color appearance. Spoken English in the U.S. consists of eleven color terms that are widely and consistently used[12]. While the number of terms used differs across cultures, there is a remarkable hierarchical organization to the order in which color names appear. Cultures with a small number of basic color names

[12] White, black, red, green, yellow, blue, brown, purple, pink, orange, gray.

always include white, black and red. Color terms such as purple and pink enter later (Berlin and Kay (1969); Boynton and Olson (1987)).

Color names are a coarse description of color experience. Moreover, names list, but do not organize, color experience. Thus, they are not helpful when we consider issues such as color similarity or color harmony. A more complete organization of color experience is based on the three perceptual attributes called: *hue, saturation*, and *brightness*. Hue is the attribute that permits a color to be classified as red, yellow, green, and so forth. Saturation describes a color's similarity to a neutral gray or white. A gray object with a small reddish tint has little saturation, while a red object, with little white or gray, is very saturated. An object's brightness tells us about the relative ordering of the object on the dark to light scale.

Based on psychological studies of the similarity of colored patches with many different hues, saturations and brightnesses, the artist Albert Munsell created a book of colored samples. The appearance of the samples is organized with respect to hue, saturation and brightness. Furthermore, the colored samples are spaced in equal perceptual steps. Munsell organized the samples within his book in terms using a cylindrical organization as shown in Figure 15. The *Munsell Book of Colors* is published and used as a reference in many design and engineering applications.

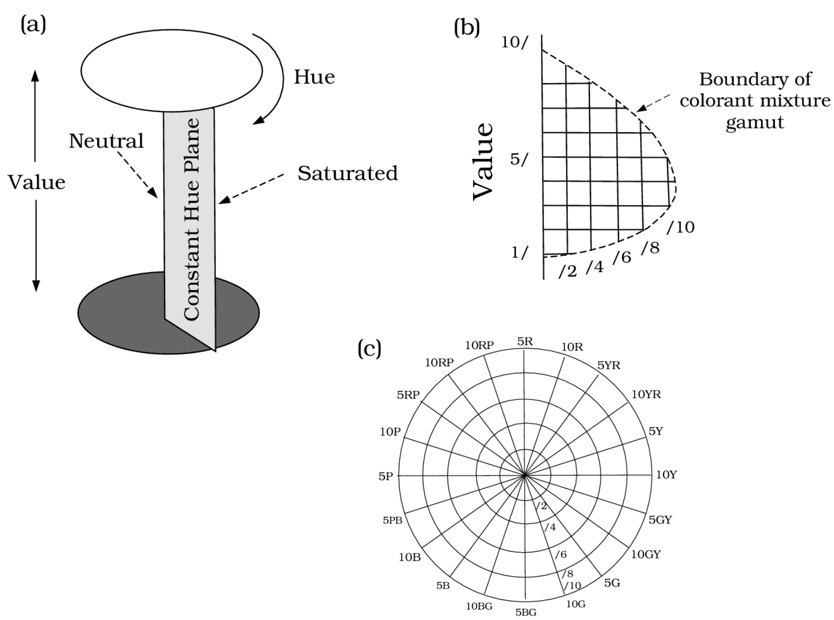

Figure 15: The Munsell Book of Colors is a collection of colored samples organized in terms of three perceptual attributes of color. The samples are arranged using a cylindrical geometry with respect to these attributes. The main axis of the cylinder codes lightness; the distance from the center of the cylinder to the edge codes the Munsell property called value (saturation); the position around the circumference of the cylinder codes the Munsell property called chroma (hue).

Perceptually, both saturation and brightness can be arranged using a linear ordering from small to large; hue, however, does not follow a linear ordering. So, Munsell organized lightness along the main axis of the cylinder, and saturation as the distance from the center of the cylinder to the edge. The circular hue dimension was mapped around the circumference of the cylinder. The Munsell Book of Colors notation is widely used in industry and science.

Munsell developed a special notation to refer to each of the samples in his book. To distinguish his notation from the colloquial usage, Munsell substituted the word *value* for lightness and the word *chroma* for saturation. He retained the word hue, apparently finding no adequate substitute. In the Munsell notation, the words hue, chroma and value have specific and technical meanings. Each colored paper is described using a three-part syntax of hue chroma/value. For example, 3YR 5/3 refers to a colored paper with the hue called 3YR, the chroma level 5, and the value level 3.

The Munsell Book was created before the CIE color standards described in Chapter . With the advent of the CIE measurement standard, based on the color-matching functions, there was a need for a method to convert the Munsell representation into the CIE standard representation. A committee of the Optical Society, led by Nickerson, Newhall and Evans, measured the CIE values of the Munsell samples in the published book, and the Munsell Corporation agreed to produce the colored samples to measurement standards defined by the Optical Society of America. The new standard for the Munsell Book, based on CIE values rather than pigment formulae, is called the *Munsell Renotation System*. Calibration tables that describe the color measurements of the Munsell Book samples are tabulated, for example, Wyszecki and Stiles (1982).

Opponent-Colors

One of the most remarkable and important insights about color appearance is the concept of *opponent-colors*, first described by E. Hering (1878). Hering pointed out that there is a powerful psychological relationship between the different hues. While some pairs of hues can coexist in a single color sensation, others cannot. For example, orange is composed of red and yellow while cyan is composed of blue and green. But, we never experience a hue that is simultaneously red and green. Nor do we experience a color sensation that is simultaneously blue and yellow. These two hue pairs, red-green and blue-yellow, are called *opponent-colors*.

There is no physical reason why these two opponent-colors pairs must exist. That we never perceive red and green, while we easily perceive red and yellow, must be due to the neural representation of colors. Hering argued that opponent-colors exist because the sensations of red and green are encoded in the visual pathways by a single pathway. The excitation of the pathway causes us to perceive one of the opponent-colors; inhibition of the pathway causes us to perceive the other.

Hering made his point forcefully, and extended his theory to explain various other aspects of color appearance, as well. But, his insights were not followed by a set of quantitative studies.

Perhaps for this reason, his ideas languished while the colorimetrists used color-matching to set standards for all of modern technology. This is not to say Hering's work was forgotten. Colorimetrists who thought about color appearance invariably turned to Hering's insights. In a well-known review article, the eminent scientist D. B. Judd, wrote

> The Hering (1905) theory of opponent colors has come to be fairly well accepted as the most likely description of color processes in the optic nerve and cortex. Thus this theory reappears in the final stage in the stage theories of von Kries-Schrodinger (von Kries (1905); Schrodinger, 1925), Adams (1923, 1942) and Muller (1924, 1930). By far the most completely worked out of these stage theories is that of Muller. ... There is slight chance that all of the conjectures are correct, but, even if some of the solutions proposed by Muller prove to be unacceptable, he has nevertheless made a start toward the solution of important problems that will eventually have to be faced by other theorists. [(Judd (1951), pg. 836)].

Hue Cancellation

Several experimental observations, beginning in the mid-1950s, catapulted opponent-colors theory from a special-purpose model, known only to to color specialists, to a central idea in vision science.

The first was a behavioral experiment that defined a procedure for measuring opponent-colors, the *hue cancellation* experiment. The hue cancellation experiment was developed in a series of papers by Jameson and Hurvich (Jameson and Hurvich (1955); Hurvich and Jameson (1957)). By providing a method of quantifying the opponent-colors insight, Hurvich and Jameson made the idea accessible to other scientists, opening a major line of inquiry.

In the hue cancellation experiment, the observer is asked to judge whether a test light appears to be, say, reddish or greenish. If the test light appears reddish, the subject adds green light in order to cancel precisely the red appearance of the test. If the light appears greenish, then the subject adds red light to cancel the green appearance. The added light is called the *canceling* light. Once the red or green hue of the test light is canceled, the test plus canceling light appear yellow, blue, or gray. The same experiment can be performed to measure the blue-yellow opponent-colors pairing. In this case the subject is asked whether the test light appears blue or yellow, and the canceling lights also appear blue and yellow.

Figure 16 shows a set of hue cancellation measurements obtained by Jameson and Hurvich (Jameson and Hurvich (1955); Hurvich and Jameson (1957)). Subjects canceled the red-green or blue-yellow color appearance of a series of spectral lights. The vertical axis shows the relative intensity of the canceling lights, scaled so that when equal amounts of these lights are superimposed the result did not appear, say, red or green. The canceling lights always have positive intensity, but the intensity of the green and blue canceling lights are plotted as negative to permit you to distinguish which canceling light was used.

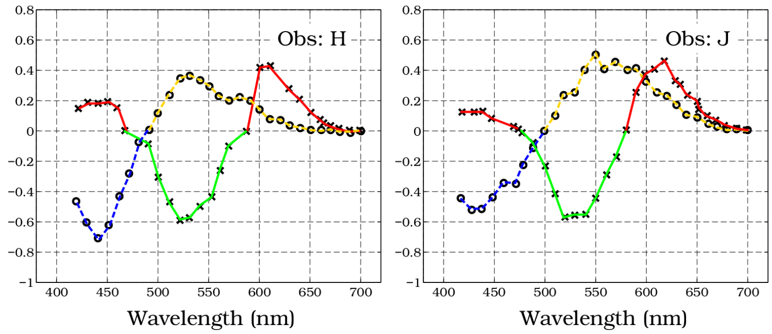

Figure 16: Measurements from the hue cancellation experiment. An observer is presented with a monochromatic test light. If the light appears red then some amount of a green canceling light is added to cancel the redness. If the light appears green, then a red canceling light is added to cancel the greenness. The horizontal axis of the graph measures the wavelength of the monochromatic test light, and the vertical axis measures the relative intensity of the canceling light. The entire curve represents the red-green appearance of all monochromatic lights. A similar procedure is used to measure blue-yellow. (Source: Hurvich and Jameson (1957)).

To what extent can we generalize from red-green measurements using monochromatic lights to other lights? The answer to this question we must evaluate the linearity of the hue cancellation experiment. If the experiment is linear, we can use the data in Figure 16 to predict whether any test light will appear red or green (blue-yellow) since all lights are the sum of monochromatic lights. If the experiment is not linear, then the data represent only an interesting collection of observations.

To evaluate the linearity of the hue cancellation experiment, one can perform the following experiment: Suppose the test light t_1 appears neither red nor green, and the test light t_2 appears neither red nor green. Does the superposition of these two test lights, $t_1 + t_2$, also appear neither red nor green? In general, the hue cancellation experiment fails this test of linearity. If we superimpose two lights, neither of which appears red or green, the result can appear red. If we add two lights neither of which appears blue or yellow, the result can appear yellow. Hence, the hue cancellation studies are a useful benchmark. But, we need a more complete (nonlinear) model before we can apply the hue cancellation data in Figure 18 to predict the opponent-colors appearance of polychromatic test lights (Larimer et al. (1975); Burns et al. (1984); Ayama and Ikeda (1989); Chichilnisky (1995)).

Opponent-colors measurements at threshold

In addition to color appearance judgments, one can also demonstrate the presence of essential opponent-colors signals behaviorally by *color test-mixture experiments*. These color experiments are direct analogues of the pattern-mixture experiments I reviewed in

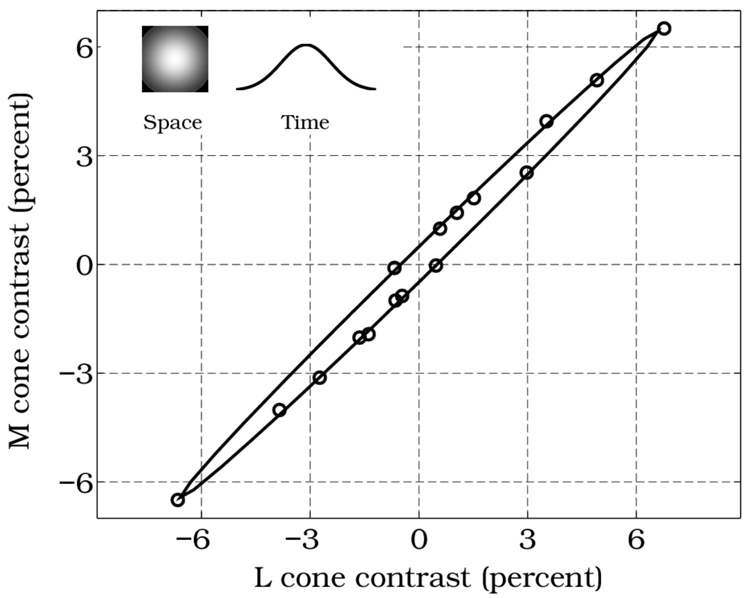

Figure 17: Color test-mixture experiments demonstrate opponent-colors processes. The axes measure percent change in cone absorption rates for the L and M cones. The points show the cone absorptions rates at detection threshold measured using different colored test lights. The smooth curve is an ellipse fit through the data points. The mixture experiment shows that the L and M cone signals cancel one another, so that lights that excite a mixture of L and M cones are harder to see than lights that stimulate just one of these two cone class (Source: Wandell (1987)).

The intersection of the ellipse with the horizontal axis, shows the relative L cone absorption rate at detection threshold. The intersection of the ellipse with the vertical axis shows the relative M cone absorption rate at detection threshold. The shape of the ellipse shows that signals that stimulate the L and M cones simultaneously are less visible than signals that stimulate only one or the other. At the most extreme points on the ellipse, the cone absorptions of the L and M cones are more than five times the rate required to detect a signal when each cone class is stimulated alone. The poor sensitivity to mixtures of signals from these two cone types shows that the signals must oppose one another. The cancellation of threshold level signals from the L and M cones, as well as between the S cones and the other two classes (not shown), have been observed in many different laboratories and under many different experimental conditions (e.g., Boynton et al. (1964); Mollon and Polden (1977); Pugh (1976), Pugh and Mollon (1979); Stromeyer et al. (1985); Sternheim et al. (1979); Wandell and Pugh (1980a), Wandell and Pugh (1980b)).

In addition to demonstrating opponent-colors, these threshold data reveal a second interesting and surprising feature of visual encoding. Two neural signals that are visible when they are seen singly become invisible when they are superimposed. It seems odd that the visual system should be organized so that plainly visible signals can be made invisible. From the figure we can see that this is a powerful effect, suppressing a signal that is more than five times threshold. This observation tells us that in many operating conditions absolute sensitivity is not the dominant criterion. The visual pathways can sacrifice target visibility in order to achieve the goals of the opponent-colors encoding.

Opponent Signals in the Visual Pathways

In addition to these two types of behavioral evidence, there is also considerable physiological evidence that demonstrates the existence of opponent-colors signals in the visual pathway.

In a report that gained widespread attention, Svaetichin (1956) measured the responses of three types of retinal neurons in a fish. He reported that the electrical responses were qualitatively consistent with Hering's notion of the opponent-colors representation. In two types of neurons, the electrical response increased to certain wavelengths of light and decreased in response to other wavelengths, paralleling the red-green and blue-yellow opponency in color perception[13]. The electrical response of a third set of neurons increased to all wavelengths of light, as in a black-white representation. Shortly after Svaetichin's report, De Valois and his colleagues established the existence of opponent-colors neurons in the lateral geniculate nucleus of nonhuman primates. There is now a substantial literature documenting the presence of color opponent-signals in the visual pathways (e.g. De Valois et al. (1958), De Valois (1965); De Valois et al. (1966); Wiesel and Hubel (1966); Gouras (1968); Derrington et al. (1984); Lennie et al. (1990)).

[13]At first, it was thought that these responses reflected the activity of the cones. Subsequent investigations showed that the responses were from horizontal cells (Svaetichin and Macnichol (1958)).

The resemblance between the psychological organization of opponent-colors measured in the hue cancellation experiment and the neural opponent-signals suggests a link from the neural responses to the perceptual organization. To make a convincing argument for the specific connection between opponent-colors and a specific set of neural opponent-signals, we must identify a linking hypothesis. The hypothesis should tell us how we can predict appearance from the activity of cells, and conversely how we can predict the activity of these cells from appearance.

A natural starting place is to suppose that there is a population of neurons whose members are excited when we perceive red and inhibited when we perceive green. From the linking hypothesis, we predict that neurons in this population will be unresponsive to lights that appear neither red nor green. There are two spectral regions that appear neither red nor green to human observers: one near 570nm and a second near 470nm. To forge a strong link between appearance and neural response, we can ask whether the candidate neural population fails to respond to lights that appear neither red nor green. Then, we might search for a second population that fails to respond to lights that appear neither blue nor yellow.

This question was studied by DeValois and his collaborators in the lateral geniculate nucleus of the monkey. In their studies, DeValois and his colleagues studied the response of neurons to monochromatic stimuli presented on a zero background. They found a weak correspondence between the neutral points of individual neurons and the perceptual neutral points (De Valois et al. (1966)). More recently, Derrington et al. (1984) measured the responses of lateral geniculate neurons using contrast stimulus presented on a moderate, neutral background. They estimated the input to these neurons from the different cone classes and confirmed the basic observations made by DeValois and his colleagues.

Derrington et al. reported that parvocellular neurons could be classified into two groups of neurons. One population of neurons receives opposing input from the L and M cones. The panel on the left of Figure 18 shows my estimate of the spectral sensitivity of this group of parvocellular neurons. For these neurons wavelengths near 570nm are quite ineffective. But, there is a great deal of variation within this cell population making it difficult to be confident in the connection. Moreover, these neurons do not show a second zero-crossing near 470nm that would parallel the human opponent-colors judgments in the hue cancellation experiment.

A second population of lateral geniculate neurons receives input from the S cones and an opposing signal from a combination of the L and M cones. For these neurons, wavelengths near 500nm are quite ineffective. The panel on the right of Figure 18 shows my estimate of the spectral sensitivity of this group of parvocellular neurons.

There was less order in the opponent-color signals of the magnocellular neurons. Many magnocellular units seemed to be driven by a difference between the L and M cones. A few parvocellular units and a few magnocellular units were driven by a positive sum of the two signals from these two cone types.

The spectral responses of these neural populations suggest that there is only a loose connection between the signals coded by these neurons and the perceptual coding into opponent-hues; it

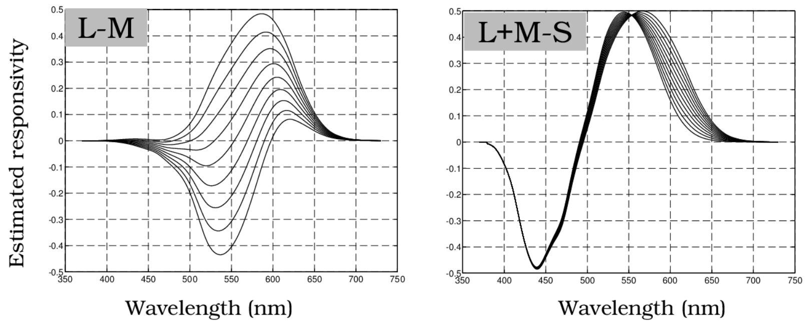

Figure 18: Opponent-signals measured in lateral geniculate nucleus neurons. These spectral response curves are inferred from the measured responses of lateral geniculate neurons to many different colored stimuli presented on a monitor. The vast majority of lateral geniculate neurons in the parvocellular layers can be divided into two groups based on their response to modulations colored lights. One group of neurons receives an opponent contribution from the L and M cones alone (panel a). The second group of neurons receives a signal of like sign from the L and M cones, and an opposing signal from the S cones (panel b) (Source: Derrington et al. (1984)).

is unlikely that the excitation and inhibition causes our perception of red-green and blue-yellow. One difficulty is the imperfect correspondence between the neural responses and the hue cancellation measurements. The second difficulty is that there is no substantial population of neurons representing a white-black signal. This is a very important perceptual dimension which must be carried in the lateral geniculate nucleus signals. Yet, no clearly identified group of neurons can be assigned this role[14].

Decorrelation of the Cone Absorptions

opponent-signals measured in the lateral geniculate nucleus probably represent a code used by the visual pathways because of its properties in communicating information from the retina to the brain. The psychological opponent-colors coding may be a consequence of the coding strategy used to communicate information from the retina to the cortex. What reason might there be for using an opponent-signals coding?

One reason to use an opponent-signal representation has to do with the efficiency of the visual encoding. Because of the overlap of the L and M cone spectral sensitivities, the absorption

[14]Some authors have suggested that a single group of lateral geniculate neurons codes a white-black sensation for high spatial frequency patterns and a red-green sensation for low spatial frequency patterns. While this is an interesting hypothesis, notice that the authors have abandoned the idea that there is a specific color sensation associated with the response of lateral geniculate neurons. Instead, they suppose that the perceived hue depends on the pattern of neural activation (Ingling and Martinez, 1984; Derrington et al. (1984)).

rates of these two cone types are highly correlated. This correlation represents an inefficiency in the visual coding of spectral information. As I described in Chapter , decorrelating the signals can improve the efficiency of the neural representation.

We can illustrate this principle by working an example, parallel to the one in Chapter . Consider the cone absorptions to a set of surfaces. Because of the overlap in spectral sensitivities, the cone absorptions between, say, the L and M cones will be correlated. To remove the correlation, we create a new representation of the signals consisting of the L cone absorptions alone, and a weighted combination of the the L, M, and S cone absorptions. We will choose the weighted combination of signals so that the new signal is independent of the L cone absorptions. As we reviewed in the earlier chapter, by decorrelating the cone absorptions before they travel to the brain, we make effective use of the dynamic range of the neurons transmitting the information (Buchsbaum and Gottschalk (1984)).

The graphs in Figure 19 (a,b) show examples of the correlation of the cone absorptions for a particular set of surfaces and illuminant. These plots represent the cone absorptions from light reflected by a Macbeth ColorChecker viewed under mean daylight illumination. The correlations shown in these two plots are typical of natural images: the L and M cone absorptions are highly correlated (panel a); the M and S cone absorptions are also correlated (panel b).

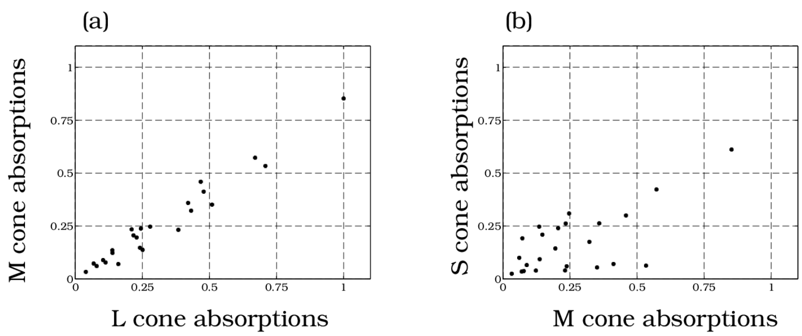

Figure 19: Absorptions in the three cone classes are highly correlated. The correlation between cone absorptions can be measured using correlograms. In this figure, correlograms are shown of the cone absorptions from the surfaces in the Macbeth ColorChecker illuminated by average daylight. (a) A correlogram of the L and M cone absorptions. (b) A correlogram of the L cone absorptions plotted versus a weighted sum of the cone absorptions that is decorrelated from the L cone absorptions, -.59L + 0.8M-.12S.

As described in Chapter , we decorrelate the signals derived from the cone absorptions by forming new signals that are weighted combinations of the cone absorptions. There are many linear transforms of the cone absorptions that could serve to decorrelate these absorptions. One such transformation is represented by the following three linear equations[^decor-svd],

% This is the matrix u in the decor sensor analysis in decorrelate.m

$$
\begin{aligned}
O_1(\lambda) &= \quad 1.0L(\lambda) + 0.0M(\lambda) + 0.0S(\lambda) \\
O_2(\lambda) &= \quad -0.59L(\lambda) + 0.80M(\lambda) + -0.12S(\lambda) \\
O_3(\lambda) &= \quad -0.34L(\lambda) + -0.11M(\lambda) + 0.93S(\lambda)
\end{aligned} \tag{0.16}
$$

or, written in matrix form,

$$
\begin{pmatrix} O_1(\lambda) \\ O_2(\lambda) \\ O_3(\lambda) \end{pmatrix} = \begin{pmatrix} 1.00 & 0.00 & 0.00 \\ -0.59 & 0.80 & -0.12 \\ -0.34 & -0.11 & 0.93 \end{pmatrix} \begin{pmatrix} L(\lambda) \\ M(\lambda) \\ S(\lambda) \end{pmatrix} \tag{0.17}
$$

The new signals, $O_i(\lambda)$, are related to the cone absorptions by a linear transformation. These three signals are decorrelated with respect to this particular collection of surfaces and illuminant.

$$
\begin{aligned}
O_1(\lambda) &= \quad 1.0L(\lambda) + 0.0M(\lambda) + 0.0S(\lambda) \\
O_2(\lambda) &= \quad -0.59L(\lambda) + 0.80M(\lambda) + -0.12S(\lambda) \\
O_3(\lambda) &= \quad -0.34L(\lambda) + -0.11M(\lambda) + 0.93S(\lambda)
\end{aligned}
$$

{#eq-decor-opponent-signals}

or, written in matrix form,

$$
\begin{pmatrix} O_1(\lambda) \\ O_2(\lambda) \\ O_3(\lambda) \end{pmatrix} = \begin{pmatrix} 1.00 & 0.00 & 0.00 \\ -0.59 & 0.80 & -0.12 \\ -0.34 & -0.11 & 0.93 \end{pmatrix} \begin{pmatrix} L(\lambda) \\ M(\lambda) \\ S(\lambda) \end{pmatrix} \tag{0.18}
$$

The new signals, $O_i(\lambda)$, are related to the cone absorptions by a linear transformation. These three signals are decorrelated with respect to this particular collection of surfaces and illuminant.

The spectral sensitivity of the three decorrelated signals are shown in Figure 20. The two opponent spectral sensitivities are reminiscent of the hue cancellation measurements and the opponent-signals measured in the lateral geniculate nucleus. One of the sensors has two zero-crossings, near 570nm and 470nm. A second sensor has one zero-crossing near 490nm. The third sensor has no zero-crossings, as required for a white-black pathway. The similarity between the decorrelated signals, the opponent-signals in the lateral geniculate nucleus, and the hue cancellation experiment suggest a purpose for opponent-colors organization. Opponent-colors may exist to decorrelate the cone absorptions and provide an efficient neural representation of color (Buchsbaum and Gottschalk (1984); Derrico and Buchsbaum (1991)).

The opponent-colors representation is a universal property of human color appearance, just as the need for efficient coding is a simple and universal idea. We should expect to find a

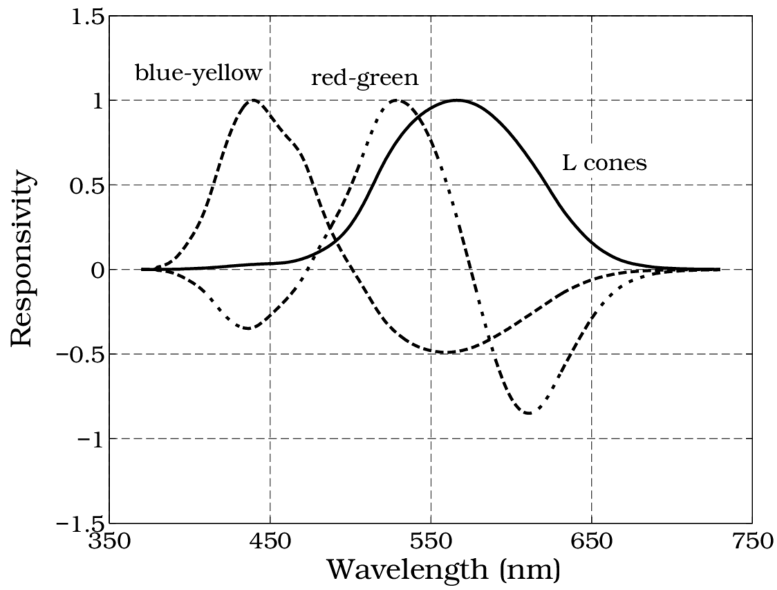

Figure 20: The spectral responsivity of a set of color sensors whose responses to the Macbeth ColorChecker under mean daylight are decorrelated. The spectral sensitivities of these sensors resemble the spectral sensitivities of lateral geniculate neurons and the color appearance judgments measured in the hue cancellation experiment.

precise connection between opponent-colors appearance and neural organization in the central visual pathways. The hue cancellation experiment provides us with a behavioral method of quantifying opponent-colors organization. Hue cancellation measurements establish a standard for neurophysiologists to use when evaluating opponent-signals in the visual pathways as candidates for the opponent-colors representation. Opponent-colors organization is a simple and important idea; pursuing its neural basis will lead us to new ideas about the encoding of visual information.

Spatial Pattern and Color

Color Plate 2 (Albers) and Figure 1 show that the color appearance at a location depends on the local image contrast, that is, the relationship between the local cone absorptions and the mean image absorptions. The targets we used to demonstrate this dependence are very simple spatial patterns, squares or lines, with no internal spatial structure of their own. In this section, we will review how color appearance can also depend on the spatial structure, such as the texture or spatial frequency, of the target itself.

Color Plate 6 shows two squarewaves composed of alternating blue and yellow bars. One squarewave is at a higher spatial frequency than the other. The average signal reflected from the regions containing the squarewaves is the same, that is, these are pure contrast modulations about a common mean field. If you examine the squarewaves from a close distance, you will see that bars in the squarewave patterns are drawn with the same ink. If you place this book a few meters away from you, say across the room, the color of the bars in the high spatial frequency pattern will appear different from the color of the bars in the low spatial frequency pattern. The bars in the high spatial frequency pattern will appear to be light and dark modulations about the green average. The bars in the low spatial frequency pattern will continue to look a distinct blue and yellow[15].

[15]You can also alter the relative color appearance of the patterns by moving the book rapidly up and down. You will see that the low frequency squarewave retains its appearance while the high frequency squarewave becomes a green blur.

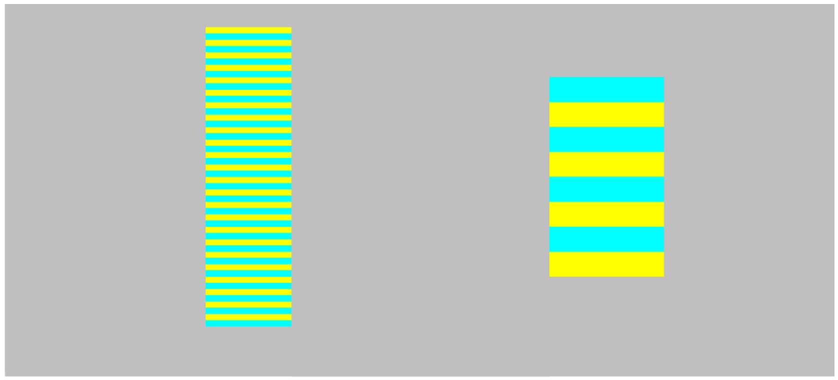

Figure 21: **Color Plate 6.** Color appearance covaries with spatial pattern. The bars printed in these two squarewaves are the same. Yet, whether the bars appear the same or not depends on their spatial frequency which you can control by altering the viewing distance. Also, you can influence the color appearance in the two patterns by moving the book rapidly up and down while you look at the patterns. (Source: Poirson and Wandell (1993)).

Poirson and Wandell (1993) used an asymmetric color-matching task to study how color appearance changes with spatial frequency of the squarewave pattern. Subjects viewed squarewave patterns whose bars were colored modulations about a neutral gray background; that is, the average of the two bars comprising the pattern was equal to the mean background level. Subjects adjusted the appearance of a 2 degree square patch to have the same color appearance as each of the bars in the pattern.

Two qualitative observations stood out in this study. First, spatial patterns of moderate and high spatial frequency patterns (above 8 cpd) appear mainly light-dark, with little saturation. Thus, no matter what the relative cone absorptions of a high spatial frequency target, the target appeared to be a light dark variation about the mean level. Second, the spatially asymmetric color appearance matches are not photopigment matches. This can be deduced from the first observation: Because of axial chromatic aberration, moderate frequency squarewave contrast patterns (4 and 8 cpd) cannot stimulate the S cones significantly. Yet, subjects match the bars in these high frequency patterns using a 2 deg patch with considerable S cone contrast. The asymmetric color-matches are established at neural sites central to the photoreceptors.

Poirson and I explained the asymmetric spatial color matches using a pattern-color separable model. In this model, we supposed that the color appearance of the target was determined by the response of three color mechanisms, and that the response of each mechanisms was separable with respect to pattern and color. We derived the spatial and spectral responsivities of these pathways from the observers color-matches; the estimated sensitivities are shown in Figure 22.

Interestingly, the three color pathways that we derived from the asymmetric matching experiment correspond quite well to the opponent-color mechanisms derived from the hue cancellation experiment. One pathway is sensitive mainly to light-dark variation; this pathway has the best spatial resolution. The other two pathways are sensitive to red-green and blue-yellow variation. The blue-yellow pathway has the worst spatial resolution. Granger and Heurtley (1973), Mullen (1985), Sekiguchi et al. (1993a), and Sekiguchi et al. (1993b) made measurements that presupposed the existence of opponent-color pathways and estimated similar pattern sensitivities of the three mechanisms. Notice that the derivation of the opponent-colors representation in this experiment did not involve asking the observers any questions about the hue or saturation of the targets. The observers simply set color appearance matches; the opponent-colors mechanisms were needed to predict the color matches.

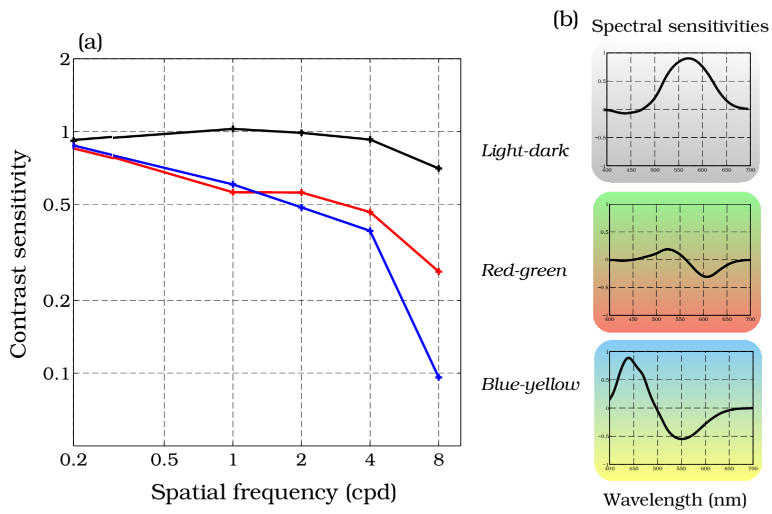

Figure 22: Estimates of the pattern-color separable sensitivity of pathways mediating color appearance. By measuring spatially asymmetric color-matches, it is possible to deduce the pattern and color sensitivity of three visual mechanisms that mediate color appearance judgments. The pattern and wavelength sensitivity of a light-dark, red-green, and blue-yellow mechanism derived from experimental measurements are shown here. (Source: Poirson and Wandell (1993)).

One of the more striking aspects of opponent-colors representations is that the apparent spatial sharpness, or focus, of a color image depends mainly on the sharpness of the light-dark component the image; apparent sharpness depends very little on the spatial structure of the opponent-color image components. This is illustrated in the three images shown in Color Plate 7. These images were created by converting the original image, represented as three spatial patterns of cone absorptions, into three new images corresponding to a light-dark representation and two opponent-colors representations. The image in Color Plate 7 (a) shows the result of spatially blurring the light-dark component and then reconstructing the image; the result appears defocussed. The images in Color Plate 7 (b,c) show the result of applying the same spatial blurring to the red-green and blue-yellow opponent-colors representations and then reconstructing. These images look spatially focused, though their color appearance has been changed somewhat.

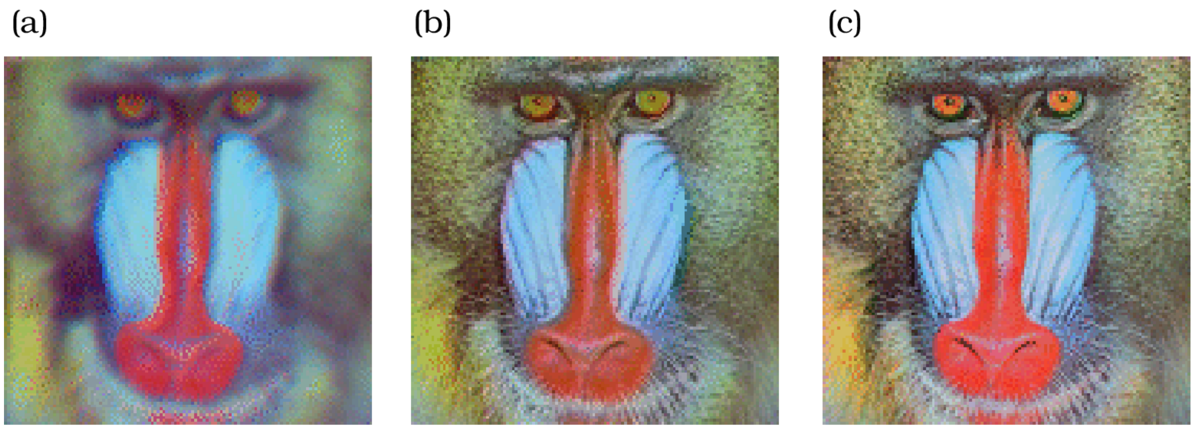

Figure 23: **Color Plate 7.** The apparent spatial sharpness (focus) of a color image depends mainly on the light-dark component of the image, not the opponent-colors components. A colored image was converted to a light-dark, red-green and blue-yellow representation. To create the three images, the light-dark (a), red-green (b), or blue-yellow (c) components were spatially blurred and then the image was reconstructed. The light-dark image looks defocused, but the same amount of blurring does not make the other two images look defocused. (Source: H. Hel-Or, personal communication).

We can take advantage of the poor spatial resolution of the opponent-colors representations when we code color images for image storage and transmission. We can allocate much less information about the opponent-colors components of color images without changing the apparent spatial sharpness of the image. This property of human perception was important in shaping broadcast television standards and digital image compression algorithms. As a quantitative prediction, we should expect to find that neurons in the central visual pathways that represent light-dark information should be able to represent spatial information at much higher resolution than neurons that code opponent-colors information. Consequently, we should expect that the largest fraction of central neurons encode light-dark, rather than the other two opponent-colors signals.

The differences between the light-dark encoding and the opponent-colors encoding are of great perceptual significance. Consequently, several authors have studied hypotheses based on the idea that opponent-colors signals and light-dark signals are found in separate areas of the brain. In the final section of this chapter, we will consider some of the evidence concerning the representation of color information in the visual cortex.

The Cortical Basis of Color Appearance

Clinical studies

In 1974 J.C. Meadows reviewed case studies of fourteen patients who had lost their ability to see colors due to a brain injury. For some patients, the colors of objects appeared wrong. Other patients saw the world entirely in shades of gray. Yet, these patients still had good visual acuity.

The syndrome Meadows reviewed, which I will call *cerebral dyschromatopsia*, had been described in reports spanning a century[16] (Zeki (1990)). But, the cases were rare, poor methods were used to study the patients, and the color loss was not well-dissociated from other visual deficits. Consequently, at the time Meadows wrote his review, several well-known investigators had expressed doubt about even the existence of cerebral dyschromatopsia[17](e.g. Teuber et al. (1960)). By bringing together a number of new cases and studying them with much better methods, Critchley (1965), Meadows (1974), Zeki (1990) and others (e.g. Green and Lessell (1977); Damasio et al. (1980); Victor et al. (1987); Mollon et al. (1980); Heywood et al. (1987); Heywood et al. (1992)) have removed any doubt about the existence and significance of the syndrome.

Congenital Monochromacy

Usually, observers are dichromats or monochromats because they are missing one of the cone photopigments (see e.g. Alpern (1974); Smith and Pokorny (1972)). There are also reports of congenital cone monochromacy of central origin. In a thorough and fascinating study, R. A. Weale (1953) searched England for individuals who (a) could not tell color photographs from black and white, (b) were not photophobic, and (c) had good visual acuity. (Requirements (b) and (c) eliminated rod monochromats). Weale found three cone monochromats, that is individuals who could adjust the intensity of a single primary light to match the appearance of any other test light. Yet, based on direct measurements of the photopigment in the eye of one of the observers, as well as behavioral measurements, some of these cone monochromats were shown to have more than one cone photopigment (Weale (1959); Gibson (1962); see

[16]Some of the terms used to describe color loss vary between authors. The terms trichromacy, dichromacy and monochromacy are precise, referring to the number of primary lights necessary to complete the color matching experiment. Some authors use the phrase *cerebral achromatopsia*, meaning “without color vision”, to describe a loss of color vision while others use cerebral dyschromatopsia. I prefer the second term because in these cases insensitivity to hue is often not complete and because these patients still distinguish the colors white and black. When the behavioral evidence warrants it, one might append a modifier, such as *monochromatic* dyschromatopsia, to describe the the color loss more precisely.

[17]In his book and in a long article, Zeki argued that the skepticism concerning cerebral dyschromatopsia was caused by their acceptance of a profoundly misguided theory concerning the significance of visual area V1. I agree with Meadows’ gentler assessment; the early evidence in support of cerebral dyschromatopsia is spotty and poorly argued. There was room for some skepticism.

also Alpern (1974)). Hence, Weale's subjects had a congenital dyschromatopsia caused by deficiencies central to the photopigments. At present, we know little more about them.

Regularities of the Cerebral Dyschromatopsia Syndrome

When color loss arises from damage to the brain, the distortion of color appearance can take several forms. In some cases, patients report that colors have completely lost their saturation and hue and the world becomes gray. In other cases, color appearance may become desaturated. Some observer can perform some simple color discrimination tasks, but they report that the colors of familiar objects do not appear right. In many cases the loss is permanent, but there are also reports of transient dyschromatopsia. For example, Lawden and Cleland (1993) recently reported on the case of a woman who suffers from migraines. During the migraine attacks, her world becomes transiently colorless.

The variability in the case studies suggest that there are a variety of mechanisms that may disturb color appearance. Across this variability, however, there are also some regularities. First, Meadows (1974) observed that every patient with dyschromatopsia was blind in some portion of the upper visual field.

Second, Meadows examined the reverse correlation: do patients with purely upper visual field losses tend to have cerebral dyschromatopsia? In the literature, he found twelve patients with a purely upper visual field loss, seven had dyschromatopsia. Of sixteen patients with a purely lower visual field loss, none had dyschromatopsia. In humans, the upper visual field is represented along the lower part of the calcarine sulcus (Chapter). The correlation between field loss and dyschromatopsia suggests that the damage that leads to dyschromatopsia is either near the lower portion of the calcarine or somewhere along the path traced out by the nerve fibers whose signal enters the lower portion of the calcarine cortex.

Third, many of the patients suffer from a syndrome called *prosopagnosia*, the inability to recognize familiar faces. Twelve of the fourteen patients described by Meadows had this syndrome. The patient with migraines also has transient prosopagnosia (Lawden and Cleland (1993)). The co-occurrence of dyschromatopsia and prosopagnosia suggests that the neural mechanisms necessary for recall of familiar faces and color are located close to one another or that they rely on the same visual signal.

Based on his review of the literature, Meadows concluded that

> The evidence on localization in cases of cerebral achromatopsia points to the importance of bilateral, inferiorly placed, posterior lesions of both cerebral hemispheres. (Meadows (1974), p. 622) [18]

[18] As S. Zeki points out, Meadows' conclusion echoes a disputed suggestion made a century earlier. While studying a patient who reported a loss of color vision, the French physician, Verrey concluded, > Le centre du sense chromatique se trouverait dans la partie la plus inferieure du lobe occipital, probablement dans la partie posterieure des plis lingual et fusiforme. (Verry, 1888, cited in Zeki (1990), p. 1722) *Translation: The*

Behavioral studies of patients with cerebral dyschromatopsia

Patients with cerebral dyschromatopsia often fail to identify any of the test patterns on the Ishihara plates[19]. Mollon et al. (1980) reported on a patient who failed to identify the targets on the Ishihara plates (Chapter) at reading distance, but who could distinguish the targets when the plates were viewed from 2 meters. At the 2 meter viewing distance, the neutral areas separating the target and background are barely visible and the target and background appear contiguous. Twelve years after the original study, Heywood et al. (1992) replicated the finding on the same patient. They also showed that the patient can discriminate contiguous colors, but not colors separated by a gray stripe. Hence, in this patient cerebral dyschromatopsia involves color and pattern together (see also Victor et al. (1987)).

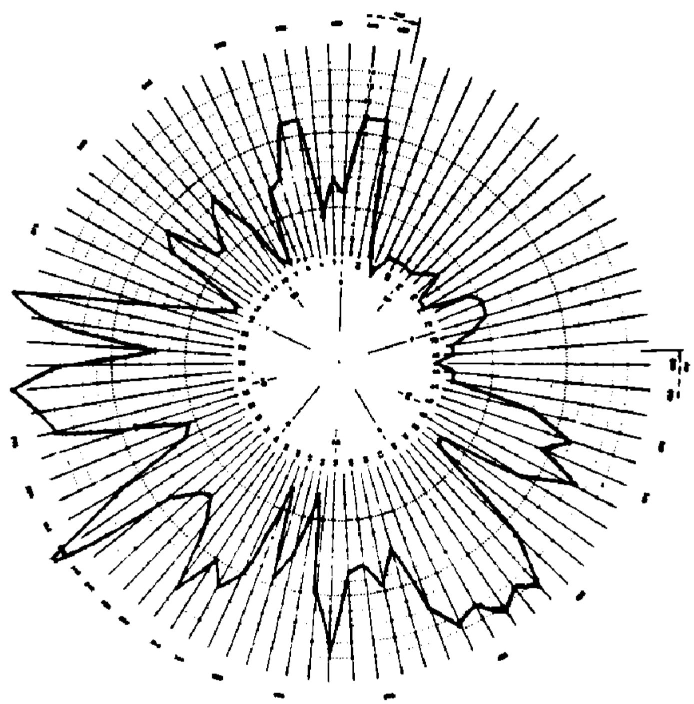

Figure 24: Results of the Farnsworth test measured on a patient suffering cerebral dyschromatopsia. The patients error scores are high in all hue directions. This pattern of scores is not consistent with any of the usual pattern of errors observed by cone dichromats who are missing one of their cone photopigments (Source: Meadows (1974)).

center of the chromatic sense will be found in the inferior part of the occipital lobe, probably in the posterior part of the lingual and fusiform gyrus.

[19]But, Meadows (1974) and Victor et al. (1987) describe patients who could read all of the plates.

Cerebral dyschromatopsics score quite poorly on the Farnsworth-Munsell hue test (see Chapter). The pattern of errors does not correspond to the errors made by any class of dichromat. The results of the test of one such patient is shown in Figure 24. The errors are large in all directions though there is some hint that the errors may be somewhat larger in the blue and yellow portions of the hue circle.

How many cone types are functional?

The patients' errors on the Ishihara color plates and the Farnsworth-Munsell hue test are not consistent with a visual pigment loss. Nonetheless, we cannot tell from their performance on these tests whether the separate cone classes are functioning or whether the loss of color perception is due, in part, to cone dysfunction.

Gibson (Gibson (1962); Alpern (1974); Mollon et al. (1980)) developed a behavioral test to infer whether the patients with cerebral dyschromatopsia had more than a single class of functioning cones. The logic of their behavioral test is based on the fact the cone signals are scaled to correct for changes in the ambient lighting conditions. For example, in the presence of a long-wavelength background, the sensitivity of the L cones is suppressed while the sensitivity of the S cones remains unchanged.

Now, suppose a subject has only a single type of cone. For this observer wavelength sensitivity is determined by the spectral sensitivity a single cone photopigment. Changes of the background illumination will not change the observer's relative wavelength sensitivity. This is the situation for normal observers under scotopic viewing conditions when we see only through the rods. Under scotopic conditions wavelength sensitivity is determined by the rhodopsin photopigment; changing the background does not change in the relative sensitivity to different test wavelengths[20].

If an individual has two functional cone classes, however, changes in the sensitivity of one cone class relative to the other will change the behavioral wavelength sensitivity. Hence, we can detect the presence of two cone classes by measuring wavelength sensitivity on two different backgrounds and noting a change in the observer's relative wavelength sensitivity.

Mollon et al. (1980) measured a cerebral dyschromatopsic's relative wavelength sensitivity to test wavelengths (510nm and 640nm) on two different backgrounds (510nm and 650nm). I have replotted their data in Figure 25. When the background changes, the relative test wavelength sensitivity changes showing that the subject has at least two functional cone classes, like Weale's and Alpern's congenital monochromats.

[20] In a beautiful series of experiments, W.S. Stiles (Stiles (1939); Stiles (1959); Stiles (1978)) studied how sensitivity varies as one changes the wavelength and intensity of a test and background lights. He developed a penetrating analysis of this experimental paradigm and identified candidate processes which he believed might describe photoreceptor adaptation. He referred to these processes as π-mechanisms, "p" for process and π for p.

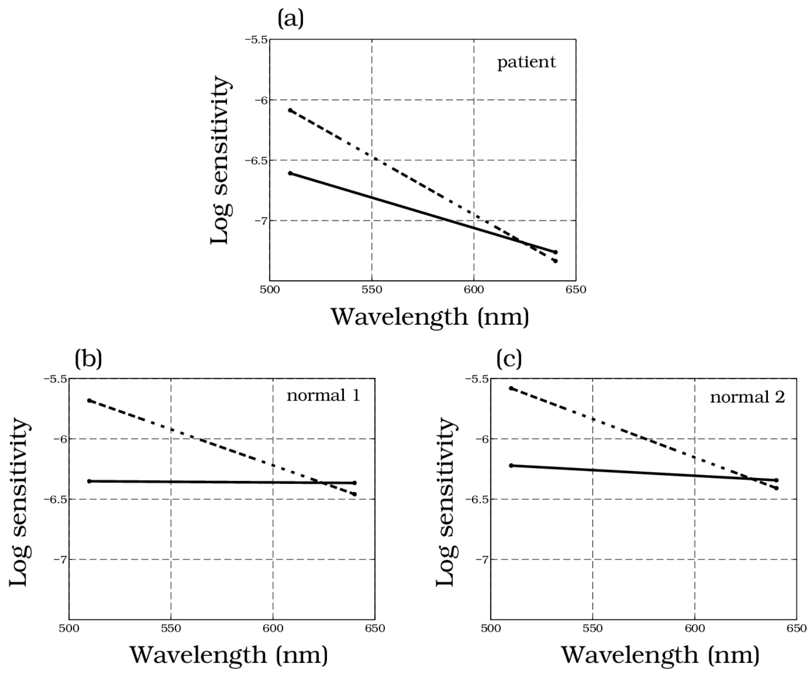

Figure 25: Experimental demonstration that a patient with cerebral dyschromatopsia has more than a single functioning cone class. (a) The patient's threshold sensitivity was measured to two monochromatic test lights on two different backgrounds. The change in background illumination changed the patient's relative wavelength sensitivity. (b) The results of performing the same experiment on a normal observer are shown. The results from the normal observer and the patient are quite similar (Source: Mollon et al. (1980)).

Clinical studies of cerebral dyschromatopsia shows that central lesions can disturb color vision severely, while sparing many other aspects of visual performance. This clinical syndrome suggests that some of the neural mechanisms essential to the sensation of color appearance may be anatomically separate from the mechanisms required for other visual tasks, such as acuity, motion and depth perception. But, clinical lesions are not neat and orderly, and the syndrome of cerebral dyschromatopsia is quite varied. Alternative hypotheses, for example that neurons carrying color information are more susceptible to stroke damage than other neurons, are also consistent with the clinical observations (Mollon et al. (1980)). To pursue the question of the neural representation of color information, we need to consider other forms of evidence concerning the localization of color appearance.

Physiological studies of color appearance

Much of the agenda for modern research on the cortical representation of color appearance has been set by Zeki via a hypothesis he calls *functional segregation* (Zeki (1974), Zeki (1993); Chapter .

Zeki argues that there is a direct correlation between the neural responses in cortical areas beyond V1 and various perceptual features, such as color, motion and form. This is not the only hypothesis we might entertain for the relationship between brain structures and perceptual function. An alternative view has been expressed by Livingstone and Hubel (Livingstone and Hubel (1984a), Livingstone and Hubel (1984b); Hubel and Livingstone (1987)) who argued that perceptual function can be localized to groups of neurons residing within single visual areas. Specifically, they have argued that differences in the density of the enzyme cytochrome oxidase within cell bodies serves as a clue to the localization of perceptual processing (see Chapter). This criterion for identifying neural segregation of function seems relevant in areas V1 and V2 since the the anatomical interconnections between these areas appear to respect the differences in cytochrome oxidase density (Burkhalter (1989)).

Livingstone and Hubel's hypothesis need not conflict with Zeki's since information may be interwined within peripheral visual areas only to be segregated later. But, the presence of subdivisions within areas V1 and V2 raise the question of whether more detailed study might not reveal functional subdivisions within areas V4 and MT as well (see e.g. Born and Tootell (1992)).

The principle line of evidence used to support Zeki's hypothesis of functional segregation is Barlow's neuron doctrine: namely, that the receptive field of a neuron corresponds to the perceptual experience the animal will have when the neuron is excited (Chapter). Based on this doctrine, neurophysiologists frequently assume that neurons with spatially oriented receptive fields are responsible for the perception of form; neurons that are inhibited by some wavelengths and excited by others are responsible for opponent-color percepts; neurons with motion selective receptive fields are responsible for motion perception.

Zeki's suggestion that monkey area V4 is a color center and area MT is a motion center is based on differences in the receptive field properties of neurons in these two areas. The overwhelming majority of neurons in area MT show motion direction selectivity. Zeki reported that many neurons in area V4 reported an unusual wavelength selectivity (Zeki (1974), Zeki (1980), Zeki (1990)).

As we have already seen, qualitative observations concerning receptive neural wavelength selectivity is not a firm basis to establish these neurons as being devoted mainly to color. For example, the vast majority of neurons in the lateral geniculate nucleus respond with opponent-signals, and these neurons have no orientation selectivity. Yet, we know that these neurons surely represent color, form and motion information.

Moreover, the quality of the receptive field measurements in area V4 has not achieved the same level of precision as measurements in the retina or area V1. Because these cells appear to be highly nonlinear, there are no widely agreed upon methods for fully characterizing their responses. And, there have been disputes concerning even the qualitative properties of area V4 receptive fields. For example, Desimone and Schein (1987) report that many cells are selective to orientation, direction of motion, and spatial frequency. Like Zeki, these authors too accept the basic logic of the neuron doctrine. They conclude from the variation of receptive field properties that "V4 is not specialized to analyze one particular attribute of a stimulus; rather, V4 appears to process both spatial and spectral information in parallel." They then develop an alternative notion of the role of area V4 and later visual areas.

Reasoning about Cortex and Perception

While hypotheses about the role of different cortical areas in perception are being debated, and experiments have begun, we are at quite an early stage in our understanding of cortical function. This should not be too surprising, after all the scientific investigation of the relationship between cortical responses and perception is a relatively new scientific endeavor, perhaps less than 100 years old. At this point in time we should expect some controversy and uncertainty regarding the status of early hypotheses. Much of the controversy stems from is due to our field's inexperience in judging which experimental measurements will prove to be a reliable source of information and which will not.

In thinking about what we have learned about cortical function, I find it helpful to consider these two questions:

- What do we want to know about cortical function?
- What are the logical underpinnings of the experimental methods we have available to determine the relationship between cortical responses and perception?

When one discovers a new structure in the brain, it is almost impossible to refrain from asking: what does this part of the brain do? Once one poses this question, the answer is naturally formulated in terms of the *localization* of perceptual function. Our mindset becomes one of asking what happens here, rather than asking what happens. Hypotheses concerning the localization of function are the usual way to begin a research program on brain function. Moreover, I think any fair reading of the historical literature will show that hypotheses about what functions are localized within the brain region serve the useful purpose of organizing early experiments and theory.

On the other hand, in those portions of the visual pathways where our understanding is relatively mature, localization is rarely the central issue. We know that the retina is involved in visual function, and we know that some features of the retinal encoding are important for acuity, adaptation, wavelength encoding, and so forth. Our grasp of retinal function is sufficiently powerful so that we no longer frame questions about retinal function as a problem of localization. Instead, we pose problems in terms of the flow of information; we try to understand how information is represented and transformed within the retina.

For example, we know that information about the stimulus wavelength is represented by the relative absorption rates of the three cone photopigments. The information is not localized in any simple anatomical sense: no single neuron contains all the necessary information, nor are the neurons that represent wavelength information grouped together. Perhaps, one might argue that acuity is localized since acuity is greatest in the fovea. Even so, acuity depends on image formation, proper spacing of the photoreceptors, and appropriate representation of the photoreceptors on the optic tract. Without all of these others components in place, the observer will not have good visual acuity. The important questions about visual acuity are questions about the nature of the information and how the information is encoded and transmitted. That the fovea is the region of highest acuity is important, but not a solution to the question of how we resolve fine detail.

The most important questions about vision are those that Helmholtz posed: What are the principles that govern how the visual pathways make inferences from the visual image? How do we use image information to compute these perceptual inferences? We seek to understand these principles of behavior and neural representations with the same precision as we understand color-matching and the cone photopigments. We begin with spatial localization of brain function so that we can decide where to begin our work, not how to end it.

Thus, as our understanding becomes more refined we no longer formulate hypotheses based on localization of function alone. Instead, we use quantitative methods to compare neural responses and and behavioral measurements. Mature areas of vision science relate perception and neural response by demonstrating correlations between the information in the neural signals and the computations applied to those signals. The information contained in the neural response, and the transformations applied to that information, is the essence of perception.

Summary and Conclusions

Color appearance, like so much of vision, is an inference. Mainly, color is a perceptual representation of the surface reflectance of that object. There are two powerful obstacles that make it difficult to infer surface reflectance from the light incident at the eye. First, the reflected light confounds information about the surface and illuminant. Second, the human eye has only three types of cones to encode a spectral signal consisting of many different wavelengths.

We began this chapter by asking what aspects of color imaging might make it feasible to perform this visual inference. Specifically, we studied how surface reflectance might be estimated from the light incident at the eye. We concluded that it is possible to draw accurate inferences about surface reflectance functions when the surface and illuminant spectral curves are regular functions that can be well-approximated by low dimensional linear models. When the input signals are constrained, it is possible to design simple algorithms that use the cone absorptions to estimate accurately surface reflectance.

Next, we considered whether human judgments of color appearance share some of the properties used by algorithms that estimate surface reflectance. As a test of the correspondence between these abstract algorithms and human behavior, we reviewed how judgments of color appearance vary with changes in the illumination. Experimental results using the asymmetric color-matching method show that color appearance judgments of targets seen under different illuminants can be predicted by matches between scaled responses of the human cones. The scale factor depends on the difference in illumination. To a large degree, these results are consistent with the general principle we have observed many times: judgments of color appearance are described mainly by the local contrast of the cone signals, not their absolute level. By basing color appearance judgments on the scaled signal, which approximates the local cone contrast, color appearance correlates more closely with surface reflectance than with the light incident at the eye.

Then, we turned to a more general review of the organizational principles of color appearance. There are two important means of organizing color experience. Many color representations, like the Munsell representation, emphasize the properties of hue, saturation and lightness. A second organizational theme is based on Hering's observation that red-green and blue-yellow are opponent-colors pairs, and that we never experience these hues together in a single color. The opponent-colors organization has drawn considerable attention with the discovery that many neurons carry opponent-signals, increasing their response to some wavelengths of light and decreasing in response to others.

In recent years, there have been many creative and interesting attempts to study the representation of color information in visual cortex. Most prominent amongst the hypotheses generated by this work is the notion that opponent-colors signals are spatially localized in the cortex. The evidence in support of this view comes from two types of experiments. First, clinical observations show that certain individuals lose their ability to perceive color although they still retina high visual acuity. Second, studies of the receptive fields of individual neurons suggest that opponent-colors signals are represented in spatially localized brain areas. These hypotheses are new and unproven. But, whether they are ultimately right or wrong, these hypotheses are the important opening steps in the modern scientific quest to understand the neural basis of conscious experience.

Motion and Depth

Motion and depth overview

The perception of motion, like the perception of color, is a visual inference. The images encoded by the photoreceptors are merely changing two-dimensional patterns of light intensity. Our visual pathways *interpret* these two-dimensional images to create our perception of objects moving in a three-dimensional world. How it is possible, even in principle, to infer three-dimensional motion from the two-dimensional retinal image is one important puzzle of motion; how our visual pathways actually make this inference is a second.

In this chapter we will try first to understand abstractly the retinal image information that is relevant to the computation of motion estimation. Then, we will review experimental measurements of motion perception and try to make sense of these measurements in the context of the computational framework. Many of the experiments involving judgment of motion suggest that visual inferences concerning motion use information about objects and their relationships, such as occlusion and texture boundaries, to detect and interpret motion. Finally, we will review a variety of experimental measurements that seek to understand how motion is computed within the visual pathways. Physiologists have identified a visual stream whose neurons are particularly responsive to motion; in animals, lesions of this pathway lead to specific visual deficits of motion. The specific loss of motion perception, without an associated loss of color or pattern sensitivity, suggests that a portion of the visual pathways is specialized for motion perception.

It is useful to begin our review of motion with a few of the many behavioral observations that show motion is a complex visual inference, and not a simple representation of the physical motion. One demonstration of this, called *apparent motion*, can be seen in many downtown districts. There you will find displays consisting of a sequence of flashing marquis lights that appear to be moving, drawing your attention to a theater or shop. Yet, none of the individual lights in the display are moving; the lights are fixed in place, flashing in sequence. Even though there is no physical motion, the stimulus evokes a sense of motion in us. Even a single pair of lights, flashing in alternation, can provide a distinct visual impression of motion.

A second example of a fixed stimulus that appear to move can be found in *motion aftereffects*. Perhaps the best known motion aftereffect is the waterfall illusion, described in the following passage.

> Whilst on a recent tours of the highlands of Scotland, I visited the celebrated Falls of Foyers near Loch Ness, and there noticed the following phaenomenon. Having steadfastly looked for a few seconds at a particular part of the cascade, admiring the confluence and decussation of the currents forming the liquid drapery of waters, and then suddenly directed my eyes to the left, to observe the vertical face of the sombre age-worn rocks immediately contiguous to the waterfall, I saw the rocky surface as if in motion upwards, and with an apparent velocity equal to that of the descending water, which the moment before had prepared my eyes to behold this singular deception Addams (1834).

Notice that in the waterfall illusion, the object that appears to move (the rock) does not have the same shape or texture as the object that causes the motion aftereffect (the waterfall). The waterfall Addams described is shown in Figure 1.

A third way to convince yourself that motion is an inference is to consider the fact that many behavioral experiments show that perceived velocity, unlike physical velocity, depends on the color and contrast of an object. We know that the color of an object or its contrast relative to the background, are not good cues about motion. Indeed, the physical definition of motion does not depend on color or contrast at all. Yet, there are many motion demonstrations that perceived velocity depends on contrast and color. Some of the effects are quite large. For example, by the proper selection of the color and pattern a peripheral target moving at 1 degree per second can be made to appear as though it were still. These effects show that the visual inference of motion is imperfect because it is influenced by image features that are irrelevant to physical motion (Cavanagh and Anstis (1991)).

Motion computations and stereo depth perception are closely related. For example, as an observer moves the local motion of image points contain useful visual information about the distance from the observer to various points in the scene. As the observer moves, points in the image change in a predictable way that depends on the direction of the observer's motion and the distance of the point from the observer. Points that are further away generally move smaller amounts than points that are closer; and, points along the direction of heading move less than points far away from the direction of heading. Information from the image motion informs us about the position of objects in space relative to the viewer (Gibson (1950)).

The collective motion of points in an image from one moment to the next is called the *motion flow field*. By drawing our attention to this source of depth information, Gibson (1950) established an important research paradigm that relates motion and depth perception: define an algorithm for measuring the motion flow field, and then devise algorithms to extract information about observer motion and object depth from the motion flow field. In recent years, this problem has been substantially solved. It is now possible to use motion flow fields to estimate both an observer's motion through a static scene and a depth map from the observer to different points within the scene (Heeger and Jepson (1992), Tomasi and Kanade (1992); Koenderink (1990)).

Figure 1: The Falls of Foyers where Addams observed the motion aftereffect called the waterfall illusion. The illusion demonstrates that perceived motion is different from physical motion; we see motion in the aftereffect although there is no motion in the image (Source: (2009)).

These computational examples show that motion and stereo depth algorithms are related by their objectives: both inform us about the positions of objects in space and the viewer's relationship to those objects. Because motion and stereo depth estimation have similar goals, they use similar types of stimulus information. Stereo algorithms use the information in our two eyes to recover depth, relying on the fact that the two images are taken from slightly different points of view. Motion algorithms use a broader range of information that may include multiple views obtained as the observer moves or as objects change their position with respect to the viewer. Most of this chapter is devoted to a review of the principles in the general class of motion estimation algorithms. In a few places, because the goals of motion and stereo depth are so similar, I have inserted some related material concerning stereo depth perception.

Computing Motion

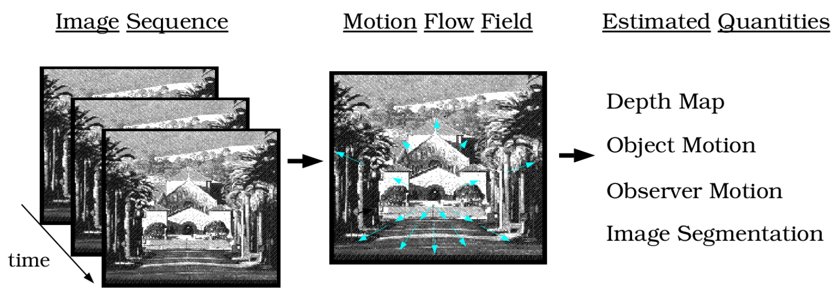

Figure 2: The overall logic of motion estimation algorithms. (a) The input stimulus consists of an image sequence. (b) The motion flow field at each moment in time is computed from the image sequence. (c) Various quantities relating to motion and depth can be calculated from the motion flow fields.

Figure 2 shows an overview of the key elements used in motion estimation algorithms. Figure 2 (a) shows the input data, a series of images acquired over time. Because the observer and objects move over time, each image in the sequence is a little different from the previous one. The image differences are due to the new geometric relationship between the camera, objects, and light source. The goal of most motion and depth estimation algorithms is to use these changes to infer motion of the observer, the motion of the objects in the image, or the depth map relating the observer to the objects.

The arrows drawn in Figure 2 (b) show the motion flow field. These arrows represent the changes in the position of points over small periods of space and time. The direction and length of the arrows correspond to the local motions that occur when the observer travels forward, down the road.

Figure 2 (c) is a list of several quantities that can be estimated from the motion flow fields. As I have already reviewed, the motion flow field contains information relevant to the depth map and observer motion. In addition, the motion flow field can be used to perform, *image segmentation*, that is to identify points in the image are part of a common object. In fact, we shall see that the motion flow field defined by a set of moving points but devoid of boundaries and shading is sufficient to give rise to an impresson of a moving three-dimensional object.

Finally, the motion flow field contains information about object motion. This information is important for two separate reasons. First, as we have already reviewed, an important part of motion algorithms is establishing the spatial relationship between objects and the viewer. Second, object motion information is very important for guiding *smooth pursuit* eye movements. The structure of our retina, in which only the fovea is capable of high spatial resolution, makes it essential that we maintain good fixation on targets as we move or as the object moves in our visual field. Information derived from motion estimation is essential to guide the eye movement system as we track moving objects in a dynamic environment (Movshon et al. (1990); Komatsu and Wurtz (1989); Schiller and Lee (1994)).

Stimulus Representation: Motion Sampling

We begin this review of motion algorithms by asking a simple question about the input data. In any practical system, the input stimulus is a sampled approximation of the continuous motion. The sampling rate should be rapid enough so that the input images provide a close approximation to the true continuous motion. How finely do we need to sample temporally the original scene in order to create a convincing visual display?

Beyond its significance for the science of motion perception, this question is also of great practical interest to people who design visual displays. A wide variety of visual display technologies represent motion by presenting a temporal sequence of still images. For example, movies and television displays both present the observer with a set of still images, each differing slightly from the previous one. In designing these display systems, engineers must select a temporal sampling rate for the display so that the observer has the illusion of smooth motion[1].

To answer the question of how finely we should sample an image sequence, we must include specifications about the image sequence and the human observer. First, consider why the answer must depend on the image sequence. Suppose that we are trying to represent a scene in which both objects and observer are still. In that case, we only need to acquire a single image. Next, suppose the image sequence contains a rapidly moving object. In that case, we need to acquire many images in order to capture all of the relevant scene information. If the

[1]Different display technologies solve this problem using various special purpose methods. For example, television in the U.S. displays a sequence of thirty static images per second. Each image is displayed in two frames, even numbered lines in the image are presented in one frame and odd numbered lines in the second frame. Hence, the display shows 60 frames (30 images) per second. Movie projectors display only twenty-four images per second, but each image is flashed three times so that the temporal flicker rate is 72 frames per second. Modern computer displays present complete images at seventy-two frames per second or higher. This rate is fast enough that they rarely need special tricks to avoid temporal flicker artifacts for typical image sequences.

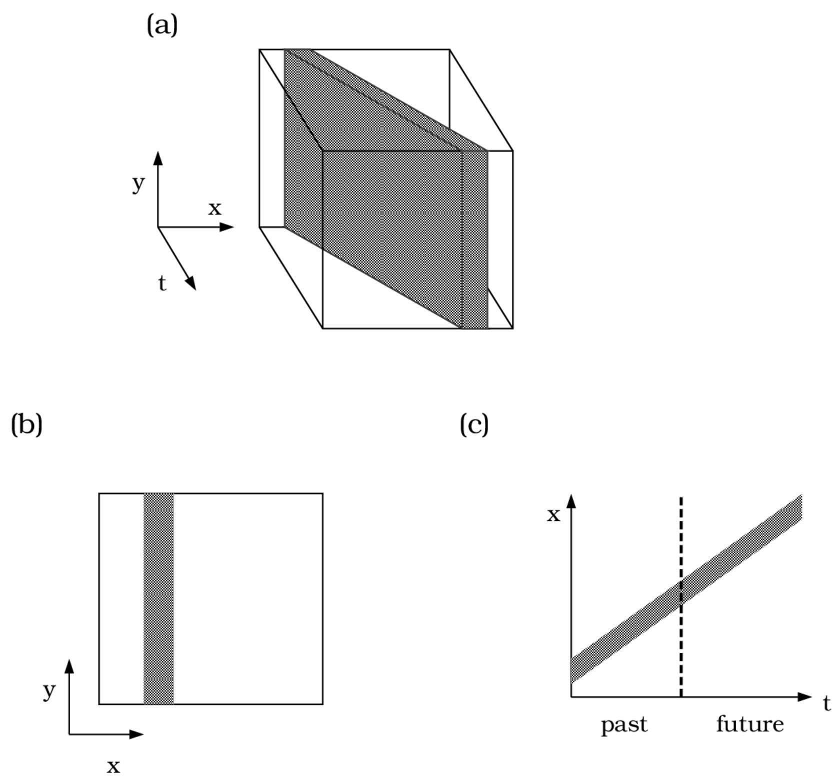

Figure 3: A motion sequence is a series of images measured over time. (a) The motion sequence of images can be grouped into a three-dimensional volume of data. Cross sections of the volume show the spatial pattern at a moment in time (panel b) time (t) plotted against one dimension (x) of space (panel c). When the spatial pattern is one-dimensional, the (t,x) cross-section provides a complete representation of the stimulus sequence.

image sequence contains rapidly moving objects, or if the observer moves rapidly, we must use high temporal sampling rates.

We will analyze the information in an image sequence using several simple representations shown in Figure 3. When we analyze the image sequence in order to estimate motion, we can call the image sequence the *motion signal* or *motion sequence.* Figure 3 (a) represents the motion sequence as a three-dimensional data set: the volume of data includes two spatial dimensions and time (x, y, t). Each point in this volume sends an amount of light to the eye, $I(x, y, t)$. The data in Figure 3 (a) illustrates an image sequence consisting of a dark bar on a light background moving to the right.

Next, consider two simplified versions of this three-dimensional data. Figure 3 (b) shows a cross-section of the data in the (x, y) plane. This image represents the dark bar at a single moment in time. Figure 3 (c) shows a cross-section of the motion volume in the (t, x) plane at a fixed value of y. In this plot time runs from the left (past) to the right (future) of the graph. The present is indicated by the dashed vertical line. The image intensity along the `$x$` direction is shown as the gray bar across the vertical axis.

When the spatial stimulus is one-dimensional, (i.e., constant in one direction) we can measure only the motion component perpendicular to the constant spatial dimension. For example, when the stimulus is an infinite vertical line, we can estimate only the motion in the horizontal direction. In this case, the (t, x) cross-section is the same at all levels of y so that the (t, x) cross-section contains all of the information needed to describe the object's motion. In the motion literature, the inability to measure the motion along the constant spatial dimension is called the *aperture problem*[2].

We can use the (t, x) plot to represent the effect of temporal sampling. First, consider the (t, x) representation of a smoothly moving stimulus shown in Figure 4. Now, suppose we sample the image intensities regularly in time. The sampled motion can be represented as a series of dashes in the (t, x) plot, as shown in Figure 4 (b). Each dash represents the bar at a single moment in time, and the separation between the dashes depends on the temporal sampling rate and target velocity. If the sampling rate is high, the separation between the dashes is small and the sequence will appear similar to the original continuous image. If the sampling rate is low, the separation between the dashes is large and the sequence will appear quite different from the continuous motion.

The separation between the dashes in the sampled representation also depends on the object's velocity. As the bar pattern moves faster, the dashes fall along a line of increasing slope. Thus, for increasing velocities the separation between the dashes will increase. Hence, the difference between continuous motion and sampled motion is larger for faster moving targets.

[2]The name "aperture problem" is something of a misnomer. It was selected because experimentally it is impossible to create infinite one-dimensional stimuli. Instead, subjects are presented finite one-dimensional patterns, such as a line-segment, through an aperture that masks the terminations of the line segment and making the stimulus effectively one-dimensional. The source of the uncertainty concerning the direction of motion, however, is not the aperture itself but rather the fact that the information available to the observer is one-dimensional.

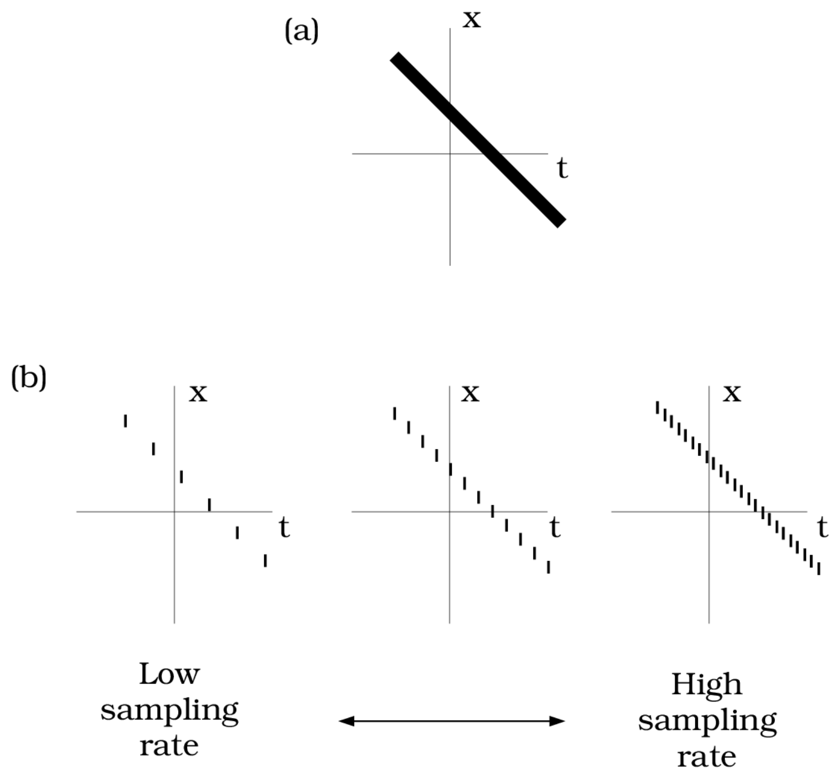

Figure 4: The representation of continuous and temporally sampled motion. (a) The continuous space-time plot of a moving line. (b) Temporal sampling of the continuous stimulus is represented by a series of dashes. As the temporal sampling rate increases (from left to right), the sampled stimulus becomes more similar to the continuous stimulus.

The Window of Visibility

Next, we will use measurements of visual spatial and temporal sensitivity to predict the temporal sampling rate at which a motion sequence appears indistinguishable from continuous motion. The basic procedure reviewed here has been described by several independent sources; Watson et al. (1983) call the method *the window of visibility* (see also Pearson (1975); Fahle and Poggio (1981))

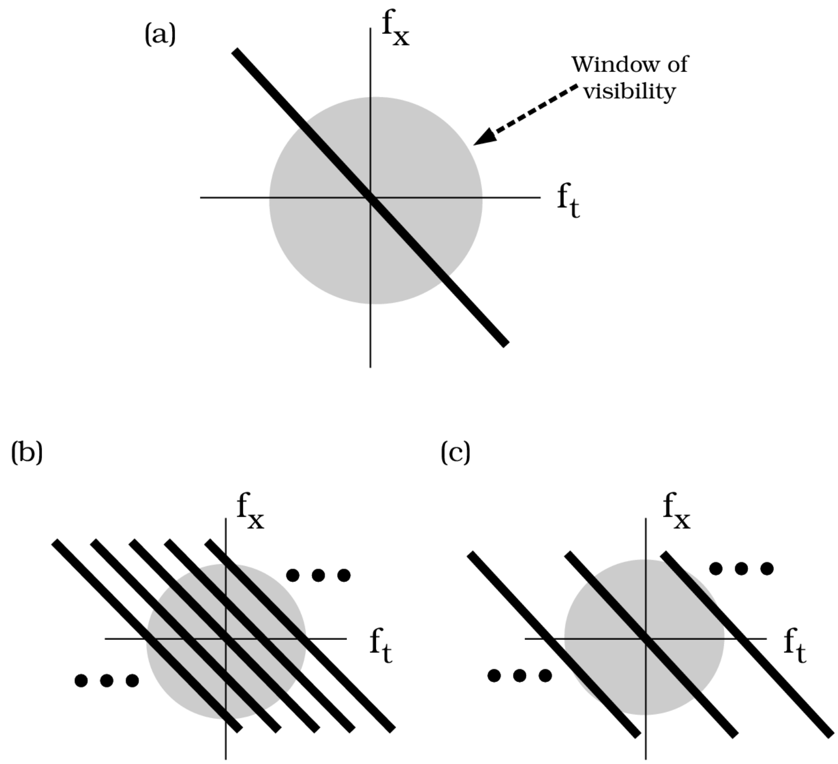

Figure 5: A graphical method to decide when sampled motion can be discriminated from continuous motion. The axes of the graphs represent the spatial and temporal frequency values of the stimulus. (a) The solid line represents the spatial and temporal frequency content of a vertical line moving continuously. The shaded area represents the range of visible spatial and temporal frequencies, that is, the window of visibility. (b,c) Temporally sampling the image introduces replicas. The spacing of the replicas depends on the temporal sampling rate. When the rate is low, the replicas are closely spaced and there is significant energy inside the window of visibility. When the sampling rate is high, the replicas are widely spaced and there is little energy inside the window of visibility. If the replicas fall outside the window, then the sampled and continuous motion will be indistinguishable.

The window of visibility method begins by transforming the images from the $ (t,x) $ representation into a new representation based on spatial and temporal harmonic functions. We can convert from the (t, x) representation to the new representation by using the Fourier transform (see Chapter and the Appendix). In the new representation, the stimulus is represented by its intensity with respect to the spatial and temporal frequency dimensions, (f_t, f_x). We convert the motion signal from the $ (t,x) $ form to the (f_t, f_x) form because, as we shall see, it is easy to represent the effect of sampling in the latter representation.

In the $((t, x))$ graph, a moving line is represented by a straight line whose slope depends on the line's velocity. In the $((f_t, f_x))$ graph, a moving line is also represented by a straight line whose slope depends on the line's velocity. You can see how this comes about by considering the units of spatial frequency, temporal frequency, and velocity. The units of f_t and f_x are *cycles/sec* and *cycles/deg*, respectively. The units of velocity, v, are *deg/sec*. It follows that spatial frequency, temporal frequency and velocity are related by the linear equation

$$f_t = v f_x \tag{0.1}$$

Now, a still image has zero energy at all non-zero temporal frequencies. Suppose an object begins to translate at velocity v. Then, each spatial frequency component associated with the object moves at this same velocity and creates a temporal modulation at the frequency $v f_x$. Consequently, an object moving at v will be represented by its spatial frequencies, f_x, and the corresponding temporal frequencies, $f_t = v f_x$. In the (f_t, f_x) graph this collection of points defines a line whose slope depends on the velocity, as shown in Figure 5 (a)[3].

We use the $((f_t, f_x))$ representation because it is easy to express the sampling distortion in that coordinate frame. A basic result of Fourier Theory is that temporally sampling a continuous signal creates a set of replicas of the original continuous signal in the $((f_t, f_x))$ representation[4]. The temporal sampling replicas are displaced from the original along the f_t axis; the size of the displacement depends on the sampling rate. When the sampling is very fine, the replicas are spaced far from the original. When the sampling is very coarse, the replicas are spaced close to the original.

Figure 5 (b,c) contain graphs representing temporally sampled motion. In panel b, the temporal sampling rate is low and the replicas are spaced close to the original signal. At this sampling rate, the sampled motion is plainly discriminable from the continuous motion. In panel c, the temporal sampling rate is high and the replicas are far from the original signal. To make the sampled image appear like continuous motion, we must set the temporal sampling rate high enough so that the sampling distortion is invisible. The problem that remains is to find the sampling rate at which the replicas will be invisible.

[3]Speaking more precisely, the Fourier Transform maps the intensities in the $((t, x))$ plot into a set of complex numbers. The plot shown in this figure represents the locations of the nonzero components of the data after applying the Fourier Transform.

[4]Temporally sampling a signal in the time domain produces periodic replicas of its spectrum in the frequency domain, spaced by the sampling frequency.

The shaded area in each panel of Figure 5 shows a region called the *window of visibility*. The window describes the spatio-temporal frequency range that is detectable to human observers. The boundary of the window is a coarse summary of the limits of space-time sensitivity that we reviewed in Chapter . Spatial signals beyond roughly 50 cycles per degree, or temporal frequency signals beyond roughly 60 cycles per second, are beyond our perceptual limits. If the sampling replicas fall outside the window of visibility, they will not be visible and the difference between the continuous and sampled motion will not be perceptible. Hence, to select a temporal sampling rate at which sampled motion will be indiscriminable from continuous motion, we should select a temporal sampling rate such that the replicas fall outside of the window of visibility.

The window of visibility method is a very useful approximation to use when we evaluate the temporal sampling requirements for different image sequences and display technologies. But, the method has two limitations. First, the method is very conservative. There will be sampled motion signals that fail to contain energy within the window and yet the sampled motion will still appear to be continuous motion. This will occur because the energy that unwanted sampling energy that falls within the window of visibility may be masked by the energy from the continuous motion (see Section for a discussion of masking).

Second, the method is a limited description of motion. By examining the replicas, we can decide that the stimulus does look the same as the original continuous motion. But, the method doesn't help us to decide the motion looks like, i.e., the velocity and direction. We analyze how to estimate motion from image sequences next.

Image Motion Information

What properties of the data in an image sequence suggest that motion is present? We can answer this question by considering the representation of a one-dimensional object, say a vertical line, in the $((t, x))$ plot. When the observer and object are still, the intensity pattern does not change across time. In this case the $((t, x))$ plot of the object's intensity is the same for all values of t and is simply a horizontal line. When the object moves, its spatial position, x, changes across time so that in the $((t, x))$ the path of the moving line includes segments that deviate from the horizontal. The value of the orientation of the trajectory in the $((t, x))$ plot depends on the object's velocity. Large velocities are near the vertical; small velocities are near the horizontal orientation of a still object. Hence, *orientation* in the $((t, x))$ representation informs us about velocity (Adelson and Bergen (1985); Watson and Ahumada (1985)).

The connection between orientation in the (t, x) plot and velocity sensitivity suggests a procedure for estimating motion. Suppose we wish to create a neuron that responds well to motion at a particular velocity but responds little to motion at other velocities. Then, we should create a neuron whose space-time receptive field is sensitivity to signals with the proper orientation in the (t, x) plot.

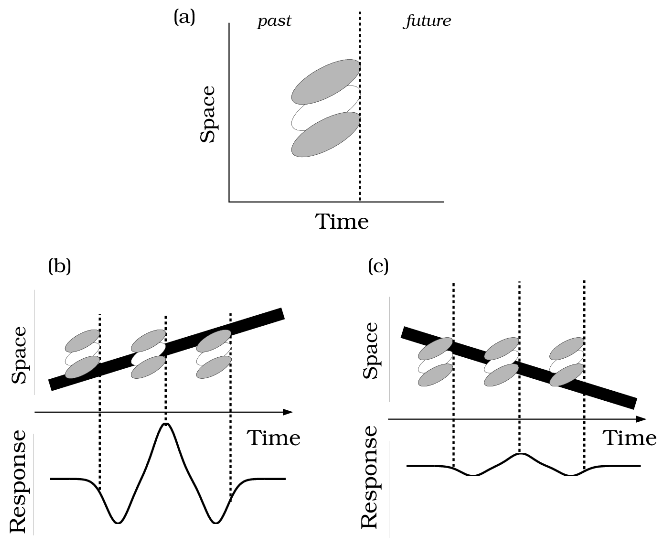

Figure 6: Space-time oriented receptive field. (a) The space-time receptive field of a neuron is represented on an (t,x) plot. The neuron always responds to events in the recent past, so the receptive field moves along the time axis with the present. The dark areas show an inhibitory region and the light area shows an excitatory region. (b) The upper portion of the graph shows an (t,x) plot of a moving line and the space-time receptive field of a linear neuron. The neuron's receptive field is shown at several different moments in time, indicated by the vertical dashed line. The common orientation of the space-time receptive field and the stimulus motion produce a large amplitude response, shown in the bottom half of this graph. (c) When the same neuron is stimulated by a line moving in a different direction, the stimulus motion aligns poorly with the space-time receptive field. Consequently, the response amplitude is much smaller.

Figure 6 shows the idea of a space-time oriented receptive field. In Figure 6 (a), I have represented the space-time receptive field of the neuron using the same conventions that we used to represent the space-time receptive field of neurons in Chapter and Chapter): The excitatory regions of the receptive field are shown as the light area and the inhibitory regions are shown as the shaded area. The horizontal axis represents time, and the dashed line represents the present moment in time. The receptive field of the neuron always responds to recent events in the past, and so it travels along with the line denoting the present, trailing just behind. This graph has much in common with the ordinary notation showing an oriented two-dimensional spatial receptive field. The graph is somewhat different from the conventional spatial receptive field because the space-time receptive field always travels in time just behind the present.

Neurons with oriented space-time receptive fields respond differently to stimuli moving in different directions and velocities. Figure 6 (b) shows the response to a line moving in a direction that is aligned with space-time receptive field. The upper portion of the graph shows the relationship between the stimulus and the neuron's receptive field at several points in time. Because the stimulus and the receptive field share a common orientation, the stimulus fills the inhibitory, excitatory, and then inhibitory portions of the receptive field in turn. Consequently, the neuron will have a large amplitude response to the stimulus, as shown in the lower portion of Figure 6 (b).

Figure 6 shows the response of the same neuron to a stimulus moving in a different direction. The space-time orientation of this stimulus is not well-aligned with the receptive field, so the stimulus falls across the inhibitory and excitatory receptive field regions simultaneously. Consequently, the response amplitude to this moving stimulus is much smaller. Just as neurons with oriented receptive fields in (x, y) respond best to bars with the same orientation, so too neurons with oriented receptive fields in (t, x) respond best to signals with a certain velocity.

It is possible, in principle, to create neurons with space-time oriented receptive fields by combining the responses of the simple cells in area V1 of the cortex. One of many possible methods is shown in Figure 7 (a). Consider an array of neurons with adjacent spatial receptive fields. The spatial receptive fields are shown at the top of panel (a). The responses of these neurons are added together after a temporal delay, δt. The sum of these responses drives the output neuron shown at the bottom.

Figure 7 (b) shows the (t, x) receptive field of the output neuron. In panel (b), the receptive field plotted along the x dimension are the one-dimensional receptive fields of the neurons in panel (a), that is the receptive fields measured using a one-dimensional stimulus that is constant along the y axis. The spatial receptive fields of the input neurons are adjacent to one another, so they are shifted along the x dimension of the graph. The temporal response of the neurons, measured at each point in the receptive field is also shown in panel (b). Since the input neurons are delayed prior to being summed, the temporal receptive fields are shifted along the t dimension. The shift in both the x and t dimensions yield an output receptive field that is oriented in the space-time plot.

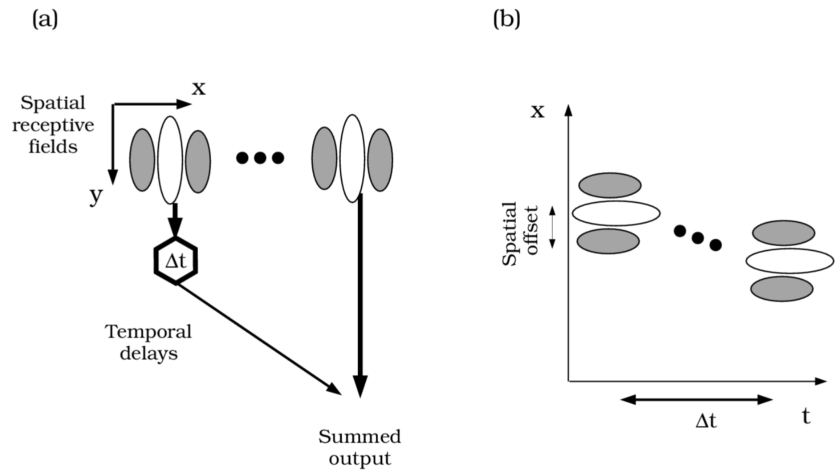

Figure 7: A method for creating a space-time oriented receptive field. (a) A pair of spatial receptive fields, displaced in the x-direction, is shown at the top. The response of the neuron on the left is delayed and then added to the response of the neuron on the right. (b) The (t,x) receptive field of the output neuron in panel (a) is shown. The temporal response of the neuron on the left is delayed compared to the temporal response of the neuron on the right. The combination of spatial displacement and temporal delay yield an output neuron whose receptive field is oriented in space-time.

When a neuron has a space-time oriented receptive field, its response amplitude varies with the image velocity (see Figure 6). Thus, to measure stimulus velocity we need to compare the response amplitudes of an array of neurons, each with its own preferred motion. There are various methods of computing the amplitude of the time-varying response of a neuron and comparing the results among different neurons. Generally, these methods involve simple squaring and summing operations applied to the responses. In recent years, several specific computational methods for extracting the amplitude of the neural responses have been proposed (Adelson and Bergen (1985); Watson and Ahumada (1985); van Santen and Sperling (1985)). We will return to this topic again after considering a second way to formulate the problem of motion estimation.

The Motion Gradient Constraint

The (t, x) representation of motion clarifies the requirements for a linear receptive field that discriminates among motion in different directions and velocities. There is a second way to describe the requirements for motion estimation that provides some additional insights. In this section, we will derive a motion estimation computation based on the assumption that in small regions of the image motion causes a displacement of the point intensities without changing the intensity values. This assumption is called the *motion gradient constraint*.

The motion gradient constraint is an approximation, and sometimes not a very good approximation. As the relative positions of the observer, objects and light sources change, the spatial intensity pattern of the reflected light changes as well. For example, when one object moves behind another the local intensity pattern changes considerably. Or, as we saw in Chapter , if we are viewing a specular surface the spatial distribution of the light reflected to our eye varies as we change position. As a practical matter, however, there are often regions within an image sequence where the motion gradient constraint is a good approximation. In some applications the approximation is good enough so that we can derive useful information.

To estimate local velocity using the motion gradient, we reason as follows. We describe the image intensities in the sequence as $I(a, b, t)$, the intensity at location (a, b) and time t. Suppose the velocities in the x and y directions at a point (a, b, t) are described by the *motion vector*, (v_x, v_y). Further, suppose that images in the motion signal are separated by a single unit of time. In that case the intensity at point (a, b) will have shifted to a new position in the next frame,

$$I(a, b, t) = I(a + v_x, b + v_y, t + 1) \tag{0.2}$$

(Remember that v_x and v_y depend on the spatial position and the moment in time, (a, b, t).)

Our goal is to use the changing image intensities to estimate the motion vector, (v_x, v_y), at each position. We expand the right hand side of Equation 0.2 in terms of the partial derivatives of the intensity pattern with respect to space and time,

$$I(a + v_x, b + v_y, t + 1) \approx I(a, b, t) + v_x \frac{\partial I}{\partial x} + v_y \frac{\partial I}{\partial y} + \frac{\partial I}{\partial t} \tag{0.3}$$

The terms $\frac{\partial I}{\partial x}$ and $\frac{\partial I}{\partial y}$ are the partial derivatives of $I(x, y, t)$ in the spatial and temporal dimensions, respectively. Grouping Equation 0.2 and Equation 0.3, we obtain the *gradient constraint equation*.

$$v_x \frac{\partial I}{\partial x} + v_y \frac{\partial I}{\partial y} + \frac{\partial I}{\partial t} \approx 0 \tag{0.4}$$

Equation 0.4 is a linear relationship between the space-time derivatives of the image intensities and the local velocity. Since there is only one linear equation and there are two unknown velocity components, the equation has multiple solutions. All of the solutions fall on a *velocity constraint line* shown in the graph in Figure 8.

Because the data at a single point do not define a unique solution, to derive an estimate we must combine the velocity constraint lines from a number of nearby points. There will be a unique solution, that is all of the lines will intersect in a single point, if (a) the motion gradient constraint is true, (b) nearby points share a common velocity, and (b) there is no noise in the

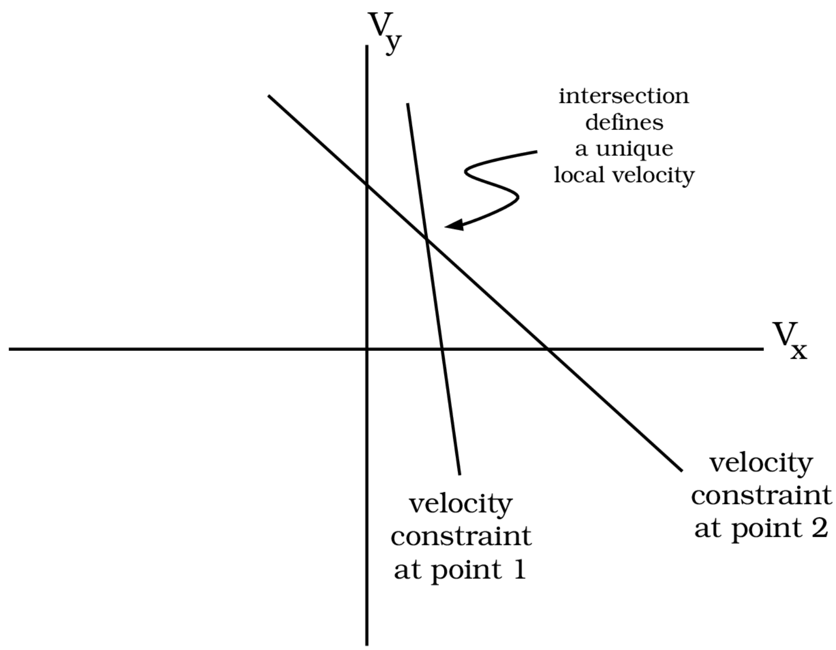

Figure 8: A graphical representation of the motion gradient constraint. According to the motion gradient constraint, the spatial and temporal derivatives at each image point constrain the local velocities to fall somewhere along a line. The intersection of the constraint lines derived from nearby points yields a local velocity estimate that is consistent with the motion of all the local points.

measurements. If the lines do not come close to a single intersection point, then the motion gradient constraint is a poor local description of the image motion or the nearby points do not share a common motion. In the Appendix, I discuss some of the issues related to finding the best solution to the motion gradient constraint equations of multiple points in the presence of measurement noise.

Space-time filters and motion gradient

Early in this chapter, we found that we can use the response amplitudes of space-time oriented linear filters to measure local image velocity. Now, studying the motion gradient constraint, we find that we can combine the spatio-temporal derivatives of the image intensities to measure the local velocity. These two methods of measuring local motion are closely linked as the following argument shows (Simoncelli (1993)).

To be able to explain the relationship using pictures, let's consider only one-dimensional spatial stimuli and use the (t, x) graph. With this simplification, the motion gradient constraint has the reduced form

$$v_x \frac{\partial I}{\partial x} + \frac{\partial I}{\partial t} = 0 \tag{0.5}$$

Since the stimuli are one-dimensional, we can only estimate a single directional velocity, v_x.

How can we express the computation in Equation 0.5 in terms of the responses of space-time receptive fields? To perform this computation, we need to compute the local spatial and temporal derivatives of the image. A receptive field that computes the spatial derivative can be computed in two steps. First, we compute a weighted average of the local image intensities over a small space-time region. We know that some space-time averaging of the image intensities must take place because of various unavoidable physiological factors, such as optical blurring and temporal sluggishness of the neural response. Suppose we describe this space-time averaging using a Gaussian weighting function $g(x, t)$. Second, we compute the spatial derivative by applying the spatial partial derivative operator to the averaged data. The space-time averaging followed by a partial derivative calculation can be grouped into a single operation, $\frac{\partial g}{\partial x}$. Similarly, we can express the temporal derivative operator as $\frac{\partial g}{\partial t}$. The space-time receptive fields that compute these two derivative operations are shown in (t, x) graphs at the top of Figure 9 (a).

One way to compute the velocity, according to Equation 0.5, is to multiply these spatial and temporal receptive fields with the image. The ratio of the responses is equal to the velocity, v_x. An equivalent way to perform this calculation is to create an array of neurons whose receptive fields are various weighted sums of the two derivative operators for different values, v_x. The receptive fields of such an array of neurons is shown in Figure 9 (a). Each receptive field is oriented in space-time, and the orientation depends on the velocity used as a weight, v_x. The pattern of response amplitudes of these neurons can be used to estimate the stimulus motion.

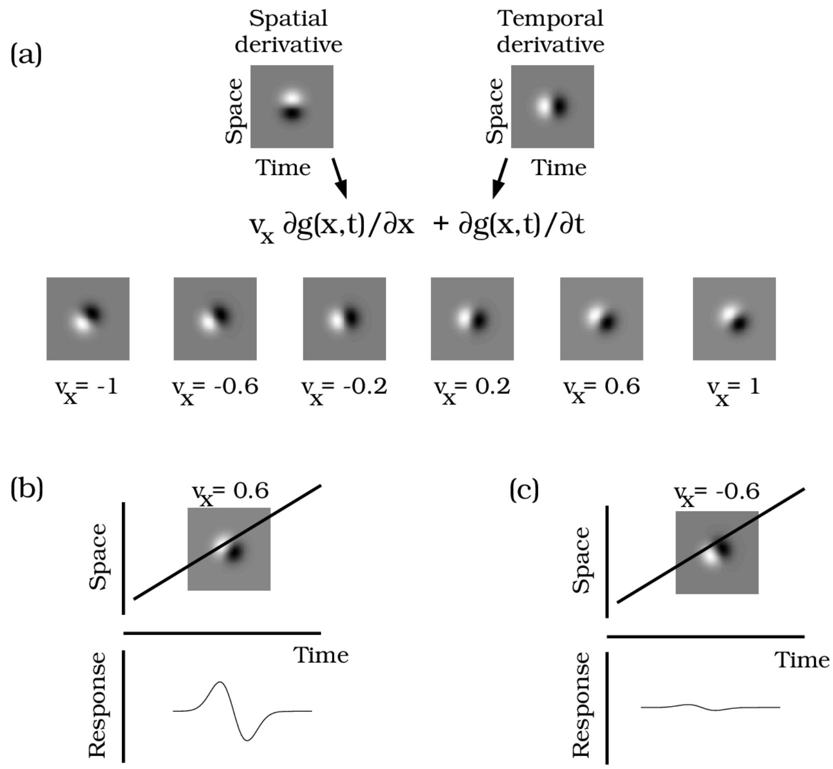

Figure 9: The motion gradient constraint represented in terms of space-time receptive fields. (a) The spatial and temporal derivatives can be computed using neurons whose (t,x) receptive fields are shown at the top. We can form weighted sums of these neural responses to create new receptive fields that are oriented in space-time. (b,c) The response amplitudes of these neurons can be used to identify the motion of a stimulus. The receptive field of the neuron represented in (b) responds strongly to the stimulus motion while the receptive field of the neuron in (c) responds weakly. By comparing the response amplitudes of the array of neurons, one can infer the stimulus motion.

For example, the neuron whose receptive field is shown in panel (b) has a receptive field that is aligned with the stimulus motion and has a large response amplitude. The neuron shown in panel (c) has a small response amplitude. We can deduce the local image velocity from the pattern of response amplitudes.

This set of pictures shows that the motion gradient constraint can be understood in terms of the responses of space-time oriented receptive fields. Hence, space-time oriented receptive fields and the motion gradient constraint are complementary ways of thinking about local motion.

Depth Information in the Motion Flow Field

We now have several ways of thinking about motion flow field estimation. But, remember that the motion flow field itself is not our main goal. Rather, we would like to be able to use the information in the motion flow field estimate to make inferences about the positions of objects in the scene. Much of the computational theory of motion and depth is concerned with how to calculate these quantities from the motion flow field. I do not provide a general review of such algorithms here. But, I do explain one principle concerning the computation of a depth map from observer motion, illustrated in Figure 10, that is important to understanding many of these algorithms (Longuet-Higgins and Prazdny (1980); Koenderink and van Doorn (1975)).

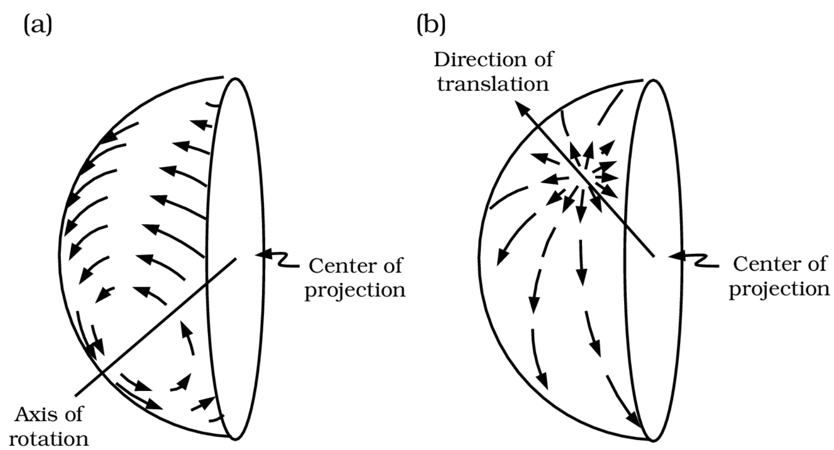

Figure 10: The motion flow field components associated with observer motion. A change in the observer's viewpoint causes two separate changes in the motion flow field. The total flow field vector is a sum of the rotation and translation components. (a) When the viewpoint rotates, the rotation component of the motion flow field is the same for all points, no matter their distance. (b) When the viewpoint translates, the motion flow vector the rotation component of the motion flow field varies with the image point distance from the observer and the direction of heading (After: Longuet-Higgins and Prazdny (1980)).

We can partition each motion flow field vector into two components that are associated with different changes in the observer's viewpoint. The first component is due to a pure rotation of the viewpoint, and the second component is due to a pure translation of the viewpoint. Each motion flow field vector is the sum of a change due to the rotational and translational viewpoint changes.

These two flow field components contain different information about the distance of the point from the viewer. The change caused by a viewpoint *rotation* does not depend on the distance to the point. When the viewpoint rotates, the local flow field of all points, not matter what their distance from the observer, rotates by same amount. Hence, the rotational component of the motion flow field contains no information about the distance to different points in the image (Figure 10 (a)).

The flow field component caused by a *translation* of the viewpoint depends on the distance to the image point in two ways. First, along each line of sight the points closer to the viewpoint are displaced more than distant points. Second the direction of the local flow field depends on the direction of the translation (Figure 10 (b)). You can demonstrate these effects for yourself by closing one eye and looking at a pair of objects, one near and one distant. As you move your head side-to-side, the image of the nearby point shifts more than the image of the distant point (i.e., motion parallax). Hence, the translational component of the motion flow field vectors contains information about the distance between the viewer and the point.

Experimental Observations of Motion

The main theoretical ideas we have reviewed concerning motion and depth each has an experimental counterpart. For example, there are behavioral studies that analyze the role of the motion gradient constraint in visual perception (Adelson and Movshon (1982)). And, the cat visual cortex contains neurons with space-time oriented receptive fields (McLean and Palmer (1994), DeAngelis et al. (1993a), DeAngelis et al. (1993b)).

In addition to confirmations of the importance of the computational ideas, the experimental literature on motion perception has provided new challenges for computational theories of motion perception. Most computational theories are based on measurements of image intensities and their derivatives. Experimental evidence suggests that motion perception depends on more abstract image features, such as surfaces or objects, as well. In Chapter we saw that surfaces and illuminants are an important component of our analysis of color vision. Similarly, the experimental literature on motion perception shows us that we need to incorporate knowledge about surfaces and objects to frame more mature theories of motion perception (Ramachandran et al. (1988); Stoner et al. (1990); Anderson and Nakayama (1994); Hildreth et al. (1995); Treue et al. (1995)).

The experimental work defines new challenges and guidelines for those working on the next generation of computational theories. As we review these results, we shall see that motion perception is far from perfect; we make many incorrect judgments of velocity and direction. Moreover, perception of surfaces and occlusion are an integral part of how we interpret motion and depth. A complete computational theory of motion perception will need to include representations of surfaces and objects, as well as explanations of why image features such as contrast and color influence motion perception.

Motion gradients: The intersection of constraints

Adelson and Movshon (1982) studied how the some of the ideas of the motion gradient constraint apply to human perception. Their experiment is a motion superposition experiment that measures how people integrate motion information from separate image features when observers infer motion. The principle behind Adelson and Movshon's measurements is shown in Figure 11.

The motion of a one-dimensional pattern is ambiguous. We cannot measure whether a one-dimensional pattern, say a bar, has moved along its length. The graph in Figure 11 (a) shows three images from an image sequence of a moving bar, and the dashed line in Figure 11 (b) shows the set of possible velocities that are consistent with the image sequence. The graph is called a *velocity diagram*, and the set of possible motions are called the *constraint line*. The image sequence constrains the bar's horizontal velocity, but the data tell us nothing about the bar's vertical velocity. Although the information in the image sequence is ambiguous, subjects' perception of the motion is not ambiguous: the bar appears to move to the right. This perceived velocity is indicated on the velocity diagram by the black dot.

Figure 11 (c,d) shows the image sequence and constraint line of a horizontal bar. In this case, the stimulus information is only informative about the the vertical motion. This stimulus defines a different constraint line in the velocity diagram, and in this case, subjects see the line moving upward.

Figure 11 (e,f) shows the superposition of the two lines. In this stimulus, each bar separately determines a single constraint line; the *intersection of constraints* is the only point in the velocity diagram that is consistent with the image sequence information. The only consistent interpretation that groups the two lines into a single stimulus is to see the pair of lines moving up and to the right. This is what subjects see.

Adelson and Movshon (1982) described a set of measurements in which they evaluated whether observers generally saw the motion of the superimposed stimuli moving in the direction predicted by the intersection of constraints. In their original study, they used one-dimensional sinusoidal gratings as stimuli, rather than bars[5]. They altered the contrast, orientation and spatial frequency of the two gratings. As parameters varied, observers generally saw motion near the direction of the intersection of constraints. Often, however, observers saw the two gratings as two different objects, sliding over one another, an effect called *motion transparency*.

[5]The superposition of two gratings at different orientations looks like a plaid, so this design is often called a *motion plaid experiment*.

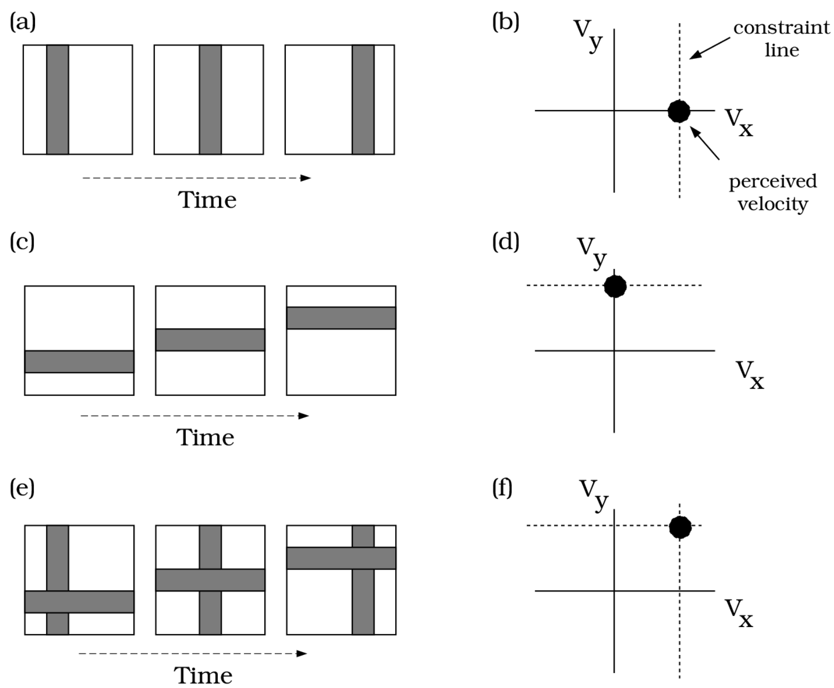

Figure 11: The intersection of constraints. The physical motion of a one-dimensional stimulus is inherently ambiguous. The physical motion in the display is consistent with a collection of possible velocities that plot as a line in velocity space. (a) A set of images of a vertical line moving to the right. (b) The set of physical motions consistent with the stimulus information plots along the velocity constraint line. The dot shows the perceived physical motion. (c,d) A similar set of graphs for a horizontal line. (e,f) When we superimpose the two lines, there is only a single physical motion that is consistent with the stimulus information. That motion plots at the intersection of the two velocity constraint lines.

Transparency is a case in which the observer perceives two motions at each point in the image. This fact alone has caused theorists to scurry back to their chalkboards and reconsider their computational motion algorithms.

The behavioral experiments show that calculations like the intersection-of-constraints are helpful in some cases. But, even in these simple mixture experiments observers see objects and surfaces, concepts that are not represented in the motion computations, are important elements of human motion perception. A second way to see the close relationship between motion an surfaces is through a visual demonstration, described in Figure 12, called a *random dot kinematogram*.

The demonstration described in Figure 12 consists of an image sequence in which each individual frame is an array of dots. From frame-to-frame, the dots change position as if they were painted on the surface of a moving object. In a single frame the observer sees nothing but a random dot pattern; the only information about the object is contained in the dot motions. The motions of the dots painted on the surface of a transparent cylinder are shown in Figure 12. The cylinder is also shown, though in the actual display the cylinder outline is not shown.

Random dot kinematograms reveal several surprising aspects of how the visual system uses motion information. First, the visual system seems to integrate local motions into globally coherent structures. The ability to integrate a set of seemingly independent local motions into a single coherent percept is called *structure from motion.* The demonstration described in Figure 12 is particularly impressive on this point. The image sequence contains a representation of dots on a transparent object. Because some of the dots are painted onto the front and some onto the back of the transparent object, each region of the image contains dots moving in opposite directions. Despite the apparent jumble of local motions, observers automatically segregate the local dot motions, and interpret the different directions and speeds, yielding the appearance of the front and back a rotating and transparent object.

Second, the ability to integrate these dot motions into an object seems to be carried out by a visual mechanism that infers the presence of a surface without being concerned about the stability of the surface texture. We can draw this conclusion from the fact that the stability and temporal properties of the individual dots has very little effect on the overall perception of the moving object. Single dots can be deleted after only a fraction of a second; new dots can be introduced at new surface locations on the implicit surface without disrupting the overall percept. Even as dots come and go, the observer sees a stable moving surface. The local space-time motions of the dots are important for revealing the object, but the object has a perceptual existence that is independent of any of the individual dots (Treue et al. (1991)).

The shapes we perceive using random dot kinematograms are very compelling, but they do not look like real moving surfaces. The motion cue is sufficient to evoke the shape, but many visual cues are missing and the observer is plainly aware of their absence. Random dot kinematograms are significant because they seem to isolate certain pathways within the visual system. Random dot kinematograms may permit us to isolate the flow of information between specialized motion mechanisms and shape recognition. By studying motion and depth

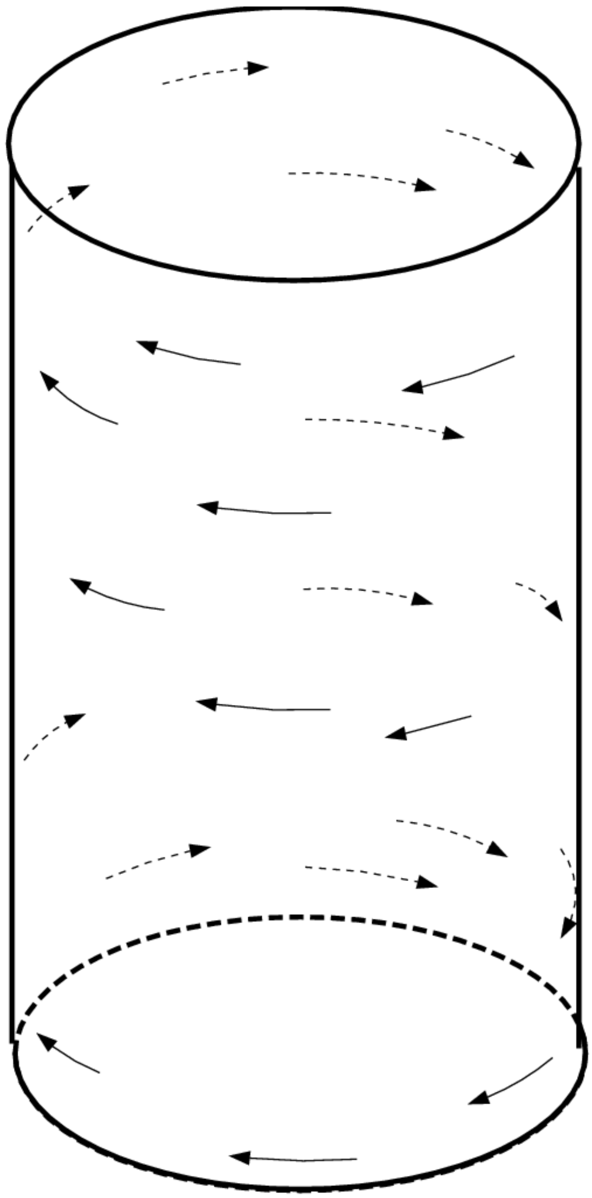

Figure 12: Description of a random dot kinematogram. Suppose that an observer views a random collection of dots, and that each dot is moving as if it is attached to the surface of a transparent cylinder. Observers perceive the surface of an implicit rotating cylinder, even though there is no shading or edge information in the image. Because the cylinder is transparent, dots move in both directions in each local region of the image. The dots are perceived as being attached to the near or far surface consistent with their direction of motion.

perception using these stimuli, we learn about special interconnections in the visual pathway. Studies with these types of stimuli have played a large role in the physiological analysis of the visual pathways, which we turn to next.

Contrast and Color

The color or contrast of an object is not a cue about the object's velocity. While velocity judgments should be independent of contrast and color, in fact perceived velocity depends on these stimulus variables. Models of human performance must be able to predict this dependence and to explain why judged velocity depends on these extraneous variables.

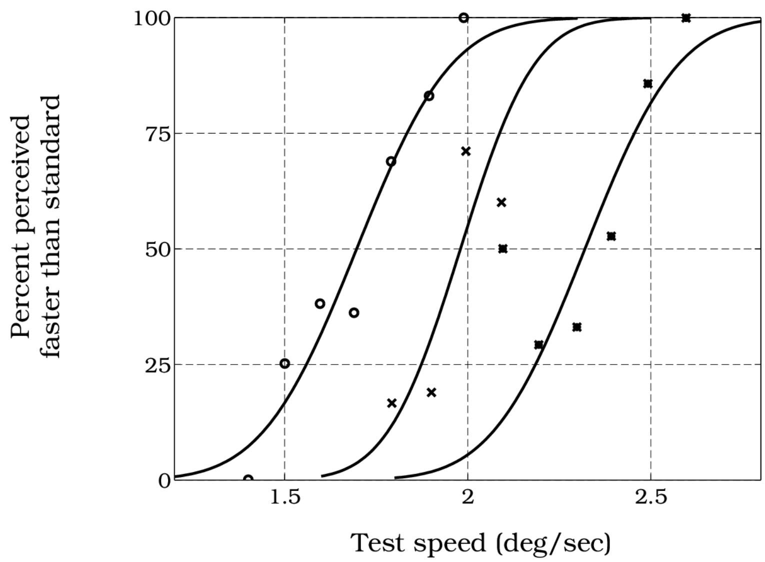

Figure 13: Perceived speed depends on stimulus contrast. The horizontal axis measures the velocity of a test grating. The vertical axis measures the probability that the test grating appears to be moving faster than a standard grating whose speed is always 2 deg/sec. The three separate curves show measurements for test gratings at three different contrasts. The curve on the left is for a test at 7 times the contrast of the standard; the curve on the middle is for a test at the same contrast as the standard; the curve on the right is for a test at one seventh the contrast of the standard. The spatial frequency of the test and standard were always 1.5 cpd. (Source: Stone and Thompson (1992)).

Stone and Thompson (1992) measured how perceived speed depends on stimulus contrast. Subjects compared the speed of a standard grating drifting at 2 deg/sec with the speed of a test grating. The data points measure the chance that the test appeared faster than the standard as a function of the speed of the test grating. The data points near the curve in the middle of the figure are a control condition in which the test and standard had the same contrast. In the control condition, the test and standard had the same apparent speed when they had the same physical speed. The curve on the left shows the results when the test grating had seven times more contrast than the standard. In this case the test and standard had equal perceived speed when the test speed was 1.6 deg/sec, significantly slower than the standard. The data points near the curve on the right shows the results when the test grating had one-seventh the contrast of the standard grating. In this condition the test had equal perceived speed to the standard speed at 2.4 deg/sec, considerably faster than the standard. High contrast targets appear to move faster than low contrast targets.

Our velocity judgments also depend on other irrelevant image properties, such as the pattern of the stimulus (e.g. Smith and Edgar (1991)) and the color of the stimulus (e.g. Moreland (1980); Cavanagh et al. (1984)). Taken together these experiments suggest that some properties of the peripheral representation, intended to be helpful in representing color and form information, have unwanted side-effects on motion perception. The initial encoding of the signal by the visual system must be appropriate for many different kinds of visual information. Given these practical requirements, interactions between irrelevant image properties and motion estimation may be unavoidable.

Long and Short Range Motion Processes

Creative science often includes a clash between two opposing tendencies. The search to unify phenomena in a grand theory is opposed by the need to distinguish phenomena with separate root explanations. The tension is summarized in Einstein's famous remark: A theory should be as simple as possible, but no simpler. Perhaps the best known effort to classify motion into different processes is Braddick's (Braddick (1974)) classification into *short-range* and *long-range* motion processes.

Since Exner's (Exner (1875)) original demonstrations, psychologists have known that even very coarsely sampled motion still generates a visual impression of motion. Such motion is easily distinguished from continuous motion, but there is no doubt that the something appears to be moving. The motion impression created by viewing coarsely sampled stimuli is called *apparent motion*[6]. The properties of apparent motion were studied by many of the Gestalt Psychologists, such as Wertheimer (1912) and Korte (1915), who describe the conditions under which the motion illusion is most compelling.

Braddick (1974) found that the spatial and temporal sampling necessary to perceive motion when using large spots is quite different from the limits using small displays with small spatial patterns, such as random dot kinematograms. Specifically, Braddick (1974) found that subjects perceive motion in a random dot kinematogram only when the spatial separations between frames are less than about 15 minutes of arc. When the spatial displacements are larger than this, observers see flickering dots but no coherent motion. This is a much smaller spatial limit

[6]This term is peculiar since all perceived motion is apparent.

than the sampling differences at which subjects report seeing apparent motion. The upper limit on the spatial displacement at which motion is perceived is called D_{max} in the motion literature.

Braddick also noted a second difference between the motion perceived in random dot kinematograms and apparent motion. Suppose we present an alternating pair of large spots to elicit apparent motion. We perceive the motion when the two spots are presented either to the same eye or when they are presented alternately to two eyes. Alternating frames of a random dot kinematogram between the two eyes, however, is less effective at evoking a sense of motion (Braddick (1974)). A wide range of experimental findings have been interpreted within this classification of motion (see e.g., Braddick (1980); Anstis (1980); Nakayama and Silverman (1984)).

From our earlier analysis of temporal sampling of motion (see Figure 5) we learned that the ability to discriminate continuous from sampled motion will depend on the spatial and temporal properties of the image display. It is not too surprising, then, to find that the ability to perceive motion at all should depend on the spatiotemporal properties of the stimulus as well. Cavanagh and Mather (1989) review a set of measurements that suggest the difference between short- and long-range processes can be explained by the spatiotemporal organization of the visual system to stimuli of different spatial size and pattern, rather than by a subdivision within the visual pathways. For example, the value of D_{max} appears to be proportional to the size of the elements in the random-dot field for dot sizes larger than 15 min rather than an absolute value that divides the sensitivity of the two motion systems (Cavanagh et al. (1985)).

Based on their review of a variety of experiments, Cavanagh and Mather conclude that the measurements that give rise to the definition of the long- and short-range processes are a consequence of differential visual sensitivity, not of motion classification. The long and short-range processes classification is still widely used, so understanding the classification is important. Because, I suspect that the classification will not last (see also, Chang and Julesz (1985); Shadlen and Carney (1986)).

First and Second order motion

Several authors have proposed a classification of motion based on whether or not a stimulus activates neurons with space-time oriented receptive fields followed by simple squaring operations (Anstis (1980); Chubb and Sperling (1988)). According to this classification, whenever a stimulus creates a powerful response for these types of sensors, the motion can be perceived by the *first-order* motion system. Chubb and Sperling (1988) show precisely how to create stimuli that are ineffective at stimulating the first-order system but that still appear to move. They propose that these moving stimuli are seen by a *second-order* motion system[7].

[7] In their original paper, Chubb and Sperling (1988) called the two putative neural pathways *Fourier* and *non-Fourier* motion systems. Cavanagh and Mather (1989) used the terms *first-* and *second-order* motion

Figure 14 describes an example of a stimulus that is ineffective at stimulating space-time oriented filters and yet appears to move. At each moment in time, the stimulus consists of a single uniform texture pattern. The stimulus appears to contain a set of vertical boundaries because the local elements in different bands move in opposite (up/down) directions. In addition to this up/down motion, the positions of the bands drift from left-to-right. This stimulus does not evoke a powerful left-right response from space-time oriented filters. Yet, the pattern plainly appears to drift left-to-right (Cavanagh and Mather (1989)).

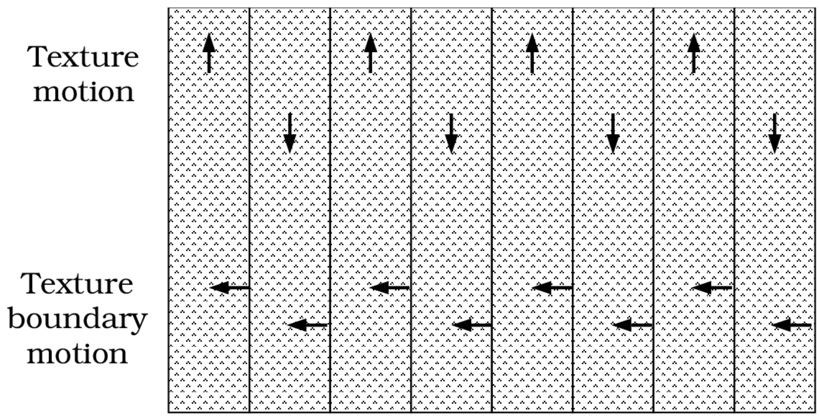

Figure 14: A second-order motion stimulus. The stimulus consists only of a set of texture patterns that are set into motion in two different ways. First, the texture in the separate bands moves up or down, alternately. The up and down motion of the texture bands defines a set of boundaries that are easily perceived even though there is no line separating the bands. (In the actual stimulus, there is no real edge to separate the texture bands. The lines are only drawn here to clarify the stimulus). The boundaries separating the texture bands moves continuously from right to left. This motion is also easily perceived. The leftward motion of the stimulus is very ineffective at creating a response from linear space-time oriented filters (Source: Cavanagh and Mather (1989)).

These second-order motion stimuli can also be interpreted as evidence that surfaces and objects play a role in human motion perception. The motion of the bars is easy to see because we see the bars as separate objects. We perceive these objects because of their local texture pattern, not because of any luminance variation. Computational theorists have not come to a consensus on how to represent objects and surfaces. Thus, the motion of these second-order stimuli cannot be easily explained by conventional theory. We might take the existence of these second-order stimuli, then, as a reminder that we need to extend current theory to incorporate a notion of perceived motions that includes concepts that connect local variations to broader ideas concerning surfaces and object (Fleet and Langley (1994); Hildreth et al. (1995)).

systems to refer to a broad class of similar motion phenomena. This terminology seems to be gaining wider acceptance, and it has other advantages.

Because we perceive the motion of borders, including borders defined by texture and depth, we must find ways to include signals derived from the outputs of texture in theories of motion perception. Cavanagh and Mather (1989) suggest that we might reformulate the classification into first and second-order processes as a different and broader question: Can motion perception can be explained by a single basic motion detection system that receives inputs from several types of visual subsystems, or are there multiple motion sensing systems each with its own separate input. There is no current consensus on this point. Some second-order phenomena can be understood by simple amendments to current theory (Fleet and Langley (1994)), But, phenomena involving transparency, depth, and occlusion may need significant new additions to the theory (Hildreth et al. (1995)). At present, then, I view the classification into first and second-order motion systems as a reminder that many different signals lead to motion perception, and that at present our analyses have only explored a few types of these signals.

Binocular Depth

> It will now be obvious why it is impossible for the artist to give a faithful representation of any near solid object, that is, to produce a painting which shall not be distinguished in the mind from the object itself. When the painting and the object are seen with both eyes, in the case of the painting two *similar* pictures are projected on the retinae, in the case of the solid object the two pictures are *dissimilar*; there is therefore an essential difference between the impressions on the organs of sensation in the two cases, and consequently between the perceptions formed in the mind; the painting therefore cannot be confounded with the solid object (Wheatstone (1838), p. 66).

Wheatstone (1838) was the first to analyze thoroughly the implications of the simple but powerful fact that each eye images the world from a slightly different position. For near objects, the different perspective obtained by each eye provides us with an important cue to depth, namely *retinal disparity* (see Chapter). The differences between a pair of stereo images, and the differences seen when the observer translates, have much in common. In the case of stereo depth we refer to the differences as retinal disparity, and in the case of motion sequence we refer to the differences as a motion flow field. In both cases the differences between the two images arise due to translation and rotations of the viewpoint associated with the different images.

Depth Without Edges

Just as there has been some debate concerning the role of surfaces and edges in motion perception, so too there has been a debate on the role of these different levels of representation in

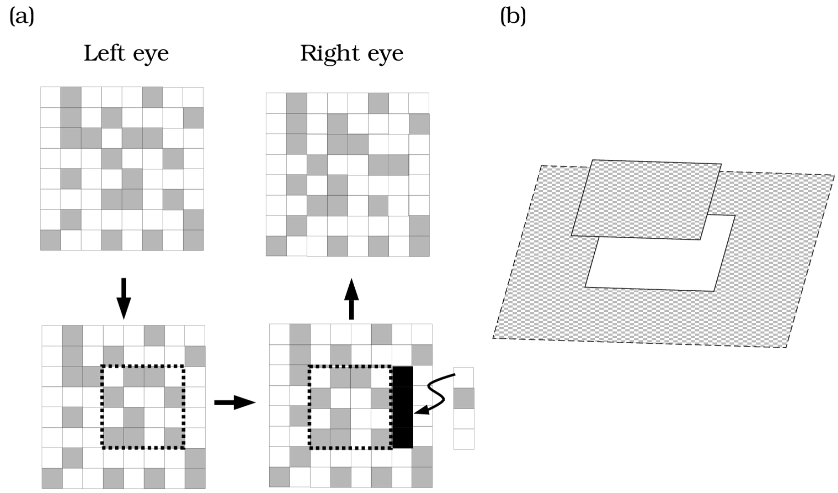

Figure 15: Construction of a random dot stereogram. (a) A random dot stereogram is created in a series of steps. First, a random dot pattern is created to present to, say, the left eye. The stimulus for the right eye is created by copying the first image, displacing a region horizontally, and then filling the gap with a random sample of dots. (b) When the right and left images are viewed simultaneously, the shifted region appears to be in a different depth plane from the other dots.

perceiving depth. Until the mid-1960s, psychologists generally supposed that the visual pathways first formed an estimate of surface and edge properties within each monocular image. It was assumed that disparity, and ultimately stereo depth, were calculated from the positions of the edge and surface locations estimated in each of the monocular images (Ogle (1964)).

Julesz (Julesz (1960), Julesz (1971)) introduced a stimulus, the *random dot stereogram*, that proves that an object can be seen in stereo depth even though we cannot perceive the object's edges are invisible in the monocular images. The random dot stereogram consists of a pair of related random dot patterns as shown in Figure 15. Each image seen separately appears to be a random collection of black and white dots. Yet, when the two images are presented separately to the two eyes, the relationship between the two collections of dots is detected by the visual pathways and the observer can perceive the surface of the object in depth.

Figure 15 shows how to create the two images comprising a random dot stereogram. First, create a sampling grid and randomly assign a black or white intensity to each position in the grid. This random image of black and white dots will be one image in the stereo pair. Next, select a region of the first image. Displace this region horizontally, over-writing the original dots. Displacing this region of dots leaves some unspecified positions; fill in these unspecified positions randomly with new black and white dots.

Random dot stereograms are a fascinating tool for vision science because the patterns we see in these stereo pairs are computed by signals that are carried separately by the two eyes.

First, they demonstrate the simple but important point that even though we cannot see any monocular edge or surface information of the object, we can still see the object based on the disparity cue. Second, they provide an interesting tool for anatomically localizing different types of perceptual computations. Recall that the earliest binocular cells are in the superficial layers of area V1 (Chapter). Hence, any part of the surface or edge computation that is performed in the monocular pathways prior to area V1 cannot play a role in the representation of edges and surfaces seen in random dot stereograms[8].

Depth With Edges

That observers perceive depth in random dot stereograms does not imply that edge detection or surface interpretation plays no role in depth perception. This is quite analogous to the experimental situation in motion perception. Observers perceive motion in random dot kinematograms, but surfaces and edge representations appear to be an important part of how we perceive motion.

We can see the relationship between surface representations and depth by considering the role of surface *occlusion*. Occlusion is one of the most powerful *monocular* cues to image depth since when one object blocks the view of another, it is a sure sign of their depth relationship. Shimojo and Nakayama (Shimojo and Nakayama (1990a), Shimojo and Nakayama (1990b); He and Nakayama (1994a), He and Nakayama (1994b)) have argued that occlusion relationships play an important role in judgments of *binocular* vision, too.

Their demonstrations of the role of occlusion in stereo depth are based on the simple physical observations shown in Figure 16 (a). Leonardo Da Vinci used this drawing in his *Trattato della Pittura* to describe the relationship between occlusion, half-occlusion, and transparency.

> if an object C be viewed by a single eye at A, all objects in the space behind it … are invisible to the eye at A; but when the other eye at B is opened, part of these objects become visible to it; those only being hid from both eyes that are included … in the double shadow CD cast by two lights at A and B. … [Because] the angular space EDG beyond D being always visible to both eyes … the object C seen with both eyes becomes, as it were, transparent, according to the usual definition of a transparent thing; namely, that which hides nothing beyond it. (Da Vinci (1970)).

Da Vinci points out that when an observer looks at an object, each eye encodes a portion of the scene that is not encoded by the other eye. These are called *half-occluded* regions of the image (Belhumeur and Mumford (1992)). When one looks beyond a small object, there is a small region that is fully occluded, and another region that both eyes can see. When examining points in this furthest region, the small object is, effectively, transparent.

There are several simple rules that describe the location and properties of the half-occluded image regions. First, half-occluded regions seen by the left eye are always at the left edge

[8]Julesz (1971) calls the inference of anatomical localization from psychological study "psychoanatomy."

of the near object, while half-occluded regions seen by the right eye are always at the right edge of the near object. The other two local possibilities (left eye sees an occlusion at the right edge, right eye sees an occluded region at the left edge) are physically impossible (see Figure 16 (b)).

Second, the relative size of the half-occluded regions varies systematically with the distance of the near and far objects. As the near object is placed closer to the observer, the half-occluded region becomes larger (see Figure 16 (c)). Hence, both the position and the size of half-occluded regions contain information that can be used to infer depth[9].

Shimojo and Nakayama (1990a) and Shimojo and Nakayama (1990b) found that surface occlusion information influences observers judgment of binocular depth. In their experiments, observers viewed a stereogram with physically unrealizable half-occlusions. They found that when the half-occlusion was, say, a pattern seen only by the right eye but near the left edge of a near object, observers suppressed the visibility of the pattern. When they presented the same pattern at the right edge of the near object, where it could arise in natural viewing, the pattern was seen easily. Anderson and Nakayama (1994) summarize a number of related observations, and they conclude that occlusion configurations, that is a property of surfaces and objects, influence the earliest stages of stereo matching.

Perceived depth, like motion and color, is a visual inference. These results show that the visual inference of depth depends on a fundamental property of surfaces and objects, namely that they can occlude one another.

Head and Eye Movements

Our eyes frequently move, smoothly tracking objects or jumping large distances as we shift our attention. To judge the motion of objects in the image, it is essential for the visual pathways to distinguish motion present in the image from motion due to eye movements.

Helmholtz (1865) distinguishes several ways the visual system might incorporate information about eye position into judgments of motion. When we move our eyes, the motor system must generate a signal that is directed from the central nervous system to the eye muscles. This outgoing signal is one potential source of information about eye movements. Helmholtz referred to this signals as denoting the *effort of will*. He reasoned that a copy of this motor signal may be sent to the brain centers responsible for motion perception, and that this willful signal may be combined with retinal signals to estimate motion. This hypothetical signal is called the *corollary discharge*.

[9] Random dot stereograms contain two half-occluded regions that are usually consistent with the image depth. When we displace the test region, we overwrite a portion of the original random dot image. The overwritten dots are half-occluded because they are only seen by the eye that views the first image. The dots that are added to complete the second image are half-occluded because they are only seen by the eye that views the second image.

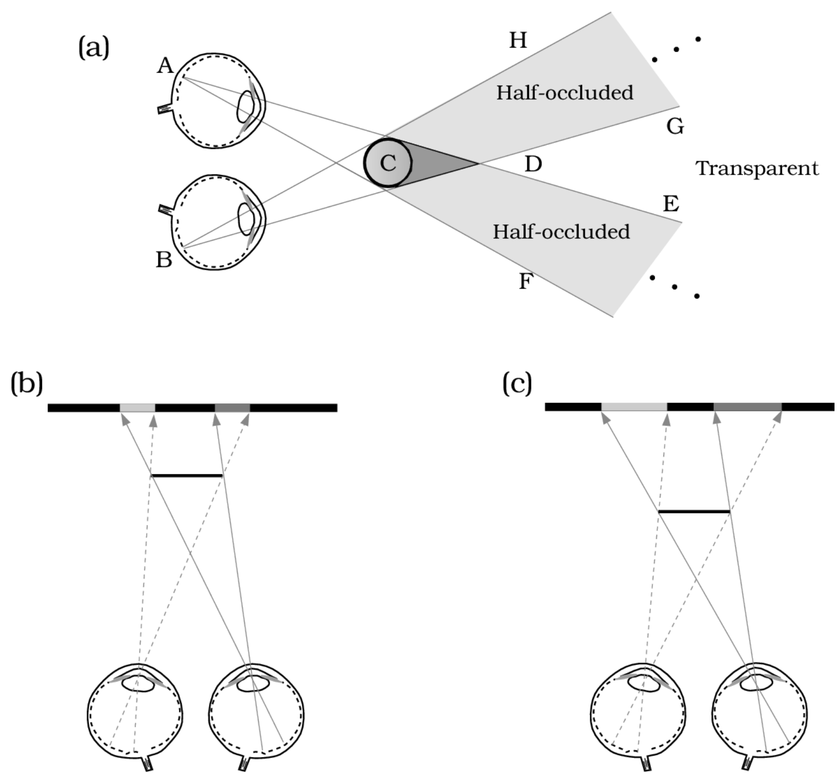

Figure 16: Half-occluded regions. In normal viewing, there will be regions of the image that are seen by both eyes, neither eye, or only one eye. (a) When viewing a small, nearby object, there is a fully occluded region just beyond the object (dark shading). There are a pair of half-occluded regions (light gray-shading). Well beyond the small object, both eyes see the image so that the object is, effectively, transparent (After: Da Vinci (1970)) (b) The half-occluded regions seen by the right eye fall near the right edge of the near object, while the half-occluded regions seen by the left eye fall near the left edge of the near object. (c) The size of the half-occluded region depends on the distance between the observer, the near object, and the far object.

A second possible source of information are nerve cells that are attached to the muscles that control eye movements. Neural sensors may measure the tension on the muscles, or the force exerted by the muscles, and the responses of these sensors may be sent to the brain centers responsible for motion perception. These are incoming sources of information, so that we can distinguish these two theories with the names *outflow theory* and *inflow theory* (Gregory (1990)).

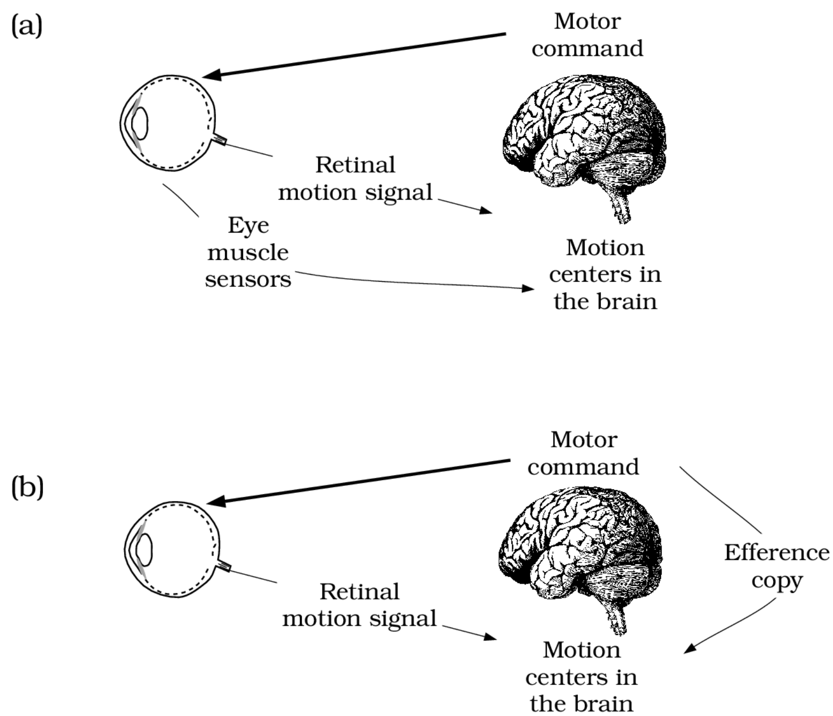

Figure 17: Inflow and Outflow theories for discounting eye movement. (a) According to inflow theory, signals from the retina and the muscles controlling eye movement are at the motion centers in the brain. By comparing these two signals, the motion centers discount eye movements and infer object motion. (b) According to outflow theory, signals from the retina and an efference copy of the motor signal are sent to motion centers in the brain. By comparing these two signals, the motion centers discount eye movements and infer object motion.

Helmholtz lists several simple experimental demonstrations in favor of outflow theory. First, when we rotate the eye by pushing on it with our finger, the world appears to move. In this case, the retinal image moves but there is no willful effort to rotate the eye. According to outflow theory we should interpret the field as rotating, and it does. Second, if we create a stabilized retinal image, say by creating an afterimage, rotating the eyeball does not make the afterimage appear to move. In this case there is no retinal image motion, and no willful effort to rotate the eye. Hence, no motion is expected. Third, Helmholtz finds support for the outflow theory in the experience of patients whose eye muscles have been paralyzed. He writes

> … in those cases where certain muscles have suddenly been paralyzed, when the patient tries to turn his eye in a direction in which it's powerless to move any longer, apparent motions are seen, producing double images if the other eye happens to be open at the time (Helmholtz, 1865, p. 245).

There is good support, then, for the basic outflow theory. This raises a second interesting question concerning how the visual system infers the changing position of the eye. The nervous system has two types of information about eye position. One type of information is based on the retinal image and computed by the motion flow field. As I reviewed earlier in this chapter and in the Appendix, it is possible to estimate the observer's motion from the motion flow field. Now, we find that it is also possible to estimate the motion of the eye from an efferent signal from the motor pathways. Which one does the visual system use?

The answer seems to be very sensible. There are times when the information about eye position from the motor system is more reliable than information from the motion flow field. Conversely, sometimes motion flow information is more reliable. Human experimental measurements suggest that under some conditions observers use motion flow information information alone to estimate heading; under other conditions extra-retinal signals, presumably from the oculomotor pathways, are combined with motion flow signals (Warren and Hannon (1988); Royden et al. (1992)).

Vision during saccadic eye movements

There is an interesting and extreme case in which the oculomotor system dominates retinal signals you can observe yourself. First, find a small mirror and a friend to help you. Ask your friend to hold the mirror close to his or her eyes. Then, have your friend switch gaze between the left and right eye repeatedly. As your friend shifts gaze, you will see both eyes move. Then, change roles. While your friend watches you, shift your gaze in the mirror from eye to eye. Your friend will see your eyes shift, but you will not be able to see your own eyes move. As your eyes saccade back and forth and watch in the mirror, you cannot see your own eyes move at all.

There have been several different measurements of sensitivity loss during saccades. To measure the loss of visual sensitivity one needs to separate out the visual effects from the simple effects having to do with the motion of the eye itself. The motion of the eye in, say, the horizontal direction changes the effective spatiotemporal signal in the direction of motion. By measuring sensitivity using horizontal contrast patterns, however, one can separate out the effect of the eye movement on the signal from the suppression by the visual pathway. The suppressive effects caused by neural, rather than optical, factors is called *saccadic suppression*.

Sensitivity loss during saccades shows two main features that relate to the motion pathway. First, during saccades contrast sensitivity to low frequency light-dark patterns is reduced

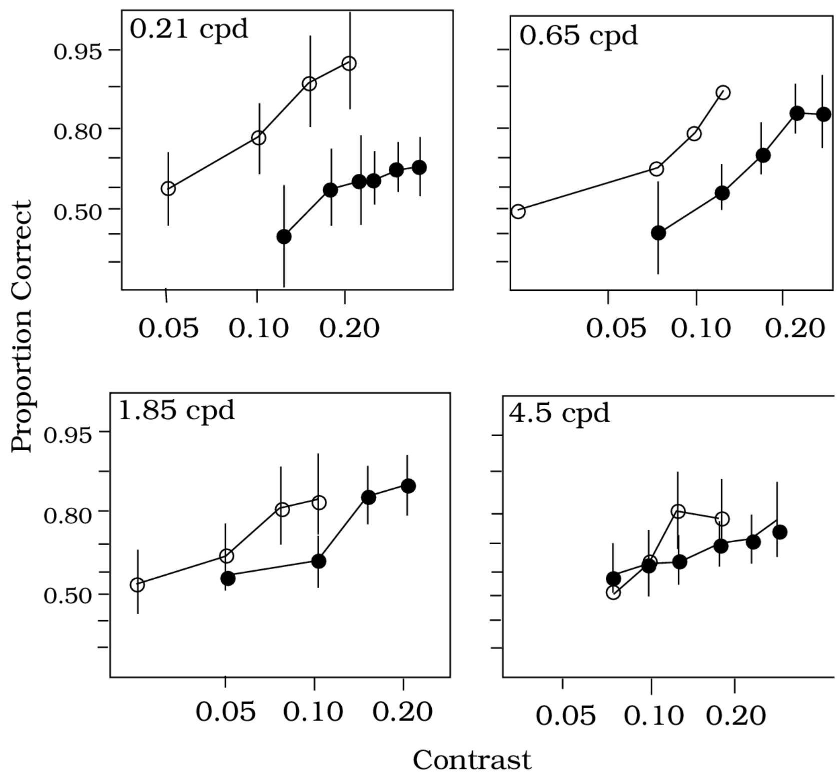

Figure 18: Contrast sensitivity is suppressed during a saccade. Each panel plots the probability of detection as a function of signal contrast while the observer is fixating (open symbols) or executing a saccade (filled symbols). The data are combined from three observers and the vertical lines through the points represent 95% confidence limits. The separate panels show measurements using patterns with different spatial frequencies. (Source: @{volkmann1978-saccadic)

strongly, while sensitivity to high spatial frequency patterns is not significantly changed (Volkmann et al. (1978); Burr et al. (1994)). Second, there is no sensitivity loss to colored edges during a saccade (Burr et al. (1994)).

The curves in Figure 18 measure probability of detecting a luminance grating as a function of the target contrast. The filled circles show measurements made during steady fixation and the open circles show measurement made during a 6 deg saccade. To see the target during the saccade, subjects need to increase the target contrast. Plainly, the suppression is strongest for the low spatial frequency targets. Suppression acts mainly on low spatial frequency targets, and there is little suppression of colored patterns. Lesion studies described in Chapter suggested that these stimuli are detected mainly by signals on the M-pathway, a component of the motion pathway. Based on the parallel loss of visual sensitivity from these lesions and during saccadic eye movements, Burr et al. (1994) suggested that saccadic suppression takes place within the motion pathway.

The oculomotor and motion systems must work together to establish a visual frame of reference. Saccadic suppression illustrates that in some cases the visual system judges the retinal information to be unreliable and suppresses the retinal signal until a more stable estimate of the reference frame can be obtained. But, as we turn our head, the world remains visible and observers can detect image displacements as small as two or three percent. Hence, although we suppress quite large displacements during saccades, we remain sensitive to displacements as we turn our heads or move about (Wallach (1987)).

The Cortical Basis of Motion Perception

More than any other visual sensation, motion seems to be associated with a discrete visual portion of the visual pathway. A visual stream that begins with the parasol cells in the retina and continues through cortical areas V1 and MT seems to have a special role in representing motion signals. This *motion pathway*[10] has been studied more extensively than any other portion of the visual pathways, and so most of this section of the chapter is devoted to a review of the responses of neurons in the visual stream from the parasol cells to area MT.

Before turning to the physiological literature, I will describe an interesting clinical report of a patient who cannot see motion.

Acquired Motion Deficits

Zihl et al. (1983) described a patient (LM) who, following a stroke, had great difficulty in perceiving certain types of motion. There have been a few reports of individuals with a

[10] While I will call this visual pathway a "motion pathway," following common usage, the certainty implied by the phrase is premature. Other portions of the visual pathways may also be important for motion, and this pathway may have functions beyond motion perception.

diminished ability to perceive motion as a consequence of stroke, and transient loss of motion perception can even be induced by magnetic stimulation of the brain. But Zihl's patient, LM, has been studied far more thoroughly than the others and so we will focus on her case (Beckers et al. (1992); Vaina et al. (1990); Zeki (1991)).

LM's color vision and acuity remain normal, and she has no difficulty in recognizing faces or objects. But, she can't see the coffee flowing into a cup. Instead, the liquid appears frozen, like a glacier. Since she cannot perceive the fluid rising, she spills while pouring. LM feels uncomfortable in a room with several moving people, or on a street, since she cannot track changes in positions, "people were suddenly here or there but I have not seen them moving." She can't cross the street for fear of being struck by a moving car. "When I'm looking at the car first, it seems far away. But then, when I want to cross the road, suddenly the car is very near."

There are very few patients with a specific motion loss and so few generalizations are possible[11]. Patient LM succeeds at certain motion tasks but fail at others. Patient LM has a difficult time segregating moving dots from stationary dots, or segregating moving dots from a background of randomly moving dots. Patient LM has no difficulty with stereo. (Zihl et al. (1983); Hess et al. (1989); Baker et al. (1991))

Patient LM has a lesion that extends over a substantial region of visual cortex, so that this case does not localize sharply the regions of visual cortex that are relevant to her defects. However, it is quite surprising that the loss of motion perception can be dissociated from other visual abilities, such as color and pattern. This observation supports the general view that motion signals are represented on a special motion pathway. To consider the nature of the neural representation of motion further, we turn to experimental studies.

The motion pathway

The starting point for our current understanding of the motion pathway is Zeki's discovery that the preponderance of neurons in cortical area MT are *direction selective*; they respond vigorously when an object or a field of random dots move in one direction, and they are silent when the motion is in a different direction. These neurons are relatively unselective for other aspects of the visual stimulus, such as color or orientation (Dubner and Zeki (1971); Zeki (1974)).

In other visual areas prior to MT, direction selective neurons represent only a fraction of the population. For example, about one-quarter of the neurons in area V1 are direction selective, and these neurons fall within a subset of the cortical layers in V1 (Hawken et al. (1988)) . The proportion of direction-selective neurons appears to be even lower in area V2. Area MT appears to be the first area in which the vast majority of neurons, distributed throughout the anatomical area, are direction selective.

[11] Zeki (1991) calls the syndrome *akinetopsia*. His review makes clear that the evidence for the existence of this syndrome is much weaker than the evidence for dyschromatopsia.

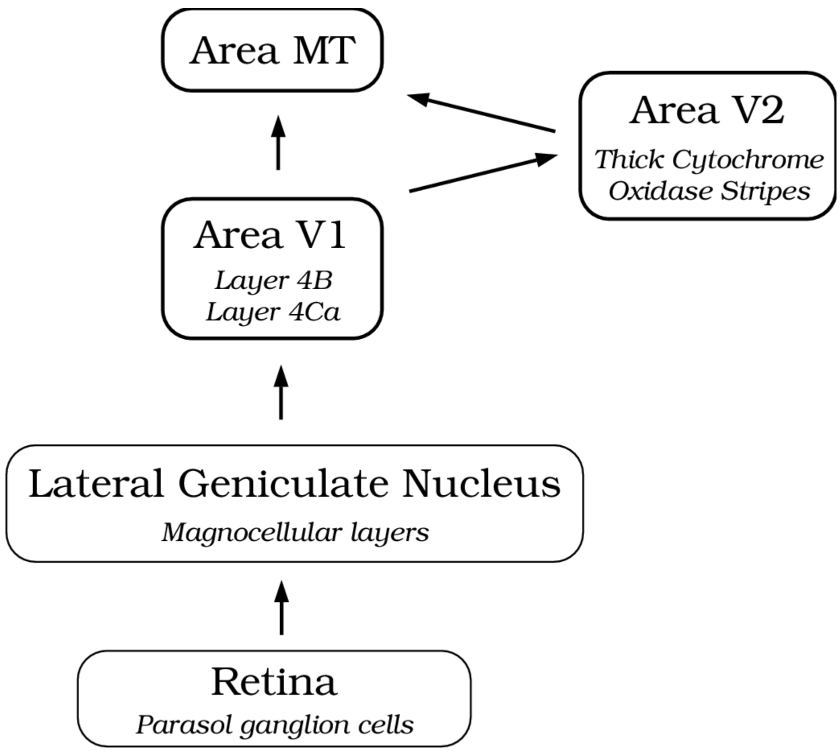

Figure 19: Anatomy of the motion pathway. The signal from parasol ganglion cells follow a pathway a discrete pathway into the brain. Their signals can be traced through the parvocellular layers of the lateral geniculate nucleus and within area V1 to area MT. Neurons in area MT respond more strongly to parasol than midget ganglion cell signals.

The neurons in area MT are principally driven by signals originating in the magnocellular pathway (see Figure 19). Recall from Chapter and Chapter that the magnocellular pathway terminates in layer 4Ca of primary visual cortex. The output from 4Ca passes to layer 4B, and the output from 4B is communicated either directly to area MT, or first through regions within area V2 and then to area MT. The majority of direction selective neurons in area V1 fall within the same layers of V1 that communicate with area MT. Hence, the direction selective neurons in area V1 appear to send their output mainly to area MT[12].

There is one further piece of evidence concerning the significance of motion and area MT. The direction-selectivity of neurons within area MT is laid out in an organized fashion. Nearby neurons tend to be selective for motion in the same direction (Albright et al. (1984)). This is analogous to the retinotopic organization evident in cortical areas V1 and V2 (see [Chapter). Taken together, the evidence argues that area MT plays an important role in motion perception (Merigan and Maunsell (1993)).

As we measure from the periphery to visual cortex, we find that the receptive field properties of the neurons within the motion pathway respond to increasingly sophisticated stimulus properties. The first major transformation is direction selectivity, which appears within neurons in layer 4B of area V1. Direction selectivity is a new feature of the receptive field, a feature which is not present in the earlier parts of the pathway.

Earlier in this chapter we saw that it is possible to estimate motion flow fields using neurons with receptive fields that are oriented in space-time (Figure 7). DeAngelis et al. (DeAngelis et al. (1993a), DeAngelis et al. (1993b); see also McLean and Palmer (1994)) measured the space-time receptive fields of neurons in cat visual cortex, and they found that some direction selective neurons have linear space-time oriented receptive fields. Some of their measurements are illustrated in Figure 20. The sequence of images in that figure shows the two-dimensional spatial receptive field of a neuron measured at different moments in time following the stimulus. Below the volume of measurements is the space-time receptive field for one-dimensional stimulation, shown in the (t, x) representation. This receptive field is also shown at the right where it is easy to see that the receptive field is oriented in the space-time plot.

Movshon et al. (1985) discovered a new feature of the receptive fields in some MT neurons that represents an additional property of motion analysis. They call the neurons that have this new receptive field property *pattern-selective* neurons to distinguish them from simple direction-selective neurons, such as we find in area V1, that they call *component-selective*. They identified these two neuronal classes in area MT using a simple mixture experiment.

First they measured the direction-selective tuning curves of neurons in area MT using one-dimensional sinusoidal grating patterns. Figure 21 shows the tuning curves of two MT neurons. In these polar plots, the neuron's response to a stimulus is plotted in the same direction from

[12]The parvocellular pathway does make some contribution to MT responses. This has been shown by blocking magnocellular pathway responses and observing responses to signals in the parvocellular pathway. But, by biological standards the separation is rather impressive (Maunsell et al. (1990)).

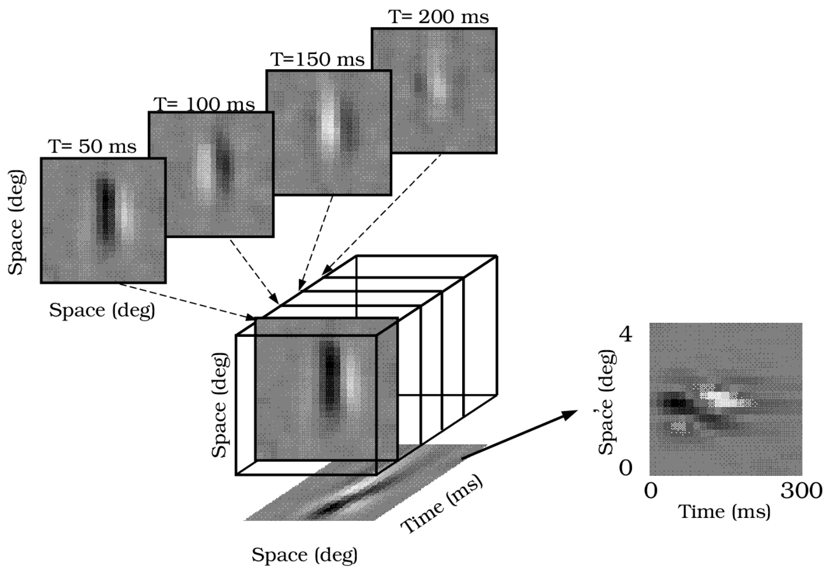

Figure 20: Space-time oriented receptive field in cat cortex. The images on the upper left show the spatial receptive field measured at different moments in time following stimulation. Taken together, these measurements form a space-time volume representation of the neural receptive field. The space-time receptive field for one-dimensional spatial stimulation is shown at the bottom of the volume and again on the right. In this (t,x) representation, the receptive field is oriented, implying that the neuron has a larger amplitude response to stimuli moving in some directions than others (After: DeAngelis et al. (1993a), DeAngelis et al. (1993b)).

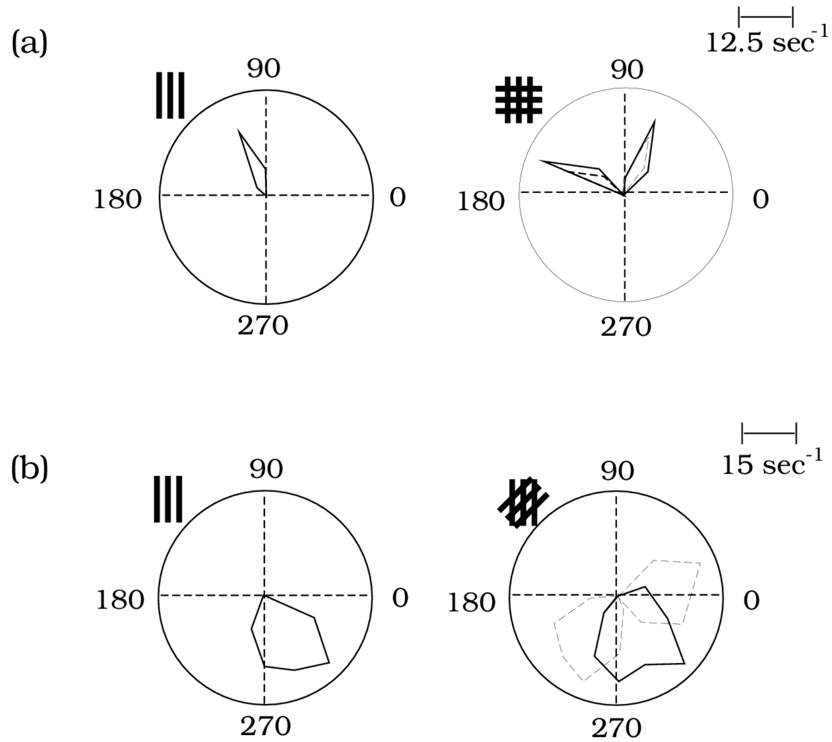

Figure 21: Direction selectivity in area MT. (a) The direction tuning of a component-selective neuron in area MT. The neuron responds to a grating moving up and to the left, but not to a plaid moving in the same direction. Instead, the neuron's responses to the plaid are predicted by its direction selectivity to the components of the pattern. The predicted responses, based on the components, are shown as dashed lines. This response pattern is typical of direction selective cells in area V1 and about half of the cells in area MT. (b) The direction tuning of a pattern-selective neuron in area MT. This neuron responded well to single gratings moving down and to the right. The cell also responded well to a plaid, whose components were separated by 135 deg, moving down and to the right. Neither component of the plaid alone evokes a response from this neuron. Hence, this neuron responds to the direction of motion of the pattern, not to the direction of motion of the components.

the origin as the stimulus motion. A point's distance from the origin indicates the size of the neuron's response. The inner circle on the plot indicates the neuron's spontaneous firing rate. The direction-selective tuning curves of these neurons are similar to the tuning curves of neurons in area V1.

Having measured the tuning curve, Movshon and his colleagues asked the basic linear systems question: can we use the tuning curve to predict the neuron's response to other patterns? To answer this question, they used new patterns formed by adding together individual grating patterns.

Consider the response of a *component-selective* MT neuron, shown on the top of Figure 21. This neuron responded well only to a narrow range of directions of a sinusoidal pattern, upward and to the left. Movshon and his colleagues measured the neuron's response to a plaid consisting of components separated in orientation by 90 degrees. This MT neuron responds well to the plaid stimulus whenever one of the plaid components moves upward and to the left. But, the neuron did not respond well when the pattern as a whole was moving upward and to the left since in that case neither of the plaid components is moving up and to the left.

Recall that when people view a moving plaid, it appears to move approximately in the direction predicted by the intersection of constraints (see Figure 11). The component-selective neuron's activity does not correlate with the perceived direction of motion. The component-selective neuron responds well only when the individual components appear to be moving upward and to the left. It does not respond well when the plaid appears to move in this direction.

The response of a pattern-selective neuron, shown on the bottom of the figure, does correlate with the perceived direction of motion. The pattern-selective neuron's response is large when a single sinusoidal grating moves down and to the right. The neuron also responded well to a 135 degree plaid pattern moving down and to the right. Remember, when the plaid is moving down and to the right, the plaid components are moving in directions that are outside of the response range of this neuron. If we isolate the components of the 135 motion plaid moving down and to the right and present them to the neuron, neither will evoke a response. Yet, when we present them together they result in a powerful response from the neuron. The nonlinear neuron response correlates with the perceived direction of motion of the stimulus.

In their survey of area MT, Movshon and his colleagues found that approximately 25% of the neurons in area MT were pattern-selective, half the neurons were classified as component-selective and the rest could not be classified. Having understood the signal transformation, we are now poised to understand the circuitry that implements the transformation. We would like to understand how pattern-selectivity is implemented, just as we now understand how direction-selectivity can be implemented.

Motion Perception and Brain Activity

Lesions of area MT

Lesion studies provide further evidence that area MT plays a role in motion perception. A lesion in area MT causes performance deficits on various motion tasks with no corresponding loss in visual acuity, color perception, or stereoscopic depth perception (Newsome and Paré (1988); Siegel and Andersen (1986); Schiller (1993)).

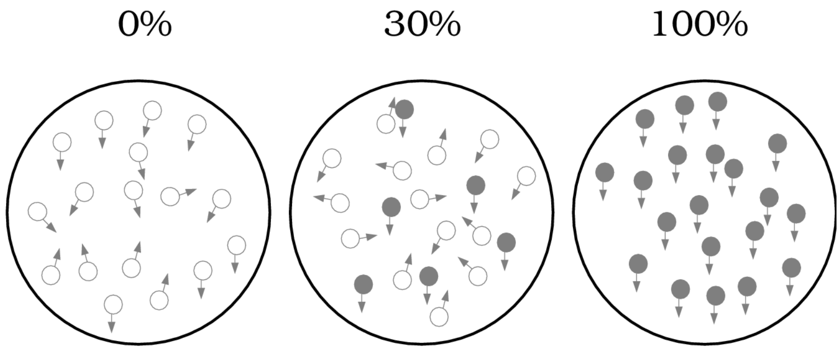

Figure 22: A random dot kinematogram used to measure motion sensitivity. Each dot is flashed briefly at random positions on the screen. When the correlation is zero, a dot is equally likely to move in any direction in the next frame. The experimenter can introduce motion into the stimulus gradually by increasing the correlation between dots presented in successive frames. Because the correlated dots (shown as filled circles) all move in the same direction, the fraction of correlated dots controls the net motion signal in the display. In the actual display, the correlated and uncorrelated dots in a frame appear the same; the filled and open dots are used in the figure only to explain the principle (Source: Newsome and Paré (1988)).

Newsome and Paré (1988) found profound deficits when the animal was forced to discriminate motion using the random dot kinematogram shown in Figure 22. In this type of kinematogram, each dot is flashed briefly at random positions on the screen. The correlation of the dot positions from frame to frame is the independent variable. When the correlation is zero, a dot is equally likely to appear anywhere on the screen in the next frame. At this correlation level, there will be some local motion signals, by chance, but the average motion will be zero. The experimenter can introduce net motion in the stimulus by correlating some of the dot position in adjacent frames. When the correlation is positive, some fraction of the dots, the *correlated dots*, reappear displaced by a fixed amount in one direction. Hence, the correlated dots introduce a net motion direction into the display.

Ordinarily, the monkey is asked to discriminate whether the net direction of dot motions is in one of two directions. When few of the dot motions are correlated, performance is near chance (50 percent correct). When many of the dot motions are correlated, performance is nearly perfect (100 percent correct). The investigators measure threshold by varying the number of correlated dots required for the monkey to judge the correct direction of motion on 75% of the trials.

There are two MT areas, one on each side of the brain. Each area receives input from the opposite visual hemifield. After lesioning area MT on one side of the brain, Newsome and Pare found that threshold for detecting motion increased by a factor of roughly 4 for stimuli in the relevant hemifield. Threshold for stimuli in the other hemifield remained at pre-operative performance levels, as does the animal's performance on non-motion tasks, such as orientation discrimination (Newsome and Wurtz (1988)).

In Newsome and Pare's experiment, the motion deficit is transient; performance returns to pre-operative levels within a week or two following the lesion. In other motion tasks, such as speed discrimination, the lesion-induced deficit can be permanent (Schiller (1993)). The transient loss of function in certain tasks affords the opportunity to study neural plasticity. Presumably, following removal of MT, however, some of the functions of the lost area are taken over by existing areas.

There is evidence of functional reorganization of many cortical functions For example, Gilbert and Wiesel (1992) have shown that after a retinal lesion that created a blindspot in the animal's visual field, the receptive fields of neurons within area V1 reorganize fairly quickly. Neurons whose receptive fields were driven by retinal signals originating in the lesioned area begin to respond to the signals from surrounding retinal areas. This plasticity seems to be a fundamental and special capability of the cortex, since the reorganization was not present in the subcortical lateral geniculate nucleus.

Probably, this ability to reorganize the visual pathways is a fundamental component of the visual system. We know, for example, that visual development depends upon receiving certain types of visual stimulation (e.g. Freeman et al. (1972); Shatz (1992); Stryker and Harris (1986)). The recovery of the animals in the Newsome and Pare study, as well as the rapid reorganization of receptive fields in Gilbert et al. described above, suggest that this reorganization may be a pervasive feature of the visual representation in adult animals as well.

Behavior and Neural Activity

The visual pathways are constantly inferring the properties of the objects we perceive. These algorithms are essential to vision, but mainly, they are hidden from our conscious awareness. We have spent most of our time trying to understand these algorithms, and how they are implemented in the visual pathway.

There is a second important and intriguing question about the cortical representation of information: this is the question of our *conscious experience*. At some point, the visual inference is complete; the motor pathways must act, and perhaps our conscious awareness must be informed about the inference. What is the nature of the representation that corresponds to the final visual inference? Which neural responses code this representation?

There is a growing collection of papers that probe the relationship between behavior and neural responses. An important part of the ability to perform such studies has been the development of techniques to measure the neural activity of alert, behaving monkeys. To obtain such measurements, the experimenter implants a small tube into the animal's skull. During experimental sessions the experimenter inserts a microelectrode through the tube to record neural activity. The electrode insertion is not painful so there is no need to anesthetize the animal. In this way, the experimenter can measure neural activity while monkeys are engaged in performing simple perceptual tasks. These experiments provide an opportunity to compare behavior and neural activity within a single, alert and behaving animal (Britten et al. (1992); Parker and Hawken (1985)).

The relationship between performance and neural activity has been studied for the detection of contrast patterns, orientation discrimination, and motion direction discrimination (e.g. Barlow et al. (1987); Britten et al. (1992); Hawkins et al. (1990); Parker and Hawken (1985); Tolhurst et al. (1983); Vogels (1990)). In the motion experiment reported by Britten et al. (1992), for example, the experimenter first isolated a neuron in area MT and determined the neuron's receptive field and best motion direction. The monkey was then shown a random dot kinematogram moving in one of two directions within the receptive field of the neuron. The animal made a forced-choice decision concerning the perceived direction of motion, and at the same time the experimenters recorded the activity of the neuron.

The response of individual neurons did not predict the animals response on any single trial. But, using a simple statistical model Britten et al. discovered that, on average, the response of a single MT neuron discriminated the motion direction as well as the whole animal can discriminate the motion direction.

Considerably more information is encoded by a single MT neuron about motion than is encoded by a single V1 neuron about pattern. For example, the sensitivity of individual V1 neurons to sinusoidal contrasting gratings is substantially lower than the animal's sensitivity. The similarity between behavioral and neural sensitivity on the motion task supports the view that area MT is specialized to represent motion perception. The finding also raises some interesting questions about how information is pooled within the nervous system to make behavioral decisions. In area MT alone there are many hundreds of neurons with equivalent sensitivity to this stimulus. If the responses of these neurons are largely independent, then pooling their outputs would improve performance substantially. Yet, the animal's performance is not much better than we would expect if the animal were simply using the output of a single neuron. Perhaps this is so because the neural responses are correlated (Zohary et al. (1994)).

Microstimulation Studies of Motion and MT

Generally, observations based on correlations are a weaker form of evidence than observations based on direct experimental manipulations. Newsome and his collaborators extended their analysis beyond correlational by manipulating the neural responses during behavioral trials (Salzman et al. (1992)).

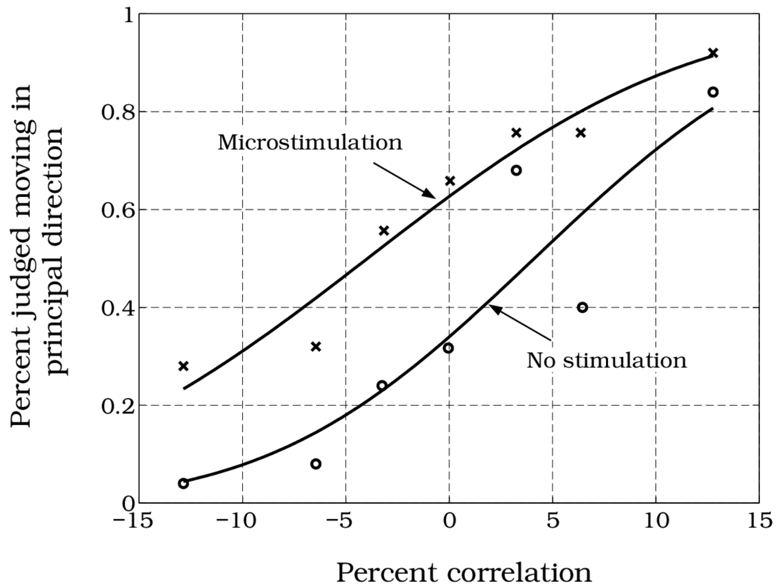

Figure 23: The effect of electrical stimulation in area MT on motion perception. An alert behaving monkey judged the direction of motion of a random dot kinematogram. Judgments made without electrical stimulation are shown by the open symbols; judgments made in the presence of small amounts of electrical stimulation within area MT are shown by the filled symbols. In this experiment, the microstimulation had the same effect as increasing fraction of correlated dots by 10 percent (Source: Salzman et al. (1992)).

As in the correlational experiments, the investigators first isolated a neuron in area MT. Within area MT, nearby neurons tend to have similar direction selectivity (Albright et al. (1984)). The experimenters used a test stimulus whose direction corresponded to the best direction of the isolated neuron; the presumption is that this direction defines the best direction of the receptive field for most of the nearby neurons.

Again, the monkey made a forced-choice decision between kinematogram motion in the best direction of the neuron or in the opposite direction. On one half of the trials, randomly selected, the investigator injected a small amount of current into the brain, stimulating the neurons near the electrode. The microstimulation changed the monkey's performance, as if the current strengthened the motion signal in the direction of the local neurons' best direction sensitivity.

The open and filled symbols in the Figure 23 show the monkey's performance on trials with and without the current injection, respectively. The monkey was more likely to say the stimulus moved in the direction preferred by the neurons in the presence of microstimulation than in its absence. In this particular experimental condition, the microstimulation was equivalent to increasing the percentage of dots moving in the test direction by ten percent.

There are two reasons why this experiment is very significant. First, the method involves a direct experimental manipulation of the animal's behavior, rather than an inference based on a correlation. The investigator actively controls the state of the neurons and observes a change in the behavior. Second, the method reminds us of the hope of someday designing visual prosthetic devices. By understanding the perceptual consequences of visual stimulation, we may be able to design visual prosthetic devices that generate predictable and controlled visual sensations.

Conclusion

Many important aspects of motion perception can be understood and predicted based on computations using only the local space-time variations of image intensities. Many of the computational elements of motion calculations, such as space-time oriented linear filters and velocity constraint lines, have a natural counterpart in the receptive fields of neurons within the motion pathway.

But the results of many behavioral experiments suggest that the surface and object representations also provide a source of useful information for the computation of motion and depth. Observers see moving surfaces sliding transparently across one another, they see motions of texture elements defined by implicit edges, they infer three-dimensional shapes and depth from the limited information in sets of random dots. It seems to me that we must understand how to incorporate surfaces in our computational theories, and we must understand how surfaces are represented in the neural pathways, to arrive at our next level of understanding of motion perception. The coupling of computational, behavioral and neural measurements has served us well this far, and I suspect that trying to incorporate surface representations using all of these methods will continue to be our best chance of understanding motion.

Taken together, it is evident that our inferences of motion and depth are not an isolated visual computations, but rather they are part of a web of visual judgments. We perceive motion in a way that depends on contrast, color, and other more abstract image features such as surface, edge and transparency. Integrating this information requires some sophisticated neural processing, and we are just at the beginning of studying this process both behaviorally and neurophysiologically. In the next chapter, we will review some of the more interesting but complex aspects of how we integrate different types of visual cues in order to make sense of the retinal image.

Seeing

Seeing overview

Seeing is a collection of inferences about the world. Motion, color and depth are important individual judgments. To see, however, we must connect these inferences into a unified explanation of the image. Until we integrate the separate inferences of pattern, color, motion and depth into a description of objects and surfaces, the world remains a disconcerting jumble of unconnected events.

It is easy to recognize the importance of integrating our visual inferences into a coherent view of the scene, but it is much harder to understand the process by which we perceive objects and surfaces. Because there is no current consensus on a theoretical approach to this topic, I have chosen to spend this chapter reviewing phenomena that I believe will be important in defining a computational theory of seeing.

In the first section of this chapter I will discuss clinical cases that illustrate the importance of being able to integrate information from different locations within an image and images acquired at different times. To those who are sighted from birth, the ability to integrate image information acquired from different viewpoints at different points in time is easy and automatic. As we walk about, we see a single object and not a collection of independent images. The computational complexity of the visual inference that integrates the different information is made quite plain, however, when we read about the difficulties of patients who were blind as infants but "cured" later in life. The tragic stories of these individuals, as they struggle to learn to see, provide us with some understanding of the complexity of object perception.

In the second section of this chapter, I will review a set of visual illusions. Visual illusions help us understand how the visual pathways organize images into objects. I have selected a series of illusions that show how the visual system uses integrates image information concerning occlusion, transparency, and boundaries to integrate judgments of brightness and shape. While I have mentioned the significance of many of these aspects of vision in earlier chapters, the illusions we will review here provide some clues about the rules for combining visual inferences into a complete description of the scene. And, there is a second reason for devoting this time to studying illusions: they are fun.

Miracle Cures

In 1963, Gregory and Wallace wrote a monograph describing a miracle cure. As an infant, the patient SB had lost effective sight in both eyes from a corneal disease. At the age of 52, he received a corneal graft that restored his optics. After living most of his life without sight, SB looked upon his wife for the first time (Gregory and Wallace (1963)).

While the case of SB is one of the best studied, there have been a few similar cases described over the last few centuries. There is considerable uniformity, and some real surprises, concerning several aspects of these "miracle cures" (Senden (1960); Valvo (1971); Sacks (1993)).

First, patients who have been blind most of their lives do not see well after their optics have been repaired. Even after months or years, they continue to struggle at tasks those blessed with sight at birth find effortless. Some visual measures, such as acuity and color vision, can be within the normal range. But patients do not perceive depth, motion, or the relationship among features effortlessly. They have difficulty recognizing a face, or judging the movement of traffic. Their visual world is a jumble from which they can occasionally glean a useful pattern or bit of information. The description of these cases suggests that many patients never acquire a good facility at grouping together features from different positions within the image, or features scene at different points in time from different perspectives. They have great difficulty integrating information from different visual perspectives, over time, into a coherent description of the scene.

The difficulty in integrating information is not a small thing. The restoration of the elements of sight without this integrative ability is a disconcerting emotional experience. Most of the patients experience severe depression, and even those patients who overcome the depression, wonder whether the returned sight was worth the effort. In summarizing the cases he studied, Valvo (1971) wrote,

> "The congenitally blind person especially, has to face the prospect of a difficult struggle before reaching a stage at which his vision permits him to understand the world around him. For a period of time varying with each patient, these people experience a confusing proliferation of perceptions, and they must learn to see as a child learns to walk. Moreover, personalities and character armors built up as a blind person have to be shed, and they often find it difficult to change their ways of living. As one of our patients put it, "I had to die as a blind person to be reborn as a seeing person." " [page 4]

Gregory and Wallace heard about SB's restoration of sight from a story in a London newspaper. They managed to get to the hospital after the first operation, in which the optics of one eye were repaired, but before the operation on the second eye (the original monograph is difficult to obtain. But, it is reprinted, along with additional material in a collection of Gregory's writings "Concepts and Mechanisms of Preception" (Gregory (1974)). They continued to visit with SB and examine his vision, when his health and mood permitted. Fairly quickly, SB managed to recognize various forms including upper case letters and the face of a clock. His ability to recognize such patterns quickly was apparently due to his ability to transfer his understanding of these shapes based on touch into a corresponding visual sensation. This happened automatically and quickly, at a rate that astonished Gregory and Wallace. It suggested to them that he had a good facility for integrating information into objects and patterns when the information corresponded to his tactile experience.

Equally surprisingly, SB could recognize the shapes in the Ishihara color plates quite easily. He learned to identify color names, and in fact some colors were already known to him because, even though when blind he could not see pattern, he could detect the difference between light and dark. Also, during opthalmological exams during his blindness the strong light gives yields a red appearance that was probability familiar to him as well.

Many of our most important perceptual abilities, however, were beyond SB's reach. We take for granted our ability to judge the shape of objects as we change our viewpoint. As we walk around a house, or a tree, or a person, each image that we see is different. Yet, we integrate the information we acquire into a single unified description of an object or a person. But, SB seemed to experience a different world as he moved around an object.

> "Quite recently he had been struck by how objects changed their shape when he walked round them. He would look at a lamp post, walk round it, stand studying it from a different aspect, and wonder why it looked different and yet the same." [(Gregory (1974), pg. 111)]

To see a moving object, we must also see the connection between the object at different moments in time. As the object moves further and further, we often see it from different perspectives and we must be able to integrate the different retinal images of the object into a single coherent description. Patients with restored sight have a difficult time learning to perceive motion and depth. Saks quotes from a patient with restored sight, Virgil, who wrote in his journal,

> "During these first weeks [after surgery] I had no appreciation of depth or distance; street lights were luminous stains stuck to the window panes and corridors of the hospital were black holes. When I crossed the road the traffic terrified me, even when I was accompanied. I am very insecure while walking; indeed I am more afraid now than before the operation."

Gregory's description of SB is striking in its similarity.

> "He [SB] found the traffic frightening, and would not attempt to cross even a comparatively small street by himself. This was in marked contrast to his former behaviour, as described to us by his wife, when he would cross any street in his own town by himself. In London, and later in his home town, he would show evident fear, even when led by a companion whom he trusted, and it was many months before he would venture alone. We heard that before the operation he

> would sometimes injure himself by walking briskly into a parked vehicle, or other unexpected obstruction, and he generally did not carry a white stick. As a blind man he was unusually active and aggressive. We began to see that this assurance had at least temporarily left him; he seemed to lack confidence and interest in his surroundings."

To perceive motion, the visual system must be able to integrate information over space and time. To perform this integration, then, requires a means of short term visual storage that can be used to represent recent information and visual inferences. If this visual storage fails, perhaps because it did not develop normally during early blindness, motion perception will be particularly vulnerable; more so, say, than color perception. One of Valvo's patients, HS, describes his difficulties with short term visual visual memories as he learned to read. He wrote in his journal,

> "My first attempts at reading were painful. I could make out single letters, but it was impossible for me to make out whole words; I managed to do so only after weeks of exhausting attempts. In fact, it was impossible for me to remember all the letters together, after having read them one by one. Nor was it possible for me, during the first weeks to count my own five fingers: I had the feeling that they were all there, but ... it was not possible for me to pass from one to the other while counting."

These clinical cases are important for the qualitative information they provide us. We learn that patients can identify colors, or even individual letters. Yet, they have difficulty integrating their visual experiences into a single whole. As they walk around an object, it appears to be a series of different shapes, not a single unitary thing. Moving objects do not have any continuity of existence. Distance, which also requires a relative judgment, is impossible to judge accurately. The experience of these patients shows us how important the processes that integrate information over space and time are to seeing. To understand seeing, we must understand the processes that link our inferences of pattern, color, motion and depth into a unified description of the world.

Illusions

Illusions are fun. They draw people into our discipline, they inspire new algorithms, they fill us with wonder. They are the children of our professional lives. And like children, illusions are a bit unruly. They do unpredictable things and defy a simple organization. You can try to insist that an illusion clean up its room, but a few minutes later you will discover another idea thrown haphazardly on the floor, or a theory turned upside down.

Of the many illusions known to vision scientists, only a fraction are suitable for the printed page. Of that portion, I have included mainly illusions to make some points about how we see objects. To understand seeing we must understand how we integrate all of the different inferences concerning pattern, color, motion and depth into a single description of the world.

Seeing the Three-Dimensional World

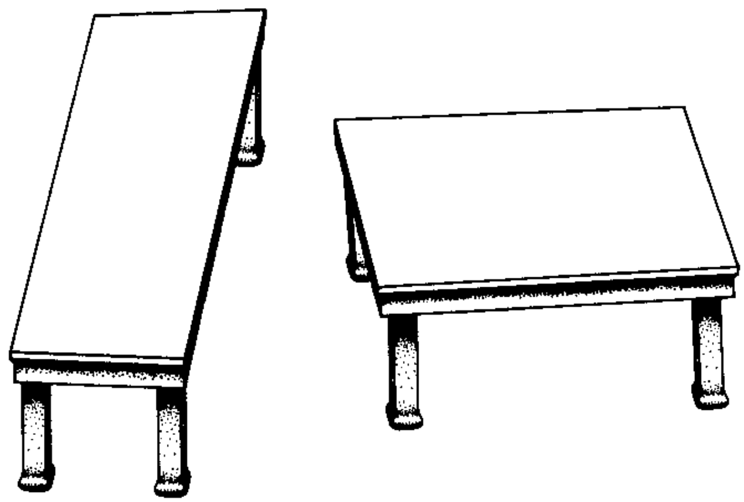

Figure 1: We assume two-dimensional shapes describe three dimensional objects. Drawn on the two-dimensional page, the table tops are the same except for a rotation. Convince yourself that the shapes are the same on the page by making a cut-out equal in size to one of the tables. Then, rotate the cut-out and place it on the other table. (Source: Shepard (1990)).

A central premise of object perception is that we see objects in a three-dimensional world. If there is an opportunity to interpret a drawing or an image as a three-dimensional object, we do. This principle is illustrated by the drawing created by Shepard (1990) shown in Figure 1. The two table tops have precisely the same two-dimensional shape on the page, except for a rigid rotation. Nobody believes this when they first look at the illusion. To convince yourself that the shapes of the table tops are are truly the same, trace one of them on an overhead transparency or tracing paper, and then rotate the tracing around. Or, make a cutout that covers one table-top and then rotate it and place it on the other. The illusion shows that we don't see the two-dimensional shape drawn on the page, but instead we see the three-dimensional shape of the object in space. This experience, which is inescapable for us, appears to be unattainable for individuals like patient SB whose case was described in the previous section.

Boring (1964) illustrated the way we automatically interpret size and depth using an image like the one shown in Figure 2. When we copy the image of the distant figure and place it next to

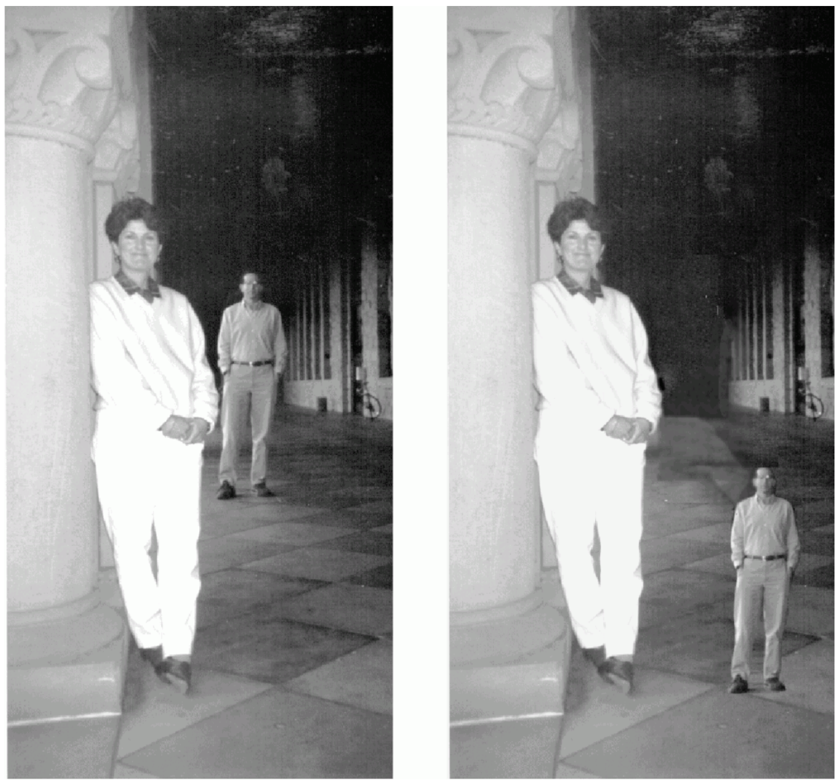

Figure 2: Judging size. Seen in its proper context, we can use the image to infer the man's height accurately and we are unaware of the size of the man's image on the page. We are made aware that the man's image is small when we translate the image to a new position with improper depth cues (After Boring (1964)).

the closer figure, we are surprised to see the size of the distant figure on the page. Boring and Shepard's illusions show that we interpret the size of the distant figure in terms of the three-dimensional cues in the image. It is hard for us to see the image on the page because, in most cases, we infer the size of things as if they were projections of three-dimensional objects.

Shadows and Edges

Not just size, but most visual inferences are based on the interpretation of image data as arising from objects in a three-dimensional world. Even judgments that seem simple, such as brightness, may depend on interpreting the scene as consisting of objects in a three-dimensional world.

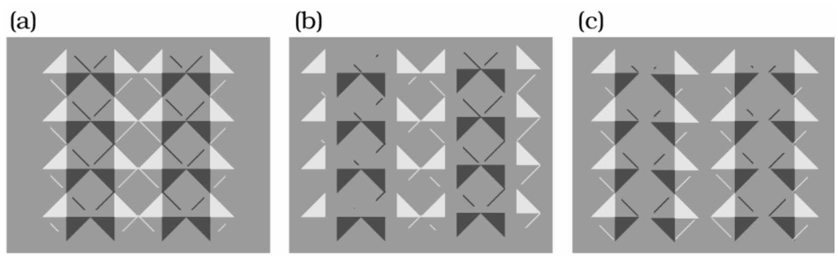

Figure 3: Brightness and shadows. (a) The intensity of the light reflected by the diamond regions in the middle and right columns is the same. Yet, the diamonds in the middle column appear darker than the diamonds in the right column. (b) When we displace the columns and destroy the interpretation of the image as containing shadows, the brightness illusion is decreased greatly. (c) When we displace the columns but maintain the perceived shadows, the brightness illusion remains strong. (After: Adelson (1993))

Figure 3 is an example of a brightness judgment that depends on our interpretation of the objects in the image (Adelson (1993)). Consider the middle and right columns of diamond shapes in Figure 3 (a). The physical intensity of the light reflected these two sets of diamonds is the same. But, the diamonds in the middle column appear darker than the diamonds in the right column.

Adelson (1993) suggests the brightness difference between the columns arises because of a transparency, that is some columns appear to be seen through light and dark strips overlayed on the image. Another interpretation of the differences between the columns is that some columns are seen under a cast shadow (Marimont, personal communication). In either event, the brightness of the local regions appears to depend on the global interpretation of the image. This is shown by the images in Figure 3 (b,c), which are variations of the image in (a). The image in (b) has no shadow edge, (b) while the image in (c) changes the image without destroying the perception of a shadow (c). The brightness difference is diminished when the shadow is destroyed, but the difference is maintained in when the shadow is present (c).

As I described in Chapter , brightness and color appearance are better predicted by reflectance than the light incident at the eye. If the visual system's objective is to associate brightness with reflectance, then the visual system should take transparency into account when judging an object's brightness. If the physical intensity of the light from a surface seen through the semi-transparent object has the same intensity as light from a surface seen directly, then the surface behind the transparency (right column) must be more reflective and hence judged brighter. The example in Figure 3 (a) shows that even image interpretations as complex as shadows or transparency can influence the brightness of a target.

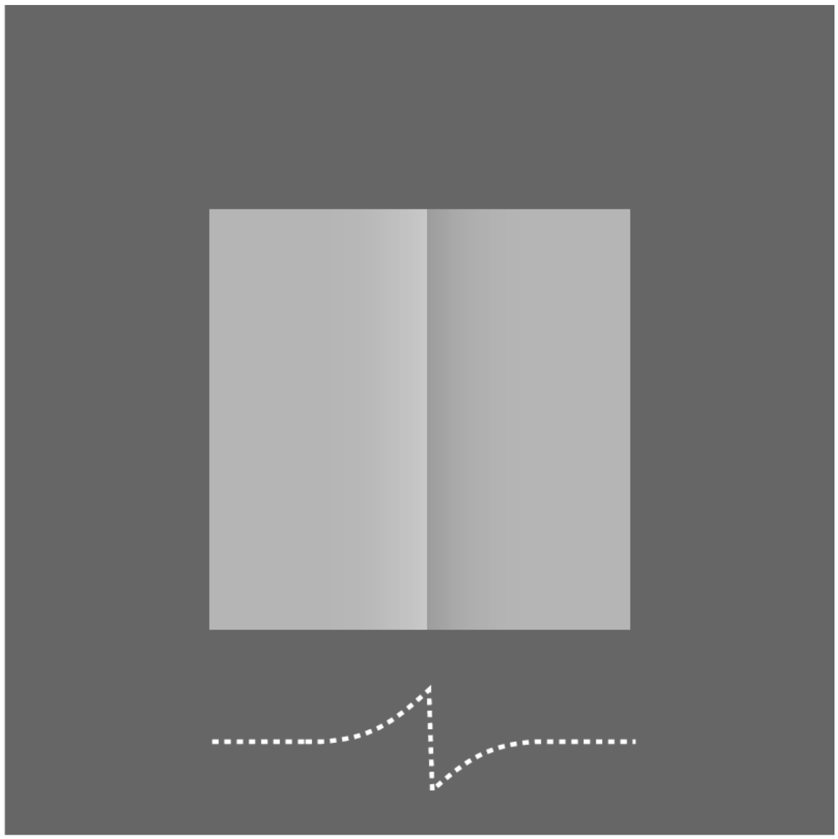

Figure 4: Edges can influence the brightness of a large region. The relative physical intensities of the inset region is shown by the trace. The intensities of the regions are equal but they are separated by a transient that defines an edge. Even though the intensities are equal, the region on the right appears darker. To confirm that the physical intensities of the areas are equal, cover the edge transient.

The illusion in Figure 4 is named for three individuals who discovered it separately: *Craik, O'Brien, and Cornsweet.* The illusion shows that surface boundaries influence brightness. The two areas on opposite sides of the border have the same physical intensity. Yet, the region on the right appears darker. The reason for this is that the intensity pattern at the border, shown at the bottom of the figure, suggests a spatial transition from a light to dark edge. This transition only occupies a small part of the image, and the intensity within the two regions away from the edge is the same. But, the visual system extends the inference from the boundary to a brightness judgment of the two large regions. It is quite surprising that the inference made using the boundary transition overrides the intensity levels within the individual regions. The inference from the boundary spreads across a large region and influences our perception of the entire object (Craik (1966); O'Brien (1958); Cornsweet (1970); Burr (1987)).

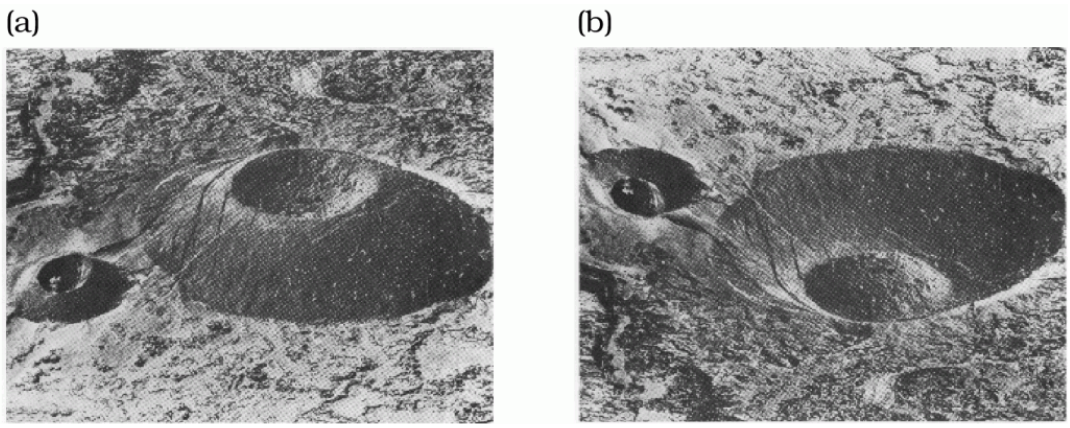

Figure 5: Shading influences shape. The image in (a) has the appearance of mound of dirt with a small indentation. The image in (b) appears to contain a crater with a mound at the top. Yet, the two images are the same except for an up-down flip. If you rotate the book 180 deg, the image containing the mound will now appear to contain a crater, and conversely the image with a crater will appear to contain a mound. The spatial relationship between the light and dark regions of the mound/crater is the main source of information defining it as convex or concave. Rotating the image rotates the shading cue and thus changes the shape we infer (After: Rittenhouse (1786)).

Figure 3 and Figure 4 show that judgments of transparency and boundaries can influence judgments of brightness. Figure 5 shows that brightness judgments can influence the perception of shape. Panel (a) shows an image containing a mound of dirt with a small dimple at the top. Panel (b) shows a second image containing a small crater with a mound at the bottom. The images in Figure 5 a & b are the same except for being flipped (not rotated) up and down using a simple image processing program.

If you rotate this book by 180 degrees, you will see that the mound in Figure 5 (a) changes into a crater, and conversely the crater in Figure 5 (b) changes into a mound. When we interpret these shapes, we assume that the illuminant is elevated. This assumption about the position of the illuminant guides our inference about the shape of objects in the image. The distinction between mound and crater in these images is mediated mainly by the shading differences. Hence, rotating the images changes the shading relationship and we reinterpret the shape. Ramachandran et al. (1988) (see also Knill and Kersten (1991)) has demonstrated this phenomenon in a number of different ways. He argues further that the brain simplifies the interpretation of images by assuming the illumination consists of a single light source.

Shapes

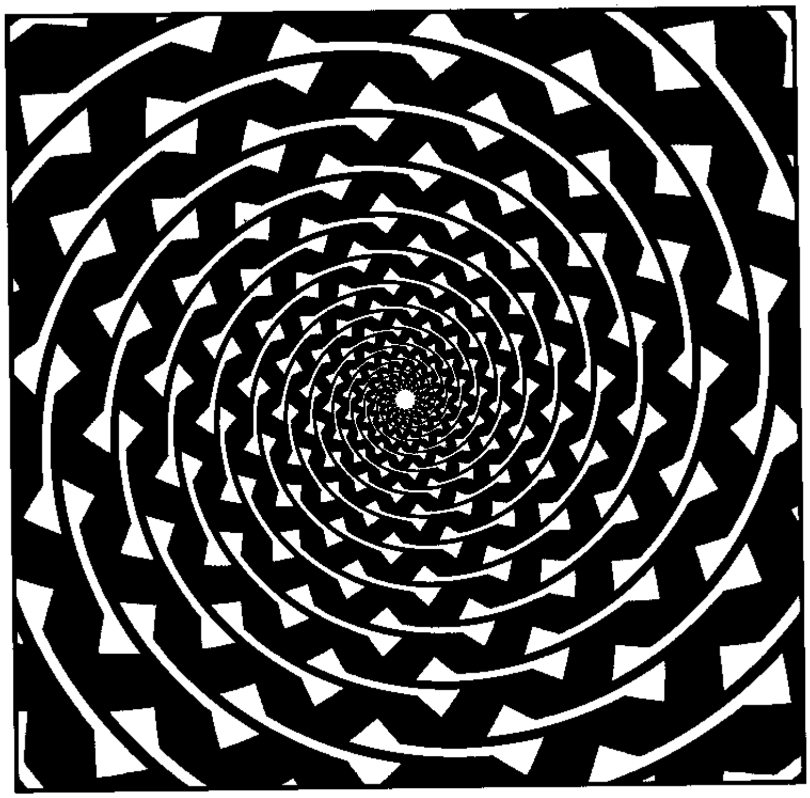

Figure 6: The Fraser spiral. The figure consists of a set of concentric circles, not a spiral at all. Yet, because of the local pattern within the circles, we perceive the overall pattern as if it were a single spiral.

The Fraser *spiral* is named after the *perceived* form in Figure 6. In fact, there is no spiral in the figure at all; the apparent spiral is really a set of concentric circles. (To persuade yourself of this, take your finger and carefully trace one of the patterns that you believe to be part of the spiral.) The light dark structure of the patterns within each circle suggest an inward spiral. But this curvature is not present in the global shape. Visual inferencing mechanisms fail to notice that the local features do not join properly into a single global spiral. This image, like the many famous drawings by Escher (1967), show that the visual mechanisms for interpreting objects in images can yield globally inconsistent solutions.

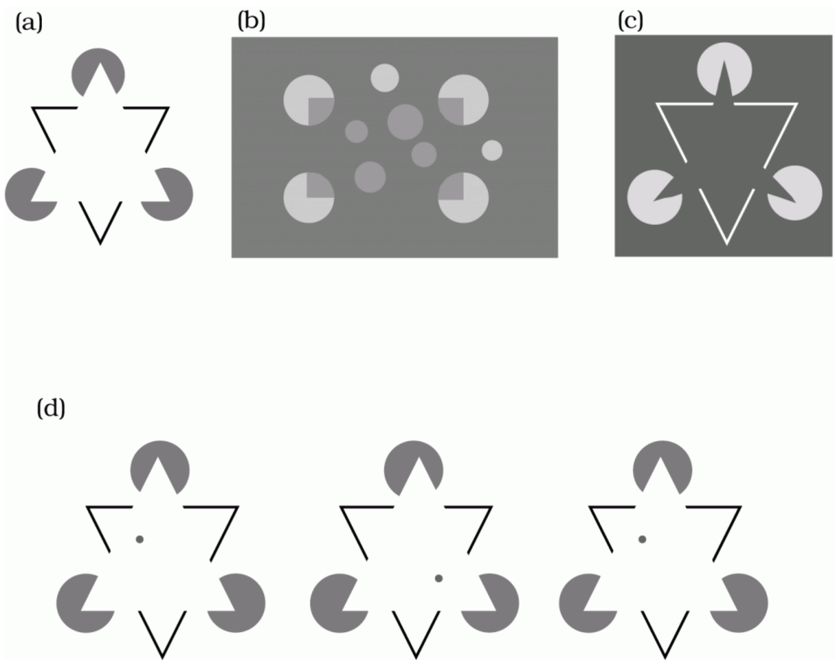

Figure 7: Subjective contours. These subjective contours are inferred from occlusion and transparency cues in the images. (a,b,c) A triangle is suggested by occlusion, a rectangle is suggested by transparency, and a curved object is suggested by occlusion. (After: Kanizsa (1979)) (d) Stereo pairs of subjective contours. By diverging your eyes beyond the page, the image pair on the right (left) will fuse and you will see the subjective contours of a triangle in front (behind) of the circles. The subjective contour is somewhat more vivid when the depth cue is added. If you converge your eyes to fuse, the depth relationships will reverse. (After: He and Nakayama (1994b)).

The objects you see in Figure 7 are visual inferences derived by integrating cues concerning occlusion and transparency. Figure 7 (a) show an image of a white triangle occluding three disks. We see the triangle even though no edges are present in the image to support the hypothesis that the triangle is present. Compare this figure with Figure 4. There, boundary information influenced the judgment of brightness. Here, occlusion information influences the judgment of a boundary and brightness. Figure 7 (a) shows that visual inferences accept the occlusion information as highly informative, even though there is missing edge and brightness information.

The transparency cues in Figure 7 (b) are enough to infer the presence of a rectangle. Figure 7 (c) shows that occlusion information can be used to infer rather complicated curved shapes, not just straight edges.

Figure 7 (d) contains stereo pairs of the subjective contour in panel (a). When the depth cue is added, the subjective contour becomes somewhat more compelling (He and Nakayama (1994b)). Fusing a stereo pair takes some practice. Try placing a piece of paper perpendicular to the page and between the two images you wish to fuse. Put your noise against the edge of the paper so that each eye sees only one of the patterns. If you then relax, and look through the page, the two images will fuse into a single depthful image. If you see both dots on the two figures, you will know that you have merged the two images, not just suppressed one of them. If you fuse the pair on the right, the triangle will appear to be in a plane floating above the page. The pair on the left shows the subjective triangle behind the page*.

> * If you fuse these stereo pairs by converging, rather than by diverging, your eyes, the depth relationships reverse.

Normally, we think of occlusion as removing information and thereby making it harder to detect an object. However, the two examples Figure 8 show the presence of an occluding object can help us explain image information and see an object that might otherwise be difficult to discern. The pattern on the left of Figure 8 (a) appears to be a set of two-dimensional drawings. When the gaps between the drawings are filled in by an occluding object, however, we can integrate the different drawings into a single three-dimensional shape of a cube. The only difference between the two drawings in panel (a) is that the white gaps separating the sections on the left have been filled in by the dark bars.

The patterns on the left of Figure 8 (b) are drawn as if they were separate parts. Precisely the same patterns are present on the right, but this time they are separated by dark bars that suggest an occluding object. Again, it is much easier to recognize the pattern as a collection of B's when the occlusion is made visually explicit. Occlusion is a very important clue for visual inferences having to do with objects.

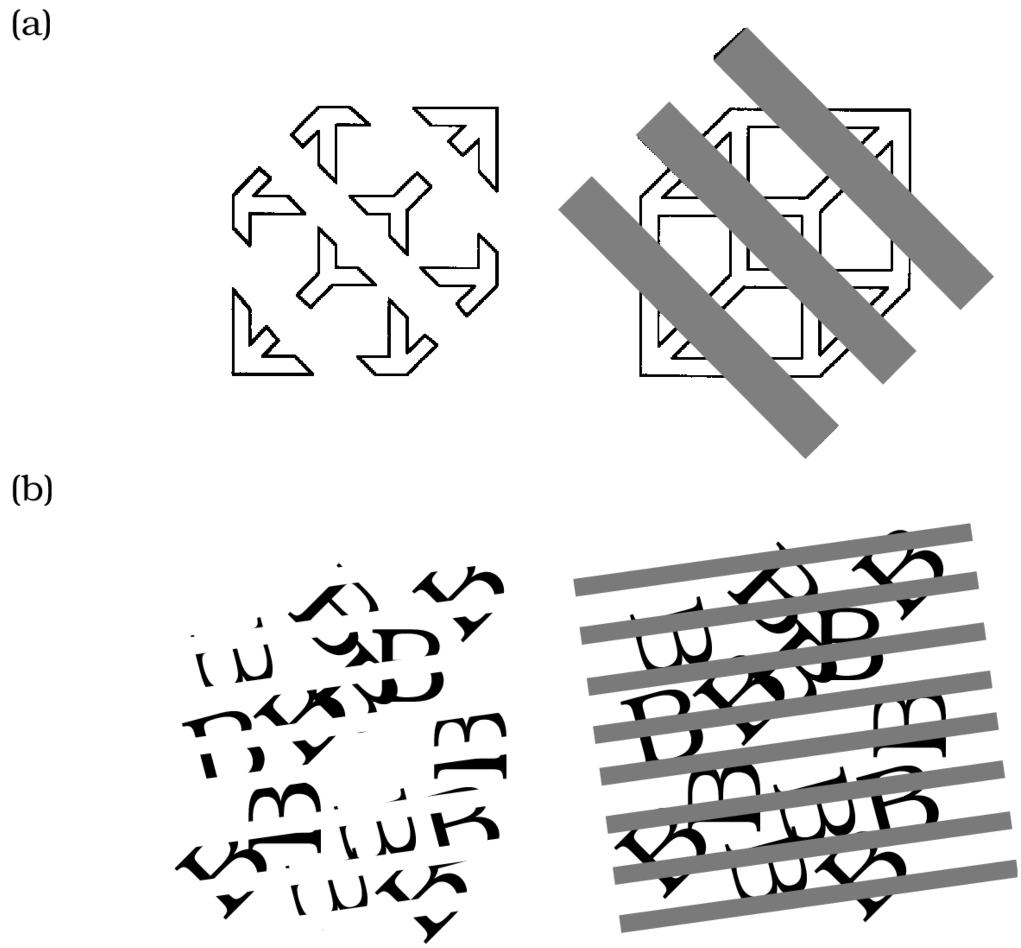

Figure 8: Occlusion and object recognition. The presence of a clearly visible occluding surface helps us to integrate otherwise fragmentary image components. (a) When the line segments are seen without an occlusion cue, they appear as a set of uncorrelated two-dimensional patterns. By overlaying occluding boundaries, the pattern is seen as part of an object, namely a three-dimensional cube (After: Kanizsa (1979)). (b) When the pattern on the left is seen on its own, it appears as a jumble of unconnected curves and lines. By placing an occluding object over the white spaces, it is much easier to see that the occluded pattern is a collection of "B's." (After: Bregman (1981)).

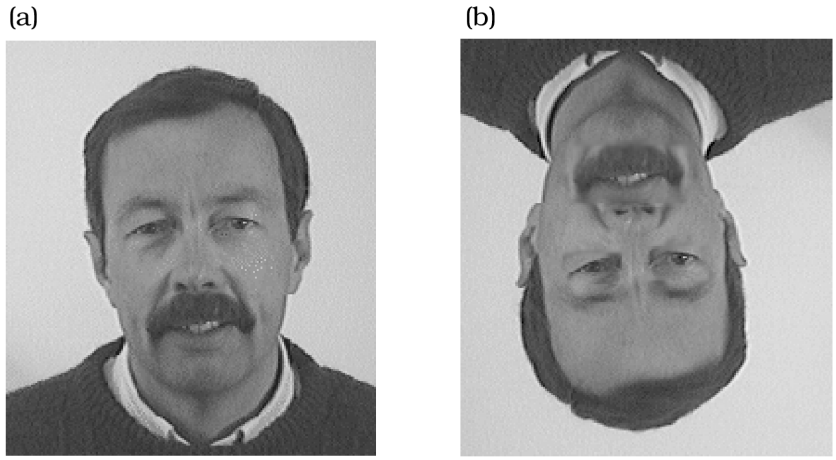

Figure 9: Face recognition illusion. (a) A face. (b) An edited version of the face in (a). Can you integrate the features when the face is inverted and predict the expression that will appear when you rotate the book? (After: Thompson (1980)).

Integrating cues

Much of object perception requires us to integrate image information for image features that are separated in space or in time. In some cases, when we integrate separate visual features into an object, we rely on certain implicit assumptions about the object. An interesting example that reveals our implicit assumptions can be revealed by the images in Figure 9. The image in (a) shows a face in its normal upright pose. The image in (b) shows the same face with several of the features, namely the eyes and mouth, edited. In this form, it is recognizable as the same face, and it seems clear that there is something amiss with the individual features. But, we cannot infer what the expression on the face will be when the inverted face is rotated into the upright position (Thompson (1980)). You will be surprised at the appearance of the face in (b) when you rotate the book and see the face in its upright pose.

This may be an illusion that has to do with faces. The clinical syndrome of *prosopagnosia*, the inability to recognize familiar faces, is further evidence that our brain has specialized circuitry for integrating the components of an image when we recognize and interpret faces. It seems more likely to me, however, that this illusion has to do with the integration of spatially segregated features. When we see a familiar object made up of many separate features in an unlikely pose, it is very difficult to judge the object's structure (Kanizsa (1979)).

Geometric Illusions

Gregory (1966) suggested that the simple and unassuming Muller-Lyer illusion, shown in Figure 10 (a), results from basic perceptual assumptions we make when we perceive depth. The two vertical lines shown in the illusion have the same length, but the line segment on the right appears longer. Gregory argues that the lines appear of different length because we cannot escape interpreting even such trivial images as three-dimensional objects. As the image in Figure 10 (b) illustrates, in the natural environment the edges that define a near corner are similar to the lines on the left of Figure 10 (a). The edges that define a far corner are similar to the lines on the right. Gregory explains the illusion as a consequence of our relentless interpretation of images as arising from a three-dimensional world. Lines that sweep out equal retinal angle, but that are at different depths, must have different physical size. Gregory suggests that even the impoverished stimulus in the Muller-Lyer illusion invokes the visual systems inferences of objects and depth. The improper application of a good principle causes the equal line segments to appear different.

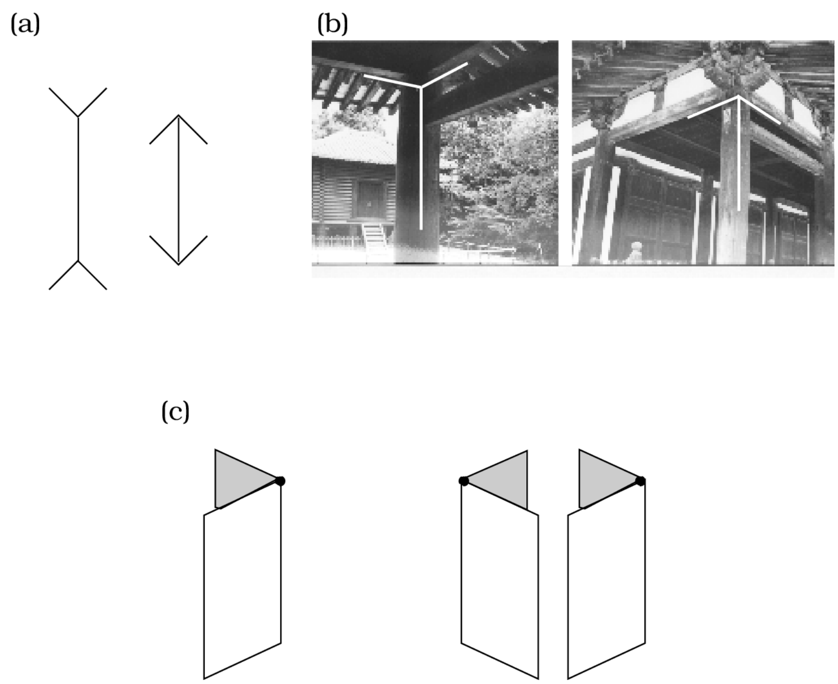

Figure 10: The Muller-Lyer illusion. (a) The classic Muller-Lyer illusion is shown. The line with the arrows pointed outward appears longer to most people, but the line lengths are the same. (b) The left and right parts of the image show two views of a corner of a building. From the outside, when the corner is relatively close to the viewer, the edges between the corner and the ceiling are oriented like closed arrows. From the inside, when the corner is relatively far from the viewer, the edges are oriented like open arrows. (c) A three-dimensional analogue of the Muller-Lyer is shown. The separations between the middle dot and the dots on either side are the same. In this rendering of the illusion, the open and closed arrow shapes are not a cue for depth. Yet, the Muller-Lyer illusion is quite powerful (Source for panel c: DeLucia and Hochberg (1991)).

Gregory's hypothesis is important because it reminds us that the basic function of visual inferences is to see objects in three-dimensions. The interpretation of visual illusions, however, is never straightforward. To test Gregory's suggestion, DeLucia and Hochberg (1991) created the version of the Muller-Lyer shown Figure 10 (c). In the two separations between the three dots are equal. Yet, just as in the Muller-Lyer the separation between the two dots attached by the closed arrow form appears smaller than the separation between the dots connected by the open arrow form. In this schematic three-dimensional image, there is little chance that the separation between the dots has to do with different depths. Gregory's hypothesis and this counter-example are a wonderful exchange that illustrates how qualitative hypotheses concerning the mechanisms of visual illusions can be tested and become part of the scientific study of vision.

Summary

Throughout this chapter, we have seen the importance of integrating separate visual inferences into a single explanation of the contents of a scene. Patients who cannot integrate visual information may identify color or a shape, but they feel that they cannot see because they cannot integrate the separate inferences into a sensible interpretation of the objects and surfaces in the scene. Many of the illusions we have reviewed show us that to see as a whole, we we must resolve conflicting information. We do not see a two-dimensional shape properly because we insist on interpreting the data as a three-dimensional shape. We do not see the physical intensity properly because we insist on interpreting a shadow or an edge.

I have chosen the illusions here to emphasize several important principles that the visual system uses to combine different visual inferences. We integrate shape and depth cues assuming that we perceive objects in a three-dimensional world; we use shadows, occlusions and edges, to interpret the properties of objects; we build up global interpretations from many local properties; yet, we also use familiar poses of objects and typical locations of illuminations help us to interpret ambiguous images.

The rules governing our sight reflect the physics of the world we see. These rules describe the interactions of objects at a physical scale within the domain of the psychologist and engineer, a human scale. This is not the physics of the sub-atomic or the physics of the galactic, but it is the physics of the world in which we live and interact. By studying the rules of this human-centered physics of perceived objects, we learn how we might see. By making neural and behavioral measurements of our brain and our perceptions, we learn how we do see.

References

(2009) Falls of foyers. Wikipedia

Abdelhamed A, Punnappurath A, Brown MS (2021) Leveraging the availability of two cameras for illuminant estimation. In: 2021 IEEE/CVF conference on computer vision and pattern recognition (CVPR). IEEE, pp 6637–6646

Addams R (1834) LI. An account of a peculiar optical phænomenon seen after having looked at a moving body. Lond Edinb Philos Mag J Sci 5:373–374

Adelson E, Bergen J (1985) Spatiotemporal energy models for the perception of motion. J Opt Soc Am A 2:284–299

Adelson EH (1993) Perceptual organization and the judgment of brightness. Science 262:2042–2044

Adelson EH, Movshon JA (1982) Phenomenal coherence of moving visual patterns. Nature 300:523–525

Ahnelt PK, Kolb H, Pflug R (1987) Identification of a subtype of cone photoreceptor, likely to be blue sensitive, in the human retina. Journal of Comparative Neurology 255:18–34

Albers J (1975) Interaction of color: Revised edition. Yale University Press

Albrecht DG, Geisler WS (1991) Motion sensitivity and the contrast-response function of simple cells in the visual cortex. Visual Neuroscience 7:531–546

Albrecht DG, Hamilton DB (1982) Striate cortex of monkey and cat: Contrast response function. J Neurophysiol 48:217–237

Albright TD, Desimone R, Gross CG (1984) Columnar organization of directionally selective cells in visual area MT of the macaque. Journal of Neurophysiology 51:16–31

Alpern M (1974) What is it that confines in a world without color? Invest Ophthalmol 13:648–674

Anderson BL, Nakayama K (1994) Toward a general theory of stereopsis: Binocular matching, occluding contours, and fusion. Psychol Rev 101:414–445

Andrews TJ, Halpern SD, Purves D (1997) Correlated size variations in human visual cortex, lateral geniculate nucleus, and optic tract. J Neurosci 17:2859–2868

Anstis SM (1980) The perception of apparent movement. Philos Trans R Soc Lond B Biol Sci 290:153–168

Ayama M, Ikeda M (1989) Dependence of the chromatic valence function on chromatic standards. Vision Res 29:1233–1244

Azzopardi P, Cowey A (1993) Preferential representation of the fovea in the primary visual cortex. Nature 361:719–721

Bak M, Girvin JP, Hambrecht FT, et al (1990) Visual sensations produced by intracortical microstimulation of the human occipital cortex. Medical & Biological Engineering & Computing 28:257–259

Baker C, Hess R, Zihl J (1991) Residual motion perception in a “motion-blind” patient, assessed with limited-lifetime random dot stimuli. J Neurosci 11:454–461

Banks MS, Geisler WS, Bennett PJ (1987) The physical limits of grating visibility. Vision Research 27:1915–1924

Barlow HB (1972) Single units and sensation: A neuron doctrine for perceptual psychology? Perception 1:371–394

Barlow HB, Blakemore C, Pettigrew JD (1967) The neural mechanisms of binocular depth discrimination. J Physiol 193:327–342

Barlow HB, Fitzhugh R, Kuffler SW (1957) Change of organization in the reveptive fields of the cat’s retina during dark adaptation. J Neurophysiology 137:338–345

Barlow H, Földiák P (1989) Adaptation and decorrelation in the cortex. In: The computing neuron. Addison-Wesley Longman Publishing Co., Inc., USA, pp 54–72

Barlow H, Kaushal TP, Hawken M, Parker A (1987) Human contrast discrimination and the threshold of cortical neurons. J Opt Soc Am A 4:2366–2371

Baylor DA (1987) Photoreceptor signals and vision. Proctor lecture. Investigative Ophthalmology and Visual Science 28:34–49

Baylor DA, Nunn BJ, Schnapf JL (1987) Spectral sensitivity of cones of the monkey macaca fascicularis. J Physiology 390:145–160. https://doi.org/10.1113/jphysiol.1987.sp016691

Beckers G, Canavan AGM, Zangemeister WH, Homberg V (1992) Transcranial magnetic stimulation of human frontal and parietal cortex impairs programming of periodic saccades. Neuroophthalmology 12:289–295

Bedford RE, Wyszecki G (1957) Axial Chromatic Aberration of the Human Eye. Journal of The Optical Society of America 47:564–565

Belhumeur PN, Mumford D (1992) A bayesian treatment of the stereo correspondence problem using half-occluded regions. Proc IEEE Comput Soc Conf Comput Vis Pattern Recognit

Berlin B, Kay P (1969) Basic color terms: Their universality and evolution

Berns RS, Gorzynski ME, Motta RJ (1993a) CRT colorimetry. Part II: metrology. Color Research & Application 18:315–325

Berns RS, Motta RJ, Gorzynski ME (1993b) CRT colorimetry. Part I: Theory and practice. Color Res Appl 18:299–314

Bishop PO (1973) Neurophysiology of binocular single vision and stereopsis. In: Jung R (ed) Handbook of sensory physiology: Central procession of visual information. Springer-Verlag, Germany, pp 255–304

Bishop PO (1984) Processing of visual information within the retinostriate system. In: Darien-Smith I (ed) Hangbook of physiology: The nervous system. pp 257–316

Blakemore C, Campbell FW (1969) On the existence of neurones in the human visual system selectively sensitive to the orientation and size of retinal images. J Physiol 203:237–260

Blakemore C, Nachmias J, Sutton P (1970) The perceived spatial frequency shift: Evidence for frequency-selective neurones in the human brain. J Physiol 210:727–750

Blakemore C, Sutton P (1969) Size adaptation: A new aftereffect. Science 166:245–247

Blasdel GG (1992) Differenital imaging of ocular dominance and orientation selectivity in monkey striate cortex. Journal of Neuroscience 12:3115–3138

Boring EG (1964) Size-constancy in a picture. Am J Psychol 77:494–498

Born R, Tootell R (1992) Segregation of global and local motion processing in primate middle temporal visual area. Nature 365:279–279

Bowne SF (1990) Contrast discrimination cannot explain spatial frequency, orientation or temporal frequency discrimination. Vision Res 30:449–461

Boycott BB, Wässle H (1974) The morphological types of ganglion cells of the domestic cat's retina. J Physiol 240:397–419

Boynton RM, Olson CX (1987) Locating basic colors in the OSA space. Color Res Appl 12:94–105

Boynton RM, Schafer W, Neun ME (1964) Hue-wavelength relation measured by color-naming method for three retinal locations. Science 146:666–668

Bracewell RN (1986) The Hartley Transform. Clarendon Press, Oxford

Braddick O (1974) A short-range process in apparent motion. Vision Res 14:519–527

Braddick OJ (1980) Low-level and high-level processes in apparent motion. Philos Trans R Soc Lond B Biol Sci 290:137–151

Brainard DH (1989) Calibration of a computer controlled color monitor. Col Res Appl 14:23–34

Brainard DH, Freeman WT (1994) Bayesian method for recovering surface and illuminant properties from photosensor responses. In: Rogowitz BE, Allebach JP (eds) Human vision, visual processing, and digital display v. SPIE

Brainard DH, Wandell BA (1986) Analysis of the retinex theory of color vision. Journal of the Optical Society of America A, Optics and Image Science 3:1651–1661

Brainard DH, Wandell BA (1991) A bilinear model of the illuminant's effect on color appearance. In: Landy MS (ed) Computational models of visual processing (pp. MIT Press, xii, pp 171–186

Brainard DH, Wandell BA (1992) Asymmetric color-matching: How color appearance depends on the illuminant. Journal of the Optical Society of America A 9:1433–1448

Bregman AS (1981) Asking the "what for" question in auditory perception. In: Kubovy M, Pomerantz JR (eds) Perceptual organization. Lawrence Erlbaum, NJ, pp 99–118

Brewer WL, Lyle Brewer W (1954) Fundamental response functions and binocular color matching. 44:207

Brindley G (1960) Physiology of the retina and the visual pathway

Brindley GS (1970) Physiology of the Retina and Visual Pathway. Williams & Wilkins

Brindley GS, Lewin WS (1968) The sensations produced by electrical stimulation of the visual cortex. 196:479–493

Britten KH, Shadlen MN, Newsome WT, Movshon JA (1992) The analysis of visual motion: A comparison of neuronal and psychophysical performance. J Neurosci 12:4745–4765

Bruner JS, Potter MC (1964) Interference in visual recognition. Science 144:424–425

Buchsbaum G (1980) A spatial processor model for object colour perception. Journal of The Franklin Institute-engineering and Applied Mathematics 310:1–26

Buchsbaum G, Gottschalk A (1984) Chromaticity coordinates of frequency-limited functions. J Opt Soc Am A 1:885–887

Burkhalter A (1989) Intrinsic connections of rat primary visual cortex: Laminar organization of axonal projections. J Comp Neurol 279:171–186

Burnham RW, Evans RM, Newhall SM (1957) Prediction of color appearance with different adaptation illuminations. Journal of the Optical Society of America 47:35–42

Burns S, Elsner A, Pokorny J, Smith V (1984) The abney effect: Chromaticity coordinates of unique and other constant hues. Vision Res 24:479–489

Burr D (1987) Implications of the craik-O'brien illusion for brightness perception. Vision Res 27:1903–1913

Burr D, Morrone M, Ross J (1994) Selective suppression of the magnocellular visual pathway during saccadic eye movements. Nature 371:511–513

Burt PJ (1988) Smart sensing within a pyramid vision machine. Proc IEEE Inst Electr Electron Eng 76:1006–1015

Burt PJ, Adelson EH (1983b) A multiresolution spline with application to image mosaics. ACM Trans Graph 2:217–236

Burt PJ, Adelson EH (1983a) The laplacian pyramid as a compact image code. Inst Electrical Electronics Engrs Trans on Communications 31:532–540

Byram GM (1944) The physical and photochemical basis of visual resolving power. Part 2: Visual acuity and the photochemistry of the retina. Journal of the Optical Society of America 34:718–738

Campbell FW, Green DG (1965) Optical and retinal factors affecting visual resolution. J Physiol 181:576–593

Campbell FW, Gubisch RW (1966) Optical quality of the human eye. J Physiol 186:558–578

Campbell FW, Robson JG (1968) Application of fourier analysis to the visibility of gratings. J Physiol 197:551–566

Carlbom I, Terzopoulos D, Harris KM (1994) Computer-assisted registration, segmentation, and 3D reconstruction from images of neuronal tissue sections. IEEE Trans Med Imaging 13:351–362

Cavanagh P, Anstis S (1991) The contribution of color to motion in normal and color-deficient observers. Vision Res 31:2109–2148

Cavanagh P, Boeglin J, Favreau OE (1985) Perception of motion in equiluminous kinematograms. Perception 14:151–162

Cavanagh P, Mather G (1989) Motion: The long and short of it. Spat Vis 4:103–129. https://doi.org/https://doi.org/10.1163/156856889x00077

Cavanagh P, Tyler CW, Favreau OE (1984) Perceived velocity of moving chromatic gratings. Journal of the Optical Society of America A, Optics and Image Science 1:893–899

Chang JJ, Julesz B (1985) Cooperative and non-cooperative processes of apparent movement of random-dot cinematograms. Spat Vis 1:39–45

Chichilnisky EJ (1995) Perceptual measurements of neural computations in color appearance

Chubb C, Sperling G (1988) Drift-balanced random stimuli: A general basis for studying non-fourier motion perception. J Opt Soc Am A 5:1986–2007

Cicerone CM, Nerger JL (1989) The relative numbers of long-wavelength-sensitive to middle-wavelength-sensitive cones in the human fovea centralis. Vision Research 29:115–128

Cohen J (1964) Dependency of the spectral reflectance curves of the Munsell color chips. Psychonomic Science 1:369–370

Coletta NJ, Williams DR (1987) Psychophysical estimate of extrafoveal cone spacing and cone spacing and the visual resolution limit. Journal of the Optical Society of America 4:1503–1523. https://doi.org/10.1364/JOSAA.4.001503

Cornsweet TN (1970) Visual perception. Academic Press, San Diego, CA

Cowan WB, Rowell ML (1986) Phosphor constancy in color video monitors. Color Res Appl

Craik KJ (1966) The nature of psychology. Cambridge University Press

Critchley M (1965) Neurology's debt to F. J. Gall (1758-1828). Br Med J 2:775–781

Curcio CA, Allen KA (1990) Topography of ganglion cells in human retina. Journal of Comparative Neurology 300:5–25

Curcio CA, Allen KA, Sloan KR, et al (1991) Distribution and Morphology of Human Cone Photoreceptors Stained with Anti-BLue Opsin. 312:610–624

D'Zmura M, Iverson G (1993a) Color constancy. I Basic theory of two-stage linear recovery of spectral descriptions for lights and surfaces. Journal of the Optical Society of America A, Optics, Image Science, and Vision 10:2148–2165

D'Zmura M, Iverson G (1993b) Color constancy II Results for two-stage linear recovery of spectral descriptions for lights and surfaces. 10:2166

D'Zmura M, Iverson G (1994) Color constancy III General linear recovery of spectral descriptions for lights and surfaces. 11:2389

D'Zmura M, Lennie P (1986) Shared pathways for rod and cone vision. Vision Res 26:1273–1280

Da Vinci L (1970) The Notebooks of Leonardo Da Vinci. Dover, New York

Dacey DM (1993) Morphology of a small-field bistratified ganglion cell type in the macaque and human retina. Visual Neurosci 10:1081–1098

Dacey DM, Lee BB (1994) The 'blue-on' opponent pathway in primate retina originates from a distinct bistratified ganglion cell type. Nature 367:731–735

Dacey DM, Petersen MR (1992) Dendritic field size and morphology of midget and parasol ganglion cells of the human retina. Proceedings of the National Academy of Sciences of the United States of America 89:9666–9670

Damasio A, Yamada T, Damasio H, et al (1980) Central achromatopsia: Behavioral, anatomic, and physiologic aspects. Neurology 30:1064–1071

Daubechies I (1990) The wavelet transform, time-frequency localization and signal analysis. IEEE Transactions on Information Theory 36:961–1005. https://doi.org/10.1109/18.57199 de Lange H (1958) Research into the dynamic nature of the human fovea-cortex systems with intermittent and modulated light. I. Attenuation characteristics with white and colored light. Journal of the Optical Society of America 48:777–784

De Valois KK (1977) Spatial frequency adaptation can enhance contrast sensitivity. Vision Res 17:1057–1065

De Valois RL (1965) Analysis and coding of color vision in the primate visual system. Cold Spring Harb Symp Quant Biol 30:567–579

De Valois RL, Abramov I, Jacobs GH (1966) Analysis of response patterns of LGN cells. J Opt Soc Am 56:966–977

De Valois RL, Albrecht DG, Thorell LG (1982) Spatial frequency selectivity of cells in the macaque visual cortex. J Opt Soc Am 67:779–784

De Valois RL, De Valois KK (1990) Spatial vision

De Valois RL, Jacobs GH (1971) Vision. Behavior of Nonhuman Primates 107–157

De Valois RL, Smith CJ, Kitai ST, Karoly AJ (1958) Response of single cells in monkey lateral geniculate nucleus to monochromatic light. Science 127:238–239

DeAngelis GC, Ohzawa I, Freeman RD (1993b) Spatiotemporal organization of simple-cell receptive fields in the cat's striate cortex. II. Linearity of temporal and spatial summation. J Neurophysiol 69:1118–1135

DeAngelis GC, Ohzawa I, Freeman RD (1993a) Spatiotemporal organization of simple-cell receptive fields in the cat's striate cortex. I. General characteristics and postnatal development. J Neurophysiol 69:1091–1117

DeAngelis G, Ohzawa I, Freeman R (1991) Depth is encoded in the visual cortex by a specialized receptive field structure. Nature 352:156–159

DeLucia PR, Hochberg J (1991) Geometrical illusions in solid objects under ordinary viewing conditions. Percept Psychophys 50:547–554

Derrico JB, Buchsbaum G (1991) A computational model of spatiochromatic image coding in early vision. J Vis Commun Image Represent 2:31–38

Derrington AM, Henning GB (1989) Some observations on the masking effects of two-dimensional stimuli. Vision Res 29:241–246

Derrington AM, Krauskopf J, Lennie P (1984) Chromatic mechanisms in lateral geniculate nucleus of macaque. J Physiol 357:241–265

Derrington AM, Lennie P (1984) Spatial and temporal contrast sensitivities of neurons in the lateral geniculate nucleus of macaque. J Physiol 357:219–240

Desimone R, Schein SJ (1987) Visual properties of neurons in area V4 of the macaque: Sensitivity to stimulus form. J Neurophysiol 57:835–868

Dixon ER (1978) Spectral distribution of Australian daylight. Journal of The Optical Society of America 68:437

Dobelle WH, Turkel J, Henderson DC, Evans JR (1979) Mapping the representation of the visual field by electrical stimulation of human cortex. American Journal of Ophthalmology 88:727–735

Drew MS, Funt B (1992) Variational approach to interreflection in color images. Journal of The Optical Society of America A-optics Image Science and Vision 9:1255–1265

Dubner R, Zeki SM (1971) Response properties and receptive fields of cells in an anatomically defined region of the superior temporal sulcus in the monkey. Brain Res 35:528–532

Emerson RC, Bergen JR, Adelson EH (1992) Directionally selective complex cells and the computation of motion energy in cat visual cortex. Vision Research 32:203–218

Engel SA, Rumelhart DE, Wandell BA, et al (1994) fMRI of human visual cortex. Nature 369:525

Enroth-Cugell C, Hertz G, Lennie P (1977) Cone signals in the cat's retina. J Neurophysiol 269:273–296

Enroth-Cugell C, Pinto LH (1970) Algebraic summation of centre and surround inputs to retinal ganglion cells of the cat. Nature 226:458–459

Enroth-Cugell C, Robson JG (1966) The contrast sensitivity of retinal ganglion cells of the cat. 187:517–552

Enroth-Cugell C, Robson JG (1984) Functional characteristics and diversity of cat retinal ganglion cells. Basic characteristics and quantitative description. Investigative Ophthalmology and Visual Science 25:250–267

Enroth-Cugell C, Robson JG, Schweitzer-Tong DE, Watson AB (1983) Spatio-temporal interactions in cat retinal ganglion cells showing linear spatial summation. 341:279–307

Escher MC (1967) The graphic work of m. C. escher. Oldbourne, London

Esteban D, Galand C (1977) Application of quadrature mirror filters to split band voice coding schemes. In: ICASSP '77. IEEE international conference on acoustics, speech, and signal processing. pp 191–195

Exner S (1875) Experimentelle Untersuchung der einfachsten psychischen Processe. Archiv für die gesamte Physiologie des Menschen und der Tiere 11:403–432

Fahle M, Poggio T (1981) Visual hyperacuity: Spatiotemporal interpolation in human vision. Proceedings of the Royal Society of London Series B: Biological Sciences 213:451–477

Farrell JE, Desmarais M (1990) Equating character-identification performance across the visual field. J Opt Soc Am (A) 7:152–159

Farrell TJ, Patterson MS, Wilson B (1992) A diffusion theory model of spatially resolved, steady-state diffuse reflectance for the noninvasive determination of tissue optical properties in vivo. Medical Physics 19:879–888

Felleman DJ, Van Essen DC (1991) Distributed hierarchical processing in the primate cerebral cortex. Cerebral Cortex 1:1–47

Ferster D (1981) A comparison of binocular depth mechanism in areas 17 and 18 of the cat visual cortex. Journal of Physiology 311:623–655

Fitzpatrick D, Itoh K, Diamond IT (1983) The laminar organization of the lateral geniculate body and the striate cortex in the squirrel monkey. J Neurosci 3:673–702

Flamant F (1955) Étude de la répartition de lumière dans l'image rétinienne d'une fente. Revue d'Optique Theorique et Instrumentale 34:433–459

Fleet DJ, Langley K (1994) Computational analysis of non-fourier motion. Vision Res 34:3057–3079

Foley JM, Legge GE (1981) Contrast detection and near-threshold discrimination in human vision. Vision research 21:1041–1053

Foster DH, Nascimento SM (1994) Relational colour constancy from invariant cone-excitation ratios. Proc Biol Sci 257:115–121

Fox PT, Raichle ME (1984) Stimulus rate dependence of regional cerebral blood flow in human striate cortex, demonstrated by positron emission tomography. J Neurophysiol 51:1109–1120

Freeman RD, Mitchell DE, Millodot M (1972) A neural effect of partial visual deprivation in humans. Science 175:1384–1386

Freeman RD, Ohzawa I (1990) On the neurophysiological organization of binocular vision. Vision Res

Geisler WS (1987) Ideal-observer analysis of visual discrimination. Frontiers of visual science

Geisler WS (1989) Sequential ideal-observer analysis of visual discriminations. Psychological Review 96:267–314

Gibson IM (1962) VISUAL MECHANISMS IN CONE-MONOCHROMAT. In: JOURNAL OF PHYSIOLOGY. p 10P

Gibson JJ (1950) The perception of the visual world. Houghton Mifflin, Boston, MA

Gilbert CD, Wiesel TN (1992) Receptive field dynamics in adult primary visual cortex. Nature 356:150–152

Gilinsky AS (1968) Orientation-specific effects of patterns of adapting light on visual acuity. Journal of the Optical Society of America 58:13–18

Goldstein E (1989) Sensation and perception. Belmont, CA, US: Wadsworth/Thomson Learning Sensation and perception 3:598

Goodman JW (1968) Introduction to fourier optics. McGraw-Hill, San Francisco

Gouras P (1968) Identification of cone mechanisms in monkey ganglion cells. J Physiol 199:533–547

Gouras P, Evers HU (1989) Neural systems detecting spectral contrast independently of effective energy contrast: Where and how does color vision begin. In: Kulikowski JJ (ed). Pergamon Press, Oxford

Graham N, Nachmias J (1971) Detection of grating patterns containing two spatial frequencies: A comparison of single-channel and multiple-channels models. Vision research 11:251–IN4

Graham N, Robson JG, Nachmias J (1978) Grating summation in fovea and periphery. Vision Research 18:815–825

Graham NV (1989) Visual pattern analyzers

Granger EM, Heurtley JC (1973) Letters to the editor: Visual chromaticity-modulation transfer function. J Opt Soc Am 63:1173–1174

Green GJ, Lessell S (1977) Acquired cerebral dyschromatopsia. Arch Ophthalmol 95:121–128

Gregory R (1966) Eye and brain: The psychology of seeing. McGraw-Hill

Gregory R (1990) Eye and brain: The psychology of seeing. Princeton University Press, Princton, NJ

Gregory R (1974) Concepts and mechanisms of perception. Charles Scribner's Sons, New York, NY

Gregory RL, Wallace JG (1963) Recovery from early blindness. Experimental psychology society monograph 2:65–129

H. SSO (1956) Optical and photoelectric analog of the eye. Journal of the optical Society of America 46:721–739

Hartline HK (1938) THE RESPONSE OF SINGLE OPTIC NERVE FIBERS OF THE VERTEBRATE EYE TO ILLUMINATION OF THE RETINA. American Journal of Physiology-Legacy Content 121:400–415

Hawken MJ, Parker AJ, Lund JS (1988) Laminar organization and contrast sensitivity of direction-selective cells in the striate cortex of the old world monkey. J Neurosci 10:3541–3548. https://doi.org/10.1523/JNEUROSCI.08-10-03541.1988

Hawkins HL, Hillyard SA, Luck SJ, et al (1990) Visual attention modulates signal detectability. J Exp Psychol Hum Percept Perform 16:802–811

He ZJ, Nakayama K (1994a) Apparent motion determined by surface layout not by disparity or three-dimensional distance. Nature 367:173–175

He ZJ, Nakayama K (1994b) Perceived surface shape not features determines correspondence strength in apparent motion. Vision Res 34:2125–2135

Hecht S, Schlaer S, Pirenne MH (1942) Energy, quanta and vision. Journal of the Optical Society of America 38:196–208

Heeger DJ (1992) Normalization of cell responses in cat striate cortex. Visual Neuroscience 9:181–197

Heeger DJ (1994) The representation of visual stimuli in primary visual cortex. Current Directions in Psychological Science 3:159–163

Heeger DJ, Jepson AD (1992) Subspace methods for recovering rigid motion I: Algorithm and implementation. Int J Comput Vis 7:95–117

Helmholtz H (1866/1911) Treatise on physiological optics. Optical Society of America, Rochester, NY

Helson H (1938) Fundamental problems in color vision. I. The principle governing changes in hue, saturation, and lightness of non-selective samples in chromatic illumination. J Exp Psychol 23:439–476

Hendry SH, Yoshioka T (1994) A neurochemically distinct third channel in the macaque dorsal lateral geniculate nucleus. Science 264:575–577

Hering E (1964) Outlines of a theory of the light sense. Harvard University Press, Cambridge, MA, US

Hess R, Baker CV, Zihl J (1989) The "motion-blind" patient: Low-level spatial and temporal filters. J Neurosci 9:1628–1640

Heywood CA, Wilson B, Cowey A (1987) A case study of cortical colour "blindness" with relatively intact achromatic discrimination. J Neurol Neurosurg Psychiatry 50:22–29

Heywood C, Gadotti A, Cowey A (1992) Cortical area V4 and its role in the perception of color. J Neurosci 12:4056–4065

Hildreth EC, Ando H, Andersen RA, Treue S (1995) Recovering three-dimensional structure from motion with surface reconstruction. Vision Res 35:117–137

Holmes G (1918) DISTURBANCES OF VISION BY CEREBRAL LESIONS. British Journal of Ophthalmology 2:353–384

Holmes G (1945) The organization of the visual cortex in man. Proc R Soc Lond Ser B 132:348–361

Horton JC, Hoyt WF (1991a) Quadrantic visual field defects. A hallmark of lesions in extrastriate (V2/V3) cortex. Brain : a journal of neurology 114 (Pt 4):1703–1718

Horton JC, Hoyt WF (1991b) The representation of the visual field in human striate cortex. A revision of the classic Holmes map. Archives of Ophthalmology 109:816–824

Hubbard R, Wald G (1951) The mechanism of rhodopsin synthesis. Proceedings of the National Academy of Sciences of the United States of America 37:69–79

Hubel DH (1982) Exploration of the primary visual cortex, 1955-1982. Nature 299:515–524

Hubel DH (1988) Eye, brain, and vision. W. H. Freeman; Company, New York

Hubel DH, Livingstone MS (1987) Segregation of form, color, and stereopsis in primate area 18. J Neurosci 7:3378–3415

Hubel DH, Wiesel TN (1965) Binocular interaction in striate cortex of kittens reared with artificial squint. Journal of Neurophysiology 26:1041–1059

Hubel DH, Wiesel TN (1959) Receptive fields of single neurons int he cat's striate cortex. Journal of Neurophysiology 148:574–591

Hubel DH, Wiesel TN (1962) Receptive fields, binocular interaction and functional architecture in the cat's visual cortex. Journal of Neurophysiology 160:106–154

Hubel DH, Wiesel TN (1968) Receptive fields and functional architecture of monkey striate cortex. 195:215–243

Hubel DH, Wiesel TN (1977) Ferrier lecture. Functional architecture of macaque monkey visual cortex. Proceedings of the Royal Society of London Series B: Biological Sciences 198:1–59

Hubel DH, Wiesel TN (1979) Brain mechanisms of vision. Scientific American 241:150–162

Hubel DH, Wiesel TN, LeVay S (1977) Plasticity of ocular dominance columns in monkey striate cortex. Phil Trans R Soc Lond Series B 278:131–163

Hubel DH, Wiesel TN, Stryker MP (1978) Anatomical demonstration of orientation columns in macaque monkey. J Comp Neurol 177:361–380

Humphrey NK (1974) Vision in a monkey without striate cortex: A case study. Soc Neurosci Abstr 6:315

Hurvich LM, Jameson D (1957) An opponent-process theory of color vision. Psychol Rev 64, Part 1:384–404

IJspeert JK, Van Den Berg T, Spekreijse H (1993) An improved mathematical description of the foveal visual point spread function with parameters for age, pupil size and pigmentation. Vision Research

Inouye T (1909) Die Sehstorungen bei Schussverletzungen der kortikalen Sehsphare

Jameson D, Hurvich L (1955) Some quantitative aspects of an opponent-colors theory. I. Chromatic responses and spectral saturation. Journal of the Optical Society of America 45:546–552

Jenkins FA, White HE (1937) Fundamentals of optics. 12–30

Jennings FA, Charman WN (1981) Off-axis image quality in the human eye. Vision Res 21:445–455

Joshua DE, Bishop PO (1970) Binocular single vision and depth discrimination. Receptive field disparities for central and peripheral vision and binocular interaction on peripheral single units in cat striate cortex. Exp Brain Res 10:389–415

Judd DB (1951) Basic correlates of the visual stimulus. In: Stevens SS (ed) Handbook of experimental psychology. Wiley, pp 811–867

Judd DB (1960) Appraisal of Land's work on two-primary color projections. Journal of The Optical Society of America 50:254–268

Judd DB (1940) Hue saturation and lightness of surface colors with chromatic illumination. J Opt Soc Am, JOSA 30:2–32

Judd DB, MacAdam DL, Wyszecki G, et al (1964) Spectral distribution of typical daylight as a function of correlated color temperature. Journal of The Optical Society of America 54:1031

Judd DB, Wyszecki G (1975) Color in business science and industry, 3rd edn. Wiley-Interscience

Julesz B (1971) Foundations of cyclopean perception. U. Chicago Press, Chicago, Illinois

Julesz B (1960) Binocular depth perception of computer-generated patterns. Bell Syst Tech J 39:1125–1162

Kalmus H (1965) Diagnosis and genetics of defective colour vision. Pergamon Press, Oxford

Kanizsa G (1979) Organization in vision. Praeger, NY

Kaplan E, Shapley RM (1982) X and y cells in the lateral geniculate nucleus of macaque monkeys. Journal of Physiology 330:125–143

Kaplan E, Shapley RM (1986) The primate retina contains two types of ganglion cells, with high and low contrast sensitivity. Proc Natl Acad Sci USA 83:2755–2757

Kelly D, Burbeck C (1984) Critical problems in spatial vision. CRC Critical Review of Biomedical Engineering 10:125–177

Kelly DH (1979a) Motion and vision. I. Stabilized images of stationary gratings. Journal of the Optical Society of America 69:1266–1274

Kelly DH (1979b) Motion and vision. II. Stabilized spatio-temporal threshold surface. Journal of the Optical Society of America 69:1340–1349

Kelly DH (1971b) Theory of flicker and transient responses. II. Counterphase gratings. Journal of the Optical Society of America 61:632–640

Kelly DH (1971a) Theory of flicker and transient responses. I. Uniform fields. J Opt Soc Am 61:537–546

Kelly DH (1966) Frequency doubling in visual responses*†. J Opt Soc Am, JOSA 56:1628–1633

Kelly DH (1961b) Visual responses to time-dependent stimuli.* II. Single-channel model of the photopic visual system. Journal of the Optical Society of America 51:747–754

Kelly DH (1961a) Visual response to time-dependent stimuli. I. Amplitude sensitivity measurements. Journal of the Optical Society of America 51:422–429

Kersten D (1987) Predictability and redundancy of natural images. J Opt Soc Am A 4:2395–2400

Klinker GJ, Shafer SA, Kanade T (1988) The measurement of highlights in color images. International Journal of Computer Vision

Knill DC, Kersten D (1991) Apparent surface curvature affects lightness perception. Nature 351:228–230

Koenderink JJ (1990) Solid shape. MIT Press, London, England

Koenderink J, van Doorn A (1975) Invariant properties of the motion parallax field due to the movement of rigid bodies relative to an observer. Optica Acta: International Journal of Optics 22:773–791

Kolb H, Nelson R, Fernandez E (2011) Webvision: The organization of the retina and visual system

Komatsu H, Wurtz RH (1989) Modulation of pursuit eye movements by stimulation of cortical areas MT and MST. J Neurophysiol 62:31–47

Korte A (1915) Kinematoskopische untersuchungen. Zeitschrift für Psychologie 72:194–296

Kouyama N, Marschak DW (1992) Bipolar cells speciffic for blue cones in the macaque retina. J Neurosci 12:1233–1252

Kuffler SW (1953) Discharge patters and functional organization of mammalian retina. J Neurophysiology 16:37–68

Kwong KK, Belliveau JW, Chesler DA, et al (1992) Dynamic magnetic resonance imaging of human brain activity during primary sensory stimulation. Proceedings of the National Academy of Sciences of the United States of America 89:5675–5679

Lachica EA, Beck PD, Casagrande VA (1992) Parallel pathways in macaque monkey striate cortex: Anatomically defined columns in layer III. Proc Natl Acad Sci USA 89:3566–3570

Land E (1977) The retinex theory of color vision. Sci Am 237:108–128

Land EH (1986a) Recent advances in Retinex theory. Vision Research 26:7–21

Land EH (1986b) An alternative technique for the computation of the designator in the retinex theory of color vision. Proceedings of the National Academy of Sciences of the United States of America 83:3078–3080

Land EH (1959) Color vision and the natural image. Part i. Proc Natl Acad Sci U S A 45:115–129

Larimer J, Krantz D, Cicerone CM (1975) Opponent process additivity—II. Yellow/blue equilibria and nonlinear models. Vision Res 15:723–731

Lawden MC, Cleland PG (1993) Achromatopsia in the aura of migraine. J Neurol Neurosurg Psychiatry 56:708–709

Lee H-C (1986) Method for computing the scene-illuminant chromaticity from specular highlights. J Opt Soc Am A 3:1694–1699

Legge GE, Foley JM (1980) Contrast masking in human vision. J Opt Soc Am 70:1458–1471

Legge GE, Foley JM (1981) Contrast making in human vision. J Opt Soc Am 70:1458–1471

Legge G, Kersten D (1987) Contrast discrimination in peripheral vision. J Opt Soc Am A 4:1594–1598

Lennie P (1980) Parallel visual pathways: A review. Vision Research 20:561–594

Lennie P, Krauskopf J, Sclar G (1990) Chromatic mechanisms in striate cortex of macaque. J Neurosci 10:649–669

Leventhal AG, Thompson KG, Liu D, et al (1993) Form ans color are not segregated in monkey striate cortex. Inv Ophthalmol Vis Sci 34:4 (Abstract No. 233)

Levi D, Klein S, Aitsebaomo AP (1985) Vernier acuity, crowding and cortical magnification. Vision Res 25:963–977

Levinthal AG, Rodieck RW, Dreher B (1981) Retinal ganglion cell classe in the old world monkey. Science 213:1139–1142

Livingstone M, Hubel D (1984a) Anatomy and physiology of a color system in the primate visual cortex. J Neurosci 4:309–356

Livingstone M, Hubel D (1984b) Specificity of intrinsic connections in primate primary visual cortex. J Neurosci 4:2830–2835

Livingstone M, Hubel D (1988) Segregation of form, color, movement, and depth: Anatomy, physiology, and perception. Science 240:740–749

Longuet-Higgins HC, Prazdny K (1980) The interpretation of a moving retinal image. Proc R Soc Lond B Biol Sci 208:385–397

Ludvigh E (1941) Extrafoveal visual acuity as measured with snellen test-letters. American Journal of Ophthalmology 24:303–310

Lynch JJ, Silveira LCL, Perry VH, Merigan WH (1992) Visual effects of damage to p ganglion cells in macaques. Vis Neurosci 8:575–583

Lyons NP, Farrell JE Linear systems analysis of CRT displays. SID Digest 220–222

Macleod DIA, Williams DR, Makous W (1992) A visual nonlinearity fed by single cones. Vision Research 32:347–363

Mallat SG (1989) A theory for multiresolution signal decomposition: the wavelet representation. IEEE Trans Pattern Anal Mach Intell 11:674–693

Maloney LT (1986) Evaluation of linear models of surface spectral reflectance with small numbers of parameters. Journal of The Optical Society of America A 3:1673–1683

Malpeli LT, Schiller PH, Colby CL (1981) Response properties of single cells in monkey striate cortex during reversible inactivation of individual lateral geniculare laminae. J Neurophysiol 46:1102–1119

Marc RE, Sperling HG (1977) Chromatic organization of primate cones. Science 196:454–456

Mariani AP (1984) Bipolar cells in the monkey retina selective for the cones likely to be blue-sensitive. Nature 308:184–186

Marimont DH, Wandell BA (1992) Linear models of surface and illuminant spectra. Journal of the Optical Society of America A, Optics and Image Science 9:1905–1913

Marimont D, Wandell B (1993) Matching color images: The effects of axial chromatic aberration. Journal of the Optical Society of America A, Optics and Image Science 12:

Marr D (2010) Vision: A computational investigation into the human representation and processing of visual information. MIT Press

Martin KAC (1992) Visual cortex parallel pathways converge. Curr Biol 2:555–557

Maunsell J, Nealey T, DePriest D (1990) Magnocellular and parvocellular contributions to responses in the middle temporal visual area (MT) of the macaque monkey. J Neurosci 10:3323–3334

McCamy CS, Marcus H, Davidson JG (1976) A color-rendition chart. J App Photog Eng 2:95–99

McCann JJ, McKee SP, Taylor TH (1976) Quantitative studies in retinex theroy. A comparison between theoretical predictions and observer responses to the “color mondrian” experiments. Vision Res 16:445–458

McLean J, Palmer LA (1994) Organization of simple cell responses in the three-dimensional (3-D) frequency domain. Vis Neurosci 11:295–306

Meadows JC (1974) Disturbed perception of colours associated with localized cerebral lesions. Brain : a journal of neurology 97:615–632

Merbs SL, Nathans J (1992) Absorption spectra of human cone pigments. Nature 356:433–435

Merigan WH, Byrne CE, Maunsell JH (1991a) Does primate motion perception depend on the magnocellular pathway? Journal of Neuroscience 11:3422–3429. https://doi.org/10.1523/JNEUROSCI.13-07-03180.1993

Merigan WH, Katz LM, Maunsell JH (1991b) The effects of parvocellular lateral geniculate leasions on the acuity and contrast sensitivity of macaque monkeys. Journal of Neuroscience

11:994–1001

Merigan WH, Maunsell JH (1993) How parallel are the primate visual pathways? Annual Review of Neuroscience, Vol 34 16:369–402

Milgram DL (1975) Computer methods for creating photomosaics. IEEE Transactions on Computers C-24:1113–1119. https://doi.org/10.1109/T-C.1975.224142

Miller WH, Bernard GD (1983) Averaging over the foveal receptor aperture curtails aliasing. Vision Research 23:1365–1369

Mitchell DE (1988) Animal models of human strabismic amblyopia: Some observations concerning the interpretation of the effects of surgically and optically induced strabismus in cats and monkeys. In: Shinkman PG (ed) Advances in neural and behavioral development. pp 209–269

Mollon J, Bowmaker J (1992) The spatial arrangement of cones in the primate fovea. Nature 360:677–679

Mollon JD, Polden PG (1977) An anomaly in the response of the eye to light of short wavelengths. Philos Trans R Soc Lond B Biol Sci 278:207–240

Mollon J, Newcombe F, Polden P, Ratcliff G (1980) On the presence of three cone mechanisms in a case of total achromatopsia. In: Verriest G (ed) Colour vision deficiencies v: Chapter 3. Hilger, Bristol

Monasterio FM de, Schein SJ, McCrane EP (1981) Staining of blue-sensitive cones of the macaque retina by a fluorescent dye. Science 213:1278–1281

Moreland JD (1980) Spectral sensitivity measured by motion photometry. Colour Deficiencies 5:299–305

Mountcastle VB (1957) Modality and opographic properties of single neurons of cat's somatic sensory cortex. Neurophysiology 20:408–434

Movshon JA, Adelson E, Gizzi MS, Newsome WT (1985) The analysis of moving visual patterns. Experimental Brain Research 117–151

Movshon JA, Lisberger SG, Krauzlis RJ (1990) Visual cortical signals supporting smooth pursuit eye movements. Cold Spring Harb Symp Quant Biol 55:707–716

Movshon JA, Thompson ID, Tolhurst DJ (1978a) Spatial summation in the receptive fields of simple cells in the cat's striate cortex. 283:53–77

Movshon JA, Thompson ID, Tolhurst DJ (1978b) Receptive field organization of complex cells in the cat's striate cortex. 283:79–99

Movshon JA, Van Sluyters R (1981) Visual neural development. Annual Review of Psychology 32:477–522

Mullen KT (1985) The contrast sensitivity of human colour vision to red-green and blue-yellow chromatic gratings. J Physiol 359:381–400

Nachmias J, Kocher EC (1970) Visual detection and discrimination of luminance increments. J Opt Soc Am 60:382–389

Nachmias J, Rogowitz BE (1983) Masking by spatially-modulated gratings. Vision Res 23:1621–1629

Nachmias J, Sansbury R, Vassilev A, Weber A (1973) Adaptation to square-wave gratings: In search of the elusive third harmonic. Vision research 13:1335–1342

Naiman AC, Makous W (1992) Spatial nonlinearities of gray-scale CRT pixels. In: Rogowitz BE (ed) Human vision, visual processing, and digital display III. SPIE

Naka K-I, Rushton WAH (1966) An attempt to analyse colour reception by electrophysiology. J Physiol 185:625–660

Nakayama K, Silverman GH (1984) Temporal and spatial characteristics of the upper displacement limit for motion in random dots. Vision Res 24:293–299

Nathans J, Merbs SL, Sung C-H, et al (1992) Molecular genetics of human visual pigments. 26:403–424

Nayar SK, Bolle RM (1993) Computing reflectance ratios from an image. Pattern Recognit 26:1529–1542

Nealey T, Maunsell JHR (1994) Magnocellular and parvocellular contributions to the responses of neurons in macaque striate cortex. J Neurosci 14:2069–2079

Neitz J, Neitz M, Jacobs GH (1993) More than three different cone pigments among people with normal color vision. Vision Research 33:117–122

Nes FV van, Bouman MA (1967) Spatial modulation transfer in the human eye. Journal of the Optical Society of America 57:401–406

Newsome WT, Paré EB (1988) A selective impairment of motion perception following lesions of the middle temporal visual area (MT). J Neurosci 8:2201–2211

Newsome W, Wurtz R (1988) Probing visual cortical function with discrete chemical lesions. Trends Neurosci 11:394–400

Newton I (1984) The optical papers of isaac newton vol. I: The optical iectures 1670-1672. Cambridge University Press, Cambridge

Nielsen KR, Wandell BA (1988) Discrete analysis of spatial-sensitivity models. J Opt Soc Am A 5:743–755

Noorlander C, Koenderink JJ (1983) Spatial and temporal discrimination ellipsoids in color space. Journal of The Optical Society of America 73:1533–1543

O'Brien V (1958) Contour perception, illusion and reality. J Opt Soc Am 48:112

O'Keefe J, Levitt JB, Kiper DC, et al (1993) Functional organization of owl monkey LGN and visual cortex. Inv Ophthalmol Vis Sci 34:4 (Abstract No. 1021

Obermayer K, Blasdel GG (1993) Geometry of orientation and ocular dominance columns in monkey striate cortex. Journal of Neuroscience 13:4114–4129

Ogawa S, Tank DW, Menon RS, et al (1992) Intrinsic signal changes accompanying sensory stimulation: Functional brain mapping with magnetic resonance imaging. Proc natl Acad Sci USA 89:5951–5955

Ogle KN (1964) Researches in binocular vision. Hafner

Packer O, Williams DR (2003) Light, the retinal image, and photoreceptors. In: Shevell SK (ed) The Science of Color, 2nd edn. Optical Society of America; Elsevier Ltd, Oxford, pp 41–102

Palmer CR, Davis TL (1981) Receptive-field structure in cat striate cortex. Journal of Neurophysiology 46:260–276

Pantle A, Sekuler R (1968) Size-detecting mechanisms in human vision. Science 162:1146–1148

Parker A, Hawken M (1985) Capabilities of monkey cortical cells in spatial-resolution tasks. J Opt Soc Am A 2:1101–1114

Parkkinen JPS, Hallikainen J, Jaaskelainen T (1989) Characteristic spectra of munsell colors. J Opt Soc Am A, JOSAA 6:318–322

Pasternak T, Merigan WH (1981) The luminance dependence of spatial vision in the cat. Vision Research 21:1333–1340

Pearson DE (1975) Transmission and display of pictorial information. Wiley, NY

Perkins ME, Landy M (1991) Nonadditivity of masking by narrow-band noises. Vision Res 31:1053–1065

Perry VH, Cowey A (1980) The projection of the fovea to the superior colliculus in rhesus monkeys. Vision Research 5:53–61

Perry VH, Cowey A (1981) The morphological correlates of x- and y-like retinal ganglion cells in the retina of monkeys. Exp Brain Res 43:226–228

Perry VH, Cowey A (1984) Retinal ganglion cells that project to the superior colliculus and pretectum in the macaque monkey. Neuroscience 12:1125–1137

Perry VH, Oehler R, Cowey A (1984) Retinal ganglion cells that project to the dorsal lateral geniculate nucleus in the macaque monkey. Neuroscience 12:1101–1123

Phillips G, Wilson HR (1984) Orientation bandwidths of spatial mechanisms measured by masking. J Opt Soc Am A 1:226–232

Poggio GF, Fischer B (1977) Binocular interaction and depth sensitivity in striate and prestriate cortex of behaving rhesus monkey. J Neurophysiol 40:1392–1405

Poggio GF, Talbot WH (1981) Mechanisms of static and dynamic steropsis in foveal cortex of the rhesus monkey. J Physiol 315:469–492

Poirson A, Wandell BA (1993) Appearance of colored patterns: Pattern-color separability. J Opt Soc Am A-optics Image Sci Vis 10:2458–2470

Pokorny JS, Smith V, Verriest G, Pinckers A (1979) Congenital and acquired color vision defects. Grune; Stratton, NY

Polyak SL (1941) The retina: The anatomy and the histology of the retina in man, ape and monkey, including the consideration of visual functions, the history of physiological optics, and the histological laboratory technique. University of Chicago Press, Chicago, IL

Polyak SL (1957) The vertebrate visual system. University of Chicago Press, Chicago, IL

Popova M (2017) Beautiful brain: The stunning drawings of neuroscience founding father santiago ramón y cajal

Posner MI, Raichle ME (1994) Images of mind. W. H. Freeman & Co, Scientific American Library, NY

Post DL, Calhoun CS (1989) An evaluation of methods for producing desired colors on CRT monitors. Color Res Appl 14:172–186

Pugh EN Jr (1976) The nature of the pi1 colour mechanism of W.S. stiles. J Physiol 257:713–747

Pugh EN Jr, Mollon JD (1979) A theory of the pi1 and pi3 color mechanisms of stiles. Vision Res 19:293–312

Ramachandran VS, Cobb SVG, Rogers-Ramachandran D (1988) Perception of 3-D structure from motion: The role of velocity gradients and segmentation boundaries. Percept Psychophys 44:390–393

Reichenbach A, Bringmann A (2022) Retina: Neuroanatomy and physiology. 955–1027. https://doi.org/https://doi.org/10.1007/978-3-030-88832-9_22

Reid RC, Shapley RM (1992) Spatial structure of cone inputs to receptive fields in primate lateral geniculate nucleus. Nature 356:716–718

Richards W (1971) Anomolous stereoscopic depth perception. J Opt Soc Am 61:410–414

Rittenhouse D (1786) Explanation of an optical deception. Trans Am Philos Soc

Robson J (1966) Spatial and temporal contrast-sensitivity functions of the visual system. Journal of the Optical Society of America 56:1141–1142

Rockland KS, Pandya DN (1979) Laminar origins and terminations of cortical connections of the occipital lobe in the rhesus monkey. Brain Research 179:3–20

Rodieck RW (1965) Quantitative analysis of cat retinal ganglion cell responses to visual stimuli. Vision Research 5:583–601

Rodieck RW, Binmoeller KF, Dineen JD (1985) Parasol and midget ganglion cells of the human retina. J Comp Neurol 233:115–132

Rodieck RW, Brening RK, Watanabe M (1993) The origin of parallel visual pathways. MIT Press, Cambridge, MA

Rovamo J, Virsu V (1979) An estimation and application of the human cortical magnification factor. Expl Brain Res 37:495–510

Rovamo J, Virsu V, Nasaren R (1978) Cortical magnification factor predicts the photopic contrast sensitivity of peripheral vision. Nature 271:54–56

Royden CS, Banks M, Crowell J (1992) The perception of heading during eye movements. Nature 360:583–585

Rushton WAH (1965) The sensitivity of rods under illumination. Journal of Physiology 178:141–160

Sacks O (1993) To see and not see. The New Yorker 59–72

Salzman CD, Murasugi CM, Britten KH, Newsome WT (1992) Microstimulation in visual area MT: Effects on direction discrimination performance. J Neurosci 12:2331–2355

Sastri VDP, Das SR (1966) Spectral distribution and color of north sky at Delhi. Journal of The Optical Society of America 56:829

Schein SJ (1988) Anatomy of macaque fovea and spatial densities of neurons in foveal representation. Journal of Comparative Neurology 269:479–505

Schiller PH (1993) The effects of V4 and middle temporal (MT) area lesions on visual performance in the rhesus monkey. Vis Neurosci 10:717–746

Schiller PH, Lee K (1994) The effects of lateral geniculate nucleus, area V4, and middle temporal (MT) lesions on visually guided eye movements. Vis Neurosci 11:229–241

Schiller PH, Logothetis NK (1990) The color-opponent and broad-based channels of the primate visual system. Trends Neurosci 10:392–398

Schiller PH, Malpeli JG (1978) Functional specificity of lateral geniculate nucleus laminae of the rhesus monkey. Journal of Neurophysiology 41:788–797

Schwartz E (1977) Voltage noise observed in rods of the turtle retina. J Physiol 272:217–246

Sekiguchi N, Williams DR, Brainard DH (1993a) Aberration-free measurements of the visibility of isoluminant gratings. J Opt Soc Am A Opt Image Sci Vis 10:2105–2117

Sekiguchi N, Williams DR, Brainard DH (1993b) Efficiency in detection of isoluminant and isochromatic interference changes. J Opt Soc Am (A) 10:2118–2133

Sekuler R, Blake R (1985) Perception. A.A. Knopf

Senden M von (1960) Space and sight: The perception of space and shape in the congenitally blind before and after operation. Free Press of Glencoe

Shadlen M, Carney T (1986) Mechanisms of human motion perception revealed by a new cyclopean illusion. Science 232:95–97

Shafer SA (1985) Using color to separate reflection components. Color Res Appl 10:210–218

Shapley RM (1990) Visual sensitivity and parallel retinocortical channels. Annu Rev Psy 41:635–658

Shatz C (1992) The developing brain. Sci Am 267:60–67

Shatz CJ, Stryker MP (1978) Ocular dominance in layer IV of the cat's visual cortex and the effects of monocular deprivation. J Physiol 281:267–283

Shepard RN (1990) Mind sights: Original visual illusions, ambiguities, and other anomalies, with a commentary on the play of mind in perception and art. W H Freeman & Co

Sherman SM, Koch C (1990) Thalamus. In: Shepherd GM (ed) The synaptic organization of the brain. Oxford University Press, New York

Shimojo S, Nakayama K (1990a) Real world occlusion constraints and binocular rivalry. Vision Res 30:69–80

Shimojo S, Nakayama K (1990b) Amodal representation of occluded surfaces: Role of invisible stimuli in apparent motion correspondence. Perception 19:285–299

Siegel RM, Andersen RA (1986) Motion perceptual deficits following ibotenic acid lesions of the middle temporal area (MT) in the behaving rhesus monkey. Soc Neurosci Abstr 12:1183

Simoncelli EP (1993) Distributed analysis and representation of visual motion. Unpublished doctoral dissertation, Dpt. Elect. Eng. and Comp. Sci., MIT

Simoncelli EP (1988) Orthogonal sub-band image transforms. M.S. thesis, Dpt. Elect. Eng. and Comp. Sci., Massachusetts Institute of Technology,

Simoncelli EP, Adelson EH (1990) Non-separable extensions of quadrature mirror filters to multiple dimensions. Proceedings of the IEEE 78:652–664. https://doi.org/10.1109/5.54805

Skottun BC, De Valois RL, Grosof DH, et al (1991) Classifying simple and complex cells on the basis of response modulation. Vision Res 31:1079–1086

Smith AT, Edgar GK (1991) Perceived speed and direction of complex gratings and plaids. J Opt Soc Am A 8:1161–1171

Smith VC, Pokorny J (1972) Spectral sensitivity of color-blind observers and the cone photopigments. Vision Research 12:2059–2071

Spillmann L,).WJ (2012) Visual perception: The neurophysiological foundations

Sprague JM, Levy J, DiBerardino A, Berlucchi G (1977) Visual cortical areas mediating form discrimination in the cat. J Comp Neurl 172:441–488

Sterling P, Calkins DJ, Klug KJ, et al (1994) Parallel pathways from primate fovea. In: INVESTIGATIVE OPHTHALMOLOGY & VISUAL SCIENCE. pp 2001–2001

Sternheim CE, Stromeyer CF, K. KMC (1979) Visibility of chromatic flicker upon spectrally mixed adapting fields. Vision Research 19:175–183

Stevens JK, Gerstein GL (1976) Spatiotemporal organization of cat lateral genicular receptive fields. J Neurophysiol 39:213–238

Stevens SS (1962) The surprising simplicity of sensory metrics. American Psychologist 17:29–39

Stiles WS (1959) Color vision: The approach through increment-threshold sensitivity. Proc Natl Acad Sci U S A 45:100–114

Stiles WS (1978) Mechanisms of colour vision. Academic Press, London, England

Stiles WS (1939) The directional sensitivity of the retina and the spectral sensitivity of the rods and cones. Proceedings of the Royal Society of London Series B 127:64–105

Stiles WS, Burch JM (1959) NPL colour-matching investigation: Final report (1958). Optica Acta 6:1–26

Stockman A, MacLeod DI, Johnson NE (1993) Spectral sensitivities of the human cones. Journal of the Optical Society of America A, Optics, Image Science, and Vision 10:2491–2521

Stone L, Thompson P (1992) Human speed perception is contrast dependent. Vision Res 32:1535–1549

Stoner G, Albright T, Ramachandran V (1990) Transparency and coherence in human motion perception. Nature 344:153–155

Strang G (1993) Introduction to linear algebra. Wellesley-Cambridge Press

Strang G (1974) Solving least squares problems. Prentice-Hall, New York

Stromeyer CF 3rd, Cole GR, Kronauer RE (1985) Second-site adaptation in the red-green chromatic pathways. Vision Res 25:219–237

Stryker M, Harris W (1986) Binocular impluse blockade prevents the formation of ocular dominance columns in cat visual cortex. J Neurosci 6:2117–2133

Svaetichin G (1956) Spectral response curves from single cones. Acta Physiol Scand Suppl 39:17–46

Svaetichin G, Macnichol EF (1958) Retinal mechanisms for chromatic and achromatic vision. Ann N Y Acad Sci 74:385–404

Tanimoto S, Pavlidis T (1975) A hierarchical data structure for picture processing. Comput Graph Image Process 4:104–119

Teller DY (1990) The domain of visual science. In: Spillmann L (ed) Visual perception: The neurophysiological foundations. Academic Press, pp 11–21

Teuber HL, Battersby WS, Bender MB (1960) Functioning versus plotted fields. In: Visual field defects after penetrating missile wounds of the brain. Harvard University Press, Cambridge, MA; London, England, pp 83–112

Thibos LN, Ye M, Zhang X, Bradley A (1992) The chromatic eye: A new reduced-eye model of ocular chromatic aberration in humans. Applied Optics 31:3594–3600

Thomas I, Simoncelli E, Bajcsy R (1994) Spherical retinal flow for a fixating observer. PENNSYLVANIA UNIV PHILADELPHIA DEPT OF COMPUTER AND INFORMATION SCIENCE

Thompson P (1980) Margaret thatcher: A new illusion. Perception 9:483–484

Tolhurst DJ, Dean AF (1987) Spatial summation by simple cells in the striate cortex of the cat. Exp Brain Res 66:607–620

Tolhurst DJ, Movshon JA, Dean AF (1983) The statistical reliability of signals in single neurons in cat and monkey visual cortex. Vision Res 23:775–785

Tomasi C, Kanade T (1992) Shape and motion from image streams under orthography: A factorization method. Int J Comput Vis 9:137–154

Tominaga S, Wandell B (1989) Standard surface-reflectance model and illuminant estimation. Journal of The Optical Society of America A-optics Image Science and Vision 6:576–584

Tominaga S, Wandell B (1990) Component estimation of surface spectral reflectance. Journal of The Optical Society of America A-optics Image Science and Vision 7:312–317

Toyama K, Tokashiki S, Matsunami K (1969) Synaptic action of commissural impulses upon association efferent cells in cat visual cortex. Brain Research 14:518–520. https://doi.org/10.1016/0006-8993(69)90128-0

Treue S, Andersen RA, Ando H, Hildreth EC (1995) Structure-from-motion: Perceptual evidence for surface interpolation. Vision Res 35:139–148

Treue S, Husain M, Andersen R (1991) Human perception of structure from motion. Vision Res 31:59–75

Vaina LM, Lemay M, Bienfang DC, et al (1990) Intact "biological motion" and "structure from motion" perception in a patient with impaired motion mechanisms: A case study. Vis Neurosci 5:353–369

Valvo A (1971) Sight restoration after long-term blindness : The problems and behavior patterns of visual rehabilitation. American Foundation for the Blind

Van Essen DC, Anderson CH, Felleman DJ (1992) Information processing in the primate visual system: An integrated systems perspective. Science 255:419–423

van Santen JP, Sperling G (1985) Elaborated reichardt detectors. J Opt Soc Am A 2:300–321

Vetterli M (1986) Filter banks allowing perfect reconstruction. Signal Processing 10:219–244

Vetterli M, Metin UZ K (1992) Multiresolution coding techniques for digital television: A review. Multidimens Syst Signal Process 3:161–187

Victor JD, Maiese K, Shapley R, et al (1987) Acquired central dyschromatopsia: Analysis of a case with preservation of color discrimination. Clinical Vision Sciences 4:183–196

Virsu V, Rovamo J (1979) Visual resolution, contrast sensitivity, and the cortical magnification factor. Exp Brain Res 37:475–494

Vogels R (1990) Population coding of stimulus orientation by striate cortical cells. Biol Cybern 64:25–31

Volkmann FC, Riggs LA, White KD, Moore RK (1978) Contrast sensitivity during saccadic eye movements. Vision Res 18:1193–1199

von Baumgarten R, Jung R (1952) Microelectrode studies on the visual cortex. Rev Neurol 87:151–155

von der Heydt R, Adorjani C, Hanny P, Baumgartner G (1978) Disparity sensitivity and receptive field incongruity of units in the cat striate cortex. Exp Brain Res 31:523–545

von Kries J (1905) Influence of adaptation on the effects produced by luminous stimuli. handbuch der Physiologie des Menschen 3:109–282

Vrhel MJ, Trussell HJ (1994) Filter considerations in color correction. IEEE Transactions on Image Processing 3:147–161. https://doi.org/10.1109/83.277897

Wald G (1968) The molecular basis of visual excitation. Nature 219:800–807. https://doi.org/https://doi.org/10.1038/219800a0

Wald G, Brown PK (1958) Human rhodopsin. Science 127:222–226

Wald G, Griffin DR (1947) The Change in Refractive Power of the Human Eye in Dim and Bright Light. Journal of The Optical Society of America 37:321–336

Wallach H (1987) Perceiving a stable environment when one moves. Annu Rev Psychol 38:1–27

Walls GL (1960) “Land! Land! Psychological Bulletin 57:29–48

Wandell BA (1987) The synthesis and analysis of color images. IEEE Transactions on Pattern Analysis and Machine Intelligence 9:2–13

Wandell BA, Pugh E (1980a) A field-additive pathway detects brief-duration, long-wavelength incremental flashes. Vision Res 20:613–624

Wandell BA, Pugh E (1980b) Detection of long-duration, long-wavelength incremental flashes by a chromatically coded pathway. Vision Res 20:625–636

Warren WH Jr, Hannon DJ (1990) Eye movements and optical flow. J Opt Soc Am A 7:160–169

Warren WH Jr, Hannon DJ (1988) Direction of self-motion is perceived from optical flow. Nature 336:162–163

Wassef EGT (1958) Investigation into the theory of prediction of the appearance of colours and its bearing on the theory of colour vision. Opt Acta (Lond) 5:101–108

Wassef EGT (1952) Application of the binocular matching method to the study of the subjective appearance of surface colours. Optica Acta 2:144–150

Wassef EGT (1959) Linearity of the relationship between the tristimulus values of corresponding colours seen under different conditions of chromatic adaptation. Opt Acta (Lond) 6:378–386

Wässle H, Boycott BB (1991) Functional architecture of the mammalian retina. Physiological Reviews 71:447–480. https://doi.org/10.1152/physrev.1991.71.2.447

Wässle H, Grünert U, Röhrenbeck J, Boycott BB (1990) Retinal ganglion cell density and cortical magnification factor in the primate. Vision Research 30:1897–1911

Watanabe M, Rodieck R (1989) Parasol and midget ganglion cells of the primate retina. J Comp Neurol 289:434–454

Watson AB (1983) Detection and recognition of simple spatial forms. In: Physical and biological processing of images. Springer Berlin Heidelberg, Berlin, Heidelberg, pp 100–114

Watson AB (1990) Perceptual-components architecture for digital video. J Opt Soc Am A 7:1943–1954

Watson AB, Ahumada AJ Jr (1985) Model of human visual-motion sensing. J Opt Soc Am A 2:322–341

Watson AB, Ahumada AJ Jr (1989) A hexagonal orthogonal-oriented pyramid as a model of image representation in visual cortex. IEEE Trans Biomed Eng 36:97–106

Watson AB, Ahumada AJ Jr, Farrell JE (1983) The window of visibility: A psychological theory of fidelity in time-sampled visual motion displays. NASA

Watt RJ, Morgan MJ (1985) A theory of the primitive spatial code in human vision. Vision Res 25:1661–1674

Weale RA (1953) Spectral sensitivity and wave-length discrimination of the peripheral retina. J Physiol 119:170–190

Weale RA (1959) Photo-sensitive reactions in foveae of normal and cone-monochromatic observers. Opt Acta (Lond) 6:158–174

Wertheimer M (1912) Experimentelle studien über das sehen von bewegung. Zeitschrift fur Psychologie 61:161–165

Westheimer G (1986) The eye as an optical instrument. In: Thomas J (ed) Handbook of perception and human performance. Wiley, New York, pp 4.1–4.20

Westheimer G (1960) Modulation thresholds for sinusoidal light distributions on the retina. J Physiol 152:67–74

Westheimer G (1979) The spatial sense of the eye. Proctor lecture. Invest Ophthalmol Vis Sci 18:893–912

Westheimer G (1990) The grain of visual space. Cold Spring Harb Symp Quant Biol 55:759–763

Westheimer G, McKee SP (1977) Spatial configurations for visual hyperacuity. Vision Research 17:941–947

Westheimer G, Tanzman IJ (1956) Qualitative depth localization with diplopic images. Journal of The Optical Society of America 46:116–117

Wheatstone C (1838) XVIII. Contributions to the physiology of vision. —part the first. On some remarkable, and hitherto unobserved, phenomena of binocular vision. Philos Trans R Soc Lond 128:371–394

Wiesel TN, Hubel DH (1966) Spatial and chromatic interactions in the lateral geniculate body of the rhesus monkey. J Neurophysiol 29:1115–1156

Williams DR (1985b) Visibility of interference fringes near the resolution limit. J Opt Soc Am A 2:1087–1093

Williams DR (1985a) Aliasing in human foveal vision. Vision Res 25:195–205

Williams DR (1986) Seeing through the photoreceptor mosaic. Trends in Neurosciences 9:193–198

Williams DR, Brainard DH, McMahon MJ, Navarro R (1994) Double-pass and interferometric measures of the optical quality of the eye. Journal of the Optical Society of America A, Optics, Image Science, and Vision 11:3123–3135

Williams DR, Collier RJ (1983) Consequences of spatial sampling by a human photoreceptor mosaic. Science 221:385–387

Williams DR, MacLeod DIA, Hayhoe MM (1981) Foveal tritanopia. Vision Research 19:1341–1356

Wilson H, McFARLANE D, Phillips G (1983) Spatial frequency tuning of orientation selective units estimated by oblique masking. Vision Res 23:873–882

Wilson HR, Gelb DJ (1984) Modified line-element theory for spatial-frequency and width discrimination. Journal of the Optical Society of America A 1:124–131

Wilson HR, Regan D (1984) Spatial-frequency adaptation and grating discrimination: Predictions of a line-element model. Journal of the Optical Society of America A 1:1091–1096

Wolff LB (1994) Relative brightness of specular and diffuse reflection. Opt Eng 33:285

Wülfing EA (1892) Ueber den kleinsten Gesichtswinkel

Wyszecki G, Stiles WS (1982) Color Science: Concepts and Methods, Quantitative Data and Formulae, 2nd edn. John Wiley & Sons, New York

Yamashita M, Wässle H (1991) Responses of rod bipolar cells isolated from the rat retina to the glutamate agonist 2-amino-4-phosphonobutyric acid (APB). J Neurosci 11:2372–2382

Yap Y, Levi D, Klein S (1989) Peripheral positional acuity: Retinal and cortical constraints on 2-dot separation discrimination under photopic and scotopic conditions. Vision Res 29:789–802

Yellott JI (1982) Spectral analysis of spatial sampling by photoreceptors: Topological disorder prevents aliasing. Vision Research 22:1205–1210

Yellott JI, Wandell BA, Cornsweet TN (1984) The beginnings of visual perception: The retinal image and its initial encoding. In: Darien-Smith I (ed) Handbook of Physiology: The Nervous System. Easton, New York, pp 257–316

Young T (1804) I. The Bakerian Lecture. Experiments and calculations relative to physical optics. 94:1–16

Zeki S (1974) Functional organisation of a visual area in the posterior bank of the superior temporal sulcus of the rhesus monkey. J Physiol 236:549–573

Zeki S (1978) Uniformity and diversity of structure and function in rhesus monkey prestriate visual cortex. J Physiol 277:273–290

Zeki S (1990) Parallelism and functional specialization in human visual cortex. Cold Spring Harbor Symposia on Quantitative Biology 55:651–661

Zeki S (1991) Cerebral akinetopsia (visual motion blindness). A review. Brain : a journal of neurology 114 (Pt 2):811–824

Zeki S (1980) The representawtion of colours in the cerebral cortex of the monkey. Nature 284:412–418

Zeki S (1983) The distribution of wavelength and orientation selective cells in different areas of monkey visual cortex. Proc R Soc Lond Ser B 217:449–470

Zeki S (1993) A vision of the brain: The visible world and the cortex. Blackwell Science, Philadelphia, PA

Zihl J, Cramon D von, Mai N (1983) Selective disturbance of movement vision after bilateral brain damage. Brain 106:313–340

Zohary E, Celebrini S, Britten KH, Newsome WT (1994) Neuronal plasticity that underlies improvement in perceptual performance. Science 263:1289–1292

Appendix

Appendix

Appendix

The appendix consists of five sections. In Section I review several properties of shift-invariant linear systems and outline proofs of these properties. This appendix also includes a brief discussion of the Discrete Fourier Series, a method for representing functions as the weighted sum of harmonic functions. Section contains a review of the main aspects of visual display calibration for psychophysical experiments. Section contains a description of the basic results in classification theory, Bayes Rule and linear discriminant functions. Section provides a geometric interpretation of vector and matrix multiplication as well as a brief introduction to signal estimation. Section outlines how to compute a motion flow field that arises when an observer moves through a fixed environment.

Shift-Invariant Linear Systems

Many of the ideas in this book rely on properties of shift-invariant linear systems. In the text, I introduced these properties without any indication of how to prove that they are true. I have two goals for this section. First, I will sketch proofs of several important properties of shift-invariant linear systems. Second, I will describe *convolution* and the *Discrete Fourier Series*, two tools that help us take advantage of these properties.[1]

Definitions

Shift-invariance is a system property that can be verified by experimental measurement. For example, in Chapter I described how to check whether the optics of the eye is shift-invariant by the following measurements. Image a line through the optics onto the retina, and measure the linespread function. Then, shift the line to a new position, forming a new retinal image. Compare the new image with the original. If the images have the same shape, differing only by a shift in position, then the optics is shift-invariant over the measured range.

We can express the empirical property of shift-invariance using the following mathematical notation. Choose a stimulus, $\mathbf{p}_i$ and measure the system response, $\mathbf{r}_i$. Now, shift the stimulus

[1]The results in this appendix are expressed using real harmonic functions. This is in contrast to the common practice of using complex notation, specifically Euler's complex exponential, as a shorthand to represent sums of harmonic functions. The exposition using complex exponentials is brief and elegant, but I believe it obscures the connection with experimental measurements. For this reason, I have avoided the development based on complex notation.

by an amount j and measure again. If the response is shifted by j as well, then the system may be shift-invariant. Try this experiment for many values of the shift parameter, j. If the experiment succeeds for all shifts, then the system is shift-invariant.

If you think about this definition as an experimentalist, you can see that there are some technical problems in making the measurements needed to verify shift-invariance. Suppose that the original stimulus and response are represented at N distinct points, $i = 1, \ldots, N$. If we shift the stimulus three locations so that now the fourth location contains the first entry, the fifth the second, and so forth, how do we fill in the first three locations in the new stimulus? And, what do we do with the last three values, $N-2, N-1, N$, which have nowhere to go?

Theorists avoid this problem by treating the real observations as if they are part of an infinite, periodic set of observations. They assume that the stimuli and data are part of an infinite periodic series with a period of N, equal to the number of original observations. If the data are infinite, the first three entries of the shifted vector are the three values at locations $-3, -2, \text{and} - 1$. If the data are periodic with period N, these three values are the same as the values at $N-3, N-2, \text{and} N-1$.

The assumption that the measurements are part of an infinite and periodic sequence permits the theorist to avoid the experimentalist's practical problem. The assumption is also essential for obtaining several of the simple closed-form results concerning the properties of shift-invariant systems. The assumption is not consistent with real measurements since real measurements cannot be made using infinite stimuli: there is always a beginning and an end to any real experiment. As an experimentalist you must always be aware that many theoretical calculations using shift-invariant methods are not valid near the boundaries of data sets, such as near the edge of an image.

Suppose we refer to the finite input as, $\mathbf{p}$, and the measured output, $\mathbf{l}$, is finite. In the theoretical analysis we extend both of these functions to be infinite and periodic. We will use a hat symbol to denote the extended functions,

$$\hat{l}_{i+N} = l_i \quad \text{and} \quad \hat{p}_{i+N} = p_i. \tag{0.1}$$

The extended functions $\hat{\mathbf{l}}$ and $\hat{\mathbf{p}}$ agree with our measurements over the measurement range from $1, \ldots, N$. By the periodicity assumption, the values outside of the measurement range are filled in by looking at the values within the measurement range. For example,

$$(\ldots, \hat{l}_{-1} = \hat{l}_{N-1},\ \hat{l}_0 = \hat{l}_N,\ \hat{l}_1, \ldots, \hat{l}_N,\ \hat{l}_{N+1} = \hat{l}_1, \ldots).$$

Convolution

Next, we derive some of the properties of linear shift-invariant systems. We begin by describing these properties in terms of the *system matrix* (see Chapter). Then, we will show how the simple structure of the shift-invariant system matrix permits us to relate the input and output by a summation formula called *cyclic convolution*. The convolution formula is so important that shift-invariant systems are sometimes called *convolution systems*.[2]

In Chapter I reviewed how to measure the system matrix of an optical system for one-dimensional input stimuli. We measure the image resulting from a single line at a series of uniformly spaced input locations. If the system is shift-invariant, then the columns of the system matrix are shifted copies of one another (except for edge artifacts). To create the system matrix, we extend the inputs and outputs to be periodic functions (Equation 0.1). Then, we select a central block of size $N \times N$ to be the system matrix and we use the corresponding entries of the extended stimulus. For example, if the input stimulus consists of six values, $\mathbf{p} = (0, 0, 0, 1, 0, 0)$, and the response to this stimulus is the vector, $\mathbf{l} = (0.0, 0.3, 0.6, 0.2, 0.1, 0.0)$, then the 6×6 system matrix is

$$\hat{\mathbf{C}} = \begin{pmatrix} 0.2 & 0.6 & 0.3 & 0.0 & 0.0 & 0.1 \\ 0.1 & 0.2 & 0.6 & 0.3 & 0.0 & 0.0 \\ 0.0 & 0.1 & 0.2 & 0.6 & 0.3 & 0.0 \\ 0.0 & 0.0 & 0.1 & 0.2 & 0.6 & 0.3 \\ 0.3 & 0.0 & 0.0 & 0.1 & 0.2 & 0.6 \\ 0.6 & 0.3 & 0.0 & 0.0 & 0.1 & 0.2 \end{pmatrix} . \tag{0.2}$$

For a general linear system, we calculate the output using the summation formula for matrix multiplication in Equation 0.4,

$$\hat{r}_i = \sum_{j=1}^{N} \hat{\mathbf{C}}_{ij} \hat{p}_j \quad . \tag{0.3}$$

When the linear system is shift-invariant system, this summation formula simplifies for two reasons. First, because of the assumed periodicity, the summation is precisely the same when we sum over any N consecutive integers. It is useful to incorporate this generalization into the summation formula as

$$\hat{r}_i = \sum_{j=<N>} \hat{\mathbf{C}}_{ij} \hat{p}_j \quad , \tag{0.4}$$

[2]Since we use only cyclic convolution here, I will drop the word "cyclic" and refer to the formula simply as convolution. This is slightly abusive, but conforms to common practice in many fields.

where the notation $j = \langle N \rangle$ means that summation can take place over any N consecutive integers. Second, notice that for whichever $N \times N$ block of values we choose, the typical entry of the system matrix will be

$$\hat{\mathbf{C}}_{ij} = \hat{l}_{i-j}. \tag{0.5}$$

We can use this relationship to simplify the summation further,

$$\hat{r}_i = \sum_{j=<N>} \hat{l}_{i-j} \hat{p}_j \quad . \tag{0.6}$$

In this form, we see that the response depends only on the input and the linespread. The summation formula in Equation 0.6) is called *cyclic convolution*. Hence, we have shown that to compute the response of a shift-invariant linear system to any stimulus, we need measure only the linespread function.

Convolution and Harmonic Functions

Next, we study some of the properties of the convolution formula. Most important, we will see why harmonic functions have a special role in the analysis of convolution systems.

Beginning with our analysis of optics in Chapter , we have relied on the fact that the response of a shift-invariant system to a harmonic function at frequency f is also a harmonic function at f. In that chapter, the result was stated in two equivalent ways.

1. If the input is a harmonic at frequency f, the output is a shifted and scaled copy of the harmonic.
2. The response to a harmonic at frequency f will be the weighted sum of a sinusoid and cosinusoid at the same frequency (Equation 0.10).

We can derive this result from the convolution formula. Define a new variable, $k = i - j$, and substitute k into Equation 0.6. Remember that the summation can take place over any adjacent N values. Hence, the substitution yields a modified convolution formula,

$$\hat{r}_i = \sum_{k=<N>} \hat{l}_k \hat{p}_{i-k} \tag{0.7}$$

Next, we use the convolution formula in Equation 0.7) to compute the response to a sinusoidal input $\sin(\frac{2\pi f j}{N})$. From trigonometry we have that

$$\sin(\frac{2\pi f(i+j)}{N}) = \sin(\frac{2\pi f i}{N}) \cos(\frac{2\pi f j}{N}) + \sin(\frac{2\pi f j}{N}) \cos(\frac{2\pi f i}{N}) \ . \tag{0.8}$$

Substitute Equation 0.8 into Equation 0.7, remembering that $\sin(-k) = -\sin(k)$ and $\cos(-k) = \cos(k)$.

$$
\begin{aligned}
\hat{r}_i &= \sum_{k=<N>} \hat{l}_k \sin(\frac{2\pi fi}{N}) \cos(\frac{2\pi fk}{N}) + \sum_{k=<N>} \hat{l}_k \sin(\frac{2\pi fk}{N}) \cos(\frac{2\pi fi}{N}) \\
&= \sin(\frac{2\pi fi}{N}) \sum_{k=<N>} \hat{l}_k \cos(\frac{2\pi fk}{N}) - \cos(\frac{2\pi fi}{N}) \sum_{k=<N>} \hat{l}_k \sin(\frac{2\pi fk}{N})
\end{aligned}
\tag{0.9}
$$

We can simplify this expression to the form

$$
\hat{r}_i = a \ \sin(\frac{2\pi fi}{N}) - b \ \cos(\frac{2\pi fi}{N}) \tag{0.10}
$$

where

$$
\begin{aligned}
a &= \sum_{k=<N>} \hat{l}_k \cos(\frac{2\pi fk}{N}) \\
b &= \sum_{k=<N>} \hat{l}_k \sin(\frac{2\pi fk}{N})
\end{aligned}
\tag{0.11}
$$

We have shown that when the input to the system is a sinusoidal function at frequency f, the output of the system is the weighted sum of a sinusoid and a cosinusoid, both at frequency f. This is equivalent to showing that when the input is a sinusoid at frequency f, the output will be a scaled and shifted copy of the input, $s_f \sin(\frac{\pi fi}{N} + \phi_f)$ (see Equation 0.8). As we shall see below, it is easy to generalize this result to all harmonic functions.

The Discrete Fourier Series: Defined

In general, when we measure the response of a shift-invariant linear system we measure N output values. When the input is a sinusoid, or more generally a harmonic, we can specify the response using only the two numbers, a and b, in Equation 0.11. We would like to take advantage of this special property of shift-invariant systems. To do so, we need a method of representing input stimuli as the weighted sum of harmonic functions.

The method used to transform a stimulus into the weighted sum of harmonic functions is called the *Discrete Fourier Transform* (DFT). The representation of the stimulus as the weighted sum of harmonic functions is called the *Discrete Fourier Series* (DFS). We use the DFS to represent an extended stimulus, $\hat{\mathbf{p}}$.

$$
\hat{p}_i = \sum_{f=0}^{N-1} a_f \cos(\frac{2\pi fi}{N}) + b_f \sin(\frac{2\pi fi}{N}) \quad . \tag{0.12}
$$

We are interested in that part of the extended stimulus that coincides with our measurements. We can express the relationship between the harmonic functions and the original stimulus, $\mathbf{p}$, using a matrix equation

$$\mathbf{p} = \mathbf{Ca} + \mathbf{Sb} \tag{0.13}$$

which has the matrix tableau form

$$\begin{pmatrix} \mathbf{p} \end{pmatrix} = \begin{pmatrix} & \mathbf{C} & \end{pmatrix} \begin{pmatrix} \mathbf{a} \end{pmatrix} + \begin{pmatrix} & \mathbf{S} & \end{pmatrix} \begin{pmatrix} \mathbf{b} \end{pmatrix} \tag{0.14}$$

The vectors $\mathbf{a}$ and $\mathbf{b}$ contain the coefficients a_f and b_f, respectively. The columns of the matrices $\mathbf{C}$ and $\mathbf{S}$ contain the relevant portions of the cosinusoidal and sinusoidal terms, $\cos(\frac{2\pi fi}{N})$ and $\sin(\frac{2\pi fi}{N})$, that are used in the DFS representation.

The DFS represents the original stimulus as the weighted sum of a set of harmonic functions (i.e., sampled sine and cosine functions). We call these sampled harmonic functions the *basis functions* of the DFS representation. The vectors $\mathbf{a}$ and $\mathbf{b}$ contain basis functions *weights* or *coefficients* that specify how much of each basis function must be added in to recreate the original stimulus, $\mathbf{p}$.

The Discrete Fourier Series: Properties

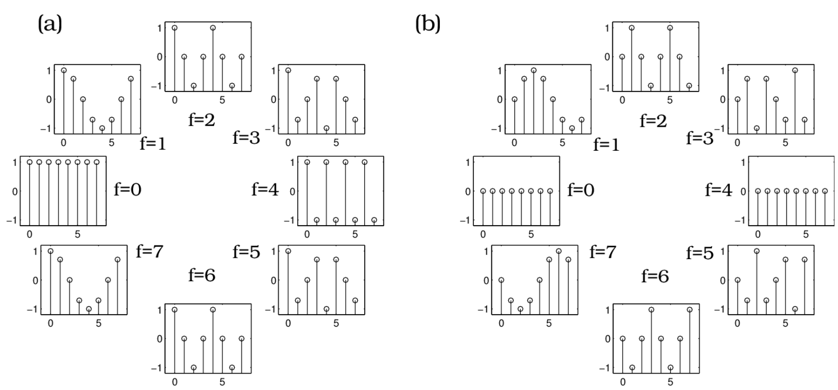

Figure 1: The basis functions of the Discrete Fourier Series. The cosinusoidal (a) and sinusoidal (b) basis functions of the discrete Fourier series representation when N=8 are shown. Notice the redundancy between the functions at symmetrically placed frequencies.

Figure 1 shows the sampled sine and cosine functions for a period of $N = 8$. The functions are arrayed in a circle to show how they relate to one another. There are a total of 16 basis functions. But, as you can see from Figure 1, they are redundant. The sampled cosinusoids in the columns of $\mathbf{C}$ repeat themselves (in reverse order); for example, when $N = 8$ the cosinusoids for $f = 1, 2, 3$ are the same as the cosinusoids for $f = 7, 6, 5$. The sampled sinusoids in the columns of $\mathbf{S}$ also repeat themselves except for a sign reversal (multiplication by negative one). There are only four independent sampled cosinusoids, and four independent sampled sinusoids. As a result of this redundancy, neither the $\mathbf{S}$ nor the matrix $\mathbf{C}$ is invertible.

Nevertheless, the properties of these harmonic basis functions make it simple to calculate the vectors containing the weights of the harmonic functions from the original stimulus, $\mathbf{p}$. To compute $\mathbf{a}$ and $\mathbf{b}$, we multiply the input by the basis functions, as in

$$\mathbf{a} = \frac{1}{N}\mathbf{C}^T\mathbf{p} \quad \text{and} \quad \mathbf{b} = \frac{1}{N}\mathbf{S}^T\mathbf{p}. \tag{0.15}$$

We can derive the relationship in Equation 0.15 from two observations. First, the matrix sum, $\mathbf{H} = \mathbf{S} + \mathbf{C}$ has a simple inverse. The columns of $\mathbf{H}$ are orthogonal to one another, so that the inverse of $\mathbf{H}$ is simply [3].

$$\mathbf{H}^{-1} = \frac{1}{N}\mathbf{H}^T = \frac{1}{N}(\mathbf{S} + \mathbf{C})^T. \tag{0.16}$$

Second, the columns of the matrices $\mathbf{C}$ and $\mathbf{S}$ are perpendicular to one another: $\mathbf{0} = \mathbf{C}\mathbf{S}^T$. This observation should not be surprising since continuous sinusoids and cosinusoids are also orthogonal to one another.

We can use these two observations to derive Equation 0.15 as follows. Express the fact that $\mathbf{H}$ and $\frac{1}{N}\mathbf{H}^T$ are inverses as follows:

$$\begin{aligned}
\mathbf{I}_{N\times N} &= \mathbf{H}\left(\frac{1}{N}\mathbf{H}^T\right) \\
&= \frac{1}{N}(\mathbf{C} + \mathbf{S})(\mathbf{C} + \mathbf{S})^T \\
&= \frac{1}{N}(\mathbf{C}\mathbf{C}^T + \mathbf{S}\mathbf{S}^T)
\end{aligned} \tag{0.17}$$

where $\mathbf{I}_{N\times N}$ is the identity matrix. Then, multiply both sides of Equation 0.17 by $\mathbf{p}$,

%cn cn' stim + sn sn' stim = stim.

$$\mathbf{p} = \frac{1}{N}(\mathbf{C}\mathbf{C}^T\mathbf{p} + \mathbf{S}\mathbf{S}^T\mathbf{p}) \tag{0.18}$$

[3]This observation is the basis of another useful linear transform method called the *Hartley Transform* (Bracewell (1986)).

Compare Equation 0.18 and Equation 0.14. Notice that the Equations become identical if we make the assignments in Equation 0.15. This completes the sketch of the proof.

Measuring a Convolution System using Harmonic Functions

Finally, we show how to predict the response of a shift-invariant linear system to any stimulus using only the responses to unit amplitude cosinusoidal inputs. This result is the logical basis for describing system performance from measurements of the response to harmonic functions. When the system is linear and shift-invariant, its responses to harmonic functions is a complete description of the system; but, this is not true for arbitrary linear systems.

Because cosinusoids and sinusoids are shifted copies of one another, the response of a shift-invariant linear system to these functions is the same except for a shift. From a calculation like the one in Equation 0.8, except using a cosinusoidal input, we can calculate the following result: If the response to a cosinusoid at frequency f is a sum of cosinusoid and sinusoid with weights, (a_f, b_f), then, the response to a sinusoid at frequency f will have weights $(b_f, -a_f)$. Hence, if we know the response to a cosinusoid at f, we also know the response to a sinusoid at f.

Next, we can use our knowledge of the response to sinusoids and cosinusoids at f to predict the response to any harmonic function at f. Suppose that the input is a harmonic function $a\cos(\frac{2\pi fi}{N}) + b\sin(\frac{2\pi fi}{N})$, and the output is, say $a'\cos(\frac{2\pi fi}{N}) + b'\sin(\frac{2\pi fi}{N})$. If the response to a unit amplitude cosinusoid is $u_f\cos(\frac{2\pi fi}{N}) + v_f\sin(\frac{2\pi fi}{N})$, then the response to a unit amplitude sinusoid is $v_f\cos(\frac{2\pi fi}{N}) - u_f\sin(\frac{2\pi fi}{N})$. Using these two facts and linearity we calculate the coefficients of the response,

$$\begin{aligned} a' = &\quad au_f + bv_f \\ b' = &\quad av_f - bu_f. \end{aligned}$$

We have shown that if we measure the system response to unit amplitude cosinusoidal inputs, we can compute the system response to an arbitrary input stimulus as follows.

- Compute the DFS coefficients of the input stimulus using Equation 0.15.
- Calculate the DFS coefficients of the output using Equation 0.19.
- Reconstruct the output from the coefficients using Equation 0.12.

You will find this series of calculations used implicitly at several points in the text. For example, we followed this organization when I described measurements of the optical quality of the lens (Chapter) and when I described measurements of behavioral sensitivity to spatiotemporal patterns (Chapter).

Display Calibration

Visual displays based on a *cathode ray tube* (CRT) are used widely in business, education and entertainment. The CRT reproduces color images using the principles embodied in the color-matching experiment (Chapter).

The design of the color CRT is one of the most important applications of vision science; thus, it is worth understanding the design as an engineering achievement. Also, because the CRT is used widely in experimental vision science, understanding how to control the CRT display is an essential skill for all vision scientists. This appendix reviews several of the principles of monitor calibration.

An Overview of a CRT Display

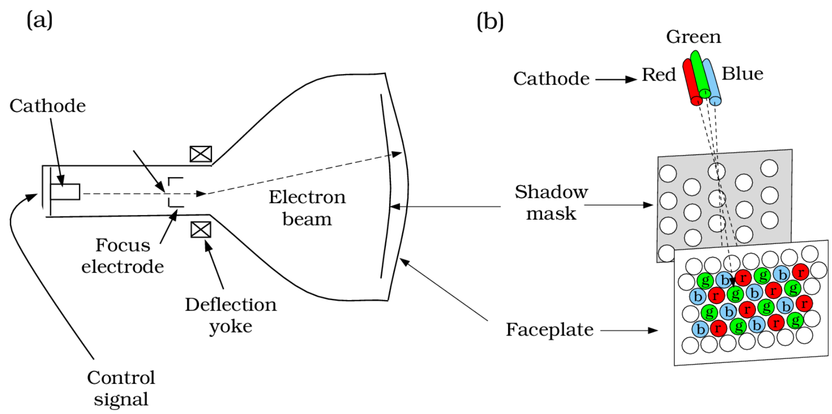

Figure 2: Overview of a cathode ray tube display. (a) A side view of the display showing the cathode, which is the source of electrons, and a method of focusing the electrons into a beam that is deflected in a raster pattern across the faceplate of the display. (b) The geometrical arrangement of the electron beams, shadow-mask, and phosphor allows each electron beam to stimulate only one of the three phosphors.

Figure 2 (a) shows the main components of a color CRT display. The display contains a *cathode*, or *electron gun*, that provides a source of electrons. The electrons are focused into a beam whose direction is deflected back and forth in a raster pattern so that it scans the faceplate of the display.

Light is emitted by a process of absorption and emission that occurs at the faceplate of the display. The faceplate consists of a phosphor painted onto a glass substrate. The phosphor absorbs electrons from the scanning beam and emits light. A signal, generally controlled from a computer, modulates the intensity of the electron beam as it scans across the faceplate. The intensity of the light emitted by the phosphor at each point on the faceplate depends on the intensity of the electrons beam as it scans past that point.

Monochrome CRTs have a single electron beam and a single type of phosphor. In monochrome systems the control signal only influences the intensity of the phosphor emissions. Color CRTs use three electron beams; each stimulates one of three phosphors. Each of the phosphors emits light of a different spectral power distribution. By separately controlling the emissions of the three types of phosphors, the user can vary the spectral composition of the emitted light. The light emitted from the CRT is always the mixture of three primary lights from the three phosphors, usually called the red, green and blue phosphors.

In order that each electron beam stimulate emissions from only one of the three types of phosphors, a metal plate, called a *shadow-mask*, is interposed between the three electron guns and the faceplate. A conventional shadow-mask is a metal plate with a series of finely spaced holes. The relative positions of the holes and the electron guns are arranged, as shown in Figure 2 (b), so that as the beam sweeps across the faceplate the electrons from a single gun that pass through a hole are absorbed by only one of the three types of phosphors; electrons from that gun that would have stimulated the other phosphors are absorbed or scattered by the shadow-mask.

The frame-buffer

In experiments, the control signal sent to the CRT display is usually created using computer software. There are two principal methods for creating these control signals. In one method, the user controls the three electron beam intensities by writing out the values of three matrices into three separate *video frame-buffers*. Each matrix specifies the control signal for one of the electron guns. Each matrix entry specifies the desired voltage level of the control signal at a single point on the faceplate. Usually, the intensity levels within each matrix are quantized to 8 bits, so this computer display architecture is called *24 bit color*, or *RGB color*.

In a second method, the user writes a single matrix into a single frame-buffer. The value at each location in this matrix is converted into three control signals sent to the display according to a code contained in in a *color look-up table*. This architecture is called *indexed color*. This method is cost-effective because it does away with two of the three frame-buffers. When using this method, the user can only select among 256 (8 bits) colors when displaying a single image.

Display Intensity

Calibrating a visual display means measuring the relationship between the frame-buffer values and the light emitted by the display. In this section we will discuss the relationship between the frame-buffer values and the intensity of the emitted light. In the next section we will discuss the relationship between the frame-buffer values and the spectral composition of the emitted light.

We can measure the relationship between the value of a frame-buffer entry and the intensity of the light emitted from the display as follows: Set the frame buffer entries controlling one of the three hosphor display intensities, say within a rectangular region, to a single value. Measure the intensity of the light emitted from the displayed rectangle. Repeat this measurement at many different frame-buffer values for this phosphor, and then for the other two phosphors.

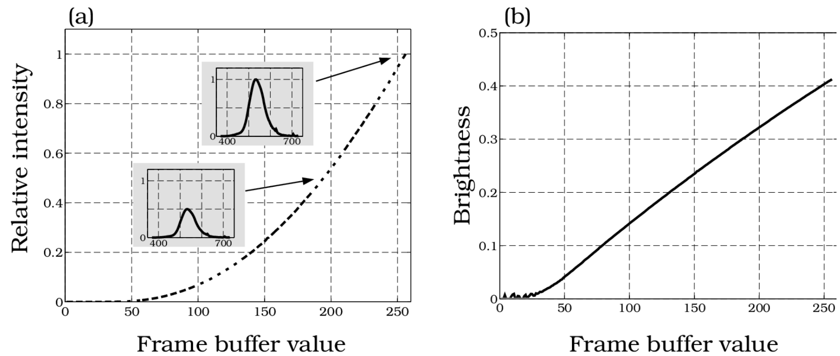

Figure 3: Frame-buffer value and display intensity. (a) The dashed curve measures the intensity of the emitted light relative to the maximum intensity. The data shown are for the green phosphor. The insets in the graph show the complete spectral power distribution of the light at two different frame-buffer levels. (b) The dashed curve describing the relative intensities is replotted, using Stevens' Power Law, to show the linear relationship between the frame-buffer value and perceived brightness.

The dashed curve in Figure 3 measures the ratio of the intensity at the highest frame-buffer level to the intensity at each of the other frame-buffer levels for the green phosphor. We can summarize the difference using this single ratio, the *relative intensity* because for over most of the range the spectral power distribution of the light emitted at one frame-buffer level is the same as the spectral power distribution of the light emitted from the monitor at maximum except for a scale factor. The insets in the graph show two examples of the spectral power distribution, measured when the frame-buffer was set to 255 and 190. These two curves have the same overall shape; they differ by a scale factor of one half.

We can approximate the curve relating the relative intensity of the light emitted from this CRT display, I, and the frame-buffer value, v, by a function of the form

$$I = \alpha v^{\gamma} + \beta \tag{0.19}$$

where α and β are two fitting parameters. For most CRTs, the exponent of the power function, γ, has a value near 2.2 (see Brainard (1989); Berns et al. (1993b), Berns et al. (1993a)).

The nonlinear function relating the frame-buffer values and the relative intensity is due to the physics of the CRT display. While nonlinear functions are usually viewed with some dread, this particular nonlinear relationship is desirable because most users want the frame-buffer values to be linear with the brightness; they don't care how the frame-buffer values relate to intensity. As it turns out, perceived brightness, B, is related to intensity through a power law relationship called *Stevens' Power Law* (Stevens (1962); Goldstein (1989); Sekuler and Blake (1985)), namely,

$$B = aI^{0.4} \tag{0.20}$$

where a is a fitting parameter. Somewhat fortuitously, the nonlinear relationship between frame-buffer values and intensity compensates for the nonlinear relationship between intensity and brightness. To show this, I have replotted Figure 3 (a) on a graph whose vertical scale is brightness, that is relative intensity raised to the 0.4 power. This graph shows that the relationship between the frame-buffer value and brightness is nearly linear. This has the effect of equalizing the perceptual steps between different levels of the frame-buffer and simplifying certain aspects of controlling the appearance of the display.

Display Spectral Power Distribution

The spectral power distribution of the light emitted in each small region of a CRT display is the mixture of the light emitted by the three phosphors. Since the mixture of lights obeys superposition, we can characterize the spectral power distributions emitted by a CRT using simple linear methods.

Suppose we measure the spectral power distribution of the red, green and blue phosphors at their maximum intensity levels. We record these measurements in three column vectors, $\mathbf{m}_i,\ i = 1, 2, 3$.

By superposition, we know that light from the monitor screen is always the weighted sum of light from the three phosphors. For example, if all three of the phosphors are set to their maximum levels, the light emitted from the screen, call it $\mathbf{t}$, will have a spectral power distribution of

$$\mathbf{m}_1 + \mathbf{m}_2 + \mathbf{m}_3. \tag{0.21}$$

More generally, if we set the phosphors to the three relative intensities $\mathbf{e} = (e_r, e_g, e_b)$, the light emitted by the CRT will be the weighted sum

$$\mathbf{t} = e_r\mathbf{m}_1 + e_g\mathbf{m}_2 + e_b\mathbf{m}_3 \tag{0.22}$$

Figure 4 is a matrix tableau that illustrates how to compute the spectral power distribution of light emitted from a CRT display. The vector $\mathbf{e}$ contains the relative intensity of each of the three phosphors. The three columns of a matrix, call it $\mathbf{M}$, contain the spectral power distributions of the light emitted by the red, green and blue phosphors at maximum intensity. The spectral power distribution of light emitted from the monitor is the product **Me**.

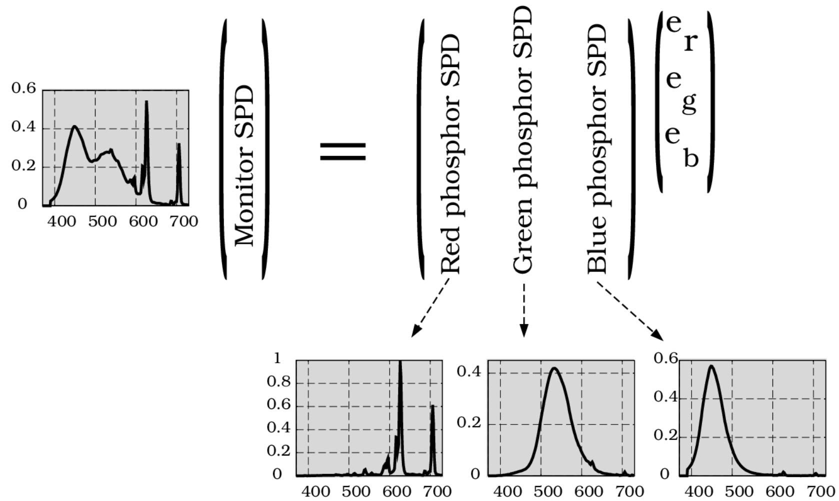

Figure 4: The spectral power distribution of light emitted from a CRT. The entries e = (er, eg, eb) are the relative intensity of the three phosphors. The columns of M contain the spectral power distributions at maximum intensity. The vector calculated by Me is the spectral power distribution of the light emitted by the CRT. The output shown in the figure was calculated for e = (0.5, 0.6,0.7)T.

The light emitted from a CRT is different from lights we encounter in natural scenes. For example, the spectral power distribution of the red phosphor, with its sharp and narrow peaks, is unlike the light we see in natural images. Nonetheless, we can adjust the three intensities of the three phosphors on a color CRT to match the appearance of most spectral power distributions, just as we can match appearance in the color-matching experiment by adjusting the intensity of three primary lights (see Chapter).

Color Calibration Matrix

In many types of psychophysical experiments, we must be able to specify and control the relative absorption rates in the three types of cones. In this section, I show how to measure and control the relative cone absorptions when the phosphor spectral power distributions and the relative cone photopigment spectral sensitivities are known.

We use two basic matrices in these calculations. We have already created the matrix **M** whose three columns contain the spectral power distributions of the phosphors at maximum intensity. We also create a matrix, **B**, whose three columns contain the cone absorption sensitivities (L, M, and S), measured through the cornea and lens (see Table~??.) Given a set of relative intensities, **e**, we calculate the relative cone photopigment absorption rates, **r** by the matrix product[4]

$$\mathbf{r} = \mathbf{B}^T \mathbf{M} \mathbf{e} = \mathbf{H} \mathbf{e}. \tag{0.23}$$

We call the matrix $\mathbf{H} = \mathbf{B}^T \mathbf{M}$, the monitor's *calibration matrix.* This matrix relates the linear phosphor intensities to the relative cone absorption rates.

As an example, I have calculated the calibration matrix for the monitor whose phosphor spectral power distributions are shown in Figure 4, and for the cone absorption spectra listed in Table~??. The resulting calibration matrix is

$$\begin{pmatrix} 0.2732 & 0.9922 & 0.1466 \\ 0.1034 & 0.9971 & 0.2123 \\ 0.0117 & 0.1047 & 1.0000 \end{pmatrix} \tag{0.24}$$

Each column of the calibration matrix describes the relative cone absorptions caused by emissions from one of the phosphors: The absorptions from the red phosphor are in the first column, and absorptions due to the green and blue phosphors are in the second and third columns, respectively.

Suppose the red phosphor stimulated only the L cones, the green the M cones, and the blue the S cones. In that case, the calibration matrix would be diagonal, and we could control the absorptions in a single cone class by adjusting only one of the phosphor emissions. In practice, the light from each of the CRT phosphors is absorbed in all three cone types and the calibration matrix is never diagonal. As a result, to control the cone absorptions we must take into account the effect each phosphor has on each of the three cone types. This complexity is unavoidable because of the overlap of the cone absorption curves and the need to use phosphors with broadband emissions to create a bright display. Consequently, the calibration matrix is never diagonal.

Example Calculations

Now, we consider two ways we might use the calibration matrix. First, we might wish to calculate the receptor absorptions to a particular light from the CRT. Second, we might wish to know how to adjust the relative intensities of the CRT in order to achieve a particular pattern of cone absorptions.

Using the methods described so far, you can calculate the relative cone absorption rates for any triplet of frame-buffer entries. Suppose the frame-buffer values are set to $ (128,128,0) $. The

[4]This calculation applies to spatially uniform regions of a display, in which we can ignore the complications of chromatic aberration. Marimont and Wandell (1993) describe how to include the effects of chromatic aberration.

pattern will look yellow since only the red and green phosphors are excited. Assuming that the curves relating relative intensity to frame-buffer level are the same for all three phosphors (Figure 3), we find that the relative intensities will be $\mathbf{e} = (0.1524, 0.1524, 0.0)^T$. The product $\mathbf{He}$ yields the relative cone absorption rates $\mathbf{r} = (0.1929, 0.1677, 0.0177)^T$. If we set the frame-buffer to $(128, 128, 128)$, which appears gray, the relative intensities are $(0.1524, 0.1524, 0.1524)$ and the relative cone absorption rates are $\mathbf{r} = (0.2152, 0.2001, 0.1702)^T$.

A second common type of calculation is used in behavioral experiments in which the experimenter wants to create a particular pattern of cone absorptions. To infer the relative display intensities necessary to achieve a desired effect on the cone absorptions, we must use the inverse of the calibration matrix, since

$$\mathbf{e} = \mathbf{H}^{-1}\mathbf{r}. \tag{0.25}$$

To continue our example, the inverse of the calibration matrix is

$$\mathbf{H}^{-1} = \begin{pmatrix} 5.8677 & -5.8795 & 0.3876 \\ -0.6074 & 1.6344 & -0.2579 \\ -0.0049 & -0.1025 & 1.0225 \end{pmatrix} \tag{0.26}$$

Suppose we wish to display a pair of stimuli that differ only in their effects on the \$ S \$ cones. Let's begin with a stimulus whose relative intensities are $\mathbf{e} = (0.5, 0.5, 0.5)^T$. Using the calibration matrix, we calculate that the relative cone absorption rates from this stimulus: they are $(.706, .656, .558)$. Now, let's create a second stimulus with a slightly higher rate of \$ S \$ cone absorptions: say, $\mathbf{r} = (.706, .656, .700)$. Using the inverse calibration matrix, we can calculate the relative display intensities needed to produce the second stimulus: they are $(0.555, 0.4634, 0.645)$.

Notice that to create a stimulus difference seen only by the S cones, we needed to adjust the intensities of all three phosphor emissions. For example, to increase the S cone absorptions we need to increase the intensity of the blue phosphor emissions. This will also cause some increases in the L and M cone absorptions, and we must compensate for this by decreasing the emissions from the red and green phosphors.

Color Calibration Tips

For most of us calibration is not, in itself, the point. Rather, we calibrate displays to describe and control experimental stimuli. If your experiments only involve a small number of stimuli, then it is best to calibrate those stimuli exhaustively. This strategy avoids making a lot of unnecessary assumptions, and your accuracy will be limited only by the quality of your calibration instrument.

In some experiments, and in most commercial applications, the number of stimuli is too large for exhaustive calibration. Brainard (1989) calculates that for the most extreme case, in which one has a 512×512 spatial array with RGB buffers at 8 bits of resolution there are $10^{1,893,917}$ different stimulus patterns. So many patterns, so little time.

Because of the large number of potential stimuli, we need to build a model of the relationship between the frame-buffer entries and the monitor output. The discussion of calibration in this appendix is based on an implicit model of the display. To perform a high quality calibration, you should check some of these assumptions. What are these implicit assumptions, and how close will they be to real performance?

Spatial Independence

First, we have assumed that the transfer function from the frame buffer values to the monitor output is independent of the spatial pattern in the frame buffer. Specifically, we have assumed that the light measurements we obtain from a region are the same if the surrounding area were set to zero or set to any other intensity level.

In fact, the intensity in a region is not always independent of the spatial pattern in nearby regions (see e.g. Lyons and Farrell, Naiman and Makous (1992)). It can be very difficult and impractical to calibrate this aspect of the display. As an experimenter, you should choose your calibration conditions to match the conditions of your experiment as closely as possible so you don't need to model the variations with spatial pattern. For example, if your experiments will use rectangular patches on a gray background, then calibrate the display properties for rectangular patches on a gray background, not on a black or white background.

If you are interested in a harsh test to evaluate spatial independence of a display, try displaying a square pattern consisting of alternating pixels with 0 and 255. When you step away from the monitor, the pattern will blur; in principle, the brightness of this pattern should match the brightness of a uniform square of the same size all of whose values are set to the frame-buffer value whose relative intensity is 0.5. You can try the test using alternating horizontal lines, or alternating vertical lines, or random dot arrays.

Phosphor Independence

Brainard (1989) points out that the spatial independence assumption reduces the number of measurements to approximately 1.6×10^7. Still too many measurements to make; but, at least we have reduced the problem so that there are fewer measurements than the number of atoms in the universe.

It is our second assumption, *phosphor independence*, that makes calibration practical. We have assumed that the signals emitted from three phosphors can be measured independently of one another. For example, we measured the relative intensities for the red phosphor and assumed that this curve is the same no matter what the state of the green and blue phosphor emissions. The phosphor independence assumption implies that we need to make only 3×256 measurements, the relative intensities of each of the three phosphors, to calibrate the display. (Once the spectral power distributions of the phosphors are known; or equivalently, the entries of the calibration matrix).

Before performing your experiments, it is important to verify phosphor independence. Measure the intensity of the monitor output to a range of, say, red phosphor values when green frame-buffer is set to zero. Then measure again when the green frame-buffer is set to its maximum value. The relative intensities of the red phosphor you measure should be the same after you correct for the additive constant from the green phosphor. In my experience, this property does fail on some CRT displays; when it fails your calibration measurements are in real trouble. I suspect that phosphor independence fails when the power supply of the monitor is inadequate to supply the needs of the three electron guns. Thus, when all three electron guns are being driven at high levels, the load on the power supply exceeds the compliance range and produces a dependence between the output levels of the different phosphors. This dependence violates the assumptions of our calibration procedure and makes calibration of such a monitor very unpleasant. Get a new monitor.

For further discussion of calibration, consult some papers in which authors have described their experience with specific display calibration projects (e.g. Brainard (1989); Cowan and Rowell (1986); Post and Calhoun (1989); Berns et al. (1993b), Berns et al. (1993a)).

Classification

Many visual judgments are classifications: an edge is present, or not; a part is defective, or not; a tumor is present, or not. The threshold and discrimination performances reviewed in Chapter are classifications as well: I saw it, or not; the stimulus was this one, or that. This appendix explains some of the basic concepts in classification theory and their application to understanding vision.

We will explore the issues in classification by analyzing some simple behavioral decisions, the kind that take place in many vision experiments. Suppose that during an experimental trial, the observer must decide which of two visual stimuli, A or B, is present. Part of the observer's decision will be based on the pattern of cone absorptions during the experimental trial. We can list the cone absorptions in a vector, $\mathbf{d}$, whose values represent the number of absorptions in each of the cones. Because there are statistical fluctuations in the light source, and variability in the image formation process, the pattern of cone absorptions created by the same stimulus varies from trial to trial. As a result, the pattern of cone absorptions from the two different stimuli may sometimes be the same, and perfect classification may be impossible.

What response strategy should the subject use to classify the stimuli correctly as often as possible? A good way to lead your life is this: *When you are uncertain and must decide, choose the more likely alternative.*

We can translate this simple principle into a statistical procedure by the following set of calculations. Suppose that we know the probability of the signal being A when we observe $\mathbf{d}$. This is called the *conditional probability*, $P(A \mid \mathbf{d})$, which is read as "the probability of A given $\mathbf{d}$." Suppose we also know the conditional probability that the signal is B is $P(B \mid \mathbf{d})$. The observer should decide that the signal is the one that is more likely given the data, namely

$$\text{If } P(A \mid \mathbf{d}) \;>\; P(B \mid \mathbf{d}) \;\text{ choose } A\text{, else } B. \tag{0.27}$$

We call the expression in Equation 0.27 a *decision rule*. The decision rule Equation 0.27 is framed in terms of the likelihood of the stimuli (A or B) given the data ($\mathbf{d}$). This formulation of the probabilities runs counter to our normal learning experience. During training, we know that stimulus A has been presented, and we experience a collection of cone absorptions. Experience informs us about probability of the data given the stimulus, $P(\mathbf{d} \mid A)$, not the probability of the stimulus given the data, $P(A \mid \mathbf{d})$. Hence, we would like to reformulate Equation 0.27 in terms of the way we acquire our experience.

Bayes Rule is a formula that converts probabilities derived from experience, $P(\mathbf{d} \mid A)$, into the form we need for the decision-rule, $P(A \mid \mathbf{d})$. The expression for Bayes Rule is

(21)

$$P(A \mid \mathbf{d}) = P(\mathbf{d} \mid A)\frac{P(A)}{P(\mathbf{d})} \tag{0.28}$$

where $P(A)$ is the probability the experimenter presents signal A (in this case one-half) and $P(\mathbf{d})$ is the probability of observing $\mathbf{d}$ quanta. As we shall see, this second probability turns out to be irrelevant to our decision.

The probabilities on the right hand side of Bayes Rule are either estimated from our experience, $P(\mathbf{d} \mid A)$, or they are a structural part of the experimental design $P(A)$. The probability that stimulus A or B is presented is called the *a priori* probability, or *base rate*. The probability $P(\mathbf{d} \mid A)$ is called the *likelihood* of the observation given the hypothesis. The probability, $P(A \mid \mathbf{d})$ is called the *a posteriori* probability. Bayes Rule combines the base rate and the likelihood of the observation to form the a posteriori probability of the hypothesis.

We can use Bayes Rule to express the decision criterion in Equation 0.27 in this more convenient form.

$$(\text{If } \; P(\mathbf{d} \mid A)\frac{P(A)}{P(\mathbf{d})} > P(\mathbf{d} \mid B)\frac{P(B)}{P(\mathbf{d})} \;\text{ choose } A\text{, else } B.) \tag{0.29}$$

Since the probability of observing the data, $P(\mathbf{d})$, divides both sides of this inequality, this probability is irrelevant to the decision. Therefore, we can re-write Equation 0.29 as

$$\frac{P(\mathbf{d} \mid A)}{P(\mathbf{d} \mid B)} > \frac{P(B)}{P(A)}. \tag{0.30}$$

The term on the left hand side of Equation 0.30 is called the *likelihood ratio*. The quantity on the right is called the *odds ratio*. The formula tells us that we should select A when the likelihood ratio, which depends on the data, exceeds the odds ratio, which depends on the a priori knowledge. A system that uses this formula to classify the stimuli is called a *Bayes classifier*.

A Bayes classifier for an Intensity Discrimination Task

In this section we will devise a Bayes classifier for a simple experimental decision. Suppose that we ask an observer to decide whether we have presented one of two brief visual stimuli; the two stimuli are identical in all ways but their intensity. We suppose that the observer decides which stimulus was presented based on the total number of cone absorptions during the trial, $\sum_{i=1}^{N} d_i = d$, and without paying attention to the spatial distribution of the cone absorptions.

Across experimental trials, the number of absorptions from A will vary. There are two sources of this variability. One source of variability is in the stimulus itself. Photons emitted by a light source are the result of a change in the energy level of an electron within the source material. Each electron within the material has some probability of changing states and yielding some energy in the form of a photon. This change in excitation level is a purely statistical event and cannot be precisely controlled. The variability in the number of emitted photons, then, is inherent in the physics of light emission and cannot be eliminated.

A second source of variability is in the observer. On different experimental trials, the position of the eye, accommodative state of the lens, and other optical factors will vary. As these image formation parameters vary, the chance that photons are absorbed within the photopigment will vary. These statistic fluctuations are unavoidable as well.

The physical variability is easy to model, while the biological variability is quite subtle. For this illustrative calculation, we ignore the effects of biological variability and consider only the stimulus variability. In this case, the number of absorptions will follow the *Poisson distribution*. The formula for the Poisson probability distribution describes the probability of emitting d quanta given a mean level of μ,

$$P(d \mid \mu) = (\mu^d/d!)e^{-\mu}. \tag{0.31}$$

(24)

$$P(d \mid \mu) = (\mu^d/d!)e^{-\mu}. \tag{0.32}$$

The value μ is called the *rate-parameter* of the Poisson distribution. The variance of the Poisson distribution is also μ.

Figure 5 shows the probability distributions of the number of cone absorptions from the two stimuli, A and B. For this illustration, I have assumed that the mean absorptions from the two stimuli are $\mu_A = 8$ and $\mu_B = 12$, respectively. Since the a priori stimulus probabilities are equal, the observer will select stimulus A whenever $P(d \mid A)$ exceeds $P(d \mid B)$. For this pair of distributions, this occurs whenever the observation is less than 9.

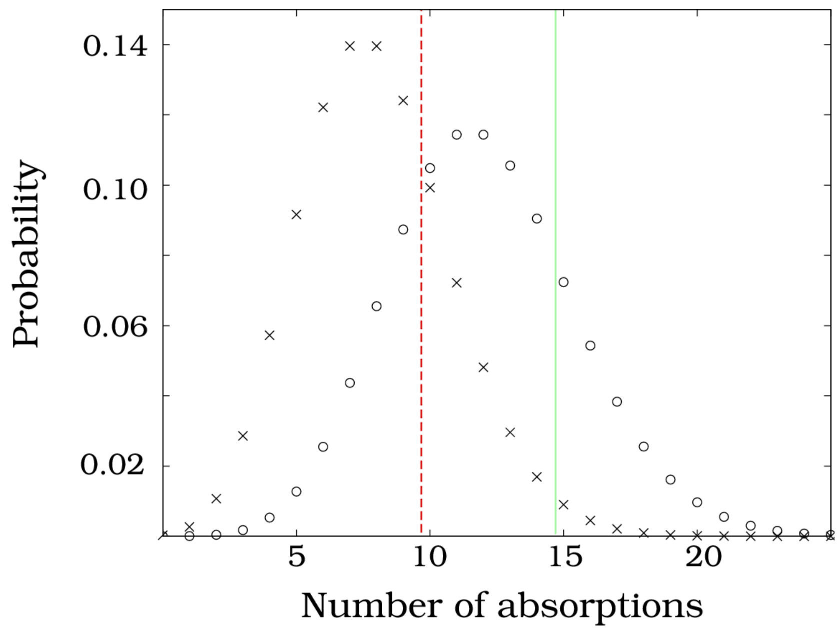

Figure 5: Bayes classifier for an intensity discrimination. The Poisson distributions of stimulus A with rate parameter muA = 8 (x's) and B with rate parameter muB = 12 (o's) are shown. When the a priori probabilities of seeing the stimuli are equal, the Bayes classifier selects B when the absorptions exceed the dashed line drawn through the graph. When the a priori probabilities are P(A) = 0.75 and P(B) = 0.25, the Bayes classifier selects B when the absorptions exceed the solid line drawn through the graph.

Now, suppose the experimenter presents A with probability 0.75 and B with probability 0.25. In this case, the subject can be right three quarters of the time simply by always guessing A. Given the strong a priori odds for A, the Bayes classifier will only choose B if the likelihood exceeds three to one. From the distributions in Figure 5 we find this occurs when there are at least 13 absorptions. The Bayes classifier uses the data and the a priori probabilities to make a decision.[5]

To find further support for their observation, Hecht et al. analyzed how the subject's responses varied across trials. They assumed that all of the observed variability was due to the stimulus, and none was due to the observer. Their account is repeated in a wonderful didactic style in Cornsweet's book. I don't think this assumption is justified; a complete treatment of the data must take into account variability intrinsic to the human observer (e.g., Nachmias and Kocher (1970)).

A Bayes classifier for a Pattern Discrimination Task

To discriminate between different spatial patterns, or stimuli located at different spatial positions, the observer must use the spatial pattern of cone absorptions. Consequently, pattern discrimination must depend on comparisons of a vector of measurements, $\mathbf{d}$, not just a single value. In this section, we develop a Bayes classifier that can be applied to a pattern discrimination task.

Again, for illustrative purposes we assume that the variability is due entirely to the stimulus. Moreover, we will assume that the variability in light absorption at neighboring receptors is statistically independent. Independence means that the probability of d_i absorptions at the i^{th} receptor and d_j at the j^{th} is

$$P(d_i \ \& \ d_j \mid A) = P(d_i \mid A) \ P(d_j \mid A). \tag{0.33}$$

We can extend this principle across all of the receptors to write the probability of observing $\mathbf{d}$ given signal A, namely

$$L_A = \prod_{i=1}^{N} P(d_i \mid A), \tag{0.34}$$

where L_A is the likelihood of observing $\mathbf{d}$ given the stimulus A.

Finally, we must specify the spatial pattern of two stimuli. The expected number of absorptions at the i^{th} cone will depend on the spatial pattern of the stimulus. We call the mean intensity of the stimulus at location i, $\mu_A i$ and $\mu_{B,i}$, respectively.

[5] In a classic paper, Hecht et al. (1942) measured the smallest number of quanta necessary to reliably detect a signal. In the most sensitive region of the retina, under the optimized viewing conditions, they found that 100 quanta at the cornea, which corresponds to about 10 absorptions, are sufficient. The quanta are absorbed in an area covered by several hundred rods; hence, it is quite unlikely that two quanta will be absorbed by the same rod. They concluded, quite correctly, that a single photon of light can produce a measurable response in a single rod.

We are ready to compute the proper Bayes classifier. The general form of the decision criterion is

$$\text{If } \frac{P(\mathbf{d} \mid A)}{P(\mathbf{d} \mid B)} > \frac{P(B)}{P(A)} \text{ choose A, else B.} \tag{0.35}$$

If the two stimuli are presented in the experiment equally often, we can re-write this equation as

$$\text{If } P(\mathbf{d} \mid A) > P(\mathbf{d} \mid B) \text{ choose } A, \text{ else } B. \tag{0.36}$$

Next, we can use independence to write

$$\text{If } \prod_{i=1}^{N} P(d_i \mid A) > \prod_{i=1}^{N} P(d_i \mid B) \text{ choose A, else B.} \tag{0.37}$$

Now, we substitute the Poisson formula, take the logarithm of both sides, and regroup terms to obtain

$$\text{If } \sum_{i=1}^{N} d_i \ln\left(\frac{\mu_{A,i}}{\mu_{B,i}}\right) > \sum_{i=1}^{N} \mu_{A,i} - \sum_{i=1}^{N} \mu_{B,i} \text{choose A, else B.} \tag{0.38}$$

Equation 0.38 can be interpreted as a very simple computational procedure. First, notice that the Equation contains two terms. The first term is the weighted sum of the photopigment absorptions,

$$\sum_{i=1}^{N} d_i w_i, \tag{0.39}$$

where $w_i = \ln\left(\frac{\mu_{A,i}}{\mu_{B,i}}\right)$. This is a very familiar computation; it is directly analogous to the calculation implemented by a linear neuron whose receptive field sensitivity at position i is w_i (see Chapter).

The second term is the difference between the total number of photopigment absorptions expected from each stimulus.

$$\sum_{i=1}^{N} \mu_{A,i} - \sum_{i=1}^{N} \mu_{B,i}. \tag{0.40}$$

This term acts as a normalizing criterion to correct for the overall response to the two stimuli. The decision rule in Equation 0.38) compares a weighted sum of cone absorptions to the normalizing criterion. If the first term exceeds the second, then choose response A, else B.

We have learned that a Bayes classifier for pattern discrimination can be implemented using the results of simple linear calculations, like the calculations represented in the outputs of some peripheral neurons. In fact, making a decision like a Bayes classifier is equivalent to comparing the response of a linear neuron with a criterion value. If response of the linear neuron with receptive field defined by w_i exceeds the criterion value, then choose stimulus A, otherwise choose B.

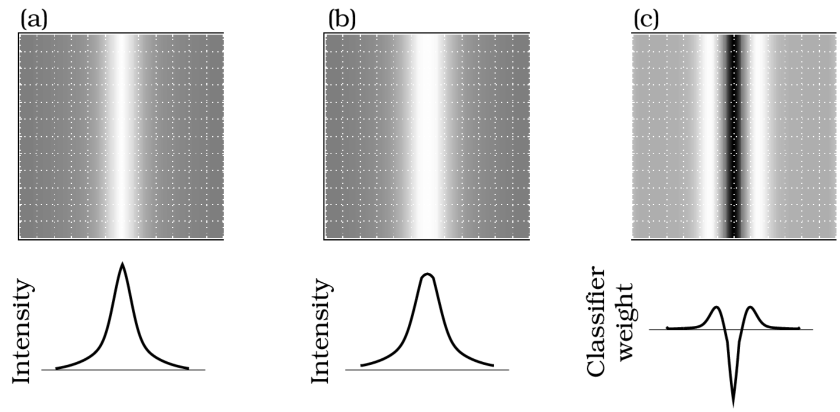

Figure 6: Bayes classifier for a spatial discrimination task. (a) The mean retinal image of a line. The grid lines are separated by 30 sec of arc, approximately the spacing of the cone inner segments in the fovea. (b) The mean retinal image of an image formed by a pair of lines separated by 30 sec of arc. The intensity of each line is one half the intensity of the line in panel (a). (c) The weights of the Bayes classifier that should be used to discriminate the stimuli in (a) and (b), given the assumptions of independent Poisson noise. (After: Geisler (1989)).

Figure 6 shows an example of a Bayes classifier computed for a simple pattern discrimination task. The two spatial patterns to be discriminated are shown in panels (a) and (b). The image in (a) is the retinal image of a line segment. Figure 6 (b) shows the retinal image of a pair of line segments, separated by 30 sec of arc. The grid marks on the image are spaced by 30 sec of arc, essentially the same spacing as the cone inner segments. The curves below the images measure the intensity of the stimuli across a horizontal section.

Figure 6 (c) shows the weights of the Bayes classifier for discriminating the two images; the weights were computing using Equation 0.39. In this image the gray level represents the value of the weight that should be applied to the individual cone absorptions: a medium gray intensity corresponds to a zero weight, lighter values are positive weights, and darker values are negative weights. The spatial pattern of weights bears an obvious resemblance to the spatial patterns of receptive fields in the visual cortex.

The Bayes classifier specifies how to obtain the optimal discrimination performance when we know the signal and the noise. Apart from the optimality of the Bayes classifier itself, observers in behavioral experiments can never know the true signal and noise perfectly. The performance of the Bayes classifier, therefore, must be equal or superior to human performance. In nearly all cases where a Bayes classifier analysis has been carried out, the Bayesian classifier performance is vastly better than human observer performance. Human observers usually fail to extract a great deal of information available in the stimulus. In general, then, the Bayes classifier does not model human performance (Banks et al. (1987)).

Why, then, is the Bayes classifier analysis important? The Bayes classifier analysis defines what information is available to the observer. Defining the stimulus is an essential part of a good experimental design. The Bayes classifier defines what the observer can potentially do, and this serves as a good standard to use in evaluating performance. The Bayes classifier helps us to understand the task; only if we understand the task, can we understand the observer's performance.

> The real power of this approach is that the ideal discriminator [Bayes classifier] measures all the information available to the later stages of the visual system. I would like to suggest that measuring the information available in discrimination stimuli with a model of the sort I have described here should be done as routinely as measuring the luminances of the stimuli with a photometer. In other words, we should not only use a light meter but we should also use the appropriate information meter. It is simply a matter of following the first commandment of psychophysics: "know thy stimulus." (Geisler (1987), p. 30)

Signal Estimation: A Geometric View

This book is filled with calculations of the general form

$$\mathbf{a}^T\mathbf{x} = \sum_{i=1}^{N} a_i x_i \quad . \tag{0.41}$$

This formula is called the *dot product* of the vectors $\mathbf{a}$ and $\mathbf{x}$. It is so important that it is often given a special notation, such as $\mathbf{a} \cdot \mathbf{x}$. Every time we multiply a matrix by a vector, $\mathbf{Ax}$, we compute the dot product $\mathbf{x}$ with the rows of $\mathbf{A}$. In this section, I want to discuss some geometric intuitions connected with the dot product operation.[6]

Although we used the dot product calculation many times, I decided not to use the dot product notation in the main portion of the book because the notation treats the two vectors symmetrically; but, in most applications the vectors $\mathbf{a}$ and $\mathbf{x}$ had an asymmetrical role. The vector $\mathbf{x}$

[6] Physicists often refer to Equation 0.42 as the scalar product because the result is a scalar; mathematicians often refer to the dot product as an inner product and write it using angle brackets $\langle \mathbf{a}, \mathbf{x} \rangle$.

was usually a stimulus, say the wavelength composition of a light or a one-dimensional spatial pattern, and the vector $\mathbf{a}$ was part of the sensory apparatus, say a photopigment wavelength sensitivity or a ganglion cell receptive field. Because the physical entities we described were not symmetric, I felt that the asymmetric notation, $\mathbf{a}^T\mathbf{x}$, was more appropriate.

The scalar value of the dot product between two vectors is equal to The inline mathematics should use the Quarto format, which is `$...$`. For equations on separate lines, use the `$$ ... $$` format and add a tag like `{#eq-dot-product}` at the end.

Here is the modified code:

$$\mathbf{a} \cdot \mathbf{x} = \|\mathbf{a}\|\|\mathbf{x}\| \cos(\theta) \tag{0.42}$$

where $\|\cdot\|$ is the vector length and θ is the angle between the vectors. To simplify the discussion in the remainder of this section, we will assume that the vector $\mathbf{a}$ has unit length.

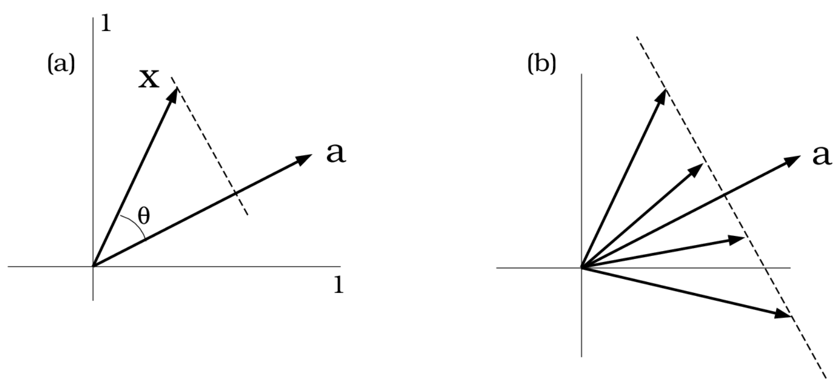

Figure 7: A geometric interpretation of the two-dimensional dot product. (a) A geometrical view of the dot product of two vectors is shown. The dashed line is a perpendicular from the tip of vector $\mathbf{x}$ to the unit-length vector $\mathbf{a}$. (b) Any vector whose endpoint falls along the dashed line yields the same scalar value when we compute the vector's dot product with $\mathbf{a}$.

Figure 7 (a) is a geometric representation of the dot product operation. The unit vector $\mathbf{a}$ and the signal vector $\mathbf{x}$ are drawn as arrows extending from the origin. A dashed line is drawn from the tip of $\mathbf{x}$ (the signal) at right angles to the vector $\mathbf{a}$ (the sensor). The length of the vector from the origin to point of intersection between the perpendicular dashed line and $\mathbf{a}$ is called the *projection* of $\mathbf{x}$ onto $\mathbf{a}$. Because we have assumed $\mathbf{a}$ has unit length, the length of the projection, $\|\mathbf{x}\| \cos(\theta)$, is equal to the dot product, $\mathbf{a} \cdot \mathbf{x} = \|\mathbf{a}\|\|\mathbf{x}\| \cos(\theta)$.

By inspecting Figure 7 (b), you can see that there are many signal vectors, $\mathbf{x}$, that have the same dot product with $\mathbf{a}$. Specifically, all of the vectors whose endpoints fall along a line that is perpendicular to $\mathbf{a}$, have the same dot product with $\mathbf{a}$. Hence, any signal represented by a vector whose endpoint is on this line will cause the same response in the sensor represented by the vector **a**.

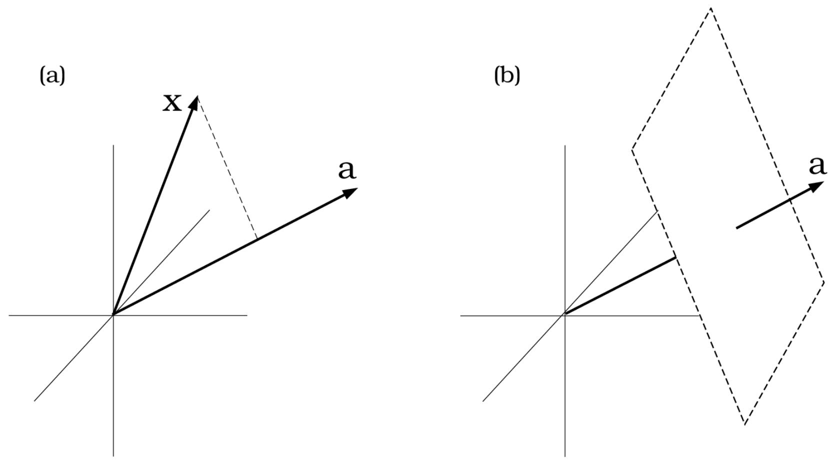

Figure 8: A geometric representation of the three-dimensional dot product. (a) The perpendicular from x to a is indicated by the dashed line. When a is a unit vector, the distance from the origin to the intersection of the dashed line with a is the scalar value of the dot product. (b) Any vector whose endpoint falls within the indicated plane yields the same scalar value when we compute the vector's dot with a.

The geometric intuition extends smoothly to vectors with more than two dimensions. Figure 8 (a) shows the dot product between a pair of three-dimensional vectors. In three-dimensions, all of the vectors whose endpoints fall on a plane perpendicular to the unit-length vector **a** have the same dot product with that vector (Figure 8 (b)). In four or more dimensions the set of signals with a common dot product value fall on a *hyperplane*.

Figure 7 (b) and Figure 8 (b) illustrate the information that is preserved and that is lost in a dot product calculation. When we measure the dot product of a pair of two-dimensional vectors, we learn that the signal must have fallen along a particular line; when we measure a three-dimensional dot-product, we learn that the signal must have fallen within a certain plane. Hence, each dot product helps to define the set of possible input signals.

By combining the results from several dot products, we can estimate the input signal. We can use the geometric representation of the dot product in Figure 7 to develop some intuitions about how to estimate the signal from a collection of sensor responses. This is a *signal estimation* problem.

First, imagine that the response of each linear neuron is equal to the dot product of a vector describing the spatial contrast pattern of a stimulus with a vector describing the neuron's receptive field. Further, suppose that the input stimuli are drawn from a set of simple spatial patterns, namely the weighted sums of two cosinusoidal gratings,

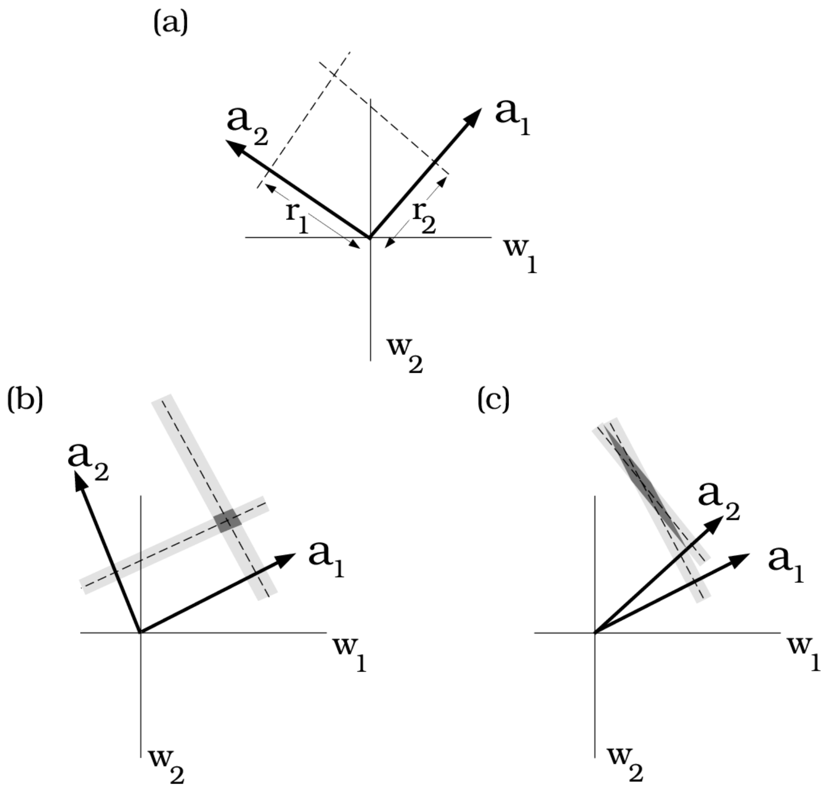

Figure 9: Signal estimation from multiple linear sensors. (a) We can infer the location of a two-dimensional signal vector from the responses of two linear sensors. (b) When the vectors representing the sensors are orthogonal, the estimation error is small. (c) When the vectors representing the sensors are nearly aligned, the estimation error tends to be quite large in the direction perpendicular to the sensor vectors.

$$w_1 \cos(2\pi f_1 x) + w_2 \cos(2\pi f_2 x) \tag{0.43}$$

We can represent each of these spatial contrast patterns using a two-dimensional vector, $\mathbf{x} = (w_1, w_2)$, whose entries are the weights of the cosinusoids. We can represent the sensitivity of each linear neuron to these spatial patterns using a two-dimensional vector, $\mathbf{a}_i$, whose two entries define the neuron's sensitivity to each of the cosinusoidal terms. Because the neurons are linear, we can compute the i^{th} neuron's response to any pattern in the set from the linear calculation in the dot product, namely, $\mathbf{a}_i{}^T\mathbf{x}$.

Figure 9 (a) shows geometrically how to use two responses to identify uniquely the two-dimensional input stimulus. Suppose that the response of the neuron with receptive field $\mathbf{a}_1$ is r_1. Then, we can infer that the stimulus must fall along a line perpendicular to the vector $\mathbf{a}_1$ and intersecting $\mathbf{a}_1$ at a distance $r_1 = \|\mathbf{x}\| \cos(\theta_1)$ from the origin.[7] If the response to the second neuron is r_2, we can draw a second line that describes a second set of possible stimulus locations. The true stimulus must be on both lines, so it is located at the intersection of the two dashed lines.

When the sensor responses have some added noise, which is always the case in real measurements, some sensor combinations provide more precise estimates than others. Figure 9 (b) shows a pair of sensors whose vectors are nearly orthogonal to one another. Because of the sensor noise, the true identity of the signal is uncertain. The lightly shaded bands drawn around the perpendicular dashed lines show the effect of sensor noise on the estimated region from the individual measurements. The darkly shaded region is the intersection of the bands, showing the likely region containing the signal. For these orthogonal sensors, the dark band that is likely to contain the signal is fairly small.

Figure 9 (c) shows the same representation but for a pair of sensors represented nearly parallel vectors. Such a pair of sensors is said to be *correlated*. When the sensors are correlated in this way, the shaded region can be quite large in the direction perpendicular to the sensor vectors. In the presence of noise, correlated sensors provide a poor estimate of the signal.

Matrix equations

Ordinarily, we use matrix multiplication to represent a collection of dot products. Many aspects of the signal estimation problem can be expressed and solved using methods developed for matrix algebra.

[7]In general, we would place the perpendicular line at a distance of $\|\mathbf{x}\| \cos(\theta_i)/\|\mathbf{a}_i\|$, but we have assumed that $\mathbf{a}_i$ has unit length.

To see the connection between matrix multiplication and the signal estimation problem, consider the following example. Write the dot product of a two-dimensional signal and a sensor in the tableau format,

$$r_1 = \begin{pmatrix} x_1 & x_2 \end{pmatrix} \begin{pmatrix} a_1 \\ a_2 \end{pmatrix}. \tag{0.44}$$

Now, suppose we have two sensors and two responses. Then, we can expand the tableau by adding more rows to represent the new measurements, as in

$$\begin{pmatrix} r_1 \\ r_2 \end{pmatrix} = \begin{pmatrix} a_{11} & a_{12} \\ a_{21} & a_{22} \end{pmatrix} \begin{pmatrix} x_1 \\ x_2 \end{pmatrix}, \tag{0.45}$$

where $a_{i\cdot}$ is a vector that represents the sensitivity of the i^{th} sensor. In the usual signal estimation problem, we know the properties of the sensors represented in the rows of the matrix and we know the responses in $\mathbf{r}$. We wish to estimate the signal in $\mathbf{x}$. The pair of sensor vectors represented in the rows of the matrix, call it $\mathbf{A}$, are the counterpart of the vectors shown in Figure 9 (a). Our ability to estimate the signal from the responses depends on the correlation between the rows of the matrix.

The matrix tableau in Equation 0.45 shows a special case in which there are two sensors and two unknown values of the signal. In general, we might have more sensors or more unknowns in the signal. Having more sensors would force us to add more rows to the matrix; having more unknowns in the signal would force us to change the lengths of the sensor and signal vectors. Each of these changes might change the general shape of the matrix tableau. We can write the general case, without specifying the number of sensors or unknowns, using the concise representation

$$\mathbf{r} = \mathbf{A}\mathbf{x} \tag{0.46}$$

Again, in the (linear) signal estimation problem we know the responses ($\mathbf{r}$) and the sensors in the rows of $\mathbf{A}$ and we wish to estimate the signal ($\mathbf{x}$).

Many topics we have reviewed in the text can be framed as linear estimation problems within the matrix Equation 0.46. For example, you might imagine that the rows of the matrix are retinal ganglion receptive fields, the responses are neural firing rates, and the input is a spatial contrast pattern (Chapter). The brain may then need to estimate various properties of the contrast pattern from the neural firing patterns. Or, you might imagine that the rows of the matrix represent the spectral responsivities of the three cone types, the responses are the cone signals, and the signal is a spectral power distribution (Chapter and Chapter). Or, you might imagine that each row of the matrix represents the receptive field of a space-time oriented neuron, the output is the neuron's response, and the signal are the two velocity components of the local motion flow field (Chapter).

There are many matrix algebra tools that are useful for solving matrix equations like Equation 0.46. To choose the proper tool for a problem, one must take into account a variety of specific properties of the measurement conditions. For example, in some cases there are more sensors than there are unknown entries in the vector $\mathbf{x}$. We can represent this estimation problem using matrix tableau as

$$\begin{pmatrix} \\ \\ \mathbf{r} \\ \\ \\ \end{pmatrix} = \begin{pmatrix} & & \\ & & \\ & \mathbf{A} & \\ & & \\ & & \end{pmatrix} \begin{pmatrix} \\ \mathbf{x} \\ \\ \end{pmatrix}. \tag{0.47}$$

$$\begin{pmatrix} \\ \\ \mathbf{r} \\ \\ \\ \end{pmatrix} = \begin{pmatrix} & & \\ & & \\ & \mathbf{A} & \\ & & \\ & & \end{pmatrix} \begin{pmatrix} \\ \mathbf{x} \\ \\ \end{pmatrix}. \tag{0.48}$$

The shape of the tableau makes it plain that there are more responses in the vector $\mathbf{r}$ than there are unknowns in the vector $\mathbf{x}$. This type of estimation problem is called *over-constrained*. When there is noise in the measurements, no exact solution to the over-constrained problem may exist; that is, there may be no vector $\mathbf{x}$ such that the equality in Equation 0.48 is perfectly satisfied. Instead, we must define an error criterion and try to find a "best" solution, that is a solution that minimizes the error criterion.

In general, the best solution will depend on the noise properties and the error criterion. In some cases, say when the noise is Gaussian and the error is the sum of the squared difference between the observed and predicted responses, there are good closed form solutions to the linear estimation problem. That is, one can find an estimate of the signal without using any search algorithms, but by direct computation. If one has other error criteria or noise, a search may be necessary.

A full discussion of the problems involved in signal estimation and matrix algebra would take us far beyond the scope of this book, but there are several excellent textbooks that explain these ideas (Strang (1993); Strang (1974), Vetterli and Metin UZ (1992)). Also, the manuals for several computer packages, such as *Matlab* and *Mathematica*, contain useful information about using these methods and further references. To see how some of these tools have been applied to vision science, you might consult some of the following references (Brainard and Freeman (1994), Heeger and Jepson (1992); Marimont and Wandell (1992); Nielsen and Wandell (1988); Thomas et al. (1994); Tomasi and Kanade (1992), Wandell (1987))

Motion Flow Field Calculation

The motion flow field describes how an image point changes position from one moment in time to the next, say, as an observer changes viewpoint. I reviewed several properties of the motion flow field in Chapter , and I also reviewed how to use the information in a motion flow field to estimate scene properties, including observer motion and depth maps.

In this appendix I describe how to compute a motion flow field. There are various reasons one might need to calculate a motion flow field. For example, motion flow fields are used as experimental stimuli to analyze human performance (e.g., Royden et al. (1992); Warren and Hannon (1990)). Also, algorithms designed to estimate depth maps from motion flow fields must be tested using artificial motion flow fields (e.g., Tomasi and Kanade (1992), Heeger and Jepson (1992)).

To calculate the motion flow field, we will treat the eye as a pinhole camera and we will define the position of the points in space relative to the pinhole. Based on this framework, we will derive two formulae. First, we will derive the *perspective projection* formula. This formula describes how points in space project onto locations in the image plane of the pinhole camera. Second, we will derive how translating and rotating the pinhole camera position, i.e., the *viewpoint*, changes the point coordinates in space. Finally, we combine these two formulae to predict how changing the viewpoint changes the point locations in the image plane, thus creating the motion flow field.

Imaging Geometry and Perspective Projection

We base our calculations on ray-tracing from points in the world onto an image plane in a pinhole camera (see Chapter). To simplify some of the graphics calculations, it is conventional to place the pinhole at the origin of the coordinate frame and the imaging plane in the positive quadrant of the coordinate frame. Figure 10 (a) shows the geometric relationship between a point in space, the pinhole, and the image plane.

We define the pinhole to be the origin of the imaging coordinate frame. The image plane is parallel to the X-Y plane at a distance f along the Z axis. A ray from $\mathbf{p} = (p_1, p_2, p_3)$ passes towards the pinhole and intersects the image plane location (u, v, f). Since the third coordinate, f, is the same for all points in the image plane, we can describe the image plane location using only the first two coordinates, (u, v).

Figure 10 (b,c) show the geometric relationship between a point in space and its location in the image plane from two different views: looking down the Y axis and X axis, respectively. From both views, we can identify a pair of similar triangles that relate the position of the point in three space and the image point position. There are two equations that relate the point coordinates, $\mathbf{p} = (p_1, p_2, p_3)$, the distance from the pinhole to the image plane f, and the image plane coordinates (u, v),

$$u = (p_1/p_3)f \quad \text{and} \quad v = (p_2/p_3)f. \tag{0.49}$$

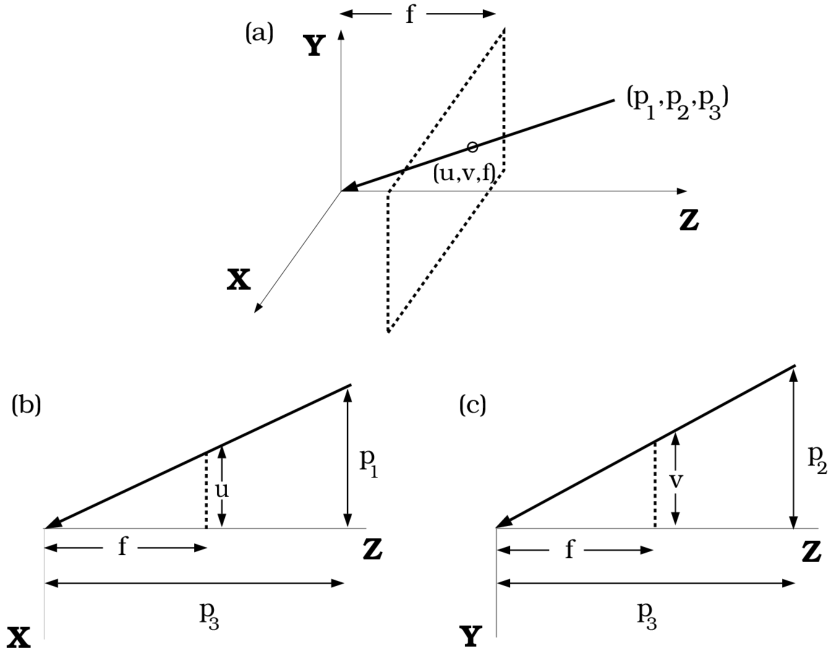

Figure 10: Perspective calculations of a pinhole camera. The coordinate frame is centered at the pinhole, and the image plane is located at a distance f in front of the pinhole parallel to the X-Y plane. (a) A ray from a point (p_1, p_2, p_3) that passes through the pinhole will intersect the image plane at location (u, v). (b) From a view along the Y axis we find a pair of similar triangles. These triangles define an equation that relates the image plane coordinate, u, the point coordinates, and the distance from the pinhole to the image plane, f. (c) From a view along the X axis, we find an analogous pair of similar triangles and an analogous equation for v.

Imaging Geometry, Camera Translation and Rotation

The coordinate frame is centered at the pinhole. Hence, when the pinhole camera moves, each point in the world is assigned a new position vector. Here, we calculate the change in coordinates of the points for each motion of the pinhole optics. We will use the new coordinate to calculate the change in the point's image position, and then the motion flow field vectors.

At each moment in time we can describe the motion of the camera using two different terms. First, there is a translational component that describes the direction of the pinhole motion. Second, there is a rotational component, that describes how the camera rotates around the pinhole. We use two vectors to represent the camera's velocity. The vector $\mathbf{t} = (t_1, t_2, t_3)^T$

represents the translational velocity. Each term in this vector describes the velocity of the camera in one of the three spatial dimensions. The vector $\mathbf{r} = (r_x, r_y, r_z)^T$ represents the angular velocity. Each term in this vector describes the rotation of the camera with respect to one of the three spatial dimensions. The six values in these vectors completely describe the rigid motion of the camera.

We can compute the change in the coordinate, $\Delta\mathbf{p} = (\Delta p_1, \Delta p_2, \Delta p_3)^T$, given the translation, rotation, and point coordinates as follows.

$$\begin{aligned} \Delta p_1 &= r_z p_2 - r_y p_3 - t_1 \\ \Delta p_2 &= r_x p_3 - r_z p_1 - t_2 \\ \Delta p_3 &= r_y p_1 - r_x p_2 - t_3 \end{aligned} \tag{0.50}$$

These formulae apply when the rotation and translation are small quantities, measuring the instantaneous change in position.

Motion Flow

Finally, we compute motion flow by using Equation 0.50 to specify how the change in position in space maps into a change in image position. The original point $\mathbf{p}$ mapped into an image position (u, v); after the observer moves, the new coordinate, $\mathbf{p} + \ \mathbf{p}$, maps into a new image position, (u', v'). The resulting motion flow is the difference in the two image positions, $\mathbf{m}(u, v) = (u - u', v - v')^T$.

Equation 0.51 defines how the motion of the pinhole camera and the depth map combine to create the motion flow field (Heeger and Jepson (1992)).

$$\mathbf{m}(u, v) = \frac{1}{p_3(u, v)} \mathbf{A}(u, v)\mathbf{t} + \mathbf{B}(u, v)\mathbf{r}. \tag{0.51}$$

The term $p_3(u, v)$ is the value of p_3 for the point in three space with image position (u, v). The entries of the 2×3 matrices $\mathbf{A}(u, v)$ and $\mathbf{B}(u, v)$ depend only on known quantities, namely the distance from the pinhole to the image plane and the image position, (u, v).

$$\mathbf{A}(u, v) = \begin{pmatrix} -f & 0 & u \\ 0 & -f & v \end{pmatrix} \tag{0.52}$$

$$\mathbf{B}(u, v) = \begin{pmatrix} -(uv)/f & -(f + u^2/f) & v \\ (f + v^2/f) & -(uv)/f & -u \end{pmatrix} \tag{0.53}$$

Equation 0.51 expresses a relationship we have seen already: The local motion flow field is the sum of two vectors (see Figure 10). One vector describes a component of the motion flow field caused by viewpoint translation, $\mathbf{t}$. The second vector describes a component of the motion flow field caused by viewpoint rotation, $\mathbf{r}$. Only the first component, caused by translation, depends on the distance to the point, $p_3(u, v)$. The rotational component is the same for points at any distance from the viewpoint. Hence, all of the information concerning the depth map is contained in the motion flow field component that is caused by viewpoint translation.

Useful numbers

Units

1. Radiometric units represent physical energy (e.g., radiance has units of watts sr^{-1} m^{-2})
2. Colorimetric units adjust radiometric units for visual wavelength sensitivity (e.g. luminance has units of cd m^{-2} scotopic units are proportional to rod absorptions; photopic luminance units are proportional to a weighted sum of the L and M cone absorptions
3. Typical ambient luminance levels (in cd m^{-2}): starlight 10^{-3}; moonlight 10^{-1}; indoor lighting 10^2; sunlight 10^5; max intensity of common CRT monitors, 10^2
4. One Troland (Td) of retinal illumination is produced on the retina when the eye looks at a surface of 1 cd m^{-2} through a pupil of area 1 mm^2.
5. Lens focal length: f (meters); lens power $= 1/f$ (diopters)
6. Conversion of linear units (X) to decibels: $Y = 20\ log\ 10(X)$; a change of 0.3 log10 units is a factor of 2, or 6 dB

Image Formation

1. The eyes are 6 cm apart and half-way down the head
2. Visual angle of the sun or moon = 0.5 deg
3. At arm's length: thumbnail = 1.5 deg; thumb joint = 2.0 deg; fist $= 8 - 10\ deg$
4. Monocular visual field measured from central fixation: 160 deg (w) x 175 deg (h)
5. Binocular visual field measured from central fixation: 200 deg (w) x 135 deg (h)
6. Region of binocular overlap: 120 deg (w) x 135 deg (h)
7. Range of pupil diameters: 2mm - 8mm.
8. Refractive indices: air 1.000; glass 1.520; water 1.333; cornea 1.376
9. Optical power (diopters): cornea, 43; lens, 20 (relaxed); whole eye, 60
10. Change in power due to accommodation, 8 diopters
11. Axial chromatic aberration over the visible spectrum: 2 diopters

Retina

1. Retinal size: 5 $cm \times 5$ cm; 0.4 mm thick

2. One degree of visual angle = 0.3 mm on the retina
3. Number of cones in each retina: 5×10^6
4. Number of rods in each retina: 10^8
5. Diameter of the fovea: 1.5 mm (5.2 deg); rod-free fovea: 0.5 mm (1.7 deg); foveola (rod-free, capillary-free fovea): 0.3 mm (1 deg); size of the optic nerve head: 1.5 mm $\times 2.1$ mm (5 deg (w) x 7 deg (h)) location of the optic nerve head: 15 deg nasal
6. Peak cone density: 1.6×10^5 $cones/\text{mm}^2$;
7. Foveal cone size: 1-4 μm $(diameter) \times 50 - 80$ μm (length); extrafoveal cone size: 4-10 μm (diameter) x 40 μm (length)
8. Size of rods near fovea: 1 μm (diameter) x 60 μm (length)
9. S cone spacing (foveal): 10 arc min
10. L and M cone spacing (foveal): 0.5 arc min
11. Number of $(L + M)$ cones / Number of S $cones = 14$ (though the ratio may be higher in the foveola)
12. 1.5×10^6 optic nerve fibers/retina; ratio of receptors to ganglion cell in fovea 1:3; ratio of receptors to ganglion cells for whole retina, 125:1

Cortex

1. Area of entire cortex: 1.3×10^5 mm^2 1.7 mm thick
2. Total number of cortical neurons: 10^{10}; density: 10^5 neurons /mm^3
3. Synapses: 5×10^8 synapses /mm^3 4×10^3 synapses/neuron;
4. Axons: 3 kilometers /mm^3
5. Number of corpus callosum fibers: 5×10^8
6. Number of macaque visual areas: 30
7. Size of each area V1: 3cm by 8 cm
8. Half of area V1 represents the central 10 deg (2% of the visual field)
9. Width of a human ocular dominance column 0.5-1.0 mm; width of a macaque ocular dominance column 0.3 mm

Sensitivity

1. Minimum number of absorptions for: scotopic detection 1-5; detectable electrical excitation of a rod 1; photopic detection 10-15
2. The number of photoisomerisations per rod (per sec?) required to saturate the retinal rod circuit: 1
3. Following exposure to a sunny day, dark adaptation to a moonless night involves: 10 minutes (photopic); 40 minutes (scotopic); change in visual sensitivity 6 log10 units μm
4. Highest detectable spatial frequency at high ambient light levels, 50-60 cpd; low ambient light levels, 20-30 cpd

5. The contrast threshold (Delta L/L) for a static edge at photopic luminances is 1%.
6. Highest detectable temporal frequency: high ambient large field, 80 Hz; low ambient, large field 40 Hz.
7. Typical localization threshold: 6 arc sec (0.5 μm on the retina)
8. Minimum temporal separation needed to discriminate two small, brief light pulses from a single equal-energy pulse: 15-20 ms
9. Stereoscopic depth discrimination: step threshold, 3 arc sec; point threshold, 30 arc sec

Color

1. Visible spectrum: 370-730 nm
2. Peak wavelength sensitivity: 507nm (scotopic) and 555 nm (photopic)
3. Spectral equilibrium hues: 475 nm (blue), 500 nm (green), 575 nm (yellow), no spectral equilibrium red
4. Number of basic English color names: 11
5. Incidence of: anomalous trichromacy, 10^{-2} (male), 10^{-4} (female); protanopia and deuteranopia, 10^{-2} (male), 10^{-4} (female); tritanopia, 10^{-4}; rod monochromacy, 10^{-4}; cone monochromacy, 10^{-5}

Online Teaching Resources

The links below take you to class lectures and online tutorials. These are related to topics Joyce Farrell and I teach in Psych 221, Image Systems Engineering. The collection, like the Programming Examples, is a work in progress.

Lectures

Links to various public lectures. Maybe the ISETBio tutorials that are on YouTube.

Online tutorials

Put links to videos here.